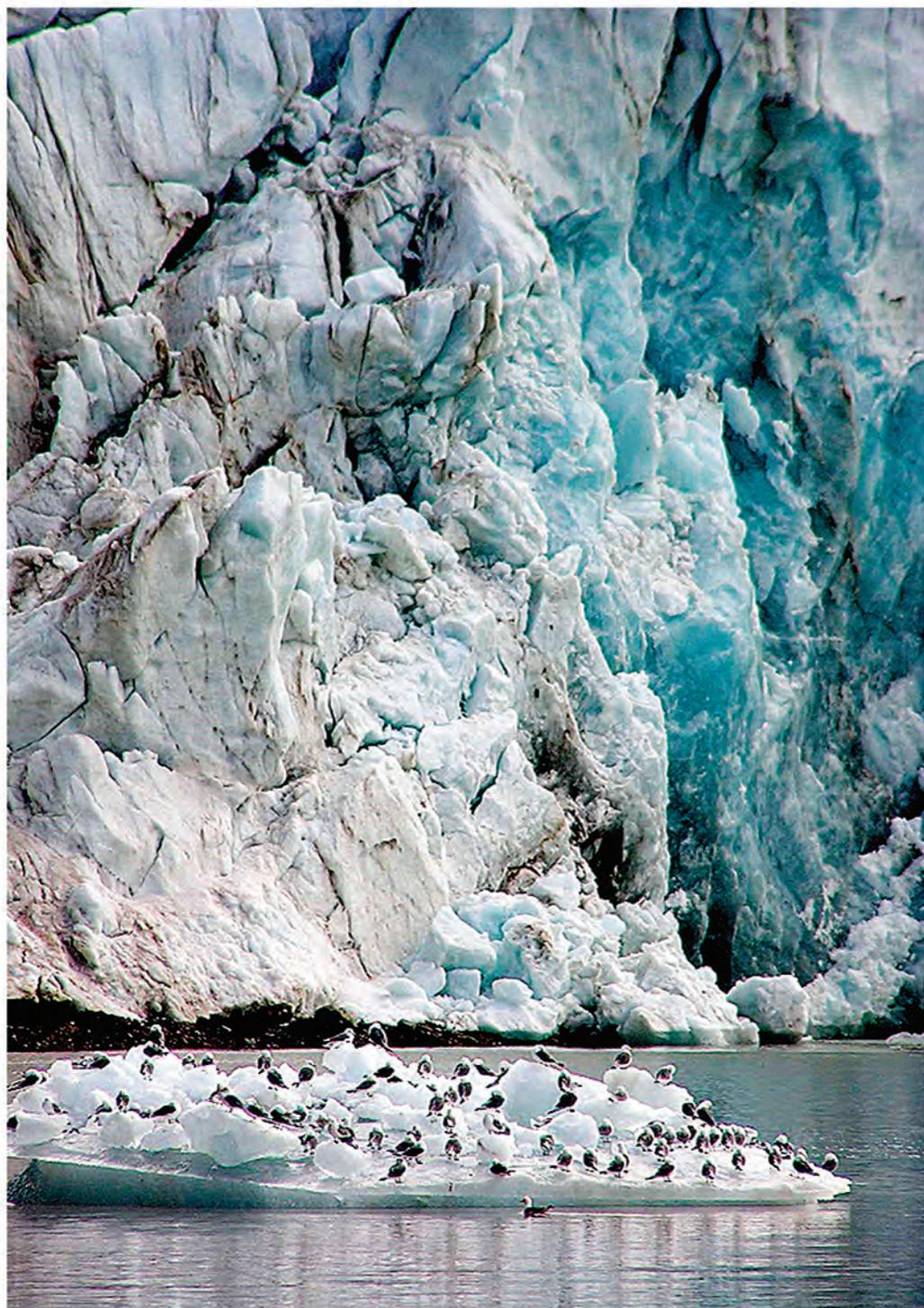


**CURRENT STATE
OF THE NATURAL ENVIRONMENT
ON SPITZBERGEN ARCHIPELAGO**



MINISTRY OF NATURAL RESOURCES AND ENVIRONMENT
OF THE RUSSIAN FEDERATION
FEDERAL SERVICE
FOR HYDROMETEOROLOGY
AND ENVIRONMENTAL MONITORING



STATE RESEARCH CENTER
ARCTIC AND ANTARCTIC RESEARCH INSTITUTE



**CURRENT STATE
OF THE NATURAL ENVIRONMENT
ON SPITZBERGEN ARCHIPELAGO**

*To the 100th anniversary
of the Arctic and Antarctic Research Institute*

*Under the general editorship
of Ph.D. in Geographical Sciences, L.M. Savatyugin*

Saint Petersburg
AARI
2021

UDK [504.5+550.3+551.32+551.46+551.5+556.5](481-922.1)

The current state of the natural environment on Spitzbergen archipelago multi-authored monograph [under the general editorship of L.M. Savatyugin]. St. Petersburg: AARI, 2020. 302 pages, ill.

Reviewers: *Candidate of Geography Sciences, N.I. Osokin*
 (Institute of Geography, Russian Academy of Sciences)
 Candidate of Physical and Mathematical Sciences I.M. Ashik
 (Arctic and Antarctic Research Institute)

Redactor: *I.Yu. Solovyanova*

Translator: *A.V. Sutrimina*

The results of scientific studies on the current state of the natural environment of the Spitsbergen archipelago, carried out by specialists of Rosgidromet in recent decades, are presented.

The publication is of interest to a wide range of specialists: oceanologists, hydrometeorologists, geomorphologists, geophysicists, glaciologists, as well as teachers and students of specialized universities.

ISBN 978-5-98364-101-3

© State Research Center
“Arctic and Antarctic Research Institute”, 2021

TABLE OF CONTENTS

Introduction	5
Chapter 1. Modern climate and characteristics of climate changes	
1.1. Spitsbergen archipelago (brief physical and geographical characteristic) (L.M. Savatyugin, I.Yu. Solovyanova).....	8
1.2. Factors influencing climate formation and change in the Spitsbergen archipelago area (G.V. Alekseyev, N.I. Glok, A.V. Smirnov, S.I. Kuzmina, A.Ye. Vyazilova).....	25
1.3. Analytical review of hydrometeorological characteristics of West Spitsbergen (according data of “Barentsburg” Hydrometeorological observatory) (A.R. Antsiferova, Ye.D. Siekkinen, O.M. Chaus).....	33
1.4. Comparison of the first and modern warming in the Arctic on the example of the Spitsbergen archipelago (B.V. Ivanov, D.I. Tislenko, P.N. Svyashchennikov, K. Isaksen, Ye. Forland, O. Nordli, H. Gjetlen)	49
1.5. Analysis of climate continentality and abnormality in the western Spitsbergen area by observing data of surface air temperature in the second half of the XX century (D.I. Tislenko, B.V. Ivanov)	60
Chapter 2. Variability of oceanological parameters in the marine areas of the Spitsbergen	
2.1. The present oceanological conditions of West Spitzbergen fjords (E.V. Bloshkina, K.V. Filchuk).....	66
2.2. Seasonal and periodic change in the ice cover in the Spitzbergen archipelago (D.I. Tislenko, B.V. Ivanov, V.M. Smolyanitsky, P.N. Svyashchennikov, A.V. Vesman, K. Isaksen, H. Gjelten)	87
Chapter 3. Inland waterways, glaciers, and permafrost of West Spitsbergen	
3.1. Dynamics of the depth of seasonal thawing of permafrost on West Spitsbergen in the conditions of modern climate change (P.V. Bogorodsky, V.Yu. Kustov)	96
3.2. Characteristics of the contemporary glaciation of Nordenskiöld land on the West Spitzbergen (S.R. Verkulich)	110
3.3. The permafrost of Spitzbergen and its monitoring at the cryospheric testing area in Barentsburg (N.E. Demidov, S.R. Verkulich, V.E. Demidov, D.A. Solovyeva, S. Vatterikh)	126
3.4. The mechanics of the Nordenskiöldbreen destruction and the formation of icebergs (V.G. Korostelyov, V.N. Smirnov, A.N. Pavlov).....	141
3.5. The hydrological and hydrochemical regime of the rivers in Grøn fjorden (M.V. Tretyakov, O.F. Golovanov, V.A. Grigoryeva, K.V. Romashova).....	156
3.6. Maximum snow storage at the catchment basin of Grøn fjorden (M.V. Tretyakov, O.F. Golovanov, V.A. Grigoryeva, K.V. Romashova).....	173
Chapter 4. Monitoring of the ionosphere on the Spitsbergen archipelago	
4.1. Influence of artificial ionospheric disturbances caused by impact on the propagation of radio waves of the decameter range of the SPEAR complex on Spitzbergen (N.F. Blagoveshchenskaya, T.D. Borisova, A.S. Kalishin)	182

4.2. Polar ionosphere modification induced by powerful HF radio waves: research results on the Spitsbergen archipelago (N.F. Blagoveshchenskaya, T.D. Borisova, A.S. Kalishin).....	195
4.3. State of the upper atmosphere on Spitzbergen (R.Yu. Lukianova)	221
Chapter 5. The ecological state of the natural environment in the area of the Spitsbergen archipelago	
5.1. Assessment of environmental pollution on Spitzbergen in the area of Barentsburg and adjacent territories (B.N. Demin, A.S. Demeshkin, S.V. Vlasov, K.A. Bazhukov).....	234
5.2. Aerosol component of the atmosphere in Barentsburg (V.F. Radionov, O.R. Sidorova, L.P. Golobokova, O.I. Khuriganova, T.V. Khodzher, S.M. Sakerin, D.M. Kabanov, D.G. Chernov, V.S. Kozlov, M.V. Panchenko)	268

INTRODUCTION



The Spitsbergen archipelago is one of the northernmost land areas in the Northern Hemisphere, only 1,020 km from the North Pole to its rocky shores. The northern point of Spitsbergen is located at latitude $80^{\circ} 49' N$, the southern one at latitude $76^{\circ} 29'$. Located in the western part of the Central Polar Basin, at the junction of the Arctic Ocean and its marginal seas, the Greenland and Barents Seas, the Spitsbergen archipelago, due to its unique geographical position, is the most significant object to assess climate change in the Arctic region, study

and forecast hydrometeorological and heliophysical processes in the atmosphere, ocean, near-Earth, and outer space, and monitor the state of the environment.

The Spitsbergen archipelago, in particular the West Spitsbergen Island, where Barentsburg is located, is the most representative territory for conducting comprehensive hydrometeorological studies necessary to assess climate change, their impact on the archipelago's environment for the subsequent development of recommendations for rational nature management, timely forecasting early warning and minimizing the negative consequences of climate change. In this regard, it is essential to study the interaction in the chain of natural processes and phenomena, such as, for example, heat fluxes from the ocean, cyclonic atmospheric circulation, precipitation, glaciers, snow cover, freshwater runoff, soil and vegetation cover, and human adaptation. It is relevant to carry out work on reference and local monitoring of pollution and measures to protect the environment in the areas of economic activity of Russian enterprises on the archipelago. The specialists of Rosgidromet from AARI, North-West Branch of Research and Production Association "Typhoon", Murmansk AHMEM carry out such scientific research on West Spitsbergen.

Rosgidromet organizations organize several expeditions on Western Spitsbergen both in winter and spring and summer every year, and the Barentsburg hydrometeorological observatory of the Murmansk AHMEM and the wintering team of the Russian scientific Arctic expedition to the Spitsbergen archipelago (RAE-Sh, AARI) conduct observations all year round.

The permanent and active presence of Russia in this region contributes to ensuring full participation in solving international issues related to Spitsbergen. In 2008, the Government of the Russian Federation approved the project "Strengthening the Russian Presence on the Spitsbergen Archipelago", which provides for the creation of the Russian Scientific Center on the Spitsbergen Archipelago (RSCS), which made it possible to combine the efforts of 12 Russian scientific organizations within the framework of a scientific consortium. The main goal of the RSCS is to increase the efficiency of Russian scientific research on Spitsbergen through better coordination and cooperation between institutes,

the creation of a unified infrastructure to monitor natural processes, and the state of the natural environment in the Spitsbergen region and the water area of the Arctic Ocean. Rosgidromet was appointed the coordinator of the consortium's work, and AARI is the head organization of the consortium with the newly created structural unit RAE-Sh (Russian scientific Arctic expedition to the Spitsbergen archipelago) as an information, coordination and logistics center. In Barentsburg, a chemical-analytical laboratory equipped with the most modern equipment was built to carry out almost all types of chemical analyzes of environmental monitoring, the introduction of new directions of research directly on-site.

At present, Russian scientific research and work on the Spitsbergen archipelago are carried out by specialists from organizations of Rosgidromet, the Ministry of Science and Higher Education of the Russian Federation and the Ministry of Natural Resources of Russia. Rosgidromet organizations carry out regular hydrometeorological and environmental monitoring in the area of Barentsburg, Piramiden, Colesbay, the Grumant mine, and adjacent fjord waters; scientific knowledge was obtained on the problem of climatic changes, in particular, new data on the temperature regime, circulation of coastal waters, thickness, under-ice relief, the internal structure of glaciers and ice reserves in the archipelago, data on the evolution and stability of ecosystems, data on the level of pollutants in the components of the natural environment (atmospheric air, snow cover, sea, lake and river waters, sea and freshwater bottom sediments, sea and freshwater ice cover, soils, soil waters, terrestrial vegetation), as well as the main hydrochemical indicators of sea waters and surface water bodies.

Thus, the studies mentioned above made it possible to collect objective field information on the main climatic characteristics of the study area and create an integrated environmental monitoring system on the West Spitsbergen Island.

The scientific knowledge and observational data obtained in previous years, the availability of the infrastructure of the established Russian Scientific Center, the need to implement government programs (Strategy of the Russian presence on the Spitsbergen archipelago until 2020 in the sphere of fundamental and applied scientific research) make it necessary and possible to organize further complex scientific research on the archipelago, increasing their efficiency and international significance, even though Russian scientific expeditionary activities are complicated by the requirements of the Norwegian Law on Nature Conservation of the Spitsbergen Archipelago, according to which, in particular, scientists are prohibited to access most of the archipelago.

This monograph presents the scientific results of research carried out by specialists of Rosgidromet in recent decades.

*Director of the Arctic and Antarctic Research Institute,
Ph.D. in Geographical Sciences*

A.S. Makarov

Chapter 1

Modern climate and characteristics of climate changes

1.1. SPITSBERGEN ARCHIPELAGO (BRIEF PHYSICAL AND GEOGRAPHICAL CHARACTERISTIC)

L.M. Savatyugin, I.Yu. Solovyanova

Spitsbergen archipelago (German *Spitzbergen*), also Svalbard (Norwegian *Svalbard*), Spitsbergen (Dutch *Spitsbergen*), Grumant (ancient Russian Pomor name) is one of the largest polar archipelagos. Its islands in the Arctic Ocean range from 76° 26' to 80° 50' north latitude and from 10 to 32° east longitude. The total land area is about 63,000 km². It has thousands of islands, islets, and skerries. Still, there are only five large islands: West Spitsbergen (39,044 km²), North East Land (Nordaustlandet) (14,530 km²), Edge Island (Edgeøya) (5030 km²), Barents Island (Barentsøya) (1330 km²) and Prins Karls Forland (640 km²). The archipelago is washed by the waters of the Arctic Ocean, the Greenland, Norwegian, and Barents Seas (Fig. 1.1.1).



Fig. 1.1.1. Physiological map of the Spitsbergen archipelago.

Only 1020 km separate the Ross Island (Rossøya) (the northernmost point of the archipelago) from the North Pole (Pechurov, 1983). Some of its islands are beyond the eightieth degree of northern latitude. Only the north of Greenland and the Ellesmere Island (Canada) are located even closer to the North Pole.

The relief of the West Spitsbergen is close to the alpine type. A significant dissection of the surface is typical for it due to the tectonic structure, the alternation of a complex system of ridges and plateau-like hills, on which there are glaciers, deeply incised valleys, and sharp mountain peaks. The highest point of the island (and the entire archipelago) is Newton Peak (1713 m). It is located in the northeastern part of the island on Olav V Land. At the same time, about 43 % of the archipelago land is located at less than 300 m above sea level. The same type of relief is typical for the Prins Karls Forland, whose maximum elevation (Mount Monaco) is 1084 m. Smoother relief of tabular hills framed by marine plains is typical for the Nordaustlandet, Edgeøya, and the Barentsøya Islands. The maximum elevations of these islands peaks are 637, 578, and 610 m, respectively.

An integral and characteristic feature of Spitsbergen is extensive glaciation, the total area of which exceeds 35,000 sq. km. About 60 % of the Spitsbergen surface is covered with many meters of ice, which gives its nature extraordinary beauty and attractiveness. The total ice reserve in the glaciers of the archipelago is about 7.5 thousand km³. The reserve of “solid” water concentrated in glaciers is 30 times higher than the annual flow of the Volga River (Singer, 2006).

The Spitsbergen, Franz Josef Land, Novaya Zemlya, and Severnaya Zemlya archipelagos are all part of the same glaciological province (Glaciation of the Spitsbergen (Svalbard), 1975). However, Spitsbergen is the first among them to receive intense rainfall brought by cyclones from the North Atlantic to the Eurasian Arctic. Thus, the glaciation processes of the three Russian archipelagos and Spitsbergen are interconnected.

The study of the conditions of existence and development of active Spitsbergen glaciers is a great importance for understanding the patterns and characteristics of the evolution of glaciation throughout the Eurasian Arctic. Fluctuations in polar glaciers appear as a sensitive natural indicator of global climate change. Incredibly diverse in morphology, behavior, and dynamics, the glaciation makes Spitsbergen a unique glaciological object in the entire Arctic. We can find here almost all the various types of glaciers that exist on the globe. Such diversity is due to differences in the relief and climate of the archipelago.

By the nature of the glaciation, Spitsbergen is divided into three broad areas: cover, mountain-cover, and mountain (mountain-valley) glaciation (Glaciation of the Spitsbergen (Svalbard), 1985; Koryakin, 1988). The Nordaustlandet island belongs to the area of cover glaciation. Three large ice caps (Austfonna, Vestfonna, and Sørfonna) with a total area of about 11,000 km² occupy up to 80 % of the territory of this second-largest island of the archipelago. The volume of ice concentrated in them is 44 % of the total volume of ice on the archipelago. Mountain-cover glaciation occurs on the West Spitsbergen, Prins Karls Forland, Barentsøya and Edgeøya Islands (Fig. 1.1.2). The bulk of the glaciers of the archipelago (more than 60 %) are located on the island of the West Spitsbergen. The area of mountain glaciation occupies its central part, stretching from south to north.

Many glaciers in winter have internal and subglacial runoff and naled ice. The presence of water lubrication stimulates the sliding of ice masses, which contributes to their mechanical instability. Ultimately, this causes a sudden regular movement (pulsation) of the glacier – surge. Literature sources and numerous observations indicate that almost



Fig. 1.1.2. Mountain-cover area of glaciation of West Spitsbergen
(photo by I.Yu. Solovyanova).

90 % of Spitsbergen glaciers can be classified as surging type glaciers. Just in the period from 1860 to 1992, surges were recorded on 88 glaciers (Glacier atlas of Svalbard and Jan Mayen, 1993), and using indirect signs of surges, movements were detected on 345 glaciers of the archipelago (Sevestre and Benn, 2015).

The surge of the Skobreen and Paulabreen that took place between 2003 and 2005 is described in detail. Glaciers are located at the top of the Van Mijenfjorden. The area of the glaciers is 64.6 and 18.2 km, and the length is 16 and 8 km, respectively, with the Skobreen being the left, lower outlet glacier of the Paulabreen. The Skobreen initiated the movement, dragging along the more powerful Paulabreen. To study this movement, we used both time-lapse video recording of the displacement of the glacier front and three-time aerial photography, as well as from the ASTER satellite images of various phases of the movement. Over the study period, the glacier surface moved 2800 m at a speed of about 3.2 m/day (Kristensen and Benn, 2012). Fig. 1.1.3 shows the final stage of the surge; one can clearly see that the surface of the glacier is still covered with numerous radial cracks, but they are already “healed” by snow.

The most famous of the archipelago’s glaciers are located on the Nordaustlandet, it is the Austfonna ice cap (together with Vegafonna) with a total area of 8450 sq. km. It ranks second most significant in Europe and seventh-most significant in the world. The dome of the ice cap is located at an altitude of about 800 m above sea level; the ice thickness is about 600 m (Moholdt and Kääb, 2012; Dowdeswell et al., 1986). The alimentation line of the Austfonna passes at an altitude of 300–400 m. The glacier belongs to the polythermal type; it has a “warm” layer of ice in the central part and “cold” ice in the marginal parts



Fig. 1.1.3. Skobreen and Paulabreen, July 2006
(photo by I.Yu. Solovyanova).

of the cap (Schellenberger et al., 2017). Between 2012 and 2017, the Austfonna ice cap “lost weight” by more than 50 m equal to one-sixth of the thickness of the entire ice cap. Over the past two decades, the loss of snow in the southeastern part of Austfonna has accelerated significantly. The area of thinning of ice has spread more than 50 km into the upper parts of the glacier. Now it is located at a distance of only 10 km from its peak. The outlet glacier, the moving part of the Austfonna, also accelerated 25 times (Fig. 1.1.4). If, in 2012, the outlet glacier moved at a speed of 150 m per year, then in the summer of 2016, its speed reached 8.9–11.4 m/day. The maximum recorded speed was 18.8 m/day (Schellenberger et al., 2017).

The total length of the marginal parts of the outlet glaciers on the archipelago is more than 1030 km. These glaciers produce a vast number of icebergs, but most of the small icebergs, debris and pieces of icebergs that break into the fjords are destroyed there, not reaching the open sea (Dowdeswell, 1989). There are individual relationships between the morphometric parameters of the iceberg and the glacier that generated it. Outlet glaciers located in the fjords produce icebergs of small size (less than 50 m long) and often of irregular shape (Dowdeswell, 1992). The ice flow at producing fronts is estimated at $3 \pm 1 \text{ km}^3/\text{year}$. Thus, the total loss of ice due to the discharge of icebergs is $4 \pm 1 \text{ km}^3/\text{year}$ (Hagen et al., 2003).

However, even small icebergs can pose risks to maritime traffic. So, in the summer of 2006, a part of the glacier collapsed on a tourist ship that came close to the front of the Nordenskiöldbreen in the Billefjorden. One person was seriously injured, and the



Fig. 1.1.4. The edge of one of the outlet glaciers of the Austfonna ice cap (photo from open sources).

vessel suffered great material damage. After this incident, the Governor of Svalbard issued a decree on the need to maintain the minimum distance that is allowed to approach the glacial front on boats and ships. The minimum permissible distance is 200 m, and this distance should be increased if the work is carried out in a narrow or shallow fjord or when the height of the glacier front is more than 40–50 m.

The necessity to know the features of glaciers regime and structure when designing villages, mines, roads, bridges, power lines causes the practical study of archipelago glaciers. It is also required to take into account the valuable reserves of “solid” water because most of the settlements of Spitsbergen use melted snow and glacial waters for water supply. Finally, glaciers can also be considered a recreational area of the archipelago, as they are a favorite place for islanders and tourists to ride fast snowmobiles and to ski.

A characteristic feature of the archipelago is the presence of fjords. Fjords include narrow, winding, and deeply cut into the land sea bays and straits with rocky shores, typical for upland countries in high latitudes. Generally, the length of the fjords is several times greater than their width. The largest fjords of the archipelago are the Storfjorden (132 km), Wijdefjorden (108 km), Isfjorden (107 km) (Fig. 1.1.5), Van Mijenfjorden (83 km), Woodfjorden (64 km).

Oceanographic conditions in the fjords are closely related to the characteristics of sea currents around the archipelago (Tislenko, Ivanov, 2015). The West Spitsbergen Current brings to the fjords a large amount of heat and salts; it is a northern branch of the Norwegian Current (Fig. 1.1.6). The water temperature in the warm core of this current (at depths of 100–600 m) reaches 5 °C in winter and rises to 7 °C in summer. Warm and salty Atlantic waters in the system of the West Svalbard current spread to the north, clinging to the continental (western) slope of the West Spitsbergen. That is why the waters west of the archipelago are generally free of ice. In recent decades, there has been a steady increase



Fig. 1.1.5. View of the Isfjorden mouth
(photo by A.S. Izmailov).

in temperature and salinity of Atlantic waters both in the West Spitsbergen Current and, in fact, in the fjords of the West Spitsbergen Island, where these waters are classified as transformed Atlantic waters (Pavlov et al., 2010).

The presence of drifting ice in the waters washing the Spitsbergen archipelago affects the formation of features of the oceanographic regime in Arctic waters (Zhichkin, 2015; Zhichkin, 2016). The southern distribution boundary of drifting ice lies in the area of the archipelago. It changes its location significantly from year to year, sometimes moving over considerable distances. To the west of Spitsbergen, the boundary line of drifting ice under the influence of the warm West Spitsbergen Current is substantially shifted to the north. In particular winters favorable for ice; solid ice cover may be absent near the western coast of the archipelago. Drifting ice is almost always observed along the southern tip of the archipelago (Sørkapp).

The most massive fjords of West Spitsbergen, bordering the Fram Strait, such as the Kongsfjorden, Isfjorden, Bellsund, and Hornsund, are usually covered with ice (fast ice) in November–January, and in May–June they are free of ice. In some years (recently, it has become a consistent pattern), steady fast ice in the fjords of West Spitsbergen does not form throughout the winter season (Pavlov et al., 2010). It is explained by the fact that one of the branches of the warm North Atlantic Current, a continuation of the Gulf Stream, approaches its western coast (Fig. 1.1.6). Warm waters penetrate deep into the fjords and warm them up.

The river system in the archipelago is poorly developed. The largest rivers flow on the West Spitsbergen island: Reindalselva (about 50 km long), Sassanelva (40 km), and Adventelva (35 km). The rivers on Spitsbergen have glacier- and snow-feeding, most of them begin at the glaciers fronts. According to the degree of glaciation of the catchment,

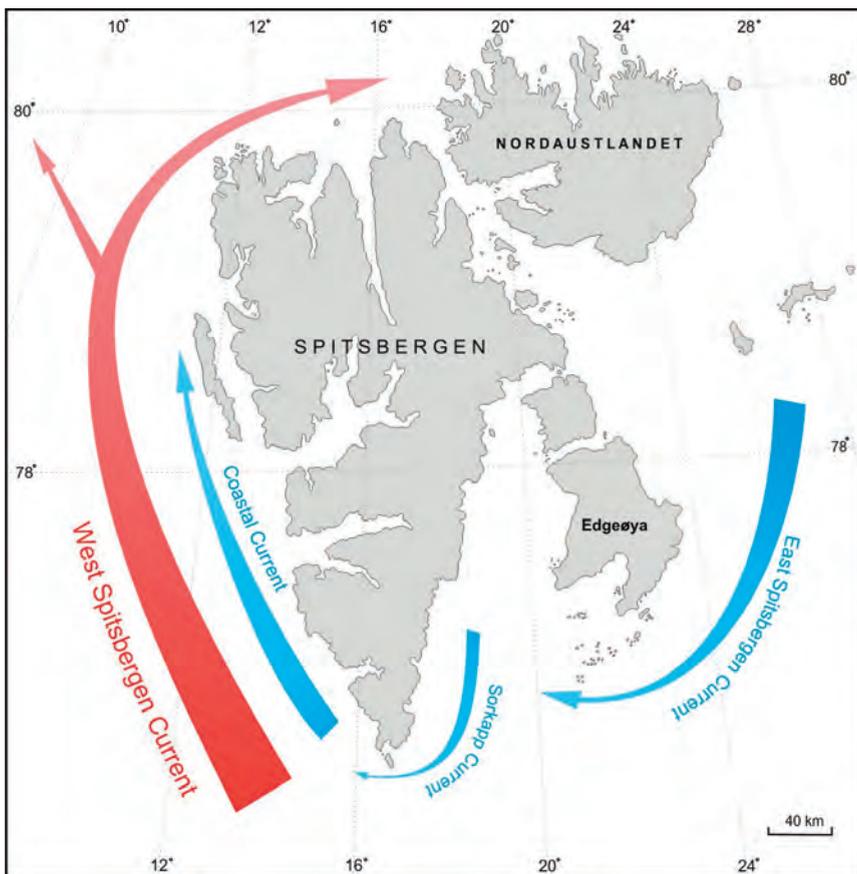


Fig. 1.1.6. Scheme of the main currents in the area of Spitsbergen (Svendsen, 2002).

Red arrows indicate warm sea currents, blue arrows the cold ones.

one can divide the rivers of Spitsbergen into three types: with a catchment glaciated for more than 60 %, less than 60 %, but more than 5 %, with zero glaciation.

Rivers typically have seasonal and daily level fluctuations. In late spring and early summer, when there is an active melting of the snow cover (Fig. 1.1.7), the rivers are full of water and carry a large amount of suspended material into the fjords. In mid-summer and autumn, rivers become shallow, and sometimes turn into small streams or completely dry up. However, on days with sustainable rainfall in the middle of summer, flood peaks are noted.

In winter, rivers and streams generally freeze to the bottom, but despite this, in winter, there is runoff at the some glacier terminus on Spitsbergen. One can see it as extensive naled ice in the marginal parts of the polythermal glaciers. Still, its share in the total volume of river runoff is insignificant and amounts to about 1–5 % (Solovyanova, Mavlyudov, 2007). The river valleys within the mountainous part are V-shaped, in the plain and coastal parts they are U-shaped. Landforms of river origin in broad valleys are represented exclusively by floodplains. Generally, rivers do not have a single bed. Numerous channels and branches cut the floodplain.



Fig. 1.1.7. Grøndalen, April 2006
(photo by A.S. Izmailov).

The results of hydrometric and glaciological measurements show that in river basins with a low degree of glaciation, the average runoff layer is in the range of 300–350 mm, reaching 1200–1500 mm in catchment basins with glaciers (Hodgkins, 1997). River runoff for 60 % glaciated catchment basins depends not only on precipitation but to a large extent on glacier ablation. By definition, negative-balance glaciers release more water than they get in the form of snow or rain. A good example is the catchment basin of the Bayelva, where additional runoff due to the negative mass balance, is estimated at 200 mm / year (Sund, 2008). It increases the total volume of river runoff by about 20 %. According to measurements at the Bayelva for two summer seasons, the average monthly distribution of runoff can be represented as follows: May 0.8 %, June 17.4 %, July 46.4 %, August 33.2 %, and September 2.2 % (Hodson, 1994).

The main inland water reservoirs are shallow (less than 2 m deep) ponds, and small lakes formed as a result of permafrost thawing. They often produce a lot of insects and crustaceans, and they can be significant biotopes for birds (Smith et al., 2005). Fish do not live in these lakes since, in winter, they freeze to the bottom. The only freshwater fish, the Arctic char, is found in non-freezing lakes (more than 2 m deep) with access to the sea. Arctic char (lat. *Salvelinus alpinus*) – a species of actinopterygian fish of the salmon family, a predator eating fingerlings of other fish and small fish.

The largest lakes in the archipelago include Linnévatnet (Fig. 1.1.8), Femmilsjøen, and Lakssjøen.

The widespread distribution of permafrost causes the development of specific relief forms associated with the formation of frost cracks, heaving, solifluction, thermokarst, and frosty weathering. The depth of natural thawing of soils in the summer period ranges from 0.5 to 2.5 m (Savchenko, 2008). Due to the freezing of the seasonally thawed layer, the



Fig. 1.1.8. Linne Lake (Linnévatnet)
(photo by I.Yu. Solovyanova).

stresses arising in the soils cause the formation of heaving mounds up to 0.6 m high and 2–3 m wide. In the places of the year-round outlet of highly saline waters, huge pingos form. So, in the Adventdalen, there is a pingo up to 28 m high and 410 m wide (Rossi et al., 2018). In late winter and early spring, such pingos form large naled fields with a high volume of meltwater between the icy layers and salt flowers on the surface (Fig. 1.1.9).

The thickness of permafrost on Spitsbergen varies from 100 m in coastal areas and along the bottoms of broad valleys up to 400–500 m in mountainous areas. The exception is massive glaciers, under which taliks are located. Although the archipelago is located to the north of 76° N, the climate there is quite mild. Climatic conditions are determined not only by the high latitude position of the archipelago, the marine environment, but also the influence of the warm Spitsbergen Current (Gulf Stream branch) and the atmospheric circulation regime (Alekseyev, 2003). Basically, the climate of the archipelago refers to the marine type. However, one can observe significant climatic differences between the particular regions of the archipelago. In the west, due to the influence of the Spitsbergen Current (northeastern continuation of the North Atlantic current), climatic conditions are milder than in the east. For the central areas of the archipelago, a continental climate is typical. One can observe relatively cold and humid climatic conditions in the southeast of the archipelago, and in the northeast, the climate is typically arctic. Here is the “cold pole” of Spitsbergen. Even in high summer, the temperature in this area rarely exceeds 0 °C, and in winter, it sometimes drops below –40 °C. According to observations of the “Barentsburg” meteostation, the average annual air temperature for the period 1960–2000



Fig. 1.1.9. Salt flowers on the surface of the naled ice in the Grøndalen (photo by I.Yu. Solovyanova).

equal to $-5.8\text{ }^{\circ}\text{C}$ (Semyonov et al., 2002). The average temperature of the warmest month (July) is $8\text{ }^{\circ}\text{C}$. The absolute maximum temperature ($20.3\text{ }^{\circ}\text{C}$) was recorded in July 1999. The coldest month is February: the average monthly temperature is $-18\text{ }^{\circ}\text{C}$. The minimum temperature ($-39.8\text{ }^{\circ}\text{C}$) was noted in Barentsburg in March 1986. According to long-term average data, a steady transition of temperature through $0\text{ }^{\circ}\text{C}$ towards the positive values occurs on 5 June, and towards negative values on 18 September. Due to the features of atmospheric circulation (the invasion of warm cyclones) in winter, periodic thaws can be observed.

The amount of precipitation is not the same for particular parts of the archipelago. If one moves from the center of the archipelago to the west coast of Spitsbergen, the number of precipitation increases, and to the south, southeast and, especially, northeast, decreases, again increasing slightly only on the easternmost coast. The west coast of Spitsbergen has about 400 mm of precipitation annually, and the island of Nordaustlandet has just over 200 mm annually. South and southwest winds bring the maximum precipitation.

The yearly average precipitation is 563 mm. December (62.2 mm) and January (59.5 mm) have the highest amount of precipitation, May (29.0 mm) has the average minimum (Antsiferova et al., 2016). The mountains have 2.5–3 times as much precipitation as flat areas, which has a significant effect on the mass balance of glaciers. Precipitation comes mainly in the form of weak but long-term snowfalls. Heavy snowfalls and rains are rare. Annually, the archipelago has about 240 days of precipitation, including 170 days with snow and 70 days with rain.



Fig. 1.1.10. Prominent representatives of the archipelago flora.

a – polar willow, *b* – birch mushroom in the thickets of dwarf arctic birch, *c* – cyanosis boreal, *d* – mountain avens.

Cloudy weather prevails on Spitsbergen throughout the year. A maximum cloud cover occurs in the summer (August). Thunderstorms are possible at this time. The average annual amount of clouds is 7–8 points (Semyonov et al., 2002).

The large-scale and local atmospheric circulation is determined by the position of the Icelandic low of pressure and high-pressure areas over Greenland and the Arctic Ocean, which determine the intensity of warm and moist air from the North Atlantic towards the Norwegian and Barents Seas. The significant temperature difference between the Atlantic and Arctic air masses causes significant fluctuations in weather conditions, especially in winter. The West Spitsbergen Current is the reason for the absence (minimum amount) of drifting ice along the west coast of the archipelago almost throughout the year to the north of Spitsbergen (polynya “Whale Bay”).

When it comes to geobotanics, the Spitsbergen stands out as an autonomous region of the Arctic tundra (except for Nordaustlandet, belonging to the southern strip of the polar deserts).

Despite the apparent scarcity and harsh natural conditions, the flora of the archipelago is quite rich. Most of West Spitsbergen is represented by the northern zone of the arctic tundra, and only in the Isfjorden area, one can find the extrazonal “spots” of the southern arctic tundra. Numerous mosses, lichens, mushrooms, freshwater algae, and more than 170 species of vascular plants belonging to 29 families grow on the archipelago (Korolyova et al., 2008).

All this diversity occupies a layer with a thickness of a maximum of several dozens of centimeters above the ground. Among the representatives, one can note plants such

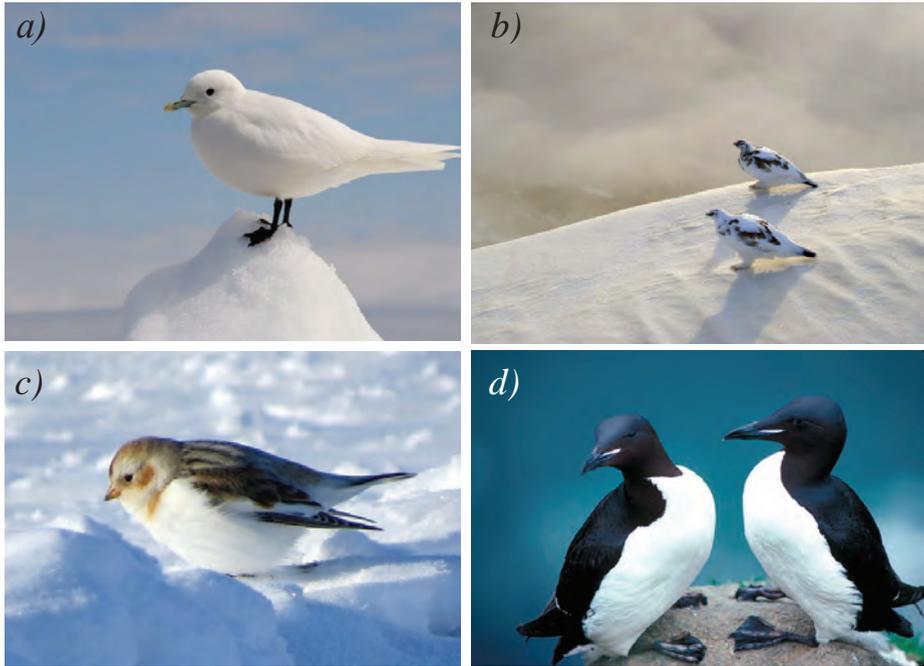


Fig. 1.1.11. Representatives of the avifauna of Spitsbergen.

a – ivory gull, *b* – rock ptarmigan in autumn, *c* – snow bunting, *d* – thick-billed murres.

as polar willow (*Salix polaris*), a low-growing shrub with tiny leaves, as well as a dwarf birch (*Betula nana*) (Fig. 1.1.10). Quite often there are white and yellow polar poppies (*Papaver polare*) and dryads (*Dryas octopetala*), blooming in the middle of August, that is almost before the onset of winter, the cushion pink (*Silene acaulis*), forming pink pillows, etc. (Korolyova et al., 2008; Savatyugin, Dorozhkina, 2009).

On the Spitsbergen in the summer months, there are about 90 species of birds, 30 of which constantly nest on the archipelago (Kovacs, 2005). The most numerous of the seabirds of the archipelago are the guillemots, little auks, puffins, fulmars, kittiwakes, and other types of seagulls. The common eiders, Arctic terns, barnacle geese, and purple sandpipers are closely connected with the sea. One of the beautiful representatives of seabirds is an ivory gull (Fig. 1.1.11). This bird is listed in the Red Data Book of Russia, Canada, Greenland, and Norway. The ivory gull nests in small colonies on inaccessible rocks among glaciers and even on sea ice, wintering on the edge of the sea ice and in the polynyas. As a result of climate warming and a decrease in the area of sea ice, as well as due to harmful egg collection and pollution, there is a global decrease in the number of ivory gulls (Gavrilo, Ström, 2004; Gavrilo, 2011).

The typical land birds are the rock ptarmigan and the snow bunting (Fig. 1.1.11).

Mammal species on Spitsbergen are relatively few. First of all, it is a polar bear. The polar bear population in the archipelago has several thousand individuals (Fig. 1.1.12). Most times, polar bears are found in its northwestern part. Seals serve as their usual prey, but bears are frequent visitors to the outskirts of the settlements (especially in winter), where they come to search for edible waste. Some of the bears are marked with radio beacons, which allows to track their movements, and the places where they have cubs are



Fig. 1.1.12. Road sign in Longyearbyen
(photo by L.M. Savatyugin).

the most protected on Spitsbergen. Moreover, since polar bears spend most of their lives on drifting sea ice, they are not classified as terrestrial animals but are considered marine fauna, although they still give birth to cubs on the land, in snow dens.

Hunting for a polar bear was widely practiced on Spitsbergen. In some years, the number of killed bears exceeded 800 individuals. Such uncontrolled hunting led to a sharp decrease in the population, which forced the Norwegian government to impose a complete ban on bear hunting in 1973. Nevertheless, despite the complete prohibition of hunting, almost every year, there are cases of death of animals either during human self-defense or, in agreement with the Governor, during the culling of sick, wounded animals or for scientific purposes.

There are only two species of terrestrial animals here – reindeer and arctic fox (Fig. 1.1.13). Reindeer belong to an independent subspecies, are found everywhere on the archipelago; often they even go into the settlements and let people approach at a distance of several meters. Unlike the deer on the mainland, local reindeer have thick fur and short legs; they never form large herds, and one can usually see them in pairs or a couple plus young animals. The maximum number of herds observed was about a dozen individuals.

In the period from 1860 to 1925, a dramatic decrease in the population was observed. Due to it, a complete ban for reindeer hunting was imposed 1925 and 1983. It led to the restoration of the reindeer population, and they recolonized their former ranges. Annual monitoring of the number of reindeer in the Adventdalen (1979–2013) showed that the population size ranges from 400 to 1200 individuals. Similar numbers and population dynamics are also recorded in the neighboring Reindalen. The number of reindeer is so high



Fig. 1.1.13. Representatives of the fauna of Spitsbergen.
a – Arctic fox changing its pelage; *b* – Spitsbergen reindeer.

that in Spitsbergen, where nature conservation conditions are stringent, there is a hunting season for them. And the shed antlers are all over the ground at the places of feeding.

The Arctic fox population on the archipelago is stable enough. While it is not possible to make a complete calculation of the level of the entire Arctic fox population in Spitsbergen, however, their population density in just one area of Adventdalen – Sassendalen (about 900 km²) is estimated at 1–1.5 individuals per 10 km². The Arctic fox is an active nomadic species, in search of food, they can move for long distances. These animals are found on the coastal lowlands and high in the mountains, however, their favorite habitat is the cliff bottoms with colonies of birds, where they eat eggs and chicks. Arctic foxes are carriers of parasites transmitted to humans, such as rabies and tapeworm *Echinococcus multilocularis*, as well as toxoplasmosis. Outbreaks of rabies in the archipelago were recorded in 1980 and 2011. Due to this reason, house cats are prohibited on the island. It is allowed to hunt Arctic foxes on Spitsbergen. According to the Svalbard Governor, up to 120 animals are hunted annually (Meet the Svalbard Archipelago, 2012).

They tried to relocate other land mammals, in particular polar hares and muskoxen from Greenland, to the archipelago, but these attempts were unsuccessful.

Seals (ringed seal, bearded seal, harbor seal), walruses, and beluga whales inhabit the coastal waters of the archipelago (Yezhov, 2016). Shoals of cod and herring, halibut, and haddock come to the shores of the archipelago together with a warm current, and seals come after them: Greenland seal and bearded seal. On pebble beaches under the rocks, tusk walruses arrange their haulout sites (Fig. 1.1.14), and in the open sea, you can often whale spouting. There are many whales up to the present day, although fleets of whalers have been hunting in these places since the days of Willem Barentsz and Henry Hudson. Most of them are belugas and killer whales, but one can also see the famous “sea-unicorn”, the narwhal. The head of this whale ends with a sharp two-meter bone growth that looks like a horn.

The only fish species found in the rivers and lakes of West Spitsbergen is the Arctic char (*Salvelinus alpinus*). Cod (*Gadus morhua*), capelin (*Mallotus villosus*), haddock (*Melanogrammus aeglefinus*), Atlantic halibut (*Hippoglossus hippoglossus*), rockfish (*Sebastes marinus*) are found in the sea.



Fig. 1.1.14. Walrus haulout site at Forlandet National Park (Prins Karls Forland) (photo from open sources).

Spitsbergen has a very rich and diverse geological history, so it is often called a real geology reserve. Here you can find subsurface rocks of almost all periods of the Earth's development, and the richest deposits of coal indicate the fact that once the archipelago was definitely located in a zone with a warmer climate.

Since the vegetation cover here is very scarce, and human activity is limited, most of the unique natural formations have survived to this day in almost pristine condition. To preserve this unique nature, about 65 % of the surface of Spitsbergen is given for protected areas, including seven national parks, six nature reserves (Northeast and Southeast Svalbard, three floristic regions, and one marine reserve), 15 specialized bird sanctuaries, and one geological nature reserve. Svalbard Environmental Protection Act, 2001, regulates the pattern of utilization of these reserves, most of the provisions of the Act apply to the protection of the entire nature of the archipelago. In all these areas, there is a complete ban on the use of motor vehicles and any commercial activity.

REFERENCES

- Buzin I.V., Glazovskij A.F., Gudoshnikov Ju.P., Danilov A.I., Dmitriev N.E., Zubakin G.K., Kubyshkin N.V., Naumov A.K., Nesterov A.V., Skutin A.A., Skutina E.A., Shibakin S.I. Icebergs and glaciers of the Barents Sea: Recent studies. Part 1. The main producing glaciers, distribution and morphometric features of icebergs. *Problemy Arktiki i Antarktiki*. Problems of Arctic and Antarctic. 2008, 1 (78): 66–80. [In Russian].
- Alekseev G.V. Studies of climate change in the Arctic in the twentieth century. *Trudy AARI*. Proc. of AARI. 2003, 446: 6–21. [In Russian].
- Antsiferova A.R., Siekkinen Ye.D., Chaus O.M. Climate pattern of the distribution of precipitation on the Spitsbergen archipelago according to the “Barentsburg” hydrometeorological observatory. *Kompleksnye issledovanija prirody Shpicbergena*. Comprehensive studies of the nature of Spitsbergen. 2016, 13: 26–31. [In Russian].
- Gavrilo M.V. *Belaja chajka Pagophila eburnea* (Phipps, 1774) v *Rossijskoj Arktike: osobennosti gnezdovanija vida v sovremennom optimume areala*. Ivory gull *Pagophila eburnea* (Phipps, 1774) in the Russian Arctic: features of species nesting in the best modern range. PhD thesis, 2011. [In Russian].
- Demidov N.Je., Karaevskaja E.S., Verkulich S.R., Nikulina A.L., Savatjugin L.M. The first results of permafrost observations at the cryosphere test site of the Russian Scientific Center on the Spitsbergen archipelago (RSCS). *Problemy Arktiki i Antarktiki*. Problems of Arctic and Antarctic. 2016, 4 (110): 67–79. [In Russian].
- Yezhov A.V. Some features of the presence of pinnipeds in the Grønfjorden (Spitsbergen) in the late winter and spring. *Kompleksnye issledovanija prirody Shpicbergena*. Comprehensive studies of the nature of Spitsbergen. 2016, 16: 128–132. [In Russian].
- Zhichkin A.P. Dynamics of ice coverage in the area of the Spitsbergen archipelago and the adjacent shelf at the beginning of the 21st century. *Kompleksnye issledovanija prirody Shpicbergena*. Comprehensive studies of the nature of Spitsbergen. 2016, 16: 140–144. [In Russian].
- Zhichkin A.P. Features of interannual and seasonal fluctuations in ice coverage anomalies of the Barents Sea. *Meteorologija i gidrologija*. Meteorology and Hydrology. 2015, 5: 52–62. [In Russian].
- Zinger Ye.M. *Shpicbergen — ledovij arhipelag*. The ice archipelago Spitsbergen. Moscow: Penta, 2006: 302 p. [In Russian].
- Bore P.P. (ed.). *Meet the Svalbard Archipelago*. Oslo, 2012. 28 p. [In Russian].
- Koroljova N.E., Konstantinova N.A., Savchenko A.N., Belkina O.A., Lihachev A.Ju., Davydov D.A., Urbanavichene I.N. *Flora i rastitel'nost' poberezh'ja zaliva Grjon-f'ord (arhipelag Shpicbergen)*. Flora and vegetation of the coast of the Grønfjorden (Spitsbergen). Apatity: Publishers K&M, 2008: 132 p. [In Russian].

- Koryakin V. S. *Ledniki Arktiki*. Glaciers of the Arctic. Moscow: Nauka, 1988: 157 p. [In Russian].
- Nikiforov E.G., Shpeiher A.O. *Zakonomernosti formirovaniya krupnomasshtabnyh kolebanij gidrologicheskogo rezhima Severnogo Ledovitogo okeana*. Patterns of formation of large-scale fluctuations in the hydrological regime of the Arctic Ocean. Leningrad: Gidrometeoizdat, 1980: 269 p. [In Russian].
- Kotljakov V.M. (ed.) *Oledenenie Shpicbergena (Sval'barda)*. Glaciation of Spitsbergen (Svalbard). Moscow: Nauka, 1975: 276 p. [In Russian].
- Pavlov A.K., Ivanov B.V., Zhuravskij D.M., Tverberg V.K. Warming in the bays of West-Spitsbergen: a short-term phenomenon or a steady trend. *Problemy Arktiki i Antarktiki*. Problems of Arctic and Antarctic. 2010, 3: 1–13. [In Russian].
- Pechurov L.V. Spitsbergen. Moscow: Mysl', 1983: 150 p. [In Russian].
- Savatyugin L.M., Ugryumov Ju.V. Research and work of the Federal Service for Hydrometeorology and Environmental Monitoring (Rosgidromet) organizations on the Spitsbergen archipelago. *Rossijskie poljarnye issledovanija. Informacionno-analiticheskij sbornik*. Russian Polar Research. Information analysis collection. 2018, 1 (31): 9–12. [In Russian].
- Savatyugin L.M., Dorozhkina M.V. *Arhipelag Shpicbergen: rossijskie imena i nazvanija*. Spitsbergen archipelago: Russian names and titles. St. Petersburg: Nauka, 2009: 259 p. [In Russian].
- Savchenko A.N. Natural environment. *Flora i rastitel'nost' poberezh'ja zaliva Grøn'fjord (arh. Shpicbergen)*. Flora and vegetation of the coast of the Grøn'fjorden (Spitsbergen). Apatity: Publishers K&M, 2008: 9–10. [In Russian].
- Semjonov A.V., Antsiferova A.R., Davydov A.A. The climate of Barentsburg. Changes in the main characteristics over the past 40 years (according to observations of the “Barentsburg” meteorostation). *Kompleksnye issledovanija prirody Shpicbergena*. Comprehensive studies of the nature of Spitsbergen. 2002, 2: 139–145. [In Russian].
- Solovyanova I.Ju., Mavludov B.R. River runoff on Spitsbergen in winter. *Meteorologija i gidrologija*. Meteorology and hydrology. 2006, 4: 100–109. [In Russian].
- Tislenko D.I., Ivanov B.V. Long-term variability of the temperature of Atlantic waters in the fjords of the West Spitsbergen during the period of the first (1920–1940) and modern warming in the Arctic. *Problemy Arktiki i Antarktiki*. Problems of Arctic and Antarctic. 2015, 2 (104): 93–101. [In Russian].
- Arctic fox (*Vulpes lagopus*). Available at: <http://www.npolar.no/en/species/arctic-fox.html>. Title from the screen (accessed 7.09.2018).
- Dowdeswell J. On the Nature of Svalbard Icebergs. *J. Glaciology*. 1989, 35 (120): 224–234; DOI: 10.3189/S00221430000455X.
- Dowdeswell J., Forsberg C.F. The size and frequency of icebergs and bergy bits derived from tidewater glaciers in Kongsfjorden, northwest Spitsbergen. *Polar Research*. 1992, 11 (2): 81–91; DOI: 10.3402/polar.v11i2.6719.
- Hagen J.O., Kohler J., Melvold K., Winther J.-G. Glaciers in Svalbard: mass balance, runoff, and freshwater flux. *Polar Research*. 2003, 22 (2): 145–159.
- Hagen J.O., Lafauconnier B. Reconstructed runoff from High Arctic basin Bayelva in Svalbard based on mass balance measurements. *Nord. Hydrol*. 2002, 26: 285–296.
- Hodgkins R. Glacier hydrology in Svalbard, Norwegian high arctic. *Quaternary Sci. Reviews*. 1997, 16 (9): 957–973; DOI:10.1016/S0277-3791(97)00032-2.
- Hodson A. Climate, hydrology and sediment transfer process interactions in a sub-polar glacier basin, Svalbard. Unpublished PhD thesis. University of Southampton. 1994.
- Jiskoot H., Murray T., Boyle P. Controls on the distribution of surge-type glaciers in Svalbard. *J. Glaciology*. 2000, 46 (154): 412–422.
- Kovacs K. Birds and mammals of Svalbard. Published by the Norwegian Polar Institute as No. 13 in the series “Polar Handbooks”. 2005: 203 p.

- Kristensen L., Benn D.I.* A surge of the glaciers Skobreen-Paulabreen, Svalbard, observed by time-lapse photographs and remote sensing data. *Polar Research*. 2012, 31 (1): 11106; DOI:10.3402/polar.v31i0.11106.
- Liestøl O.* Open-system pingos in Spitsbergen. *Norsk Geografisk Tidsskrift*. 1996, 50 (1): 81–84; DOI: 10.1080/00291959608552355.
- Pettersson L.-E.* Hydrological Investigations in Svalbard. Proc. Nordic Hydrological Conference. NHP-report 34/94.
- Rossi G., Accaino F., Boaga J., Petronio L., Romeo R., Wheeler W.* Seismic survey on an open Pingo system in Adventdalen Valley, Spitsbergen, Svalbard. *Near Surface Geophysics*. 2018, 16; DOI: 10.3997/1873–0604.2017037.
- Schellenberger T., Dunse T., Kääb A., Schuler T.V., Hagen J.O., Reijmer C.H.* Multi-year surface velocities and sea-level rise contribution of the Basin-3 and Basin-2 surges, Austfonna, Svalbard. *The Cryosphere Discuss*. 2017, 5 p.; DOI: 10.5194/tc.
- Sevestre H., Benn D.I.* Climatic and geometric controls on the global distribution of surge-type glaciers: implications for a unifying model of surging. *J. Glaciology*. 2015, 61: 646–662; DOI: 10.3189/2015JG14J136.
- Smith L.C., Sheng Y., MacDonald G.M., Hinzman L.D.* Disappearing Arctic lakes. *Science*. 2005, 308: 1429–1429; DOI: 10.1126/science.1108142.
- Svendsen H., Beszczynska-Møller A., Hagen J.-O., Lefauconnier B., Tverberg V., Gerland S., Ørbæk J.-B., Bischof K., Papucci C., Zajaczkowski M., Azzolini R., Bruland O., Wiencke C.* The physical environment of Kongsfjorden – Krossfjorden, an Arctic fjord system in Svalbard. *Polar Research*. 2002, 21 (1): 133–166; DOI: 10.3402/polar.v21i1.6479.
- Sund M.* Polar hydrology. Report Norwegian Water Resources and Energy Directorate’s work in Svalbard. Oslo: 2008, 66 p.
- Svalbard reindeer (*Rangifer tarandus platyrhynchus*). Available at: <http://www.npolar.no/en/species/svalbard-reindeer.html>. Title from the screen (accessed 7.09.2018).
- Vidar B., Cherenkov A.E., Gavrilov M.V., Koryakin A.S., Krasnov J.V., Nikolaeva N.G., Pokrovskaya I.V., Semashko V.J., Tertitski G.M.* Seabird colony database of the Barents Sea Region and the Kara Sea. *Norsk Polarinstitutt Rapportserie*. Tromsø, 2000, 78 p.

1.2. FACTORS THAT INFLUENCE CLIMATE FORMATION AND CHANGE IN THE SPITSBERGEN ARCHIPELAGO AREA

G.V. Alekseev, N.I. Glok, A.V. Smirnov, S.I. Kuzmina, A.Ye. Vyazilova

The climate in the area of the Spitsbergen archipelago, as in the entire Arctic, is formed under conditions of significantly reduced supply of heat from the Sun than the climate in non-polar regions. The heat coming with atmospheric and oceanic circulation makes the most significant contribution to compensating for the shortage of solar energy here. Due to this process, the climate of the Arctic is much warmer than it would be in the absence of advection (Alekseev, 2014; Alekseev, Podgorny, 1991). Increased heat and moisture transfer from low latitudes sets back-coupling in the Arctic climate system into action. It is an increase in the influx of long-wave radiation to the surface due to an increase in the concentration of atmospheric water vapor and the absorption of heat from the Sun as a result of an increase in open water in summer. In Fig. 1.2.1 schematically presents the processes forming Arctic climate.

With modern warming, special attention is drawn to the degradation of the sea ice cover in the Arctic Ocean (Arctic Ocean), which is sharply responsive to climate change. Analysis of historical data on marine Arctic ice reveals significant changes in ice distribution in the past. In the twentieth century, there are four stages in the development of Arctic sea ice in the Atlantic region: two stages of ice cover expansion (1900–1918 and 1938–1968) and two stages of its reduction (1918–1938 and 1968–1999), appearing against the background of a century-old reduction in the area of Arctic ice (Zakharov, 2004). The earliest estimates of ice distribution are from the Greenland, Norwegian, and Barents Seas and surrounding areas (Løyningetal, 2003; Vinje, 2001). According to these estimates, in 1920–1940 ice area in summer in the region from 30° W up to 70° E and to the south of 80° N declined. The maximum in the stage of reduction of the sea ice cover (1918–1938) occurred in the warming of the 1930s. Vize V.Yu. was the first to indicate an increase in the

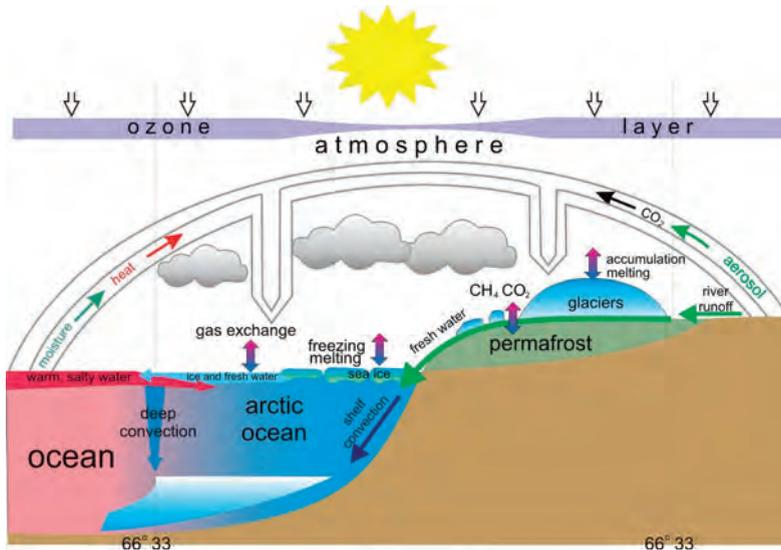


Fig. 1.2.1. The processes involved in the formation of the Arctic climate (Alekseev, 2003).

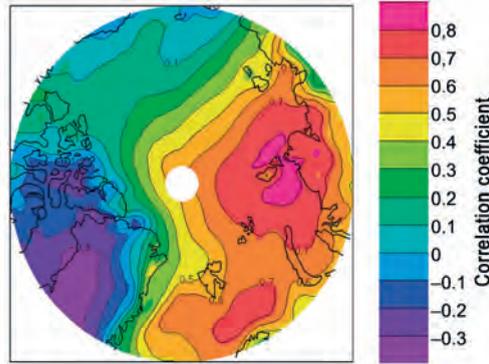


Fig. 1.2.2. The correlation coefficient between the influx of apparent heat through the Atlantic “gate” on the isobaric surface of 1000 hPa and near-surface air temperature in December – February 1979–2014 in the Arctic, calculated according to the ERA/Interim reanalysis data (Alekseev et al., 2016b).

circulation of the atmosphere and the ocean as the leading cause of Arctic warming and, as a result, a reduction in the area of sea ice cover in the Atlantic part of Arctic (Vize, 1937).

The influence of atmospheric circulation on climate change in the Arctic is confirmed by calculations of the contribution of atmospheric transport to the formation of Arctic energy balance. According to estimates, meridional transport in the atmosphere forms the main incoming part of the energy balance for the Earth system – the atmosphere at high latitudes of the Northern Hemisphere (Marchuk et al., 1988; Khrol, 1992; Nakamura and Oort, 1988; Serreze et al., 2007).

Calculations of atmospheric transport of apparent and latent heat to the Arctic through a latitude of 70° N, performed by Alekseev et al. (2016b) showed that the main influx of atmospheric heat in winter is through the Atlantic “gate” (from 0 to 80° E) and has the most significant impact on changes in winter air temperature in the Atlantic part of Arctic (Fig. 1.2.2).

Interannual changes of this influx show an increase, especially noticeable after 1997 (Fig. 1.2.3 a). It corresponds with interannual changes in the average air temperature north of 70° N (Fig. 1.2.3 b).

Obviously, the influx of atmospheric heat through the Atlantic “gate” is associated with the warming influence of the North Atlantic, from where warm saltwater enters the Norwegian and Greenland seas and further into the Barents Sea. Over this water flows of warm and humid air spread and move further to the water of the Arctic seas and the Arctic basin. Water with a positive temperature on the surface of the North European Basin (NEB) in the cold part of the year is a powerful “heater” of the region. However, the power of this “heater” fluctuates after changes in the circulation of the atmosphere and water masses in the North Atlantic, providing heat transfer from low latitudes to high ones.

Due to long-term oceanographic observations at NEB, begun at the end of the 19th century, changes in the thermohaline state of water masses in this region of the World Ocean are relatively well documented. Especially valuable data on fluctuations in the influx of Atlantic water (AW) were obtained as a result of observations at the section along the Kola meridian (33° 30' E), which were started in the 1900s and are still ongoing (Bochkov, 1982; Karsakov, 2009).

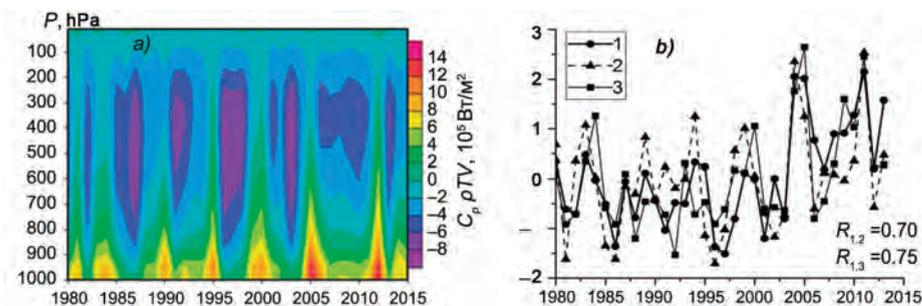


Fig. 1.2.3. The influx of heat through the Atlantic “gate” to the Arctic, affecting near-surface air temperature.

a – distribution of winter-averaged values averaged over the interval 0° – 80° E the transfer of apparent heat through a vertical unit area at isobaric levels; *b* – normalized values of the average air temperature at the surface in January – February (1) and estimates of the transfer of apparent (2) and latent (3) heat on the surface $p = 1000$ hPa in December – February. R – correlation coefficient between air temperature and transport (Alekseev et al., 2016b).

In recent years, a series of works has been published on the study of variability in the NEB climate characteristics and their causes. Particular attention is paid to the variability of characteristics of the sea ice cover (SIC) under the influence of both the atmosphere and the ocean. At the same time, the role of each factor is discussed, including as a possible initial cause.

A relationship was found between the temperature of Atlantic water in the Barents Sea and atmospheric circulation, and the effect of heat fluxes into the atmosphere on anomalies in ocean surface temperature (OST) in the Norwegian Sea was noted (Schlichtholz and Houssais, 2011). Later, it was concluded that the ocean plays a crucial role in the formation of variability in the characteristics of the troposphere over NEB in winter (Schlichtholz, 2014). The authors (Ivanova et al., 2012) came to the opposite conclusion; they found that the contribution of heat flow anomalies in winter to sea ice edge variability is four times greater than of the OST anomalies brought to the Greenland and Barents Seas.

In several papers study the inverse effect of changes in sea ice cover in the Barents Sea on atmospheric circulation over the sea and beyond (Semyonov et al., 2012; Inoue et al., 2012; Liptak, Strong, 2014; Petoukhov, Semyonov, 2010; Semyonov et al., 2015). At the same time, it is noted that when the Barents Sea is ice-free at the beginning of winter, cyclonic circulation prevails in the atmosphere. It is accompanied by a western shift of the spur of the Siberian anticyclone with inflows of cold air along its western periphery, leading to winter cooling in Europe.

Not all experiments with Atmospheric General Circulation Model (AGCM) and global climate models confirm the strong influence of the Barents Sea on temperate climate. In experiments, the reaction of the atmosphere of high and moderate latitudes to changes in the area of sea ice (ASI) in the Arctic and OST was studied in the Northern Hemisphere of AGCM (Baidin, Meleshko, 2014; Meleshko, Baidin, 2013). As a result of the calculations, no connection was found between the reduction in ice area and cold winters in Europe. According to the authors, these events are more likely associated with changes in the atmospheric circulation under the influence of an increase in OST and increased meridional heat transfer.

The results of experiments with global collaborative climate models for the study of sensitivity to external influences are more trustworthy than experiments with AGCM since they do not artificially break the changes in OST and ASI. There were experiments with the Norwegian global climate model to assess the influence of ocean heat influx on sea ice in the Arctic. They showed that an increase in the supply of Atlantic water (AW) to NEB has a strong effect on the area of sea ice, as ice formation is reduced. Thus, the ocean affects changes in ice mass more than the atmosphere, both its average value and variability (Sandø et al., 2014).

The complexity of processes that form climate variability in the region appears in significant discrepancies in the model and observed climate, revealed by comparing the results of calculations on global collaborative models. The maximum discrepancy between the simulated and observed climate for 1981–2000 was in the Barents Sea: the model air temperature was 6–8 °C lower here, and the sea ice area is much larger than the observed values (Chapman et al., 2007). A new generation of global CMIP5 models better simulates the observed climate in the Barents Sea, but the discrepancy with the results of observations remains one of the most significant in the Arctic (Pavlova et al., 2014; Semyonov et al., 2015).

Visual evidence of the influence of AW inflow on sea ice distribution in the Atlantic region of the Arctic is presented on combined maps of the distribution of water salinity on the surface of the Barents, Norwegian and Greenland Seas and the position of the ice boundary in June (Fig. 1.2.4). The figure shows that with an increase in the distribution area of more saline AW (Fig. 1.2.4 *b*), the ice boundary recedes and, vice versa, with its reduction, the ice occupies a large water area (Fig. 1.2.4 *a*). June was chosen as an example since, for this month, there is the most considerable amount of oceanographic observation data and, at the same time, the period of summer when sea ice is just beginning to melt.

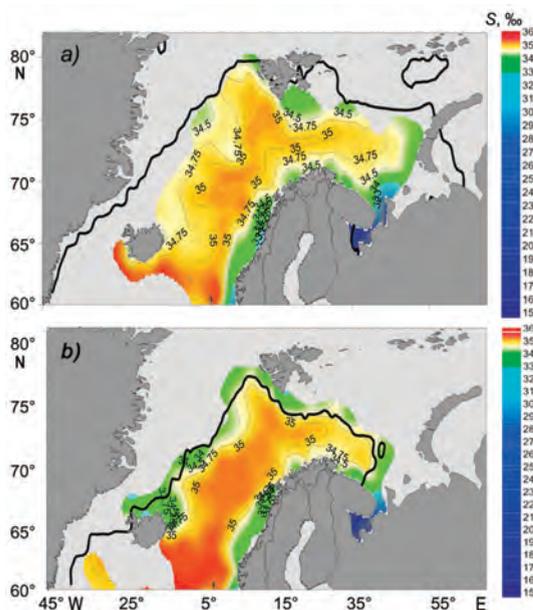


Fig. 1.2.4. Distribution of salinity (‰) of water on the surface of NEB and the position of the ice boundary (black curve) in June 1989 (*a*) and 1969 (*b*).

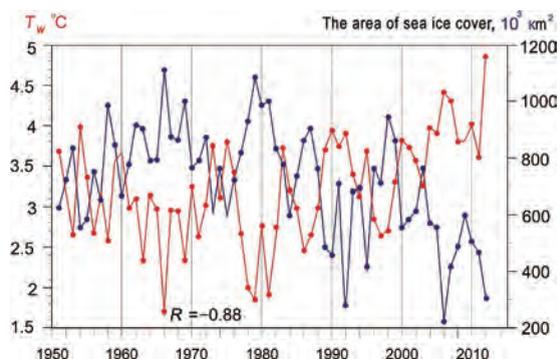


Fig. 1.2.5. The average monthly water temperature in the section along the Kola meridian (T_w) and sea ice area (ASI) in the Barents Sea in May (Alekseev et al., 2016a).

A quantitative assessment of the influence of fluctuations in the influx of AW on changes in the ice area showed that the closest relationship (correlation coefficient -0.88) was observed between them in May when the increase in the area of sea ice cover stops and melting just begins (Fig. 1.2.5) (Alekseev and et al. 2016a).

Since the influx of AW influences on the variability of characteristics of the regional climate, it is assumed that there is a connection of it with anomalies in the characteristics of the AW in the areas of their formation in the temperate and low latitudes of the North Atlantic. In the work of Alekseev et al. (2016a), according to the results of a multivariate correlation and factor analysis of the fields of the average monthly HadISST OST, together with the characteristics of sea ice and water temperature in NEB, two such regions were found. One of these regions is located in the area of the beginning of the North Atlantic Current south of Newfoundland, and the other one is in the equatorial part of the North Atlantic (Fig. 1.2.6). The influence of the first of these areas on the temperature regime of the region affects after nine months, and the second one after 27 months.

Anomalies of OST in the equatorial region have the most noticeable effect on the area of Arctic sea ice in winter in three years (Fig. 1.2.7). It is equivalent to the effect on the area of ice in the Atlantic region of the Arctic since the variability of ice area in the Arctic Ocean in winter is due to changes in the Atlantic region of the Arctic.

The influence of regional atmospheric circulation on changes in the sea ice area and air temperature in the Barents Sea, which was estimated using three different atmospheric indicators, turned out to be insignificant compared to the contribution of the influx of AW (Alekseev et al., 2016a). The most noticeable effect is the meridional component of atmospheric circulation, estimated by the pressure difference between Spitsbergen and Franz Josef Land, the winter anomaly of which affects the temperature of water and ASI for almost the entire year. The influence of changes in circulation over the Barents Sea, described by the main component of the pressure field in the winter months, shows itself in the variability of T_{KM} (water temperature in the section along the Kola meridian) from April to November, and in the variability of ASI from February to May.

Comparison of the contribution of changes in AW inflow and atmospheric circulation fluctuations using calculations of multiple regression T_{KM} and circulation indicators (alternately) on ASI showed that 76 % of ASI variability in May is associated with

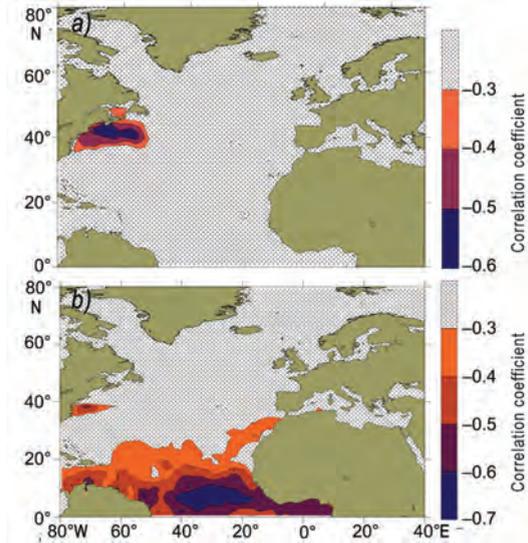


Fig. 1.2.6. Areas in the North Atlantic where the average monthly OST in October affects the area of sea ice in the Barents Sea after nine months (a) and 27 months (b).

The color shows the correlation coefficient for 1950–2014.

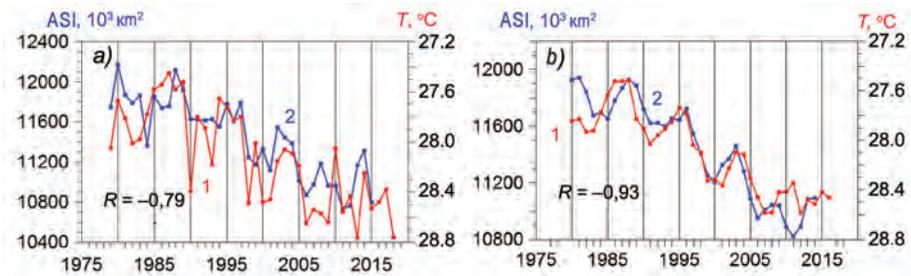


Fig. 1.2.7. Changes in OST (T) in the equatorial region of the North Atlantic in October and the ice area in the Arctic Ocean (ASI) in December after three years (a) and the same, but on a three-year moving-average basis (b).

R is the correlation coefficient.

changes in water temperature and about 10 % with a regional atmospheric circulation of water temperature. The main reason for the weaker regional atmospheric influence on the interannual variability of ASI is understandable if we compare the spectral structure of the interannual variability of T_{KM} , ASI, and near-surface air temperature in the Barents Sea and atmospheric circulation indicators. 50 % of the interannual variability of the first two characteristics fall upon fluctuations with a period of more than ten years, no more than 15 % fall upon fluctuations with a period of fewer than three years. In the interannual variability of the characteristics of regional atmospheric circulation, up to 40 % fall upon fluctuations with a period of fewer than three years, which include weather noise from not completely excluded synoptic fluctuations. Also, the calculation of the pressure difference between points at a relatively small distance weakens the large-scale components of the pressure variability and enhances random fluctuations.

CONCLUSIONS

The waters washing Spitsbergen, are under the warming influence of the North Atlantic. Warm salt water flows through the Faroe-Scottish and Faroe-Iceland straits to the Norwegian and Greenland Seas and further to the Barents Sea and the Arctic Basin. Over this water flows of warm and humid air spread and move further to east and northeast to the Arctic seas and the Arctic basin. Water on the surface of the Norwegian and Barents seas, whose temperature is above 0 °C, is powerful “heater” of the region in the cold part of the year. However, the power of this “heater” fluctuates after changes in the circulation of the atmosphere and water masses in the North Atlantic, providing heat transfer from low latitudes to high ones. Changes in the influx of Atlantic water determine the main part of the interannual variability of the sea ice area, water temperature in the cold part of the year, and the average annual air temperature in the region.

The effect of regional atmospheric circulation on the interannual variability of these climate characteristics is modest, including due to a significant proportion of weather noise in their variability. In particular, in May, 76 % of interannual variability in the area of ice in the Barents Sea is associated with changes in water temperature, and about 10 % with the regional atmospheric circulation of water.

The connection between the variability of sea ice area and water temperature in the region with OST anomalies in the area south of Newfoundland and in the equatorial region of the North Atlantic has been found. Their influence is delayed from several months to several years, which creates the prerequisites for developing methods for climate forecast of sea ice area and water temperature in the region.

An increase in meridional atmospheric heat transfer through the Atlantic “gate” makes the main contribution to an increase in air temperature in the Atlantic region of the Arctic in winter and determines a large part of the trend of winter average air temperature north of 70° N in 1994–2014.

REFERENCES

- Alekseev G.V.* Studies of climate change in the Arctic in the twentieth century. *Trudy AARI. Proc. of AARI.* 2003, 446: 6–21. [In Russian].
- Alekseev G.V., Glok N.I., Smirnov A.V., Vyazilova A.Ye.* The influence of the North Atlantic on climate fluctuations in the Barents Sea and their predictability. *Meteorologija i gidrologija.* Meteorology and Hydrology. 2016a, 8: 38–56. [In Russian].
- Alekseev G.V., Kuzmina S.I., Urazgildeyeva A.V., Bobylev L.P.* The effect of atmospheric heat and moisture transfers on the intensification of warming in the Arctic in the winter. *Fundamental'naja i prikladnaja klimatologija.* Fundamental and Applied Climatology. 2016b, 1: 43–63. [In Russian].
- Alekseev G.V., Podgornyj I.A.* The role of advection and other factors in the formation of the polar climate. *Klimaticheskij režim Arktiki na rubezhe XX i XXI vekov.* Climatic regime of the Arctic at the turn of the 20th and 21st centuries. St. Petersburg: Gidrometeoizdat, 1991: 4–18. [In Russian].
- Alekseev G.V.* Dynamic intensification of global warming. *Trudy Mezhduнародnoj konferencii pamjati akad. A.M. Obuhova.* Proc. International Conference in Memory of Academician A.M. Obukhov. Moscow: GEOS, 2014: 290–306. [In Russian].
- Bajdin A.V., Meleshko V.P.* The reaction of the atmosphere in high and middle latitudes to a reduction in the area of sea ice and an increase in the surface temperature of the oceans. *Meteorologija i gidrologija.* Meteorology and Hydrology. 2014, 6: 5–8. [In Russian].

- Bochkov Yu.A.* A retrospective of the water temperature in the 0–200 m layer at the Kola Meridian section in the Barents Sea (1900–1981). *Trudy PINRO*. Proc. of PINRO (Knipovich Polar Research Institute of Marine Fisheries and Oceanography). 1982: 113–122. [In Russian].
- Vize V.Yu.* Causes of Arctic warming. *Sovetskaja Arktika*. Soviet Arctic. 1937, 1: 1–7. [In Russian].
- Zakharov V.F.* Changes in the distribution of Arctic sea ice during the twentieth century. *Formirovanie i dinamika sovremennogo klimata Arktiki*. Formation and dynamics of the modern climate of the Arctic. St. Petersburg: Gidrometeoizdat, 2004: 112–159. [In Russian].
- Karsakov A.L.* *Okeanograficheskie issledovanija na razreze “Kol’skij meridian” v Barencevom more za period 1900–2008 gg.* Oceanographic studies at the Kola Meridian section in the Barents Sea for the period 1900–2008. Murmansk: Publishers PINRO, 2009: 139 p. [In Russian].
- Marchuk G.I. Kondratyev K.Ja., Kozoderov V.V.* *Radiacionnyj balans Zemli, ključevye aspekty*. Earth radiation balance, key aspects. Moscow: Nauka, 1988. 216 p. [In Russian].
- Meleshko V.P., Baidin A.V.* The atmosphere’s climate response to the reduction of ice in the Arctic and other external influences over the past decades. *Trudy Glavnoj geofizicheskoj observatorii*. Proc. of the Main State Hydrometeorological Observatory. 2013, 568: 80–113. [In Russian].
- Pavlova T.V., Kattsov V.M., Meleshko V.P., Shkolnik I.M., Govorkova V.A., Nadezhina E.D.* A new generation of climate models. *Trudy Glavnoj geofizicheskoj observatorii*. Proc. of the Main State Hydrometeorological Observatory. 2014, 575: 5–64. [In Russian].
- Semyonov V.A., Mokhov I.I.* The role of sea ice boundaries and ocean surface temperature in changes in the regional climate in Eurasia over recent decades. *Izvestija RAN. Fizika atmosfery i okeana*. Izvestiya RAS. Physics of the atmosphere and the ocean. 2012, 48 (4): 403–421. [In Russian].
- Khrol V.P.* *Atlas jenergetičeskogo balansa Severnoj poljarnoj oblasti*. Atlas of the energy balance of the Northern polar region. Leningrad: Gidrometeoizdat, 1992: 52. [In Russian].
- Chapman W.L., Walsh J.E.* Simulations of Arctic temperature and pressure by global coupled models. *J. Climate*. 2014, 20: 609–632. DOI: 10.1175/JCLI4026.1.
- Inoue J., Hori M.E., Takaya K.* The role of Barents sea ice in the wintertime cyclone track and emergence of a warm – Arctic cold–Siberian anomaly. *J. Climate*. 25 (7): 2561–2568.
- Ivanova D.P., McClean J.L., Hunke E.C.* Interaction of ocean temperature advection, surface heat fluxes, and sea ice in the marginal ice zone during the North Atlantic Oscillation in the 1990s: A modeling study. *Geophys. Res.* 117. C02031, DOI: 10.1029/2011JC007532.
- Liptak J., Strong C.* The Winter Atmospheric Response to Sea Ice Anomalies in the Barents Sea. *J. Climate*. 27: 914–924. DOI: 10.1175/JCLI-D–13–00186.1.
- Løyning T.B., Dick C., Goodwin H., Pavlova O., Vinje T., Kjærnlid G., Villinger T.* “ACSYS HISTORICAL ICE CHART ARCHIVE (1553–2002)”. Tromsø, Norway. IACPO Informal Report. 2003, 8: 35 p.
- Nakamura N., Oort A.H.* Atmospheric heat budgets of the polar regions. *J. Geophys. Res.* 93 (D8): 9510–9524.
- Petoukhov V., Semenov V.A.* A link between reduced Barents – Kara sea ice and cold winter extremes over northern continents. *J. Geophys. Res.* 115: D21111; DOI: 10.1029/2009JD013568.
- Sandø A.B., Gao Y., Langehaug H.R.* Poleward ocean heat transports, sea ice processes, and Arctic sea ice variability in NorESM-M simulations. *J. Geophys. Res. Ocean.* 2014, 119 (3): 2095–2108.
- Schlichtholz P., Houssais M.N.* Forcing of oceanic heat anomalies by air-sea interactions in the Nordic Seas area // *J. Geophys. Res.* // *J. Climate*. 2011, 27: 8686–8706.
- Semenov V.A.* et al. Arctic sea ice area in CMIP3 and CMIP5 climate model ensembles – variability and change. *Cryosph. Discuss.* 2015, 9: 1077–1131.
- Serreze M.C.* et al. The large-scale energy budget of the Arctic. *J. Geophys. Res.* 112. No. D11122.
- Vinje T.* Anomalies and trends of sea – ice extent and atmospheric circulation in the Nordic seas during the period 1864–1998 // *J. Climate*. 2001, 14 (3): 255–267.

1.3. ANALYTICAL REVIEW OF HYDROMETEOROLOGICAL CHARACTERISTICS OF WEST SPITSBERGEN (ACCORDING DATA OF “BARENTSBURG” HYDROMETEOROLOGICAL OBSERVATORY)

A.R. Antsiferova, Ye.D. Siekkinen, O.M. Chaus

The first regular Russian meteorological observations on Spitsbergen were carried out during the work of the Russian-Swedish expedition to measure the meridian arc in 1899–1902. In addition to astronomers – surveyors, the expedition included a group of meteorologists led by physicist M.A. Bayer, an employee of the Pulkovo Observatory. The observations were carried out on the shore of Gåshamna in Hornsund (76° 56' N and 15° 53' E), where the settlement Konstantinovskiy (Konstantinovka) was built with residential buildings and meteorological and magnetic observatories. The main meteorological parameters were measured: temperature and humidity, atmospheric pressure, wind speed and direction. Moreover, meteorologists conducted visual observations of various atmospheric phenomena every hour, in particular polar lights and changes in the magnetic field. According to these data, M.A. Bayer compiled observations book. The functional role of meteorological observations was also to determine the visual range of visibility during triangulation geodetic measurements when signals were sent from the tops of the surrounding mountains or other points of the triangulation system (Savatyugin, Dorozhkina, 2009).

In 1899, the icebreaker Ermak, commanded by Admiral S.O. Makarov sailed to the shores of Spitsbergen. On the shore of Advent Bay, sailors set an age-long mark to observe sea level fluctuations.

The first Soviet meteorological station was organized in 1932 in the Grumant settlement. In 1933, the station was moved to the Barentsburg (78° 04' N, 14° 15' E).

During World War II, the “Barentsburg” hydrometeorological station was mothballed; and polar explorers were evacuated from the archipelago.

In 1947, the station resumed its work as the Barentsburg High Latitude Observatory and came under the jurisdiction of the General Hydrometeorological Service (Semyonov, 2009). In December of 1947 the aerological group began to work, it had the most significant personnel and technological infrastructure. In some facilities, the “Malachit” direction-finding device with a rangefinder adapter and a gas generation point were located. For the first time in this region, it became possible to study the state of the upper atmosphere (from the Earth’s surface up to 30–40 km, which significantly exceeded the upper boundary of all aircraft in the world). It was done using the first and only instrument at that time to study the characteristics of the upper atmosphere – RZ–049 radio probe designed by Professor Molchanov.

This radio sounding station has been operating continuously for many decades. They gradually installed more modern radiosondes there (RZ–049 was replaced by A–22–III, A–22–IV, MR3, MAR3). The “Meteorit” radar replaced the “Malachit” direction-finding device, and later the aerological computer complex AVK-1.

Since 1963, the station has been part of the Murmansk Territorial Administration for Hydrometeorology and Environmental Monitoring under the USSR State Committee. In July 1983, they opened the “Barentsburg” Regional Hydrometeorological Observatory (RHMO) at the premises of the polar station.

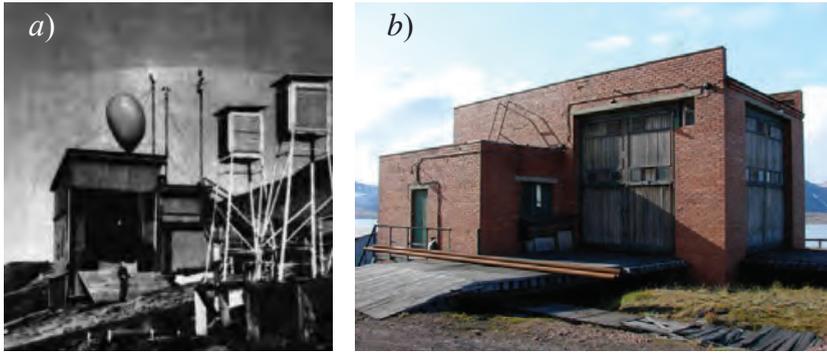


Fig. 1.3.1. Aerological pavilions in Barentsburg: the aerological pavilion at 1947 (a), and the building of the gas-generating at 2002 (b).

The most detailed observations were carried out in the period from 1985 to 1990, when regular meteorological, geophysical, oceanographic, aerological, actinometric, and other types of observations were carried out with the prompt transfer of data to forecasting centers. The personnel of the RHMO in this period was 25–28 people.

In the early 1990s, when the country faced economic difficulties, many types of observations at the RHMO were suspended, only meteorological observations were carried out, and the staff was reduced to three people. Only since 2000, after regulation of the Government of the Russian Federation “On financing the activities of Russian organizations in the Spitsbergen archipelago” was enacted, sea and actinometric observations, as well as sea level observations, were resumed.

Since 2000, the Murmansk Administration for Hydrometeorological and Environmental Monitoring (AHMEM) in the area of Barentsburg village regularly monitors the state of air pollution, precipitation, snow cover, surface water on the lakes of Stemmevatnet and Kopan, as well as the sea waters of the Grønfjorden according to hydrochemical indicators and detection of pollutants. Since 2001, geophysical observations have been resumed, modern measuring systems record magnetic field variations, cosmic radiation levels are measured, and signals from the oblique sounding of the atmosphere are received.

On January 1, 2004, the study of the hydrological regime of Stemmevatnet began.

The “Barentsburg” Hydrometeorological Observatory conducts meteorological observations following the “Manual on Hydrometeorological Stations and Posts”, issue 3, part 1 (1985), in full, within the deadlines established by the World Meteorological Organization: 00, 03, 06, 09, 12, 15, 18, 21 hours UTC (Universal Time Coordinated).

The department of meteorology and climate of the Federal State Budgetary Institution (FSBI) “Murmansk UGMS” processes and accumulates meteorological information using the program “PERSONA MIS” developed at the FSBI “RIHMI-WDC”. From October 1, 2013, under the order of the FSBI “Murmansk UGMS”, observations of temperature and humidity, atmospheric pressure, wind characteristics, and soil temperature are carried out using an automated meteorological complex (AMC). Observations of visibility, cloud characteristics, and atmospheric phenomena are carried out visually according to the Manual.

According to the Barentsburg Hydrometeorological Observatory, work on climate studies in the Spitsbergen in Murmansk UGMS started in 2002 and is currently ongoing. In their studies, the specialists of the Murmansk UGMS used methods for assessing changes

in the main meteorological parameters proposed by leading experts of Rosgidromet. Much attention is paid to the formation and updating of the database of meteorological parameters. Large datasets of regular meteorological observations make it possible to more accurately assess the trends in climate changes occurring on the Spitsbergen.

At the first stage of the work, preparation of an analysis of changes in the average annual and average seasonal air temperature, it became necessary to divide the year into climatic seasons. In this regard, the method proposed by B. A. Yakovlev for determining the climatic seasons on the Kola Peninsula (Yakovlev, 1961). The main criterion is the average monthly variability of the average daily air temperature calculated by the formula:

$$\Delta T = \frac{1}{n} \sum_{k=1}^{k=n+1} [T_{k=1} - T_k], \tag{1.3.1}$$

here n is the number of days in a month; $\sum_{k=1}^{k=n+1} [T_{k=1} - T_k]$ – is the sum of the absolute values of the difference in the values of the average daily temperature for neighboring days from the first day of the current month to the first day of the next month.

Table 1.3.1. shows the values of day-to-day variability of air temperature generalized by months for the observation period from 1948 to 2015.

Table 1.3.1

**Day-to-day variability of average daily air temperature ($T^{\circ}\text{C}$)
at “Barentsburg” Hydrometeorological observatory**

Month.....	I	II	III	IV	V	VI	VII	VIII	IX	X	XI	XII
$T^{\circ}\text{C}$	3.2	3.5	3.2	2.6	1.4	0.9	1.1	0.9	1.3	2.0	2.6	3.0

The Table shows that in the period from October to April, the values of day-to-day variability are maximum and exceed the average annual value; this period entirely refers to the winter season. In May, the value of day-to-day variability decreases drastically, and this month was assigned to the spring season. In June and August, the values of day-to-day variability are approximately equal and reach the minimum values for the year; this period refers to the summer season; in September, the value of day-to-day variability increases drastically, and that month refers to the fall season.

Regardless of the characteristic of day-to-day variability of the average daily air temperature, the year was divided into season in the same way according to the average monthly frequency of wind direction.

The increase in average annual air temperature, which is observed throughout the territory of the Russian Federation, is maximum on the coast of the Arctic Ocean (Report on the climate in the Russian Federation for 2015, 2016). Analysis of data on changes in anomalies in average annual air temperature in the Spitsbergen confirms that the average annual air temperature increases faster in recent decades (Fig. 1.3.2).

The rate of average annual air temperature rise in Barentsburg since the mid-1970s is estimated by the value of the coefficient of the linear trend of anomalies in average annual air temperature, which is 0.92 $^{\circ}\text{C}$ for ten years for the observation period from 1976 to 2015. For comparison, we present data for the Kola Peninsula, where the rate of average annual air temperature rise is 0.60 $^{\circ}\text{C}$ for ten years (Fig. 1.3.3), and on average throughout the Russian Federation (according to the Rosgidromet report on climate change in 2015) it is 0.45 $^{\circ}\text{C}$ for ten years.

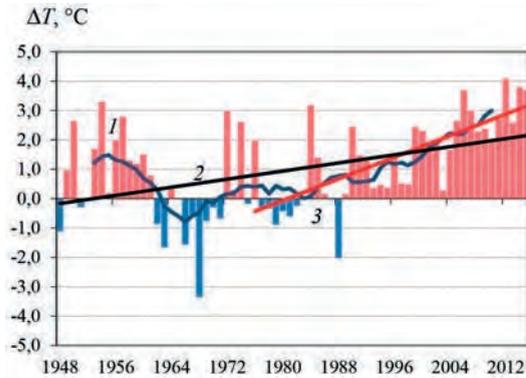


Fig. 1.3.2. Anomalies in the average annual (January–December) air temperature (°C) for the observation period from 1948 to 2015, according to “Barentsburg” Hydrometeorological observatory.
 1 – the results of the 11-year moving average, 2 and 3 – linear trends for the periods of 1948–2015 (2) and 1976–2015 (3).

In the 21st century, many records of average annual air temperature were broken on Spitsbergen: the year 2012 in Barentsburg became the warmest for the entire observation period (Antsiferova et al., 2014): a positive anomaly in the average annual air temperature was 4.1 °C. The second warmest year was 2014, the anomaly in which was only 0.3 °C less than in the record year 2012. The third place was shared by 2006 and 2015, with an average annual air temperature anomaly of 3.7 °C.

The average monthly and annual air temperatures in the 21st century (2001–2015), in comparison with the climate norm (1961–1990), are shown in Fig. 1.3.4 and Table. 1.3.2. Table 1.3.2 shows that the most enormous increase in average monthly air temperature is observed in the winter months. The average seasonal temperature in the 21st century in winter is 3.5 °C higher than the climatic norm, in spring – 1.8 °C, in summer – 1.1 °C, in fall – 1.2 °C.

The maximum rate of average seasonal air temperature rise in Barentsburg is observed in winter: the value of the linear trend coefficient for the observation period

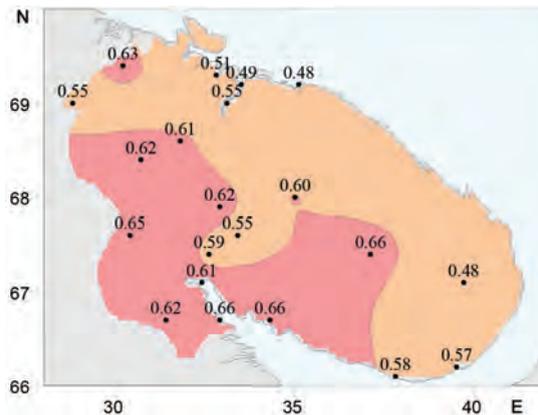


Fig. 1.3.3. The rate of average annual air temperature rise (°C for ten years) on the Kola Peninsula.

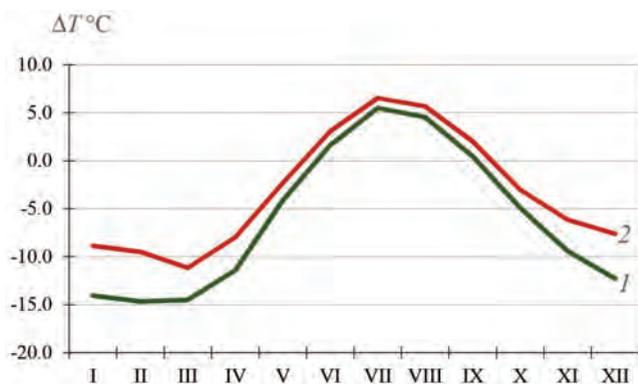


Fig. 1.3.4. The average monthly air temperature.

1 – the average for the observation period of 1961–1990, 2 – the average for the observation period of 2001–2015.

Table 1.3.2

The average monthly and annual air temperature (°C) in Barentsburg during the observation periods of 1961–1990 and 2001–2015

Period	I	II	III	IV	V	VI	VII	VIII	IX	X	XI	XII	Year
1961—1990	-14.1	-14.7	-14.5	-11.4	-4.1	1.6	5.5	4.5	0.5	-4.9	-9.4	-12.3	-6.1
2001—2015	-9.1	-9.9	-11.5	-8.1	-2.4	3.0	6.4	5.7	1.7	-3.6	-6.7	-7.9	-3.5

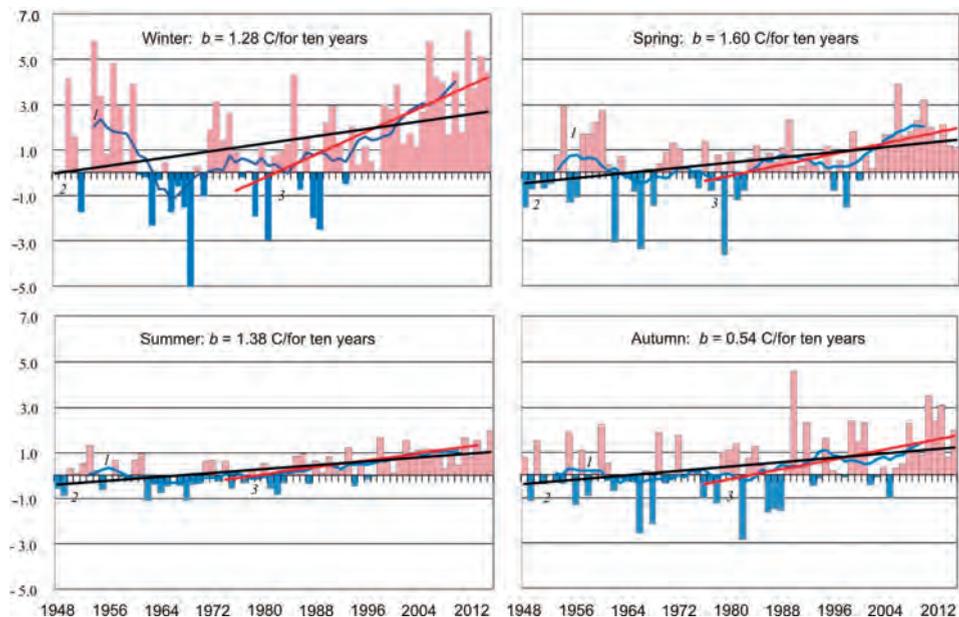


Fig. 1.3.5. Anomalies in seasonal air temperatures (°C) for the observation period from 1948 to 2015, according to “Barentsburg” Hydrometeorological observatory.

1 – the results of the 11-year moving average, 2 and 3 – linear trends for the periods of 1948–2015 (2) and 1976–2015 (3); b – the coefficient of the linear trend.

1976–2015 is 1.28 °C/10 years; in summer, the coefficient value is 0.38 °C/10 years, in the spring – 0.60 °C/10 years and in fall 0.54 °C/10 years.

Fig. 1.3.5 shows the series of seasonal air temperature anomalies in Barentsburg. Anomalies are calculated as a deviation from the average for 1961–1990.

For an almost seventy-year observation period in Barentsburg, six of the ten warmest winters were recorded from 2001 to 2015. The warmest was winter 2011–12 when the anomaly in the average seasonal air temperature was 6.3 °C (Antsiferova et al. 2014).

ANALYSIS OF THAWS DURATION IN THE WINTER PERIOD

An increase in air temperature leads to a significant increase in the number of days with a thaw in the winter months, i.e., such days when contrasted with steady sub-zero temperature, the air temperature rises to 0 °C and above. Table 1.3.3 presents the values of the average and the largest number of days with a thaw for the observation period from 2001 to 2015 in comparison with the climate norm for 1961–1990.

Table 1.3.3

The average and the largest number of days with a thaw in the winter (October–April)

Specifics	X	XI	XII	I	II	III	IV	Winter
The largest number of days is 2001–2015	17	15	14	18	11	9	20	75
The average number of days is 1961–1990	9.9	5.2	3.6	3.7	2.8	3.4	3.0	31.4
The average number of days is 2001–2015	10.6	6.7	6.7	6.9	4.1	2.9	5.7	43.8

An increase in the average number of thaw days is observed in all winter months except March. In mid-winter, the average number of days with a thaw was almost double as much as the climatic norm. In January 2006, 2010, 2012, and 2014, there were from 13 to 18 days with a thaw. Generally, such a significant increase in air temperature in the middle of winter is associated with the advection of warm, humid air from the North Atlantic. In recent years, weather forecasters have noted a shift in the trajectory of North Atlantic cyclones to higher latitudes; the frequency of intense cyclones increases, and warm and humid air enters Spitsbergen with a south wind.

ANALYSIS OF CHANGE IN EXTREMELY HIGH AND EXTREMELY LOW AIR TEMPERATURE BY SEASONS OF THE YEAR

When contrasted with an increase in the average annual and average seasonal values of air temperature, the most interesting is the change in the frequency of extreme temperature values. The limits of the temperature extremes for each season were determined from the series of maximum and minimum daily air temperatures in ascending order for the observation period from 1948 to 2015. The meteorological value corresponding to the 95 or 5 % interval was considered limiting (Table. 1.3.4). The number of days for each season of each year was calculated when the values of the daily minimum and maximum air temperatures exceeded the limit value. Such an approach to the values of the series, when a 5 % part of it is considered extreme, was also used by Bulygina et al. (2000).

Table 1.3.4

The limits of the seasonal temperature extremes at Barentsburg

Temperature	Winter	Spring	Summer	Fall
T_{\max} , °C	2.5 ... 8.5	3.1 ... 9.9	11.5 ... 20.3	7.5 ... 12.1
T_{\min} , °C	-26.2 ... -39.8	-13.6 ... -22.5	-1.7 ... -9.2	-5.8 ... -12.2

Table 1.3.5

The average and the maximum number of days with extremely high values of air temperature by seasons compared to climate norm

The number of days per season	Winter	Spring	Summer	Fall
Average for the period 1961–1990	9.7	1.5	4.9	1.3
Average for the period 2001–2015	13.1	1.6	6.1	2.7
The largest number for the period 2001–2015	26	9	13	8

Table 1.3.6

The average and the maximum number of days with extremely low minimum air temperatures by seasons compared to climate norm

The number of days per season	Winter	Spring	Summer	Fall
Average for the period 1961–1990	17.0	2.5	5.9	2.2
Average for the period 2001–2015	1.6	0.1	1.1	0.9
The largest number for the period 2001–2015	11	1	8	5

Table 1.3.5 and 1.3.6 present the average and the largest number of days with extreme values of the maximum and minimum air temperatures for different observation periods.

During the observation period from 2001 to 2015, the average and the maximum number of days with extremely high values of air temperature in winter exceeds the climatic norm by almost 1.4 and 2.7 times, respectively.

In spring, the average number of days with extremely high values of air temperature in comparison with the climate norm has changed little.

In summer, the number of days with extremely high air temperatures in the 21st century increased by 1.2 days compared to the climate norm. In summer 2015, 13 such days were recorded.

In fall, the average number of days with extremely high air temperatures in comparison with the climate norm doubled, and the largest number was noted in the warmest year of 2012 for the entire observation period.

During the observation period from 2001 to 2015, the average number of days with extremely low values of air temperature in winter decreased by more than ten times. Even the largest observed number of days with extremely low air temperatures (11 days in winter 2003–04) is less than the climatic norm.

On average, during the observation period from 1961 to 1990, 2.5 days with extremely low air temperatures were observed in spring. Over the past fifteen years, only two cases have been recorded – in 2002 and 2003.

In summer, the number of days with extremely low air temperatures decreased by more than five times compared with the climate norm. Only eight such days were noted in the summer of 2001.

In fall, extremely low air temperatures began to be observed two times as less as during the observation period from 1961 to 1990. Only five days with extremely low air temperatures were noted in 2005.

The results of a study of changes in the temperature regime on the Spitsbergen indicate ongoing warming. The increase in average annual air temperature in Barentsburg is higher than on the Kola Peninsula and higher than the average in the Russian Federation. The highest rate of increase in average air temperature is observed in winter, which in Barentsburg lasts from October to April inclusive. In the 21st century, there has been an

increase in the number of days with a thaw in winter, as well as an increase in the number of days with extremely high values of maximum air temperature and a decrease in the number of days with extremely low values of minimum air temperature in all seasons.

ANALYSIS OF CHANGE IN ANNUAL (SEASONAL) PRECIPITATION TOTAL

Spitsbergen belongs to the area of excessive moistening. According to the “Barentsburg” Hydrometeorological Observatory, on average, the archipelago has about 570 mm of precipitation per year, the number of days with total precipitation of at least 0.1 mm is 198. Precipitation in the form of snow prevails. The snow cover reaches its maximum in April. According to long-term average data, the formation of a stable snow cover takes place in the last days of September, and the melting occurs in the middle of June.

The climate seasons on Spitsbergen are significantly different from the calendar ones: the period from October to April is the winter season, May is spring, June to August is summer, September is fall. Therefore, the assessment of changes in the precipitation regime in Barentsburg was carried out for two periods: warm (June through September inclusive), when liquid precipitation prevails, and cold (October through May), when the main precipitation form is snow. The change in annual precipitation total was estimated for the calendar year (January through December). To simplify the comparison of data for different periods, the data are averaged within the periods. Precipitation totals are expressed in mm/month, i.e., are scaled to monthly precipitation totals.

Fig. 1.3.6. shows the time dependence of changes in the anomalies of annual precipitation and precipitation for the warm and cold periods. Anomalies are calculated as deviations from the average for 1961–1990. The smoothed curve is obtained by an 11-year moving average. Linear trends are based on data for the periods 1966–2015 and 2001–2015.

In the cold season, the linear trend of precipitation anomalies is practically zero. In the warm season, there is a decrease in precipitation. However, the dynamics of precipitation over the past fifteen years are of particular interest, since during this period, one can observe the highest increase in the average air temperature both for the whole year and for each season.

The observation period from 2001 to 2015 tends to the increase of precipitation both in the cold and warm periods of the year. The values of the linear trend coefficient are 2.7 mm/month for ten years for the cold season and 9.8 mm/month for ten years for the warm period.

Comparing the precipitation regime in Barentsburg and the Kola Peninsula, one should note that the Kola Peninsula generally has 2–2.5 times as much precipitation in the summer months as in winter, and its intensity is much higher. In summer, daily precipitation of more than 10 mm is typical. This amount of precipitation may occur several times a season. In winter, days with total precipitation of more than 10 mm are much rarer; by far not every year daily precipitation of up to 0.5 mm prevails (Yakovlev, 1961).

In Barentsburg, the situation is the opposite: in the winter months, precipitation is 1.5–2 times as much as in summer. Intensive precipitation (10 mm or more per day) is observed annually in almost every month of the cold season. In the warm period, such precipitation is much less common. During the warm period, June through September, the average precipitation is 146 mm, and 1998 became the “driest” year when archipelago had less than 44 mm of precipitation (July 1998 became the warmest over the entire observation period). The warm 1980 was the rainiest year; it had 265 mm of precipitation. The cold period has, on average, 424 mm of precipitation. The cold period of 2011–2012 had the most significant amount of precipitation (563 mm). Moreover, in general, 2012

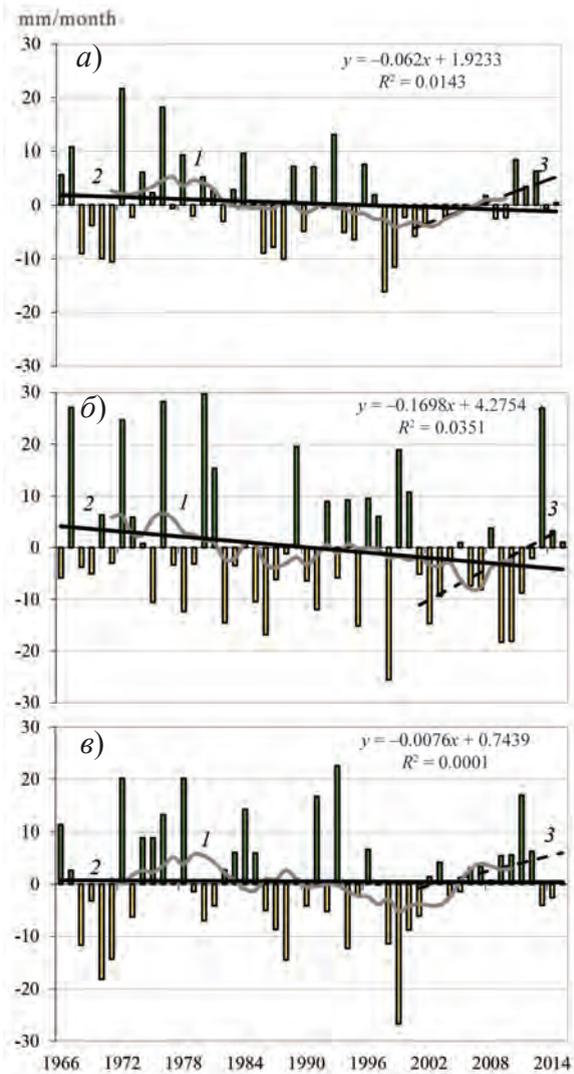


Fig. 1.3.6. Anomalies in the annual precipitation total (a) and precipitation total for the cold (b) and warm (c) period (mm/month).

1 – the results of the 11-year moving average, 2 and 3 – linear trends for the periods of 1948–2015 (2) and 1976–2015 (3).

(and, in particular, winter 2011/12) was the warmest year for the entire observation period in Barentsburg. The cold period of 1986–1987 had the least precipitation (234 mm).

Table 1.3.7 shows the average annual and monthly precipitation for two periods: 1961–1990 (climate norm) and 2001–2015, as well as deviation from the norm (ΔR).

There were no changes in the average annual precipitation compared to the climate norm. A significant deviation from the norm is observed only in particular months: in June – a decrease in the average precipitation by 28 %, and in October and November – an increase by 20 and 17 %.

Table 1.3.7

Average monthly and annual precipitation (mm) for 1961–1990 (R_1) and 2001–2015 (R_2) and deviation from the norm (ΔR %)

Parameter	I	II	III	IV	V	VI	VII	VIII	IX	X	XI	XII	Год
R_1 mm	59	56	57	43	27	25	30	39	53	60	60	58	567
R_2 mm	60	52	58	38	27	18	29	34	50	72	70	58	566
ΔR %	102	93	102	88	100	72	97	87	94	120	117	100	100

The main factor for precipitation formation on the Spitsbergen in the cold season is the advection of warm and humid air from the North Atlantic. Southern air streams that bring saturated air “provide” a large amount of precipitation in Barentsburg. In the warm period, cyclonic activity decreases, and the amount of precipitation decreases accordingly.

ANALYSIS OF CHANGE IN DURATION OF HEAVY PRECIPITATION (TOTAL OF 10 MM AND MORE)

Heavy snowfalls and rains cause additional difficulties for conducting business on a climatically difficult inaccessible territory. During the observation period from 1966 to 2015, there was a tendency to a decrease in the total number of days with precipitation in the warm period. This trend is noted both for light precipitation, the daily amount of which does not exceed 0.5 mm, and for heavy precipitation (total of 10 mm or more). During the observation period from 2001 to 2015, the number of days with precipitation increased (Fig. 1.3.7).

In the cold season, the number of days with precipitation over the 50-year observation period has changed little, but over the past fifteen years, it has increased. The value of the linear trend coefficient is small, so we can only talk about the emerging trend.

In Barentsburg, solid and mixed precipitation is possible in any of the months of the warm period, as well as liquid precipitation is possible in any of the months of the cold season. According to long-term average data, the duration of liquid precipitation in the warm season is about 400 hours or 69 % of the total duration of all types of precipitation; solid precipitation is about 100 hours (17 %), mixed – 80 hours (14 %). In the cold season, the duration of liquid precipitation is only 6 %, mixed – 6 %, solid – 88 %.

From 2001 to 2015, during the cold season, there is an increase in the duration of solid and mixed precipitation, and the duration of liquid precipitation is practically

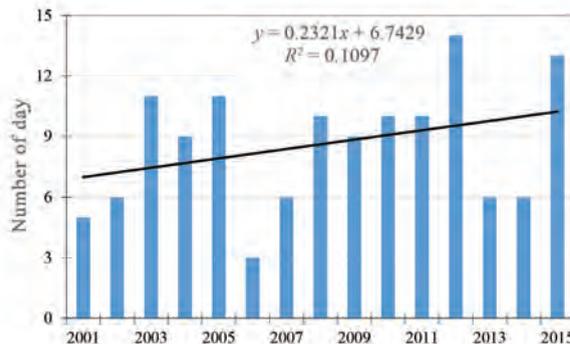


Fig. 1.3.7. The number of days with daily precipitation of 10 mm or more in the cold season. A straight line shows a linear trend.

unchanged. In the warm season, an increase in the duration of liquid and mixed precipitation and a decrease in the duration of solid precipitation is observed. Thus, the analysis of changes in precipitation in Barentsburg allows us to draw the following conclusions. The observation period from 2001 to 2015 tends to the increase of precipitation both in the cold and warm periods of the year and a slight increase in the number of days with heavy precipitation. The duration of liquid precipitation in the cold season is practically unchanged; the amount of solid and mixed precipitation increases. During the warm season, the duration of liquid and mixed precipitation increases, and the duration of solid precipitation decreases.

**ANALYSIS OF CHANGE IN THE HEIGHT
OF THE SNOW COVER
(BY THE PERMANENT SNOW STAKE IN THE METEOROLOGICAL PLATFORM)**

Snow cover has a significant impact on the formation of temperature during the cold season. When snow cover is established, a more significant cooling is usually observed than in the same weather, but there is no snow. Melting of the snow cover requires a significant input of heat brought by the masses of warm air or coming from solar radiation. Therefore, when there is snow cover in spring and winter, thaws are less intense than if there is no snow (Yakovlev, 1972).

During the observation period from 2001 to 2015, stable snow cover in Barentsburg was observed on average from September 30 to June 12. In some years, depending on weather conditions, the dates of formation and destruction of stable snow cover can vary significantly. So, in 2006 the snow cover melted on May 27 and in 2008 on July 1st. However, for a short time, snow cover can be formed in any of the summer months.

“Barentsburg” Hydrometeorological observatory conducts daily observations of the height of the snow cover at the meteorological platform, determines the extent of snow coverage in the visible neighborhood of the station.

In Fig. 1.3.8 presents the average decade and the largest average decade height of the snow cover at the meteorological platform for the observation period from 2001 to 2015.

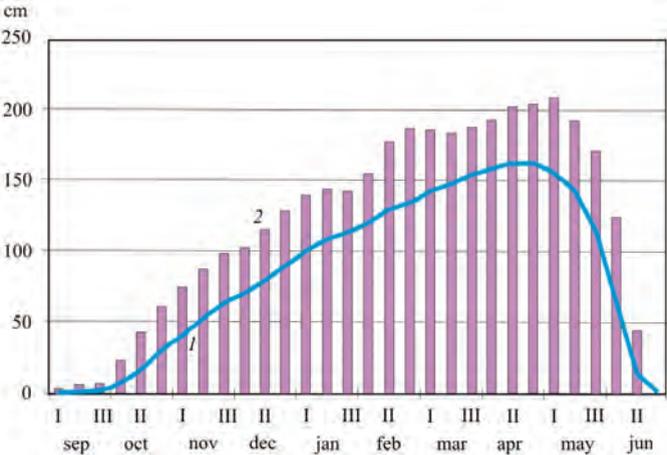


Fig. 1.3.8. The average (1) and the greatest (2) decades-long snow height (cm) at a meteorological platform.

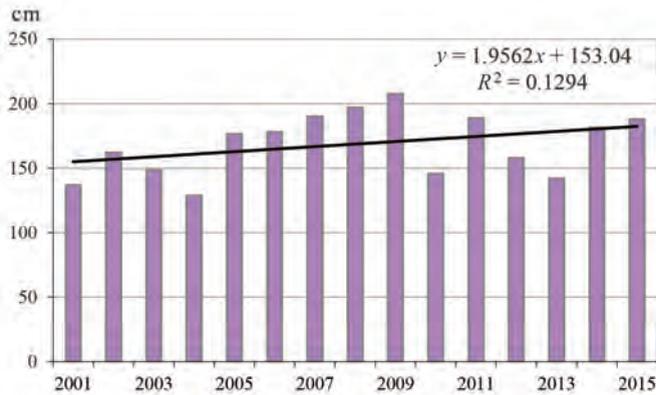


Fig. 1.3.9. The highest decade snow height (cm) at the meteorological platform for the observation period 2001—2015.

A straight line shows a linear trend.

Snow cover reaches its highest level in the second and third decades of April. In some years, at the end of the winter period, snow height can be more than 200 cm. Figure 1.3.9 presents the change in the largest average decade snow height for the observation period from 2001 to 2015.

A positive value of the linear trend coefficient indicates a tendency to increase the highest decade winter snow height in the 21st century. The maximum level (208 cm) was recorded in 2009. Over the entire observation period at this meteorological platform, the maximum snow height was recorded in 1993 and amounted to 235 cm.

Thus, when contrasted with an increase in average seasonal air temperature in winter and a tendency to increase precipitation in the cold season, in Barentsburg, there is an increase in the highest decade winter snow height for winter.

CHARACTERISTIC OF WIND PATTERN

Very difficult terrain affects the features of the wind pattern of the Barentsburg. The hydrometeorological observatory is located near the coast of the Greenland Sea on the eastern shore of the Grønfjorden, which is the southern branch of the Isfjorden – the largest on the Spitsbergen.

The surrounding area has mountainous relief. The height of the mountain peaks ranges from 200–800 m above sea level. Mountain peaks are cut by numerous valleys with broad slopes and screes, some of which are covered with glaciers. The Barentsburg is located on the terrace-shaped section of the coast at the foot of the bordering the mountain area. The central part of the village is located on the terrace with elevations of 60–70 m above sea level.

Fig. 1.3.10 and Table 1.3.8 present the average seasonal frequency of the wind direction, expressed in fractions (%) of the total number of observations for the season excluding the windless conditions. The frequency of windless conditions is given in fractions (%) of the total number of observations for the period 2001–2015.

The frequency of the north wind in all seasons of the year is practically unchanged. In winter, the wind of eastern directions prevails, the total frequency of which exceeds 60 %. The direction of the transfer of air masses largely depends on the distribution of

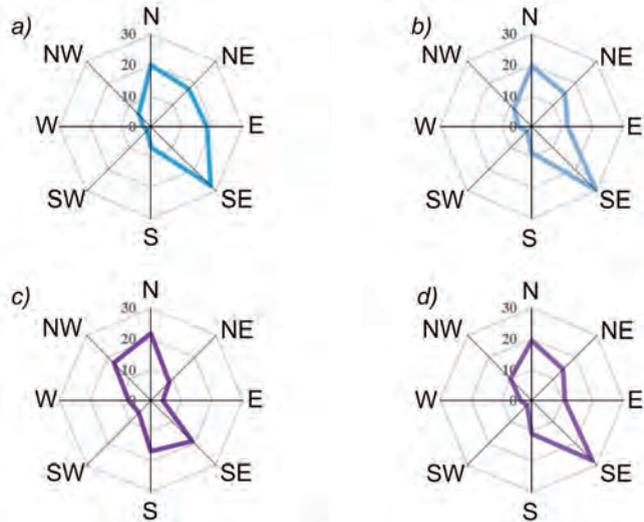


Fig. 1.3.10. Average seasonal frequency (%) of wind direction.
a – winter, *b* – spring, *c* – summer, *d* – fall.

Table 1.3.8

Average seasonal frequency of wind direction and windless conditions (%)

Season	Points of the compass								Windless conditions
	N	NE	E	SE	S	SW	W	NW	
Winter	20	17	18	27	7	2	2	6	12
Spring	20	15	12	30	9	2	4	8	13
Summer	22	8	4	19	17	6	7	17	9
Autumn	20	14	11	28	11	2	4	10	13
Year	20	15	14	26	10	3	4	9	11

atmospheric pressure on the earth's surface. In Barentsburg, the lowest pressure falls upon December–January, when the frequency and intensity of cyclones moving from the West Atlantic increase. As a rule, east winds are associated with the trajectory of the cyclones, which in winter passes south of the Spitsbergen.

In spring, the frequency of the eastern winds begins to decrease, the frequency of the western winds increases. The highest pressure falls upon in May. In the summer, the frequency of the south wind and the winds of the western directions increases. In fall, the synoptic processes switch to a winter regime, and the frequency of eastern winds increases again.

The average wind speed has a well-defined annual course with its maximum in the winter and its minimum in summer (Fig. 1.3.11).

An increase in the intensity and frequency of cyclones in winter also leads to an increase in the number of days with a gale (with gusts of 15 m/s or more) (Table 1.3.9). On average, one can observe 4–7 days with a gale a month. In some years, the number of days with a gale reached 17 (December 2001), and in general, in 2001 amounted to 70 days.

In summer, due to a decrease in the frequency of cyclones and an increase in the frequency of anticyclones, the number of days with a gale is sharply reduced. The average number is less than one day, and the largest does not exceed three days.

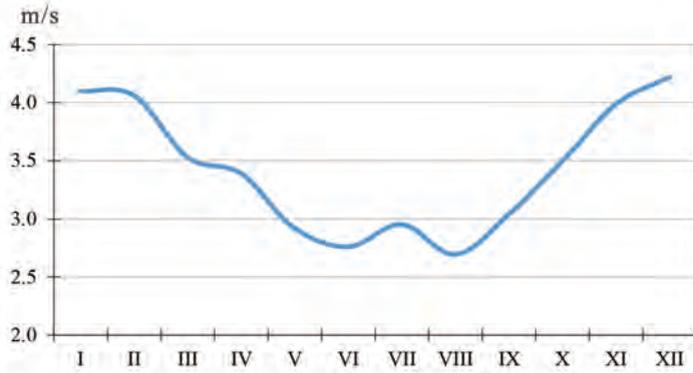


Fig. 1.3.11. The annual course of the average wind speed (m/s).

Table 1.3.9

The average monthly and the annual number of days with a gale for the observation period of 2001–2015

Month...	I	II	III	IV	V	VI	VII	VIII	IX	X	XI	XII	Year
Number of days...	6.7	5.2	5.5	3.6	1.4	0.7	0.7	0.7	2.3	3.7	6.3	6.6	43.3

According to the list of dangerous meteorological phenomena and their criteria, in the area of responsibility of the Murmansk UGMS, the most frequently repeated dangerous meteorological phenomenon is strong wind (maximum wind speed in gusts is at least 25 m/s). According to the long-term average data summarized for the observation period 2001 through 2015, in Barentsburg, one day a year has wind with a gust of 25 m/s or more. In some years, one could note up to three days with a strong wind. The repeatability of strong winds has a well-defined annual course with its maximum in the cold season and its minimum in warm weather (Table 1.3.10).

Table 1.3.10

The average and the largest number of days with a maximum gust of wind of 25 m/s or more

Month...	I	II	III	IV	V	VI	VII	VIII	IX	X	XI	XII	Year
The average number...	0.4	0.1	0.3	0.1	0	0	0	0	0	0	0	0.1	1.0
The largest num-ber...	2	1	3	1	0	0	0	0	0	0	0	1	3

The frequency of dangerous wind in Barentsburg is less than, for example, in Murmansk or on the coast of the Barents Sea (Teriberka Hydrometeorostation (HMS)). In Murmansk, there are about three days per year with a gust of 25 m/s or more, and in some years, one noted up to eight days with a strong wind. According to the Teriberka HMS, on average, over a year, there are more than twenty days with a maximum gust of 25 m/s or more per day. Of course, the small frequency of dangerous winds in Barentsburg is associated with the specifics of the geographical location of the village as well as its surrounding, the mountains.

REFERENCES

Antsiferova A.N., Mokrotovarova O.I., Siekkinen E.D. Climate change on the Spitsbergen archipelago. Climate pattern during winter of 2013-14. *Kompleksnyye issledovaniya prirody Shpitsbergena*. Comprehensive studies of the nature of Spitsbergen. 2014, 12: 16–21. [In Russian].

Bulygina O.N., Korshunova N.N., Razuwayev V.N., Shaimardanov M.Z., Shvets N.V. Variability of extreme climatic phenomena on the territory of Russia. Trudy VNIIGMI — MCD. Proc. of the RIHMI – WDC (All-Russian Research Institute of Hydrometeorological Information – World Data Centre). 2000, 187: 16–31. [In Russian].

Davydov A.A., Antsiferova A.R. Climate change in Barentsburg from 1960 to 2005 in the values of average annual temperature and temperature extremes. *Kompleksnye issledovaniya prirody Shpicbergena*. Comprehensive studies of the nature of Spitsbergen. 2007, 7: 140–148. [In Russian].

Doklad ob osobennostyah klimata na territorii Rossijskoj Federacii za 2015 god. Report on the climate in the Russian Federation for 2015. Moscow, 2016: 107 p. [In Russian].

Oganesyan V.V. Climate changes in Moscow from 1879 to 2002 in the values of the extremes of temperature and precipitation. *Meteorologija i gidrologija*. Meteorology and Hydrology. 2004, 9: 31–37. [In Russian].

Savatyugin L.M., Dorozhkina M.V. Arhipelag Shpicbergen: rossijskie imena i nazvanija. Spitsbergen archipelago: Russian names and titles. St. Petersburg: Nauka, 2009: 259 p. [In Russian].

Semyonov A.V. *Gidrometeorologicheskie nabljudenija na arhipelage Shpicbergen*. Hydrometeorological observations on the Spitsbergen archipelago. *Nauka na Shpicbergene: Istorija rossijskih issledovanij*. Science on Spitsbergen: History of russian studies. St. Petersburg: GAMAS, 2009: 390–394. [In Russian].

Semyonov A.V., Antsiferov A.R., Davydov A.A. The climate of Barentsburg. Measurements of the main characteristics over the past 40 years (according to observations of the “Barentsburg” Hydrometeorological Observatory). “*Materialy II Mezhdunarodnoj konferencii Kompleksnye issledovaniya prirody Shpicbergena*”. Proc. of the II International Conference “Comprehensive Studies of the Nature of Spitsbergen”. 2002, 2: 139–145. [In Russian].

Yakovlev B.A. *Klimat Murmansknoj oblasti*. The climate of the Murmansk region. Murmansk: Murmansk Book Publishing House, 1961: 200. [In Russian].

Yakovlev B.A. *Klimat Murmanska*. The climate of Murmansk. Leningrad: Gidrometeoizdat, 1972: 108. [In Russian].

1.4. COMPARISON OF THE FIRST AND MODERN WARMING IN THE ARCTIC ON THE EXAMPLE OF THE SPITSBERGEN

B.V. Ivanov, D.I. Tislenko, P.N. Svyashchennikov, K. Isaksen, Ye. Forland, O. Nordli, H. Gjetlen

In recent decades, the climate of our planet has been undergoing major changes. The most noticeable climatic changes are observed in the Arctic region, and in particular, a record decrease in the area of ice cover, an increase in the temperature of Atlantic waters (AW), and an increase in surface air temperature (SAT). All this together indicates significant warming observed in the Arctic in the last decades of the 20th century and the first decade of the 21st century. Russian and foreign researchers have already recorded similar processes in 1920–1940, and they aroused great scientific interest, which resulted in some hypotheses about the causes of the observed phenomenon.

Before proceeding to a review of previous studies on the causes of warming in the Arctic, recorded in the first half of the 20th century and the modern period, we clarify such an important concept as the climate norm. Per the fundamental works (Gruza, 2012; Gruza, Rankova, 2012), a 30-year time interval (1961–1990) is used as a standard period for assessing the climatic variables characterizing the modern climate. The term “climate norm” or “WMO norm” means the average value of a variable for the period specified above, and the deviation of this value from the norm is called an anomaly. According to the leading climate scientists (Gruza, 2012; Gruza, Rankova, 2012), taking into account the current state of the climate system and the observed changes, the time interval for determining the *modern climate* needs to be clarified. Hereafter we specify this new time interval.

REVIEW OF PREVIOUSLY PUBLISHED STUDIES

The Arctic is an essential part of the planetary climate system connected with other parts through the transfer of heat and moisture in the atmosphere and ocean (Alekseev, 2003; Nikiforov and Speicher, 1980).

The observed climate changes in the Arctic over the past decades amid global warming are of great interest to modern researchers. This section attempts to summarize the views of some modern Russian and foreign scientists on the main climate changes (climate trends) observed in the Arctic region over the 20th century and the first decade of the 21st century using the example of the Spitsbergen archipelago.

To assess climate change on a regional scale, the most frequently used information is SAT (Alekseev, 2003; Gruza, Rankova, 2012). Fluctuations in air temperature on the Spitsbergen archipelago, measured during a century, indicate two main periods of warming: 1920–1940s and 1980–2010s (Nordli, Isaksen, 2012; Nordli et al., 2014). The average annual air temperature varied significantly throughout the twentieth century and reached maximum values in the periods 1920–1940 and 1980–2010.

It should be noted that the so-called first warming attracted the attention of researchers in the first half of the last century. So, V.Yu. Vize, in his work “Causes of Arctic Warming” (1937) described this period as the most considerable climatic fluctuation, recorded at that time by regular meteorological observations. He noted that air temperature increased not only in the cold season but also on average per year; at the same time, the average annual

air temperature on Svalbard turned out to be 1.7 °C higher than the long-term average. The author concluded that the warming of the Arctic was the result of an increase in the general circulation of the atmosphere on the globe. It is associated with the intensification of all atmospheric action centers, in particular the Icelandic minimum and the Siberian maximum, at which the flow of water and ice from the Arctic basin (AB) to the Greenland Sea was enhanced. Searching for the cause of that severe anomaly, which resulted in such exceptional warming in the Arctic and a decrease in the ice cover of the Arctic seas, V.Yu. Vize suggested that, since the anomaly covered the entire globe, the cause should be sought outside the Earth – most likely, in changes in solar activity (Vize, 1937).

Some studies examine climatic changes in the Arctic that occur during modern warming (from the late 1980s to the present) (Alekseev et al., 2009; Alekseev, 2015). The authors note that during this period, there is a sharp reduction in the area occupied by sea ice at the end of the summer period, as well as the spread of positive water temperature anomalies in the intermediate layer of AW in AB. It was shown that there is a sharp increase in the average values of the SAT for the winter (after 1998) and summer (after 1996) months. The maximum values were recorded in 2012. Comparison of the warming periods of 1920–1940 and 1990–2000 was carried out on the example of data from 30 weather stations located north of 60° N (Alekseev et al., 2010). The analysis was performed both for individual seasons of the year: winter (average SAT for November–March) and summer (average SAT for June–August), and for average values for the year. Linear trends estimated the rate of warming development for specific periods (growth phases of SAT). Based on the analysis done, it was concluded that the first warming was faster than warming in the period 1980–2000.

The phases of the so-called low-frequency fluctuations of the climate system with a period of 50–80 years are considered as one of the causes of the identified warming (Polyakov et al., 2004). The positive phase of the low-frequency fluctuation includes an increase in the influx of warm AW and warm air from the North Atlantic to the Arctic, the rise of the upper AW border to the surface and the intensive removal of excess ice and freshwater through the Fram Strait due to increased cyclonic activity. An increase in anticyclonic ice drift and anticyclonic surface circulation, the convergence of surface currents, and also deepening of the AW layer are typical for the negative phase. A significant similarity between the variability of AW temperature and the variability of key atmospheric parameters suggests a close connection between large-scale atmospheric circulation and ice and ocean conditions.

When assessing the role of meridional transport in the atmosphere in enhancing warming in the northern region, it was shown that the intensification of meridional transport makes a significant contribution to the observed trend of the average SAT in the Arctic in the modern period (Alekseev, 2015).

V.Yu. Vize developed a hypothesis that the intensification of atmospheric circulation and solar activity are the leading causes of the first warming in the Arctic. This hypothesis is also used by other Russian specialists (Gudkovich et al., 2012). It is noted that a typical feature of climate change in our era is its cyclical nature, and cycles at intervals of 60 and 200 years are the most significant (Raspopov et al., 2004; Bashkirtsev, Mashnich, 2004). The first cycle is associated with a change in warm and cold periods, mainly in the polar and temperate latitudes, and the second one is the secular tendency, which occurs especially in temperate and low latitudes (Frolov et al., 2010b). According to some

authors, at the end of the 20th and beginning of the 21st century, the positive maxima of both cycles coincided. It ultimately led to a significant increase in the SAT, in particular, in the Arctic (Gudkovich et al., 2012). By this point of view, several Russian experts, considering modern climate changes, express an opinion on the upcoming change in the warming trend in the Arctic as a whole, and in the Spitsbergen archipelago in particular (Frolov et al., 2009; Gudkovich, Kovalev, 2002; Lyubushin, Klyashtorin, 2012). The state of polar vortices has a demonstrable effect on climate change, and the vortices themselves substantially depend on solar activity (Frolov et al., 2010a). An increase in solar activity leads to the intensification of polar vortices and an increase in western transport in the atmosphere, and a decrease in solar activity, on the contrary, leads to their weakening. In this case, the weakening of polar vortices is accompanied by an increase in the frequency of polar anticyclones and their shift to the west. Gudkovich et al. (2013) represented an analysis of the development of meteorological conditions in the Arctic for the period 2007–2013 when there was an increase in the Arctic anticyclone in the winter half of the year and its shift to the west by a distance of about 1,500 km. The intensification of the Arctic anticyclone and its shift to the west, according to the authors of this work, lead to the blocking of Atlantic cyclones. It results in intense heat transfer to the zone of the Spitsbergen archipelago and the seas of the Western Arctic (Barents, Kara).

Matishov et al. (2014) present ideas about modern climatic trends observed in the Arctic. Since the beginning of the 21st century, a prolonged warm anomaly has persisted in the Western Arctic, which is comparable in intensity to the above-mentioned first warming of the Arctic (Matishov et al., 2011; Serezze and Barry, 2011). This statement is consistent with the opinion of the AARI specialists on the existence of 60-year and 200-year cycles associated with changes in the influx of solar radiation (Gudkovich et al., 2012). According to some authors, a superposition of these cycles gives reason to believe that by 2030–2040 we will more likely have not an increase in warming, but, on the contrary, a decrease in the SAT (Matishov et al., 2014). *The modern* warming of the Arctic in the 1990s – 2000s is taking place under conditions of intensive western transport in the middle latitudes. In recent years, periodicity and, especially, the duration of anticyclonic blocking over Eurasia have increased. And it contributes to the intensification of the continental climate (Matishov et al., 2014). It is noted that the trajectories of the North Atlantic cyclones are shifted to high latitudes, which contributes to the formation of positive SAT anomalies, water surface temperature, and a decrease in the ice cover of the Arctic seas both in the warm and cold periods of the year.

A lot of Russian and foreign scientific publications are devoted to the study of climate in the area of the Spitsbergen archipelago. Changes in various components of the climatic system of the Spitsbergen archipelago during the 20th century and the first decade of the 21st century are examined in Nordli et al. (2014); Nordli, Isaksen (2012); Ivanov, Zhuravsky (2010); Tislenko, Ivanov (2015). Analysis of the temporal variability of the SAT for the period 1898–2012 was presented by Nordli et al. (2014). Based on the results obtained, one can conclude that in terms of a linear trend, we can observe an increase in the SAT by 2.6 °C for the region of the Spitsbergen archipelago over the past 100 years.

The long-term regime of the SAT is characterized by the presence of two periods of warming (1931–1960 and 1990–2010) and two periods of cooling (1901–1930 and 1961–1980). The coldest period is 1901–1930, and the modern period is characterized as a period of intensive increase in the SAT. Moreover, many authors estimated the period 2005–2014 as the warmest for all time of instrumental monitoring on the Spitsbergen archipelago.

Positive anomalies were observed, as indicated above, in other components of the archipelago’s climate system. So, in the Grøn fjorden, where the Russian mining village Barentsburg is located, according to some fundamental ice characteristics, one can observe a noticeable softening of the ice situation (Ivanov, Zhuravsky, 2010). A stable ice cover (fast ice) in most winters was absent in this period.

From the presented review, devoted to the main features of climate change in the Spitsbergen, we can conclude that long-term changes in the SAT for the entire previous period of instrumental monitoring tended to warm. The climate of the Spitsbergen archipelago tends to become milder, and this tendency is generally consistent with the well-known concept of the rapid warming of the Arctic from the 1980s to 2015 (Alekseev, 2014, 2015; Zhichkin, 2014, 2015; Polyakov et al., 2002; Bekryaev et al., 2010).

USED DATA AND PROCESSING METHODS

In this work, we used the data of NMI published in open sources (Hanssen-Bauer, 2002; Nordli, Isaksen, 2012; Nordli et al., 2014), AWI (Alfred Wegener Institute) (Maturilli et al., 2013), PAN (Polish Academy of Sciences) (Mars, Styszyńska, 2013), State Funds of SRC “AARI”, RIHMI-WDC.



Fig. 1.4.1. SAT Observation Points on West Spitsbergen.

Below you can find information on the SAT for the entire period of instrumental monitoring (including reconstructed datasets) for the following weather stations located on the Spitsbergen archipelago: Norway (Ny-Ålesund, 1934–2014; Isfjord Radio, 1934–2014; Longyearbyen, 1898–2014; Russia (Barentsburg, 1911–1930, 1932–2014; Piramiden, 1940–2014); Poland (Hornsund, 1939–2014).

The most extended series of observations (Longyearbyen) is available for monthly average SAT values (Nordli et al., 2014). The series was obtained by combining observational data carried out in Longyearbyen, as well as at the temporary observation points (expeditions of hunters, geologists, etc.) in the nearest part of archipelago. The series was formed using special interpolation methods to fill in the available gaps (Nordli et al., 2014). All of the above points are located on West Spitsbergen, the largest island of the archipelago (Fig. 1.4.1).

Until 1936, observations at weather stations were carried out three times a day: at 07, 13, 19 local solar time. From 1936 to 1966, observations were made four times a day: at 01, 07, 13, 21 local solar time. Finally, from 1966 to the present, observations are carried out eight times a day: at 00, 03, 06, 09, 12, 15, 18, 21 Moscow time (winter standard time (Manual ..., 1985).

Changes in the timing of observations and their numbers can cause systematic discrepancies in the estimates of the average daily and monthly mean values of the SAT. Usually, three- and four-time observations due to the neglect of low nighttime air temperatures at high and temperate latitudes lead to an overestimation of the actual values of the average daily SAT. Moreover, these differences depend on the season of the year, geographical latitude, and some other factors (topography, etc.). As a rule, this introduces corrections to the average values obtained as a result of three- and four-times observations, to bring them to the actual average daily or monthly values. For this, corrections are introduced into the average values of the SAT calculated based on three- and four-times observations, which correspond to the difference between the actual average and average calculated according to the data of three- and four-times observations. The actual average SAT value is calculated over ten years from hourly observations from a station thermograph. To bring the SAT to its actual value at stations where the use of a thermograph is not provided, corrections are calculated using data from nearby stations with a similar landscape where there is a thermograph (Alisov et al., 1952; Drozdov et al., 1989).

For the observation point in Barentsburg, the period 1911–1930 is represented only by long-term annual averages. These data relate to observations made at the Norwegian weather station “Spitsbergen Radio” (“Green Harbor”), located at a distance of 1.5 km south of Barentsburg at Finneset. To compare the series in 1935–1936, the specialists of the Barentsburg weather station carried out a comparative series of parallel observations at Finneset and in Barentsburg. In 2013–2015, a similar series was repeated in the framework of the Agreement and the Joint Research Program of Rosgidromet and NMI (2013–2015) by specialists of the SRC AARI. Statistical analysis methods were used (Greshilov et al., 1997; Rozhkov, 2002) to analyze the long-term variability of the SAT. The 11-year moving average was used to identify long-term trends in the time series of the SAT, represented by average values for a year or a month. The 11-year averaging period is used due to the existence of a well-known cycle of changes in solar activity (Vitinsky et al., 1986; Monin, 1969; Priest, 1985). The analysis of the long-term variability of the SAT was carried out by calculating linear trends. The coefficient α , ($^{\circ}\text{C}/\text{year}$), characterizing the angle of the trend line (Greshilov et al., 1997; Rozhkov, 2002), is taken as a numerical characteristic of a linear trend.

ANALYSIS OF TEMPORARY VARIABILITY OF SAT IN THE AREA OF SPITSBERGEN ARCHIPELAGO

Since the most extended continuous series of instrumental monitoring data on the Spitsbergen archipelago is the series obtained for Longyearbyen, it was used to objectively analyze the trends in SAT changes in the 20th century and the first decade of the 21st century. The interval from 1889 to 1900 was excluded from the series used for statistical analysis. It is due to a significant number of uncertainties in the data for this period due to the lack of reliable information about the measurement methodology, the instruments used, their accuracy class, etc. Thus, the most extended time series of average monthly SAT values covers the period from 1900 to 2014.

Fig. 1.4.2 *a* shows the temporal variability of the average annual SAT values, as well as charts constructed using a 5- and 11-year moving average filter for the indicated characteristic. The use of filters is explained by the significant interannual variability of the SAT and the need to identify the long-term patterns of temporal variability, which are interesting for us.

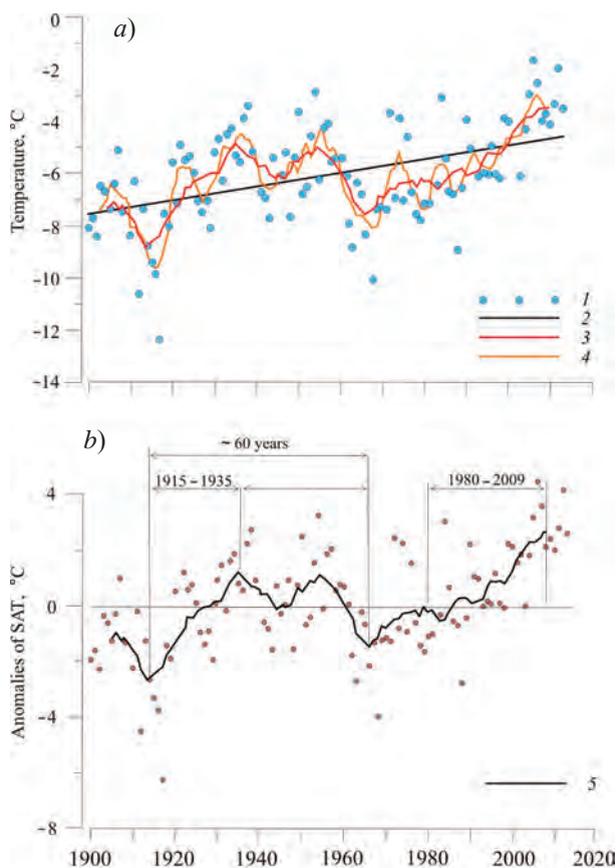


Fig. 1.4.2. The variability of annual averages (*a*) and anomalies (*b*) of SAT for the period from 1900 to 2014.

1 – surface air temperature; 2 – linear trend; 3 и 5 – 11-year moving averages; 4 – 5-year moving average.

The most marked increase in SAT is observed from about the mid-1980s to our time. It is the so-called modern period of warming. This period of a significant increase in the SAT in the area of the Spitsbergen archipelago coincides with the period of the well-known *Arctic amplification*, which is a significant increase in air temperature in 1980–2010 across the entire Arctic (Serezze, Barry, 2011). A chart of an 11-year moving average describes variability with scale over 11 years, excluding high-frequency fluctuations with a shorter period. The 11-year averaging period was chosen, as already mentioned above, is due to the existence of a well-known cycle of changes in solar activity (Monin, 1969; Vitinsky et al., 1986; Priest, 1985). The calculation of the linear SAT trend showed that warming occurred on average at a rate of 0.026 °C/year and amounted to 2.9 °C for the entire observation period (Table 1.4.1). In terms of deviations from the average, *modern* warming is more powerful compared to the *first one* (Fig. 1.4.2 b). The figure shows precisely the phases of the increase in the SAT (1915–1935 and 1980–2009) for both periods of warming, highlighted in the charts after applying the filter. The maximum deviations for the period of *modern* warming were 4.4 and 4.1 °C and were observed in 2006 and 2012, respectively. Positive deviations during the period of the *first* warming in the Arctic are much lower and amount to 2.7 and 3.2 °C (1938 and 1954). The prevalence of negative SAT anomalies corresponds to the time intervals of 1900–1925 and 1965–1980. The maximum negative deviation is 6.3 °C and was observed in 1917.

Warming values were analyzed in the area of the Spitsbergen archipelago for each month of the year separately for the selected period of instrumental monitoring. Table 1.4.1. presents the results of the analysis. The most significant warming was observed in February, March, April, and November: the SAT increase for the indicated months was 4–5 °C per century. The obtained linear trends turned out to be statistically significant at the level of $P < 0.05$. An exception is trends for January and December, which are statistically significant at the level of $P < 0.15$.

Separate analysis and comparison of the intensity were carried out according to the warming phases (1915–1935 and 1980–2009). Table 1.4.2 presents the results. The corresponding linear regression equations were calculated for time series obtained using

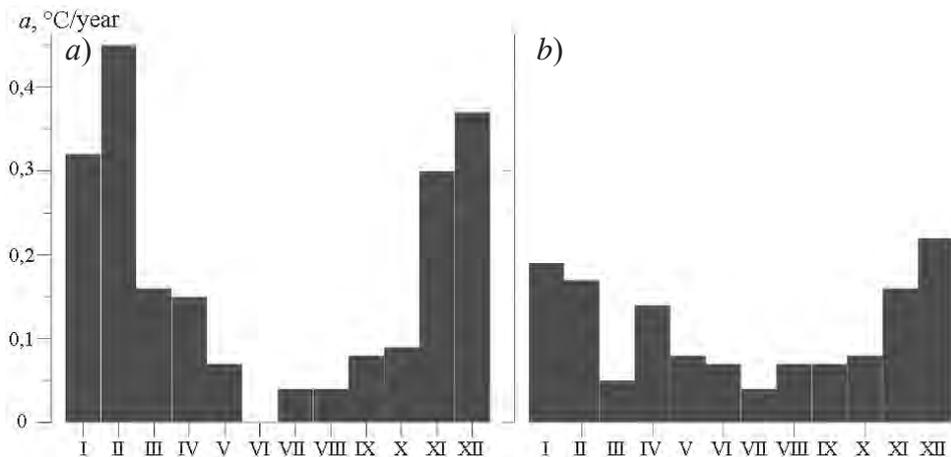


Fig. 1.4.3. Coefficients of linear trends of the monthly average SAT in the area of the Spitsbergen archipelago for the *first* (a) and *modern* (b) warming periods.

Table 1.4.1

Warming characteristic for individual periods	
Period	Coefficient a of a linear trend, °C / year
<i>January</i>	<i>0.021</i>
February	0.052
March	0.048
April	0.038
May	0.029
June	0.009
July	0.015
August	0.011
September	0.020
October	0.016
November	0.040
<i>December</i>	<i>0.019</i>
Annual average	0.026
All period (1900–2014)	2.9

Note. The months for which the linear regression equations are not statistically significant at the level of $P < 0.05$ are in italics..

Table 1.4.2

Comparison of warming periods for the Spitsbergen area		
Period	Coefficient a of linear trend,	
	°C/year	1980–2008
<i>January</i>	<i>0.32</i>	<i>0.19</i>
February	0.45	0.17
March	0.16	0.05
April	0.15	0.14
May	0.07	0.08
June	0.00	0.07
July	0.04	0.04
August	0.04	0.07
September	0.08	0.07
October	0.09	0.08
November	0.30	0.16
<i>December</i>	<i>0.37</i>	<i>0.22</i>
Year	0.17	0.11

Notes. The months for which the linear regression equations are not statistically significant at the level of $P < 0.05$ are in italics.

an 11-year moving average filter. Comparing the results obtained concerning the average annual SAT values in the area of the Spitsbergen archipelago, one may state that a more marked increase in temperature is observed for both warming periods than in general for the entire observation period (1900–2014). For the *first* warming, the coefficient of the linear SAT trend is 0.17 °C / year, for the *modern* one, it is 0.11 °C / year. Thus, both warming periods occurred at similar speeds, but at the same time, significantly

faster than in general over the entire period of instrumental monitoring ($0.026\text{ }^{\circ}\text{C} / \text{year}$). Fig. 1.4.3 presents a comparison of the manifestations of warming periods in particular months for the selected intervals. A check for statistical significance showed that trends are statistically significant at the level of $P < 0.05$, except for June during the period of the first warming. The most significant rate of SAT change is observed in the following months: November, December, January, February, March, April.

The most marked increase in SAT occurs in February for the period of the first warming and equals $0.45\text{ }^{\circ}\text{C}/\text{year}$. In general, according to monthly average estimates, both warming periods occur at a similar speed; two periods are distinguished: warm (April–October) and cold (November–March). The months from April to March are characterized by almost equal values of the rate of change in the SAT for both time intervals. For the cold period, the values of the rate of change in the SAT during the *first* warming are 1.5–2 times as much as those during the period of *modern* warming.

Let us consider the results obtained for the area of the Spitsbergen archipelago in comparison with the results presented in other works devoted to the consideration of the rate of change in the SAT in the Arctic in the 20th century. The paper presents data on current trends in the SAT in the form of the geographical distribution of linear trend coefficients in Russia for 1976–2006. (Evaluation report ..., 2008). It is worth noting that over the indicated period, for most of the territory of the Russian Arctic, there are positive values of the coefficients of the linear trend both on an annual and seasonal average, which corresponds to the modern SAT changes in Spitsbergen. Moreover, a comparison of the rate of change in the SAT in absolute value showed that modern warming is slightly more intense in the region of Spitsbergen, while the values of the linear trend coefficient are comparable. For example, the average annual values for modern warming for the Kola Peninsula region are $0.6\text{--}0.7\text{ }^{\circ}\text{C}/10\text{ years}$, and for Spitsbergen, they are $1.1\text{ }^{\circ}\text{C}/10\text{ years}$.

CONCLUSIONS

Within the scope of the analysis, we can draw the following conclusions.

According to estimates of the coefficient of linear regression for the entire period of instrumental monitoring on Spitsbergen, one can reveal an increase in SAT by $2.9\text{ }^{\circ}\text{C}$. The most significant increase in SAT is observed in February, March, April, and November and amounts to $4\text{--}5\text{ }^{\circ}\text{C}$ per century.

The rate of increase in SAT during the period of the *first* warming was $0.17\text{ }^{\circ}\text{C} / \text{year}$, and during the period of *modern* warming equals $0.11\text{ }^{\circ}\text{C} / \text{year}$. Analysis of the rate of change in the SAT for particular months of the year showed that the most marked increase in the SAT during the *first* warming is in February and amounts to $0.45\text{ }^{\circ}\text{C} / \text{year}$, which is 2.5 times as much as the average annual values for this period. Only in May and August, the period of *modern* warming is characterized by higher values of the rate of change in the SAT compared with the first warming.

The intensity of the increase in the average annual SAT in the modern period (1990–2014) is, on average, three times as much as similar estimates for the entire observation period (1900–2014). It indicates an intensification of climate warming in the archipelago in recent decades.

REFERENCES

Alekseev G.V. The Arctic Measuring of Global Warming. *Led i sneg*. Ice and Snow. 2014, 2: 53–68. [In Russian].

- Alekseev G.V. Studies of climate change in the Arctic in the twentieth century. *Trudy AANII*. Proc. of AARI. 2003, 446: 6–19. [In Russian].
- Alekseev G.V. Manifestation and intensification of global warming in the Arctic. *Fundamental'naja i prikladnaja klimatologija*. Fundamental and Applied Climatology. 2015, 1: 11–26. [In Russian].
- Alekseev G.V., Ivanov N.E., Pnyushkov A.V., Balakin A.A. Climate change in the marine Arctic at the beginning of the XXI century. *Problemy Arktiki i Antarktiki*. Problems of Arctic and Antarctic. 2010, 3 (86): 22–34. [In Russian].
- Alisov B.P., Drozdov O.A., Rubinshtein E.S. *Kurs klimatologii. Uchebnik. Chast' I, II*. Climatology course. Study book. Part I, II. Leningrad: Gidrometeoizdat, 1952: 487 p. [In Russian].
- Bashkirtsev V.S., Mashnich G.P. The changeability of the Sun and the climate of the Earth. *Solnechno-zemnaja fizika*. Solar-terrestrial physics. 2004, 6: 135–137. [In Russian].
- Vize V.Yu. Causes of Arctic warming. *Sovetskaja Arktika*. Soviet Arctic. 1937, 1: 10–19. [In Russian].
- Vitinskij Yu.I., Kopecky M., Kuklin G.V. *Statistika pjatnoobrazovatel'noj dejatel'nosti Solnca*. Statistics of sunspot activity of the Sun. Moscow: Nauka, 1986: 295 p. [In Russian].
- Greshilov A.A., Stakun V.A., Stakun A.A. *Matematcheskie metody postroenija prognozov*. Mathematical methods for forecasting. Moscow: Radio i svyaz, 1997: 112 p. [In Russian].
- Gruza G.V. Study of climate and its changes. *Izmenenie klimata*. Climate change. 2012, 31: 5–8. [In Russian].
- Gruza G.V., Rankova E.Ya. *Nabljudajemye i ozhidaemye izmenenija klimata Rossii: temperatura vozduha*. Observed and expected climate changes in Russia: air temperature. Obninsk: Publishing House RIHMI – WDC, 2012. 194 p. [In Russian].
- Gudkovich Z.M., Karklin V.P., Mironov Ye.U., Ivanov V.V., Losev S.M., Dymant L.N., Smolyanitsky V.M., Frolov S.V., Yulin A.V., Usoltseva E.A. The development of ice and meteorological conditions in the Arctic in the period 2007–2013. *Problemy Arktiki i Antarktiki*. Problems of Arctic and Antarctic, 2013, 2 (96): 90–102. [In Russian].
- Gudkovich Z.M., Karklin V.P., Smolyanitsky V.M., Frolov I.Ye. What is happening to the Earth's climate? *OOS: Izmenenie klimata*. EP (environment protection): Climate change. 2012, 5: 34–41. [In Russian].
- Gudkovich Z.M., Kovalev E.G. About some mechanisms of cyclic climate changes in the Arctic and Antarctic. *Okeanologija*. Oceanology. 2002, 42 (6): 1–7. [In Russian].
- Drozdov O.A., Vasilyev V.A., Kobysheva N.V., Raevsky A.N., Smekalova L.K., Shkolny Ye.P. *Klimatologija*. Climatology. Leningrad: Gidrometeoizdat, 1989: 567 p. [In Russian].
- Zhichkin A.P. Ice conditions in the Franz Josef Land archipelago. *Trudy Kol'skogo nauchnogo centra. Okeanologija*. Proc. of the Kola Science Center. Oceanology. 2014, 2 (4): 82–89. [In Russian].
- Zhichkin A.P. Features of interannual and seasonal fluctuations in ice coverage anomalies of the Barents Sea. *Meteorologija i gidrologija*. Meteorology and Hydrology. 2015, 5: 52–62. [In Russian].
- Ivanov B.V., Zhuravsky D.M. Ice conditions in the Grøn fjorden (Spitsbergen) during 1974–2008. *Problemy Arktiki i Antarktiki*. Problems of Arctic and Antarctic. 2010, 2 (85): 27–31. [In Russian].
- Matishov G.G., Dzhenjuk S.L., Zhichkin A.P., Moiseev D.V. The climate of the seas of the Western Arctic at the beginning of the XXI century. *Izvestija RAN. Serija geogr.* Izvestia RAS. Geography series. 2011, 3: 17–32. [In Russian].
- Matishov G.G., Dzhenjuk S.L., Moiseev D.V., Zhichkin A.P. About the nature of significant hydrometeorological anomalies in the northern and southern seas of Russia. *Izvestija RAN. Serija geogr.* Izvestia RAS. Geography series. 2014, 1: 36–46. [In Russian].
- Monin A.S. *Prognoz pogody kak zadacha fiziki*. Weather forecast as a task of physics. Moscow: Nauka, 1969: 184 p. [In Russian].
- Nastavlenie gidrometeorologicheskim stancijam i postam. Vyp. 3. Chast' 1. Meteorologicheskie nabljudenija na stancijah*. Manual on Hydrometeorological Stations and Posts. Issue 3. Part 1. Meteorological observations at stations. Leningrad: Gidrometeoizdat, 1985: 300 p. [In Russian].

- Nikiforov E.G., Speicher A.O. *Zakonomernosti formirovaniya krupnomasshtabnyh kolebanij gidrologicheskogo rezhima Severnogo Ledovitogo okeana*. Patterns of formation of large-scale fluctuations in the hydrological regime of the Arctic Ocean. Leningrad: Gidrometeoizdat, 1980: 269 p. [In Russian].
- Ocenochnyj doklad ob izmenenijah klimata i ih posledstvijah na territorii Rossijskoj Federacii. Tom. 1. Izmeneniya klimata*. Evaluation report on climate change and its consequences in the Russian Federation. V. 1. Climate change. Moscow: Rosgidromet Publishing House, 2008: 227. [In Russian].
- Priest E.R. *Solnechnaja magnitogidrodinamika*. Solar magnetohydrodynamics. Moscow: Mir, 1985: 592 p. [In Russian].
- Rozhkov V.A. *Teorija i metody statisticheskogo ocenivaniya verojatnostnyh harakteristik sluchajnyh velichin i funkcij s gidrometeorologicheskimi primerami. Kniga 2*. Theory and methods of statistical estimation of probabilistic characteristics of random variables and functions with hydrometeorological examples. Book 2. St. Petersburg: Gidrometeoizdat, 2002: 780 p. [In Russian].
- Tislenko D.I., Ivanov B.V. *Vremennaja izmenchivost' prizemnoj temperatury vozduha v rajone arhipelaga Shpichbergen v uslovijah pervogo (1920–1940) i sovremennogo poteplenija v Arktike*. Temporary variability of surface air temperature in the area of the Spitsbergen archipelago under the conditions of the first (1920–1940) and modern warming in the Arctic. *Kollektivnaja monografija po materialam mezhdunarodnoj nauchno-prakticheskoj konferencii "LXIX Gercenovskie chtenija", posvjashhennoj 115-letiju so dnja rozhdenija S.V. Kalesnika*. Multi-authored monograph based on the materials of the international scientific-practical conference "LXIX Herzen Readings" dedicated to the 115th birthday of S.V. Kalesnik. St. Petersburg: Publishing house of Herzen Russian State Pedagogical University, 2016: 243–247. [In Russian].
- Frolov I.Ye., Gudkovich Z.M., Karklin V.P., Smolyanitsky V.M. Climate change in Arctic and Antarctic is the result of natural causes. *Problemy Arktiki i Antarktiki*. Problems of Arctic and Antarctic. 2010a, 2: 52–61. [In Russian].
- Frolov I.Ye., Gudkovich Z.M., Karklin V.P., Smolyanitsky V.M. Climate change is the result of natural causes. *Jekologicheskij Vestnik Rossii*. Ecological Bulletin of Russia. 2010b, 1: 49–54. [In Russian].
- Alekseev G.V., Danilov A.I., Kattsov V.M., Kuzmina S.I., Ivanov N.E. Changes in the Climate and Sea Ice of the Northern Hemisphere in the 20th and 21st Centuries from Data of Observations and Modeling. *Izvestia Atmospheric and Oceanic Physics*. 2009, 45 (6): 675–686.
- Bekryayev R.V., Polyakov I.V., Alekseev V.A. Role of Polar Amplification in Long-Term Surface Air Temperature Variations and Modern Arctic Warming. *J. Climate*. 2010, 23: 3888–3906.
- Davidson K. et al. (ed). Calculation of monthly 30-year standard normal. WMO–TD 341. World Meteorological Organization, 1989: 12 p.
- Frolov I.Ye., Gudkovich Z.M., Karklin V.P., Kovalev Ye.G., Smolyanitsky V.M. Climate change in Eurasian Arctic Shelf seas. Praxing Publishing Ltd., 2009: 164 p.
- Gjelten H., Nordli Ø., Isaksen K., Førland E., Sviashchennikov P., Wyszynski P., Prokhorova U., Przybylak R., Ivanov B., Urazgildeeva A. Air temperature variations and gradients along the coast and fjords of western Spitsbergen. *Polar Research*. 2016, 35; DOI: 10.3402/polar.v35.29878.
- Hanssen-Bauer I. Temperature and precipitation in Svalbard 1912–2050: Measurements and scenarios. *Polar Record*. 38 (206): 2002, 225–232; DOI: 10.1017/S0032247400017757.
- Lyubushin A.A., Klyashutorin L.B. Short Term Global DT Prediction using 60–70 Years Periodicity. *Energy and Environment*. 2012, 23 (1): 2–12.
- Marsz A., Styszyńska A. (eds.). *Climate and Climate Change at Hornsund, Svalbard Gdynia*. Gdynia Maritime University, 2013: 402 p.
- Maturilli M., Herber P., Langlo G.-K. Climatology and time series of surface meteorology in Ny-Ålesund, Svalbard. *Earth System Science Data*. 2013, 5(1); DOI: 10.5194/essd-5-155-2013.
- Nordli Ø., Przybylak R., Ogilvie A., Isaksen K. Long-term temperature trends and variability on Spitsbergen: the extended Svalbard Airport temperature series, 1898–2012. *Polar Research*. 2014, 33 (1); DOI: 10.3402/polar.v33.21349.

Polyakov I.V., Alekseev G.V., Timokhov L.A., Bhatt U.S., Colony R.L., Simmons H.L., Walsh D., Walsh J.E., Zakharov V.F. Variability of the Intermediate Atlantic Water of the Arctic Ocean over the Last 100 Years. *J. Climate*. 2004, 17: 4485–4497.

Polyakov I.V., Alekseev G.V., Bekryaev R.V., Bhatt U., Colony R., Johnson M. A., Karklin V.P., Makshtas A.P., Walsh D., Yulin A.V. Observationally based assessment of polar amplification of global warming. *Geophys. Res. Lett.* 2002, 29: 1878–1891.

Przybylak R., Arazny A., Nordli Ø., Finkelburg R., Kejna M., Budzik T., Migala K., Sikora S., Puczko D., Rymerg K., Rachlewicz G. Spatial distribution of air temperature on Svalbard during 1 year with campaign measurements. *Int. J. Climatology*. 2014, 33: 3702–3719; DOI: 10.1002/joc.3937.

Raspopov O.M., Dergachev V.A., Kolstrom T.H. Hale Cyclicity of Solar Activity and Its Relation to Climate Variability. *Solar Physics*. 2004, 224: 455–463.

Serezze M.C., Barry R.G. Processes and impacts of Arctic amplification: A research synthesis. *Global and planetary change*. 2011, 77: 85–96.

Tislenko D.I., Ivanov B.V. Long-term variability of Atlantic water temperature in the Svalbard fjords in conditions of past and recent global warming. *Czech Polar Reports*. 2015, 5 (2): 134–142.

1.5. ANALYSIS OF CLIMATE CONTINENTALITY AND ABNORMALITY IN THE WESTERN SPITSBERGEN AREA BY OBSERVING DATA OF SURFACE AIR TEMPERATURE IN THE SECOND HALF OF THE XX CENTURY

D.I. Tislenko, B.V. Ivanov

A 30-year period, in particular 1961–1990, is used as a standard period for assessing climatic variables characterizing the *current* or *modern* climate, on the recommendation of the World Meteorological Organization (WMO). Currently, this period is still considered to be a basic one. The average value of a variable for this period is called the *norm* by default. The deviation of this value from the norm is called an *anomaly* (Gruza, 2012; Gruza and Rankova, 2012). In recent years, as per observed climate changes, there is an opinion that it is rational to recalculate the climate norm based on the standart period (1961–1990), and move it closer in time to the current moment (“modern” climate). Table 1.5.1 present the norm of surface air temperature (SAT) for the period 1961–1990 for the main observation points on the Spitsbergen.

Table 1.5.1

The values of the climate norm of SAT (°C) for the region of Spitsbergen archipelago

Isfjord Radio	Hornsund	Barentsburg	Ny-Ålesund	Longyearbyen	Piramiden
-5.0	-5.4	-6.1	-6.3	-6.7	-6.8

The lowest average annual SAT values are observed at the Piramiden station (a station with a nominally *continental* climate), and the highest values one can observe at the Isfjord Radio station (a station with a nominally *marine* climate). Fig. 1.5.1 shows the distribution of SAT anomalies for an observation point in Barentsburg for the period 1948–2014.

Similar distributions of anomalies were obtained for all other points of regular long-term observations of the SAT in the archipelago. 1948 is chosen as the reference start point

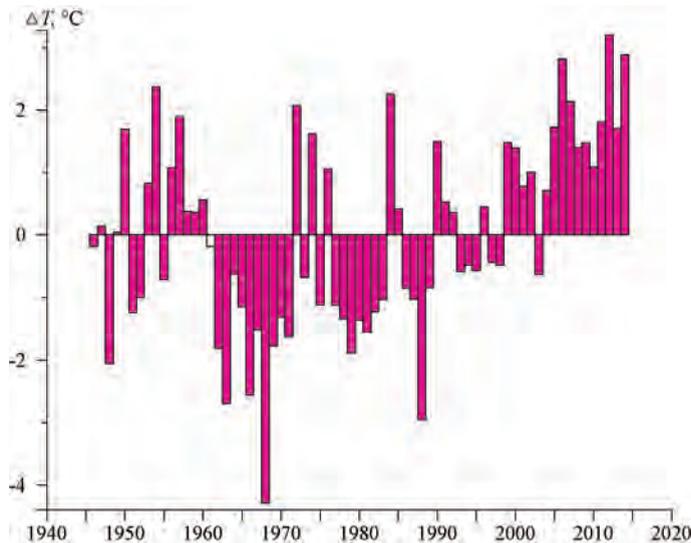


Fig. 1.5.1. Distribution of SAT anomalies for the Barentsburg point (1948–2014).

Estimates of the linear regression equations a calculated for all observation points

Observation point	1990—2014 гг.		1948—2014 гг.	
	R^2	a	R^2	a
Hornsund	0.4464	0.1073	0.2106	0.0366
Isfjord Radio	0.4598	0.0892	0.1573	0.0287
Barentsburg	0.4615	0.1048	0.1531	0.0310
Longyearbyen	0.4805	0.1293	0.2038	0.0422
Piramiden	0.4538	0.1088	0.1478	0.0329
Ny-Ålesund	0.4440	0.0948	0.1562	0.0309

Note. R^2 — coefficient of determination; a — coefficient that characterizes the angle of the trend line.

since the climatic series for all observation points have no gaps and can be considered homogeneous from this moment in time (year). Table 1.5.2 presents the estimates of the linear regression equations (trends) calculated for each observation point for two intervals: the entire series and the period of *modern* changes (1990–2014). The values of anomalies were used as initial data.

The table shows that the rate of increase in the average annual SAT values in the *modern period* (the value of coefficient a) is, on average, three times as high as similar estimates for the entire observation period. It indicates an increase in the climate warming process in the archipelago in recent decades. Considering that the SAT is one of the most frequently used characteristics for assessing climate changes on a regional scale, and the interaction in the *ocean–atmosphere–sea ice* system determines its changes, the spatial and temporal changes in the SAT for the of West Spitsbergen area were analyzed according to available data.

We estimated the time variations in the difference in the mean annual SAT values between the extreme northern (Ny-Ålesund) and southern (Hornsund) observation points – *latitudinal* difference, as well as between western (Isfjord Radio) and eastern (Piramiden) observation points – *meridional* difference. Linear differential trends (the difference in the average annual SAT values) were calculated for both series. Table 1.5.3 presents the results.

As the above table shows, meridional differences increase, while latitudinal differences decrease. The latter indicates a certain equalization of the climate from the point of view of its continentality. Climate warming in the area of Piramiden, where the lowest average annual temperature is observed (see Table 1.5.1), it occurs somewhat faster than at Isfjord Radio station (the warmest station per Table 1.5.1) for the entire observation period. The opposite situation we can observe in the meridional section. Higher rates of warming are recorded in the southern part of the archipelago (Hornsund station), where the average annual SAT is higher compared to Ny-Ålesund (see Table 1.5.1). We can give you some preliminary findings that the peaking of the meridional gradient of the SAT can cause a more intense transport of air in the surface layer from west to east, i.e., from the sea zone of the Isfjord (the area adjacent to the Fram Strait) to the inner part of its water area (the area of Piramiden).

Table 1.5.3

Estimates of the linear regression equations (a) characterizing the changes in the difference between the SAT along the latitude and meridian

Station	a
Hornsund – Ny-Ålesund	0.006
Isfjord Radio – Piramiden	–0.004

The average values of the difference between the maximum and minimum SAT values during the year (the entire available observation period)

Station	Peak-to-peak value, °C	Observation period
Isfjord Radio	18.8	1935–1940, 1947–2014
Barentsburg	21.8	1932–1940, 1947–2014
Longyearbyen	24.4	1899–2014
Piramiden	25.0	1940, 1948–2014
Hornsund	18.7	1935–1940, 1947–2014
Ny-Ålesund	21.1	1935–1940, 1947–2014

Table 1.5.4 presents the average values of the difference between the maximum and minimum SAT values during the year (monthly average values). As the table shows, there is an increase in climate continentality as we move eastward, which is quite logical, for four observation points located in the water area of the Isfjord (nominally *meridional* section). So, in the Isfjord Radio station area, located at the entrance to the Isfjord, the peak-to-peak value of the SAT is 18.8 °C. When moving deeper into the bay (to the east), the peak-to-peak value of the SAT increases and reaches 25.0 °C (Piramiden station). Hornsund Station is located in the south of West Spitsbergen. The peak-to-peak value for this point is 18.7 °C. Ny-Ålesund station is located in the northern part of West Spitzbergen. Still, its location, at some distance from the entrance to the fjord from the side of the Fram Strait, is more similar to the Barentsburg station, which is also confirmed by the average peak-to-peak values in the monthly average SAT (21.1 °C).

The estimates obtained are generally consistent with the results of previous studies (Przubulak et al., 2016; Gejtlen et al., 2016; Tislenko, Ivanov, 2016).

Since the available data provides the most comprehensive description of the SAT changes for West Spitzbergen starting in the second half of the XX century, a preliminary analysis of the anomalous climate was carried out for this period. Two well-known indices were used to describe the anomalous climate. The first of these is the CAI (Climate Anomaly Index), which is defined as the Euclidean distance between a point describing the current state of the climate and a point representing the state of a time-average value (norm) (Gruza and Rankova, 2012):

$$CAI = \sqrt{\frac{1}{n} \cdot \sum_{i=1}^n \left(\frac{\Delta T_i}{\sigma} \right)^2}, \quad (1.5.1)$$

where n – is number of stations, i – is station serial number, ΔT_i is SAT anomaly, σ – is standard deviation (SD).

The larger the CAI, the farther away the point, representing the instantaneous state of the climate, is from the “center” of points – climate states. The calculation of the center position for a given index is most often carried out over the entire available observation period (Gruza and Rankova, 2012).

As the second integral characteristic describing the anomalous temperature field for the region of West Spitsbergen, the Tokarev parameter was chosen (K_T), allowing to take into account not only the value of the anomaly but also its sign (Tokarev, 1983):

$$K_T = \frac{1}{N + M} \left[\sum_{i=1}^n \left(\frac{\Delta T_{+i}}{\sigma_i} \right)^2 - \sum_{i=1}^n \left(\frac{\Delta T_{-i}}{\sigma_i} \right)^2 \right], \quad (1.5.2)$$

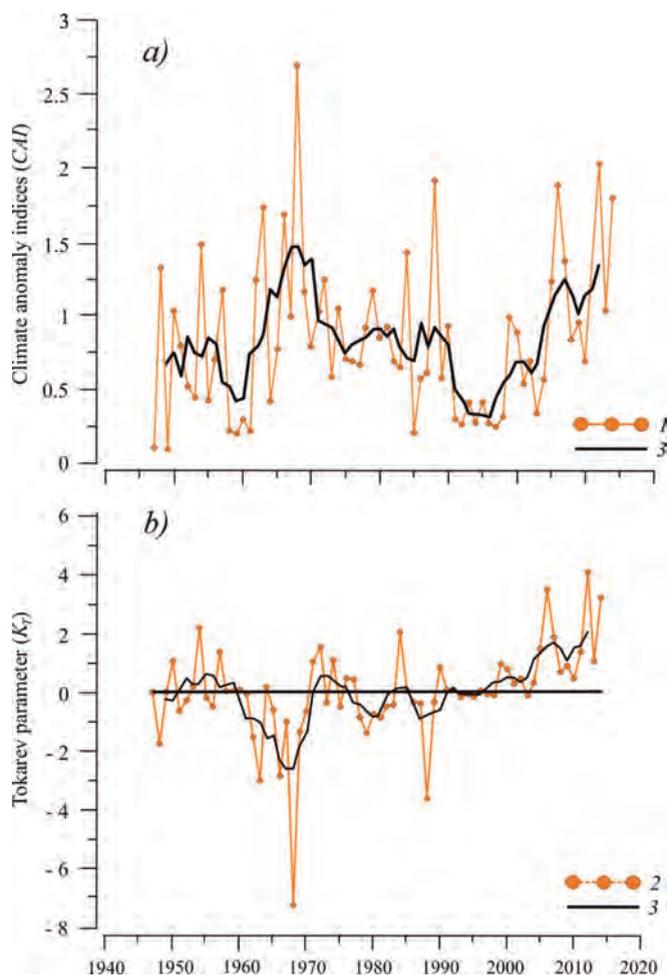


Fig. 1.5.2. Time course of climate anomaly indices CAI (a) and K_T (b) in the region of West Spitsbergen for the period 1947–2014.

1 – CAI; 2 – Tokarev parameter; 3 – 5-year moving average.

where N – is the number of points with a positive anomaly ΔT_{+i} ; M – is the number of points with a positive anomaly ΔT_{-i} ; i – is station serial number.

Deviations of the SAT values (ΔT_i) were determined as the difference between the actual temperature and the norm (average SAT value for 1947–2014). Then, the obtained values of the anomalies were normalized to the SD to obtain a more homogeneous comparable picture. Fig 1.5.2 presents the time course of the calculated values of the indices CAI and K_T .

One used a 5-year moving average filter to more clearly identify periods with an intense anomaly in terms of SAT. The presented figures show that the maximum anomalous climate in the Spitsbergen area corresponds to two intervals: 1960–1970 and 2005–2014. For the first period, the maximum absolute values of the indices CAI and K_T fall upon 1968. For the second period, similar values were observed in 2012. The total number of years when the CAI index > 1 (i.e., the calculated average value of the anomaly exceeds the SD),

for the Spitsbergen area is 22, which is 32 % of the entire time series. Moreover, in 1968 and 2012, cases were recorded when the *CAI* index > 2 (3 % of the entire time series).

Based on the analysis of the *CAI* index values, it is also possible to identify significant and very significant anomalies (*extremums*) in the second half of the 20th century. Thus, the extreme anomaly ($> 2\sigma$) of the temperature field in the region of West Spitsbergen is recorded in 1968, 1988 and 2012 (the value of the anomaly in 1968 is three times as much as the SD).

REFERENCES

Gruza G.V. Study of climate and its changes. *Izmenenie klimata*. Climate change. 2012, 31: 5–8. [In Russian].

Gruza G.V., Rankova E.Ja. *Nabljudаемые и ожидаемые изменения климата России: температура воздуха*. Observed and expected climate changes in Russia: air temperature. Obninsk, 2012: 194 p. [In Russian].

Tislenko D.I., Ivanov B.V. Temporary variability of surface air temperature in the area of the Spitsbergen archipelago under the conditions of the first (1920–1940) and modern warming in the Arctic. *Kollektivnaja monografija po materialam mezhdunarodnoj nauchno–prakticheskoj konferencii “LXIX Gercenovskie chtenija”, posvjashhennoj 115-letiju so dnja rozhdenija S.V. Kalesnika*. Multi-authored monograph based on the materials of the international scientific-practical conference “LXIX Herzen Readings” dedicated to the 115th birthday of S.V. Kalesnik. St. Petersburg: Publishing house of the Herzen Russian State Pedagogical University, 2016: 243–247. [In Russian].

Tokarev V.G. On the variability and anomalies of the average seasonal air temperature in the first half of summer in Western Siberia. *Trudy ZapSibNII*. Proc. of the West Siberian Regional Research Institute. 1983, 59: 20–26. [In Russian].

Gjelten H., Nordli Ø., Isaksen K., Førland E., Sviashchennikov P., Wyszynski P., Prokhorova U., Przybylak R., Ivanov B., Urazgildeeva A. Air temperature variations and gradients along the coast and fjords of western Spitsbergen. *Polar Research*. 2016, 35; DOI: 10.3402/polar.v35.29878.

Przybylak R., Arazny A., Nordli Ø., Finkelnburg R., Kejna M., Budzik T., Migala K., Sikora S., Puczko D., Rymerg K., Rachlewicz G. Spatial distribution of air temperature on Svalbard during 1 year with campaign measurements. *J. Climatology*. 2014, 33; DOI: 10.1002/joc.3937.

Chapter 2
Variability of oceanological parameters
in the marine areas
of the Spitsbergen archipelago

2.1. THE PRESENT OCEANOGRAPHIC CONDITIONS OF WEST SPITSBERGEN FJORDS

E.V. Bloskhina, K.V. Filchuk

Several factors that influence the water masses of the West Spitsbergen fjords are: the inflow of warm salty Atlantic waters, the inflow of fresher and colder Arctic waters, river runoff, and the processes of ice formation and melting.

Atlantic waters (AW) are the main source of heat in the study area. AW originates from the West Spitsbergen Current (WSC), which is a continuation of the Norwegian Current. By the latest estimates of researchers, it is precisely the waters of the WSC that carry most of the total volume of AW entering the Arctic basin (Schauer et al., 2008) and this water the primary heat transfer to the Arctic Basin (Aagaard and Greisman, 1975; Walczowski and Piechura, 2007). Thus, the Fram Strait, through which AW enters the Arctic Ocean, is a key region for water and heat exchange between the North Atlantic and the Arctic basin (Tislenko, Ivanov, 2015).

Arctic waters that are less saline and colder than AW flow into the continental shelf of West Spitsbergen with the East Spitsbergen Current (Haarpaintner et al., 2001), spreading over the continental shelf of the archipelago from south to north and creating a kind of barrier to West Spitsbergen fjords, preventing the constant influence of AW. A frontal zone known as the Arctic front forms between AW and Arctic waters (Saloranta and Svendsen, 2001). Water exchange through this front is associated with northern winds leading to the occurrence of upwelling in the WSC. As shown in some studies, a change in the horizontal density gradient and, accordingly, the pressure gradient initiates this exchange (Cottier et al., 2005; Svendsen et al., 2002). Nilsen et al. (2016), based on the analysis of observational data and the results of model calculations, proposed to consider atmospheric forcing as a mechanism that determines the AW intrusion into the archipelago fjords. The passages of strong cyclones in the Fram Strait cause an upsurge of water to the coastline of West Spitsbergen, which modulates the barotropic branch of the WSC at the shelf brake (Nilsen et al., 2016). It leads to topographically guided currents into the troughs of West Spitsbergen. The further AW intrusion into the fjords depends on various factors: relief, atmospheric circulation, and characteristics of local water masses. For example, for the Isfjorden, it was shown that the horizontal pressure gradient could regulate the process of AW inflow into the fjord. This gradient arises between the AW and the local waters that form directly inside the fjord in the winter as a result of ice formation in the polynya (Nilsen et al., 2006).

River runoff has the most considerable influence on the thermohaline characteristics of fjord waters in the summer-autumn period when continental glaciers are actively melting. It leads to an increase in the volume of freshwater entering the fjords and the freshening of the surface layer. Sea ice melting processes usually begin in the fjords in May – June and also lead to the freshening of the surface layer. Sea ice formation processes, resulting in the formation of water mass with low temperature and high salinity, usually begin in November (Moiseyev, Bobrov, 2015; Moiseyev, Gromov, 2009).

However, in recent years, abnormally warm winters have been observed on Svalbard: ice cover is not formed every year and not in all fjords, the temperature of the AW

coming to the shores of the archipelago rises, the AW inflow into the fjords becomes more regular, their volume increases. These changes have a profound effect on the structure and functioning of the entire ecosystem of the fjords (Hop et al., 2002; Berge et al., 2005; Łącka et al., 2016; Pavlov et al., 2010; Pavlov, 2011).

AREA OF STUDY

Oceanographic studies of West Spitsbergen fjords were carried out according to the Long-Term Monitoring Program at the oceanographic polygon in the coastal waters of Svalbard. They were a part of the project to create a Russian scientific center on Svalbard, and a continuation of the AARI systematic expeditionary observations of the state of the waters in the fjords resumed in 2006. The research objects are the water areas included in the oceanographic polygon of the Russian Science Center on Svalbard (RSCS). Figure 2.1.1 shows the location of the objects in the polygon.

Isfjorden is the largest fjord of Svalbard, stretching from the southwest to the northeast. The length of the Isfjorden along the axis is about 100 km. The coastline of the Isfjorden is strongly indented and forms several smaller fjords: Grønfjorden and Adventfjorden on the south side; Sassenfjorden, passing into the Tempelfjorden, and Billefjorden, ending in Mimerbukta, Petuniabukta, Adolfbukta in the northeast; Nordfjorden, passing into the Ekmanfjorden and the Dicksonfjorden in the north. Water masses from the adjacent continental shelf can freely penetrate into the Isfjorden due to the absence of the topographic barrier at its entrance.

Billefjorden is about 30km long and 5–8 km wide. This fjord is unique because it is the only fjord in the Isfjorden system that has two topographic barriers at the entrance: an external (70 m) and an internal (40 m), which prevents the free exchange of water with adjacent water areas. The average depth of the fjord is 160 m. The area of the Billefjorden is 182 km² (5.9 % of Isfjorden area), and the volume of water is 13 km³ (3.5 % of the volume of the Isfjorden) (Nilsen et al., 2008).

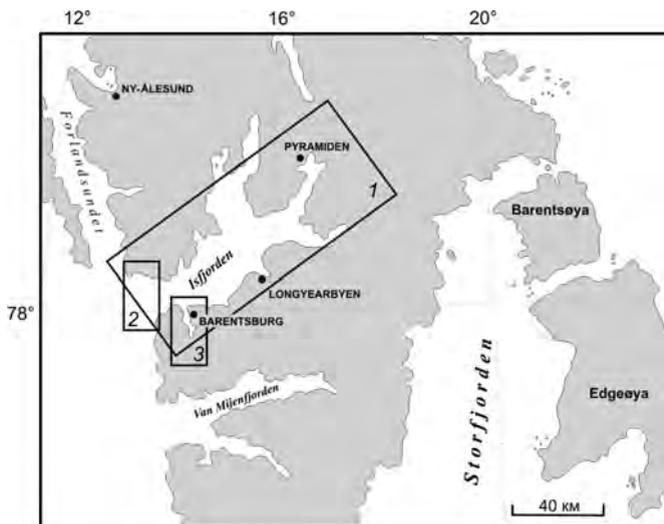


Fig. 2.1.1. Objects of the oceanographic polygon of RSCS: Isfjorden and Billefjorden (1), the mouth of Isfjorden (2), Grønfjorden (3).

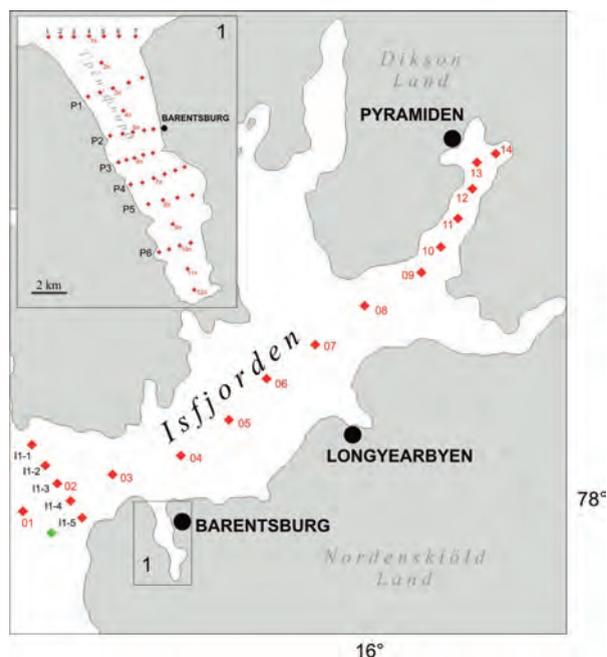


Fig. 2.1.2. The station map of Isfjorden and Billefjorden.

The red diamonds show oceanographic stations; the green diamond shows the position of the current meter moorings.

Fig. 2.1.2 shows the layout of the oceanographic polygon of RSCS in the waters of the Isfjorden and Billefjorden. Red diamonds show oceanographic stations; a green diamond shows the position of the current meter mooring.

The Grøn fjorden is a relatively small fjord located on the south side of the Isfjorden close to its mouth. The fjord has meridian direction; its length is approximately 16.5 km. The width and depth of the fjord increase from the south to the north (exit to the Isfjorden), from 1.8 to 5.4 km and from 50 to 170 m, respectively. There is no barrier in the mouth of the Grøn fjorden, which allows free exchange with the water masses of the Isfjorden. Several streams and rivers flow into the fjord.

From 2011 to 2017, four summer sections in the Isfjorden, including the Billefjorden, as well as seven summer and six winter sections in the Grøn fjorden, were made.

THERMOHALINE CHARACTERISTICS WATER MASSES AND ITS VARIABILITY IN THE WEST SPITSBERGEN FJORDS

The Svedsen classification (Svedsen, 2002) was used to distinguish water masses in the studied fjords. He developed the classification for the Kongsfjorden-Krossfjorden fjords system, which also belongs to the West Spitsbergen fjords. Nilsen et al. (2008) also used Svedsen classification to analyze water masses in the Isfjorden.

We provide here a brief overview of the water masses in the West Spitsbergen fjords:

Atlantic Water (AW), transported by the West Spitsbergen Current, characterized by high temperature ($> 3 \text{ }^{\circ}\text{C}$) and salinity ($> 34.9 \text{ psu}$);

Transformed Atlantic Water (TAW), formed as a result of the mixing of AW and Arctic waters: $1 < T < 3 \text{ }^{\circ}\text{C}$, $34.7 < S < 34.9 \text{ psu}$;

Surface Water (SW), formed in late spring and summer under the influence of increased volume of river runoff, melting sea ice and solar radiation heating: $T > 1\text{ }^{\circ}\text{C}$, $S < 34\text{ psu}$;

Intermediate Water (IW), formed as a result of mixing SW and AW (TAW): $T > 1\text{ }^{\circ}\text{C}$, $34 < S < 34.9\text{ psu}$;

Local Water (LW), which forms directly in the fjord by convectional processes during autumn/winter as a result of cooling of SW or IW with salinity close to 34 psu, $-0.5 < T < 1\text{ }^{\circ}\text{C}$, $S < 34.8\text{ psu}$;

Winter Cooled Water (WCW), formed as a result of winter cooling and the sea ice formation, $T < -0.5\text{ }^{\circ}\text{C}$, $S > 34.3\text{ psu}$.

ISFJORDEN AND BILLEFJORDEN

Open access data from Internet were used to analyze the state of water in the 1990s and 2000s (Boyer et al., 2013; ICES, 2014; Moiseyev, Ionov, 2006; Meshcheryakov et al., 2014). Since the observations were irregular and were carried out in different months and years (23 stations in total), only *TS* diagrams were used to analyze the distribution of water masses (Fig. 2.1.3).

In the 1990s, as a result of observations in the Isfjorden (in its mouth and along the axis of the fjord), the following water masses were identified in the summer months: SW, the minimum salinity was 28 psu (August 1993), and IW, which had temperatures from 1 to 5.5 °C (June–July 1997). AW was recorded only in August 1994 and July 1998; in other years, AW was not observed. In this years, the maximum temperature of AW was 3.5 °C. The salinity of LW in the 1990s ranged from 33.5 to 34.8 psu.

In April 1999, only two stations were carried out in the outer part of Isfjorden. TAW, LW, and WCW were identified. In March 2016 and 2017 years, two water masses were observed: LW and TAW (Fig. 2.1.3).

Isfjorden water masses distribution in the 2000s are shown in Fig. 2.1.4, and Fig. 2.1.5. The features of the temperature and salinity distribution are similar to each other. SW was observed from the surface to a depth of 25–50 m along the axis of the entire fjord. The maximum temperature (up to 6.5 °C) was observed in 2003 in the central part of the fjord. The minimum salinity (up to 29.5 psu) was recorded in 2006 in the inner part of the fjord. AW was identified during these years with a maximum temperature of 6 °C (2006) in the western part of the section. The minimum volume of AW was observed in 2009. There was WCW in the Billefjorden in the layer from a depth of 60–70 m to the bottom. LW was above it (on the depth of 50–70 m), the minimum salinity of which (34.2 psu) was recorded in 2009. The maximum volume of TAW was observed in 2006, the minimum – in 2003.

Compared with the 1990s, AW was represented in the fjord in a larger volume and was observed almost every year. AW temperature and salinity were higher than in the 1990s. Higher temperatures were also typical for SW and IW.

In June 2014, only one water mass – AW – was identified in the Isfjorden characterized by a temperature of 0.5–4.5 °C and salinity of about 35.1 psu (Fig. 2.1.6; 2.1.7 *a, b* and 2.1.8 *a, b*). The low temperature of AW (less than 3 °C) at a depth of more than 50–100 m can be explained by the fact that the AW occupied fjord for a long time. As a result, it cooled due to heat exchange with the atmosphere. These cooled layers sank beneath the warmer ones. Similar conditions were recorded in the Kongsfjorden (West Spitsbergen

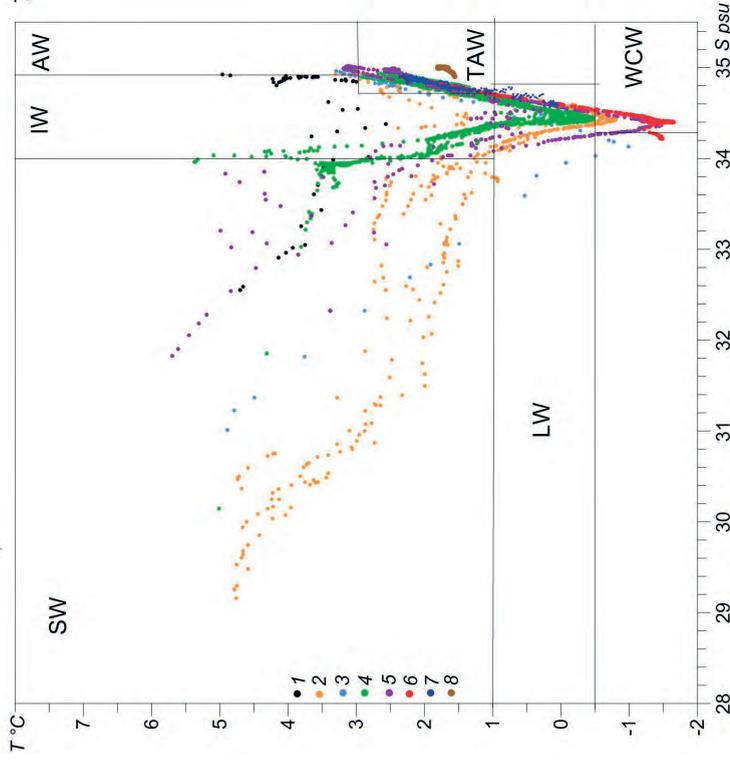


Fig. 2.1.3. TS-diagram based on measurements from the Isfjorden in the 1990s and 2010s.

1 – July 1991, 2 – August 1993, 3 – August 1994, 4 – June and July 1997, 5 – July 1998, 6 – April 1998 and April 1999, 7 – March 2016, 8 – April 2017..

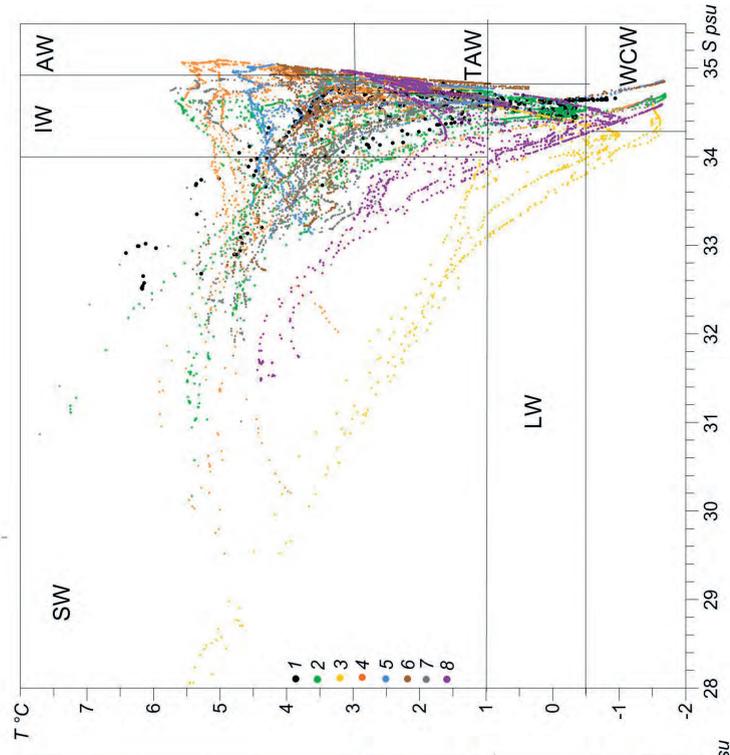


Fig. 2.1.4. TS-diagram based on measurements in the Isfjorden during the summer months of the 2000s.

1 – 2002, 2 – 2003, 3 – 2004, 4 – 2006, 5 – 2007, 6 – 2008, 7 – 2009, 8 – 2010.

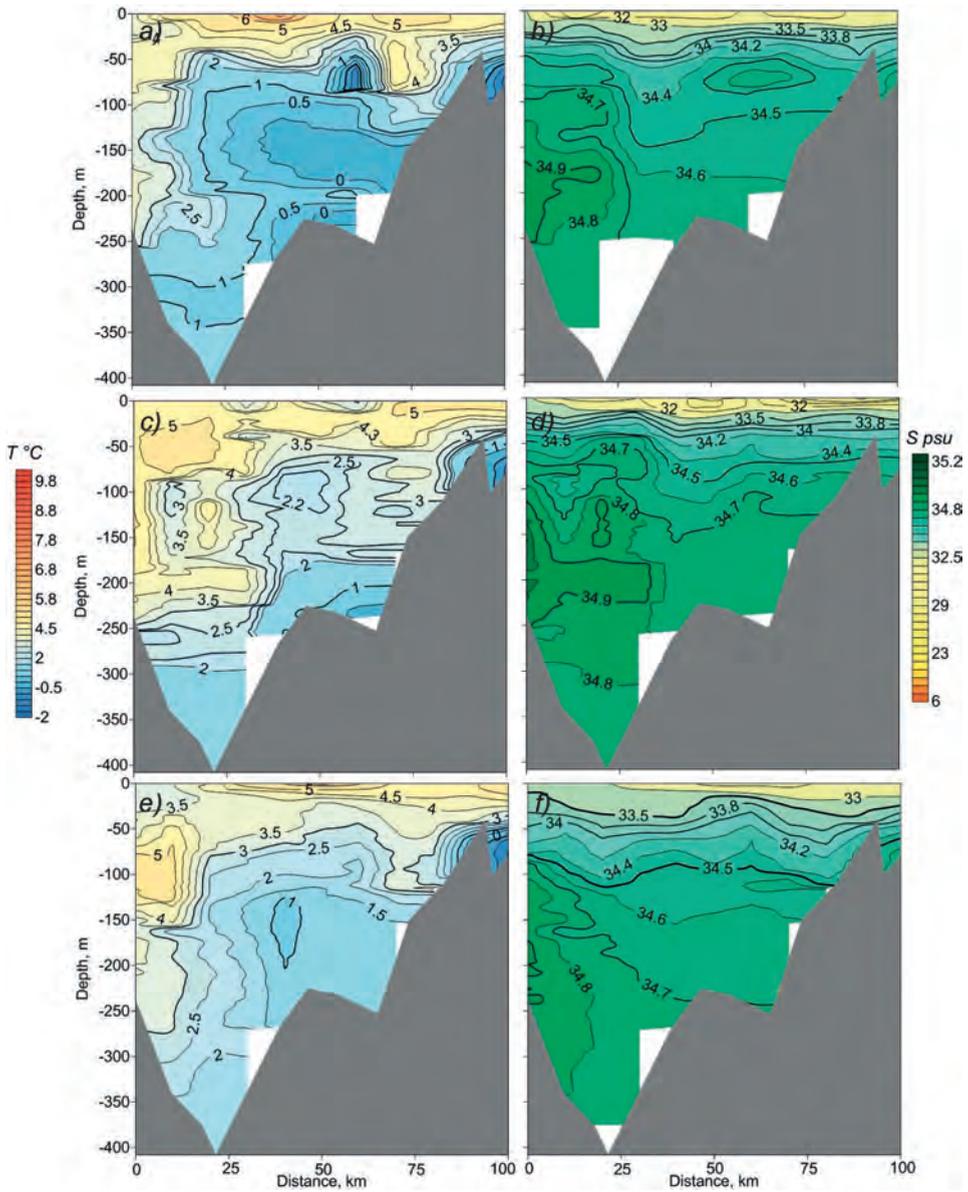


Fig. 2.1.5. Distribution of temperature, °C (a, b, c) and salinity, psu (b, d, f) along the axis of the Isfjorden in August 2003 (a, b), August 2006 (c, d) and August 2009 (e, f).

All sections are oriented west-east.

fjord, located northwest of the Isfjorden) in April 2007. Tverberg et al. (2007) described the mechanism of how such conditions form.

As noted above, the Billefjorden has a 40 m topographic barrier at the entrance, which prevents the water exchange with the Isfjorden. In the summer months, the Billefjorden from a depth of 40–50 m to the bottom is occupied by local water masses that form here in the autumn/winter period: LW and WCW (Fig. 2.1.7). Salinity in the surface layer decreased. It is due to the influence of the melting of the Nordenskjöldbreen into Adolfbukta. In 2014 in Billefjorden layer of 20–40 m, was occupied by AW, which penetrates here from the Isfjorden (Fig. 2.1.7 *a, b*). Unlike June 2014, when AW occupied the entire Isfjorden, measurements were carried out in September 2015 (only a section in the mouth of the Isfjorden), in August 2016 and in July 2017 showed three more water masses in the fjord: SW, IW and TAW (Fig. 2.1.7 *c, d, e, f*, and 2.1.8 *c, d, e, f*).

In September 2015 (measurements were made only in the mouth of the Isfjorden to a depth of 128 m), in the water layer from the surface to the depth of 40–50 m there was SW with temperature from 2 to 4.4 °C and salinity from 31.4 up to 34 psu (see Fig. 2.1.8 *c, d*). AW (temperature of 4–5 °C) was identified under IW.

In August 2016, SW (0–25 m) in the mouth of Isfjorden, 0–40 m in the Billefjorden) was characterized by temperatures from 3 to 7 °C and salinity from 25 to 34 psu (Fig. 2.1. 7 *c, d*). TAW was identified under the IW; TAW temperature varied from 2 to 2.5 °C. In the western part of the section, AW (temperature of 4–4.3 °C) was located at a depth of 120–170 m.

In the Billefjorden, as in 2014, the water layer, starting from a depth of 60 m to the bottom, was occupied by waters of local origin: LW (60–75 m, $T = -0.5 \dots -1$ °C, $S = 34.5 \dots 34.6$ psu) and WCW (from 75 m to the bottom, $T = -1 \dots -0.5$ °C, $S = 34.6 \dots 34.7$ psu).

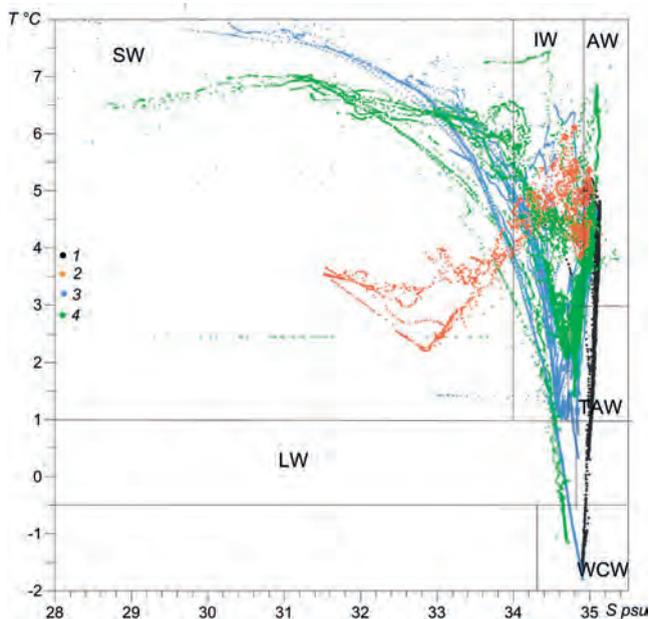


Fig. 2.1.6. TS-diagram based on measurements in the Isfjorden during the summer months in 2014–2017.

1 – June 2014; 2 – September 2015; 3 – August 2016; 4 – July 2017.

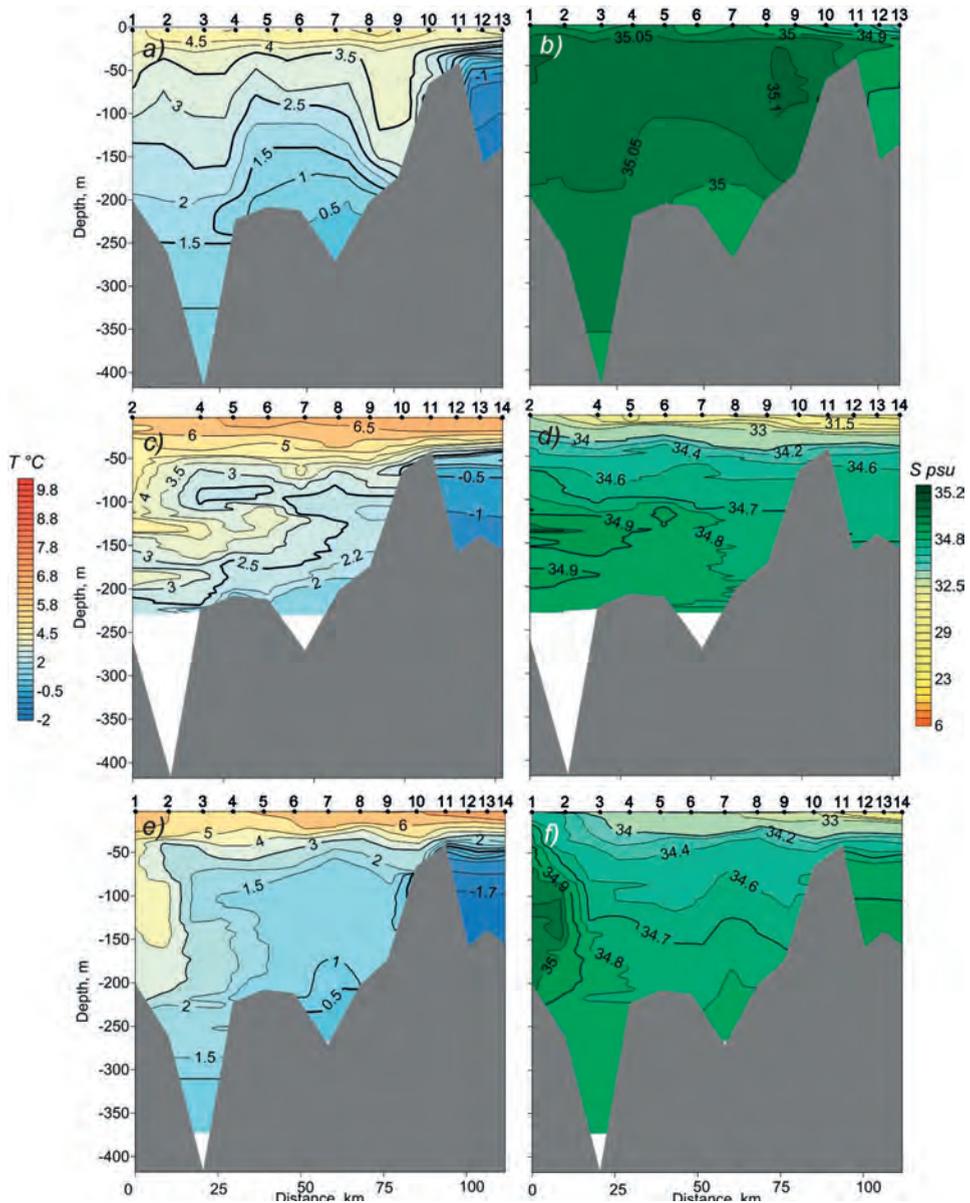


Fig. 2.1.7. Distribution of temperature, °C (*a, b, c*) and salinity, psu (*b, d, f*) along the axis of the Isfjorden in June 2014 (*a, b*), August 2016 (*c, d*), and August 2017 (*e, f*).

All sections are oriented west-east.

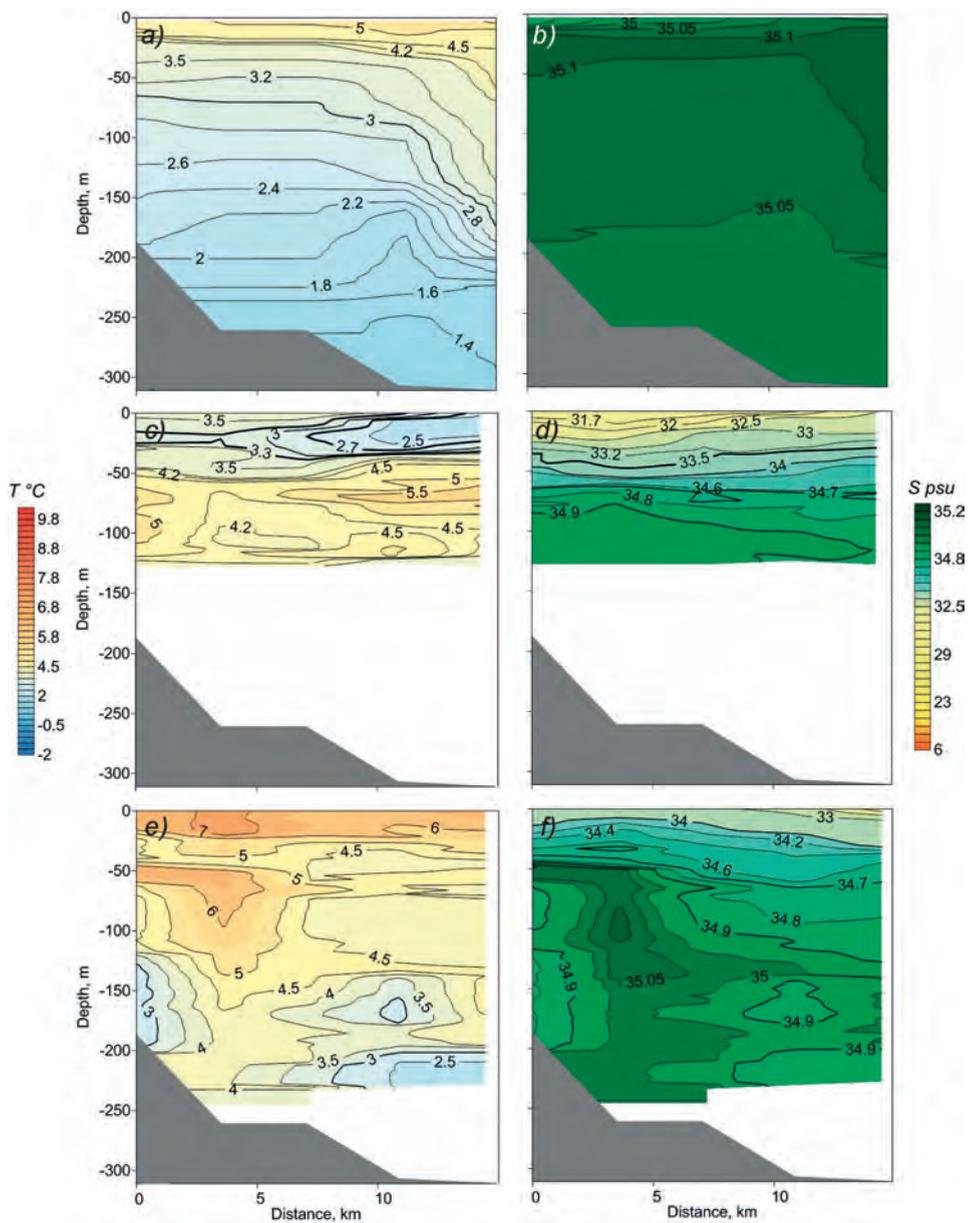


Fig. 2.1.8. Distribution of temperature, °C (*a, b, c*) and salinity, psu (*b, d, f*) in the mouth of the Isfjorden in June 2014 (*a, b*), September 2015 (*c, d*), and August 2016 (*e, f*). All sections are oriented north-south.

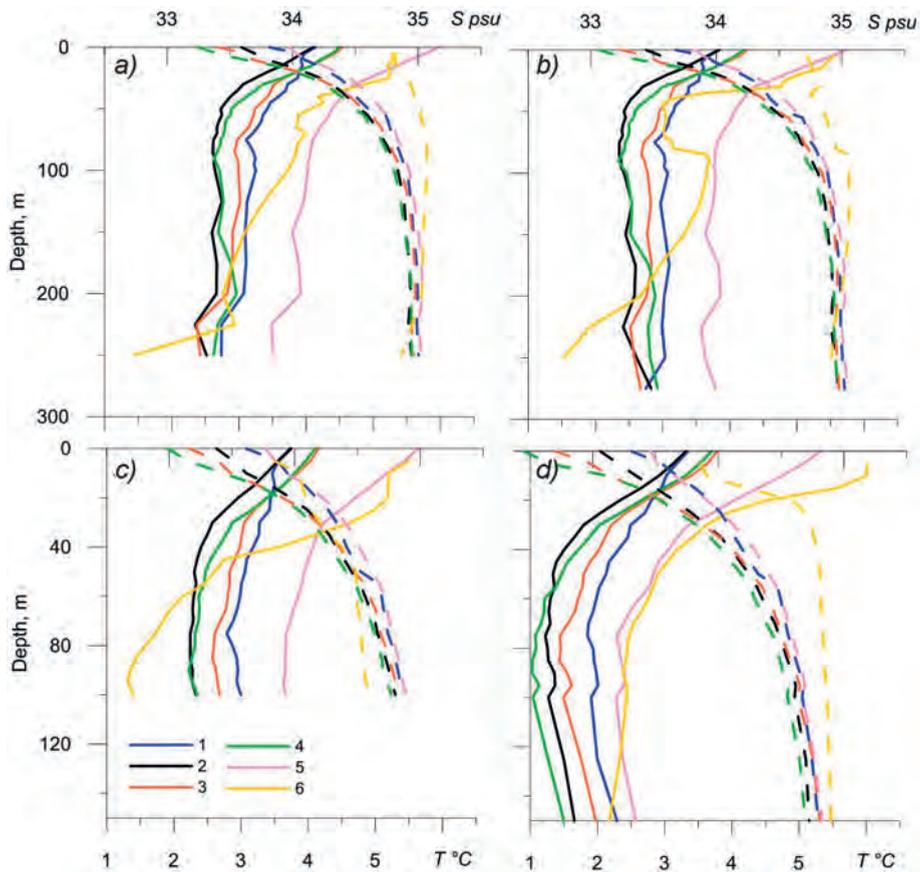


Fig. 2.1.9. Vertical distribution of averaged temperature (T °C, solid lines) and averaged salinity (S psu, dashed lines) according to climatic data and measurement results in 2014–2017 in Isfjorden at points No.1 (a), No. 2 (b), No. 3 (c), No. 8 (d) (Fig. 2.1.2).

1 – 1965–1974, 2 – 1975–1984, 3 – 1985–1994, 4 – 1995–2004, 5 – 2005–2012, 6 – 2014–2017.

The distribution of water masses in 2017 in the Billefjorden was similar to the distribution of the previous year (Fig. 2.1.7 e, f): SW to a depth of 30–40 m, (maximum temperature values of 7–8 °C in the Billefjorden); IW at a depth of 30–40 to 40–50 m; LW at a depth of 50–60 m, WCW in the layer from 60 m to the bottom (the minimum temperature is –1.7 °C).

In 2017 in the Isfjorden, SW was identified to a depth of 30 m. AW was observed at a depth of 40–230 m only in the westernmost part of the section (temperature 3–4 °C). In the other areas of the fjord, TAW lay under IW. In the deepest part of the section under the TAW to the bottom, there was an LW that remained here from the autumn/winter period.

In the mouth of the Isfjorden, the temperature of the AW layer, located at depth from 140–160 to 220–260 m, reached 4–4.5 °C.

To analyze the current state of the waters of the Isfjorden, we compared the climatic data for some points of the fjord with the measurement results obtained in 2014–2017. Climate data (decade average temperature and salinity) were taken from World Ocean Atlas

2013 (Boyer et al., 2013). Data were compared for four points located in the Isfjorden (Fig. 2.1.9). Averaged temperature and salinity are gradually increasing from the 1960s to the present time. For all points, the maximum temperature was observed in 2005–2017. For all points except for point No. 3, the averaged salinity for the period 2014–2017 is maximum for the entire study period.

GRØNFJORDEN

In Grønfjorden, measurements are carried out in the spring months (March–April) for the period 2012–2017.

In April 2012 (one section was made along the axis of the fjord, one section in the mouth of the fjord and four sections across the fjord), the following water masses were recorded in Grønfjorden (Fig. 2.1.10; 2.1.11 *a, b*; 2.1.12, 2.1.13 *a, b*).

TAW was observed in the entire fjord except for a southernmost section in the bottom layers (average layer depth 30 m). The maximum values of temperature (2–2.2 °C) were observed in the mouth of the fjord. LW was recorded throughout the fjord. It occupied the entire central and eastern parts of the section from the surface to a depth of 90–100 m in the mouth of the fjord. On the remaining cross-sections, LW was located above the TAW layer. WCW with temperature from –0.5 to –0.9 °C and salinity from 34.5 to 34.55 psu was recorded from the surface to the upper boundary of LW in the entire water area of the fjord (except for the areas where the LW reaches the surface).

In contrast to April 2012, in April 2013 (one longitudinal and five cross-sections were made), only two water masses were recorded in the Grønfjorden: LW and WCW (Fig. 2.1.10; 2.1.11 *c, d*; 2.1.14).

The boundary of the LW salinity had the same location as isohaline of 34.8 psu. In the southernmost section, the entire water column was occupied by WCW, the

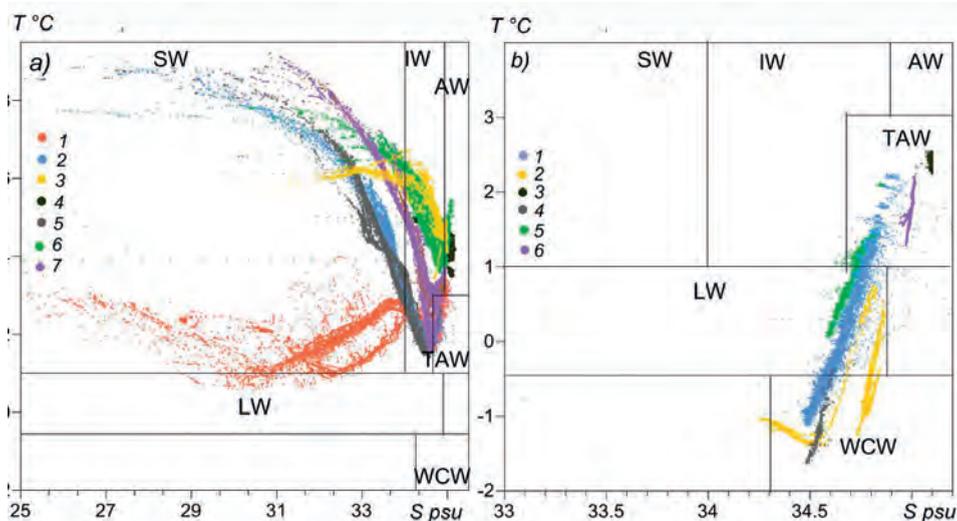


Fig. 2.1.10. TS-diagram based on measurements in Grønfjorden in the summer months 2011–2017 (*a*) in the spring months 2012–2017 (*b*).

a) 1 – August 2011, 2 – August 2012, 3 – September 2013, 4 – June 2014, 5 – August 2015, 6 – August 2016, 7 – August 2017; *b*) 1 – April 2012, 2 – April 2013, 3 – April 2014, 4 – April 2015, 5 – March 2016, 6 – March 2017.

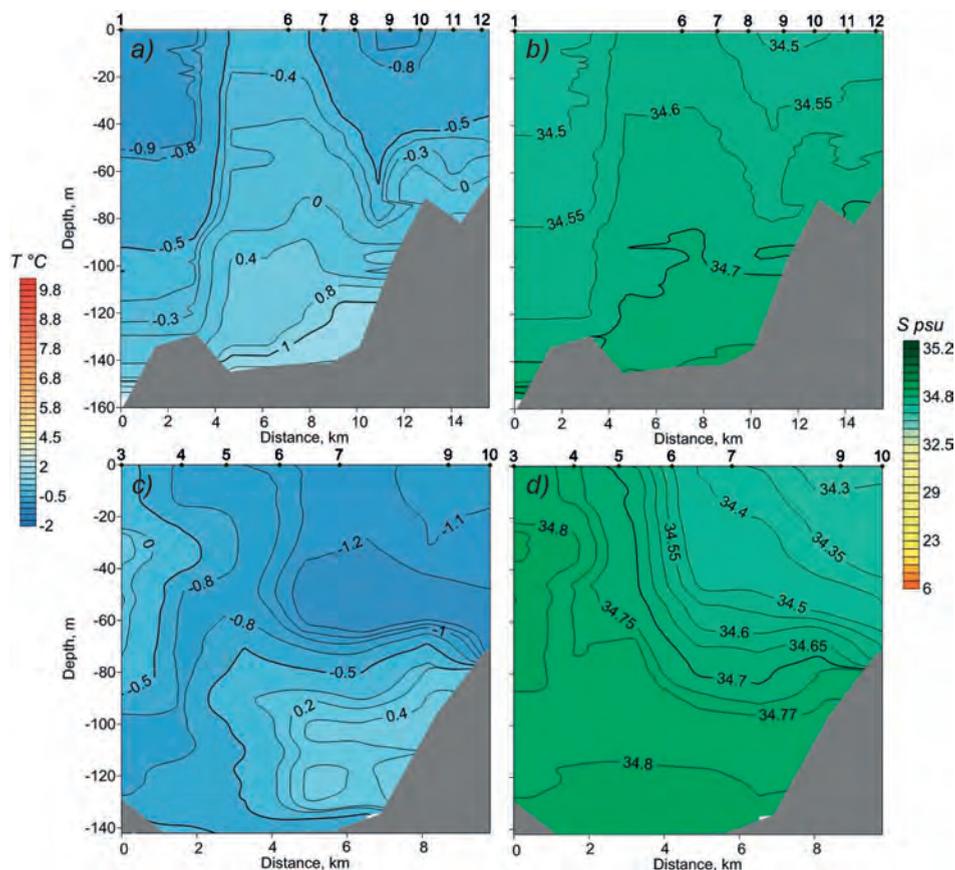


Fig. 2.1.11. Distribution of temperature, °C (*a, c*) and salinity, psu (*b, d*) along the Grøn fjorden axis in April 2012 (*a, b*) and April 2013 (*c, d*).

All sections are oriented north-south.

temperature of which varied from -1.1 to -1.3 °C, and salinity from 34.5 to 34.34 psu. In the northern sections (P1 and P2), WCW was recorded with temperatures ranging from -1.1 to -0.8 °C and salinity greater than 34.75 psu.

The sections in April 2014 (one section along the fjord axis and four cross-sections) showed that only one water mass, AW, was present in the whole Grøn fjorden, its temperature ranged from 2.2 to 2.6 °C, and salinity – from 35.04 to 35.1 psu. The explanation of the low AW temperatures was given above when analyzing the survey in the Isfjorden water area in June 2014.

In April 2016, only two sections were made in the Grøn fjorden: one along the fjord axis and one in its mouth. Two water masses were recorded along the axis of the fjord. TAW with a temperature of 1–1.4 °C and salinity of 34.73–34.81 psu and LW with temperature from 0.3 to 1 °C and salinity from 34.65 to 34.73 psu (Fig. 2.1.13 *c, d*).

In April 2017 (one along the fjord axis and one section in the mouth), Grøn fjorden showed a situation similar to April 2014, when the entire fjord was filled with water mass with high salinity (above 35 psu), its temperature was 1.5 to 2.2 °C, it was AW.

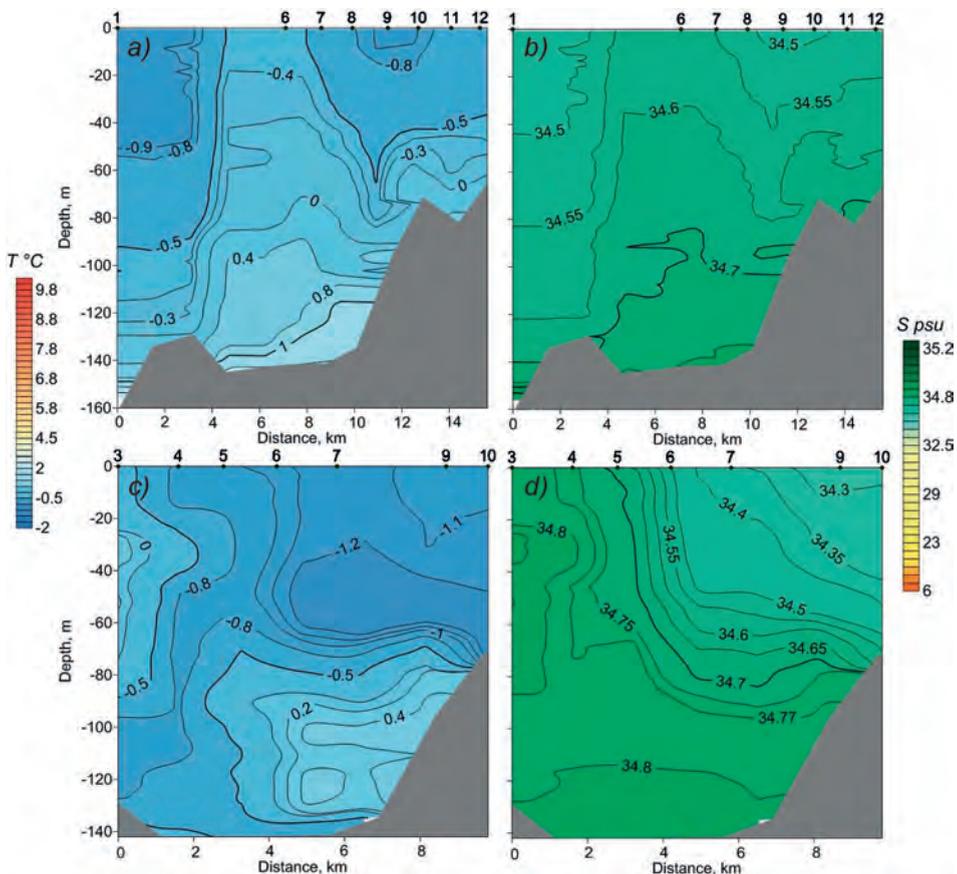


Fig. 2.1.12. Distribution of temperature (*a, c*) and salinity, psu (*b, d*) in the section P3 (*a, b*) and P4 (*c, d*) across the Grøn fjorden in April 2012.

All sections are oriented west-east.

During the summer expeditions in the Grøn fjorden, 36 sections were completed. In August 2011, there were SW, IW, TAW and AW in Grøn fjorden (one section along the fjord axis, one section in the mouth and four cross-sections). Surface water mass with minimal salinity (up to 6 psu) in the inner part of the bay was observed from the surface to a depth of 50 m. Moreover, the first 10 m of the surface layer were strongly freshened, which is associated with an increase in river runoff (Fig. 2.1.15 *a, b*).

The surface layer temperature varied from 1 to 4 °C, which is several degrees lower than the surface layer temperatures obtained in the remaining years of the survey. Most likely, this is due to the presence in 2011 in the winter–spring period of a thicker ice cover and even fast ice, which prevented the radiation heating of surface waters in comparison with other years, when mainly broken ice was observed and the water area was previously freed from the ice cover.

Under the SW, at a depth of 50 to 80–100 m, the IW lay, and on the southernmost cross section to the bottom, the water temperature in the layer varied from 1.5 to 2.5 °C. Everywhere, except for shallow areas, one could observe TAW beneath the IW at the

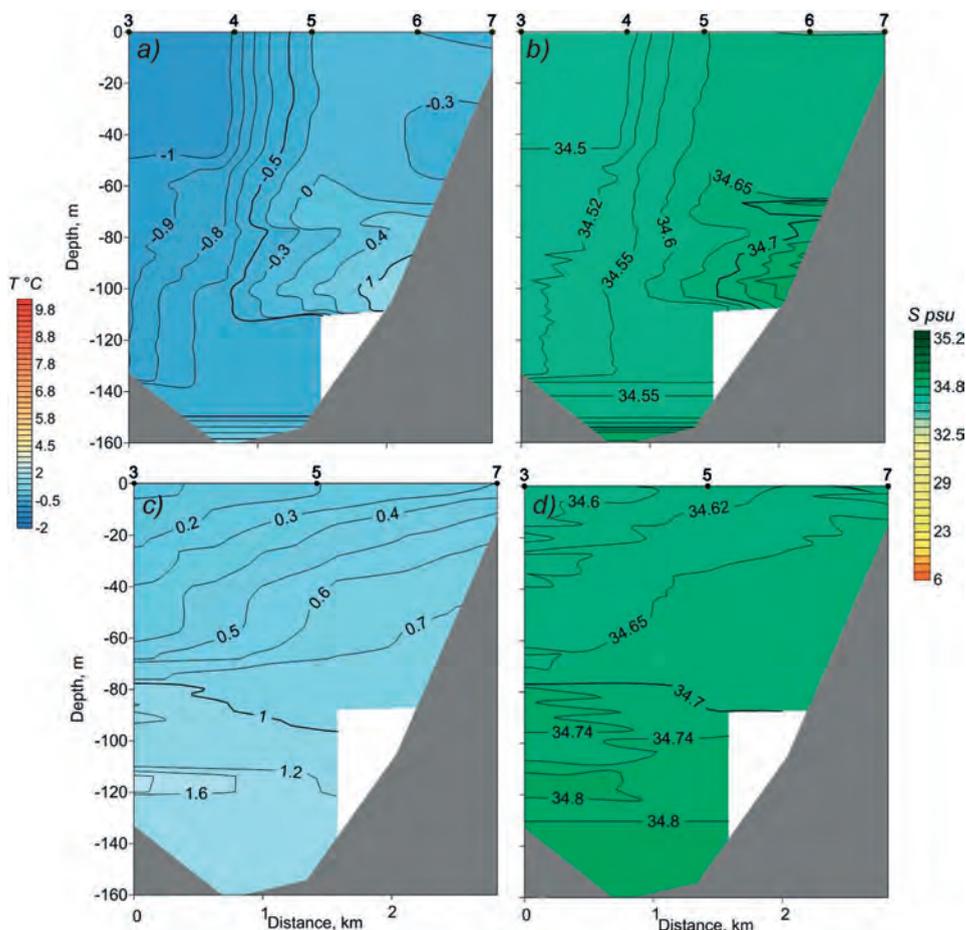


Fig. 2.1.13. Distribution of temperature, °C (a, c) and salinity, psu (b, d) in a section across the mouth of Grønfjorden in April 2012 (a, b) and April 2016 (c, d).

All sections are oriented west-east.

horizons from 80–100 m to the bottom. AW was recorded with temperatures up to 3.5 °C (Fig. 2.1.16 c, d) beneath TAW in the mouth of the fjord.

In August 2012 (one along of fjord axis and four cross-sections were made), three water masses were recorded: SW, IW and TAW. The general distribution of water masses was similar to August 2011. The lower boundary of SW was recorded at a depth of 30–35 m. The lower boundary of IW was located at a depth of 70–110 m. TAW was present beneath IW; its temperature ranged from 1.5 to 2.5 °C (Fig. 2.1.15 e, f).

In September 2013, surface water mass with minimal salinity values of up to 32 psu was observed from the surface to a depth of 40–50 m (Fig. 2.1.17 a, b). The temperature of the surface layer ranged from 6 to 6.2 °C. IW was present under SW at a depth from 40–50 to 90–110 m. The maximum temperature of AW was 4.6 °C.

In June 2014, almost the entire water column was occupied by AW in the mouth of the Grønfjorden; its temperature was from 3.5 to 4.5 °C and salinity of about 35.1 psu.

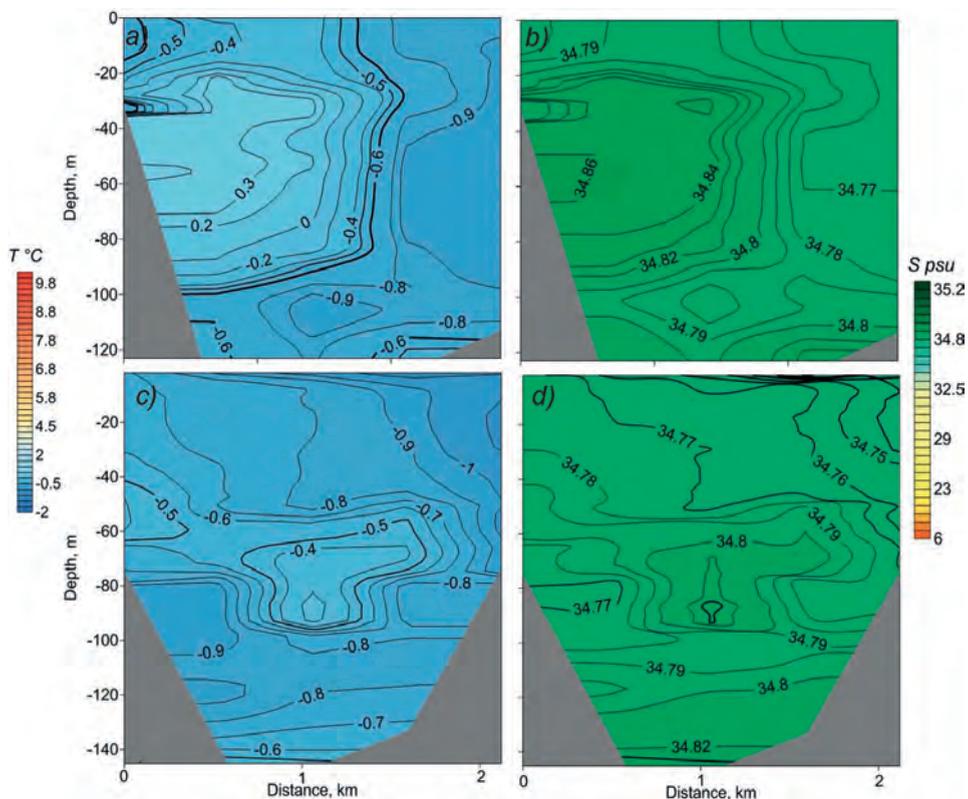


Fig. 2.1.14. Distribution of temperature (*a, c*) and salinity, psu (*b, d*) in the section P1 (*a, b*) and P2 (*c, d*) across the Grøn fjorden in April 2013.

All sections are oriented west-east.

In August 2015, there were SW, IW, and TAW in Grøn fjorden (one section along of fjord axis, one section in the mouth, and four cross-sections). The lower boundary of the SW was located at a depth of 60–80 m. The maximum temperature was 9 °C; the minimum salinity was 24 psu (Fig. 2.1.17 *c, d*). TAW was recorded over the entire water area of the fjord in the bottom layer. The temperature of TAW was 2–2.5 °C, salinity – 34.7–34.8 psu.

In August 2016, SW was located in the layer from the surface to a depth of 20–40 m. The maximum temperature was 8 °C; the minimum salinity was 30 psu. In August 2016, IW had temperatures 4.5–5.8 °C (Fig. 2.1.18. *e, f*). The lower boundary of IW was recorded at horizons of 90–130 m. AW was observed in almost all areas of the fjord. The temperature of AW was 3.9–4.9 °C.

In August 2017, there were SW, IW, TAW and AW in Grøn fjorden (one section along of fjord axis, one section in the mouth and four cross-sections). The temperature of the SW (Fig. 2.1.17 *a, b*) varied from 5 to 9 °C. IW was present beneath SW at a depth from 20–30 to 80 m TAW was observed beneath IW at a depth of 80 to 110 m. AW was identified in a bottom layer; its temperature was up to 3.5 °C and salinity up to 35.1 psu (Fig. 2.1.16 *e, f*).

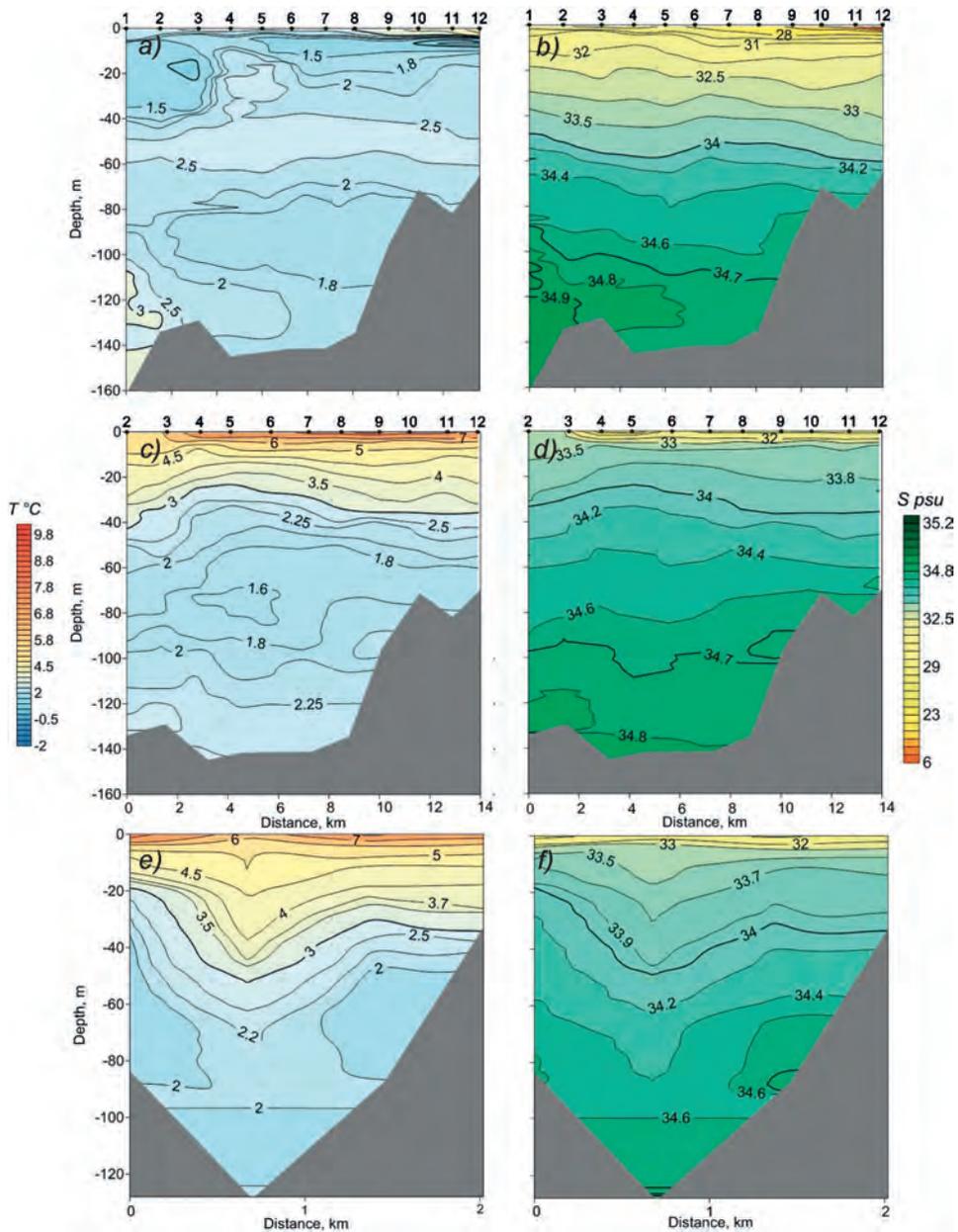


Fig. 2.1.15. Distribution of temperature, °C (a, c, e) and salinity, psu (b, d, f) along the Grøn fjorden axis in August 2011 (a, b) and August 2012 (c, d) and in cross-section P1 in August 2012 (e, f).

The sections along the axis are oriented north-south, the cross-section is oriented west-east.

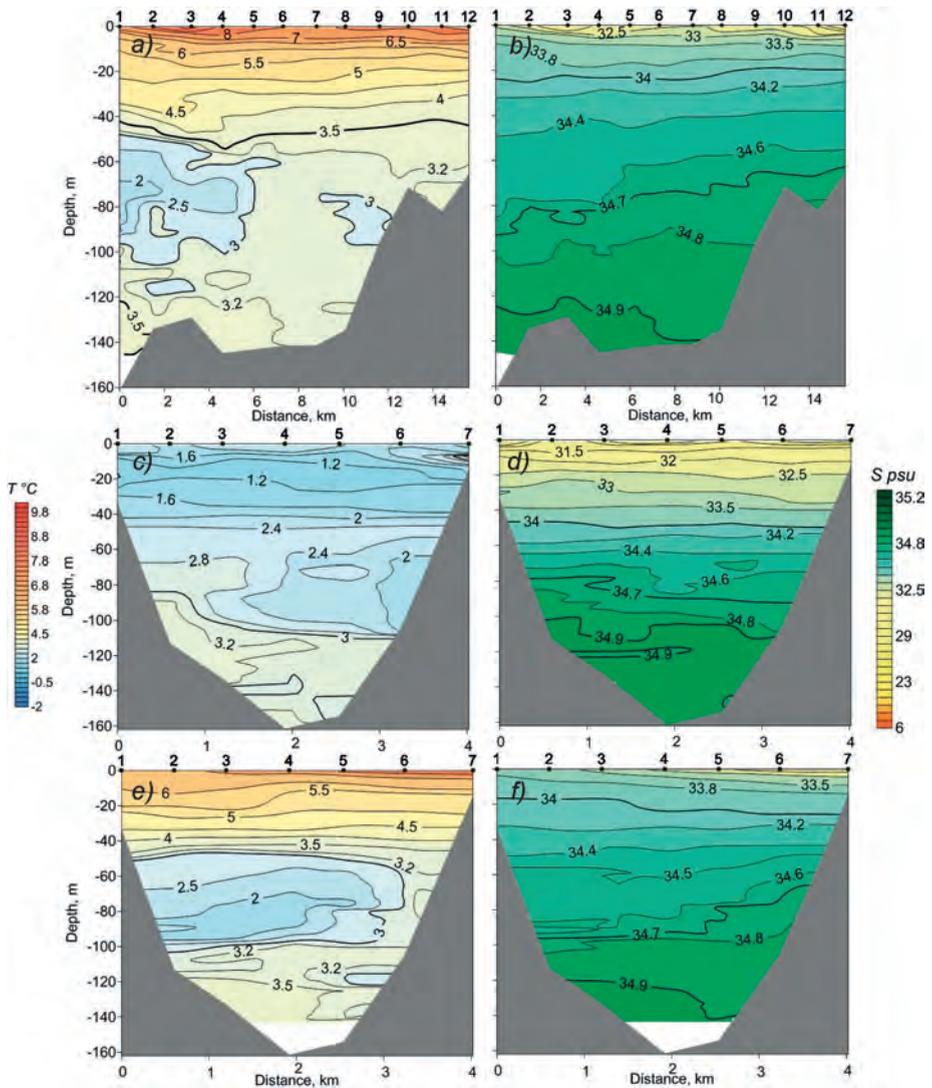


Fig. 2.1.16. Distribution of temperature, °C (a, c, e) and salinity, psu (b, d, f) along the Grøn fjorden axis in August 2017 (a, b) and in a section across the mouth of the fjord in August 2011 (c, d) and in August 2007 (e, f).

The sections along the axis are oriented north-south, the cross-section is oriented west-east.

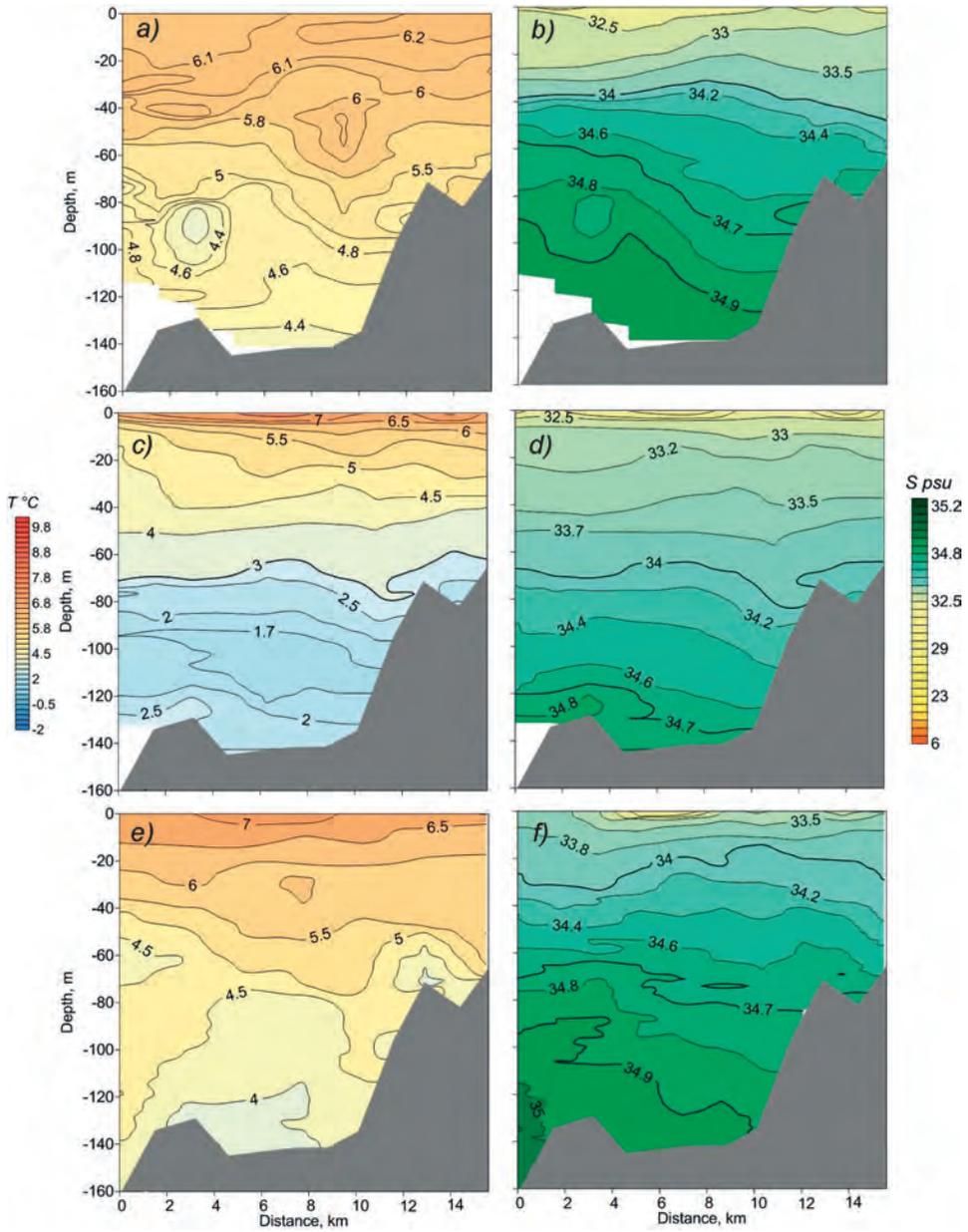


Fig. 2.1.17. Distribution of temperature, °C (a, c, e) and salinity, psu (b, d, f) along the axis of the Isfjorden in September 2013 (a, b), August 2015 (c, d), and August 2016 (e, f).

All sections are oriented north-south.

CONCLUSIONS

Based on the analysis of oceanographic measurements carried out in the Isfjorden, Billefjorden, and Grønfjorden in the spring and summer months of 2011–2017, the following conclusions can be drawn about the distribution of water masses and their thermohaline characteristics.

1. In the summer, the Billefjorden has three water masses (SW, LW, and WCW). WCW has low-temperature (up to $-1.7\text{ }^{\circ}\text{C}$) and high salinity and is located from a depth of 60–70 m to the bottom. LW forms here in the autumn/winter period and is located from a depth of 40–50 m to the upper boundary of WCW. The presence of other water masses (TAW, IW, AW) located above LW depends on the distribution of water masses in the Isfjorden.

2. In the summertime of 2014–2017, Isfjorden had typically four water masses: SW, IW, TAW and AW. The volume of AW and TAW present in the fjord has significant interannual variability. SW and IW are usually located from the surface to the horizon of 30–40 m and from 30–40 to 50–80 m, respectively. It should be noted that in 2014 an abnormal situation was observed when the entire water column of the fjord was filled only with AW of high salinity (> 35 psu).

3. During the period of study, the maximum value of the SW temperature ($8\text{ }^{\circ}\text{C}$) was recorded in July 2017 in the Billefjorden and the minimum ($2\text{ }^{\circ}\text{C}$) in the mouth of the Isfjorden in September 2015. Such low values in 2015 compared to other years, can be associated with waters coming in along the southern coast of the Isfjorden that formed during the summer period not in the fjord itself, but on the continental shelf of the archipelago.

4. The maximum temperature of AW ($6.5\text{ }^{\circ}\text{C}$) and IW ($7.5\text{ }^{\circ}\text{C}$) was observed in August 2016 in the mouth of the Isfjorden. In other years the temperature maximum in the layer of AW was $4\text{--}4.5\text{ }^{\circ}\text{C}$.

5. In spring, the Grønfjorden has two water masses: WCW with a maximum salinity of 34.85 psu was recorded in April 2013, and a minimum temperature of $-1.7\text{ }^{\circ}\text{C}$ in April 2015; LW forms here in the autumn/winter period. In the spring months of 2014 and 2017 a situation was observed when AW occupied the entire fjord, its temperature was $1.5\text{--}2.6\text{ }^{\circ}\text{C}$, and the salinity exceeded 35 psu.

6. In summer, the Grønfjorden has four water masses: SW having low salinity (the minimum value of 6 psu was recorded in the south of the fjord in August 2011), IW, TAW, and AW. The maximum temperature ($4.5\text{--}5.5\text{ }^{\circ}\text{C}$) of AW was observed in August 2016. In other years, the temperature of AW ranged from 3 to $4.5\text{ }^{\circ}\text{C}$.

7. In the spring months, the range of temperature and salinity in the fjord varies insignificantly: temperature varies from -1.7 to $2.5\text{ }^{\circ}\text{C}$, salinity ranges from 34.3 to 35.1‰. In the summer months, vice versa, temperature and salinity change a lot and range from $1\text{--}9\text{ }^{\circ}\text{C}$ and $6\text{--}35.1$ psu, respectively.

8. The interannual variability of water masses volume in the fjords varies significantly. Unlike the summer months, when in most cases, the orientation of the isotherms, isohalines, and isopycnic lines is horizontal, the frontal zones are typical for the spring months.

Based on a comparison of the data obtained in the 1990–2000s, the WOA13 data and oceanographic measurements carried out in the Isfjorden in spring and summer months of 2014–2017, the distribution of water masses and their thermohaline characteristics in Isfjorden have the following features:

- in the summer months of the 1990s, AW was recorded only in 1994 and 1998; in 2002–2017 AW was observed almost every year, which allows us to conclude that AW intrudes into the water area of the Isfjorden more often;
- the temperature of AW entering the fjord in the summer months increased from 3.5 °C in the 1990s to 4–6.5 °C in 2014–2017;
- unlike April 1997 and 1998 when LW, WCW, TAW were recorded in the Isfjorden, WCW was not recorded in the spring months of 2016 and 2017;
- in June 2014, one observed an abnormal situation when AW occupied the entire water area of Isfjorden;
- in the summer months of the 2000s and 2010s, the average temperature and salinity in the Isfjorden were highest over the entire history of observations since 1965.

REFERENCES

- Meshcheryakov N.I., Bobrov K.A., Tarasov G.A.* Sedimentological and oceanological studies in April 2014 in the Grønfjorden Bay. *Kompleksnyye issledovaniya prirody Shpicbergena i priliegajushhego shel'fa. Trudy nauchno-prakticheskoy konferencii.* Comprehensive studies of the nature of Spitsbergen and the adjacent shelf. Proc. of Research-to-Practice Conference. Moscow: GEOS, 2014, 12: 210–215. [In Russian].
- Moiseev D.V., Bobrov K.A.* Oceanographic research in the Grønfjorden Bay. *Arkticheskoe morskoe prirodopol'zovanie v XXI veke — sovremennyy balans nauchnykh traditsij i innovacij: Tezisy dokladov Mezhdunarodnoj nauchnoj konferencii.* Arctic marine nature management in the XXI century – a current balance of scientific traditions and innovations: Abstracts of reports from the International Scientific Conference (on the 80th anniversary of Murmansk Marine Biological Institute, Kola Scientific Center of the Russian Academy of Sciences (MMBI KSC RAS)). Apatity: Publishing house of KSC RAS, 2015: 168 p. [In Russian].
- Moiseev D. V., Gromov M. S.* Thermohaline conditions in the bays and fjords of West Spitsbergen in the summer of 2003 and 2008. *Kompleksnyye issledovaniya prirody Shpicbergena. Trudy nauchno-prakticheskoy konferencii.* Comprehensive studies of the Nature of Spitsbergen. Proceedings of Research-to-Practice Conference. Moscow: GEOS, 2009: 332–335. [In Russian].
- Moiseev D.V., Ionov V.V.* Some results of oceanographic studies in bays and fjords of West Spitsbergen in the summer of 2001 and 2002. *Kompleksnyye issledovaniya prirody Shpicbergena. Trudy nauchno-prakticheskoy konferencii.* Comprehensive studies of the Nature of Spitsbergen. Proceedings of Research-to-Practice Conference. Apatity: Publishing house of KSC RAS, 2006, 6: 261–270. [In Russian].
- Pavlov A.K., Ivanov B.V., Zhuravsky D.M., Tverberg V.* Warming in the bays of West Spitsbergen: a short-term phenomenon or a steady trend? *Problemy Arktiki i Antarktiki.* Problems of Arctic and Antarctic. 2010, 3 (86): 70–78. [In Russian].
- Pavlov A.K.* *Formirovanie termicheskogo rezhima vod zalivov Zapadnogo Shpicbergena.* The formation of the thermal regime of the waters of West Spitsbergen bays. PhD Thesis. St. Petersburg: Publishing house of AARI, 2011: 22 p. [In Russian].
- Tislenko D.I., Ivanov B.V.* Long-term variability of the temperature of Atlantic waters in the fjords of the West Spitsbergen during the period of the first (1920–1940) and modern warming in the Arctic. *Problemy Arktiki i Antarktiki.* Problems of Arctic and Antarctic. 2015, 2 (104): 93–100. [In Russian].
- Aagaard K., Greisman P.* Toward new mass and heat budgets for the Arctic Ocean. *J. Geophys. Res.* 1995, 80: 3821–3827.
- Berge J., Johnsen G., Nilsen F., Gulliksen B. and Slagstad D.* Ocean temperature oscillations enable reappearance of blue mussels *Mytilus edulis* in Svalbard after a 1000 year absence. *Marine Ecology Progress Series.* 2005, 303: 167–175.

Boyer T.P., Antonov J.I., Baranova O.K., Coleman C., Garcia H.E., Grodsky A., Johnson D.R., Locarnini R.A., Mishonov A.V., O'Brien T.D., Paver C.R., Reagan J.R., Seidov D., Smolyar I.V., and Zweng M.M. World Ocean Database 2013, NOAA Atlas NESDIS. Silver Spring, 2013: 209 p.; DOI: 10.7289/V5nz85mt.

Cottier F.R., Tverberg V., Inall M.E., Svendsen H., Nilsen F. and Griffiths C. Water mass modification in an Arctic fjord through cross-shelf exchange. *J. Geophys. Res. Oceans.* 2005, 110; DOI: 10.1029/2004JC002757.

Haarpaintner J., O'Dwyer J., Gascard J.C., Haugan P.M., Schauer and U. Østerhus S. Seasonal transformation of water masses, circulation and brine formation, observed in Storfjorden Svalbard. *Annales Glaciology.* 2001, 33: 437–443.

Hop H., Pearson T., Hegseth E.N., Kovacs K.M., Wiencke C., Kwasniewski S., Eiane K., Mehlum F., Gulliksen B., Wlodarska-Kowalczyk M., Lydersen C., Weslawski J.M., Cochrane S., Gabrielsen G.W., Leakey, R.J.G., Lonne O.J., Zajaczkowski, M., Falk-Petersen S., Kendal, M., Wangberg S.-A., Bischof K., Voronkov A.Y., Kovaltchouk N.A., Wiktor J., Poltermann M., di Prisco G., Papucci C., Gerland S. The marine ecosystem of Kongsfjorden, Svalbard. *Polar Research.* 2002, 21: 167–208.

ICES Dataset on Ocean Hydrography. The International Council for the Exploration of the Sea. Copenhagen, 2014. Available at: <http://ocean.ices.dk> (accessed 13.08.2018).

Łącka M., Zajaczkowski M. Does the recent pool of benthic foraminiferal tests in fjordic surface sediments reflect interannual environmental changes? The resolution limit of the foraminiferal record. *Annales Societatis Geologorum Poloniae.* 2016, 86: 59–71.

Nilsen F., Cottier F., Skogseth R. and Mattsson S. Fjord shelf exchange controlled by ice and brine production: the interannual variation of Atlantic Water in Isbille, Svalbard. *Continental Shelf Research.* 2008, 28: 1838–1853.

Nilsen F., Gjevik B., Schauer U. Cooling of the West Spitsbergen Current: isopycnal diffusion by topographic vorticity waves. *J. Geophys. Res.* 2006, 111: C08012; DOI: 10.1029/2005JC002991.

Nilsen F., Skogseth R., Vaardal-Lunde J. and Inall M. A Simple Shelf Circulation Model: Intrusion of Atlantic Water on the West Spitsbergen Shelf. *J. Physical Oceanography.* 2016, 46 (4): 1209–1230.

Saloranta T.M., Svendsen H. Across the Arctic Front west of Spitsbergen: high-resolution CTD sections from 1998–2000. *Polar Research.* 2001, 20: 177–184.

Schauer U., Beszczynska-Moller A., Walczowski W., Fahrbach E., Piechura J. and Hansen E. Variation of measured heat flow through the Fram Strait Between 1997 and 2006. *Arctic – Subarctic Ocean Fluxes.* Springer: Dordrecht, 2008: 65–85.

Svendsen H., Beszczynska-Moller A., Hagen, J.O., Lefauconnier B., Tverberg V., Gerland S., Orbaek J.B., Bischof K., Papucci C., Zajaczkowski M., Azzolini R., Bruland O., Wiencke C., Winther J.-G., Dallmann W. The physical environment of Kongsfjorden Krossfjorden, an Arctic fjord system in Svalbard. *Polar Research.* 2002, 21: 133–166.

Tverberg V., Nilsen F., Goszczko I., Cottier F., Svendsen H. and Gerland S. The warm winter temperatures of 2006 and 2007 in the Kongsfjorden water masses compared to historical data. In: 8th Ny-Ålesund seminar Polarnet technical report. Rome: Earth and Environment Department, National Research Council, 2007: 40–44.

Walczowski W. and Piechura J. Pathways of Greenland Sea warming. *Geophys. Res. Lett.* 2007, 34; DOI: 10.1029/2007GL029974.

2.2. SEASONAL AND LONG TERM CHANGE IN THE ICE COVER IN THE SPITZBERGEN ARCHIPELAGO

D.I. Tislenko, B.V. Ivanov, V.M. Smolyanitsky, P.N. Svyashchennikov, A.V. Vesman, K. Isaksen, H. Gjeltén

Numerous Russian and foreign scientific publications studied the climate of the Spitsbergen archipelago. Svyashchennikov et al. (2010, 2011); Tislenko, Ivanov (2015); Marsz, Styszyńska (2013); Nordli et al. considered changes of many central components of the climate system over the 20th century and the first decade of the 21st century. Nilsen et al. presented an analysis of the temporal variability of the surface air temperature (SAT) for the period 1898–2012. It allows us to conclude that there was an increase in the SAT by 2.6 °C for the indicated time interval in terms of a linear trend. Moreover, the period 2005–2012 is estimated as the warmest for all time of instrumental monitoring.

Ivanov and Zhuravsky (2010) analyzed the long-period variability of several essential ice characteristics for the period 1973–2008, which revealed a general softening of the ice situation using the example of Grønfjorden. Significant interannual variability is noted. So, if in the winter seasons of 2005–2007, since stable ice cover (fast ice) did not form at all, then there was an increase in the average and maximum thickness of fast ice until the spring of 2011, but in 2011–2014, stable fast ice was absent in the Grønfjorden again. Studies performed by Russian and Norwegian researchers (Pavlov et al., 2010; Tislenko, Ivanov, 2015; Pavlov et al., 2013) were devoted to the analysis of the long-period temperature variability of intermediate transformed Atlantic waters (TAW) intruding the fjords of West Spitsbergen. The calculated estimates of the long-term variability of TAW in the fjords coincide with the results presented in the well-known work of Polyakov et al. (2004). In general, the climate of the Spitsbergen archipelago tends to become milder. It corresponds to the well-known concept of “rapid warming” in the Arctic (Alekseev, 2014; Bekryaev et al., 2010; Polyakov et al., 2002).

In recent years, several serious studies have appeared (Frolov et al., 2010; Frolov et al., 2009; Haas et al., 2008; Renner et al., 2014). They are devoted to the problems of long-term changes in the area and thickness of the ice cover both in the Spitsbergen archipelago (Fram Strait) and the Arctic as a whole. For example, the average thickness of the ice cover in August–September decreased by 44 % in the region of the North Pole for the period 2001–2007, and it was proposed to consider an increase in the SAT values as a reason (Haas et al., 2008). For the Fram Strait region, a decrease in ice thickness in 2003–2012 amounted to more than 50 %, and the trend calculated for this period was 0.3 m/year (Renner et al., 2014). However, there are still no detailed researches devoted to the study of the patterns and characteristics of the seasonal and long-term ice regime of waters washing the Spitsbergen archipelago.

In recent years, the laboratory of regime manuals of AARI collected and summarized unique data on ice characteristics for the entire available period of visual and instrumental monitoring (Frolov et al., 2010; Frolov et al., 2009).

The period since 1979 provided high-quality homogeneous datasets with a high degree of spatial and temporal resolution obtained from satellite observations. This circumstance allowed the authors to quantify the spatial and temporal variability of ice conditions in the waters washing Spitsbergen archipelago for the period 1979–2015.

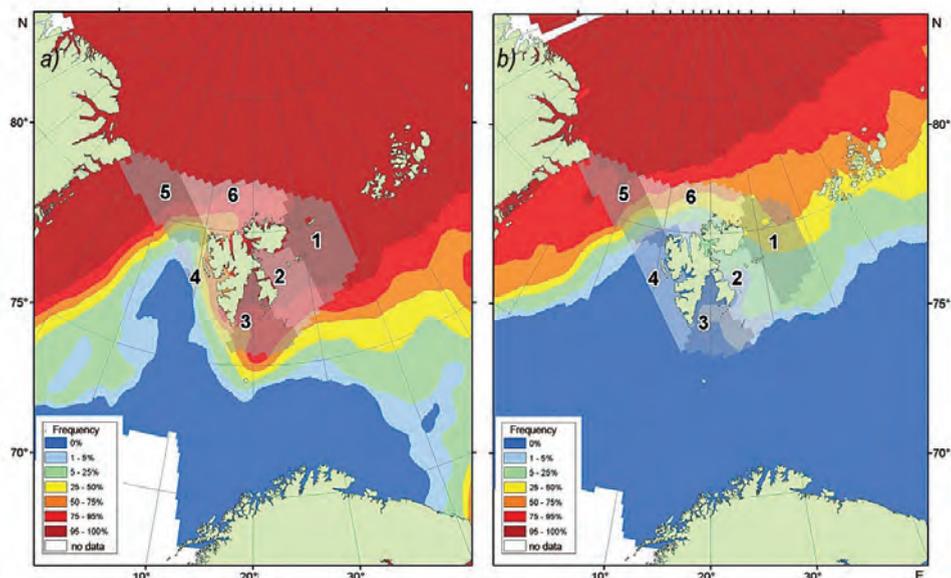


Fig. 2.2.1. The frequency of encounters with ice of any kind during periods of maximum (a) and minimal (b) development of ice cover and the accepted pattern of zoning of water areas washing Spitsbergen.

Legend 1–6 see the text.

The following open sources of information were used to obtain quantitative estimates; the resources were presented in the Global Digital Sea Ice Data Bank (Frolov et al., 2010; Frolov et al., 2009):

- regional 7–30-day ice charts from the archive of the World AARI Sea Ice Data Center (Greenland and Barents Seas for the period 1933–2013 (<http://wdc.aari.ru>));
- daily estimates of total ice concentration using the NASATEAM algorithm based on SSMR–SSM/I–SSMIS data on a 25×25 km grid over the period 1978–2015, from the NSIDC archive (ftp://sidacs.colorado.edu/DATASETS/nsidc0051_gsfc_nasateam_seaice/final-gsfc/).

The ready datasets we are studying are a product that allows us to estimate the seasonal and long-term variability of ice cover and its area in several quasihomogeneous regions neighboring Spitsbergen archipelago. The regions were selected based on expert analysis of the frequency of encounters with ice of any kind in winter (November–May) and summer (June–September), as well as in the months of maximum (March) and minimum (September) ice cover development based on ice mapping for the period 1933–2013.

In total, six regions were identified (Fig. 2.2.1), they have the following general geographic specifics (provisionally titled): 1 – East Spitsbergen region, 2 – Barents Sea region, 3 – South Spitsbergen region, 4 – West Spitsbergen region, 5 – Fram Strait region, 6 – North Spitsbergen region (“Whale Bay”). The assessment of the quality of this identification was confirmed based on an analysis of seasonal changes in ice cover, according to SSMR–SSM/I–SSMIS data. The data showed significant differences in the seasonal dynamics of absolute ice cover values and their long-term trends. A chart of the temporal variability of the average annual sea ice area for a region located off the west coast of Spitsbergen archipelago (Fram Strait, Region 4) in Fig. 2.2.2 is an example of using data from the above mentioned Global Bank.

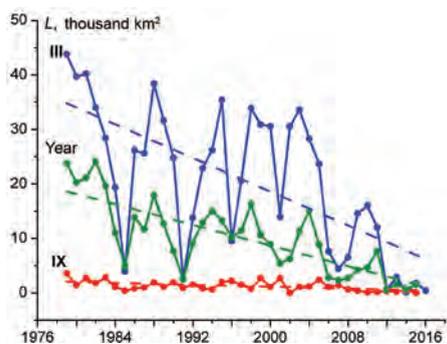


Fig. 2.2.2. Temporal variability of ice cover area for region 4 for the period from 1979 to 2015.
III – March, IX – September.

Fig. 2.2.2 shows that despite the high interannual variability in the winter period (March), there is a significant decrease in the ice cover area in winter and on average over the year for the entire considered period. In terms of a linear trend, this reduction (average annual estimates) is about 0.5 thousand km² per year. Please note that the obtained linear trends are statistically significant at the level of $P < 0.05$. The value of the coefficient of determination is 0.59, i.e., the obtained linear trend describes more than 50 % of the total variance of the analyzed time series.

Table 2.2.1 presents the values of the coefficient of the linear trend angle for both particular months and annual average values for all six regions. The reduction in the area of ice cover (average annual values) occurs at almost the same rate in all regions except for Region 5, which stands out. Here, for the period April–November, linear trends are not statistically significant, and the rate of reduction in the area of ice cover in other months of the year is 2–6 times lower than in other regions. Apparently, this nature of variability is associated with the features of water and ice circulation, which is a unidirectional stable removal of multiyear ice from the central parts of the Arctic basin by the East Greenland Current.

For the remaining regions have a generally identical pattern of variability. Trend angle coefficients are generally maximum in the cold period (October–March) and minimum in the warm period (April–September). However, for regions located east of the archipelago (1–3), high rate values of change in the ice area are typical in July–September. Maximum values were found in region 1 in July and November (–1.35 thousand and –1.37 thousand km² / year, respectively). The maximum decrease in the average annual values of the ice

Table 2.2.1

The coefficient of linear trend angle ($-a$, thousand km² / year) for six regions of the Spitsbergen archipelago

Region	I	II	III	IV	V	VI	VII	VIII	IX	X	XI	XII	Год
1	0.32	0.28	0.11	0.08	0.27	0.94	1.35	0.50	0.15	1.02	1.37	0.45	0.57
2	0.42	0.37	0.18	0.10	0.35	0.68	0.69	0.30	0.14	0.53	1.05	0.49	0.44
3	0.85	0.68	0.37	0.37	0.66	0.68	0.33	0.01	0.01	0.17	0.81	1.03	0.49
4	0.86	0.90	0.74	0.75	0.59	0.38	0.23	0.14	0.04	0.04	0.29	0.73	0.47
5	0.17	0.24	0.17	0.09	0.07	0.06	0.09	0.02	0.11	0.00	0.05	0.13	0.07
6	0.80	0.77	0.44	0.18	0.23	0.22	0.43	0.45	0.36	0.53	0.65	0.72	0.48

Note. The values of a , which are not statistically significant at the level of $P < 0.05$ are in italics.

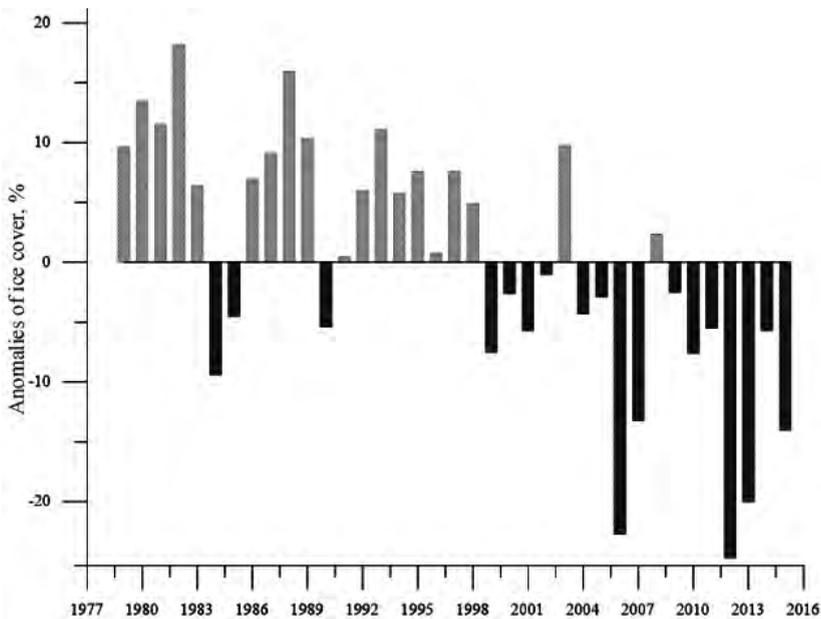


Fig. 2.2.3. Anomalies (%) of ice cover in the region of Spitsbergen for 1979–2015.

area is also observed in Region I and amounts to -0.57 thousand km^2 / year. Thus, based on the data obtained, we can conclude that in the waters surrounding Spitsbergen archipelago, over the past 35 years, ice conditions tend to become milder both on average for the year and individual seasons. Fig. 2.2.3 presents the temporal variability of the anomaly of total ice cover in the area of Spitsbergen for 1979–2015 (for all regions in general), calculated according to the method proposed in Zhichkin (2014). The approach presents the numerical values of the anomalies in percent. 100 % is the average ice cover for the entire analyzed period. Analysis of the data showed that in the waters surrounding Spitsbergen archipelago, the ice cover decreases in general over the past three decades, contrasted to its noticeable interannual variability. Moreover, on average, positive anomalies (1979–1998) decrease in absolute value, and negative ones (from 1999 to the present) increase.

Table 2.2.2 shows the statistical characteristics of total ice cover for each month of the year for the entire analyzed period.

As the presented data show, we can observe ice cover in the waters washing Spitsbergen almost throughout the year. On average, by November, most of the water

Table 2.2.2

Total ice cover statistics (%)

Characteristic	Month											
	IX	X	XI	XII	I	II	III	IV	V	VI	VII	VIII
The average	29	40	61	73	78	82	86	86	81	74	53	34
Minimum	10	16	22	29	37	43	54	53	43	34	19	9
Maximum	56	72	90	98	99	98	98	100	98	92	85	56
SD	11	16	21	18	17	15	10	8	10	13	16	12

Note. SD – Standard deviation.

area is covered with ice. However, in the last 10–15 years, the ice cover in November is often not more than 20–40 %. Separately, we can distinguish the 2006–07 season, when there was a regular increase in the area of ice cover from September to October. Then in November, the ice cover decreased by 7 to 12 %. The highest ice cover values correspond to the period of January–May (78–86 %). March and April demonstrate the maximum values. The absolute maximum was recorded in April 1979. The smallest variability is typical for the period of March–May; the standard deviation for these months is 8–10 %. The studied time interval had no ice-free months. On average, September can be considered as a month with the least ice cover (less than 30 %). The absolute minimum ice cover in the area of Spitsbergen was observed in August 2004 and amounted to 9 %. The most significant variability is typical from October through January and July; the standard deviation is 16–21 %.

Table 2.2.3

Ice cover statistics (%) for selected areas

Characteristic	Month											
	IX	X	XI	XII	I	II	III	IV	V	VI	VII	VIII
<i>Region 1</i>												
Average	21.9	44.7	77.0	91.4	94.8	96.4	98.5	98.7	96.6	88.0	55.7	27.0
Minimum	0.0	0.0	0.0	19.3	51.3	61.2	82.2	59.4	32.2	14.8	0.0	0.0
Maximum	75.7	98.1	100.0	100.0	100.0	100.0	100.0	100.0	100.0	100.0	99.5	71.9
SD	24.7	33.6	33.1	18.6	11.0	9.0	3.7	6.7	11.8	21.5	30.8	25.1
<i>Region 2</i>												
Average	5.0	24.1	65.4	84.1	89.2	91.7	95.1	96.3	92.7	81.3	43.1	9.1
Minimum	0.0	0.0	0.0	8.8	45.9	38.5	67.5	65.8	56.1	19.9	0.2	0.2
Maximum	51.8	80.0	100.0	100.0	100.0	100.0	100.0	100.0	100.0	100.0	95.5	58.5
SD	10.7	24.8	35.4	25.0	15.2	13.7	7.9	6.3	11.1	24.0	26.3	14.4
<i>Region 3</i>												
Average	1.7	5.9	32.8	60.4	73.2	79.5	85.7	86.1	74.3	52.2	17.5	3.1
Minimum	0.2	0.2	0.4	1.1	4.8	13.2	22.7	48.8	22.2	2.8	0.7	0.7
Maximum	15.3	42.6	93.7	99.8	100.0	100.0	100.0	100.0	100.0	100.0	72.3	16.8
SD	2.4	9.6	28.6	32.8	30.5	26.3	18.0	14.0	20.8	26.4	16.7	2.9
<i>Region 4</i>												
Average	2.7	1.9	8.6	22.8	38.7	43.2	45.6	38.5	23.7	17.7	10.3	6.4
Minimum	0.0	0.0	0.0	0.2	0.2	0.0	0.2	1.1	2.4	1.1	0.2	0.2
Maximum	7.8	8.4	53.2	90.9	97.6	93.1	94.8	99.4	88.7	51.9	31.0	18.4
SD	2.0	1.7	12.6	24.0	31.6	31.7	28.1	24.2	21.9	14.2	8.3	4.6
<i>Region 5</i>												
Average	72.9	80.3	82.4	82.9	82.9	85.3	86.6	87.6	86.8	88.7	83.7	72.7
Minimum	40.5	66.8	67.4	71.1	69.2	67.2	73.5	71.5	67.5	73.8	63.5	13.1
Maximum	89.3	95.9	93.9	99.4	99.6	98.7	99.7	100.0	98.9	99.1	96.4	91.0
SD	11.1	6.7	6.3	6.4	8.0	8.8	6.3	7.2	7.9	7.0	8.8	15.7
<i>Region 6</i>												
Average	48.6	58.4	71.2	76.9	73.9	79.1	89.0	92.0	90.8	91.5	81.6	62.0
Minimum	2.0	17.8	23.7	26.4	12.8	26.7	42.3	46.5	47.6	53.1	28.8	15.1
Maximum	83.7	96.6	100.0	100.0	100.0	100.0	100.0	100.0	100.0	100.0	99.9	92.7
SD	23.8	22.7	22.9	21.5	24.7	22.1	14.3	10.7	11.5	10.6	18.8	22.6

For a more detailed analysis of the spatial and temporal variability of ice conditions, a similar statistical analysis was performed individually for each of the six regions. The results are presented in table. 2.2.3. March and April demonstrate the maximum values of ice cover, August and September show the minimum ones. Regions 1–4 may have no ice cover at all from July to November. Regions 5 and 6 didn't have any months with no sea ice by monthly average values. The minimum standard deviations for individual months were recorded in Region 5; they ranged from 6 to 16 %. The most significant variability is observed in Region 4, where the standard deviation varies from 2 to 32 % during the year.

The interannual variability of ice cover in Region 4 (the eastern part of the Fram Strait), which is strongly influenced by the Atlantic waters (West Spitsbergen Current), should be described in detail. The lowest average ice cover values for all months are typical for this water area in comparison with other regions. Over the past ten years, the average ice cover of this region is not more than 7 %. It should be noted that the most significant variability is observed not in the warm period when the seasonal melting of the ice cover occurs, but in the cold one (January–April). The standard deviation for the period from January through April is from 24 to 32 % with a difference between maximum and minimum values of 91–98 %, and from July through October, it is from 2 to 8 % with a difference of 8 to 18 %, respectively. Based on Table 2.2.3, charts of changes in average ice cover were constructed, they allow to evaluate the spatial features of seasonal variability (Fig. 2.2.4). So, for regions 1–4, we can observe a well-defined seasonal variation, and the seasonal peak-to-peak value in regions 1–3 is close in absolute value but significantly higher (about two times) than in Region 4. The seasonal course of ice cover for regions 5 and 6 is not so well-defined. The reasons for the differences, as mentioned above, are due to the features of the water circulation in the strait between Greenland and Spitsbergen (Region 5) and the existence of the stationary winter polynya “Whale Bay” north of Spitsbergen archipelago (Region 6).

To assess the spatial features of the variability of ice cover, we compared our results with data typical for another vast Arctic archipelago – Franz Josef Land (FJL) (Zhichkin, 2014). A comparison of average monthly estimates of the ice cover area showed that the

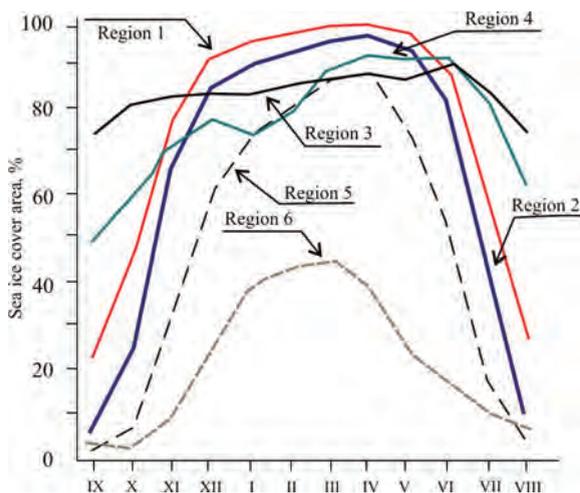


Fig. 2.2.4. Seasonal changes in ice cover in the area of the Spitsbergen archipelago.

area of the FJL has, of course, more ice. The smallest variability of ice cover in the FJL water area occurs in the cold season (November–April), the standard deviation varies from 0 to 2 %, whereas Spitsbergen archipelago maximum variability is typical for these months, especially in the period November–February (standard deviation varies from 15 to 21 %). The warm period of the year (August–September) shows the opposite situation. The difference between the maximum and minimum values of ice cover in this period is 46–48 % (SD is 11–12 %) in the area of Spitsbergen archipelago, while for the FJL archipelago, this value is equal to 90–95 % (SD is 27 %).

At the same time, there are some features typical for both regions. For example, the long-term variability of ice cover is very similar. First of all, this concerns time intervals, when ice anomalies in both regions had the same sign. Positive anomalies (“cold” phase) were observed from 1979 to 1998, negative ones (“warm” phase) – from 1999 to the present. According to the authors, this may indicate that there is one common external source of observed changes.

CONCLUSIONS

Within the scope of the analysis, we can draw the following conclusions.

In the waters surrounding Spitsbergen archipelago, over the past 35 years, ice conditions tend to become milder both on average for the year and individual seasons. The total reduction in the area of ice cover in terms of a linear trend by average annual values is 2.6 thousand km² per year.

The nature of the seasonal variability of ice cover is due to the features of water and ice circulation in the Spitsbergen archipelago area.

From 1979 to 1998, positive ice cover anomalies decrease, and from 1999 to the present, negative ice cover anomalies increase.

Differences and similarities in seasonal and long-term variability of ice cover in the Norwegian, Greenland, and Barents Seas, as well as in the Arctic basin, washing the Spitsbergen and FJL archipelagos were revealed.

REFERENCES

- Alekseev G.V. The Arctic Measuring of Global Warming. *Led i Sneg*. Ice and Snow. 2014, 2: 53–68. [In Russian].
- Alekseev G.V. Manifestation and intensification of global warming in the Arctic. *Fundamental'naja i prikladnaja klimatologija*. Fundamental and Applied Climatology. 2015, 1: 11–26. [In Russian].
- Zhichkin A.P. Ice conditions in the Franz Josef Land archipelago. *Trudy Kol'skogo nauchnogo centra. Okeanologija*. Proc. of the Kola Science Center. Oceanology. 2014, 2 (4): 82–89. [In Russian].
- Ivanov B.V., Pavlov A.K., Andreyev O.M., Zhuravsky D.M., Svyashchennikov P.N. Studies of the snow and ice cover of the Grøn fjorden (Spitsbergen): historical data, field studies, modeling. *Problemy Arktiki i Antarktiki*. Problems of Arctic and Antarctic. 2012, 2 (92): 43–54. [In Russian].
- Ivanov B.V., Zhuravsky D.M. Ice conditions in the Grøn fjorden (Spitsbergen) during 1974–2008. *Problemy Arktiki i Antarktiki*. Problems of Arctic and Antarctic. 2010, 2 (85): 27–31. [In Russian].
- Frolov I.Ye., Gudkovich Z.M., Karklin V.P., Smolyanitsky V.M. Climate change in Arctic and Antarctic is the result of natural causes. *Problemy Arktiki i Antarktiki*. Problems of Arctic and Antarctic. 2010, 2: 52–61. [In Russian].
- Svyashchennikov P.N., Ivanov B.V., Bocharov P.V., Zhuravsky D.M., Timachev V.F., Semenov A.V., Soldatova T.A., Antsiferova A.R. Study of radiation climatic factors and the meteorological regime of the Spitsbergen. *Rossijskie issledovanija po programme MPG 2007/08. T. III. Meteorologicheskie i*

- geofizicheskie issledovanija*. Russian studies under the International Polar Year (IPY) 2007/08 program. T. Sh. Meteorological and geophysical studies. 2011: 78–84. [In Russian].
- Pavlov A.K., Ivanov B.V., Zhuravsky D.M., Tverberg V. Warming in the Fjords of West Spitsbergen. Anomaly or natural variability. *Problemy Arktiki i Antarktiki*. Problems of Arctic and Antarctic. 2010, 3 (86): 78–84. [In Russian].
- Svyashchennikov P.N., Ivanov B.V., Bocharov P.V. The influence of cloud characteristics on the radiation regime of West Spitsbergen. *Priroda shel'fa i arhipelagov evropejskoj Arktiki. Kompleksnye issledovanija arhipelaga Shpicbergen*. The nature of the shelf and archipelagos of the European Arctic. Comprehensive studies of the Spitsbergen archipelago. Moscow: GEOS, 2010: 474–480. [In Russian].
- Tislenko D.I., Ivanov B.V. Long-term variability of the temperature of Atlantic waters in the fjords of the West Spitsbergen during the period of the first (1920–1940) and modern warming in the Arctic. *Problemy Arktiki i Antarktiki*. Problems of Arctic and Antarctic. 2015, 2 (104): 93–100. [In Russian].
- Bekryaev R.V., Polyakov I.V., Alekseev V.A. Role of Polar Amplification in Long-Term Surface Air Temperature Variations and Modern Arctic Warming. *J. Climate*. 2010, 23: 3888–3906.
- Frolov I.Ye., Gudkovich Z.M., Karklin V.P., Kovalev E.G., Smolyanitsky V.M. Climate change in Eurasian Arctic Shelf seas. Praxing publishing ltd., 2009. 164 p.
- Haas C., Pfaffling A., Hendricks S., Rabenstein, L., Etienne J.-L., Rigor I. Reduced ice thickness in Arctic Transpolar Drift favors rapid ice retreat. *Geophys. Res. Lett.* 2008, 35 (17): 2564–2576.
- Marsz A., Styszyńska A. Climate and Climate Change at Hornsund, Svalbard. Gdynia: Gdynia Maritime University, 2013: 402 p.
- Nordli Ø, Przybylak R., Ogilvie A., and Isaksen K. Long-term temperature trends and variability on Spitsbergen: the extended Svalbard Airport temperature series, 1898–2012. *Polar Research*. 2014, 33 (1); DOI: 10.3402/polar.v33.21349.
- Pavlov A.K., Tverberg V., Ivanov B.V., Nilsen F., Falk-Petersen S., Granskog M.A. Warming of Atlantic Water in two west Spitsbergen fjords over the last century (1912–2009). *Polar Research*. 2013, 32; DOI: 10.3402/polar.v32i0.11206.
- Polyakov I.V., Alekseev G.V., Timokhov L.A., Bhatt U.S., Colony R.L., Simmons H.L., Walsh D., Walsh J.E., Zakharov V.F. Variability of the Intermediate Atlantic Water of the Arctic Ocean over the Last 100 Years. *J. Climate*. 2004, 17: 4485–4497.
- Polyakov I.V., Alekseev G.V., Bekryaev R.V., Bhatt U., Colony R., Johnson M.A., Karklin V.P., Makshtas A.P., Walsh D., Yulin A.V. Observationally based assessment of polar amplification of global warming. *Geophys. Res. Lett.* 2002, 29: 1878–1891.
- Renner A.H., Gerland S., Haas C., Spreen G., Beckers J.F., Hansen E., Nicolaus M. and Goodwin H. Evidence of Arctic sea ice thinning from direct observations. *Geophys. Res. Lett.* 2014, 41 (14): 5029–5036.

Chapter 3

Inland waterways, glaciers, and permafrost of West Spitsbergen

3.1. DYNAMICS OF THE DEPTH OF SEASONAL THAWING OF PERMAFROST ON WEST SPITSBERGEN IN THE CONDITIONS OF MODERN CLIMATE CHANGE

P.V. Bogorodsky, V.Yu. Kustov

One of the most important natural consequences of warming is the degradation of permafrost (IPCC, 2014). Although the scenario of its future transformation at a qualitative level seems quite clear, the real picture may have significant differences due to the influence of snow cover, hydrological and soil factors and vegetation; significant spatio-temporal variability is also typical for them (Anisimov et al., 2012). In this regard, data on the dynamics of the thermal structure and thickness of the active layer (AL) of the permafrost of West Spitsbergen, they determine the intensity of geomorphological processes and the physical and mechanical properties of soils, are of great interest. Obtaining these data is the goal of several monitoring programs conducted at different times on the islands of the archipelago.

In this chapter, an attempt is made to calculate the long-term dynamics of the AL rate on West Spitsbergen according to meteorological observations at the Barentsburg station using mathematical modeling methods. With the help of the available schemes for solving the heat equation for freezing/thawing soil, the model type is selected, a calculation algorithm is constructed, the input parameters of the model are set, and the accuracy of the model reproduction of seasonal thawing of the main types of soils of West Spitsbergen is evaluated. For comparison with other areas of West Spitsbergen, similar calculations were performed according to the weather stations Longyearbyen and Ny-Ålesund.

By the soil-geographical regionalization, West Spitsbergen belongs to the so-called polar (cold) belt of Eurasia (Soil-geographical ..., 1962). The geographical location of Spitsbergen in the zone 74–81° N influences its climate. The average temperature in July ranges from 4 to 6 °C, in January – from –12 to –16 °C. Due to the warm North Atlantic Current, the temperature in Spitsbergen in the winter months is more than 20 °C higher than the average temperature for this latitudinal zone in Russia and Canada.

Glaciers cover about 60 % of the territory of Spitsbergen; the remaining areas are weak in vegetation. Landscapes of arctic deserts with fragmented vegetation cover are typical for them; they are represented by a complex of soil spots with a vegetation coverage not exceeding 25 %. Vegetation includes forms of plant communities that can exist with a minimum amount of solar heat (mosses, lichens, mushrooms, seaweed, some types of flowering plants, and occasionally shrubs).

Arctic soils are widespread in areas of West Spitsbergen not occupied by glaciers. Formed in the harsh climatic conditions of the Arctic zone of the polar region, they are characterized by poor development of soil processes, underdevelopment of the soil profile, spaced vegetation cover, consisting mainly of mosses and lichens. Permafrost has a significant influence on the formation of Arctic soils, the thickness of its layer varies from zero near the coast to 500 m at elevations; it thaws in summer to a depth of 1–1.5 m, the associated permafrost processes also influence the soil (pingos, cracking, thawing, etc.) (Humlum et al., 2003).

Obtaining data on the thermal structure and thickness of the AL in West Spitsbergen is the goal of the global monitoring of permafrost carried out within the framework of several international programs. The most ambitious program is the Circumpolar Active

Layer Monitoring (CALM) program, which is currently the main source of data on the long-term dynamics of permafrost (Brown, 2000). Within the framework of this program, since 1990 unified measurements of the depth of seasonal thawing of permafrost have been carried out in Spitsbergen at standard observation sites according to a single measurement protocol that ensures the statistical reliability of the data obtained (<http://www.gwu.edu/~calm/data/north.html>). A significant part of the data was obtained manually using the contact method based on the difference in the density of thawed and frozen soil, another part – by interpolating temperature data according to the depth of the soil. Permafrost measurements in the Spitsbergen archipelago are currently being carried out at the UNISCALM site by the University Center in Svalbard (UNIS). In addition to the CALM sites, data on the thermal regime of the active soil layer in Spitsbergen is being obtained within the framework of the TSP NORWAY permafrost observation project (<http://www.ngu.no/kart/permafrost/?lang=English>), as well as during the implementation of several UNIS research programs.

Analysis of the data on permafrost observations of West Spitsbergen shows that the depth of seasonal thawing has high spatial variability, ranging from several dozens of centimeters to one or even two meters (Gregersen and Eidsmoen, 1988; Humlum et al., 2003; Isaksen et al., 2007; Westermann et al., 2010). It is determined mainly by the thermophysical characteristics of the environmental components: ground cover (vegetation, moss, and peat) and soil. Snow cover also plays a significant role in the dynamics of soil thawing (Shmakin et al., 2013). Although there are some studies (Putkonen, 1998; Roth and Boike, 2001), the study of these factors remains insufficient.

The situation is complicated by a significant discrepancy, up to 100 % or more (Gavrilyev, 2004), in the values of the thermophysical properties of soils even within the same type and with the same parameters of moisture and density of soil skeleton. The reason for this discrepancy is the exceptional diversity of the mineral composition and dispersion of particles. The reason is primarily the conditions of formation and cryogenic structure, as well as the error of experiments, both instrumental and planned. For these reasons, soils of seasonal freezing/thawing are characterized by effective thermophysical properties, and it is an independent and rather difficult task to determine them. Today it is impossible to solve it without significant simplifications. Since the datasets on permafrost observations are not large, and the characteristics of heat and mass exchange properties are contradictory, it is natural to use mathematical modeling methods to assess the dynamics of the thermal structure of Arctic soils. Currently, there are enough models, with different degree of complexity (Machulskaya and Lykosov, 2009). The simplest of them are semi-empirical relations for calculating permafrost indices that link permafrost parameters (for example, thawing depth) with atmospheric parameters (for example, the sum of heating degree-days). The variability of the properties of soils and vegetation adds significant uncertainty in the results of such calculations, which is why they can be considered only as a first approximation for solving the problem of assessing the dynamics of permafrost. The most complex are physically complete numerical models constructed by the methods of continuum mechanics based on the fundamental law of conservation of mass, momentum and energy, and closing equations of state, taking into account many factors (for example, the possibility of overcooled pore moisture). With all the advantages of these models, calculations based on them require a large amount of data on the properties of soil, which are entirely or, for the most part, absent for the absolute majority of areas of West Spitsbergen.

MATHEMATICAL STATEMENT OF THE PROBLEM OF SEASONAL THAWING

Among the existing variety of models, one-dimensional models with a simplified description of thermodynamic processes form a particular class. They are based on approximate solutions of the heat conduction equation. In terms of complexity, they are in-between semi-empirical formulas and numerical hydrothermal models. Despite some simplifications of real processes, these models are widely used to analyze the dynamics of permafrost (Anisimov et al. 2012; Anisimov, 2008; Anisimov and Belolutskaya, 2004; Sazonova and Romanovsky, 2003). The models use a quite modest computational resource but give the results that are quite comparable in terms of accuracy with the data of both measurements and calculations by numerical models of the hydrothermal regime of the soil. For these reasons, a stationary model of an intermediate level of complexity was used for the calculations; it is developed based on the GIPL-1 model of the Permafrost Laboratory, Geophysical Institute University of Alaska Fairbanks (USA).

Calculations performed with the GIPL-1 within the ACIA program for Eastern Siberia and Alaska showed an accuracy of $\pm (0.2-0.4)^\circ\text{C}$ for the AL bottom temperature and $\pm (0.1-0.3)$ m for its thickness in comparison with both measured data and the results of calculations using one of the most physically complete numerical models (Sazonova and Romanovsky, 2003). The model is based on the well-known scheme for the analytical solution of the heat conduction equation for a layered soil by Kudryavtsev (Kudryavtsev et al., 1974).

Fig. 3.1.1 shows a block diagram of the model, the envelopes of annual temperature fluctuations, the amplitude of which exponentially decays as the heatwave propagates deeper and becomes negligible at depth X , as well as the average annual temperature profile of the active soil layer (Romanovsky and Marchenko, 1997). The calculation is carried out in stages, taking into account the effect of snow cover, vegetation, and temperature differences due to the difference in thermal conductivity coefficients of thawed and frozen soil. The boundary of AL X is geometrically located at the intersection of the envelope of the 0°C mark and is determined by solving the algebraic problem

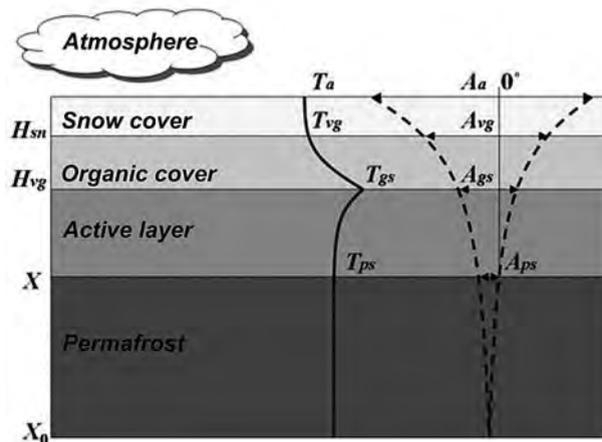


Fig. 3.1.1. The location of the layers of the environment and the vertical distribution of the average annual temperature (T) and its amplitude (A).

See tables 3.1.1 and 3.1.2. for legend.

$$X \left(2A_{ps} C_t + Q \right) = 2 \left(A_{gs} - |T_{ps}| \right) \sqrt{K_t C_t P / \pi} + \frac{\left(2A_{ps} C_t x + Q z_t \right) Q \sqrt{K_t P / \pi C_t}}{2A_{ps} C_t x + Q X + \left(2A_{ps} C_t + Q \right) \sqrt{K_t P / \pi C_t}}, \quad (3.1.1)$$

where

$$x = \frac{2 \left(A_{gs} - |T_{ps}| \right) \sqrt{K_t C_t P / \pi}}{2A_{ps} C_t + Q},$$

P is the length of the year (c). Corresponding temperature T , amplitude A and corrections to them ΔT and ΔA are functions of the input parameters of the problem and are found from the relationships presented many times in the literature (Anisimov, 2008, Kudryavtsev et al., 1974, Sazonova and Romanovsky, 2003, Romanovsky and Marchenko, 2013). Their signs according to these works are given in Tables 3.1.1 and 3.1.2.

Table 3.1.1

Model input data	
Parameter, units	Обозначение
Amplitude of annual air fluctuations, °C	A_a
Average annual air temperature, °C	T_a
Average annual snow thickness, m	H_{sn}
Duration of the warm season, s	τ_2
Thermal conductivity coefficient of snow, W/(m·K)	K_{sn}
Vegetation height, m	H_v
Thermal diffusivity coefficient of frozen/thawed vegetation, m ² /s	a_{vf}/a_{tv}
Thermal conductivity coefficient of frozen/thawed soil, W/(m·K)	K_f/K_t
Volumetric heat of phase transitions of water, J/m ³	Q
Volumetric heat capacity of snow, J/(m ³ ·K)	C_{sn}
Volumetric heat capacity of frozen/thawed soil, J/(m ³ ·K)	C_t/C_f

Table 3.1.2

Model output data	
Parameter, units	Sign
Snow cover T_a/A_a correction, °C	$\Delta T_{sn} / \Delta A_{sn}$
Vegetation T_a/A_a correction, °C	$\Delta T_v / \Delta A_v$
Seasonal temperature/temperature range at the soil surface, °C	T_{gs} / A_{gs}
Average annual permafrost temperature, °C	T_{ps}
Amplitude of annual temperature fluctuations in permafrost AL, °C	A_{ps}
AL thickness, m	X

PARAMETRIZATION OF THERMOPHYSICAL PROPERTIES OF SOILS AND GROUND COVERS

Due to the diversity of genetic varieties of soils in West Spitsbergen, for the study of thawing, it seems quite reasonable to divide soils into two (sandy and loamy) or three (sandy, sandy loam and loamy) basic types. They have characteristics in common that are universal for all dispersed materials of the permafrost zone in both frozen and thawed

state (Kersten, 1955; Gavrilyev, 1998, 2004). In addition to these works, there are data from the literature summaries, generalized in the System of Normative Documents (see, for example, SNiP 2.02.04-88 and the links given therein).

The volumetric heat capacity of non-saline soils thawed and cooled at a temperature above the ground freezing point has an additive property concerning the heat capacity of its constituent parts: the organomineral skeleton, ice and tightly bound unfrozen water:

$$C_{th} = (c_d + c_w W_{tot}) \rho_{d,th,f}, \quad (3.1.2)$$

where c_d – is the specific heat capacity of the soil skeleton; $c = 4200 \text{ J}/(\text{kg} \cdot ^\circ\text{C})$ is the specific heat capacity of water; W_{tot} – is total moisture content; $\rho_{d,th,f}$ – is the density of soil skeleton.

For non-saline soils in a frozen state, provided that the soil temperature is below or equal to the ground freezing point, the value of C_f the value of the formula is found by

$$C_f = [c_d + c_w W_w + c_i (W_{tot} - W_w)] \rho_{d,f}, \quad (3.1.3)$$

where W_w – is the moisture content of non-saline soil due to tightly bound (unfrozen) water; a – specific heat capacity of ice; $c_i = 2120 + 7.8T$.

The volumetric heat of freezing (thawing) of the soil Q (J/m^3) is taken equal to the amount of heat required for freezing water (melting ice) per unit volume of the soil, and is determined by the formula

$$Q = Q_0 (W_{tot} - W_w) \rho_{d,th}, \quad (3.1.4)$$

where $Q_0 = 3.35 \cdot 10^5 \text{ (J/kg)}$ is the specific heat of phase transitions water–ice.

The soil litter (SL) has a significant effect on the thermal regime of soils. Therefore it is also necessary to take into account the difference in its properties in the frozen and thawed state. For the sake of simplicity, in the future, a single organic vegetation cover is considered as a soil litter, including moss, lichen, and peat sublayers. The reason for this is the similarity of the thermophysical properties of moss and the peat formed as a result of its dying-off and decomposition (Anisimov and Belolutskaya, 2004), even though the available data on the heat capacity of peat are rather contradictory. This assumption allows us to consider the thawing soil to be a two-layer one, consisting of an upper organic and lower mineral parts. For simplicity, we consider the so-called dry SL, which becomes thawed by the moment the snow cover melts and gets frozen at the beginning of winter, which allows one to neglect the phase processes in it.

The value $K_{vt,vf}$ is mainly influenced by the value W_{tot} , which is described by empirical formulas

$$K_{vt} = 0.034 + 0.1257W_{tot} - 0.0227W_{tot}^2 + 0.00133W_{tot}^3, \quad (3.1.5)$$

$$K_{vf} = 0.034 + 0.132 (W_{tot} - 0.5), \quad (3.1.6)$$

where $0 \leq W_{tot} \leq 10$ for thawed moss and $0.5 \leq W_{tot} \leq 0.5$ for frozen one; when $W_{tot} \leq 0.5$ value K_{vf} becomes constant.

The value of $C_{vt,vf}$ can be calculated using formulas (2)–(3) universal for dispersed material, taking $c_d = 1.6 \cdot 10^3 \text{ J}/(\text{kg} \cdot \text{K})$, $\rho_d = 1800 \text{ kg}/\text{m}^3$, $W_w = 0$ (Gavrilyev, 2004), which allows to determine the value $a_{vt,vf}$

$$a_{vt,vf} = K_{vt,vf} / C_{vt,vf} \quad (3.1.7)$$

To specify the long-term variability of the organic cover height H_v , an approach proposed by Cornelissen et al. (2001) was used, as well as the approach used in Anisimov and Belolutskaya (2004). According to them, an increase in the thickness (biomass) of SL,

while maintaining the species composition, occurs with an increase in air temperature only to a particular threshold value. Its excess results in the displacement of mosses and lichens by more highly organized vascular plants; as a result, the organic layer stops growing and decreases both due to its shading and height. An increase of 1 °C corresponds to an increase in H_v by 5 cm but after reaching a value of 20 cm, further warming by 1 °C entails the same decrease in H_v . It was assumed that the thickness H_v cannot be less than 5 cm, and its average value (10 cm) corresponds to the average temperature over the observation period of 1985–2015 (–4.52 °C for Barentsburg, –4.61 °C for Longyearbyen and –4.78 °C for Ny-Ålesund).

Such a scenario, which assumes that the evolution of the organic layer depends on a single atmospheric parameter T_a , despite its schematic nature, nevertheless allows us to parameterize the long-term evolution of vegetation and thereby estimate its contribution to the thermoregulation of the soil. The influence of the organic layer on the conditions of snow accumulation, the reflectivity of the surface, moisture evaporation, the value of turbulent heat exchange between the soil and the atmosphere, etc., were not considered.

INPUT DATA

The areas of polar stations in West Spitsbergen were selected as objects of modeling, for which there are large datasets of meteorological observations: Barentsburg, Longyearbyen and Ny-Ålesund. Atmospheric forcing in the model was represented by the data of processing standard eight-time (every three hours) meteorological observations in the period from 1985 to 2015. The monthly average and daily average data from Barentsburg station were obtained in RIHMI-WDC (<http://meteo.ru>). To calculate the average monthly and average annual values of meteorological elements obtained at Ny-Ålesund and Longyearbyen stations, the current data of meteorological observations from the Norwegian Meteorological Institute, posted on the website (<http://eKlima.met.no>) were used. Unfortunately, a lot of information on snow accumulation was missing. For this reason, to obtain the necessary information for Longyearbyen station, a data recovery procedure was used based on the available data on atmospheric precipitation by approximating them with a sextic polynomial. For Ny-Ålesund station, the number of missing data from the sample turned out to be so large that the snow thickness for the entire thirty-year period was assumed constant and equal to its average value for the last five years for which the corresponding information was available.

It should be noted that since the cold season makes the main contribution to the formation of the average annual soil temperature, geocryology usually uses a conditional annual period, the date of the beginning of soil freezing is the beginning of this period (Konstantinov et al., 2006). In these calculations, January 1 was taken as the beginning of the year, and, accordingly, the soil parameters were calculated for this calendar year. Therefore, further in the text, tables and figures, only calendar years are given.

Of all the parameters necessary for the calculation, we can get T_a , A_a , H_{sn} , and τ_2 directly from the data of meteorological observations. Their average annual values as well as the values of the vegetation height for the study period and their linear trends are shown in Fig. 3.1.2, and the statistical characteristics – the standard deviation (SD), the coefficient of determination (R^2), and the coefficient of variation (V) – are given in Table 3.1.3. The figure shows that significant interannual variations are typical for them, reflecting the variability of atmospheric conditions in West Spitsbergen. It led to significant interannual fluctuations in the input parameters in absolute values. At the same time, only the air temperature and its amplitude demonstrate clear tendencies to increase and decrease, respectively. It can be seen that the first three parameters are quite close to each other for all selected points, which seems natural given the distance

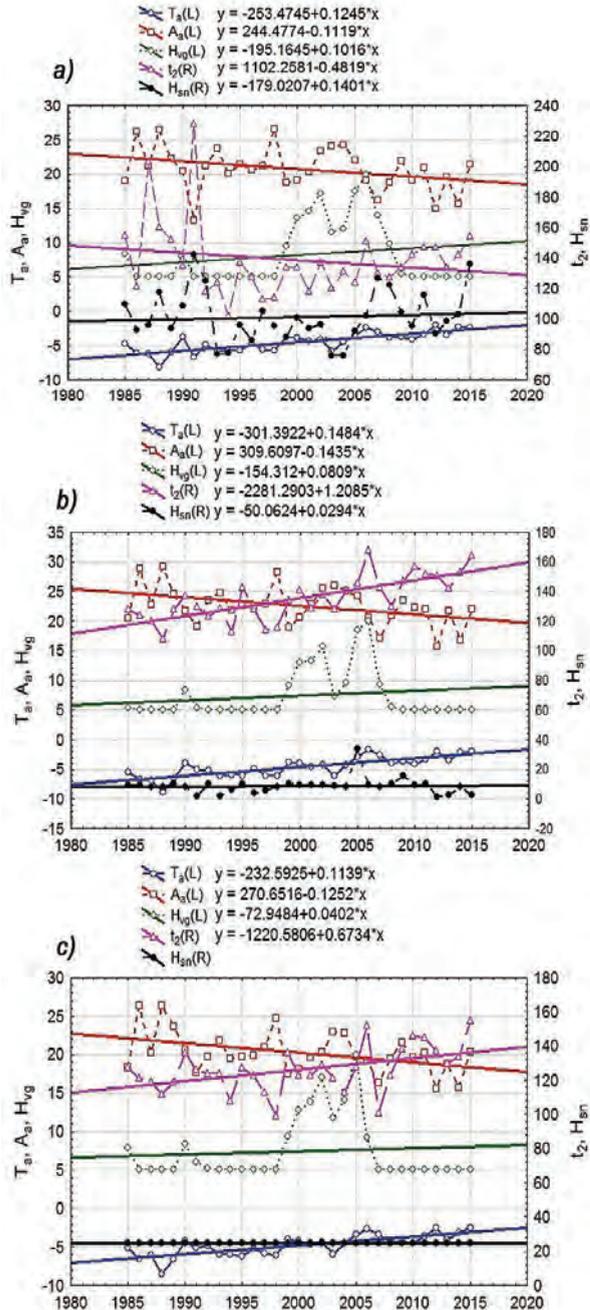


Fig. 3.1.2. Long-term dynamics of the average annual values of meteorological parameters and the vegetation height calculated from them and their linear trends at Barentsburg (a), Longyearbyen (b), and Ny-Ålesund (c) stations.

Interannual changes in meteorological characteristics for the study period

Parameter	Barentsburg			Ny-Ålesund			Longyearbyen		
	Stand	R^2	V	Stand	R^2	V	Stand	R^2	V
T_a	1.45	0.61	-32.21	1.37	0.57	-28.61	1.70	0.63	-37
A_a	3.16	0.10	15.23	2.64	0.18	13.08	3.20	0.17	14
t_2	24.92	0.03	0.01	13.22	0.21	10.47	14.85	0.55	11
H_{sn}	16.83	0.01	16.63	–	–	–	3.21	0.00	65
H_{vg}	4.60	0.04	56.55	4.13	0.01	55.51	4.27	0.03	57

between them. The exception is snow cover, the range of its average annual depth between Barentsburg and other geographic points, even taking into account the low quality of data from the latter, is quite wide. It should be noted that, despite the great interest in this issue, the problem of the representativity of the snow cover measurements in Barentsburg remains open. The peculiarity of the measurement conditions at the meteorological site of the Barentsburg station, located on the slope, is one of the possible reasons.

Calculations according to the model (3.1.1) were carried out for permafrost and seasonally thawed soils under a moss-peat SL, typical for West Spitsbergen: sand, sandy loam and loam (clay) with an admixture of gravel, pebbles and crushed stone in an amount of up to 20 % and boulders up to 10 % with an average density in natural occurrence from 1750 to 1950 kg/m³. According to Gavrilyev (2004), the specific gravity of their skeleton and the total moisture content can be taken the same and equal 1800 kg/m³ and 0.1 respectively, amount of tightly bound moisture (at $t = -10$ °C) 0.003 unit fraction for sand, 0.022 unit fraction for sandy loam and 0.049 unit fraction for loam, specific heat capacity 693, 735 and 777 J/(kg·K) respectively.

The use of these values in calculations by formulas (3.1.2) – (3.1.4) and the data of literary sources give the following values of the input parameters: $K_t = 1.97$ W/(m·°C); $K_f = 2.30$ W/(m·°C) (for sand); $K_t = 1.45$ W/(m·°C); $K_f = 1.59$ W/(m·°C) (for sandy loam); $K_t = 1.06$ W/(m·°C); $K_f = 1.26$ W/(m·°C) (for loam and clay); $C_t = 2.42 \cdot 10^6$ J/(m³·°C); $C_f = 2.04 \cdot 10^6$ J/(m³·°C) (for all types of soil), as well as $Q = 3.08 \cdot 10^7$ J/m³. For the organic layer the formulas (3.1.5) – (3.1.7) give: $a_{vf} = 50.9 \cdot 10^{-8}$ m²/s; $a_{vt} = 24.6 \cdot 10^{-8}$ m²/s.

CALCULATION RESULTS

Interannual changes in the depth of seasonal thawing and dynamics of permafrost temperature from 1985 to 2015, as well as their linear trends with regression equations for all measurement points, are shown in Fig. 3.1.3 – 3.1.5 and in Tables 3.1.4 – 3.1.6. Comparison of Fig. 3.1.2 and 3.1.3 – 3.1.5 indicate a relationship between the thermal regime of the soil and both temperature variations and the depth of snow cover (Osokin et al., 2006).

A typical feature of all distributions is considerable interannual variability, which is apparently caused by insufficiently adequate consideration of back-coupling in the model that arises due to changes in the depth of snow and organic cover, their parametrization leaves much to be desired. During the period of calculations, the standard deviation of the thawing depth was 0.3–0.4 m, and the coefficient of variation in absolute value was within 29–38. As you can see, the thawing depth is a significantly less variable characteristic than the temperature of the permafrost base, its coefficient of variation in absolute value was 41–89. In this case, the coefficients of determination for both parameters had relatively small values and their variations: 0.31–0.40 and 0.58–0.63, respectively.

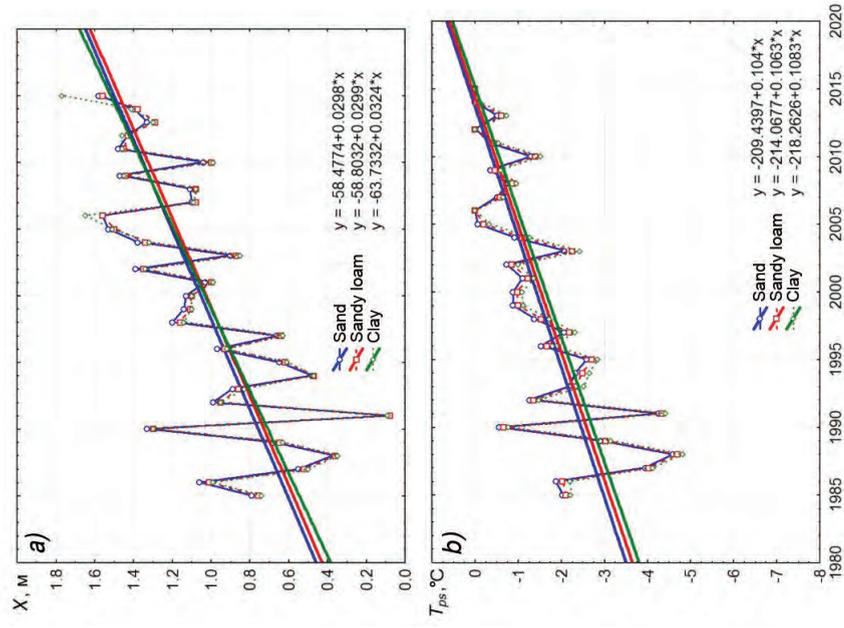


Fig. 3.1.3. Long-term dynamics of the AL rate (α) and permafrost temperature (b) of the main types of soil and their trends at Barentsburg station.

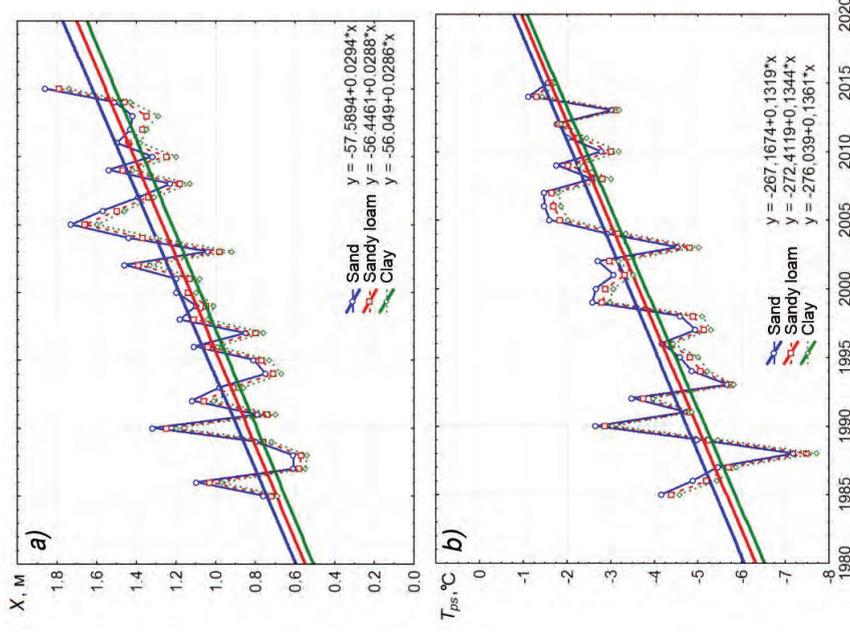


Fig. 3.1.4. Long-term dynamics of the AL rate (α) and permafrost temperature (b) of the main types of soil and their trends at Longyeacarbeyen station.

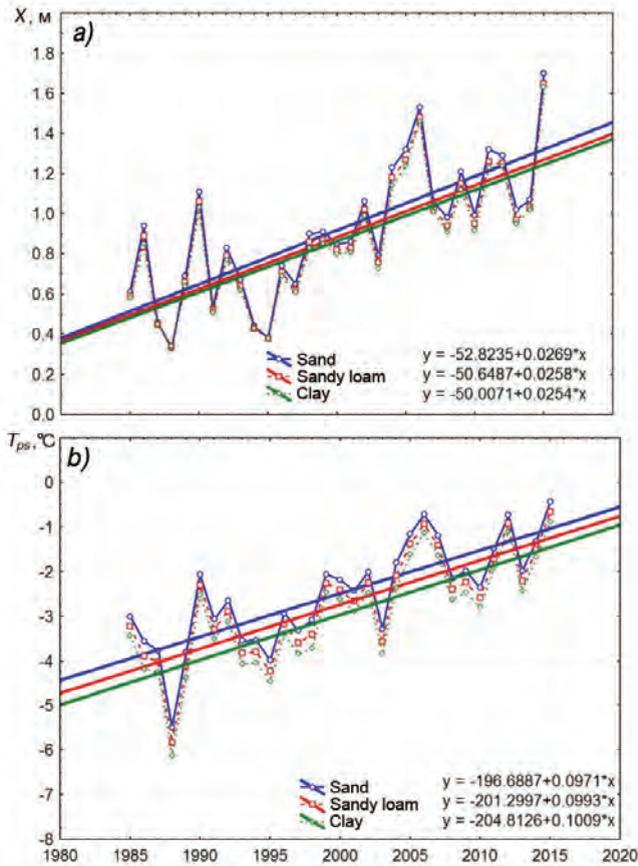


Fig. 3.1.5. Long-term dynamics of the AL rate (a) and permafrost temperature (b) of the main types of soil and their trends at Ny-Ålesund station.

The qualitative variability of the z_t and T_{ps} values is the same at all stations and is characterized by a steady increase due to the predominant increase in the average annual temperature of the surface air layer and an increase in the duration of the warm period, the amplitude of their seasonal variation also decreases. Both indicators are very similar in number, although their values for Barentsburg are slightly higher than for other stations. This difference is associated with the increased values of the thickness of the snow cover if compared to others, which was mentioned above, and, as a result, its significant warming effect.

Table 3.1.4

Interannual changes in the characteristics of seasonal thawing of sand soil for the study period

Point	X_t, m			$T_{ps}, ^\circ C$		
	SD	R^2	V	SD	R^2	V
Barentsburg	0,38	0,50	36,21	1,26	0,57	-88,70
Ny-Ålesund	0,33	0,54	36,22	1,14	0,60	-45,64
Longyearbyen	0,33	0,66	27,75	1,53	0,62	-44,71

Note. SD – Standard deviation.

Table 3.1.5

**Interannual changes in the characteristics of seasonal thawing of sandy loam soil
for the study period**

Point	X, m			$T_{ps}, ^\circ C$		
	SD	R^2	V	SD	R^2	V
Barentsburg	0,38	0,51	36,92	1,27	0,58	-79,98
Ny-Ålesund	0,32	0,54	35,99	1,16	0,60	-42,51
Longyearbyen	0,32	0,67	28,39	1,54	0,63	-42,54

Table 3.1.6

**Interannual changes in the characteristics of seasonal thawing of clay soil
for the study period**

Point	X, m			$T_{ps}, ^\circ C$		
	SD	R^2	V	SD	R^2	V
Barentsburg	0,40	0,54	38,82	1,29	0,58	-78,98
Ny-Ålesund	0,31	0,55	36,09	1,18	0,60	-39,87
Longyearbyen	0,32	0,68	29,22	1,55	0,63	-40,95

In general, the obtained distributions show that the dynamics of the AL depth in the territory of West Spitsbergen is quite the same type, and therefore its main regional trend can be identified from the calculation data at a single point. Moreover, as the figures show, despite the rather wide interannual variability X and T_{ps} , the nature of their variability at all stations is the same. Both indicators are very similar in absolute value, although their values for Barentsburg are slightly higher than for other stations. This difference is associated with the increased values of the thickness of the snow cover if compared to other stations, which was mentioned above, and, as a result, its large warming effect.

The main tendency in the course of X and T_{ps} is their increase, which has been especially noticeable since the mid-1990s of the last century. An increase in the AL depth and an increase in permafrost temperature prevail, due to a predominant increase in the average annual temperature of the surface air layer and an increase in the duration of the period with positive air temperature, as well as a decrease in the amplitude of their seasonal variation.

With a sufficiently good agreement between the calculated estimates and the literature data, it should be kept in mind that the thaw depth can have considerable spatial variability due to the variability of the thermophysical properties of soils and SL, starting from a distance of a few meters.

The theoretically calculated values obtained for each parameter in the form of one number, even though they correspond to the average values, may not be available at all within the selected point. It is due to the contradiction between the deterministic nature of the one-dimensional mathematical model, initially developed for pointwise calculations, and the stochastic nature of the physical processes that form the seasonal thawing of permafrost at a specific point in the territory. Obviously, calculations based on deterministic models are justified only when using the effective values of the parameters of soils and vegetation, provided that their natural variability is neglected. Therefore, within any station, the AL depth is, in a certain sense, a random variable with a distribution function, which, in principle, cannot be taken into account within the framework of the deterministic method used (Anisimov, 2008).

DISCUSSION AND CONCLUSION

Although the simulation results show a steady increase in the thickness of the active layer and an increase in its temperature since the 1980s, it is early to make conclusions that the rates of these changes will persist, especially since climate warming will apparently occur first of all during due to an increase in winter temperatures (IPCC, 2014). Several observations (Gerasimov, 2006) indicate an ambiguous response of the permafrost to the ongoing climatic changes due to the occurrence of back-coupling in the system “boundary layer of the atmosphere–snow cover–AL–permafrost”, preventing the rapid growth of seasonal thawing (Anisimov, Sherstyukov, 2015). Thus, the development of vegetation, caused by the predicted increase in air temperature, the amount of solar radiation, the amount of precipitation, and the concentration of carbon dioxide, can lead to a heat-insulating effect. It prevents, up to certain limits, an increase in the temperature of the soil surface and thereby compensates for the warming effect. On the other hand, an increase in soil moisture in summer and ice content in winter leads to its more intense interaction with the atmosphere, which makes it difficult to establish an unambiguous dependence between the occurring atmospheric and geocryological changes.

The simulation results allow us to make the following conclusions.

Based on model calculations, the influence of atmospheric characteristics on the dynamics of seasonal thawing of the soil of West Spitsbergen over the past 30 years has been estimated. The results obtained indicate the consistency of permafrost-climatic changes with the course of global warming and are an incentive for the expansion of permafrost research at the RSCS in Barentsburg,

With significant interannual variability of the calculated parameters, their positive trends confidently demonstrate an increase in the AL depth and an increase in its temperature. The dynamics of the AL and the temperature of the permafrost boundary in the Barentsburg region is generally synchronous with their dynamics at Longyearbyen and Ny-Ålesund stations, which indicates the same regional trend in the degradation of permafrost in West Spitsbergen.

Despite the use of several simplifying assumptions in the model, the results of the performed study show that stationary models of an intermediate level of complexity can be successfully used in the analysis of the space-time dynamics of permafrost on a regional scale.

The following main tasks require a solution to achieve this goal:

- organization of a monitoring site at the Barentsburg station that meets the standards of the Circumpolar Active Layer Monitoring Program for its subsequent inclusion in the number of Russian CALM sites;
- staging observations of the dynamics of external (meteorological, hydrological and biological) and internal (type and structure of the soil, depth of AL, dynamics of surface microrelief, etc.) concerning the geological environment of natural factors on this monitoring site, the observations should be unified by CALM standards;
- integration of the performed studies into the CALM program.

In conclusion, it should be noted that by now, the RSCS has ample opportunities to solve the above problems at the most advanced level. The station in Barentsburg has a facility for drilling wells up to 50 m deep, as well as a unique meteorological complex for measuring the parameters of energy and mass exchange of the atmosphere with the geological substrate. The data obtained with its help together with the data of permafrost

observations, as well as the results of similar measurements at Russian stations in Tiksi and on Bolshevik Island (Severnaya Zemlya archipelago), will make it possible to obtain new quantitative estimates of the impact of climate change on the evolution of permafrost of the coast and islands of the high-latitude Arctic and will allow AARI to become a full-fledged participant in any international climate programs.

REFERENCES

- Anisimov O.A. Probabilistic-statistical modeling of the thickness of the active layer in the current and future climate: results. *Kriosfera Zemli. Earth's Cryosphere*. 2009, XIII (3): 36–44. [In Russian].
- Anisimov O.A. Current and future permafrost changes: a synthesis of observations and modeling. *Problemy Arktiki i Antarktiki. Problems of Arctic and Antarctic*. 2008, 1 (78): 7–16. [In Russian].
- Anisimov O.A., Belolutskaya M.A. Modeling the effects of anthropogenic warming on permafrost: taking into account the effects of vegetation. *Meteorologija i gidrologija. Meteorology and Hydrology*. 2004, 11: 73–82. [In Russian].
- Anisimov O.A., Sherstjukov A.B. Assessment of the role of climatic factors in changes in permafrost soils. Part 1. Current state. *Kriosfera Zemli. Earth's Cryosphere*. 2015, X (3): 15–22. [In Russian].
- Anisimov O.A., Anokhin Yu.A., Lavrov S.A. et al. Mainland permafrost. *Metody ocenki posledstvij izmenenija klimata dlja fizicheskikh i biologicheskikh sistem. Methods for assessing the effects of climate change for physical and biological systems*. Moscow: Rosgidromet, 2012: 301–359. [In Russian].
- Gavriljev R.I. *Teplofizicheskie svojstva komponentov prirodnoj sredy v kriolitozone: spravocnoe posobie*. Thermophysical properties of the components of the natural environment in the permafrost zone: a reference guide. Novosibirsk: Publishing house of SB RAS, 2004: 145 p. [In Russian].
- Gavriljev R.I. *Teplofizicheskie svojstva gornyh porod i napochvennyh pokrovov kriolitozony*. Thermophysical properties of rocks and ground cover of the permafrost zone. Apatity: Publishing house of SB RAS, 1998: 280 p. [In Russian].
- Gerasimov Ye.Ju. *Mezhhodovaja izmenchivost' moshhnosti sezonnotalogo sloja "Spasskaja pad": kompleksnye issledovanija merzlotnyh landshaftov*. Interannual variability of the thickness of the seasonally active layer "Spasskaya Pad": comprehensive studies of permafrost. Yakutsk: Publishing House of Melnikov Permafrost Institute SB RAS, 2006: 100–103. [In Russian].
- Kersten M.S. Thermal properties of the soil. *Merzlotnye javlenija v grunte*. Permafrost phenomena in the soil. Moscow: Inostrannaya literatura, 1955: 200–207. [In Russian].
- Konstantinov P.Ya., Argunov R.N., Gerasimov Ye.Ju., Ugarov I.S. About the relationship between the depth of seasonal thawing and interannual variability of the average annual soil temperature. *Kriosfera Zemli. Earth's Cryosphere*. 2006, X (3): 15–22. [In Russian].
- Kudryavcev V.A., Garagulya L.S., Kondratyev K.A., Melamed V.G. *Osnovy merzlotnogo prognoza pri inzhenerno-geologicheskikh issledovanijah*. Basics of permafrost forecasting in engineering-geological research. Moscow: Nauka, 1974: 431 p. [In Russian].
- Machulskaya Ye.Ye., Lykosov V.N. Mathematical modeling of the processes of interaction between the atmosphere and the permafrost zone. *Izvestija RAN. Fizika atmosfery i okeana. Bulletin of RAS. Physics of the Atmosphere and Ocean*. 2009, 45 (6): 736–753. [In Russian].
- Mejer L.A. (ed.). IPCC Climate change, 2014: Synthesis report. Contribution of Working Groups I, II and III to the Fifth Assessment Report of the Intergovernmental Panel on Climate. Geneva, 2014: 163 p. [In Russian].
- Mikhailov I.S. Analysis of the spatial structure of some landscapes of the arctic zone *Trudy AANII. Proceedings of the AARI* 1971. 304: 147–163. [In Russian].
- Osokin N.I., Samoilo R.S., Sosnovsky A.V. Assessment of the effect of snow cover thickness on permafrost degradation during climate warming. *Izvestija RAN. Serija geograf. Bulletin of RAS. Ser. Geograph*. 2006, 4: 40–46. [In Russian].

Pochvenno-geograficheskoe rajonirovanie SSSR. Soil-geographical regionalization of the USSR. Moscow: Publishing House of the USSR Academy of Sciences, 1962: 422 p. [In Russian].

SNiP 2.02.04—88. Osnovaniya i fundamenty na mnogoletnemmerzlyh gruntah. SNiP (construction norms and specifications) 2.02.04—88. Bases and basements on permafrost soil. Moscow: Stroyizdat, 1990: 53 p. [In Russian].

Shmakin A.B., Osokin N.I., Sosnovsky A.V., Zazovskaya E.P., Borzenkova A.V. Influence of snow cover on freezing and thawing of the soil on West Spitsbergen. *Ljod i sneg*. Ice and Snow. 2013, 4 (124): 52–59.

Brown J., Hunkel K.M., Nelson F.E. The circumpolar active layer monitoring (CALM) program: research designs and initial results. *Polar Geogr.* 2000, 24: 163–258.

Cornelissen J.H.C., Callaghan T.V., Alatalo J.M. et al. Global change and arctic ecosystems: is lichen decline a function of increases in vascular plant biomass? *J. Ecology*. 2000, 89 (6): 984–994; doi: 10.1046/j.1365-2745.2001.00625.x.

Gregersen O., Eidsmoen T. Permafrost Conditions in the Shore Area at Svalbard. *Proc. Of the Fifth International Conference on Permafrost in Trondheim, Norway*. 1988, 2: 933–936.

Humlum O., Instanes A., Sollid J.L. Permafrost in Svalbard: a review of research history, climatic background, and engineering challenges. *Polar Research*. 2003, 22 (2): 191–215.

Isaksen K., Sollid J.L., Holmlund P., Harris C. Recent warming of mountain permafrost in Svalbard and Scandinavia. *J. Geophys. Res.* 2007, 112; DOI:10.1029/2006JF000522.

Putkonen J. Soil thermal properties and heat transfer processes near Ny-Ålesund, northwestern Spitsbergen, Svalbard. *Polar Research*. 1998, 17 (2): 165–179.

Romanovsky V.E., Marchenko S. The GIPL Model for Estimation of Temporal and Spatial Variability of the Active Layer Thickness and Mean Annual Ground Temperatures. Available at: <http://www.snap.uaf.edu/attachments/The%20GIPL-1%20Model-final.pdf>.

Roth K., Boike J. Quantifying the thermal dynamics of a permafrost site near Ny-Ålesund, Svalbard. *Water Resources Res.* 2001, 37 (12): 2901–2014.

Sazonova T.S., Romanovsky V.E. A model for regional-scale estimation of temporal and spatial variability of active-layer thickness and mean annual ground temperatures. *Permafrost and Periglacial Processes*. 2003, 2: 125–140.

Westermann S., Wollschläger U., Boike J. Monitoring of active layer dynamics at a permafrost site on Svalbard using multi-channel ground-penetrating radar. *The Cryosphere*. 2010, 4: 475–487.

3.2. CHARACTERISTICS OF THE CONTEMPORARY GLACIATION OF NORDENSKIÖLD LAND, IN THE WEST SPITZBERGEN

S.R. Verkulich

Glaciers cover about 60 % of the surface of Spitsbergen (Glaciology of Spitsbergen, 1985; Mavlyudov, 2006) and are the most important component of its natural environment. Changes in glaciation associated with climatic fluctuations have a significant impact on the relief, hydrological system, permafrost, flora, and fauna of the archipelago and thus affect the living conditions and human activities here. In this regard, the study and monitoring of the state of local glaciers have significant scientific and practical importance.

One of the places for long-term glaciological research on the archipelago is the area of Barentsburg (West Spitsbergen), where several glaciers are located. The Institute of Geography of the USSR Academy of Sciences started to study them in 1965, and there were periodic mass-balance observations (Glaciology of Spitsbergen, Svalbard, 1985; Zinger and Mikhailov, 1967; Koryakin and Troitsky, 1969; Mavlyudov et al., 2012; Glaciation of Spitsbergen, 1975; Troitsky, 1988a, 1988b). Since 2001, AARI specialists have begun to work here, the research continues to the present and represents a complex of studies of the characteristics and dynamics of local glaciers. Glaciological studies have covered seven



Fig. 3.2.1. Location of glaciers, objects of glaciological research by the AARI, on the Spitsbergen.

major local glaciers: Vøringbreen, Aldegondabreen, Vestre Grønfjordbreen and Austre Grønfjordbreen, Gleditschfonna, Tavlebreen, and Tungebreen. Some observations were made on the Bertilbreen in the area of Piramiden and on the Nordenskiöldbreen (Fig. 3.2.1). The Vøringbreen is a small cirque glacier on the western shore of the Grønfjorden that feeds Stemmevatnet, which supplies water to Barentsburg. It is about 1.4 km long, and about 0.7 km wide. Aldegondabreen is a mountain-valley glacier on the western shore of Grønfjorden, oriented west-east. It is about 3.2 km long, and up to 2.3 km wide, maximum ice thickness is 216 m. The upper point of the glacier is about 600 m high above sea level, and the lowest point of its tongue is about 110 m high above sea level. Vestre Grønfjordbreen is a mountain-valley glacier in the southern part of Grønfjorden. The glacier is up to 9 km long and up to 7 km wide; its lower point is 60 m above sea level, and the upper point is 749 m above sea level. Austre Grønfjordbreen is a mountain-valley glacier in the southern part of Grønfjorden, about 7 km long and up to 2.2 km wide. The tongue is located 30 m above sea level, and the upper point is 749 m above sea level. Gledichfonna is a valley glacier with an area of 2.53 km²; its maximum length is 2.45 km. The tongue of the glacier goes down to an elevation of 220 m above sea level, and the upper parts of the glacier are higher than 400 m above sea level. The Tavlebreen is located in the upper reaches of the Grøndalen. It is 6 km long, and about 2 km wide, the lowest point is 200 m above sea level, and the highest point is 700 m above sea level. The Tungebreen is located in the upper reaches on the left side of the Grøndalen, west of the Tavlebreen. A common watershed separates their upper reaches. It is 3.7 km long, and about 800 m wide, the lowest point is 200 m above sea level, and the highest point is 800 m above sea level. The Bertilbreen is a mountain-valley glacier 4.51 km long; it is maximum 1.73 km wide. The highest point of the glacier is about 700 m above sea level, and the lowest point of his tongue is 175 m above sea level. Nordenskiöldbreen is an outlet glacier with an area of about 232 km² (Mavlyudov, 2006), its tongue goes down into the sea.

BALANCE CHARACTERISTICS AND THE STATE OF GLACIATION IN THE BARENTSBURG AREA DURING THE PAST DECADE

The basis for assessing the mass-balance characteristics and the state of glaciation in the Barentsburg area are the results of long-term snow observation and glaciological research on the Aldegondabreen. According to spring snow measurements data, the thickness and distribution of snow cover on the glacier depend, in addition to the meteorological conditions of snow accumulation, on the absolute height of the surface. They are influenced by wind transfer, exposure of slopes, and surface relief; they are characterized by interannual variability. In most cases, the following things were recorded: a smooth distribution of the snow cover thickness over the glacier and the dependence between the increase in the thickness of the snow cover with an increase in the surface height, the greatest thickness of the snow cover was on the sides of the glacier. However, in some years, measurements have shown a more varied data (Fig. 3.2.2).

The distribution of water reserves in the snow cover is also uneven. It is associated, in addition to the thickness of the snow, with variations in its density, which in different years was homogeneous or increased up the glacier. The number and thickness of ice layers, which depend on the characteristics of the meteorological conditions of snow accumulation (thaws, winds, etc.), had a significant effect on the density and, consequently, on the amount of water in the snow. In some years, thanks to these layers, the water

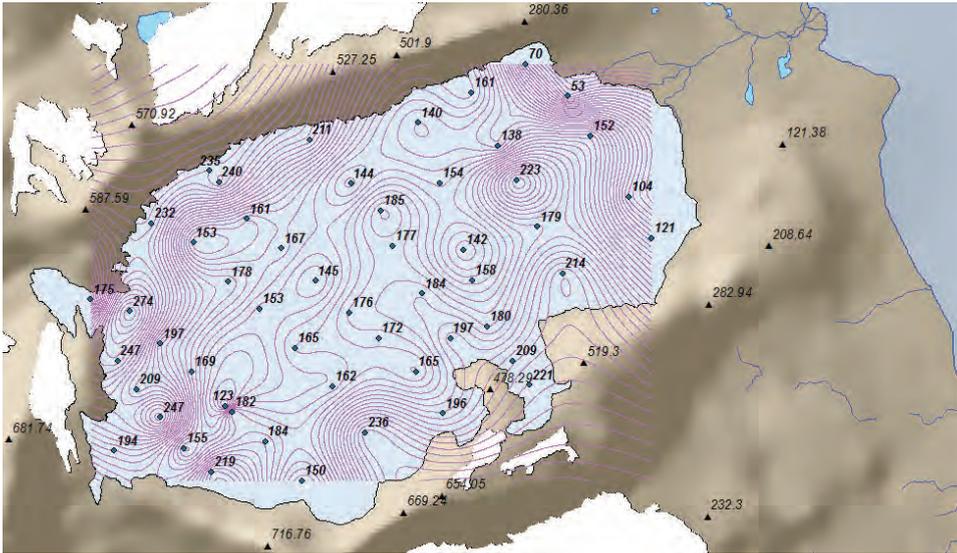


Fig. 3.2.2. Distribution of snow cover thickness (cm) on the Aldegondabreen according to survey data for 2015 (Study of the meteorological regime ..., 2015; Study of long-term changes in ..., 2015).

reserve in the snow was higher than in other years, with a smaller thickness of the snow. In general, long-term observations on the Aldegondabreen revealed interannual variability of the average water reserve in the snow cover within the range of 627–859 mm, with no apparent tendency to increase or decrease this value for the last decade.

Repeated snow measurements on the Vestre and Austre Grønfyordbreens revealed a generally smoother distribution of snow depth (Fig. 3.2.3) and its density (with an increase from bottom to top with an increase in absolute values) over their surface compared to

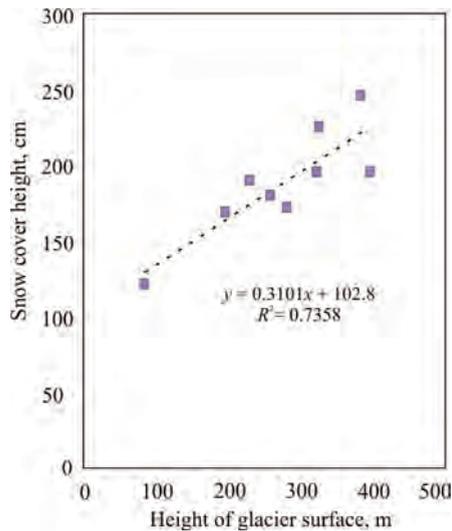


Fig. 3.2.3. Dependence of the snow cover height on the absolute height of the Vestre Grønfyordbreen surface according to survey data for 2007 (Study of the meteorological regime ..., 2007).

Table 3.1.2

Results of snow measurements on the Aldegondabreen, Austre and Vestre Grønfyordbreens

Период	Aldegondabreen			Vestre Grønfyordbreen			Austre Grønfyordbreen		
	h_s , sm	ρ_s , g/sm ³	Q , mm	h_s , sm	ρ_s , g/sm ³	Q , mm	h_s , sm	ρ_s , g/sm ³	Q , mm
30 April – 2 May 2003	130	–	–	–	–	–	–	–	–
April 2004	124	–	–	–	–	–	–	–	–
12–14 April 2005	194	0.339	658	177	0.329	545	–	–	–
26 April – 14 May 2006	153	0.467	715	–	–	–	–	–	–
15 April – 4 May 2007	184	0.467	859	178	0.398	708	–	–	–
April 2008	200	0.390	780	–	–	–	–	–	–
22 April 2009	168/180	0.368	669	–	–	–	–	–	–
27 April – 7 May 2010	180/180	0.432	777	193/196	0.430	841	–	–	–
18–30 April 2011	195/195	0.404	786	194/195	0.410	793	157/157	0.430	682
19 April – 4 May 2012	183/184	0.438	815	174/174	0.426	741	166/167	0.430	719
15–28 April 2013	–	–	–	–	–	–	129/135	0.304	378
7–25 April 2014	174/174	0.367	627	182/182	0.374	666	–	–	–
31 April – 5 May 2015	177	0.433	766	181	0.437	791	–	–	–

Note: 1. In some cases, the depth of the snow cover is given without taking into account the ice crust (numerator) and taking it into account (denominator). 2. h_s is average snow height; ρ_s is average snow density; Q – average water reserve in the snow cover.

the Aldegondabreen. For the Vestre Grønfyordbreen, this is probably due to the presence of an accumulation area above the seasonal snow boundary and an extended middle part of the glacier, which reduces the influence of slopes on the nature of snow accumulation. The relief of the surface of both glaciers is also more uncomplicated.

The range of changes in the average annual water content in the snow cover on the Vestre and Austre Grønfyordbreens measured during snow measurements is wider than in the case of the Aldegondabreen (Table 3.2.1). In general, one can note, firstly, comparable values of this parameter for the Vestre Grønfyordbreen and Aldegondabreen and, secondly, consistently lower values recorded on the Austre Grønfyordbreen during the years of joint observations on glaciers. At the same time, on the surface of the Vestre Grønfyordbreen with maximum elevations (accumulation zone), this value often exceeded all those measured in the area (Study of ..., 2011; Study of ..., 2012).

Comparison of the interannual variability of water content in the snow cover of the Aldegondabreen, the annual amounts of precipitation for the cold period of snow accumulation, the mean air temperature for the cold period and the average annual air temperature (according to the Barentsburg Hydrometeorological Observatory) shows the absence of strong connection and mutual dependence of the listed parameters (Figure 3.2.4) This may be due to methodological reasons, and in particular not very good position of the meteorostation in Barentsburg and low representativeness of meteorological parameters measured on it for the analysis of snow accumulation processes on the glaciers of the region. Such factors as wind transport and redistribution of snow (including from the slopes

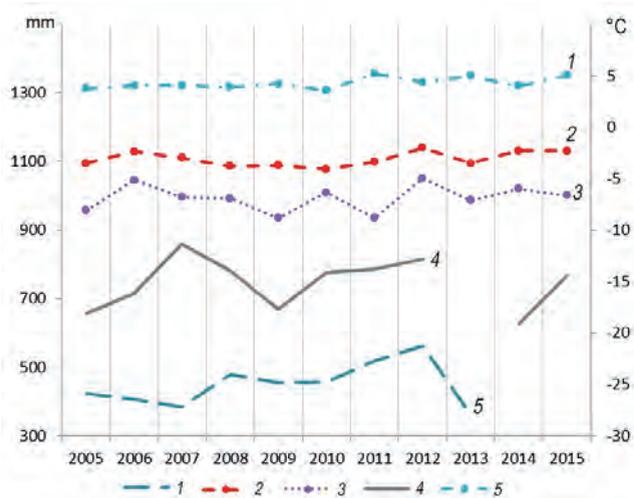


Fig. 3.2.4. The course of changes in water reserves in the snow cover of the Aldegondabreen glacier and meteorological parameters measured at Barentsburg meteorostation for 2005–2015.

1 – precipitation (mm) for the cold period (October–May); 2 – average water accumulation (mm) in the snow cover of the glacier; 3 – average annual air temperature (°C); 4 – average air temperature (°C) for the cold period (October–May); 5 – average air temperature (°C) for the warm period (June–September).

surrounding the glacier), differences in the actual duration of the cold period, periodic precipitation and conservation in the snow mass of liquid atmospheric precipitation, etc., which play a significant role in the processes of accumulation and metamorphism of snow can be a natural reason.

During summer-autumn mass-balance glaciological studies, the features of ablation process and the presence of significant interannual changes in the value of the loss in weight of the Aldegondabreen were revealed. The observation results indicate an uneven melting of the glacial surface while observing the main trend of decreasing ablation with increasing altitude. An illustration is the distribution of the total ablation value at the measurement points in 2015 (Fig. 3.2.5). Points 16 and 10 are the most distant from the trend line, located on the tongue and edge of the glacier and, accordingly, close to the moraine. The area of point no. 8 was subject to the least melting. Ablation stick no. 12 did not thaw out during the season; it is located at 458 m and is the highest point.

Fig. 3.2.6 shows the spatial distribution of total surface ablation. It shows the ablation tends to decrease in general from the north-east to the southwest of the glacier.

The ablation process during each season was uneven and depended primarily on the air temperature and the amount of liquid precipitation. Thus, in 2014, the maximum average daily surface ablation (26 mm per day) was recorded from 4 to 10 August, when the maximum average daily temperature was observed for the entire summer (9 °C), and there was no precipitation (Study of the meteorological regime ..., 2014; Study of long-term changes in ..., 2014). A slight increase in air temperature, coinciding with rainfall, can initiate active melting on the glacier even in September, which was recorded, for example, in 2015 (Table 3.2.2) (Study of the meteorological regime ..., 2015; Study of long-term changes in ..., 2015). In general, the maximum melting on the glacier occurs at the end of July–August.

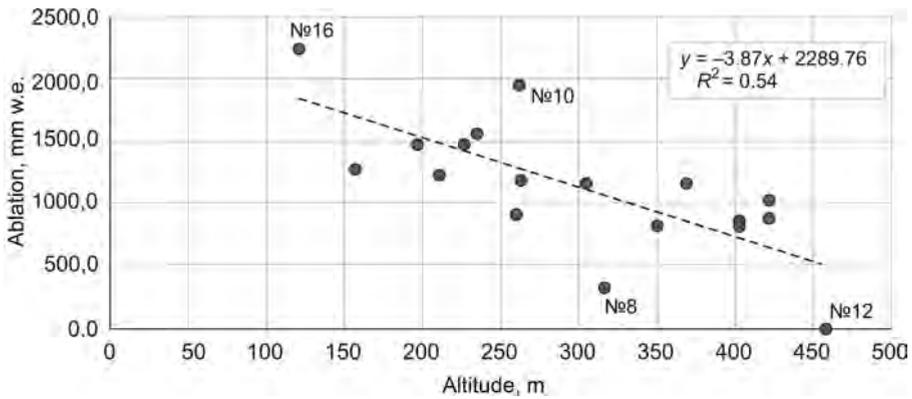


Fig. 3.2.5. Altitude distribution of the total ablation value on the Aldegondabreen according to data for 2015 (Study of the meteorological regime ..., 2015; Study of long-term changes in ..., 2015).

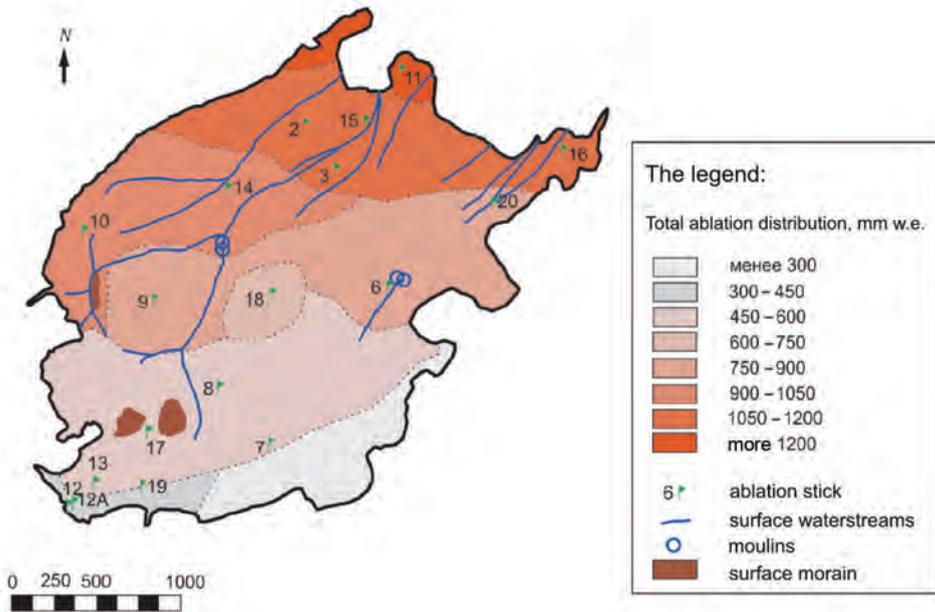


Fig. 3.2.6. Total ablation distribution diagram on the Aldegondabreen according to data for 2014 (Study of the meteorological regime ..., 2014; Study of long-term changes in ..., 2014).

Undoubtedly, the main factor determining the course of melting and annual ice loss is the interannual variability of climatic conditions. So, compared to 2009, in 2014, the snow cover from the glacier melted later; as a result, the ablation period began at the end of July, and it was less intense. The maximum average daily ablation in 2014 was 11 mm less and occurred in the first week of August, and not at the end of July, as in 2009. The average daily ablation in 2014 was 17 mm w.e. in 41 days, and in 2009 it was 24 mm w.e. in 36 days. If 2009 is characterized by a sudden change in the average daily ablation with several peaks, then in 2014, the changes were smooth with one peak interval (Fig. 3.2.7). The glacial surface started to melt 10 days later in 2014.

Ablation dynamics on the Aldegondabreen in 2015 by observation periods

Period	Number of days	Average ablation, mm w.e.	
		for a period	for a day
22.07–24.08 2015	33	851.8	25.81
24.08–10.09 2015	17	54.5	3.21
10.09–15.09 2015	5	37.5	7.50

The interannual variability of the climatic conditions of ablation and the above-mentioned features of its process led to significant differences in the values of the total weight loss of the Aldegondabreen over the years of observations (Table 3.2.3). At the same time, the studies carried out indicate a constant loss of ice on the Aldegondabreen.

Ice loss was recorded during research in 2014–2015 at the Vestre Grøn fjordbreen (Table 3.2.3), the maximum values of the melted ice mass, as well as on the Aldegondabreen, were at the end of July–August. In general, the Vestre Grøn fjordbreen is characterized by more steady seasonal and high-altitude melting than the Aldegondabreen (Fig. 3.2.8). The reason is probably that Vestre Grøn fjordbreen stretches from south to north, and the valley sides have less influence on the distribution of solar radiation over the glacier surface.

The value of the altitude gradient of the total ablation in the 2014 was 427 mm w.e. by 100 m, which is noticeably more than on the Aldegondabreen. Perhaps it is due to the lower location of the glacier front (below 100 m) and its intense melting compared to the Aldegondabreen, as well as the presence of an accumulation zone in the upper reaches of the glacier (a height of 450–600 m). Thus, despite the higher values of total ablation at the lowest observation point on the Vestre Grøn fjordbreen (Table 3.2.3), the process and volumes of surface ablation for the glaciers under study should be similar.

The measured mass-balance characteristics of glaciers make it possible to assess the current state of glaciation in the Barentsburg area over the last decade and by comparing it with previous data to reveal the features of the multi-decadal development of this glaciation. The research results show that the main distinguishing feature of the region's glaciation in the last decade is its constant degradation. In all years, a significant decrease in the mass of the Aldegondabreen and Vestre Grøn fjordbreen has been revealed (Table 3.2.3). This trend has been observed since the last century: the valley glaciers of West Spitsbergen experienced a reduction from 1936 to 2003, during which the average value of the surface decrease was 0.64 and 0.47 m/year for the Aldegondabreen and Vestre Grøn fjordbreen, respectively, and the average negative mass balance of the Aldegondabreen

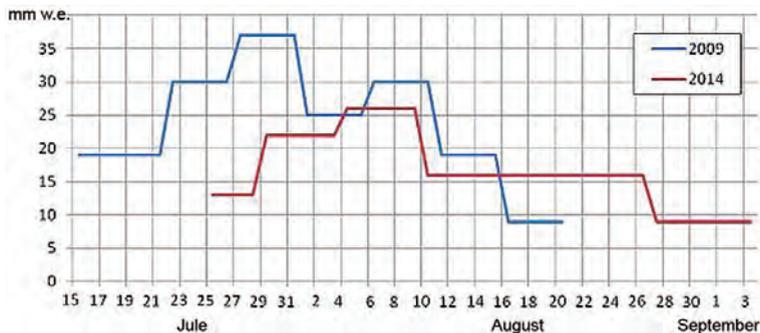


Fig. 3.2.7. Average daily ablation (mm w.e.) by periods in 2009 and 2014.

Ablation and glacier weight loss rates

Glacier	Период наблюдений	V_i mln m ³	$\text{grad}A_{h_i}$ mm w.e. for 100 m	A_{h_i} min/max/average mm w.e.
Aldegondabreen	August–16 September 2008 (29 days)	2.87	–130	100/637/409
Aldegondabreen	15 July–20 August 2009 (36 days)	8.95	–	387/1286/757
Aldegondabreen	7 August–9 September 2010 (33 days)	–	–178	90/495/264
Aldegondabreen	25 July–21 September 2014 (41 days)	5.31	–300	211/1302/754
Vestre Grønfjordbreen	22 July–26 September 2014 (66 days)	–	–427	0/1512/659
Aldegondabreen	22 July–15 September 2015 (55 days)	7.36	–	324/2241/1200
Vestre Grønfjordbreen	25 July–12 September 2015 (49 days)	–	–	0/2718/1109

Note. V – total loss of glacier volume for the balance year; $\text{grad}A_{h_i}$ is the value of the altitude gradient of the total ablation for the season; A_s – surface ablation over the observation period.

was 860 mm w.e. (Mavlyudov et al., 2012; Mavlyudov, 2006). In the period 1966–1990, ice losses for the Aldegondabreen were 40–130 cm (400–1300 mm), and for the Vestre Grønfjordbreen – 100–1400 mm (Mavlyudov, 2006; Etzelmuller and Sollid, 1996). Per the data for recent years (Table 3.2.3), the annual loss of the ice layer on the Aldegondabreen ranged from 264 to 1200 mm w.e. with an average value over five mass balance years 720 mm w.e.; on the Vestre Grønfjordbreen in 2013–2014 and 2014–2015 balance years, the average value of the ice layer loss was 659 and 1109 mm w.e., respectively. Thus, the values of ablation and glaciers weight loss in the region measured in recent years are generally within the range of long-term values.

Conditions for reducing glaciation in the Barentsburg area also have a physical and mathematical foundation over the past decade. The results of calculations of the equivalent snow thickness, at which the ablation of glaciers is compensated by solid precipitation, showed that with a snow cover thickness of 2.5 m, the ablation of the Aldegondabreen is compensated for by solid precipitation at an average air temperature of 3.7 °C in the warm period (Osokin et al., 2010). As Table 3.2.1 and Fig. 3.2.2 show, the thickness of the snow cover on the glacier in the last decade rarely reached 2.0 m. At the same time, the average temperature of the warm period exceeded 4.0 °C; it is a prerequisite for ablation and ice loss to prevail over its growth. The glaciers in the region tend to degrade, we can see it from the change in the height of the position of the snow boundary, the results of the study of it you can find below. In general, if in the 1980s, the equilibrium line of the Aldegondabreen was located at a height of about 350–400 m (Glaciology of ..., 1985). Now almost the entire surface of the glacier is in the ablation area.

Along with it, there are interannual variations in ice loss on the glaciers of the Isfjorden area, indicating a periodic change in the nature and activity of the reduction of local glaciation. So, in the lower part of the Aldegondabreen, at a height of 179 m above sea level, 222 cm of ice melted in 2004, and 158 cm melted in 2010, i.e., ice melting slowed

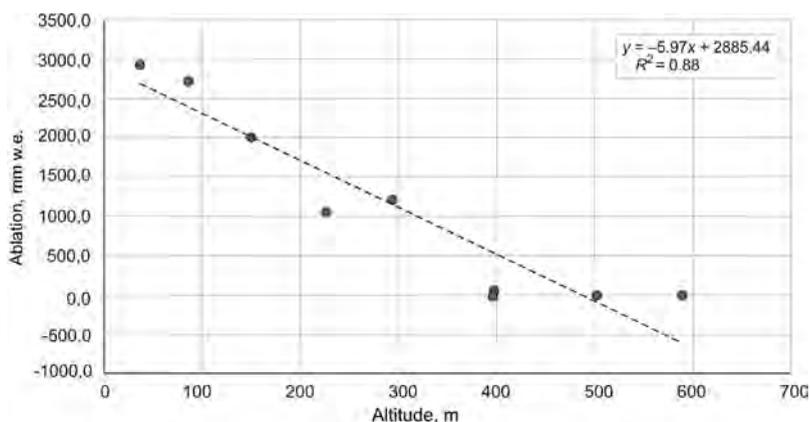


Fig. 3.2.8. Altitude distribution of the total ablation value on the Vestre Grøn fjordbreen.

down in time. So, in the upper part of the Aldegondabreen, at a height of 432 m above sea level, 121 cm of ice melted in 2004, and 28 cm melted in 2010 (a decrease of about 77 % over seven years). From these indicators, it was concluded that in the period 2004–2010, melting in the lower part of the Nordenskiöld Land glaciers changed insignificantly. In their upper part, there was a noticeable reduction in ice melting (Mavlyudov et al., 2012). Results of measurements on the Aldegondabreen in 2014 and 2015 (Study of the meteorological regime ..., 2014; Study of long-term changes in ..., 2014; Study of the meteorological regime ..., 2015; Study of long-term changes in ..., 2015) indicate that at a height of about 180 m, about 104 and 140 cm of snow, respectively melted (continued decrease in melting), while at a height of about 430 m, about 42 and 44 cm, respectively, melted (a decrease in the volume of melting compared to 2004, but an increase compared to 2010). Thus, in general, it confirms the assumption about a possible decrease in the intensity of melting and loss of glaciers over the past decade.

Observations of ablation processes supplemented summer mass-balance studies on glaciers. Observations of the dynamics of the altitude position of the snow line on the Aldegondabreen carried out in 2009, 2014 and 2015, showed its rise during ablation in late July–August up to a height of 450–455 m, which indicates the almost complete absence of an equilibrium line. According to the data for 2014, the glacier began to thaw on 9 July, by 13 July the snow line rose to a mark of 252 m, by 19 July to a mark of 350 m, and by 29 July to a height of 450 m. Above this point, the snow remained only on steep shady slopes in the south and southwest. Visual observation data showed a linear dependence of the snow line height on the total air temperature taken from the Barentsburg meteorostation (75 m), and it was reduced to the average height of the Aldegondabreen (275 m) using a temperature gradient of $-1.28\text{ }^{\circ}\text{C}/100\text{ m}$ (Study of long-term ..., 2009). As Fig. 3.2.9 shows, the rise of the snow line during the season is very steady, which is consistent with the data of visual observations. When restoring the course of the snow line, the influence of summer atmospheric precipitation was not taken into account, so one can only judge the qualitative results of making the graph.

According to the results of observations for 2014 and 2015, on the Vestre Grøn fjordbreen, the snow line also rose at the end of July–August to heights of 440–450 m, which is explained by its proximity to the Aldegondabreen. On the Bertilbreen

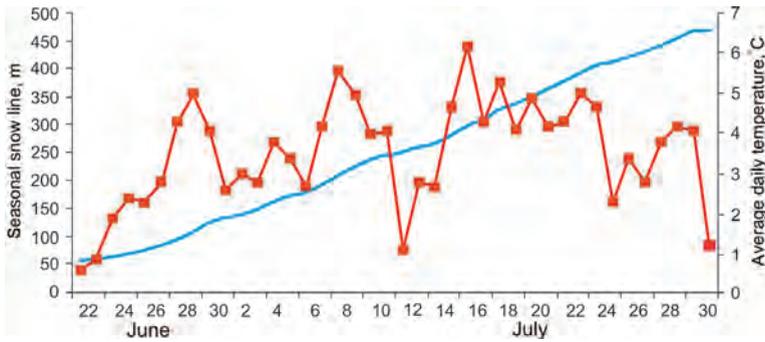


Fig. 3.2.9. The reconstructed retreat of the seasonal snow line and the course of the average daily air temperature (T_{av} , °C) on the Aldegondabreen in 2014.

(Piramiden area), the snow line at the end of the ablation season in 2014 reached the height of 520–550 m, which indicates warmer climatic conditions and other melting conditions in this area.

During observations of the surface hydrological network on the Aldegondabreen glacier in 2002–2003, 2008, and 2014 watercourses plots were made. Comparison of the plots revealed a significant change in the pattern of the surface stream network (Fig. 3.2.10), an increase in the length of the most incised channels of the first order with the formation of the main watercourse, a decrease in the number of active moulins, a shift in the main volume of runoff to the northwestern, sunny side of the glacier, simultaneously with a sharp reduction on the shadow side of the number of watercourses. Such directional long-term changes can be associated with the shrinkage of the glacier under the current climatic conditions, leading to the transformation of its ice surface relief, and an increase in the dependence of runoff on microclimatic conditions (for example, the degree of shading of various parts of the glacier by the sides of the valley).

An experimental study in 2006 of the inglacial drainage system of the Aldegondabreen and Vestre Grønfjordbreen indicated that meltwater has complex paths through the glacial body, where the meltwater redistributes and, possibly, accumulates in subglacial/intraglacial cavity. The significant interannual variability in this system is possible; it is consistent with the results of surveys of the surface hydrological network on the Aldegondabreen.

The study of periglacial naled ice (Aldegondabreen, Tavlebreen, Tungebreen, Austre, and Vestre Grønfjordbreen) showed that their sizes vary within the following limits: length 60–600 m, width 30–400 m, thickness 0.5–4.0 m. The vertical structure of naled ice is heterogeneous: the number of layers in them ranges from 3 to 12; the layers have different thicknesses and are represented by crystals of round and acicular shapes. This heterogeneity of the vertical structure indicates the waters of different genesis form the ice in the meteorological conditions that change many times and change suddenly during one year since all the studied naled ice fields annually disappears by the end of the melting season. This is probably why the analysis of samples from the naled ice fields did not reveal a connection between their structure and mineralization, on the one hand, and the temperature regime, on the other hand.

The studies of the characteristics of the heat balance and turbulent exchange on the surface of the Aldegondabreen were carried out in 2004, 2005, and 2010 and gave varied results. Gradient observations made it possible to note the inversion distribution of

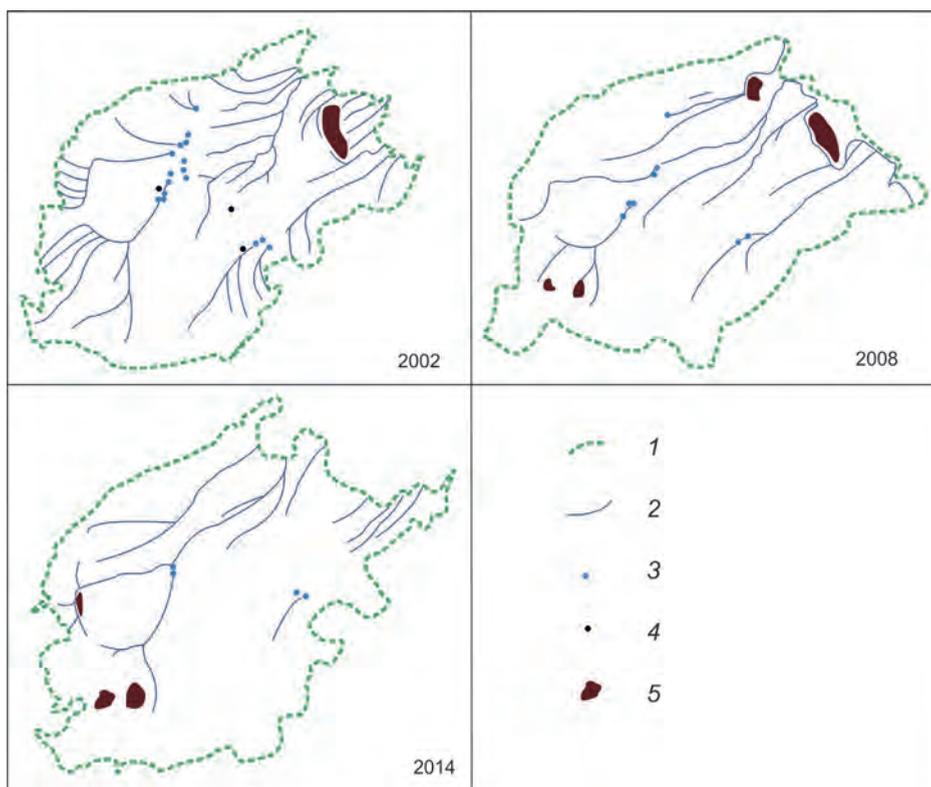


Fig. 3.2.10. Charts of surface waterstreams on the Aldegondabreen glacier in 2002, 2008, and 2014.
 1 – outlines of the Aldegondabreen glacier, 2 – surface waterstreams, 3 – glacier wells, 4 – overgrown glacial wells (chart for 2002), 5 – positive landforms – outcrops of bedrocks and moraines.

air temperature over the glacier according to the height, which is typical over the snow surface. Observations on the glacier in April showed that the temperature of the snow cover during almost the entire period decreases from approximately $-3\text{ }^{\circ}\text{C}$ at a depth of 5 cm to $-6\text{ }^{\circ}\text{C}$ at a depth of 50 cm, which corresponds to the heat flux from the surface into the depth of the snow cover. An exception is the distribution of the snow cover temperature during the sharp increase in air temperature, which began on 26 April 2004. It can be explained by the vertical structure of the snow cover at the observation point: approximately at a depth of 30 cm, there was an ice crust in the snow cover, which delayed the melting water coming from above, as a result, the temperature of the snow at this depth turned out to be close to the melting point of water.

The total heat flux at a depth of 30 cm in the central part of the Aldegondabreen is $1.5\text{--}2.0\text{ W/m}^2$; similar values were obtained in the coastal zone. However, after a sharp increase in air temperature from 27 April, the total heat flux was by an order higher. In April, the direction of the resulting flux during the observation period repeatedly changed its sign: the heat flux deep into the snow cover reached 60 W/m^2 , the heat flux from the snow surface to the atmosphere was 39 W/m^2 (the highest value). In July–August, the resulting heat flux during the entire observation period goes from the atmosphere to the ice surface and varies from 90 to 220 W/m^2 .

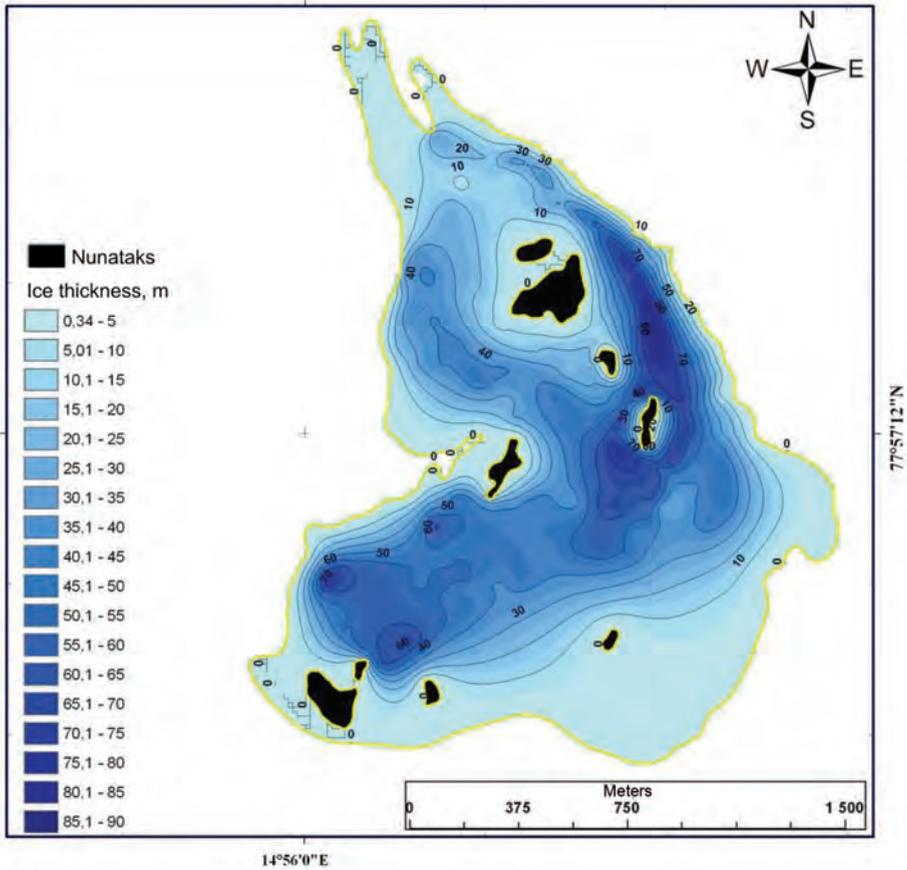


Fig. 3.2.11. Ice thickness of the Tungebreen (Study of the meteorological ..., 2011).

As a result of actinometric observations on the Aldegondabreen in 2007, the spatial distribution of albedo in the wavelength range of 0.3–3.0 μm was observed. It shows the existence of stable zones on the surface of the glacier during the melting period with the lowest albedo of 10–15 % in the areas adjacent to the terminal moraine and the southern edge of the glacier; in the northern part of the glacier, the albedo reaches up to 70 %. Such distribution affects the amount of absorbed solar radiation and, consequently, the part of glacier melting in the surface layer. The albedo in the range of 0.4–0.7 μm in slightly contaminated areas of the glacier turned out to be higher than the albedo in the entire short-wavelength range. In contaminated areas, the ratio becomes inverse, and this probably indicates the degree of difference between the considered reflective surfaces and Lambert reflection. In general, the studies have shown the presence of significant spatio-temporal variations in albedo on the glacier surface during both the day and the season, which must be taken into account when verifying high- and medium-resolution satellite images.

The radar studies in 2011 resulted in the identification of the ice thickness and the internal structure of the Tungebreen and Gledichfonna (Study of the meteorological ..., 2011). Fig. 3.2.11 shows that the Tungebreen reaches its maximum thickness (88 m) in its

middle part, near its right side, and in the upper part, the ice thickness reaches 70 m. The southernmost part of the glacier is characterized by a huge slope and, most likely, insignificant ice thickness. Most of the sounding profiles in the glacier revealed internal reflections from the cold–warm ice interface. In the southwestern part of the glacier, the thickness of the warm ice reaches 60 m. That means, practically the entire thickness of the glacier is here at the ice melting point; The warm bottom layer of ice is also confined to depressions in the bedrock, where its thickness reaches 15–30 m. The maximum ice thickness of Gledichfonna exceeds 60 m with an average thickness of 33.7 m, has a single-layer structure; the absence of internal reflections indicates its cold thermal state.

CONCLUSIONS

Long-term complex glaciological studies of the AARI have made it possible to collect a large dataset over the last decade and to reveal the characteristics of the state, changes, and structure of glaciers in the Barentsburg area (West Spitsbergen).

Mass-balance measurements and observations on the glaciers of the study area made it possible to obtain the following results.

Changes in the average annual values of water content in the snow cover of the glaciers of the region in the period 2003–2015 ranged from 627 to 859 mm w.e. The absence of a connection between these values and meteorological parameters was revealed, which may be due to both a methodological reason and natural factors: wind transfer and redistribution of snow; differences in the actual duration of the cold period; periodic liquid precipitation and its conservation in the snow mass, etc.

The annual ice loss on the Aldegondabreen for the above period ranged between 264 and 1200 mm w.e. (with an average value over five mass balance years of 720 mm w.e.). On the Vestre Grønfyordbreen in 2013–2015 balance years, the average value of ice loss was 659 and 1109 mm w.e. These data on the ice loss of the glaciers in the region are generally within the range of long-term values, which confirms that glaciation in the region keeps tending to reduce. At the same time, the data of mass balance measurements for 2010–2015 on the Aldegondabreen, in general, confirm the assumption of a possible decrease in the intensity of melting and loss of glaciers over the past decade.

Observations of the ablation processes during the above period showed the following.

The absolute height of the snow line on the Aldegondabreen for the period from 2003 to 2015 moved upward to a height of 450–455 m above sea level. It shows that there is almost no equilibrium line on the glacier, i.e., it confirms the conclusions of mass-balance observations that those glaciers in the region, equilibrium line of which is below 450 m above sea level, tend to reduce.

Long-term changes in the surface hydrological network on the Aldegondabreen and its drainage system indicate its reduction in current climatic conditions, leading to a transformation of the ice surface relief and an increase in the dependence of runoff on microclimatic conditions.

Studies of the spatial distribution of albedo, characteristics of heat balance and turbulent exchange on the Aldegondabreen indicate the presence of significant spatio-temporal variations in albedo and associated processes on the glacial surface (both during the day and during ablation seasons), depending on the pollution, illumination, sharp changes in meteorological conditions, and other factors affecting the state of the surface of the glacier and the layer of ice melting.

REFERENCES

- Kotlyakov V.M. (ed.). *Gljaciologija Shpicbergena*. Glaciology of Spitsbergen. Moscow: Nauka, 1985: 199 p. [In Russian].
- Zinger Ye.M., Mikhailov V.I. Snow accumulation on Spitsbergen glaciers. *Materialy gljaciologicheskikh issledovanij*. Materials of glaciological studies. 1967, 13: 86–100. [In Russian].
- Izuchenie meteorologicheskogo rezhima i klimaticeskikh izmenenij v rajone arhipelaga Shpicbergen. Jekspedicija "Shpicbergen-2003"*. Study of the meteorological regime and climatic changes in the area of the Spitsbergen archipelago. Expedition "Spitsbergen-2003". R&D report (supervisor S.M. Pryamikov). St. Petersburg, 2003: 214 p. (AARI Funds, Inv. No. R–5513). [In Russian].
- Izuchenie meteorologicheskogo rezhima i klimaticeskikh izmenenij v rajone arhipelaga Shpicbergen. Jekspedicija "Shpicbergen-2004"*. Study of the meteorological regime and climatic changes in the area of the Spitsbergen archipelago. Expedition "Spitsbergen-2004". R&D report (supervisor S.M. Pryamikov). St. Petersburg, 2004: 157 p. (AARI Funds, Inv. No. R–5514). [In Russian].
- Izuchenie meteorologicheskogo rezhima i klimaticeskikh izmenenij v rajone arhipelaga Shpicbergen. Jekspedicija "Shpicbergen-2005"*. Study of the meteorological regime and climatic changes in the area of the Spitsbergen archipelago. Expedition "Spitsbergen-2005". R&D report (supervisor S.M. Pryamikov). St. Petersburg, 2005: 157 p. (AARI Funds, Inv. No. R–5547). [In Russian].
- Izuchenie meteorologicheskogo rezhima i klimaticeskikh izmenenij v rajone arhipelaga Shpicbergen. Jekspedicija "Shpicbergen-2006"*. Study of the meteorological regime and climatic changes in the area of the Spitsbergen archipelago. Expedition "Spitsbergen-2006". R&D report (supervisor S.M. Pryamikov). St. Petersburg, 2007: 210 p. (AARI Funds, Inv. No. R–560). [In Russian].
- Izuchenie meteorologicheskogo rezhima i klimaticeskikh izmenenij v rajone arhipelaga Shpicbergen. Jekspedicija "Shpicbergen-2007"*. Study of the meteorological regime and climatic changes in the area of the Spitsbergen archipelago. Expedition "Spitsbergen-2007". R&D report (supervisor S.M. Pryamikov). St. Petersburg, 2007: 164 p. (AARI Funds, Inv. No. R–5637). [In Russian].
- Izuchenie meteorologicheskogo rezhima i klimaticeskikh izmenenij v rajone arhipelaga Shpicbergen. Jekspedicija "Shpicbergen-2008"*. Study of the meteorological regime and climatic changes in the area of the Spitsbergen archipelago. Expedition "Spitsbergen-2008". R&D report (supervisor S.M. Pryamikov). St. Petersburg, 2008: 191 p. (AARI Funds, Inv. No. R–5731). [In Russian].
- Izuchenie meteorologicheskogo rezhima i klimaticeskikh izmenenij v rajone arhipelaga Shpicbergen. Jekspedicija "Shpicbergen-2009"*. Study of the meteorological regime and climatic changes in the area of the Spitsbergen archipelago. Expedition "Spitsbergen-2009". R&D report (supervisor S.M. Pryamikov). St. Petersburg, 2009: 237 p. (AARI Funds, Inv. No. R–5833). [In Russian].
- Izuchenie meteorologicheskogo rezhima i klimaticeskikh izmenenij v rajone arhipelaga Shpicbergen. Jekspedicija "Shpicbergen-2010"*. Study of the meteorological regime and climatic changes in the area of the Spitsbergen archipelago. Expedition "Spitsbergen-2010". R&D report (supervisor S.M. Pryamikov). St. Petersburg, 2010: 157 p. (AARI Funds, Inv. No. R–6004). [In Russian].
- Izuchenie meteorologicheskogo rezhima i klimaticeskikh izmenenij v rajone arhipelaga Shpicbergen. Jekspedicija "Shpicbergen-2011"*. Study of the meteorological regime and climatic changes in the area of the Spitsbergen archipelago. Expedition "Spitsbergen-2011". R&D report (supervisor L.M. Savatyugin). St. Petersburg, 2011: 202 p. (AARI Funds, Inv. No. R–6005). [In Russian].
- Izuchenie meteorologicheskogo rezhima i klimaticeskikh izmenenij v rajone arhipelaga Shpicbergen: otchet o NIR (itogovyy za 2012 g.)*. Study of the meteorological regime and climatic changes in the area of the Spitsbergen archipelago: R&D report (Final report for 2012). R&D report (scientific supervisor of the topic L.M. Savatyugin). St. Petersburg, 2012: 235 p. (AARI Funds, Inv. No. R–6059). [In Russian].
- Izuchenie meteorologicheskogo rezhima i klimaticeskikh izmenenij v rajone arhipelaga Shpicbergen: otchet o NIR (itogovyy za 2013 g.)*. Study of the meteorological regime and climatic changes in the area of the Spitsbergen archipelago: R&D report (Final report for 2013). R&D report (scientific supervisor of the topic L.M. Savatyugin). St. Petersburg, 2013: 146 p. (AARI Funds, Inv. No. R–6137). [In Russian].

Izuchenie meteorologicheskogo rezhima i klimaticheskih izmenenij v rajone arhipelaga Shpicbergen: otchet o NIR (itogovyj za 2014 g.). Study of the meteorological regime and climatic changes in the area of the Spitsbergen archipelago: R&D report (Final report for 2014). R&D report (scientific supervisor of the topic L.M. Savatyugin). St. Petersburg, 2014. P. 156 (AARI Funds, Inv. No. R–6290). [In Russian].

Izuchenie meteorologicheskogo rezhima i klimaticheskih izmenenij v rajone arhipelaga Shpicbergen: otchet o NIR (itogovyj za 2015 g.). Study of the meteorological regime and climatic changes in the area of the Spitsbergen archipelago: R&D report (Final report for 2015). R&D report (scientific supervisor of the topic L.M. Savatyugin). St. Petersburg, 2015: 187 p. (AARI Funds, Inv. No. R–6289). [In Russian].

Issledovanie mnogoletnih izmenenij gidrometeorologicheskogo rezhima i sostojanija prirodnoj sredy arhipelaga Shpicbergen: otchet o NIR (promezhutochnyj za 2014 g.) Study of long-term changes in the hydrometeorological regime and the state of the natural environment of the Spitsbergen archipelago: R&D report (Interim report for 2014). R&D report (principal investigator L.M. Savatyugin). St. Petersburg, 2014: 138 p. (AARI Funds, Inv. No. R–6314). [In Russian].

Issledovanie mnogoletnih izmenenij gidrometeorologicheskogo rezhima i sostojanija prirodnoj sredy arhipelaga Shpicbergen: otchet o NIR (promezhutochnyj za 2015 g.) Study of long-term changes in the hydrometeorological regime and the state of the natural environment of the Spitsbergen archipelago: R&D report (Interim report for 2015). R&D report (principal investigator L.M. Savatyugin). St. Petersburg, 2015: 182 p. (AARI Funds, Inv. No. R–6315). [In Russian].

Issledovanija svojstv snezhnogo pokrova v rajone o. Zap. Shpicbergen: otchet ob jekspedicii "Shpicbergen-2002" (aprel' — maj 2002 g.). Research of the properties of snow cover in the area of the West Spitsbergen: Report of Expedition "Spitsbergen-2002" (April – May 2002). R&D report (supervisor S. M. Pryamikov). St. Petersburg, 2002: 121 p. (AARI Funds, Inv. No. 0–3472). [In Russian].

Koryakin V.S., Troitsky L.S. The main regularities of modern glaciation of Spitsbergen. *Materialy gljaciologicheskikh issledovanij.* Materials of glaciological studies. 1969, 15: 101–110. [In Russian].

Kuzmin P.P. Method of control (normal) snow surveying. *Trudy Zakavkazskogo nauchno-issledovatel'skogo gidrometeorologicheskogo instituta.* Proc. of Transcaucasian Hydrometeorological Research Institute. 1963, 13: 39–47. [In Russian].

Mavlyudov B.R. Glaciation in Spitsbergen at the end of the 20th century. *Materialy gljaciologicheskikh issledovanij.* Materials of glaciological studies. 2006, 101: 146–152. [In Russian].

Mavlyudov B.R., Savatyugin L.M., Solovyanova I.Ju. The reaction of the Nordenskiöld glaciers (Spitsbergen) on climate change. *Problemy Arktiki i Antarktiki.* Problems of Arctic and Antarctic. 2012, 1 (91): 67–77. [In Russian].

Nastavlenija gidrometeorologicheskimi stancijam i postam. Vyp. 6. Ch. 2. Gidrologicheskie nabljudenija i raboty na malyh rekah. Manual on Hydrometeorological Stations and Posts. Issue 6. Part 2. Hydrological observations and work on small rivers. Leningrad: Gidrometeoizdat, 1972: 266. [In Russian].

Kotlyakov V.M. (ed.). Oledenenie Shpicbergena. Glaciation of Spitsbergen. Moscow: Nauka, 1975: 276 p. [In Russian].

Osokin N.I., Sosnovsky A.V., Mavlyudov B.R., Nakalov P.R., Chernov R.A. Changes in the existence conditions for glaciers on the Spitsbergen archipelago at the beginning of the XXI century. *Priroda shel'fa i arhipelagov evropejskoj Arktiki. Kompleksnye issledovanija prirody Shpicbergena. Materialy mezhdunarodnoj nauchnoj konferencii.* The nature of the shelf and archipelagos of the European Arctic. Comprehensive studies of the Nature of Spitsbergen. Materials of the international scientific conference (Murmansk, October 27–30, 2010). Moscow: GEOS, 2010, 10: 439–444. [In Russian].

Rukovodstvo po snegomernym s#jomkam v gorah. Guide to snow measuring works in the mountains. Leningrad: Gidrometeoizdat, 1958: 57 p. [In Russian].

Troitsky L.S. Mass balance of different types of glaciers on Spitsbergen. *Materialy gljaciologicheskikh issledovanij.* Materials of glaciological studies. 1988a, 63: 117–121. [In Russian].

Troitsky L.S. On the mass balance of the Spitsbergen glaciers in 1985/86, 1986/87 and 1987/88 balance years. *Materialy gljaciologicheskikh issledovanij*. Materials of glaciological studies. 1988b, 63: 194–197. [In Russian].

Tronov M.V. *Ledniki i klimat*. Glaciers and climate. Leningrad: Gidrometeoizdat, 1966, 407 p. [In Russian].

Macheret Ju.Ja., Berikashvili V.Sh., Vasilenko E.V., Sokolov V.G. Broadband impulse radar for sounding glaciers with an optical synchronization channel and digital signal processing. *Datchiki i sistemy*. Sensors and systems. 2006, 12: 2–8. [In Russian].

Etzelmuller B., Sollid J.L. Long-term mass balance of selected polythermal glaciers on Spitsbergen, Svalbard. *Norsk Geografisk Tidsskrift*. 1996, 50: 55–66.

Paterson W.S.B. The physics of glaciers. Oxford: Pergamon, 1994: 480 p.

3.3. THE PERMAFROST OF SPITZBERGEN AND ITS MONITORING AT THE CRYOSPHERIC TESTING AREA IN BARENTSBURG

N.E. Demidov, S.R. Verkulich, V.E. Demidov, D.A. Solovyeva, S. Wetterich

Permafrost is an essential component of the natural environment of the polar regions. Its changes largely depend on different-scale and different-time transformations in the “atmosphere-ocean” climate system and, in turn, have a high impact on changes in the relief, landscapes, water balance, and other elements of the earth’s surface. Observations on how permafrost reacts to climate warming in the North Polar Region, carried out in recent decades, generally indicate an increase in the average annual ground temperature, an intensification of thermokarst and thermal abrasion of sea coasts, and an increase in the depth of seasonal thawing. The Spitsbergen archipelago is located in the North Atlantic zone of the Arctic. So the permafrost in this region is most sensitive to changes in the atmosphere and ocean, and in local geocryological conditions change faster than on other Arctic islands.

This chapter considers the history and current status of geocryological research on Spitsbergen, provides an outline of the permafrost structure of the archipelago, including the first results of research at the cryospheric testing area of the Russian Scientific Center on Spitsbergen (RSCS), and gives recommendations for further research at this testing area. Published works of Russian and international researchers, archives of the Spitsbergen Party of JSC Polar Marine Geosurvey Expedition (PMGE), and the “Arktikugol” Trust, as well as the results of the authors’ expeditionary work as part of the AARI expeditions in 2016–2018 are used.

HISTORY AND PRESENT STATUS OF PERMAFROST RESEARCH ON SPITZBERGEN

A practical necessity initiated permafrost exploration in the Soviet mines of Spitsbergen when people encountered permafrost when digging mines, designing basements, and finding water supply sources. In contrast to international companies engaged in the development of coal in Spitsbergen, Soviet geologists in the 1930s–1940s approached these issues from the position of doctrine of permafrost by M. I. Sumgin (Permafrost soil within the USSR, 1927). In 1935, just three years after the acquisition of coal plots from Holland, the Spitsbergen exploration expedition of the “Arktikugol” Trust began hydrogeological studies, which addressed a wide range of issues related to permafrost (Zenkov, 1935). During the Soviet years, researchers from RIGA, SEVMORGEО, VSEGINGEO, Institute of Geography of the USSR Academy of Sciences, and other production and R&D organizations were involved in the study of the permafrost of Spitsbergen. Despite the exploration and research work in the 1990s decreased and at the same time Norwegian geocryological research intensified, the Barentsburg and Piramiden mines remain the most studied permafrost areas on Spitsbergen.

At the Barentsburg mine, core drilling of about 350 prospecting boreholes for coal to a depth of 700 m was carried out (Mine workings plan ..., 2016). The drilling was carried out in three shifts using high concentration brine for flushing (Karpov, 1946). In some boreholes, the depth of the zero isotherm was measured by thermometers, as well as by the freezing of freshwater (Zenkov, 1935; Albul, 1947; Obidin, 1953; Obidin, 1958). Temperature measurements were made along the mine shafts and in test pits.

This network of boreholes made it possible to identify patterns in the position of the lower boundary of permafrost, depending on the terrain and distance from the sea, to obtain temperature curves, to determine the typical depth of zero amplitudes and the geothermal gradient. Six boreholes at the Barentsburg mine, two at Piramiden, and one at the Grumant mine were equipped for routine monitoring of the permafrost temperature. Conducting specialized engineering and geological surveys at the Piramiden mine was since the settlement is located on frozen quaternary deposits of several dozens of meters thick. Due to the differential settlement, most of the buildings, including a 125-apartment four-story residential building built on a pile foundation with a ventilated crawl space, had deformations (Sheko et al., 1980). Buildings were equipped with special benchmarks to monitor deformations. The study of the temperature state of the permafrost was also necessary for the calculation of thermal stabilizers (based on kerosene), which were installed in the village buildings.

Early reports also describe permafrost processes and phenomena (pingos, naled ice, frost-shattered areas, etc.). A significant amount of information was obtained on groundwater, which was divided into suprapermfrost, interpermafrost, and subpermafrost already in the reports of the 30s following the classification of N.I. Tolstikhin. The main regularities in the formation of the active layer thickness were studied depending on the granulometric composition of the sediments, the orientation of the slopes, the absolute elevations of the surface, the characteristics of the vegetation, and snow cover.

B.I. Vtyurin studied the cryogenic structure of frozen quaternary rocks and underground ice during the expeditions of the Institute of Geography of the USSR Academy of Sciences 1987–1988. It was concluded that “all types, subtypes, and types of cryogenic structure are found on Spitsbergen, although their scale differs significantly from other regions of the Arctic and Subarctic, especially continental North Asian regions” (Vtyurin, 1989; Vtyurin, 1990). It was suggested that on Spitsbergen, the conditions are most favorable for the cement type of ice formation and less favorable for the segregation and pool-like types of ice formation because of the coarse-grained nature of the deposits.

It should be noted that the works by B.I. Vtyurin are among the few published Russian theoretical works on the study of the permafrost on Spitsbergen. The work by the NIIGA employee N.I. Obidin on groundwater and permafrost of the Soviet mines in Spitsbergen based on the results of research in 1952–1954 (Obidin, 1958), one can also name a pioneering work. The other above mentioned works are mainly production reports stored in the archives of the PMGE in Barentsburg and Lomonosov, as well as in the archives of the “Arktikugol” Trust in Barentsburg and Moscow.

The history of Norwegian permafrost exploration in Spitsbergen is detailed in Humlum et al. (2003). The first information about permafrost is associated with the holding of the First International Polar Year in 1882 and the beginning of the development of the first coal deposits in 1898. Until the 1970s, researchers studied mainly individual phenomena, in some way associated with permafrost: anchor ice, solifluction, frost cracking, mudflows, springs, glacier bed, etc. In 1977, Leistol’s milestone work was published (Leistol, 1977), which systematized data on the thickness and thermal state of the Spitsbergen permafrost. Based on temperature measurements in mines, Leistol estimated the value of the geothermal gradient for central Spitsbergen as 2–2.5 °C/100 m. Also, the mentioned work discussed the issues of the spatial distribution of frozen strata, pingos, and outcrops of subpermafrost water. The existence of submarine permafrost was

discussed in Gregersen and Eidsmoen (1988); Landvik et al. (1988). Groundwater and its relationship with permafrost, including in terms of their practical use, were highlighted in Haldorsen et al. (1996); Haldorsen and Heim (1999).

In 1978, the Norwegian Committee on Permafrost began stationary observations of the temperature regime of frozen rocks in boreholes 2 and 8 m deep in the area of Svea (Bakkehoi and Bandis, 1988). Under the Permafrost and Climate in Europe (PACE) project in the central part of West Spitsbergen, in 1998, temperature measurements were made in a borehole with a depth of 100 m for paleotemperature reconstructions (Isaksen et al., 2000). In 2007, monitoring results for this borehole were published, showing an increase in temperature (Isaksen et al., 2007). Since 1972, regular measurements of the thickness of the active layer have been carried out in the Kapp Linne and Kalipsostrand regions (Christiansen et al., 2003).

A significant impetus for studying permafrost on Spitsbergen was the International Polar Year 2007, within the framework of which the TSP-Norway project was implemented for drilling and infrastructure development for long-term temperature monitoring of four more boreholes from 5 to 40 m deep. All boreholes are located in the central and western parts of West Spitsbergen at a distance of no more than 60 km from Longyearbyen (Christiansen et al., 2010).

A new stage of Russian permafrost research is associated with the scientific research activities of the AARI. Since 2016, in the area of Barentsburg, a group of permafrost scientists began to work regularly: a reconnaissance of permafrost-geological conditions, an arrangement of a cryosphere testing area with constant observations of how permafrost responds to climate changes, drilling and core sampling of frozen sediments to identify changes in the natural environment of Spitsbergen over the past tens of thousands of years. Drilling was carried out by the Russian installation UKB-12/25 “running dry”, without flushing and blowing, it ensures the preservation of the frozen state of the cores for their correct lithologic description and prevention of their chemical and biological contamination (Fig. 3.3.1). The insignificant weight and dimensions of the drilling equipment made it possible to perform work without damage to the natural environment and disturbance of the soil and vegetation layer, which could have led to a change in the temperature regime of the permafrost.



Fig. 3.3.1. Drilling a borehole using the UKB-12/25 (CDU, core drilling unit) unit in the Grøndalen in May 2017 (photo by V. Demidov).

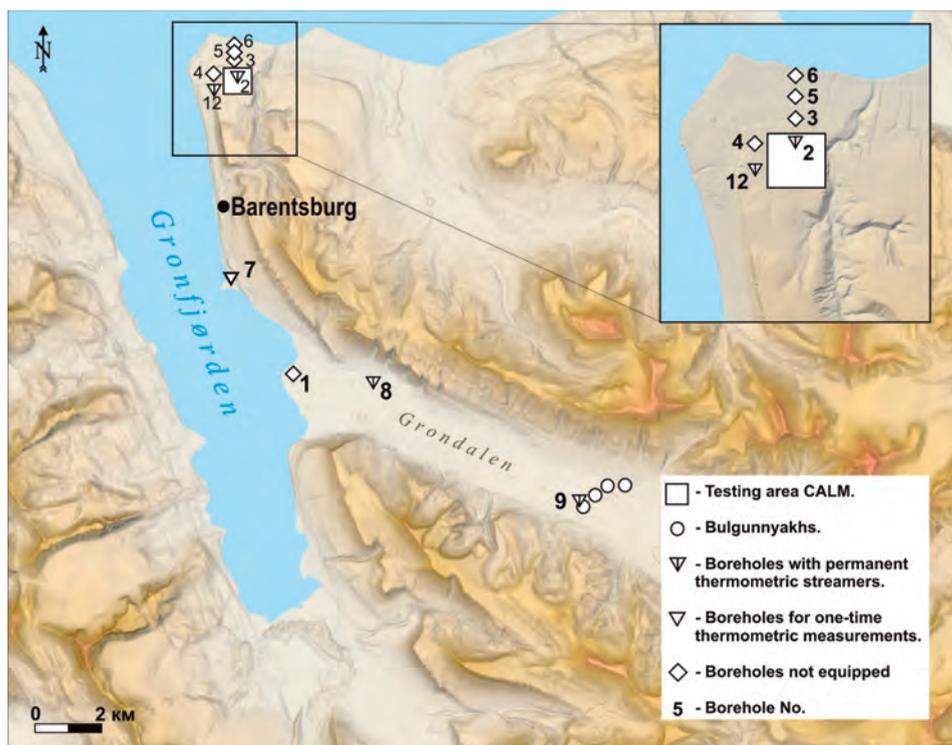


Fig. 3.3.2. The layout of monitoring points for permafrost at the cryosphere testing area of the RSCS of the AARI in the Barentsburg area.

The cryosphere testing area currently includes three thermometric boreholes with permanent thermometric streamers to monitor temperature changes at a depth of zero amplitudes; two boreholes for one-time thermometric measurements; a monitoring site for the active layer (AL) with a thermometric borehole and an automatic weather station, as well as a monitoring point for a group of frost heaving mounds (Figure 3.3.2).

FROZEN ROCKS DISTRIBUTION

The distribution of frozen rocks in glacier-free areas is uniform; subaerial permafrost occupies about 40 % of the archipelago’s area. Through taliks (subgelisols) are locally distributed under the beds of large rivers and lakes, as well as in places where thermal waters come out in the form of springs. Specific volcanic taliks are found in the north of the archipelago, where there are volcanic edifices several thousand years old (Evdokimov, 2000). The frozen rocks are also supposed to be under some glaciers (Leistol, 1976).

In general, the question of the “cold” and “warm” bed of the Spitsbergen glaciers has not been sufficiently studied yet. It is believed that warm glaciers dominate in the western part of the archipelago, under which there is a runoff of meltwater, which forms naled ice and pingos along the periphery of the glaciers (Fundamentals of geocryology, 1998). Vice versa, in the eastern part of the archipelago, the ice sheets are colder, and under them, the probability of permafrost is maximal. In the central part of the archipelago, there may be a complex situation, when frozen rocks and taliks can be simultaneously present under the glacier, along which subglacial waters runoff.

It should also be taken into account that subglacial taliks can appear and disappear, following the dynamics of the glacier thickness in rather short geological time intervals (Haldorsen et al., 2011). On the southern and western shores of Spitsbergen, the seawater temperature does not exceed 6 °C. On the northern and eastern maritime margins of the archipelago, the seawater temperature is negative (Fundamentals of geocryology, 1998). The question of the presence and distribution of the submarine permafrost in the Spitsbergen area, where the width of the continental shelf can reach 50 km, remains open.

CRYOGENIC STRUCTURE

The cryogenic structure of the frozen rocks of Spitsbergen was formed at the time of tectonic uplift and glaciation, which contributed to the denudation (washout) of loose sediments. Therefore, loose sediments on the archipelago are fragmental, and rocks dominated on the surface are characterized by low ice content and fractured cryogenic textures. Ice in rock cracks was noted during shaft work in Grumant, Barentsburg, Piramiden, and Sveagrava (Obidin, 1958).

Colluvial, solifluction, glacial, marine, alluvial and lacustrine deposits are prevalent among loose sediments on Spitsbergen. A system of marine terraces with a height of about 100 m stretches along the coastline. Smaller areas are occupied by alluvium and lacustrine deposits. The age of loose deposits is mainly Holocene, and their thickness rarely reaches the first dozens of meters. All loose sediments of Spitsbergen, except for individual facies of marine and lacustrine sediments, are characterized by coarse grain, which cement ice formation prevails over segregation ice.

Syncryogenic type of freezing is typical for glacial deposits, they have massive pore cryotexture and buried glacial ice cores. Despite the coarse-grained composition of the Spitsbergen alluvium, it is the channel margin sand that is characterized by a syngenetic type, a schlieren subtype, and a complex type of cryogenic structure. Small deposits of massive wedge ice are associated with it (Vtyurin, 1989). Lacustrine sediments freeze in both syncryogenic and epicryogenic scenarios.

Per B.I. Vtyurin, marine sediments of Spitsbergen refer mainly to the epigenetic type of freezing and less often to the complex type (Vtyurin, 1990). The cryolithologic structure of the marine terraces was studied in detail during the drilling of boreholes at the cryosphere testing area in Barentsburg (see Fig. 3.3.2). The terraces are characterized by the same type of cryolithological structure (Fig. 3.3.3), reflecting the change in the facies environment when sediments were in the process of accumulation. Above there are loams about 1.5 m thick, then there is a gravel-pebble soil with a dark sandy-silty filler and a massive cryotexture. Frozen clay with a reticular and layered cryotexture, including interlayers of ice soil and ice up to 20 cm thick, further is frozen gravel-pebble soil with a massive cryotexture, with a rocky base underneath.

To date, based on the results of the chemical analysis of the water extract of the sampled cores carried out in the laboratory of the RSCS of the AARI, we can assume that their thawing and desalination in the Holocene optimum period explain the absence of salinity in the upper layers of frozen rocks now. Thus, the geochemical boundary, at which the transition from freshened to saline sediments occurs, can be a marker of the thawing depth during the Holocene optimum period. Accordingly, the deposits located above the geochemical boundary should be considered as epigenetically frozen, while the underlying ones can be both epigenetic and syngenetic.

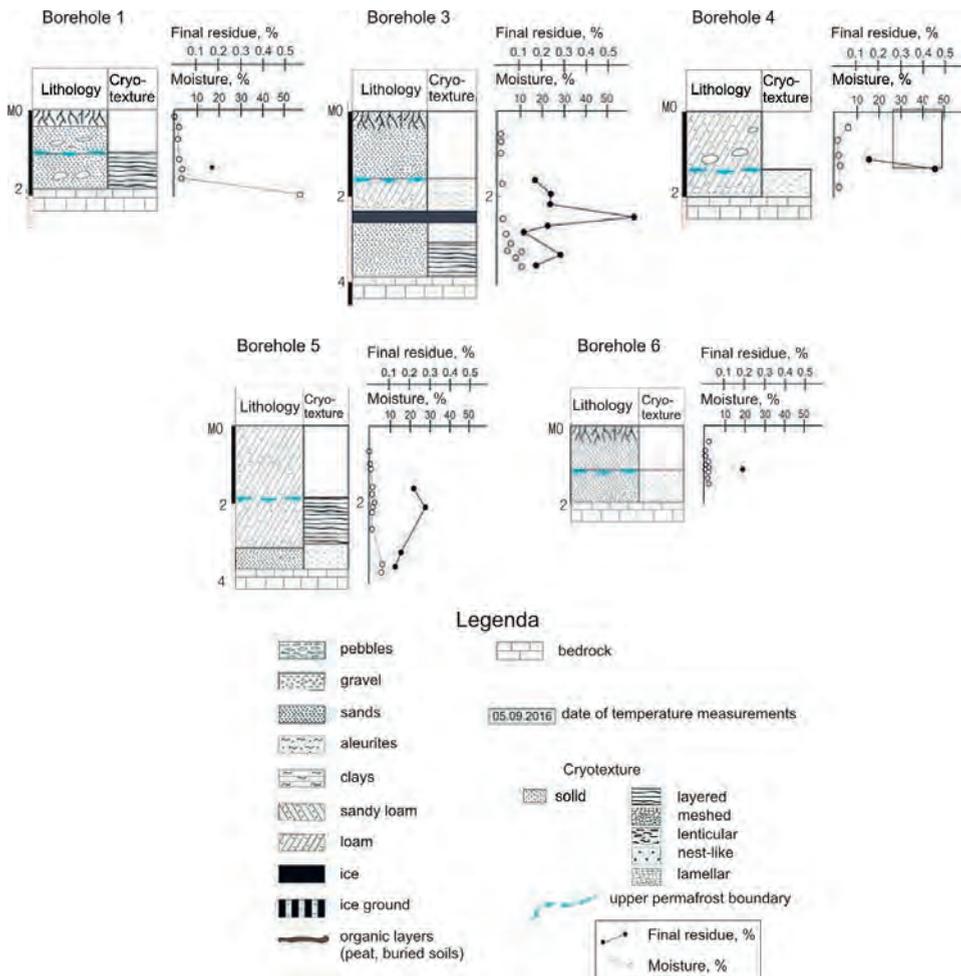


Fig. 3.3.3. Cryolithological borehole logs 1, 3, 4, 5, and 6 with the results of the final residue of the water extract and moisture.

Accumulating deposits ice of various genesis is quite widespread on Spitsbergen. Among them, there are buried primary-surface, mainly glacial, ice, and injection ice in perennial pingos – frost heaving mounds and massive wedge ice. There is evidence that the syngenetic fine-dispersed rocks of Spitsbergen contain a transitional layer 0.2–0.3 m thick, confined to the permafrost top (Fundamentals of geocryology, 1998). High ice content and reticular-layered and ataxitic cryotextures are typical for the transitional layer.

THICKNESS AND TEMPERATURE OF FROZEN ROCKS

The thickness and temperature of the frozen rocks of the archipelago have barely been studied. The data obtained in Soviet times for the areas of the Barentsburg, Colesbey, and Piramiden mines, as well as during research scientific research (Barentsburg, Kapp Linne, Ny-Ålesund, Adventdalen, Hornsund), relate only to the western and partially central part of the West Spitsbergen. On theoretical grounds, latitudinal zoning, altitudinal zoning,

distance from the coast, and the thermal regime of washing currents, ground glaciation, and breaks of heat flow anomalies are the main factors determining the permafrost thickness in the archipelago. Even the first researchers of the permafrost on Spitsbergen (Zenkov, 1935) noted the most important feature of the geocryological structure of the archipelago. The permafrost thickness in the east of the archipelago should exceed the thickness in the western part due to a decrease in the warming effect of the Gulf Stream and western air currents.

According to borehole data, the depth of the zero isotherm varies significantly in the Barentsburg and Colesbay mines. Measurements in the boreholes of the “Arktikugol” Trust in Barentsburg gave the following results: in the borehole No. 1, the 0 °C isotherm is located 120 m deep, at a distance of 4 km to the north in borehole No. 13, the transition through 0 °C was observed at a depth of 175 m, borehole No. 235 that is 230.5 m deep, was entirely in the permafrost zone. In boreholes No. 1 and 3 on Colesbay, the zero isotherm is located at a depth of 97 m and 85 m, respectively. “Thus, the lower boundary of the permafrost turns out to be a kind of curved surface with sometimes unpredictable bends” (Zenkov, 1935). The maximum permafrost thickness indicated according to measurements in boreholes to date has been identified on the Sarkofagen ridge near Longyearbyen. Here, in borehole No. 3 at a depth of 400 m, the temperature was -0.6 °C.

The average annual temperature of rocks at a depth of zero amplitudes in Spitsbergen is highly dependent on the absolute elevations and distance from the sea, among other factors. In glaciation free areas, the average annual permafrost temperature, depending on latitude and other factors, varies from -1 to -7 °C. It can be assumed that the lowest-temperature frozen rocks are widespread in the north of the archipelago, where the average annual permafrost temperature can drop to values less than -10 °C (Fundamentals of geocryology, 1998).

Table 3.3.1

**Measured and calculated values of the permafrost thickness
(Fundamentals of geocryology, 1998; Zenkov, 1935)**

Region	Geomorphological location	Thickness, m
The Adventdalen Mines Larsbreen	Highlands	250–450
	Glacier tongue, 100 m thick (temperature of glacier bed -2.4 °C)	250
Foxfallenbreen	Temperature of glacier bed -3.3 °C at a depth of 64 m	220
Bjørnøya (Bear Island) Piramiden mine (Pyramiden)	Holocene marine terraces with abs. mark 25–50 m	60–80
	Inland plateau	100
Barentsburg mine	Inland plateau	300–500
	Near the sea on laida	8–30
	Holocene marine terraces	100–120
Svea mine	Inland plateau and mountain ranges	300–450
	Marine laida off the coast	100
	Marine laida 200 m from the coast	250
Longyearbyen	Mountain slope with abs. mark 500 m	280
	Gulf coast	100
	Mountain range with an elevation of 500 m	450
	River-valley	200

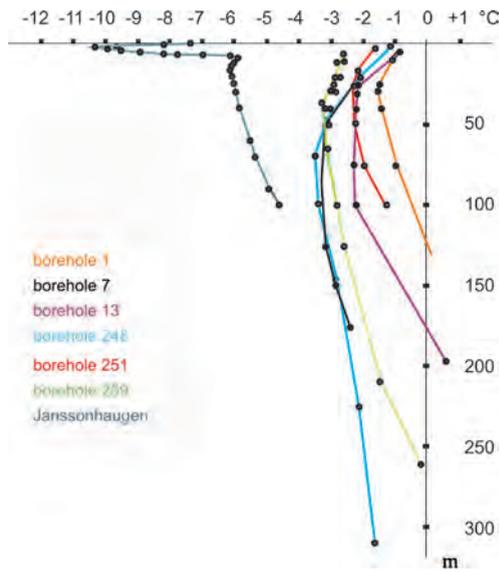


Fig. 3.3.4. Temperature curves from deep exploration boreholes of the “Arktikugol” Trust in Barentsburg and the Norwegian thermometric permafrost borehole in Janssonhaugen. The data are taken from Zenkov (1935), Obidin (1957), Isaksen et al. (2007).

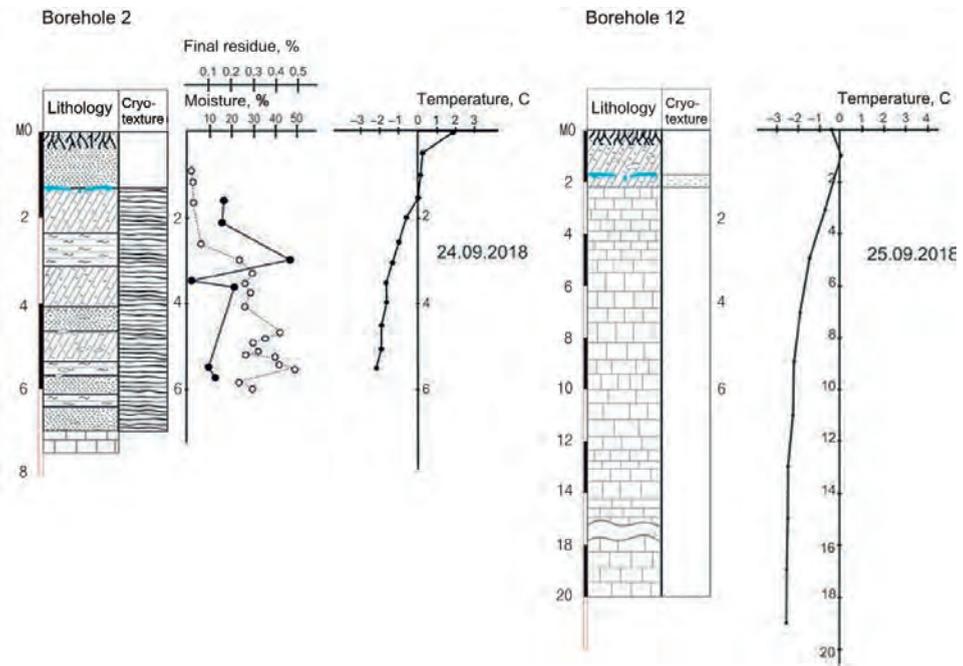


Fig. 3.3.5. Cryolithological borehole logs No. 2 (September 24, 2018) and No. 12 (September 25, 2018) with the results of thermometric measurements, determination of the final residue of the water extract, and moisture.

See Fig. 3.3.3 for legend.

A bulge towards negative temperature values characterizes temperature curves for boreholes at depths below 10–15 m, respectively, the absolute minima are below the depth of zero amplitudes (Fig. 3.3.4).

Obviously, this nature of the curves reflects the current trend of increasing surface temperature. The current increase in the permafrost temperature at a rate of 0.025–0.035 °C is also recorded in observation thermometric boreholes (Isaksen et al., 2007).

The temperature distribution in the boreholes at the RSCS testing area in Barentsburg is interesting. In borehole No. 12 (Fig. 3.3.5), drilled in rocks, the average annual temperature at a depth of 15 m in 2017 was –2.45 °C, and in the borehole No. 2 at a depth of 5.5 m, it was –2.12 °C. In the Grøndalen in a borehole No. 8 on the marine terrace, according to a single measurement in September 2017 at a depth of 14.5 m, the temperature was –3.56 °C.

In borehole No. 9, drilled at the frost heaving mound in the Grøndalen (Fig. 3.3.6), the average annual temperature in the ice core at a depth of 10 m in 2017–2018 was –2.31 °C. In borehole No. 7, drilled at a distance of 20 m from the sea’s edge at Finneset, according to a single measurement in September 2016 at a depth of 12.5 m, the temperature was –0.87 °C. That means it was more than 1 °C higher than in other boreholes in the

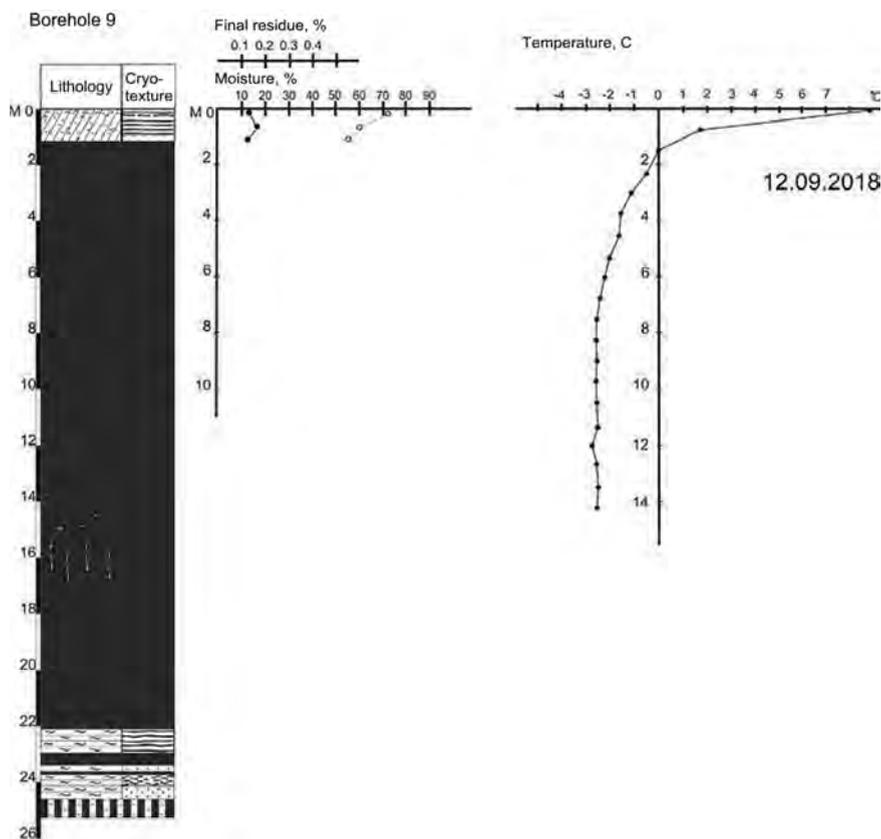


Fig. 3.3.6. Cryolithological borehole log No. 9 (September 12, 2018) with the results of thermometric measurements, determination of the final residue of the water extract, and moisture.

See Fig. 3.3.3 for legend

testing area, clearly demonstrating the warming effect of the sea. Similar values of the temperature of frozen strata in the area of Barentsburg indicate that provided the trend for an increase in the average annual air temperature by 4 °C over 100 years continues (Humlum et al., 2003), which was recorded in Spitsbergen in the last century, we have to expect the degradation of frozen strata already in the XXI century.

ACTIVE LAYER

The same factors that control the thickness and average annual temperature of the permafrost at a depth of zero amplitudes, mostly control the formation of the active layer (AL). Observations of the AL thickness on Spitsbergen are carried out mainly on the western coast of the West Spitsbergen and in several areas of its central part, which is characterized by more severe climatic conditions. At absolute elevations above 500 m, the AL thickness does not exceed several decimeters, or it does not form at all. Coarser-grained formations, due to proper aeration and filtration of groundwater, have a thicker AL. The absence of vegetation cover or underdeveloped vegetation cover also leads to an increase in the AL thickness.

On the contrary, only 0.3–0.5 m thaws under peat bogs (Vtyurin, 1990). In the most favorable conditions, the AL thickness on Spitsbergen can reach 3–4 m. The maximum AL thickness is formed in September.

The CALM site was established to monitor the AL thickness at the RSCS cryosphere testing area in Barentsburg. CALM is an international program for Circumpolar Active-Layer Monitoring, created in 1990. It is a component of the GTOS (Global Terrestrial Observing System) and GCOS (Global Climate Observing System) systems, operating under

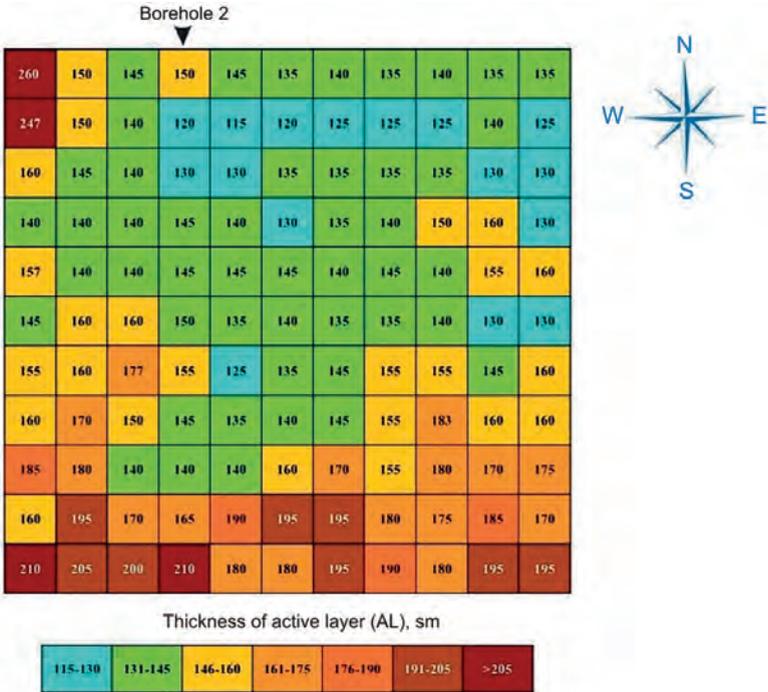


Fig. 3.3.7. Scheme of the CALM site with the results of AL thickness in September 2016.

the guidance of the World Meteorological Organization (WMO). The AL measurements were carried out for the first time at the beginning of September 2016 with the first snowfall with a step of 10 m at 121 points. Despite the significant AL thickness and the presence of gravel and pebbles in its section, one could identify the depth of the permafrost quite well when driving the probe with a sledgehammer due to the difference in the mechanical properties of thawed and frozen soil. The AL thickness varied from 1.15 to 2.60 m, with an average value of 1.56 m (Fig. 3.3.7).

In addition to Barentsburg, there is a CALM site in the Adventdalen near Longyearbyen. Also, AL is monitored in the areas of Ny-Ålesund, Kapp Linne and Hornsund, but the AL depth there is not determined by probe measurements, but is calculated based on the maximum penetration into the depth of the zero isotherm. In 2017, the AL thickness in the above five areas varied from 50 to 300 cm. High AL values are typical of rocks.

CRYOGENIC PROCESSES AND PHENOMENA

One of the visiting cards of Spitsbergen is the perennial pingos (better known in the Russian literature as hydrolaccoliths or bulgunnyakhs (frost heaving mound)). In the Reindalen, their height reaches 40 m, and they are 500 m wide. The location of some pingos correlates with warm springs of brackish groundwater. When a water-saturated AL freezes on gentle slopes, filled with weak material, at the beginning of winter seasonal pingos up to 120 cm high appear (Zenkov, 1935).

There is a group of bulgunnyakhs located at the cryosphere testing area of the RSCS in the Grøndalen, which also became an object of monitoring. Based on the nature of the section drilled by borehole No. 8 in the Grøndalen, it can be concluded that in the late Holocene, the relative sea level was higher than the present one. And relatively homogeneous clays and loams were deposited in the valley under fjord conditions, indicating favorable conditions of sedimentation. Such conditions existed until the second half of the Holocene when the fjord began to become shallow. The upper sandy-gravel layer was formed in the offshore conditions. After the valley came out from under the sea level, the freezing of marine sediments began according to the so-called open system scenario. The formation of injection pingos (bulgunnyakhs) began, supposedly in places where the groundwater was discharged along tectonic faults.

To monitor a group of bulgunnyakhs, they drilled boreholes in the middle reaches of the Grøndalselva in one of them and performed regular morphometric measurements in four others. Borehole No. 9 (see Fig. 3.3.6), drilled in the central crater of one of the bulgunnyakhs, showed that the thickness of the gravelly loams above the ice core is approximately 1.5 m, and then to a depth of 23.5 m, there is an ice core with frozen saline clays underneath. Borehole thermometry showed that in summer, the AL reaches the ice core, it thaws, and the crater deepens. Thus, it should be assumed that bulgunnyakhs are extremely sensitive to climate warming. The other known permafrost phenomenon in Spitsbergen is structural soils on high terraces and in the mountains. Under the influence of heaving, cryoturbation and frost sorting, bizarre circles – medallion spots, stripes, and polygons – appear in the active layer composed of fine earth with detrital material. Medallion spots are sometimes characterized by the concentration of finer material in the center of the circle.

In contrast, the border of the circles is formed by large fragments or moss margin. In mountainous areas, where weathering products accumulate on the slopes, stone stripes are formed down the slope. They consist of strips of fine earth separated by ribbons of coarse debris.

On the slopes composed of dispersed material, tongue-like flow-like solifluction terraces are formed. Solifluction develops when the AL is saturated with water. Therefore, it is mostly observed in the central and southwestern parts of the archipelago – where there is more atmospheric precipitation.

In the river valleys, in the places of subpermafrost waters discharge and along the periphery of warm glaciers, naled ice forms in winter. The continuous distribution of frozen rocks contributes to the concentration of underground runoff under warm glaciers and its discharge at the edge of glaciers, as well as along pressure-filtration taliks in river valleys. On the periphery of the glaciers, the thickness of naled ice reaches several dozens of meters. The thickness of naled ice from deep springs and in the valleys of freezing rivers is several meters (Fundamentals of geocryology, 1998).

Frost-shattered areas with ice veins are locally distributed throughout Spitsbergen. The most studied areas are in alluvial sediments of the largest valleys located in the central and southern parts of the West Spitsbergen: Adventdalen, Kolesdalen, Reindalen, and Sassendalen. Here they range in size from 15 to 50 m in diameter, cavern-lode ice extends 3–5 m deep from the lower boundary of the AL (Humlum et al., 2003).

DISCUSSION AND CONCLUSION

Based on the observed trend for an increase in the average annual air temperature and the data on the temperature of frozen strata obtained from the results of drilling on the West Spitsbergen, we should expect the beginning of the degradation of the strata already in the current century. This fact makes the work on monitoring permafrost on Spitsbergen extremely urgent. The review presented in this chapter allows us to outline promising areas of permafrost research that should be developed within the framework of the RSCS. It is advisable to pay special attention to the development of the Russian permafrost monitoring network both in the area of the Barentsburg and Piramiden and in remote areas where such observations are not carried out. At present, Russian and international research and monitoring points for frozen rocks are available only in the western and central parts of West Spitsbergen. At the same time, the data obtained in these areas cannot be extrapolated to the east and north of the archipelago, where it is much colder, and the formation of the climate proceeds differently.

It seems logical to organize CALM monitoring sites and thermometric boreholes on the northern and eastern coasts of the archipelago, where the climatic and, consequently, the geocryological situation is significantly different from the western coast. The UKB-12/25 drilling rig used in RSCS of the AARI is on a par with the UNIS drilling rig in tactical and technical terms. The Russian rig is not so massive (the weight of the UKB-12/25 is several times less), so this rig is quite suitable for drilling in remote areas of Spitsbergen. The general design of the observational network of the cryosphere testing area in Barentsburg can be considered complete, and its further development should improve the instrumentation of the observation posts.

If similar testing areas are also organized on the islands of the Russian Arctic, for example, on Franz Josef Land, Severnaya Zemlya, Novosibirsk Islands, and on Wrangel Island, then unique observations will be carried out along the entire continental shelf of Russia. Spitsbergen will become the westernmost point on this profile, at which the rate of change in the geocryological situation caused by climate warming is maximum. The organization of such an observing program is comparable in importance and, in many

respects, will surpass the European project of observing permafrost along the transect through continental Europe to Spitsbergen, Permafrost, and Climate in Europe (PACE).

The Barentsburg cryosphere testing area is unique because some exploration boreholes have thermometric measurements made in the 30s–80s of the last century. Repeated measurements in these boreholes will reveal the most extended trends in the temperature state of the permafrost in Spitsbergen. Similar measurements should be resumed at other Soviet mines on Spitsbergen, primarily at the Piramiden mine, where Soviet specialists carried out a reasonably large-scale study of permafrost. It is advisable to agree on plans for the development of the observation network on Spitsbergen between the Russian and Norwegian sides, and the monitoring data on the average annual temperature, and AL thickness should be integrated into the international databases of the CALM and TSP programs.

The frozen rocks of the pre-Holocene time, which could have survived at high elevations not affected by the Holocene transgression, have barely been studied to date. Pleistocene deposits are found in the near neighborhood of Barentsburg – in the area of the Linnévatnet. A correlated study paleoclimatic of lacustrine sediment logs and temperature curves in deep boreholes is of interest. It will help to reveal paleopermafrost conditions during the Holocene and explain the formation of a negative temperature extremum in boreholes at a depth of 50–100 m.

In the north of Spitsbergen, there is an area of young volcanoes. There, one can study the process of interaction of volcanism with glaciers and permafrost, unique for the earth. A similar process takes place on Mars. The study of specific landforms on Spitsbergen, formed during the interaction of volcanism and permafrost, as well as cryogenic weathering of volcanic rocks, is of considerable interest for comparative planetary science. Astrobiological work, closely related to the study of permafrost, can be carried out to isolate viable thermophilic organisms from frozen volcanic deposits. It is believed that on Mars, volcanic eruptions could lead to the ingress of potential biomarkers from subpermafrost aquifers to the surface, where they were cryopreserved in the permafrost.

So far, there is very little data on the submarine and subglacial permafrost of Spitsbergen, which in the total area may exceed the continental permafrost. Studying these issues will require large-scale geophysical and drilling operations. The first step in this direction could be a project to install bottom stations around Spitsbergen to obtain data on the average annual temperature of the seabed surface.

REFERENCES

Albul S.P. Predvaritel'nyj otchet o gidrogeologicheskikh rabotah na mestorozhdenii "Barentsburg". Preliminary report on hydrogeological works at the Barentsburg mine. *Gidroshakht*, 1947–1948, 96: 26 p. [In Russian].

Sumgin M.I. Vechnaja merzlota pochvy v predelakh SSSR. Permafrost soil within the USSR. Moscow: Publishing House of the USSR Academy of Sciences, 1937: 379 p.

Vedomstvennyye stroitel'nye normy (VSN) 61–89. Izyskanija, proektirovanie i stroitel'stvo zheleznykh dorog v rajonah vечноj merzloty. Industry-Specific Construction Standards (ISCS) 61–89. Research, design, and construction of railways in permafrost regions. Moscow, 1990. [In Russian].

Vtyurin B.I. Cryogenic structure of loose sediments of Spitsbergen. *Materialy glaciologicheskikh issledovanij.* Materials of glaciological studies. 1990, 70: 43–49. [In Russian].

- Vtyurin B.I. Underground ice of Spitsbergen. *Materialy glaciologicheskikh issledovanij*. Materials of glaciological studies. 1989, 65: 67–75. [In Russian].
- Evdokimov A.N. *Vulkany Shpicbergena*. Volcanoes of Spitsbergen. St. Petersburg: Publishing house of FSBI “VNIIOkeangeologia”, 2000: 123 p. [In Russian].
- Zenkov K. A. *Otchjot o geologorazvedochnyh rabotah na sovetskikh uchastkah ostrova Zapadnyj Shpicbergen, provedennyh v 1935—1936 gg.* Report on geological exploration in the Soviet areas of the West Spitsbergen carried out in 1935–1936. ST “Arktikugol”, 1935, 150: 70 p. [In Russian].
- Karpov A.F. *Sostojanie izuchennosti i stepen' razvedannosti mestorozhdenij uglej na o. Shpicbergen*. The state of knowledge and the degree of exploration of coal deposits on Spitsbergen. Leningrad: Glavuglerazvedka, Lenuglerazvedka Trust, 1946. [In Russian].
- Koltukov V.A. *Geologicheskoe stroenie i ugljenosnost' rajona Barenburga i tundry Bogemana*. Geological structure and coal content of the Barentsburg region and the Bogeman Tundra. GT “Arktikugol”, 1933. 41 p. [In Russian].
- Obidin N.I. *Merzlota i podzemnye vody Barenburga, Grumanta i Piramidy o-va Shpicbergen (Predvaritel'nyj otchjot po issledovanijam 1952 g.)*. Permafrost and groundwater in Barentsburg, Grumant, and Piramida (Pyramiden) on Spitsbergen (Preliminary research report 1952). Leningrad: Publishing House of the Research Institute of Geology of the Arctic (RIGA), 1953. [In Russian].
- Obidin N.I. New data on groundwater and permafrost of the Soviet mines on Spitsbergen based on research in 1952–1954. *Trudy nauchno-issledovatel'skogo instituta geologii i Arktiki*. Proc. of the Research Institute of Geology of the Arctic (RIGA). 1958, 85 (9): 129–140. [In Russian].
- Ershov Je.D. (ed.). *Osnovy geokriologii. Chast 3. Regional'naja i istoricheskaja geokriologija mira*. Fundamentals of geocryology. Part 3. Regional and Historical Geocryology of the World. Moscow: Publishing House of the Moscow State University (MSU), 1998: 575 p. [In Russian].
- Plan gornyh vyrabotok po plastu Verhnemu. M 1:5000*. Mine workings plan for the Verkhny seam. M 1:5000. ST “Arktikugol”, 2016. [In Russian].
- Respublikanskije stroitel'nye normy (RSN) 31—83. Normy proizvodstva inzhenerno-geologicheskikh izyskanij na vechnomjorzhlyh gruntah*. Republic's Construction Standards (RCS) 31–83. Production standards for geotechnical surveys on permafrost soil. Moscow: Gosstroj RSFSR, 1983. [In Russian].
- Sheko A.I., Grechishchev S.E., Postoev G.P. *Razrabotka rekomendacij po provedeniju inzhenerno-geologicheskikh issledovanij na ob#ektah rudnikov Barenburg i Piramida na Shpicbergene*. Development of recommendations for conducting engineering and geological studies at the facilities of the Barentsburg and Piramida mines on Spitsbergen. Moscow: Publishing House of the All-Union Scientific Research Institute of Hydrogeology and Engineering Geology VSEGINGEO, 1980: 98 p.
- Bakkehoi S., Bandis C. Meteorological conditions influence on the permafrost ground in Sveagruva, Spitsbergen. Oslo: Norw. Geotech. Inst. Publ., 1988, 176: 39–43.
- Christiansen H. H., Etzelmüller B., Isaksen K., Juliussen H., Farbrot H., Humlum O., Johansson M., Ingeman-Nielsen T., Kristensen L., Hjort J., Holmlund P., Sanne A.B.K., Sigsgaard C., Akerman H.J., Foged N., Blikra L.H., Pernosky M.A., Odegard R.S. The Thermal State of Permafrost in the Nordic Area during the International Polar Year 2007–2009, *Permafrost Periglac.* 2010, 21: 156–18 p. 1; DOI: 10.1002/pp. 687.
- Christiansen H.H., Akerman J.H., Repelewska-Pekalowa Y. Active layer dynamics in Greenland, Svalbard and Sweden. In: Extended abstract for the 8th International Permafrost Conference. Zurich, 2003: 19–20.
- Etzelmüller B., Schuler T.V., Isaksen K., Christiansen H.H., Farbrot H., Benestad R. Modelling past and future permafrost conditions in Svalbard. *The Cryosphere Discuss.* 2010, 4: 1877–1908. www.the-cryosphere—discuss.net/4/1877/2010/ DOI:10.5194/tcd-4-1877-2010.
- Gilbert G.L., Christiansen H.H., Neumann U. Coring of unconsolidated permafrost deposits: methodological successes and challenges. *Proc. GeoQuebec 2015. Challenges from North to South*. Quebec City, 2015.

- Gregersen O., Eidsmoen T.* Permafrost conditions in the shore area at Svalbard. Proc. 5-th International Conference on permafrost, Norway, August 2–5, 1988. Nor. Geotech. Inst. Publ. 1988, 177.
- Haldersen S., Heim M., J. van der Ploeg M.* Impacts of climate change on groundwater in permafrost areas: case study from Svalbard, Norway. In: *Climate Change Effects on Groundwater Resources: A Global Synthesis of Findings and Recommendations*, Edition: IAH — International Contributions to Hydrogeology, Chapter: 18, Publisher: CRC Press, Taylor & Francis Group, Editors: Holger Treidel, Jose Luis Martin-Bordes, Jason J. Gurdak, 2011: 323–338.
- Haldorsen S., Heim M.* An Arctic groundwater system and its dependence upon climate change: an example from Svalbard. *Permafrost and Periglacial Process*. 1999, 10: 137–149.
- Haldorsen S., Heim H., Lauritzen S.E.* Subpermafrost groundwater of western Svalbard. *Nord. Hydrol.* 1996, 27: 57–68.
- Humlum O., Instanes A., and Sollid J.L.* Permafrost in Svalbard: a review of research history, climatic background and engineering challenges. *Polar Res.* 2003, 22: 191–215.
- Isaksen K., Sollid J.L., Holmlund P. and C. Harris.* Recent warming of mountain permafrost in Svalbard and Scandinavia. *J. Geophys. Res.* 2007, 112. F02S04. doi:10.1029/2006JF000522.
- Isaksen K., Vonder Muhll D., Gubler H., Kohl T., and Sollid J.L.* Ground surface temperature reconstruction based on data from a deep borehole in permafrost at Janssonhaugen, 25 Svalbard. *Ann. Glaciol.* 2000, 31: 287–294.
- Landvik J.Y., Mangerud Y. and Salvigsen O.* Glacial history and permafrost in the Svalbard area. *Proceeding of the 5th International conference on permafrost*. Trondheim: Tapir Publishers, 1988: 194–198.
- Liestøl O.* Pingos, springs, and permafrost in Spitsbergen. *Årbok: Norsk Polarinstitut*, 1975: 7–29.

3.4. THE MECHANICS OF THE NORDENSKIÖLDBREEN DESTRUCTION AND THE FORMATION OF ICEBERGS

V.G. Korostelyov, V.N. Smirnov, A.N. Pavlov

Studying the state and activity of glaciers in the Arctic is of great importance for improving models of the modern climate and the impact of glacial processes on the environment. It is necessary to highlight the problem of ensuring the safety of navigation on the Arctic shelf due to the formation of icebergs from outlet glaciers. One of the most effective methods to study the dynamics and mechanics of glaciers is the seismometric method. It is used to register both earthquakes and “icequakes” (Vinogradov et al., 2014; Fedorov and Asming, 2015). The works on recording the parameters of seismic waves carried out in seasonal and year-round observations study this issue.

Earthquake records are typical, and they have longitudinal, transverse and surface waves in the range of 3–5, 2–4, and 0.03 Hz, respectively. It is pointed out that the waves in the open sea and the impact of the surf are the sources of the background microseismic noise. The main advantage of the methods is to ensure long-term recording of signals from the processes of cracking and the collapse of glacier fragments into the sea. “Icequakes” include large-scale/block movements of the entire mass of the glacier (surge) and local faults with the collapse of ice fragments into the sea and the formation of icebergs (calving) (Paterson, 1972; Dolgushin and Osipova, 1982). The dynamics and mechanics of glacier destruction generate elastic seismic waves. Epicentral distances of close earthquakes and icequakes can reach 150 km. There is a relationship between the nature of daily variations in the number of icequakes and air temperature; the number of ice events increases during the period of positive temperatures, and activity decreases during periods of negative temperatures. Obviously, local measurements of the parameters of each icequake are required to reveal the large-scale mechanics of glaciers. The phenomena of elastic-plastic deformation of ice, the accumulation, and release of stresses, the formation of an ordered large-scale structure of the glacier, the emission of elastic waves in the “glacier–soil–water” system are enormously important to understand the response/reaction of glaciers to climatic changes and identify physicommechanical phenomena in the “atmosphere–glaciers–land–sea” system. Such studies make it possible to create a technology for short-term forecasting of the time and place of iceberg formation in real-time.

In Korostelyov et al. (2013), the seismometric method was first used to study the local dynamics and mechanics of the Nordenskiöld glacier, located in the eastern part of the Spitsbergen archipelago, in the summer. It was shown that the movement of the glacier is intermittent, corresponding to both the period of semidiurnal tide in the earth’s crust and short-term local movements. The dynamics and mechanics of deformation and fracture of the glacier are accompanied by the formation of a group of ordered ice blocks. The nature of the glacier blocks movement is a discontinuous horizontal displacement of ice along its natural boundaries. The glacier bed and through faults in it are zones of the active generation of self-oscillations with a duration of 2–3 minutes and the emission of elastic shear waves.

This chapter reviews the summarized data and new results from improved glacier monitoring technology. The Nordenskiöldbreen belongs to the tidal outlet glaciers, the general dynamics of which is the movement of a complex system of blocks interacting



Fig. 3.4.1. Nordenskiöldbreen structure and the collapse of ice blocks on the fast ice of the fjord in winter. An ice block separates from the front of the Nordenskiöldbreen and falls into the fjord waters causing microtsunami (photo by sergeydolya.livejournal.com. 2015).

with each other, with the geological substrate (bed) and with the sides (lateral boundaries of the glacier). This movement of the glacier is called the “block–schollen movement” (Fig. 3.4.1). It can be assumed that there are almost periodic changes in the glacier, in its height, gravity and the slope of the glacier surface under the action of the tidal forces of the Moon and the Sun. Ice undergoes periodic compression, stretching, and displacement. The interaction of blocks with the fast ice of the fjord generates a wide range of oscillatory and wave processes in the “air–ice–water–soil” system.

In summer, water is continually flowing into the base of the glacier through cracks and faults. This water is formed during the melting of the glacier and erodes the edges of cracks and faults. The presence of broad boundaries between glacier blocks in summer, water in the cracks, and at the base of the glacier bed lead to an increase in the speed of movement of the glacier as a whole. Falling ice blocks form relatively small icebergs. The free wave spreads over the surface of the bay for several kilometers.

METHODS FOR OBSERVING DYNAMIC PROCESSES ON GLACIERS

Visual observations of the collapse of glaciers into the sea and the formation of icebergs were noted in the Arctic and Antarctic expeditions. The first instrumental observations of the dynamic processes of the breakdown of outlet glaciers and the formation of icebergs were carried out in the Antarctic in 1965 (Smirnov and Linkov, 1967). In the Davis Sea, near the Mirny Observatory, trains of previously unknown free surface waves were recorded using an ice tide gauge and tiltmeters installed on landfast ice 2 m thick. It was known that flexural-gravity waves with a period of up to 15 s, caused by the wind, and waves with a period of up to 35 s, caused by storms in the Indian Ocean, develop in the landfast ice. The duration of the recorded unknown oscillation trains reached 50 min, the oscillation period was 40–60 s, and the double amplitude of the wave reached 30 cm. Several cases of such events have been recorded over many months of continuous observations. Fig. 3.4.2 shows one of the long-standing unique records.

The connection between the fast ice wave trains was revealed when comparing with microseismic waves recorded at the Mirny coastal seismic station. The seismograms showed high-frequency wave trains lasting from 0.5 to 5 minutes with an amplitude of up to dozens of microns in the frequency range of 1–10 Hz (Fig. 3.4.2 *a*). The time lag of the trains of free surface waves indicated from the records of the devices relative to the appearance of seismic elastic waves made it possible to determine the distance to the epicenter of the wave generation. The narrow-band nature of the amplitude spectra of

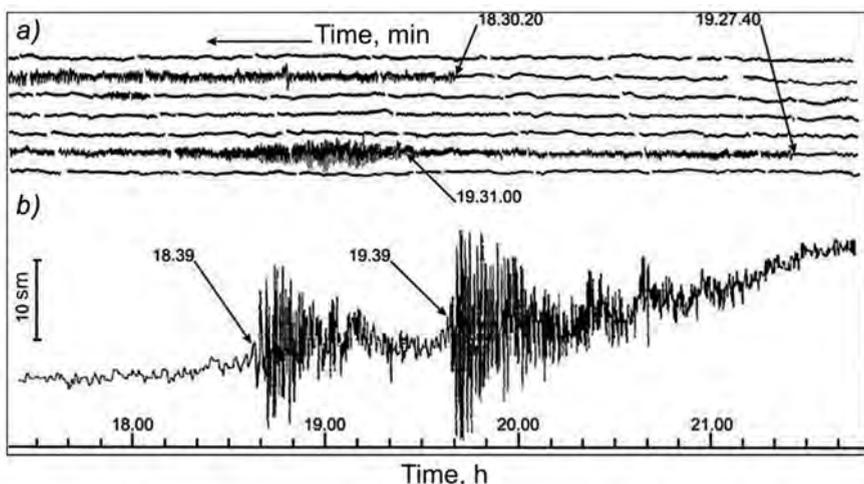


Fig. 3.4.2. Seismometer records on the rocky soil of the Antarctic coast during the movement of the outlet glacier (a) and tide gauge record on the fast ice (b).

Antarctic, Davis Sea, October 20, 1965.

The seismogram was obtained using an SVK-3 seismometer with photo registration at the Mirny seismic station.

Recording time every minute is counted from right to left.

both elastic waves and free gravitational waves indicated that the process was formed at a considerable distance from the station. We can call these free waves “ice tsunamis”.

The seismogram was obtained using an SVK-3 seismometer with photo registration at the Mirny seismic station. Recording time every minute is counted from right to left.

Based on the data obtained, it becomes obvious that one of the reasons for the formation of elastic waves in the rocky soil and free gravitational waves in the fast ice are the processes of the influence of the glacier on the bedrock, the breakaway of glacier blocks and their collapse into the sea, as well as the possible “plowing” of the seabed by the iceberg formed. Elastic microseismic waves on the coast and gravitational waves in fast ice stop in two cases. When a breakaway glacier fragment is afloat, i.e., when an iceberg appears in the sea, or when a glacier fragment penetrates the seabed and remains motionless for a long time.

A program to study the state of the Nordenskiöldbreen was created with the help of the available data on the dynamics of glaciers on Spitsbergen. For this purpose, the continuous recording of elastic vibrations of the rocky soil and the glacier surface using seismometry methods was used. In addition to traditional pendulum seismometers for recording fluctuations in the ice cover they use modern broadband three-component molecular-electronic seismometers CME-4111LT. Such seismometers record signals in the frequency range from 0.0167 to 50 Hz, i.e., waves with a period from 0.02 to 60 s. The maximum recorded signal is ± 5 mm/s. The seismometer is powered from a 12 V DC source, the consumed current is 20 mA. Operating temperature range from -40 to $+55$ °C. The permissible installation angle of the device is $\pm 15^\circ$. The device weighs 5.1 kg. Signals are registered via an ADC board to a laptop or a specialized data storage device “Baikal”.

Mobile high-resolution seismic signal recorder “Baikal-7HR” is intended for autonomous recording of signals from the CME-4111LT seismometer in a wide frequency range concerning absolute time. Such a recorder can be used for both urgent and long-term

seismic and geophysical measurements in the field in a wide temperature range. The device consumes low power from an external battery, has a large capacity of non-volatile memory, built-in highly stable generator and GPS module in conjunction with an analog-digital path, which provides high-quality performance characteristics for solving a wide range of tasks.

A seismometer – Baikal system was installed on the rocky soil of the coastal line of the fjord to establish a connection between coastal soil vibrations and glacier dynamics; Fig. 3.4.3 shows a typical example of such an installation (point C). A similar system was located on the surface of the glacier (point A). The X-axis was oriented to the north by the compass to ensure the parallelism of the sensitivity axes of seismometers (X, Y, Z). Time synchronization was carried out using GPS receivers integrated into seismic stations.

The mode of operation of the seismometer does not allow recording the constant speed of the glacier movement. Still, it can register fluctuations of the speed within the working range of the amplitude-frequency characteristic. The dynamic range of the CME4111 seismometer is 135 dB, the Baikal-7HR station has 132 dB. Calculation of the values of the amplitude-frequency characteristic of the seismometer at the value of the station gain $K = 1$ taking into account the noise level, showed that the maximum period that the CME4111 – “Baikal-7HR” system can record is eight hours.

When processing the input data, the current spectra of periodic processes are presented as a three-dimensional surface (t, f, A) , where t – current time, f – oscillation frequency, A – amplitude of signals recorded by seismometers, and in the form of wavelet-transform diagrams (two-dimensional surface with isolines of equal amplitudes on the plane f, t .)

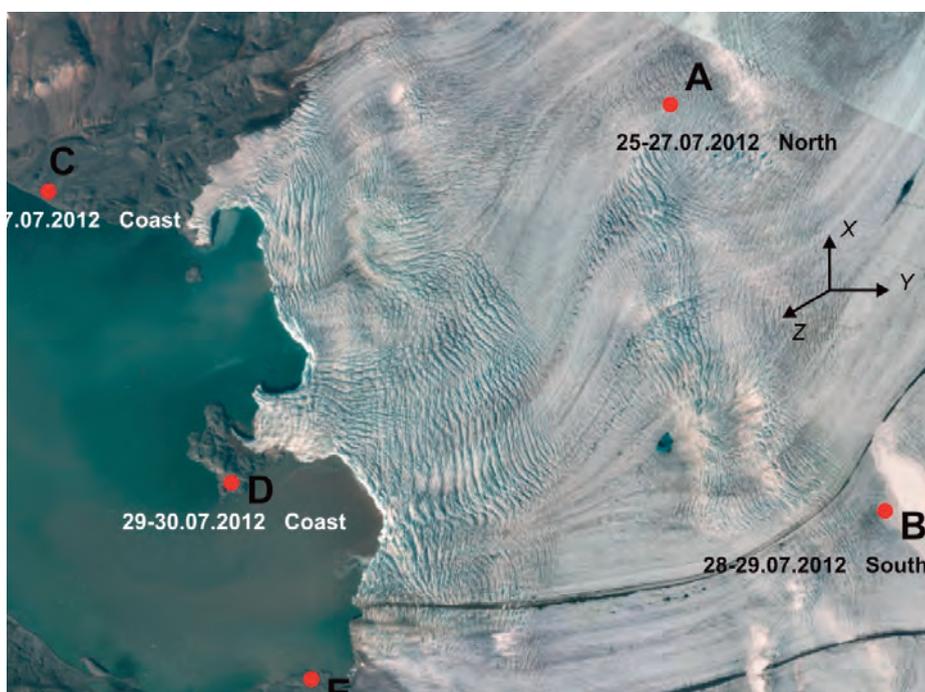


Fig. 3.4.3. Scheme of sensors placed on the surface of the Nordenskiöldbreen and the coastline of the fjord. The area of the glacier surface between seismometers on the shore (point C) and on the surface of the glacier (points A and B). Points D and E showed synchronous XYZ ground vibration components.



Fig. 3.4.4. Map of the study area for the physical and mechanical state of the Nordenskiöldbreen, indicating the location of the measuring complex on the glacier (stations 1 and 2), and on the shore (station 3) with seismometers, batteries, antennas, and a relay station to the base in Piramiden.

The seismometer on the coastal soil was located in front of the glacier front, which made it possible to record the processes associated with the fall of ice fragments into the fjord water area. The most intense registration of wave trains occurred in the *Y* direction. This direction (E–W) corresponded to the direction of the general movement of the glacier.

In addition to seismometers, a tiltmeter IN-DZa-720 was used to measure the deformations of the soil and ice on loads, which was designed to measure small angles of inclination and inclined displacements in two coordinates, as well as to measure horizontal accelerations and low-frequency seismic vibrations. The conversion factor of the electrical signal is 2 mV/mkrad. To obtain the actual values of the velocity and displacement of the glacier surface and coastal soil in a wide frequency band, the procedure “restoration of true soil movement” was used (Gaizer, 1983).

The monitoring in the area of the glacier front was organized in several versions:

- fixation of the separation of glacier fragments when the control system is located on the ground at a distance of 2 km from the glacier front;
- registration of processes in close proximity of the front (up to 100 m);
- control of soil displacement near the glacier front.

The breakaway of glacier fragments and their fall cause wave trains in the bottom soil, which are a superposition of waves of different nature. The most intense registration of impulsive non-stationary wave trains occurred in the *Y* direction. This direction (E–W) corresponded to the direction of the general movement of the glacier.

We can distinguish successive stages of the fall of a significant mass of ice in the frontal region of the glacier:

- ice fragments fall and have a vertical impact on the surface of the bay and generate elastic waves in the bottom soil;
- generation of a train of gravitational waves on the surface of the fjord.

Currently, there is a need to conduct field studies to study the identified processes and their relationship with other geophysical phenomena: tides in the earth’s crust, the impact of seismic waves as triggering mechanisms of ice dynamics, the occurrence of self-oscillation processes. In this regard, in 2016, the physical and mechanical parameters of the Nordenskiöldbreen were recorded using a measuring complex with remote signal transmission to the base of the expedition in Piramiden at a distance of 15 km. An approximate scheme for monitoring the dynamic processes of the Nordenskiöldbreen

with the transmission of data over the radio channel from the glacier and the coast to the base in Piramiden is shown in Fig. 3.4.4.

RESULTS OF FIELD OBSERVATIONS ON THE DYNAMICS AND MECHANICS OF THE GLACIER

The time-synchronous registration of fluctuations of the glacier surface and coastal soil showed the connection between natural processes. Comparing and analyzing changes in the levels of synchronously recorded fluctuations of the glacier and coastal soil in a wide frequency band showed a correlation between the parameters of the glacier movement processes and the seismic activity of the coastal zone. The frequency content of the oscillations with the maximum amplitude of the displacement velocity is below the frequency of 0.01 Hz. It has been shown that during periods of active movement of the glacier, elastic waves polarized in the horizontal plane are generated at the glacier lower boundary (Korostelyov et al., 2013). The process of their synchronous change during specific time intervals can be the criterion proving their connection.

Fig. 3.4.5 shows the current spectra of coastal soil and glacier oscillations recorded by seismometers at points C and A (Korostelyov et al., 2015). For comparative analysis, the spectra of oscillation components (X, Y, Z) are grouped in the appropriate directions: $S(f, t) X_{coast} - S(f, t) X_{glacier}$, $S(f, t) Y_{coast} - S(f, t) Y_{glacier}$ and $S(f, t) Z_{coast} - S(f, t) Z_{glacier}$.

Comparison of the spectra of ground and glacier oscillations revealed the following special features. There are well-defined components in the spectra of the coastal soil oscillation components (moments T1, T2), which are typical for the impulse. All components of the coastal seismometer recorded the maximum oscillation impulse at time T1. There is a connection between the level of oscillations of the glacier and the

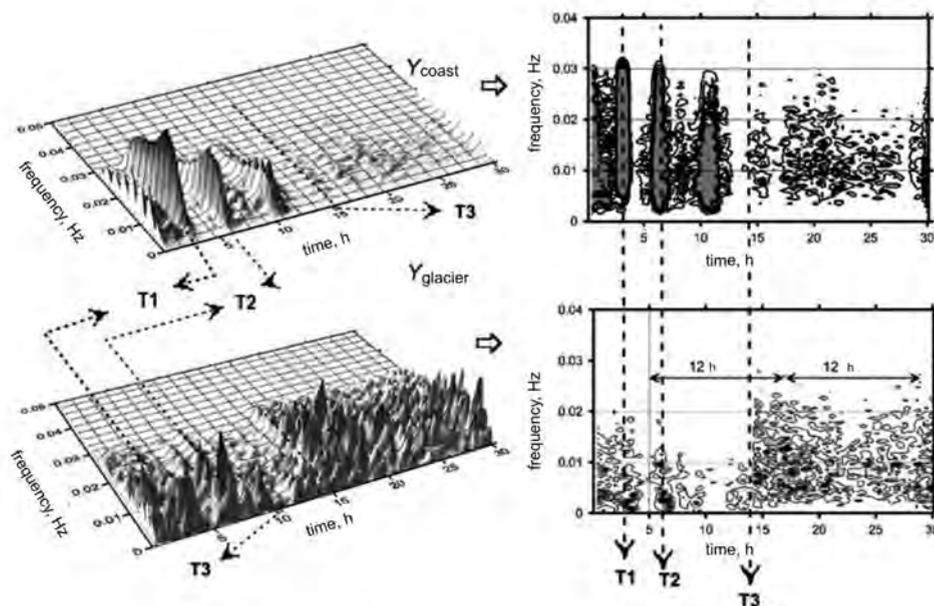


Fig. 3.4.5. Current spectra of the Y -component of coastal soil and glacier surface oscillations.

On the left – relief surfaces, on the right – the corresponding wavelet-transform diagrams.

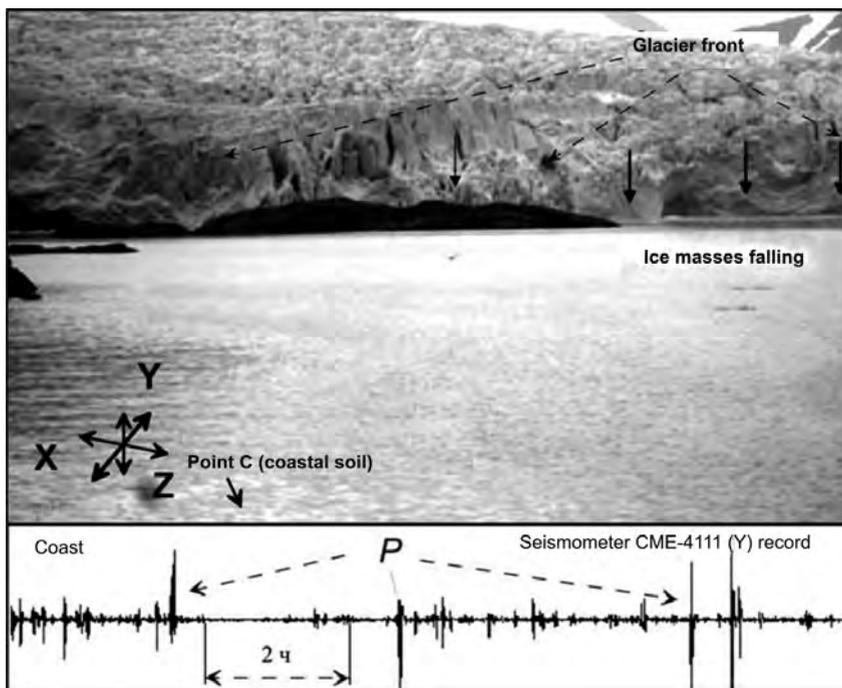


Fig. 3.4.6. View of the glacier front from the installation point of the coastal seismometer.

Y – direction to the glacier front; P – oscillation trains, generated by fracture and fall of blocks into the fjord water area.

coastal soil (T1, T2). In this case, the oscillation frequency is different. Starting from the moment T3, there is a synchronous increase in the amplitude of oscillations of the glacier surface and coastal soil. The closest connection is observed between the Y -components. There is a frequency of changes in the level of oscillations of the glacier surface with a period of 12 hours.

Processes associated with the fall of ice blocks into the fjord water area were recorded with the help of a seismometer on the coast (Fig. 3.4.6). The most intense registration of impulse non-stationary trains of waves occurred in the Y direction. This direction (E–W) corresponded to the direction of the general movement of the glacier.

The block structure of a moving glacier is characterized as an open non-linear dynamic system; such phenomena as self-organization and fractality (in space and time) are typical for it. The activity of the system involves the exchange of energy with the environment and the presence of a mechanism that changes the energy stored in the system into the energy of oscillations and waves.

The fault zones of the glacier are continuously exposed to external and internal influences of gravitational stress fields and dynamic loads as a result of earth tides. The tidal force influences the glacier more than it influences the earth's surface since the glacier is an independent inertial massif. The influence of tidal forces on the movement of glaciers is most intense in the summer period due to the presence of water along the “glacier – bed” boundary, which makes the value of the static and kinematic coefficient of friction decrease. The dissipation of external and internal energy occurs at the boundaries

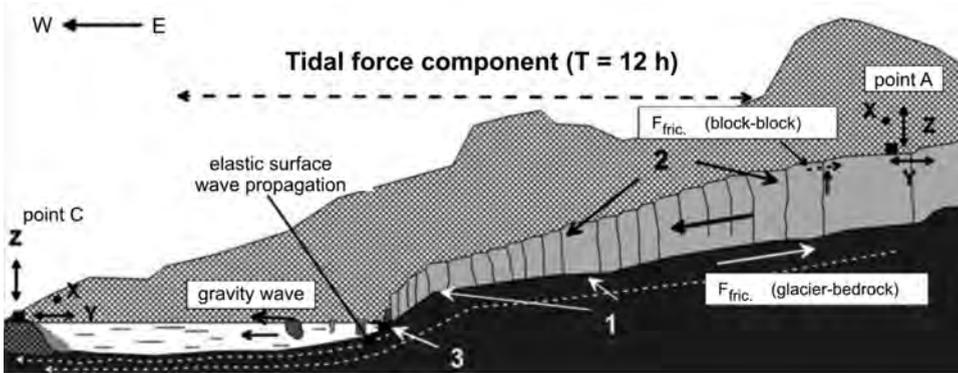


Fig. 3.4.7. Forces acting on the glacier (simplified), and the location of oscillation sources that form the natural seismic background of the fjord shoreline and glacier surface.

1 – generation area of elastic surface oscillations, 2 – generation of non-linear oscillations when ice blocks are displaced relative to each other, 3 – generation of elastic waves trains in the bottom soil and a single gravitational wave during the fall of glacier fragments.

of the glacier, bed, and adjacent blocks during periods of its active movement. The nature of the movement of the glacier changes since there is a non-linear relationship between the friction force and the speed of movement of the glacier base. In the spectra of fluctuations in the speed of movement, in addition to the main period of the semidiurnal tide (12 hours), components with a period of 6, 3, and 1.5 hours appear, which are overtones of the main process.

An ordered/self-similar structure of the glacier gradually forms over time when exposed to a non-linear dynamic system. Self-similar structures mean that the shape of their part is similar to the shape of the whole structure. The appearance of ordered structures on the glacier surface indicates the process of self-organization (see Fig. 3.4.1), which is one of the properties of an open dynamic system. Taking into account that self-organization is a process of spatial ordering in the system due to internal factors, the formation of diamond-shaped structures of various sizes on the surface indicates that a moving glacier is an open dynamic dispersion system.

Fig. 3.4.7 shows a diagram of the forces acting on the glacier and causing the pulsation of the speed of moving ice blocks, as well as the location of the supposed generation sources of oscillations and waves.

The analysis of physical processes in a dynamic glacier is presented by the results obtained using ingenious processing methods. As an example, Fig. 3.4.8 shows the spectral-temporal structure of oscillation trains generated as a result of intermittent sliding of an ice block along the boundaries with adjacent blocks and, possibly, on the boundary between the base of the glacier and its bed.

The narrow-band signal of the processes occurs by applying a band-pass filter, which contains the frequency of self-oscillations during the displacement of the glacier blocks relative to each other and the bed. The signal level generated by the amplitude detector on the comparator is compared with a predetermined value. Information about the number of pulses and their duration is transmitted to the base point for a specific time for further transmission to the base station. A set of receiving and transmitting equipment may well “serve” several similar or other systems located in different areas.

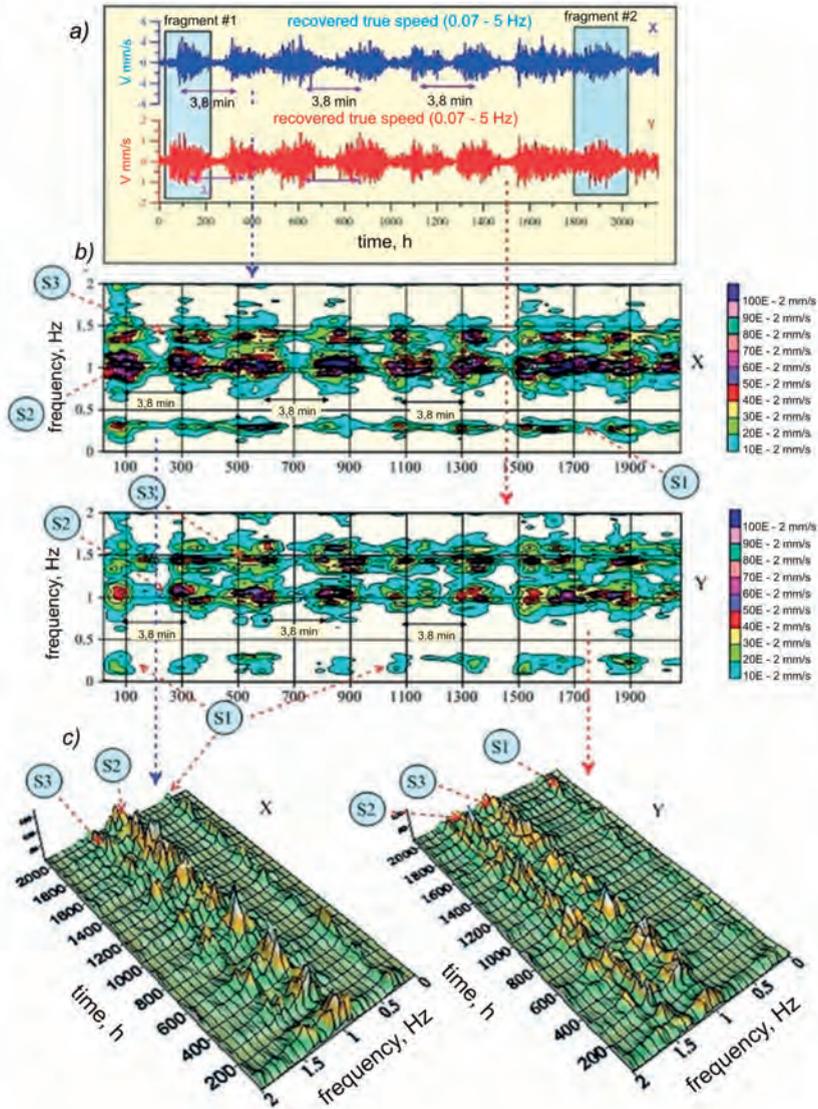


Fig. 3.4.8. A recording fragment of components of horizontally polarized oscillations (X , Y) in the frequency range 0.07–5 Hz during the period of the rapid movement of the glacier block (a), wavelet-transform diagram of the recording (b) and three-dimensional spectrum (c).

When considering the fluctuations in the speed of movement of glacier blocks with the observation time from 0.5 to 8 hours, data on self-oscillation processes were obtained. The following features are typical for the structure of the spectral composition of the glacier oscillations at two points (northern A and southern B):

- the main energy of the glacier oscillations is concentrated at frequencies below 0,01 Hz (period $T = 100$ s);

- the amplitude level of the horizontal components of oscillations (X , Y) is two orders of magnitude more than the amplitude level of the vertical component (Z); this ratio of oscillation amplitudes is maintained throughout the entire observation period;
- the nature and structure of the oscillations are non-linear, which leads to the “stratification” of the spectrum into many harmonics (overtones).

Fig. 3.4.9 shows the activation of the glacier after 3, 6, and 12 hours, due to the friction of the lower surface of the glacier on its bed and the effects of non-linear friction. From the moment T_0 the process of separation and fall of ice masses begins in the area of the glacier front, which leads to the release of the vertical load to the bed in the frontal area. The load on the soil decreases; as a result, the angle of inclination of the coastal soil decreases towards the movement of the glacier.

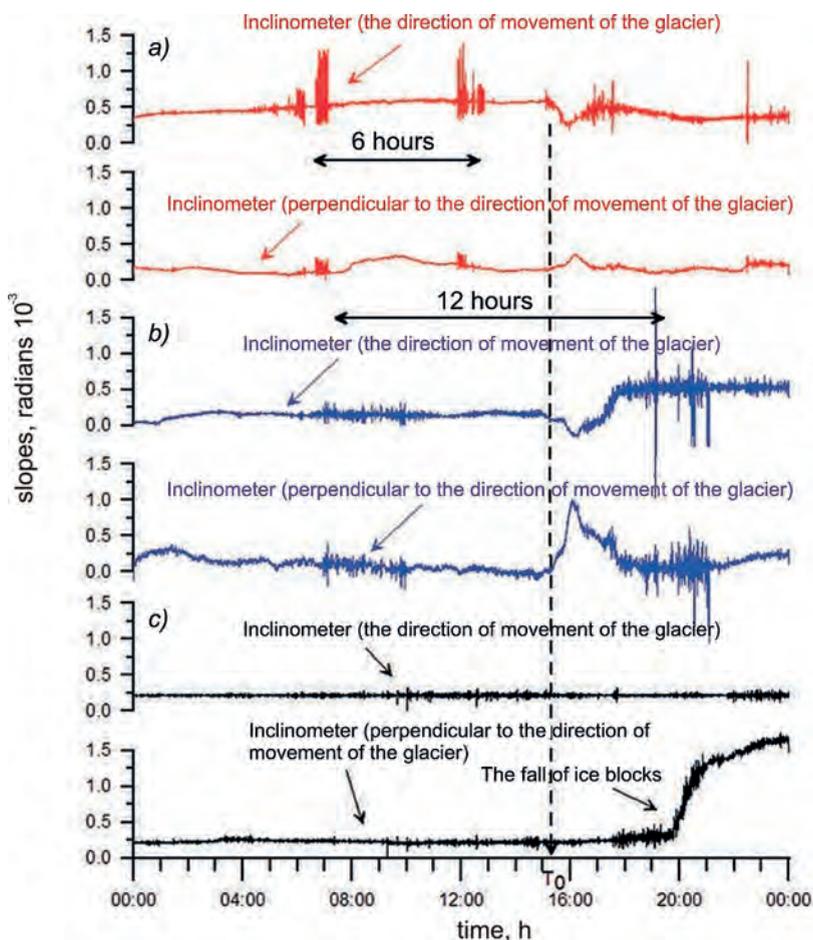


Fig. 3.4.9. Synchronous recording of the slope of the glacier surface at two points in the direction of movement and the direction perpendicular to it, as well as the coastal soil in the area of the glacier front for August 17, 2016.

a – Station No. 1 (glacier), b – Station No. 2 (glacier), c – Station No. (coastal soil), T_0 – time when the glacier starts moving actively.

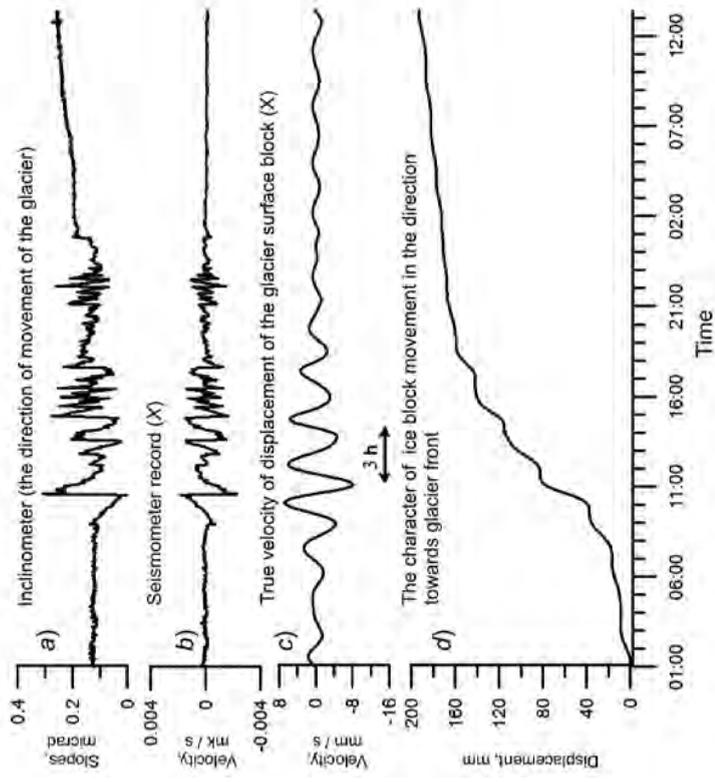
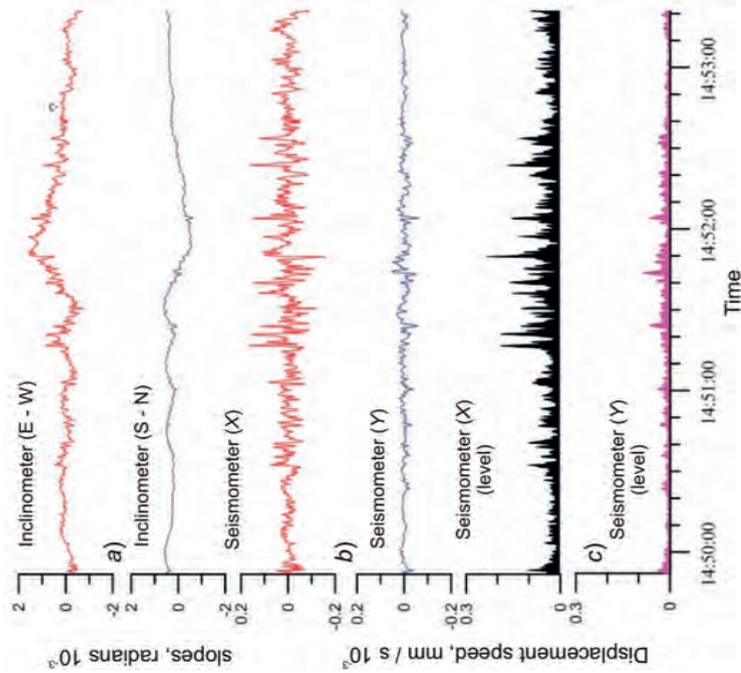


Fig. 3.4.10. The nature of the slopes and displacements during the movement of the glacier block during 12 hours on September 10, 2016, at station No. 1. *a* – slope of the block surface in the direction of travel (E – W), *b* – seismometer recording CME4311(X, (E – W), *c* – fluctuations of the actual displacement velocity in the frequency range 0.002–1 Hz, *d* – displacement of the glacier block towards the front.

Fig. 3.4.11. Fragment of the record for September 3, 2016, in the time interval ΔT_1 , illustrating the process of intermittent sliding of a glacier block.

Discontinuous oscillations can last for many hours (Fig. 3.4.10). Fig. 3.4.11 shows the recording of the glacier block movements on an enlarged scale, which is a sequence of discontinuous movements.

Let us consider the processes of how a daily tide affects the seismicity level of the coastal soil and glacier, leading to a cyclical displacement of glacier blocks and the collapse of ice into the fjord water area (Fig. 3.4.12). When the gravitational forces exceed the cohesion forces of the ice masses in the frontal region, ice fragments break off and fall. It is obvious that the decrease in the ice mass and its distribution right ahead of the glacier front reduces the pressure on the geological substrate, the bed, which leads to a slope of the coastal soil in the area of the front.

There is a connection between fluctuations/slopes of the surface of a particular glacier block; it indicates a “global” movement of the entire mass of the glacier along the bed. We can see it very clearly when considering the synchronous recording of the slope of the glacier surface and the coastal soil during the period of active displacement of the entire glacier mass (Fig. 3.4.13).

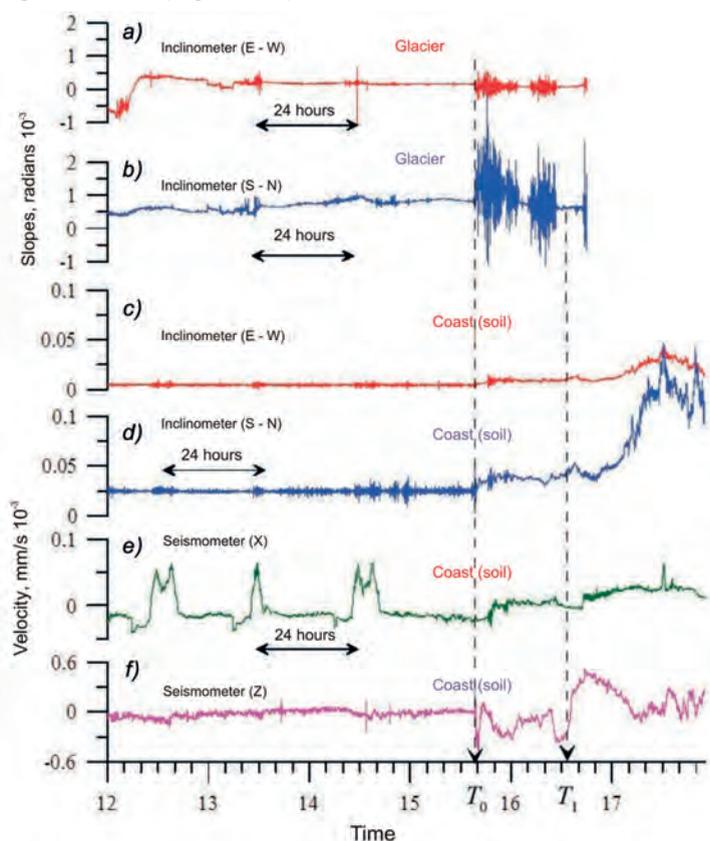


Fig. 3.4.12. Synchronous recording of slopes and elastic impulses in the “glacier–soil” system (September 2016).

a and *b* – slopes of the glacier block, *c* – *f* – slopes and displacement velocity of the coastal soil at the stage when a significant mass of ice in the front area was getting ready to breakaway, T_0 – the process beginning relative to rapid movement of the entire mass of the glacier, T_1 – the breaking away starts and ice masses in the area of the glacier front fall.

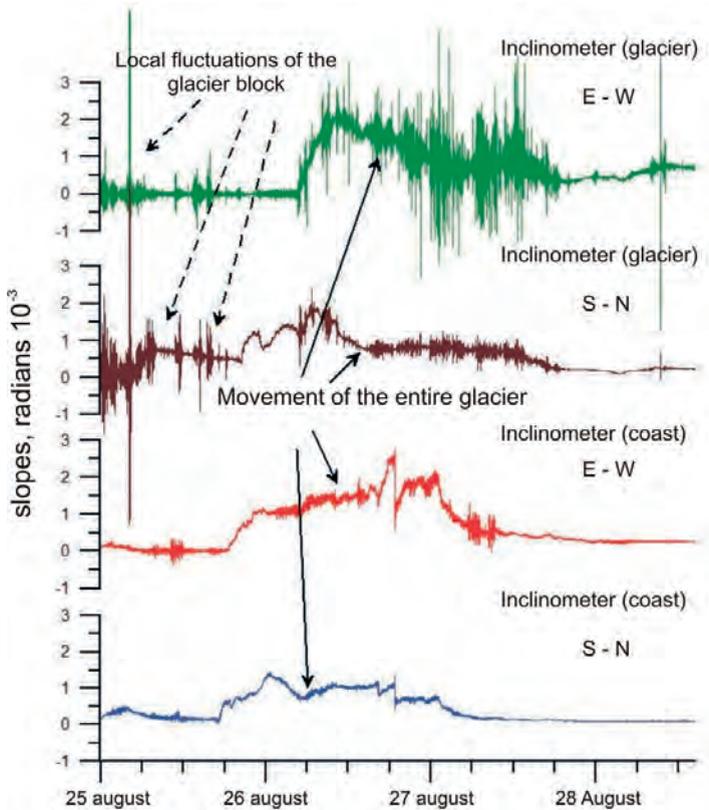


Fig. 3.4.13. Synchronous recording of the slopes of the glacier surface and coastal soil during the period of active displacement of the entire glacier mass (August 2016).

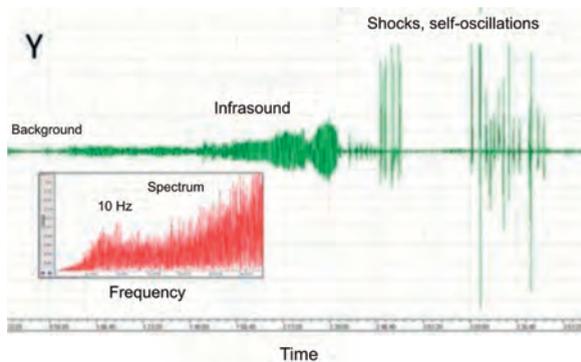


Fig. 3.4.14. Fragment of background recording, infrasonic oscillations, shocks, and self-oscillations in the Nordenskiöldbreen.

The event lasted about two hours. The amplitude spectrum ranged from 0.5 to 40 Hz.

There is no clear connection between active oscillations of the glacier block and an increase in the seismic background of the coastal soil; it indicates the local nature of the oscillations of a particular block on which the sensor is installed.

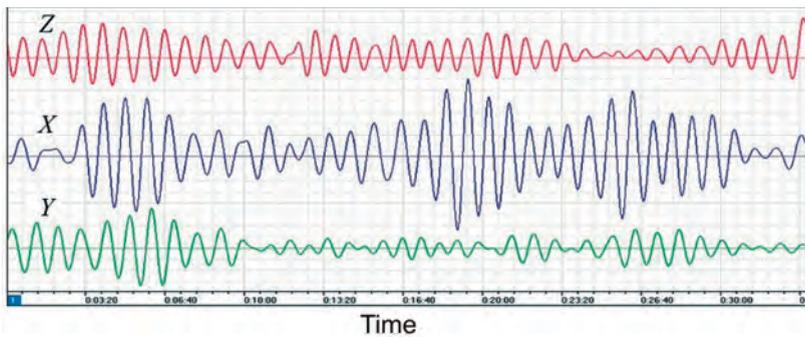


Fig. 3.4.15. Fragment of the recording of oscillations in coastal rocky soil with a period of 30–40 s in front of the glacier front – seismometer components X, Y, Z.

Low-frequency filter 0.02 Hz is applied.

It is necessary to note some of the phenomena accompanying the dynamic processes in the glacier.

Infrasonic oscillations. Seismometers on the ground and the glacier record oscillations caused by infrasonic acoustics in the range up to 40 Hz (Fig. 3.4.14). There were events when the process lasted about two hours before the phenomena of self-oscillations, shocks, and ice destruction. Infrasonic oscillations ranged from 0.5 to 40 Hz (at the Piramiden base, one could hear a typical low-frequency hum from the glacier side).

Deformation of the coastal soil. All expeditions obtained records of oscillatory processes of the rocky soil in front of the glacier front. Fig. 3.4.15 shows a typical example: Seismometer components X, Y, Z occasionally recorded oscillations with a period of 30–40 minutes. At present, the nature of these oscillations can be explained by periodic pressure on the ground due to oceanic swell waves entering the fjord from the Atlantic.

CONCLUSIONS

Instrumental monitoring of oscillatory and wave processes in the glacier massif revealed mechanical processes. They show that ice interacts not only with rocks, but also individual glacier blocks interact with each other. Gravitational forces cause all interaction processes, tidal movements in the earth's crust, elasticity, and ice creep phenomena at the boundaries of ice blocks and the bed. The general movement of the glacier has all the signs of self-oscillations, which are an internal property of the system: the system itself sets the rhythm of movement, not periodic external influence. The simultaneous increase in the level of coastal soil oscillations and block oscillations indicates the geophysical scale of the processes. Contact between ice and bedrock is one of the links in the system that generates periodic movements of the glacier.

The movements of individual ice blocks of the glacier lasting up to several minutes show themselves in horizontal displacements, the amplitudes of which can range from several millimeters to several centimeters.

Thus, under the influence of the gravity component, the stresses on the ice contacts increase, and when the maximum shear/shift stresses are reached, the glacier is displaced/shifted to the fjord. The process repeats as long as the force of gravity acts, and the contact conditions satisfy the self-oscillating system caused by pressure and sliding velocity.

In the 2016 expedition, synchronous data on the glacier dynamics were obtained using the developed technology of remote reception and transmission of signals. The

transmission of the input data was carried out by radio channel from the glacier through the fjord to the base of the expedition in Piramiden. The researchers obtained data on the dynamic processes in the Nordenskiöldbreen in the period August–September 2016.

The following basic parameters of the ice deformation and displacement mechanism should be highlighted:

- the global movement of the glacier is intermittent, the frequency of glacier movements corresponds to the period of semidiurnal earth tide – 12 hours;
- the trajectories of movement of individual glacier blocks are caused by friction and adhesion of the glacier bed with rocks;
- the movements of individual ice blocks of the glacier lasting up to several minutes show themselves in horizontal displacements, the amplitudes of which can range from several millimeters to several dozens of centimeters.
- generation of self-oscillations and waves occurs during elementary periodic displacements of the glacier block relative to the adjacent block and rocks lasting from two to three minutes;
- it is shown that self-oscillations are large-scale at a distance of up to 1 km;
- the generation of icebergs is accompanied by shocks and plowing of the seabed, emission of hydroacoustic and microseismic waves in the “water–ice–shore” system;
- there is a connection between oscillations of rocky soil near the glacier front and oscillations of glacier blocks;
- the infrasonic oscillations ranged from 0.5 to 40 Hz;
- oscillations of coastal rocky ground near the glacier front with a period of up to 30 seconds were indicated; the hypothesis about the nature of this phenomenon is the periodic impact of the oceanic swell and seiche oscillations of the bay water area on the coast and the seabed.

REFERENCES

- Gaizer V.M.* Determination of the actual seismic motion from records of strong movements in the near zone of earthquakes and explosions. *Fizika sejsmicheskikh voln i vnutrennee stroenie zemli*. Physics of seismic waves and the internal structure of the earth. Moscow: Nauka, 1983: 37–49. [In Russian].
- Dolgushin L.D., Osipova G.B.* *Pul'sirujushhie ledniki*. Surging glaciers. Leningrad: Gidrometeoizdat, 1982: 192 p. [In Russian].
- Korostel'jov V.G., Savatyugin L.M., Smirnov V.N.* Observation of the dynamics of the Nordenskiöld glacier using the seismometric method. *Problemy Arktiki i Antarktiki*. Problems of Arctic and Antarctic. 2013, 3 (101): 69–80. [In Russian].
- Vinogradov Yu.A., Asming V.E., Baranov S.V., Fedorov A.V., Vinogradov A.N.* Seismic-infrasound monitoring of the glaciers destruction (a pilot experiment on the Spitsbergen archipelago). *Sejsmicheskie pribory*. Seismic devices. 2014, 50 (1): 5–15. [In Russian].
- Smirnov V.N., Linkov E.M.* On the source of high-frequency seismic disturbances and flexural-gravity waves in Antarctica. *Izvestija AN SSSR. Fizika Zemli*. Bulletin of SSR Academy of Sciences. Physics of the Earth. 1967, 8: 25–30. [In Russian].
- Fedorov A.V., Asming V.E.* Monitoring of the Spitsbergen glaciers' activity using the seismic method. *Nauka i tehnologicheskie razrabotki*. Science and technological solutions. 2015, 94 (4): 44–52. [In Russian].

3.5. PECULIARITIES OF THE FORMATION OF THE HYDROLOGICAL AND HYDROCHEMICAL REGIME OF THE RIVERS IN GRØNFJORDEN

M.V. Tretyakov, O.F. Golovanov, V.A. Grigoryeva, K.V. Romashova

Many scientific and practical problems solved in Spitsbergen, including studies of climate, glaciation, hydrology of land and coastal areas of the sea, water resources, ecology, and many others, require knowledge of the hydrological characteristics of surface water bodies on land. The efforts of Norwegian (NPI, UNIS, etc.), Polish (Institute of Geophysics Polish Academy of Sciences), and Russian scientists are focused on solving this problem on the islands of West Spitsbergen. The Russian complex of observations of the environment status and natural conditions of West Spitsbergen is carried out by the Barentsburg hydrometeorological observatory of the Murmansk AHMEM. A seasonal glaciological expedition of the Institute of Geography of the RAS, the Kola Scientific Center of the RAS, MMBI, PMGE carried out the hydrological observations on the archipelago.

Since 2001, the AARI has resumed scientific research on Spitsbergen within the framework of the topic “Study of the meteorological regime and climatic changes in the area of the Spitsbergen archipelago”, paying great attention to hydrological research on surface streamflow and their catchments. At present, hydrological and hydrochemical observations are an integral part of the expeditionary activities of the AARI on West Spitsbergen. They include monitoring of changes in the elements of the water balance, as well as the state of water bodies on the Spitsbergen archipelago. The AARI has accumulated a significant amount of material based on expeditionary work on surface water bodies of Spitsbergen, held from 2002 to 2017. The purpose of the research is to obtain, on their basis, modern assessments of the main characteristics of the hydrological and hydrochemical regime of rivers, as well as assessments of their trends over the last decade.

The objects of hydrological research of the AARI expedition are, first of all, the surface water bodies on the land of the catchment area of the Grønfjorden, on the shore of which Barentsburg is located.

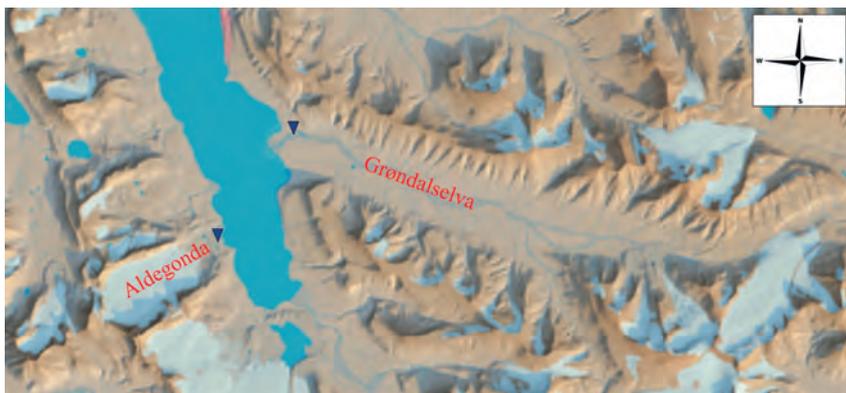


Fig. 3.5.1. Grøndalselva and Aldegonda rivers.

The black triangles indicate the location of the gauging section.

AARI hydrological studies are carried out on rivers of various types: mountain and valley rivers, rivers with varying degrees of glaciation and lakes in the watershed. As the objects of this study, two different-type rivers of the Grønfjorden basin were chosen. They reflect the specific features typical for surface of this catchment and West Spitsbergen in general. It is the Grøndalselva, which flows through a long and wide valley, the catchment area of which has a small degree of glaciation, and the Aldegonda River, which belongs to the mountain type, has a significant degree of glaciation of the catchment area, a short length, and the river channel completely fits into the framework of the moraine complex glacier of the same name (Fig. 3.5.1).

STUDY OF HYDROLOGICAL AND HYDROCHEMICAL REGIME OF SURFACE WATER OBJECTS NEAR BARENTSBURG ON SPITSBERGEN. MATERIALS AND METHODS

Determining the components of the water balance of river basins, a significant part of which may be occupied by glaciers, and observing their trends, require detailed measurements, which are incredibly difficult, especially under the conditions of Spitsbergen.

Russian observations of the hydrological regime elements, which make it possible to determine the components of the water balance, were started in 1976 by the Spitsbergen glaciological expedition of the Institute of Geography of the USSR Academy of Sciences (Glaciology of Spitsbergen, 1985). In 1983, for the first time in Spitsbergen, the study of the regime of the Mimerelva was carried out during the entire period of existence of surface runoff, and the water resources of its basin were estimated (Gokhman, 1988). In 1984 and 1985, hydrological observations were continued; they covered the Grøndalselva and Mimerelva rivers near their mouths. The results of hydrological observations made it possible to characterize the main features of the flow regime and levels of the Grøndalselva and Mimerelva rivers concerning meteorological parameters and synoptic situations. The elements of the water balance of the Mimerelva and Grøndalselva rivers for 1984 and 1985 were calculated based on the results of snow measuring works in the territory of river basins, observational data from the Barentsburg and Piramiden meteorological stations, as well as data on the balance of the Vøringbreen and Bertilbreen. In this case, evaporation at the average height of the basins was calculated according to the graphs by P.S. Kuzin. The results were extrapolated for the entire West Spitsbergen, which made it possible to estimate the total runoff from its surface. More details on the performed hydrological and water balance work in 1983–1985, you can find in Gokhman (1990, 1988) and Gokhman, Khodakov (1983).

In conditions of extreme lack of hydrological observations data on Spitsbergen and a much more complete meteorological study, estimates of the annual river runoff were carried out based on the available meteorological information using the equation of the water balance of the river basin for a long-term period (Glaciology of Spitsbergen, 1985; World water balance ..., 1974).

We should note that the hydrochemical indicators of surface water quality and the particular climatic conditions of the study area are poorly studied. At the same time, West Spitsbergen is one of the few regions in the world where glaciers have been directly involved in human economic activity for a long time, and freshwater resources are of great importance here; they are used for water supply and in heat power engineering. As a result, specialized observations of the physical and chemical indicators of the state of rivers were included in the observations carried out by the AARI expedition since 2003

at organized hydrological posts. Comprehensive monitoring of the hydrological cycle and the state of water bodies is being carried out, including the balance of river catchments of Spitsbergen. Measurements of water discharge are generally carried out here using the velocity-area method, and propeller-type current meter are used to measure the current velocity. They are recommended for such observations at the posts of the Rosgidromet observation network. Measurements of depth and flow velocity are carried out with the help of a wading measurement since the depth of rivers here rarely exceeds one meter. Suspended sediments sampling is performed with bottle sediment sampler from a wading rod integrally (Solovyanova, 2004; Tretyakov, 2010).

A database of hydrological characteristics of the elements of the water regime at the studied objects was compiled based on the results of observations carried out from 2001 to 2017. This database contains the calculated long-term series of hydrological characteristics in addition to the measured characteristics, such as the daily discharge of water and suspended sediments, spring water equivalent of snow cover in catchments, and some others.

Unfortunately, due to objective reasons, the observations of the runoff of the rivers under study are scattered. They refer to different phases of the hydrological cycle and different synoptic situations. Therefore, they do not cover the entire period of the runoff, mainly due to the lack of observations in the spring and autumn transition periods.

To restore the water flow of the Aldegonda River during periods not covered by data from direct hydrological observations, a model of its formation was developed, based on the heat balance method for calculating snow melting by P.P. Kuzmin (Kuzmin, 1961), which was also extended to the glacial surface, the method for calculating snowpack yield by G.P. Kovzel (Kovzel, 1962) and the method of transformation of the runoff by G.P. Kalinin and P.I. Milyukov (Kalinin, Milyukov, 1958).

Kuzmin's method was adapted to this region by dividing the catchment area into altitude zones, assuming that the temperature decreases on average by 0.6 °C for every 100 m of altitude. The Aldegonda River catchment area was divided into two parts: glacial (Aldegondabreen) and non-glacial (moraine). Moraine is mainly located in the lower part of the catchment area at an altitude of 0 to 80 m above sea level. The glacier is divided into four more altitude zones of 100 m each. Dividing the catchment area into altitude zones allows one to calculate snow melting and snowpack yield separately for each zone, calculating the transformation of the runoff from each zone to the closing section according to the method of G.P. Kalinin and P.I. Milyukov.

The observation of the chemical composition of surface waters, fluctuations, and tendencies of its changes is an essential component of the hydrological work of the AARI expedition on the rivers of the Grøn fjorden basin. During the expedition, samples of snow and water were taken to determine the content and changes during the field season in the content of total carbon (TC), inorganic carbon (IC), total nitrogen (TN), organic carbon (NPOC), cations (Na, NH, K, Mg, Ca) and anions (F, Cl, Br, NO₂, NO₃, PO₄, SO₄), total silicon Si (SiO), they observed the change in the pH value, the specific electrical conductivity of water, and the concentration of dissolved oxygen. Sampling for analysis to determine chemical indicators was carried out following GOST R 51592–2000; RD 52.19.595–96.

Full-fledged observations of the chemical runoff of water became possible only after the start of the functioning of the RSCS and when they organized a chemical analytical laboratory in its infrastructure, that is, starting from 2014. From that moment

on, observations of the content of chemical elements in freshwater and its changes became systematic, including the number of specified indicators and the sampling frequency.

Due to the above factors, the analysis of the chemical composition of snow masses and freshwaters flowing into the Grønfjorden is based mainly on the results of field observations that have been obtained over the past three years.

The estimation of the statistical significance of the linear trends was carried out following the recommendations set out in Polyak (1975). At the same time, to confirm the hypothesis of the presence of a linear trend, a 95 % significance level was accepted. The following formula determined the variance of the linear trend error

$$\sigma_{\beta}^2 = \frac{12\sigma^2}{N(N^2 - 1)}, \quad (3.5.1.)$$

where σ – root-mean-square deviation of the considered hydrological characteristic, N – number of years in the studied period, β – an average rate of change of the considered characteristic. The statistically significant trends meet the condition $|\beta| > 2\sigma_{\beta}$.

GENERAL HYDROLOGICAL CHARACTERISTICS

Most of the rivers and streams of Spitsbergen have fast current (1–3 m/s) and a depth of 1–1.5 m (Gokhman, 1988). The channels of mountain rivers and streams often have rapids, with waterfalls, the height of which sometimes reaches several tens of meters. The rivers flowing through wide flat valleys meander strongly, are divided into separate branches and carry a large amount of sediment during the flood period. The length of most rivers is limited to several kilometers, and only in the central part of West Spitsbergen, where glaciation is small, the length of large rivers reaches 20 km or more, and the area of their catchments is hundreds of square kilometers; their maximum discharge is more than 100 m³/s.

We can distinguish three specific periods in the annual hydrological cycle of the Spitsbergen rivers: winter – the period of snow accumulation; spring, when the snow melts; summer-autumn when the rivers are fed by meltwater from glaciers and liquid precipitation.

There is no permanent river flow in Spitsbergen during the winter period, which lasts from October to May. Winter runoff from polythermal glaciers, mainly due to the snowpack yield from the subglacial talik, accumulates in the form of periglacial ice, sometimes quite significant. The share of winter runoff in the annual volume of river water is small and can amount to 3–5 % (Solovyanova, 2004). Water equivalent of snow cover or the amount of solid precipitation during the cold part of the year is the main factor that determines the characteristics of the spring flood.

Snow starts melting on river catchments in the second half of May. In the first 10–15 days after the average daily air temperature transits through 0 °C towards positive values, it usually remains close to zero, and the water consumption on rivers usually amounts to hundreds of liters per second and does not exceed 1–2 m³/s. The flood caused by an increase in the average daily air temperature starts in the first half of June. Meltwater first flows through the snow or along the surface of the channel ice, gradually cutting through its channel to the ground. During floods, snow persists over most of the catchment area. After the peak of the flood, the snow cover of the territory and the water flow decrease rapidly. When air temperature slowly increases in the first half of summer, the snow cover melts longer, and flood with several peaks can extend for a period of up to a month.

Liquid precipitation in the polar regions sometimes referred to as “Polar deserts” do not play such a significant role as in middle latitudes. The water flow regime generally

depends on the response of glaciers to meteorological conditions in highly glaciated catchments during the warm period. Glacier melting, which is caused by the impact of atmospheric factors on it, is the most essential component of the input part of the water balance equation. Summer floods, the flow rate of which sometimes exceeds the maximum flow rate of the flood, are formed in the second half of summer with intense rainfall on days with high air temperatures.

The period of constant surface runoff on rivers lasts 5–6 months and usually ends by the end of September–October. For three summer months, more than 90 % of the runoff takes place, including 40–60 % in July. Runoff from highly glaciated catchments during the warm season is distributed more evenly; its main volumes occur in the period from mid-June to mid-August (Gokhman and Khodakov, 1983; Gokhman, 1987; Solovyanova et al., 2005).

The rivers of Spitsbergen are very turbid, which complicates the economical use of their water resources. The river sediments form and move on Spitsbergen under low-temperature conditions and the influence of glacial erosion. The presence of permafrost provokes the saturation of the active surface layer with water during snowmelt and rainfall. The amount of suspended sediment in rivers is closely related to the flow regime. Before floods start, the water in the rivers is usually clean; its turbidity varies from 0 to 10–15 mg/l. As the flood rises, the turbidity of the water increases sharply (up to 3 g/l and more). When the flood declines, water turbidity decreases. Turbidity of water increases as a result of outcropping and thawing of rocks in the active layer of slopes and moraine deposits near glaciers.

We chose the Grøndalselva and Aldegonda rivers, which are typical rivers of the valley and mountain types, respectively, to illustrate the hydrological and hydrochemical regime of the rivers in the Grøn fjorden more detailed. Hydrological observations at these objects began in 2001; at the same time in the lower reaches of these rivers, hydrological posts were organized, they were equipped with main and working benchmarks, level piles and automatic level devices.

The Grøndalselva flows through a wide flat valley, divides into separate branches, and flows into Grøn fjorden from the east. The catchment area of this river, with an area of 98 km², has a slight slope and a relatively small degree of glaciation – 13 %. The river is 23.5 km long. The river originates from the Tavlebreen. In the upper reaches, the river flows in a narrow canyon, in the middle and lower reaches, the valley expands. Along the entire length of the river, channel deformation processes are actively occurring, the multi-channel structure is developed, and the river has a circuitous course. During the flood and autumn floods, the Grøndalselva carries a large amount of sediment, which is formed as a result of the washout of a large amount of soil, peat, and vegetation from the surface of the valley. When it flows into the bay, the river forms a vast delta, extended for dozens of meters into the bay, and the river waters, mixing with the waters of the bay, moves a lot of suspended sediment, we can trace it at a considerable distance from the mouth.

In winter, the river freezes, and there is no runoff. Surface runoff begins in early June. During the flood period, one can observe small ice drift here, formed by ice floes brought by the river from the upper reaches and coastal ice. Melting snow from both the river valley and nearby glaciers forms the flood. Gradually decreasing, the runoff continues until the end of September. In the first ten days of October, when the air temperature passes through 0 °C, the river freezes over, and the runoff stops. In the second half of September, and sometimes during the whole month, autumn floods are observed here,

which are formed by intense liquid precipitation, stormy winds, and frequent fogs. The discharge of water and suspended sediment during this period can reach, and in some years even exceed the discharge of spring floods.

Aldegonda is a mountain-type river; It has a fast current and a porous channel up to 1 m deep and up to 11 m wide. Due to the high flow velocity, the water current in the river has a well-defined turbulent character. The Aldegonda River flows into the Grønfjorden from the west bank. The catchment area of the river is 9.4 km². The river originates from the Aldegondabreen (5.7 km²), pouring out in three streams – two from the sides and one in the center of the glacier. The glacier has been receding in recent decades, so the length of the river is increasing, and the degree of glaciation of its catchment is decreasing. In 2016, the Aldegonda River was 2.6 km long, and its catchment was 60 % glaciated. The river has a rather steep slope (0.040 ‰), a rapid current, and flows through a valley composed of moraine deposits. In some places, bedrocks outcrop on the surface of the catchment, which constrains the river bed, forming small canyons. The catchment area contains several small lakes with a total area of up to 100 m². When it flows into the Grønfjorden, the Aldegonda River forms a small delta, the position of which is unstable. In recent years, there has been an intensive development of the delta, a large number of small branches appeared, and the suspended sediment area in the bay increased. The gauging section is located at the site of the first bedrock outcrop, 500 m from the bay, and intercepts 97 % of the runoff from the catchment.

In winter, the river freezes entirely, and there is no runoff here. The onset of a flood depends directly on the transition of average daily air temperatures through 0 °C and starts in the first decade of June. Meltwater flows over the snow, gradually breaking through its bed. In the area of the gauging section, the resulting flow, due to the increase in the longitudinal slope, goes under the snow and flooding ice and comes out to the surface 300 meters below as a small spring. During floods, snow persists over most of the catchment area. The flood passes without ice drift; it has a rapid current, high flow velocity, and increased turbidity. After passing the peak of the spring flood, the water level gradually decreases, and its lowest values are noted in August. The water and suspended sediments runoff have a well-defined daily variation with its maximum in the afternoon and a minimum at night. Such a diurnal variation is caused by the fact that in the warm season, the flow regime of mountain rivers depends mainly on the melting of glaciers.

In the second half of September, we can observe flash floods, caused by frequent rains, strong winds, and fogs, which, in turn, cause intense melting of the glacier. When the daily air temperature decreases, the intensity of glacier melting decreases too, and hence the surface runoff. The runoff completely stops in the second half of October; it is associated with a stable transition of air temperature through 0 °C.

RIVER AND SEDIMENT RUNOFF

The volume of observation data for the discharge of the Aldegonda River is significantly larger than for other rivers flowing into the Grønfjorden. However, these data are still insufficient, and only part of the runoff period is observed. The reconstruction of the river runoff for the periods not covered by the observations was carried out using a runoff model based on heat balance calculations of the glacier surface, taking into account liquid atmospheric precipitation. Simulation of the runoff of the Aldegonda River agreed with the observation data of the river runoff in recent years (2014–2016). The reconstructed runoff for 2016 (Fig. 3.5.2) showed compliance with the observed values

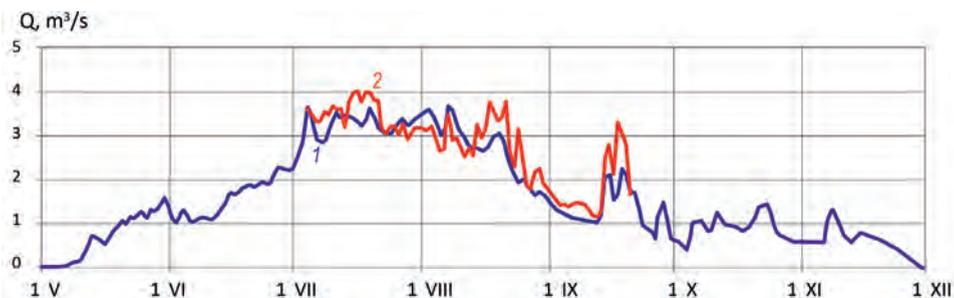


Fig. 3.5.2. The results of the calculation of the hydrograph of the runoff of the Aldegonda River for 2016 (1) and the observation data of the runoff (2).

with the Nash–Sutcliffe criterion equal to 0.67 and an average relative error of about 14 %. For previous years (2005–2013), the results of model calculations generally correspond to the data of fragmentary observations of water discharge. In some years (2005–2007), the observed water discharge turned out to be less than that calculated by the model. However, it should be noted that in those years, the methodically insufficient ion flood method was used to measure the discharge.

Calculation of snow melting and snowpack yield in the catchment area of the Aldegonda River based on snow measuring work data and standard meteorological observations at the meteorological station in Barentsburg showed that the melting process begins in late April – early May, long before the beginning of water yield from it. Water yield from snow begins almost simultaneously for the entire catchment area, although the catchment area is located in different altitude zones. The maximum snowmelt occurs in late May–early June, and by the first part of July, the snow has time to melt from all over the catchment area, without creating conditions for a positive balance of the glacier mass, which is confirmed by glaciological observations on the Aldegondabreen, which has been actively degrading in recent decades.

Further, the Aldegonda River runoff forms due to the melting of the glacier and the liquid atmospheric precipitation. The runoff regime depends entirely on the response of the glacier to meteorological conditions; in this case, summer and autumn floods are formed, the discharge of which exceeds the discharge of the flood. In autumn, when the amount of solar radiation decreases to zero, turbulent heat fluxes become the main factors in forming the runoff.

Table 3.5.1. shows the estimates of the main characteristics of the Aldegonda River runoff, obtained from the observation results, as well as the values, reconstructed based on modeling.

As you can see from the table, the most watery month is July. Up to 30 % of the runoff passes during this month. Fig. 3.5.3. shows the long-term average flow hydrograph of the Aldegonda River.

Table 3.5.1

Estimates of the runoff specifics of the Aldegonda River for the period 2001–2016

Characteristic	Month							Annual runoff
	V	VI	VII	VIII	IX	X	XI	
Runoff volume, km ³ ·10 ⁶	1.43	5.84	6.89	5.17	2.81	1.37	0.59	24.1
Runoff layer, mm	147	620	709	532	299	141	62	2510

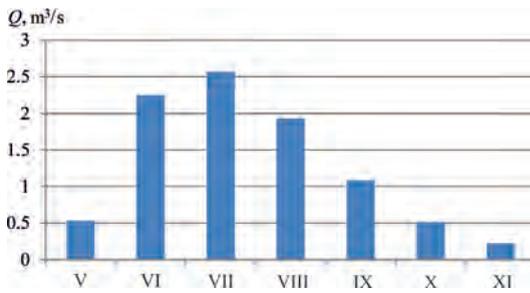


Fig. 3.5.3. The long-term average flow hydrograph of the Aldegonda River.

Concerning the sources of river feeding, according to long-term data, we can conclude that in the incoming part of the water balance, the share of snow supply accounts for an average of 26 %, the rain component is much less – about 10 %, and the main component of the incoming part is the melting of the glacier – 64 %. In the long-term view, the ratio of the river feeding sources changes insignificantly. One can note that the share of snow supply in recent years decreased and the share of supply due to glacier ablation increased (Fig. 3.5.4).

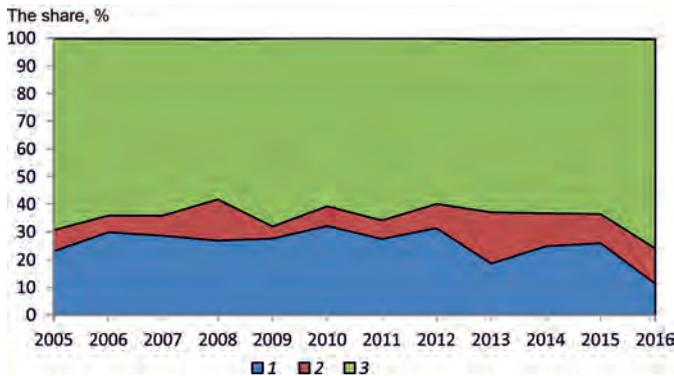


Fig. 3.5.4. The share (%) of the components of the input part of the water balance of the Aldegonda River catchment.

1 – snowmelt, 2 – liquid precipitation, 3 – glacier ablation.

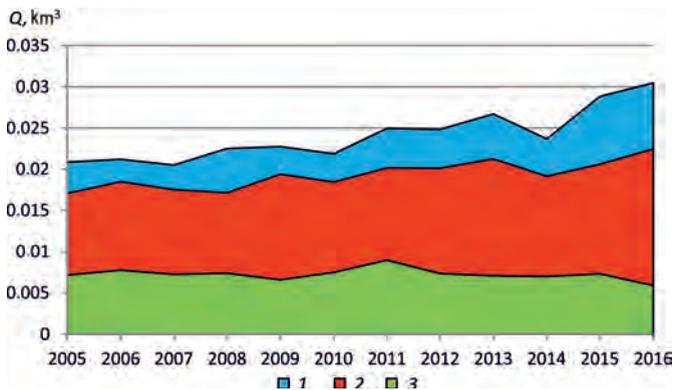
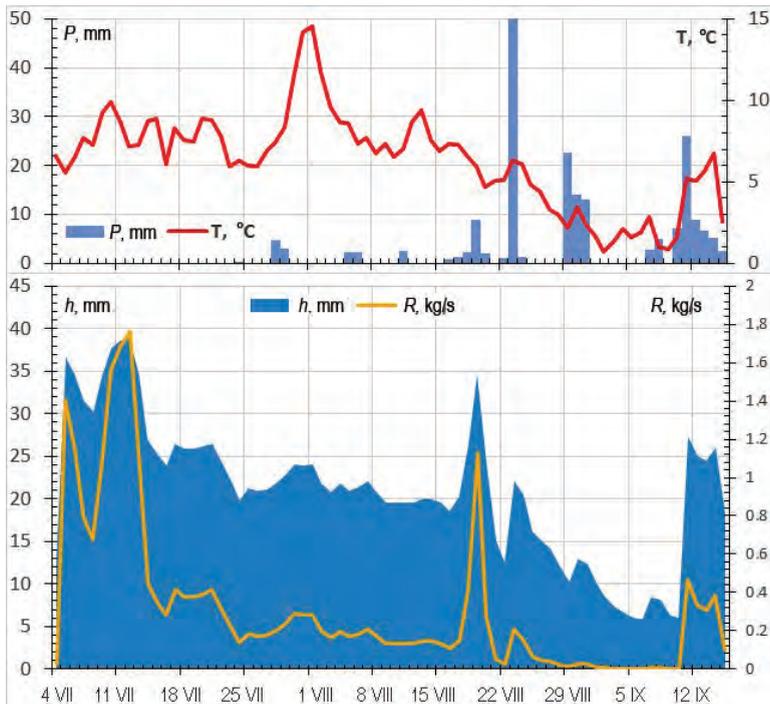


Fig. 3.5.5. Change in Aldegonda river runoff.

1 – September–November, 2 – July–August, 3 – May–June.



Change in air temperature change (T), daily precipitation amounts (P), layers of daily runoff (h) and average daily sediment discharge (R) of the Aldegonda river for the summer-autumn period 2015 (according to Barentsburg station).

Long-term changes in the runoff of the Aldegonda river show that for the period from 2005 to 2016, that runoff increased by an average of 800 thousand m^3 per year (Fig. 3.5.5). It is due to an increase in runoff in the summer and autumn months when the river is fed mainly due to the melting of the glacier. Thus, the runoff from the catchment area of the Aldegonda River clearly responds to climatic changes that have taken place in the region of Spitsbergen. The main factor behind these changes is the turbulent heat flux from the atmosphere, which increases leads to increased glacier melting.

The distribution of sediment runoff both within a day and throughout the warm period of the year is mainly determined by the nature of the distribution of water runoff. The turbidity of water in the Aldegonda River changes significantly throughout the year, which is associated with different intensity of glacier melting, uneven precipitation, different conditions of soil and vegetation, affecting the development of erosion processes in the catchment (Fig. 3.5.6). Slope erosion influences the formation of water turbidity in the Aldegonda River the most (Solovyanova, Tretyakov, 2004).

The combination of precipitation, high positive temperature values, contributing to soil thawing, and high water discharge in the river leads to an extreme increase in water turbidity (maximum observed value 2.14 g/l) and an increase in sediment discharge (up to 13.2 kg/s). It is due to both the washing off of soils from the surface of the catchment area and an increase in the size of the streamflow and the involvement of thawed soils into the flow. Such extreme situations can be observed during the entire warm period and are observed annually in the second half of September, just before the cold period.

Table 3.5.2

Estimates of the runoff specifics of the Grøndalselva for the period 2001–2016						
Characteristic	Months					Annual runoff
	V	VI	VII	VIII	IX	
Runoff volume, $\text{km}^3 \cdot 10^6$	n/d	39.1	17.8	9.62	6.14	72.7
Runoff layer, mm	n/d	398	182	98	63	741

Note. n/d – no data available.

On average, the turbidity of the Aldegonda River is 0.21 g/l. The average monthly values of turbidity for the warm period are approximately the same; therefore, the annual distribution of sediment runoff is mainly determined by the water runoff. In July, the month with the highest water content, up to 40 % of the sediment is washed out. In just a year, on average, 5.2 thousand tons of suspended sediment are washed out by the Aldegonda River.

Table 3.5.2. shows the estimates of the main characteristics of the Grøndalselva obtained from the results of runoff observations for the period 2001–2016.

As you can see from the table, the most watery month is June. Up to 50 % of the annual runoff passes during this month. According to the data on the maximum water equivalent of snow cover by the time of melting and the norm of precipitation for Barentsburg station, the share of snow supply in the incoming component of the water balance of the catchment is on average 34 %, the rain component of the runoff is about

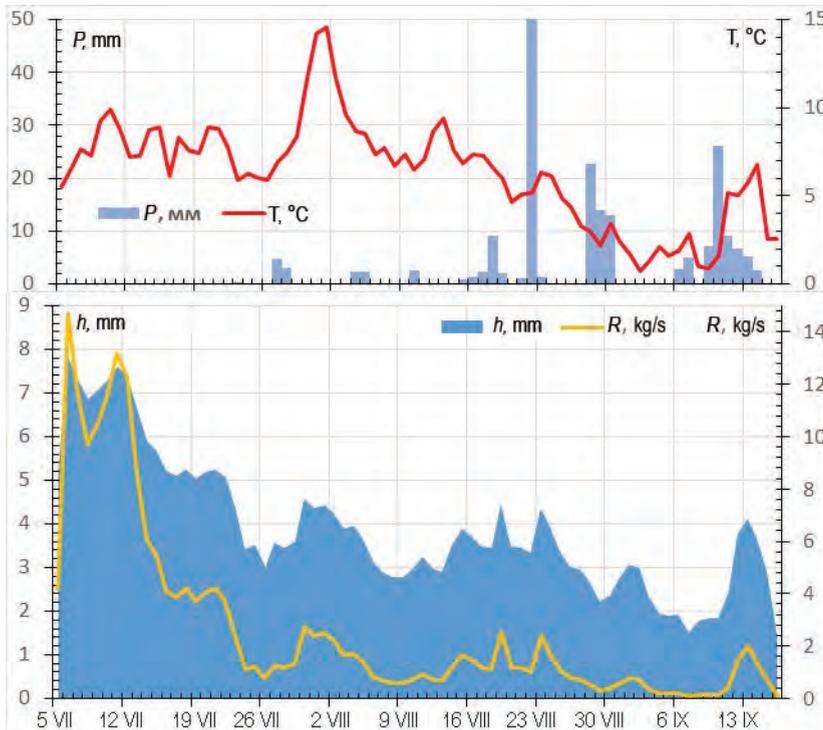


Fig. 3.5.7. Change in air temperature change (T), daily precipitation amounts (P), layers of daily runoff (h) and average daily sediment discharge (R) of the Grøndalselva for the summer-autumn period 2015 (according to Barentsburg station).

22 %; The river is fed by the melting of glaciers – 44 %. These assessments do not take into account groundwater inflow, which requires further study.

Fig. 3.5.7 shows the changes in air temperature, daily precipitation (according to the data from the Barentsburg meteorological station), and runoff layers of the Grøndalselva for the summer-autumn period of 2015.

As we can see from the figure, the highest values of water discharge and suspended sediments are observed in June, during the flood period. After the flood recession, these values also gradually decrease, reaching their minimum by September, when one observes an autumn dry weather flow on the river. However, the heavy autumn rains observed here in the second half of September intensify the melting of glaciers during this period and cause flash floods. These flash floods wash out a large amount of sediment, which, in turn, leads to a sharp increase in turbidity.

As V.V. Gokhman (Gokhman, 1988), the flash floods on the river increase turbidity to very high values, sometimes exceeding the maximum turbidity at the peak of the flood. According to the data of the 2001–2016 expeditions, the maximum turbidity of water in the Grøndalselva river was 5.7 g/l and was observed during the rain flash flood on July 29, 2003. The AARI expedition this year, with its observations, managed to cover only the decline in the flood. Still, these data also show that the highest turbidity the Grøndalselva was in June–July: this period accounts for over 75 % of the annual sediment runoff. In total, according to incomplete data, the Grøndalselva washes out about 20 thousand tons of suspended sediment per year.

HYDROCHEMICAL CHARACTERISTICS OF SURFACE WATERCOURSES IN GRØNFJORDEN BASIN

The chemical composition of meltwater on glaciers depends directly on the mineralization of ice and its contamination with moraine material. The mineralization of water in glacial streams generally corresponds to the mineralization of ice. Still, in large streams, it can be 3–4 times as much as the salinity in ice, and not so much in the small ones.

Due to the long-term seasonal snow cover, typical for this area, the contribution of the aeolian component to the actual mineralization of snow and ice is small. The mineralization of snow at the end of the cold season varies from 5 to 30 mg/l and more often does not exceed 10–15 mg/l.

The mineralization of glacial ice is also low: it varies from 4 to 35 mg/l and generally decreases down the glaciers. Snow, firn, and ice have a predominantly calcium-hydrocarbonate composition, but in some cases, the content of sulfates increases. During melting, the mineralization of the snow decreases, and freshening is most intense at the beginning of the ablation period. On Spitsbergen, the snow mineralization decreases rapidly during melting – 3–5 times in comparison with the initial one.

Numerous periglacial flooding ice in Spitsbergen is formed when glacial waters come out onto the day surface during the cold season. Mineralization of water and flooding ice increases with distance from the power source – from the glacier to the periphery. At the Aldegondabreen, the water mineralization on ice increased by 2–5 times, reaching 10 mg /l at a distance of 500 m from the glacier outlet. Mineralization increased 2–2.5 times on flooding ice in the middle part of the Grøndalselva valley.

The mineralization of water in rivers depends on the inflow of salts from tributaries and, to a large extent, on the snowiness of the territory and the share of glacial runoff. When the

**Changes in hydrochemical indicators in the rivers
of the Grønfjorden basin during the study periods in 2015 and 2016**

Parameter	Aldegonda river		Grøndalselva	
	2015	2016	2015	2016
Electrical conductivity, $\mu\text{S}/\text{cm}$	78.1–460	78.0–429	187.0–889	231–1139
pH	7.16–8.43	6.94–8.70	7.08–7.88	6.74–7.67
Total carbon (TC), mg/l	8.08–17.51	6.72–14.26	3.55–13.21	4.72–13.64
Inorganic carbon (IC), mg/l	7.45–16.60	6.06–14.05	4.88–12.08	4.00–12.92
Total organic carbon (TOC), mg/l	0.63–1.37	0.43–3.28	0.70–1.15	0.53–2.95
Total nitrogen (TN), mg/l	–	0.07–0.18	0.23–0.65	0.11–0.90
Hydrocarbonate, HCO_3^- , mg/l	30.6–108.3	31.9–74.0	14.9–80.3	21.1–68.0
Silicon, $\text{Si}(\text{SiO}_2)$, mg/l	0.33–1.24	0.29–1.58	0.88–2.08	0.79–2.87
Fluorides, F^- , mg/l	0.01–0.02	0.02–0.07	0.05–0.10	0.09–0.21
Chlorides, Cl^- , mg/l	1.77–5.45	0.84–4.41	3.34–45.80	1.67–46.18
Nitrates, NO_3^- , mg/l	0.09–0.63	0.09–0.53	0.17–2.73	0.07–4.03
Sulphates, SO_4^{2-} , mg/l	3.74–149.1	5.35–148.6	34.1–362.4	71.1–468.5
Sodium, Na^+ , mg/l	–	0.64–6.28	–	10.2–53.5
Potassium, K^+ , mg/l	0.54–1.53	0.06–2.40	1.13–2.62	0.93–5.43
Magnesium, Mg^{2+} , mg/l	1.39–13.5	1.23–12.8	2.80–48.1	11.99–64.8
Calcium, Ca^{2+} , mg/l	11.9–68.2	13.3–64.4	7.01–83.6	18.2–89.3

thawing period begins, the water mineralization decreases from 80–90 to 50–60 mg/l, and when the snow mass is soaked, and the meltwater is filtered through the top layer of the soil, it increases to 70–100 mg/l. At this time, most of the soluble impurities are washed out from the snow cover and enters streams, and then the rivers. Subsequently, the water mineralization generally reflects the runoff regime. As the flood rises, it decreases to 30–60 mg/l; during the flood decline, it increases to 60–90 mg/l.

The Aldegonda River is slightly mineralized, the conductivity value varies during the season from 78 to 460 $\mu\text{S}/\text{cm}$, and we can observe maximum values by the end of the season. The reaction of the medium is predominantly slightly alkaline – pH up to 8.7.

The river has a low content of biogenic elements (only silicon ions are identified – up to 1.48 mg/l), microcomponents, and organic matter. The dominant ions in the studied river are hydrocarbonates, chlorides, sulfates, calcium, magnesium; the potassium content is also noticeable (Table 3.5.3). Melting snow (or ice) is the main feeding of the river.

The water contains sulfates, which is explained by some reasons, we can distinguish two of them: 1) the water is drained through sedimentary rocks containing the corresponding ions; 2) the snow that feeds the river covers the territory, exposed to anthropogenic influence although to a small extent.

On the Grøndalselva, the reaction of the environment during the observation process varied from neutral to slightly alkaline. Mineralization varied widely depending on the time of observation. So the SEC values varied from 187 to 1139 $\mu\text{S}/\text{cm}$ during the season in 2015 and 2016, the average pH during the observation period was 7.42.

The main ions are hydrocarbonates, chlorides, and sulfates, the content of which is exceptionally high in the autumn period. Concentrations of calcium and magnesium are significant. The only biogenic elements were nitrates. The organic carbon content is insignificant (see Table 3.5.3).

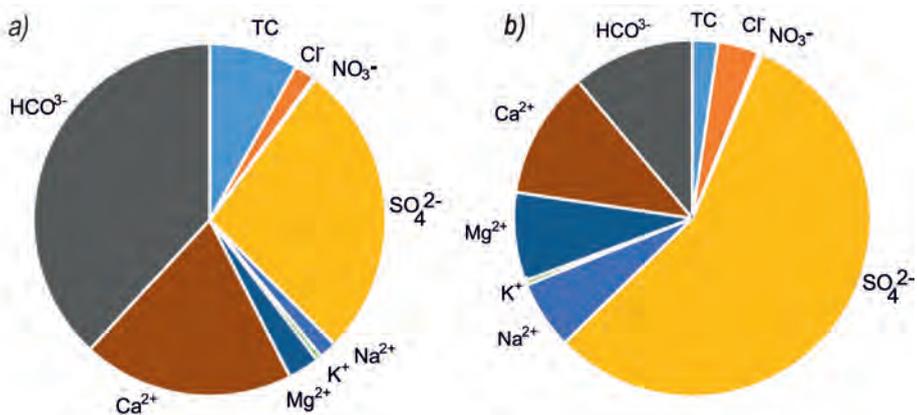


Fig. 3.5.8. Average content of basic cations and anions in the runoff of the Aldegonda (a) and Grøndalselva rivers (b) in the summer of 2016.

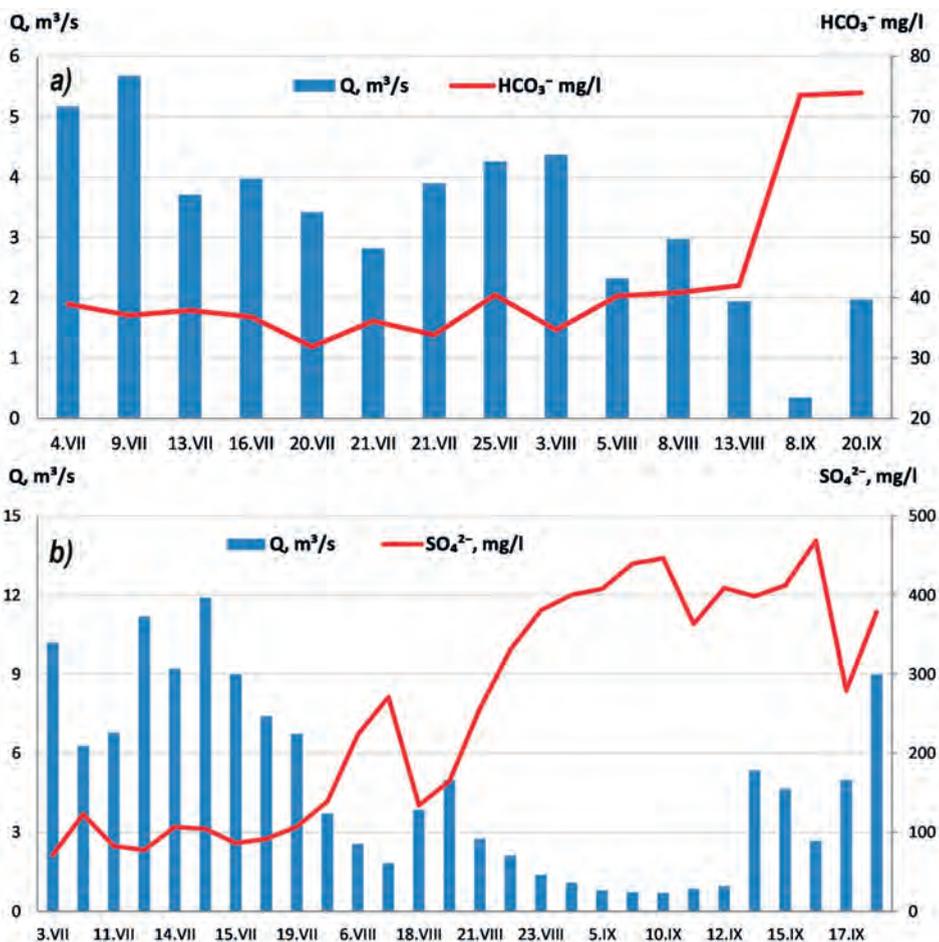


Fig. 3.5.9. Changes in the concentrations of dominant ions in the Aldegonda (a) and Grøndalselva (b) rivers in 2016.

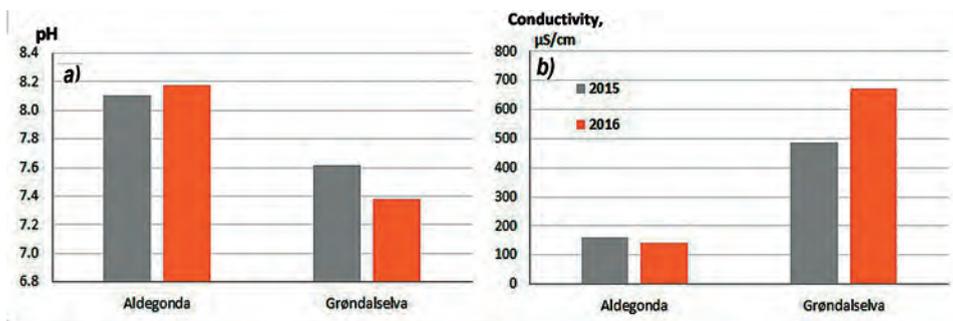


Fig. 3.5.10. Averaged values of pH (a) and specific electrical conductivity (b) in the runoff of the objects under study for 2015 and 2016.

Comparison of the sum of cations and anions in the sample showed a sharp discrepancy – the sum of cations was one and a half times higher. Perhaps this difference is due to the presence of organic acid anions – fulvic acids, naphthenic acids, etc.

According to the classification (Alekin, 1970), the waters of the Aldegonda River belong to the bicarbonate-calcium type II (the concentration of bicarbonates is about 60 mg/l on average per season). The waters of the Grøndalselva belong to the class of sulfate waters of the type II calcium group (the concentration of sulfates is about 200 mg/l on average per season). The concentration of sodium and magnesium ions in the waters of the Grøndalselva is, on average, 10 times as much as in the Aldegonda River.

On the Aldegonda River, there is a good relationship between the values and trends of river runoff changes and dominant ions (Fig. 3.5.9). When the water content of rivers decreases, the concentration of chemical substances will increase, which is associated with glacial feeding of river. The low content of biogenic elements is typical for both rivers under consideration. Thus, the concentration of nitrites, phosphates, and ammonium is beyond the detection limits of the measurement method and is less than 0.05, 0.1, and 0.25 mg/l, respectively. The concentration of nitrates reaches 1.5 mg/l (the highest content is in the Grøndalselva), and total nitrogen is 0.5 mg/l.

Representatives of typical anions – fluorides and bromides – were determined from microcomponents. Their concentration is very low: the bromide content is outside the lower limit of the method used, the fluoride content ranges insignificantly from 0.02 to 0.50 mg/l. It is often below the detection limit (see Fig. 3.5.8).

During the runoff period, the concentration of chemical elements gradually increases, while water discharge decreases (Fig. 3.5.9). In September, during the autumn flash floods, the runoff sharply increases, and the concentration of the main ions and biogenic elements decreases.

During the summer runoff, the mineralization of the studied objects greatly increases due to the channels and catchment area geology, and the maximum value for the Aldegonda River is 460 µS/cm. For the Grøndalselva, it is 1139 µS/cm (Fig. 3.5.10). The reaction of the medium is predominantly slightly alkaline: the pH slightly increases in comparison with the snow cover and reaches 8.7 in the waters of the Aldegonda River and 7.8 in the waters of the Grøndalselva.

CONCLUSIONS

To identify the features of the formation of river runoff in the catchment area of Grønfjorden, an analysis of materials from expeditionary hydrological studies for

2001–2017 was carried out. Two rivers of the bay basin of different types were studied: Grøndalselva and Aldegonda rivers.

The analysis of the materials showed that the length of the observation data series differs; they are scattered, refer to different periods and different phases of the hydrological cycle, have gaps, or are episodic. There are reasons for this situation. In particular, it is difficult to organize observations on these rivers, especially during the transitional periods of spring and autumn, conduction and optimization of hydrological observations in the conditions of Spitsbergen are not sufficiently worked out, the instrumental base is imperfect, etc. That is why it was necessary to involve a model of runoff formation, which made it possible to restore the daily values of the surface runoff of the Aldegonda River for the periods not covered by observations from the beginning of snow melting to the complete freezing of the river in autumn from 2005 to 2016.

The share of snow cover melting in the incoming water balance is 26 % for the Aldegonda River and 34 % for the Grøndalselva. Therefore, when conducting research, special attention was paid to assessing the main characteristics of snow accumulation and their long-term variability. It was revealed that at the accepted level of significance, there are no statistically significant trends in changes in the height of snow, its density, and maximum water storage in the snow for the catchments of the Aldegonda and Grøndalselva rivers.

The runoff of the Aldegonda and Grøndalselva rivers, formed by melting snow, liquid precipitation and melting of glaciers, clearly reacts to climatic changes that have taken place in the last decade in the area of Spitsbergen, the main factor of which is a turbulent heat flux from the atmosphere, which increase leads to increased melting of glaciers located on the catchments of the rivers under study. Long-term changes in the runoff of the Aldegonda river show that for the period from 2005 to 2016, that runoff increased by an average of 800 thousand m³ per year. It is due to an increase in runoff in the summer and autumn months when the river is fed mainly due to the melting of the glacier.

Observations of the runoff of suspended sediments also made it possible to determine its main characteristics. It was found that the distribution of sediment runoff both within a day and during the entire warm season for all studied rivers is mainly determined by the nature of the distribution of water runoff. The annual sediment runoff is estimated to be 5.2 thousand tons for the Aldegonda River and 90 thousand tons for the Grøndalselva.

The ionic composition of glacial waters changes significantly throughout the year. As the surface melting of the glacier decreases in autumn, the inflow of water from the glacier strata has a more significant effect; the mineralization of water also increases. Numerous periglacial flooding ice has a great influence.

On the Aldegonda River, there is a good relationship between the values and trends of river runoff changes and dominant ions. When the water content of rivers decreases, the concentration of chemical substances will increase, which is associated with glacial feeding of rivers. All studied rivers have a low content of biogenic elements.

The obtained estimates of the hydrological and hydrochemical characteristics of the studied objects record their current state and current trends in their change and can be used in the future to study the climatic changes in the environment on Spitsbergen. For this, hydrological studies of surface water bodies in the archipelago, undoubtedly, should be continued. These observations are necessary not only to obtain information about the regime and the main hydrological characteristics of surface water bodies for such still

very poorly studied areas but also to study the climate system “atmosphere–cryosphere–hydrosphere–biosphere” as a whole.

REFERENCES

- Alekin O.A. Osnovy gidrohimii. Fundamentals of hydrochemistry. Leningrad: Gidrometeoizdat, 1970: 442 p.*
- Kotlyakov V.M. (ed.). Gljaciologija Shpicbergena. Glaciology of Spitsbergen. Moscow: Nauka, 1985: 200 p. [In Russian].*
- GOST R 51592-2000. Voda. Obshhie trebovaniya k otboru prob. GOST R 51592-2000. Water. General sampling requirements. Introd. 2000-21-04. Moscow: Publishers Standartinform, 2000: 48 p. [In Russian].*
- Gokhman V.V. Vodno-lednikovyy balans Shpicbergena. Aqueo-glacial balance of Spitsbergen. PhD thesis. Moscow, 1990: 20 p. [In Russian].*
- Gokhman V.V., Khodakov V.G. Issues of analysis, forecast and conversion of winter runoff from the Bertil glacier on Spitsbergen. Materialy gljaciologicheskikh issledovanij. Materials of glaciological studies. 1983. 46: 185–193. [In Russian].*
- Gokhman V.V. Distribution and conditions for the formation of Spitsbergen glacier flooding ice. Materialy gljaciologicheskikh issledovanij. Materials of glaciological studies. 1987, 60: 68–76. [In Russian].*
- Gokhman V.V. The river runoff regime on West Spitsbergen. Materialy gljaciologicheskikh issledovanij. Materials of glaciological studies. 1988, 62: 96–103.*
- Kalinin G. P., Milyukov P. I. Priblizhennyj raschjot neustanovivshegosja dvizhenija vodnyh mass. An approximate calculation of the unsteady movement of water masses. Leningrad: Gidrometeoizdat, 1958: 72 p. [In Russian].*
- Kovzel A.G. A simplified scheme for calculating water yield from snow. Trudy Gosudarstvennogo gidrologicheskogo instituta. Proc. of the State Hydrological Institute. 1962 (99): 141–175. [In Russian].*
- Kuzmin P.P. Process tajaniya snezhnogo pokrova. Process of snow cover melting. Leningrad: Gidrometeoizdat, 1961: 345 p. [In Russian].*
- Mirovoj vodnyj balans i vodnye resursy Zemli. World water balance and water resources of the Earth. Leningrad: Gidrometeoizdat, 1974: 638 p. [In Russian].*
- Polyak I.I. Estimating the linear trend of meteorological time series. Trudy Glavnoj geofizicheskoy observatorii im. A.I. Voejkova. Proc. of the Main State Hydrometeorological Observatory. 1975 (364): 51–55. [In Russian].*
- RD 52.19.595-96. Federal'nyj perechen' metodik kolichestvennogo himicheskogo analiza, razreshennyh dlja ispol'zovanija pri analize ob#ektov okružhajushhej sredy. Federal List of quantitative chemical analysis techniques approved for use in the analysis of environmental objects. [In Russian].*
- Solovyanova I.Ju., Tretyakov M.V., Pryamikov S.M. Features of the formation of the runoff of the Aldegonda River, (Spitsbergen). Kompleksnye issledovanija prirody Shpicbergena. Comprehensive studies of the nature of Spitsbergen. Proc. of research to practice conference. Apatity: Publishing house of KSC RAS, 2005 (5): 348–355. [In Russian].*
- Solovyanova I.Ju., Tretyakov M.V. Observations of the runoff of suspended sediment in the rivers of the Groen Fjord Bay Basin. Kompleksnye issledovanija prirody Shpicbergena. Comprehensive studies of the nature of Spitsbergen. Proceedings of research to practice conference. Apatity: Publishing house of KSC RAS, 2004 (4): 230–236. [In Russian].*
- Solovyanova I.Ju., Tretyakov M.V., Svjashhennikov P.N., Andreev O.M., Ivanov B.V., Pryamikov S.M. Comprehensive hydrometeorological studies of some glacial basins on Spitsbergen. Arktika i Antarktika. Arctic and Antarctic. 2004 (3): 40–49. [In Russian].*

Solovyanova I.Ju. Osobennosti formirovaniya lednikovogo stoka arh. Shpicbergen. VI Vserossijskij gidrologicheskij s#ezd: tezis dokladov. Features of the formation of glacial runoff on Spitsbergen archipelago. VI All-Russian Hydrological Congress: abstracts of reports. St. Petersburg: Gidrometeoizdat, 2004: 127–128. [In Russian].

Tretyakov M.V. Features of the river runoff on Spitsbergen archipelago. *Geograficheskie i jekologicheskie aspekty gidrologii. Trudy nauchnoj sessii, posvjashhennoj 90-letiju kafedry gidrologii sushj SPbGU.* Geographical and environmental aspects of hydrology. Proc. of the scientific session dedicated to the 90th anniversary of the Department of Hydrology of Land, St. Petersburg State University. St. Petersburg: Publishing House of St. Petersburg State University, 2010: 217–221 p. [In Russian].

3.6. MAXIMUM WATER EQUIVALENT OF SNOW COVER AT THE CATCHMENT BASIN OF GRØNFJORDEN

M.V. Tretyakov, O.F. Golovanov, V.A. Grigoryeva, K.V. Romashova

Precipitation is an input component of the water balance of river catchment basins. The accumulation of precipitation in the solid phase during the cold part of the year determines the river runoff during the flood period, as well as, in the climatic conditions of Spitsbergen, the balance of the mass of glaciers located in the catchments. In this regard, the study of the variability of maximum water equivalent of snow cover in the river catchments of Spitsbergen is especially important.

This chapter presents studies of the maximum water equivalent of snow cover in the catchments of two different types of rivers in the Grønfjorden basin – Grøndalselva and Aldegonda rivers. The Grøndalselva flows through a long and wide valley, the catchment of which has a slight degree of glaciation. The catchment area of the Aldegonda River, which belongs to the mountain type, has significant glaciation.

STUDY OF WATER EQUIVALENT OF SNOW COVER ON SPITSBERGEN NEAR BARENTSBURG. MATERIALS AND METHODS

The first observations and calculations concerning the mass balance of the glaciers of the archipelago were carried out abroad and refer to 1934 (Glaciology of Spitsbergen, 1985), and they continued in 1958.

Similar Russian observations were started by an expedition of the Institute of Geography of the USSR Academy of Sciences in 1965–1967 and continued until 1982. The main attention was paid to the regime of glaciers, including winter, summer, and annual balance of their mass. Significant snow measuring works carried out at the same time made it possible to trace the dynamics of water equivalent of snow cover on the Vøringbreen, Bertilbreen, Bogerbreen, Brøggerbreen, Daudbreen glaciers and in the valleys of Linnédalen, Grøndalen, Adventdalen, Mimerdalen, Sassendalen, Agardhdalen in comparison with the water equivalent of snow cover at the Barentsburg, Longyearbyen, and Ny-Ålesund meteorological stations. There is a connection between the total ablation on the Vøringbreen, Bogerbreen, Bertilbreen, and Austre Brøggerbreen glaciers and the average summer (June–August) air temperature at the operating meteorological stations of West Spitsbergen (Glaciology of Spitsbergen, 1985). Russian observations of the hydrological regime elements, which make it possible to determine the components of the water balance, were started in 1976 by the Spitsbergen glaciological expedition of the Institute of Geography of the USSR Academy of Sciences (Glaciology of Spitsbergen, 1985). In 1983, for the first time in Spitsbergen, the study of the regime of the Mimerelva was carried out during the entire period of existence of surface runoff, and the water resources of its basin were estimated (Gokhman, 1990). In 1984 and 1985, snow survey was carried out in the basins of the Grøndalselva and Mimerelva. These observations showed a quite close connection between the maximum snow accumulation in the Grøndalen and the amount of precipitation in the cold period at the Barentsburg meteorological station (Gokhman, 1990).

Since 2001, the AARI has begun to study climatic changes in the archipelago area (Solovyanova et al., 2004). The expedition programs include annual spring snow survey on river catchments and glaciers.

Snow survey on the watersheds of the West Spitsbergen rivers, as well as the processing of the obtained field materials are carried out following the Manual (Manual on Hydrometeorological Stations and Posts, 1972) and the Guide to snow survey in the mountains (1958), by Method of control (normal) snow surveying (Kuzmin, 1963).

Snow and water samples were taken for analysis to determine the content of total carbon (TC), inorganic carbon (IC), total nitrogen (TN), organic carbon (NPOC), cations (Na^+ , NH^+ , K^+ , Mg^{2+} , Ca^{2+}) and anions (F^- , Cl^- , Br^- , NO_2^- , NO_3^- , PO_4^{3-} , SO_4^{2-}), total silicon Si (SiO) to ensure the study of the chemical composition of surface waters, fluctuations, and tendencies of its variability; also there were observations of changes in the pH value and the specific electrical conductivity of water.

The estimation of the statistical significance of the linear trends was carried out per the recommendations set out in Polyak (1975). At the same time, to confirm the hypothesis of the presence of a linear trend, a 95 % significance level was accepted. The following formula determined the variance of the linear trend error

$$\sigma_{\beta}^2 = \frac{12\sigma^2}{N(N^2 - 1)}, \quad (3.6.1.)$$

where σ – root-mean-square deviation of the considered hydrological characteristic, N – number of years in the studied period, β – the average rate of change of the considered characteristic. The statistically significant trends meet the condition $|\beta| > 2\sigma_{\beta}$.

MAXIMUM WATER EQUIVALENT OF SNOW COVER

Numerous reasons, such as the location and height of the terrain, the nature of the geological substrate, the effect of the wind, the exposure of slopes, avalanches, and thaws form an uneven distribution of water equivalent of snow cover over the catchment area. Also, the precipitation spreads within the archipelago unequally.

During the period of the AARI expeditionary observations on the catchment area of the Aldegonda River, it was revealed that, generally, the most significant height of snow cover is observed on the sides of the glacier. It is associated with snow transport near steep slopes and the impact of avalanches (Tretyakov and Solovyanova, 2004). The average depth of snow cover on the Aldegondabreen was 161 cm for the period 2002–2017.

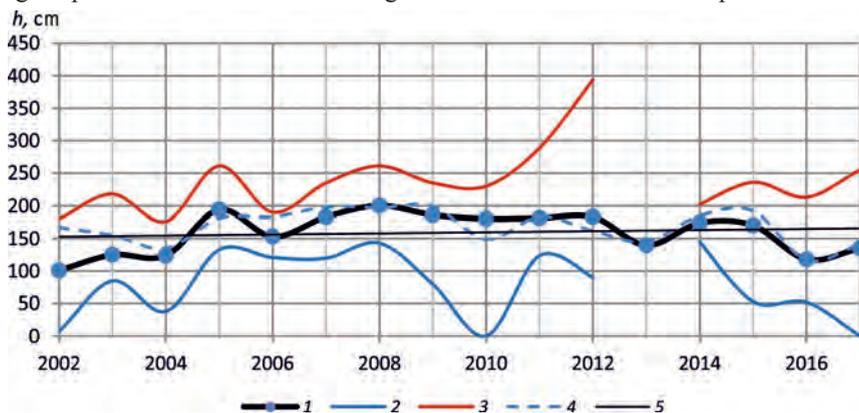


Fig. 3.6.1. Interannual variability of the average (1), minimum (2), and maximum (3) snow height in the catchment of the Aldegonda River during the period of maximum snow accumulation, as well as the maximum snow height at Barentsburg station (4) and the linear trend of the snow cover height in the Aldegonda River catchment (5).

Interannual variability of the snow cover height in the catchment area of the Aldegonda River during the period of maximum snow accumulation has a slight tendency to increase (Fig. 3.6.1). The highest average snow height in the catchment was observed in 2008 and amounted to 200 cm. The change in the average snow cover height in the catchment generally corresponds to the change in the maximum snow height for the year, measured at the Barentsburg meteorological station. The correlation coefficient between these values is 0.70. Snow cover height at the Aldegonda river catchment can be estimated from maximum snow depth h_{mB} observed in Barentsburg by $h_A = 0,85 h_{mB} + 16,9$. Density of snow in the Aldegonda River catchment at the time of its maximum accumulation, according to observations for 2002–2017 is on average $0,4 \text{ g/cm}^3$. The maximum mean density in the catchment was observed in 2004 and amounted to $0,52 \text{ g/cm}^3$, minimum – in 2016 and amounted to $0,29 \text{ g/cm}^3$ (Fig. 3.6.2).

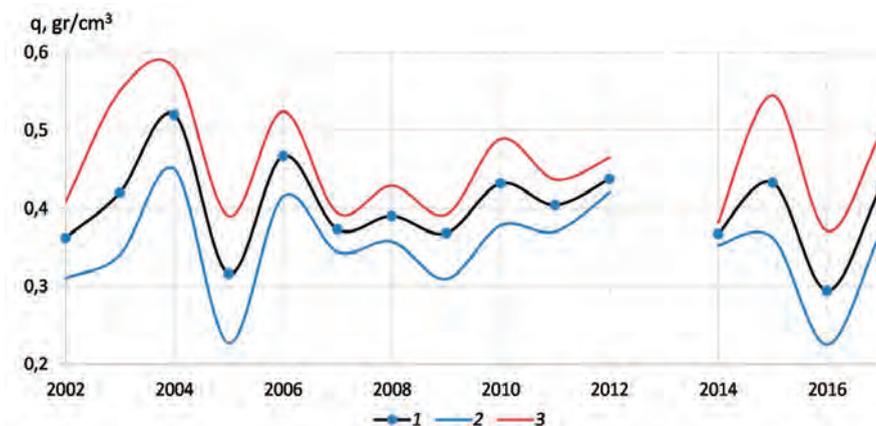


Fig. 3.6.2. Interannual variability of average (1), minimum (2) and maximum (3) snow density in the catchment area of the Aldegonda River during the period of maximum snow accumulation.

Long-term observations made it possible to reveal that the spatial distribution of the snow cover density on the surface of the Aldegondabreen clearly depends on the absolute height of the terrain. However, there is no connection between the depth of the snow cover and its density both on the glacial and non-glacial parts of the catchment.

Water equivalent of snow cover Q_s varies from 347 mm (2016) to 801 mm (2012) and averages 659 mm for the considered catchment during the observation period. There is no significant long-term trend in the change in water storage in this catchment (Fig. 3.6.3).

Relatively uneven distribution of snow cover over its area is typical for the Grøndalen. In this catchment, the average height of snow cover is significantly less than on the catchment of the Aldegonda River and averages 60 cm over the observation period. The snow cover height, as a rule, has a bimodal distribution, which indicates different conditions for the formation of snow cover on different parts of the catchment area (Tretyakov, Solovyanova, 2004). The most significant average snow height in the catchment area (92 cm) was observed in 2011, the lowest (21 cm) – in 2012. In general, there is no significant trend in the long-term variability of the snow cover height in the catchment area of the Grøndalselva (Fig. 3.6.4). The coefficient of correlation between the average height of snow cover in the catchment and its maximum height at the Barentsburg meteorological station is 0.60. The snow cover height in the Grøndalselva catchment h_G

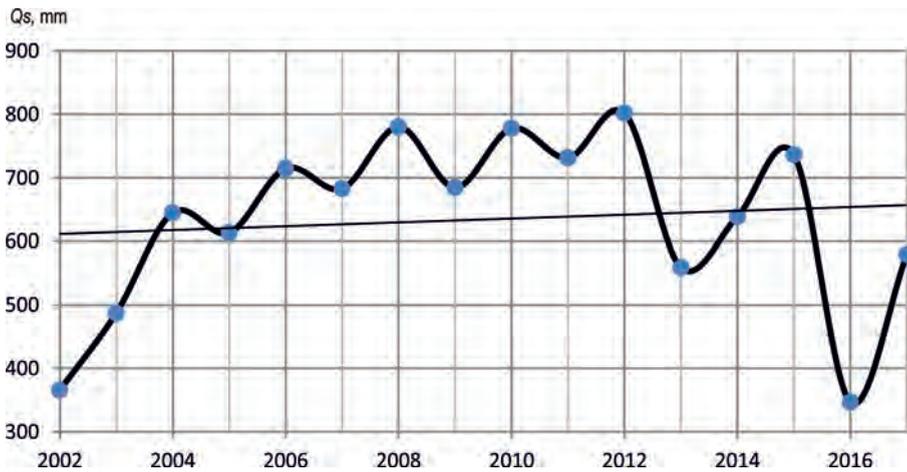


Fig. 3.6.3. Interannual variability of water equivalent of snow cover in the catchment area of the Algedonda River during the period of maximum snow accumulation.

can be estimated from the maximum snow height at the Barentsburg station according to the dependence $h_G = 0.48 \cdot h_{mB} - 22.6$.

During the observation period from 2002 to 2017, the snow density in the entire catchment of the Grøndalselva varied from 0.26 to 0.43 g/cm³ (Fig. 3.6.5). Usually, the densest snow is found in the lower part of the catchment area. The highest average density of snow cover in the catchment (0.43 g/cm³) was observed in 2015, the lowest (0.26 g/cm³) in 2016. The long-term average density for the catchment area of the Grøndalselva is 0.35 g/cm³. Generally, by the time of maximum snow accumulation, an ice crust is observed on the soil of the catchment, its thickness is quite significant in some places – up to 400 mm. It leads to significant spatial heterogeneity in the distribution of water reserves in the snow-ice cover in this catchment. The interannual variability of snow water storage is quite large and ranges from 131 to 396 mm. On average, over a long-term period, the water storage of the catchment area at the time of maximum snow accumulation is 253 mm. During the

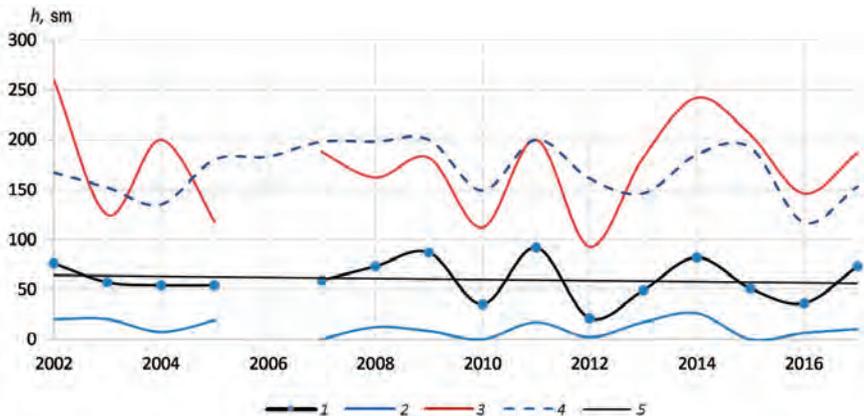


Fig. 3.6.4. Interannual variability of the average (1), minimum (2), and maximum (3) snow height in the catchment of the Grøndalselva during the period of maximum snow accumulation, as well as the maximum snow height at Barentsburg station (4) and the linear trend of the snow cover height in the Grøndalselva catchment (5).

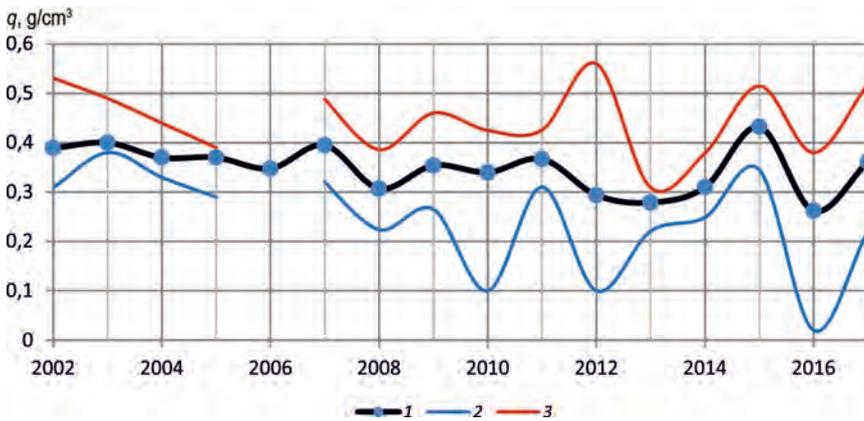


Fig. 3.6.5. Interannual variability of average (1), minimum (2), and maximum (3) snow density in the catchment area of the Grøndalselva during the period of maximum snow accumulation.

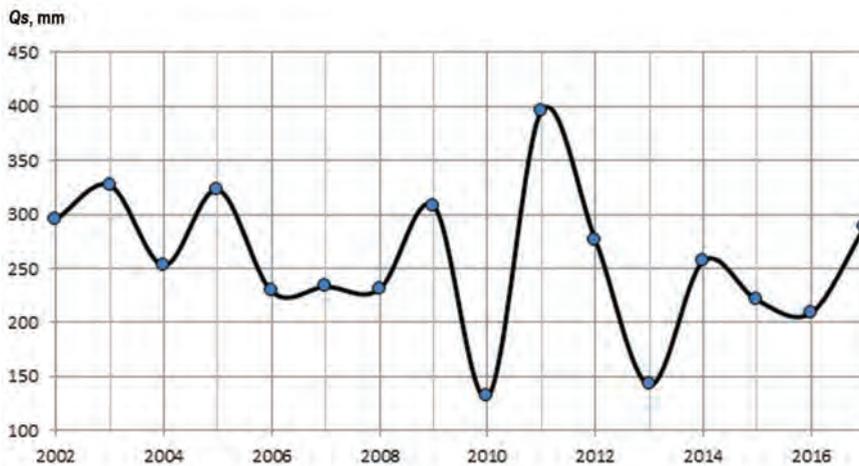


Fig. 3.6.6. Interannual variability of water equivalent of snow cover in the catchment area of the Grøndalselva during the period of maximum snow accumulation.

period of the expeditionary studies, the water storage in this catchment tended to decrease slightly (Fig. 3.6.6). This tendency is not statistically significant.

CHARACTERISTICS OF THE HYDROCHEMICAL COMPOSITION OF THE SNOW COVER IN CATCHMENT BASINS OF THE GRØNFJORDEN RIVERS

Snow cover on river catchments in the Grønfjorden basin is characterized by a slightly acidic reaction of the environment. The snow pH obtained by the authors varies from 5.5 to 6.5, which indicates low mineralization and low anthropogenic impact of the studied objects on the snow cover (Fig. 3.6.7 a).

The specific electrical conductivity (SEC) of the snow cover is directly proportional to the content of various chemical elements dissolved in sediments and indicates mineralization. On average, according to observational data for 2015–2017, the SEC values range from 12 $\mu\text{S}/\text{cm}$ in the Aldegonda River valley in 2016 to 36 $\mu\text{S}/\text{cm}$ in the Grøndalen in 2017. The electrical conductivity values are low, which indicates a low content of

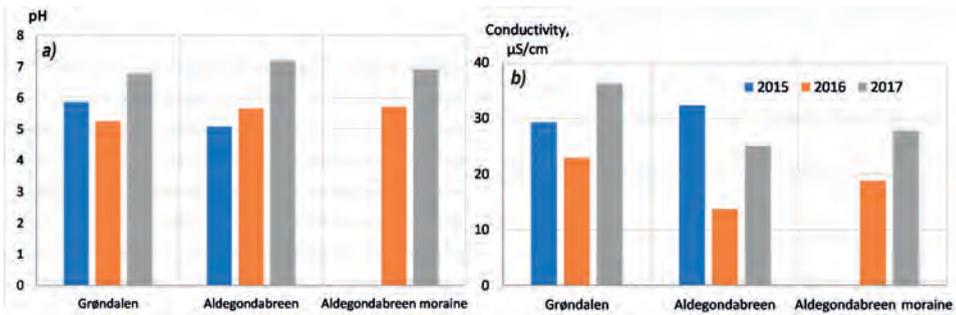


Fig. 3.6.7. Averaged values of pH (a) and specific electrical conductivity (b) of snow cover on catchments of the studied rivers in the spring of 2015–2017.

chemical elements in the snow, including ions and their oxides (Fig. 3.6.7 b). The snow cover in the Grøndalen is more mineralized than in the catchment of the Aldegondabreen. The specific electrical conductivity of snow on a glacier is 13–30 $\mu\text{S}/\text{cm}$, in the Grøndalen it is 22–36 $\mu\text{S}/\text{cm}$ on average per season. The pH values of the snow vary within 5–7.

Analyzing the obtained results of the total mineralization of the snow cover, we can say that, in general, the situation remains the same from year to year: the snow cover of the valley catchments is more mineralized than on the catchments of glaciers. For two years of observations, the difference between the average values of the snow cover mineralization for the two types of catchments does not exceed 20 mg/l. The inflow of marine aerosols from the adjacent seas plays an enormous role in the formation of the chemical composition of the snow cover of the marginal parts of the Spitsbergen archipelago. Based on the results of the observations, we can conclude that, according to the chemical composition, the snow cover of the studied catchments belongs to the sodium chloride type. The snow here is enriched with sodium-containing marine aerosols. The maximum values of the concentration of ions Na^+ and Cl^- on the surface of the Aldegondabreen are 3.08 and 15.42 mg/l, respectively (Fig. 3.6.8), in the Grøndalselva valley 5.47 and 10.31 mg/l respectively. There are about 10 times as fewer ions of Mg^{2+} and Ca^{2+} , and about 20 times as fewer ions of K^+ as Na^+ ions. A similar situation we can observe for the snow cover of the Grøndalen: There are 10 times as fewer ions of Ca^{2+} , 7 times as less Mg^{2+} , and 25 times as fewer K^+ in the snow cover as ions of Na^+ . At the same time, there is a clear correlation between the content of Na^+ and Cl^- ions in the liquid phase of snow: the correlation coefficient for the catchments of the Aldegonda and Grøndalselva rivers was 0.99.

Sulfate ions accumulate in the snow due to the deposition of sulfur dioxide aerosols from the air together with dust under the action of gravity, the content of SO_4^{2-} in the snow samples was quite insignificant. For the Aldegondabreen, catchment averaged 0.81 mg/l.

The content of nitrate ion in snow water is insignificant: for the catchment of the Grøndalselva, the average content of nitrates is 0.13 mg/l. The concentration of nitrates in the snow cover of all studied objects is extremely low (0.12 to 0.20 mg/l) and, in some cases, below the detection limit of the method used. The sulfate content is low and varies on average from 0.66 mg/l for the Vestre Grøn fjordbreen to 2.46 mg/l for the Austre Grøn fjordbreen.

In general, of all identified ions, the main part belongs to chloride ions and sodium ions. Also, total carbon and sulfates are identified in a noticeable amount; the concentration of other detected ions is insignificant. The snow cover of the investigated objects is free

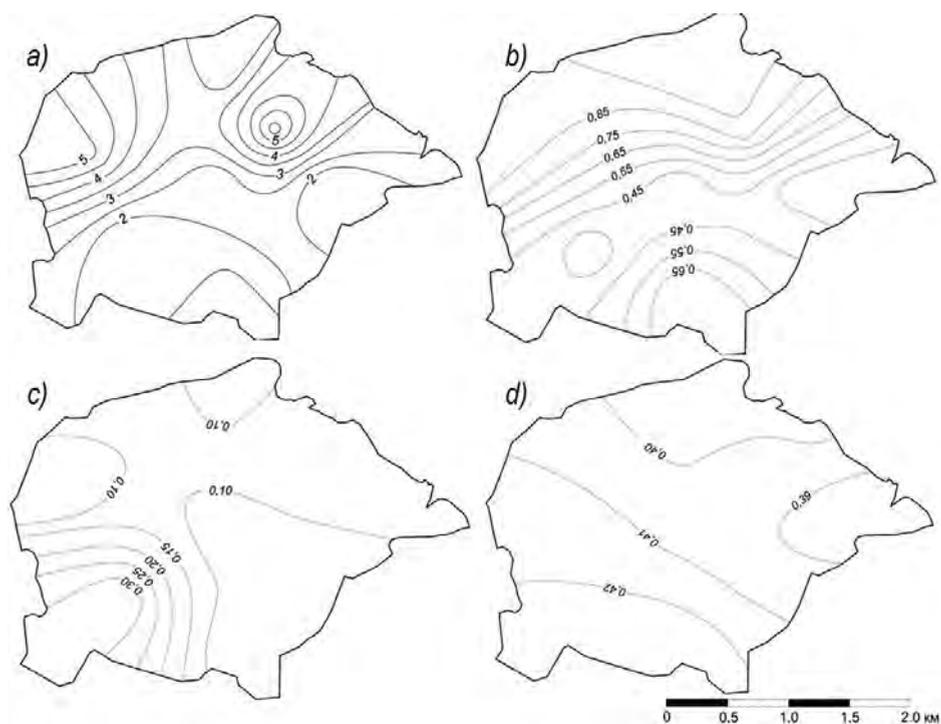


Рис. 3.6.8. Fig. 3.6.8. Distribution of the content (mg/l) of chloride ions (a), sulfates (b), nitrates (c), and ammonium (d) in the snow cover on the surface of the Aldegondabreen.

from fluorides, bromides, nitrites, phosphates, and ammonium ions; the concentrations of these ions are below the detection limit of the method used.

The highest average content of chloride ions (4.58 mg/l) was detected in snow samples taken from the moraine of the Aldegondabreen. Low concentrations of potassium, magnesium, and calcium cations were found, but it is difficult to identify any regularities since these values are close to the lower detection limit.

The content of suspended particles in the snow cover is due to factors such as atmospheric transport of solid particles from mountains, the geological substrate and ash dumps, as well as emissions of products of incomplete combustion of industrial facilities, such as thermal power plants in Barentsburg. Besides, it is highly dependent on the prevailing wind direction. The average concentration of suspended solids in snow water samples for the catchment area of the Grøndalselva is 1.95 mg/l, for the catchment of the Aldegonda River it is 1.30 mg/l. Snow from the catchment of the Grøndalselva is most polluted by undissolved mineral particles. We can observe the highest average content of suspended solids in the Grøndalen (11.63 mg/l). Moreover, in some snow samples from the Grøndalen, there were up to 67 mg/l of suspended solids. Despite the comparable values of the average content of suspended solids in objects near Barentsburg, solids in the snow cover have different origins.

CONCLUSIONS

Based on the analysis of materials from expeditionary hydrological studies for 2001–2017, the long-term characteristics of maximum snow accumulation for the catchments – the height of the snow cover, its density, and the water equivalent – were obtained for two

different-type rivers in the Grøn fjorden basin – Grøndalselva and Aldegonda. Assessment of the statistical significance of linear trends in the characteristics of maximum snow accumulation at a 95 % significance level showed there are no significant long-term changes in these characteristics over the period under study. One obtained linear equations that relate the average height of snow cover in catchments with its maximum height at the Barentsburg meteorological station.

The results of the study of the hydrochemical composition of the snow cover of the catchments for the studied rivers in the basin of the Grøn fjorden made it possible to reveal the conditions for the formation of their chemical runoff in spring. It was revealed that the snow cover in the Grøndalselva catchment, which is mainly a valley, is usually more mineralized than the snow in the Aldegonda River catchment, especially its glacial part. The modern hydrochemical composition of the snow cover is formed mainly from chloride and sodium ions; sulfates are also noticeable. The snow cover of the investigated objects is free from fluorides, bromides, nitrites, phosphates, and ammonium ions. The obtained estimates of the maximum snow accumulation and hydrochemical characteristics of the snow cover at the studied objects give an idea of their current state. They can be used in the future to study the water balance of river catchments and climatic changes in the environment on Spitsbergen.

REFERENCES

- Kotlyakov V.M.* (ed.). *Gljaciologija Shpicbergena*. Glaciology of Spitsbergen. Moscow: Nauka, 1985: 200 p. [In Russian].
- Gokhman V.V.* *Vodno-lednikovyj balans Shpicbergena*. Aqueo-glacial balance of Spitsbergen. PhD thesis. Moscow, 1990: 20 p. [In Russian].
- Kuzmin P.P.* Method of control (normal) snow surveying. *Trudy Zakavkazskogo nauchno-issledovatel'skogo gidrometeorologicheskogo instituta*. Proc. of the Transcaucasian Hydrometeorological Research Institute. 1963 (13): 39–47. [In Russian].
- Nastavlenie gidrometeorologicheskim stancijam i postam. Vypusk 6. Chast' 2. Hidrologicheskie nabljudenija i raboty na malyh rekah*. Manual on Hydrometeorological Stations and Posts. Issue 6. Part 2. Hydrological observations and work on small rivers. Leningrad: Gidrometeoizdat, 1972: 266 p. [In Russian].
- Polyak I.I.* Estimating the linear trend of meteorological time series. *Trudy Glavnoj geofizicheskoy observatorii im. A.I. Voejkova*. Proc. of the Main State Hydrometeorological Observatory. 1975, (364): 51–55. [In Russian].
- Rukovodstvo po snegomernym rabotam v gorah*. Guide to snow survey in the mountains. Leningrad: Gidrometeoizdat, 1958: 148 p. [In Russian].
- Solovyanova I.Ju., Tretyakov M.V., Svjashhennikov P.N., Andreev O.M., Ivanov B.V., Pryamikov S.M.* Comprehensive hydrometeorological studies of some glacial basins on Spitsbergen. *Arktika i Antarktika*. Arctic and Antarctic. 2004 (3): 40–49. [In Russian].
- Tretyakov M.V., Solovyanova I.Ju.* On the distribution of maximum snow reserves on Spitsbergen. *Tezisy dokladov XIII Gljaciologicheskogo simpoziuma "Sokrashhenie gljaciosfery: fakty i analiz"*. Abstracts of reports from the XIII Glaciological Symposium "Reduction of the glaciosphere: facts and analysis". St. Petersburg, 2004: 128 p. [In Russian].

Chapter 4.

Monitoring of the ionosphere on the Spitsbergen archipelago

4.1. INFLUENCE OF ARTIFICIAL IONOSPHERIC DISTURBANCES CAUSED BY IMPACT ON THE PROPAGATION OF RADIO WAVES OF THE DECAMETER RANGE OF THE SPEAR FACILITY ON SPITZBERGEN

N.F. Blagoveshchenskaya, T.D. Borisova, A.S. Kalishin

Recently, studies of the radio wave propagation in the decameter range have received a new qualitative development (Hunsucker and Hargreaves, 2003) and are relevant and important not only from a scientific but also from a practical point of view – for the justified organization of HF radio communications, solving the problems of navigation and over-the-horizon radar HF radio communication acquires particular importance in emergency situations: when organizing and carrying out emergency rescue operations, coordinating the actions of various organizations and services in areas of natural disasters.

The problem of organizing HF radio communication becomes especially acute in high latitudes – these are traditional communication systems of ships plying along the Northern Sea Route. Also, air carriers are incredibly interested in uninterrupted HF radio communications on lines crossing high latitude regions, which provide passengers with the shortest routes in time and distance between different continents of the globe.

The features of the propagation of decameter radio waves at high latitudes are caused by the complex and constantly changing state of the Earth's ionosphere, the parameters of which depend on many factors and are subject to regular and random changes. It is known that at high latitudes the ionosphere is very heterogeneous, first of all, since it consists of various large-scale structures with their specific features of behavior (the main ionosphere trough, auroral zone, polar cap, irregularities of different scales, etc.). Also, the high-latitude ionosphere is exposed to precipitating particle fluxes during magnetic storms and auroral substorms, electric fields, winds, etc. Dynamic processes in the ionosphere disrupt its regular structure and form intense horizontal (electrojet) and field-aligned currents, natural small-scale irregularities, electron density gradients, and plasma instabilities. Considerable attention is paid to studies of the specific features of the propagation of decameter radio waves at high latitudes, including during geomagnetic disturbances (Blagoveshchensky and Zhrebtsov, 1987; Blagoveshchensky, 2011).

In recent years, the study of the propagation of decameter radio waves on long and very long paths, in which it is necessary to take into account the inhomogeneous properties of the ionosphere, of both regular and random origin, has acquired increasing scientific and applied importance. Focused study of the properties of extended radio channels depending on heliogeophysical conditions, taking into account different types of disturbances in the ionosphere of natural and artificial origin, is of great importance associated with the solution of several practical tasks, supported by theoretical studies, revealing the general laws of radio wave propagation.

Irregularities and electron density gradients of the high-latitude ionosphere during radio wave propagation can cause changes in the trajectory of wave propagation in space: instead of a path along the great-circle, a new signal path (non-great circle) is formed, for example, with reflection from ionization gradients, forward ionospheric scattering or due to bi-static scatter by small-scale irregularities in the *E*- and *F*-layers of the ionosphere (Blagoveshchenskaya et al., 1991; Stocker et al., 2003; Siddle et al., 2004;

Blagoveshchensky et al., 2006; Blagoveshchensky et al., 2006; Blagoveshchensky et al., 2009). Such non-great circle signals create special trajectories of propagation of decameter radio signals, which are a significant interference to signal reception in over-the-horizon radar and navigation systems. Several papers (Blagoveshchenskaya et al., 1991; Blagoveshchensky et al., 2006) have shown the possibility of receiving decameter radio signals on the Earth on long high-latitude radio paths with a waveguide propagation mechanism when the “extraction” of radio waves from the waveguides can be carried out due to the mechanisms of bi-static scatter on small-scale ionospheric irregularities of natural origin and reflections from ionization gradients.

The impact of high-power HF radio waves emitted by specially built ground-based HF heating facilities into the *F*-layer of the ionosphere leads to the excitation of the intense artificial field-aligned irregularities (AFAI). AFAI are oriented in the direction along the magnetic field above the location of the HF heating facility. Their spatial size is 5–20 m across the Earth’s magnetic field and up to 20 km along it. The size of the artificially disturbed non-great circle signal of the ionosphere occupied by the AFAI is determined by the antenna beam width of the HF heating facility. It is about 100 km at the heights of the *F*-layer of the ionosphere.

The results of the AFAI studies excited in the polar ionosphere by powerful HF radio waves (pumping waves) of ordinary polarization (*O*-mode) of the SPEAR (Space Plasma Exploration by Active Radar) heating facility showed that the AFAI could be excited not only in the *F*-layer of the ionosphere but also in the “thick” sporadic *E_s* layers (Robinson et al., 2006; Dhillon et al., 2007; Yeoman et al., 2007; Blagoveshchenskaya et al., 2008; Blagoveshchenskaya et al., 2009). It was also found that when a powerful HF radio wave is emitted towards the Earth’s magnetic field (magnetic zenith), the generation of AFAI in the polar *F*-layer of the ionosphere can occur under the action of a pumping wave of extraordinary (*X*-mode) polarization (Borisova et al., 2012). This chapter presents a summary of the study results of the characteristics, features, and the behavior of artificial field-aligned irregularities in the polar ionosphere.

The purpose of this chapter is to study the effect of artificial small-scale ionospheric irregularities in the polar ionosphere, excited by powerful HF radio waves, both the ordinary (*O*-mode) and extraordinary (*X*-mode) polarization, on the propagation of decameter radio waves on long radio paths. The study results are based on the results of experiments carried out by the AARI specialists at the SPEAR heating facility on Spitsbergen (Borisova et al., 2012; Yeoman et al., 2007).

OBSERVATION METHODS AND TECHNICAL EQUIPMENT

The SPEAR HF heating facility (78.15° N, 16.05° E, magnetic inclination $I = 82^\circ$) was used to create artificial small-scale ionospheric irregularities in the polar ionosphere. The facility was located on Spitsbergen in close proximity of Longyearbyen (Robinson et al., 2006). A powerful HF radio wave of the ordinary (*O*-mode) or extraordinary (*X*-mode) polarization was emitted at a frequency of 4450 kHz towards the magnetic zenith (the antenna beam pattern is tilted 8° south of the vertical) by the following cycles: 2 min on/ 2 min off; 5 min on/ 5 min off. The experiments were carried out during daytime and evening hours under favorable magnetic conditions. The effective radiated power of the heating facility was $P_{\text{eff}} = 15$ MW. For the experimental conditions when the *X*-wave was emitted, the “leakage” of the *O*-mode wave did not exceed 10–15 %.

The reception of diagnostic signals scattered from AFAI was carried out by the method of bi-static scatter at the AARI Gorkovskaya observatory located at a distance of 70 km from St. Petersburg and at a distance of about 2000 km from the SPEAR facility. Fig. 4.4.1 shows the experiment geometry. On the Okeechobee (USA)–SPEAR–St. Petersburg radio path, measurements were made on 7 October in the daytime at a frequency of 13 695 kHz. The total length of the bi-static scatter path is 9210 km. The length of the Botswana (South Africa)–SPEAR–St.Petersburg bi-static scatter path is 13,150 km. The measurements on it were carried out on 29 January 2006 in the late evening hours at a frequency of 17 895 kHz. A multi-channel HF Doppler equipment (Blagoveshchenskaya et al., 2008) was used to register the heating signals from the SPEAR facility and the bi-static scattered HF signals.

To analyze and interpret the measurement results by the bi-static scatter method at the AFAI, an incoherent scatter radar (EISCAT Svalbard Radar, ESR) at a frequency of 500 MHz was used, spatially located with a SPEAR heating facility (Robinson et al., 2006; Dhillon et al., 2007). The measurements of ESR provided detailed information on the spatial and temporal variations in the ionospheric plasma parameters (density and temperature of electrons: N_e and T_e) in an artificially disturbed region of the ionosphere above the SPEAR facility. During the experiments, the ESR operated along the direction of the magnetic field in Longyearbyen (magnetic zenith).

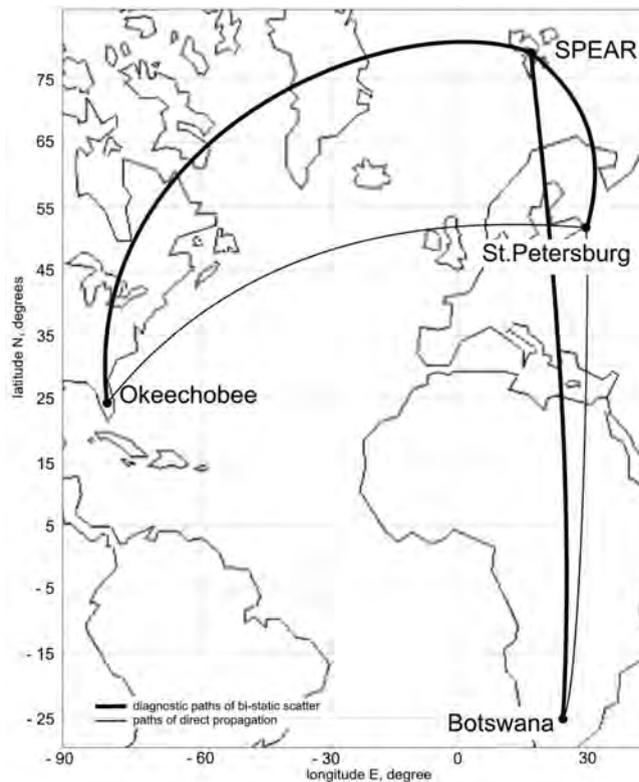


Fig. 4.1.1. Map explaining the geometry of the SPEAR heating facility location and the diagnostic paths of bi-static scatter used in the experiments, as well as the paths of direct propagation of signals from transmitters to the receiver along the great-circle.

The data of magnetic and ionospheric observations in Longyearbyen, Spitsbergen, (magnetometer and ionosonde) were used to assess the background geophysical conditions. Ionograms of vertical ionosphere sounder were taken once every four minutes in pauses between heater-on cycles.

RESULTS AND DISCUSSION

Okeechobee (USA)–SPEAR–St. Petersburg radio path

On 7 October 2010, the Scientific Research Center (SRC) Gorkovskaya, on the Okeechobee (USA)–SPEAR–St. Petersburg radio path 9210 km long, recorded HF radio signals, bi-static scattered by small-scale artificial ionospheric irregularities created in the ionosphere above SPEAR facility with the help of powerful HF radio wave of extraordinary (X -mode) polarization.

Fig. 4.1.2 *a* shows a sonogram of the HF radio signal on the Okeechobee (USA)–SPEAR–St. Petersburg radio path at frequency $f_{diag} = 13695$ kHz from 12:51 to 13:37 UT. Zero Doppler frequency f_D corresponds to the propagation of a signal from Okeechobee to St. Petersburg along the great-circle (“direct” signal). A powerful HF radio wave of X -mode polarization was emitted at a frequency of 4450 kHz towards the magnetic zenith by cycles of 5 min on, 5 min off.

Fig. 4.1.2 *a* shows that bi-static scattered signals were recorded in the heater-on cycles; they were characterized by strong diffuseness. The values of Doppler frequency f_D of bi-static scattered HF signals were mostly negative in the range from 0 to 9 Hz (except for the cycle 12:50–12:55 UT, when scattered signals were recorded both in negative and positive values of f_D).

Fig. 4.1.2 *b* shows variations in the spectral power S of the scattered HF radio signals calculated from the measured Doppler spectra for the considered observation session on 7 October 2010. The behavior of the spectral power S demonstrates its increase during the emission periods of the SPEAR facility. Fig. 4.1.2 *c* shows the temporal variations of the maximum plasma frequencies of the ionospheric layer F2 (foF2), calculated from the data of the ESR. The control of variations in the parameters of the ionospheric plasma during the operation of the SPEAR facility with the X -mode polarization was carried out by using the ESR (EISCAT Svalbard Radar) in Longyearbyen. They used the “ipy” ESR operating mode, which provided measurements every 5 s with an altitude resolution of 3–6 km in the altitude range from 90 to 500 km. For the analysis, the time variations of the data of ionospheric observations by the ESR were averaged by 30-second intervals.

Fig. 4.1.3 shows the altitude-time distributions of the electron density N_e electron temperature T_e from ESR in the altitude range from 100 to 475 km during the experiment on 7 October 2010. The figure shows changes in the electron density distribution N_e and temperature T_e along the height, related to heater-on cycles. The most significant increases N_e were observed in the layer 140–180 km, i.e., below the height of the maximum of the F2 layer ($h_m F2 \sim 225$ – 235 km). Simultaneously increasing the density N_e occurred at height $hF2$, and also significantly weaker – higher $h_m F2$, up to the height 350–375 km. In some heater-on cycles (13:00–13:05 and 13:20–13:25 UT), an increase in the electron temperature T_e was observed at the height of 200–300 km. Please note that changes in N_e and T_e during heater-on cycle 13:30–13:35 UT appeared before the facility started run and intensified during the cycle.

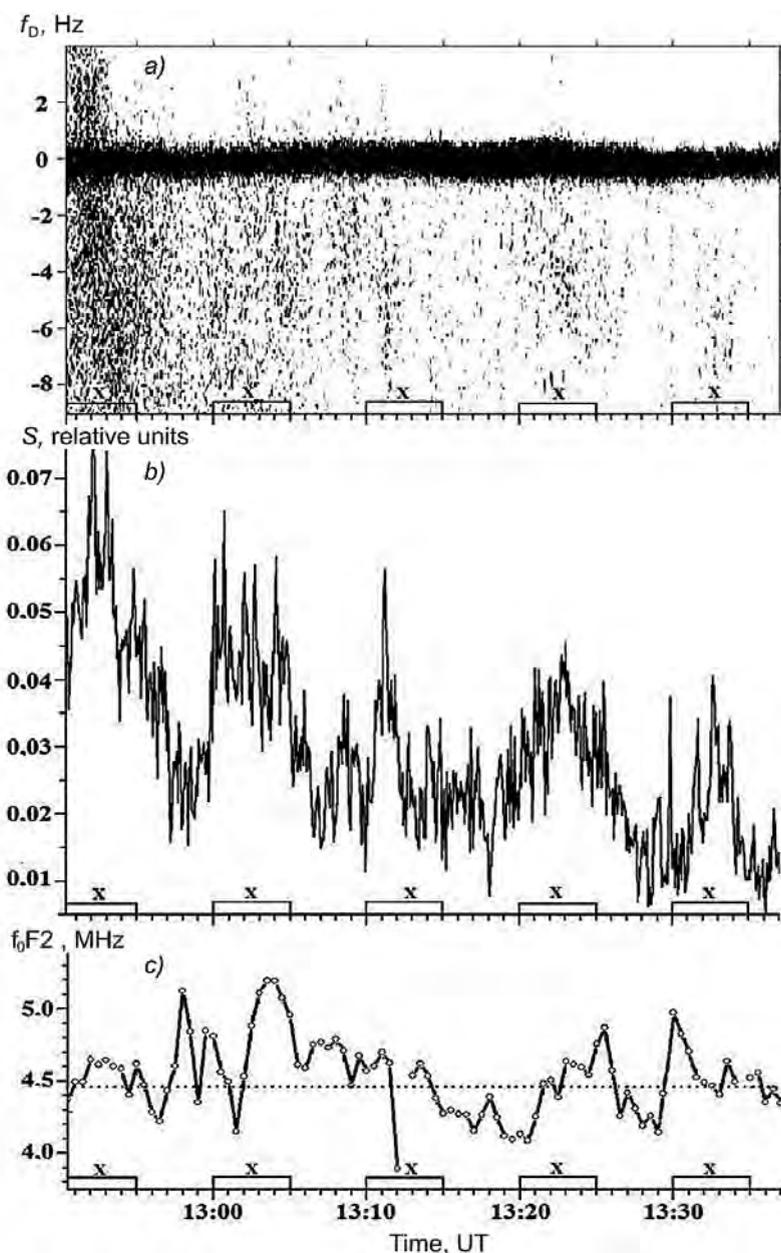


Fig. 4.1.2. Observation results during the experiment at the SPEAR facility on 7 October 2010 from 12:51 to 13:37 UT.

a) Dynamic Doppler spectra (sonogram) of diagnostic HF signals on the Okeechobee–SPEAR–St.Petersburg radio path at frequency $f_{diag} = 13695$ kHz; b) time variations in the spectral power of scattered HF signals on the Okeechobee —SPEAR–St.Petersburg radio path at frequency $f_{diag} = 13695$ kHz; c) time variations of the maximum plasma frequencies of the ionospheric layer $F2$, f_0F2 , calculated from the data of the ESR in Longyearbyen; dashed line – heating frequency; heater-on cycles and polarization of powerful HF radio waves are marked on the time axis.

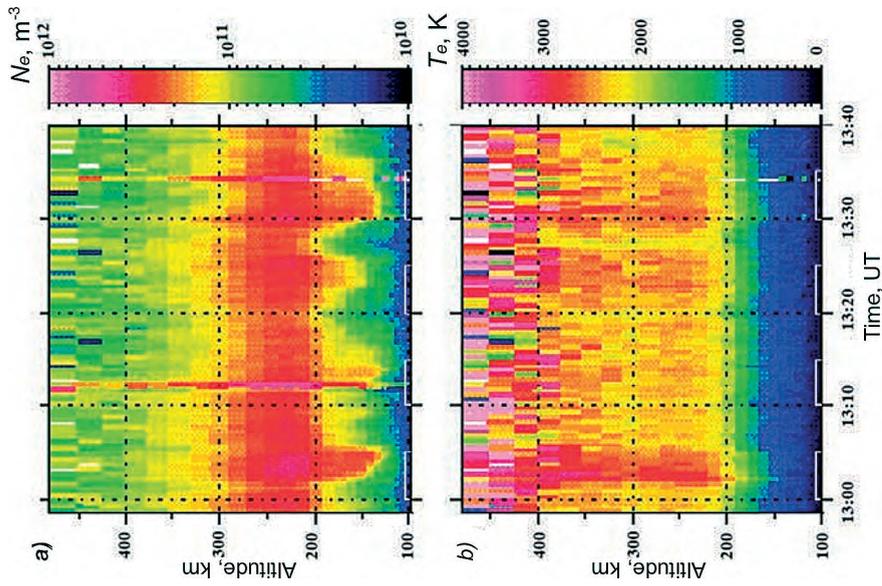


Fig. 4.1.3. Altitude-time distributions of the electron density N_e and temperature T_e as per ESR in (Longyearbyen) during the heating experiment on 7 October 2010 from 12:58 to 13:40 UT, obtained with 30-second integration time.

A powerful HF radio wave of X-mode polarization was emitted at a frequency of 4450 kHz towards the magnetic zenith. Heater-on cycles are marked on the time axis.

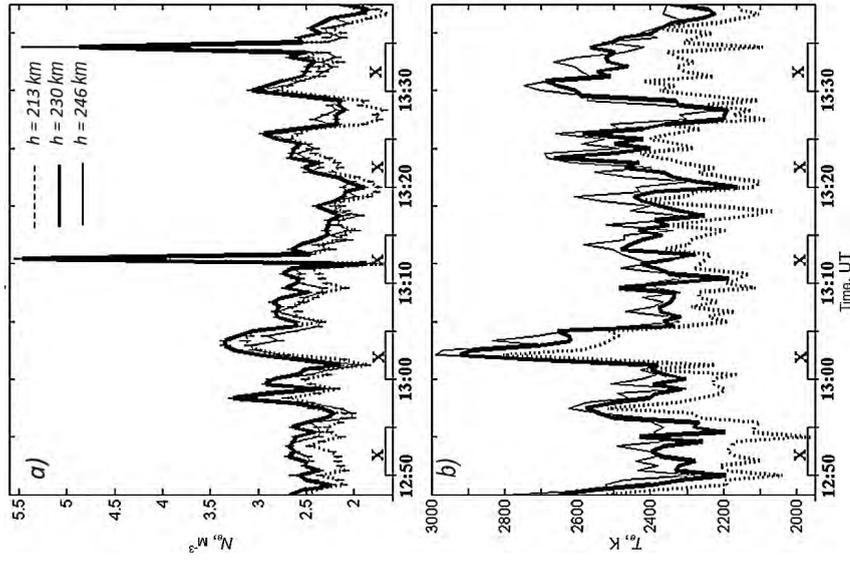


Fig. 4.1.4. Variations in electron temperature T_e (a) and density N_e (b) as per ESR at heights of 213, 230 and 246 km during the heating experiment on 7 October, 2010, from 12:51 to 13:37 UT.

The behavior of electron density N_e and temperature T_e , measured by ESR on 7 October 2010 at fixed heights of 213, 230 and 246 km, close to the maximum of the F2 layer are shown in Fig. 4.1.4. Fig. 4.1.4a shows that N_e value increases by about 20 % in the heater-on cycle 13:20–13:25 UT and by 15 % compared to background values before the heater-on cycle at 13:30–13:35 UT. The heater-on cycle at 13:00–13:05 UT showed a decrease in N_e at first. Then, from 13:01:30 to 13:05 UT, it increased.

Fig. 4.1.4 *b* shows that electron temperature T_e increases the layer F2 maximum during heater-on cycles with X-mode polarization at 13:00–13:05 UT, 13:20–13:25 UT и 13:30–13:35 UT. The value of T_e increased on average by 200–400 K relative to background values.

Let us consider the behavior of the height profiles of the electron density $N_e(h)$ in the heater-on cycles with X-mode polarization on 7 October 2010, from 12:50 to 13:35 UT. $N_e(h)$ -profiles shown in Fig. 4.1.5 in units of the plasma frequencies $f_p(h) = 8.98 \cdot N_e^{1/2}$. Please, note that the critical frequency of the regular layer E (foE) in the period from 12:50 to 13:38 UT was about 1.7–1.9 MHz, with the location of the layer maximum at the height of 120–125 km.

In the heater-on cycle at 12:50–12:55 UT, when the most intense bi-static scattered signals of the diagnostic transmitter from Okeechobee (see Fig.4.1.2) were observed, no sharp changes in the distributions of $f_p(h)$ -profiles (see Fig. 4.1.5 *a*) were observed. The critical frequencies of the F2 layer were 4.4–4.45 MHz before heating, and during the heater-on cycle foF2, they increased by 0.2–0.3 MHz. Heating frequency $f_H = 4450$ kHz was comparable to the values of the critical frequencies of foF2. After the end of the emission cycle, profile $f_p(h)$ recovered to the background state within one minute. In the interval 12:56–12:59 UT, there were sharp changes in the distributions of the ionospheric parameters $f_p(h)$ and $T_e(h)$ of a natural character.

In subsequent heater-on cycles at X-mode polarization from 13:00 to 13:35 UT (see Fig.4.1.5 *b–d*), in addition to an increase in foF2 by about 0.5 MHz, sporadic ionization layers appeared at the height of 140–180 km, with critical frequencies up to 4.3 MHz. Simultaneously with the appearance of sporadic ionization at the height below the maximum of the F2 layer, there was an increase in the electron temperature T_e at the height of the F2 layer. The height of the formation of the T_e maxima in the ionosphere corresponded to the height of the electron density maxima of the F2 layer or exceeded it by no more than 10–15 km.

To analyze and interpret the results of experimental measurements on an extended HF radio path, taking into account the bi-static scatter of radio waves at the AFAI in the ionosphere above SPEAR; ray tracing simulation was carried out on the Okeechobee (USA)–SPEAR–St. Petersburg radio path. We used a model developed at the AARI (Borisova et al., 2002; Borisova, 2014) for the calculations. The modeling is implemented within the approximation of a two-scale expansion of the geometrical optics method, which takes into account smooth horizontal ionospheric irregularities. The input parameters of the HF radio channel model are the level of solar activity, characterized by the Wolf number (W); the level of magnetic activity, represented by the three-hour index (K_p); time of day (t); day of the year; geographic coordinates of the transmitter and receiver of the diagnostic signal; geographic location coordinates of the SPEAR heating facility.

During the modeling, we searched for trajectories that implement the reception of diagnostic HF radio signals in St. Petersburg, taking into account the bi-static scatter

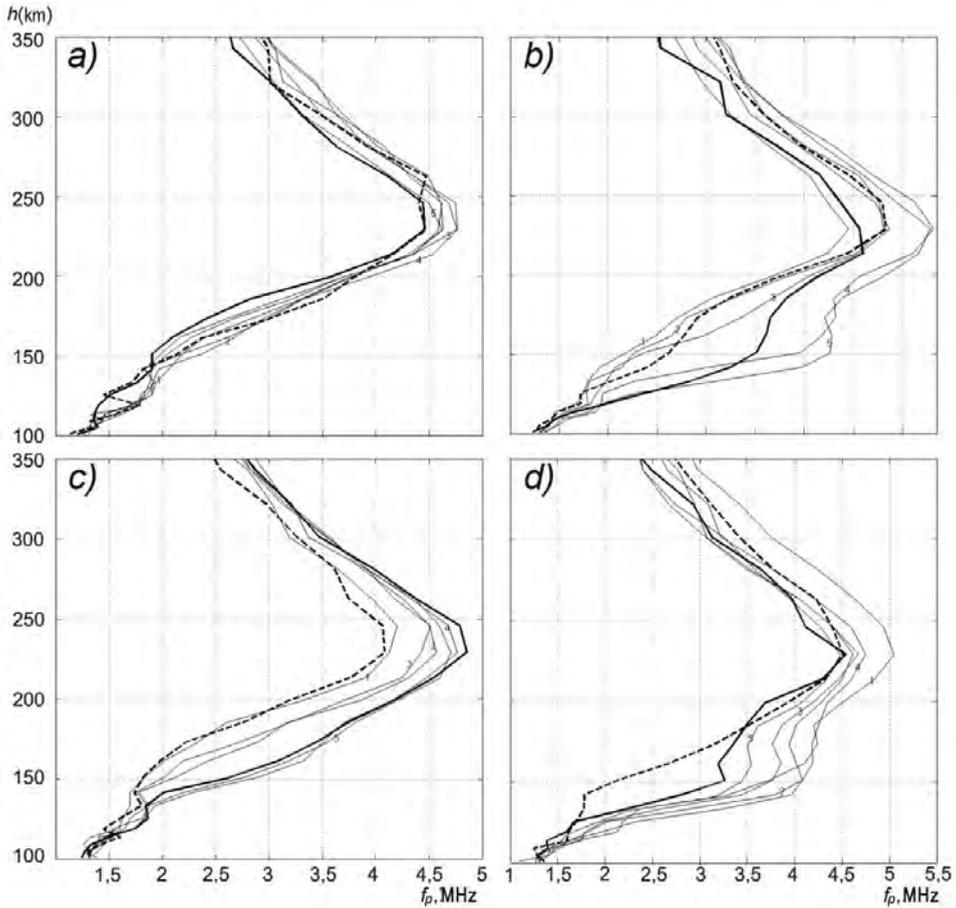


Fig. 4.1.5. The altitude profiles of the ionospheric electron density according to the data of the ESR, presented in units of the ionospheric plasma frequencies, for 7 October 2010 for the emission cycles of the SPEAR facility: *a*) from 12:50 to 12:55 UT; *b*) from 13:00 to 13:05 UT; *c*) from 13:20 to 13:25 UT; *d*) from 13:30 to 13:35 UT.

The thin curves show the profiles averaged by 1 min in the heater-on cycle; the numbers indicate the minutes of the heater-on cycle. Bold dashed curves – profiles before the heating session, solid curves – profiles after the session.

by artificial ionospheric irregularities above the SPEAR facility. The calculations were carried out for geophysical conditions corresponding to the conditions of the experiments at the SPEAR facility. The ionosphere model was corrected according to real data of vertical ionosphere sounder (VIS) in Longyearbyen and St. Petersburg. The results of calculating the propagation trajectories of HF radio signals showed that taking into account the distributions of the natural gradients of the ionosphere for HF radio signals from Okeechobee, propagation paths arose due to bi-static scatter on small-scale ionospheric irregularities above SPEAR.

Fig. 4.1.6 shows the calculated propagation trajectories of diagnostic signals from Okeechobee at a frequency of 13695 kHz received in St. Petersburg after bi-static scatter at the AFAI, created in the F-layer of the polar ionosphere above the SPEAR heating

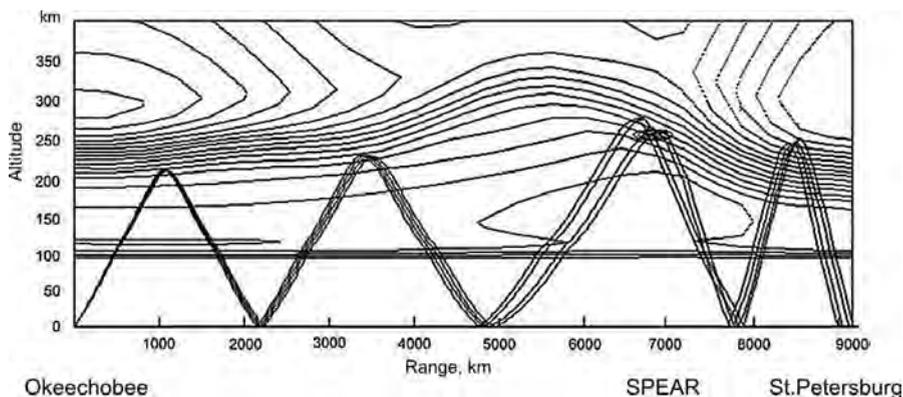


Fig. 4.1.6. The calculated propagation trajectories of diagnostic signals from Okeechobee at a frequency of 13695 kHz received in St. Petersburg after bi-static scatter at the AFAI, created in the F-layer of the polar ionosphere above the SPEAR heating facility for geophysical conditions at 13.00 UT on 7 October 2010.

facility. The calculations were carried out for geophysical conditions at 13:00 UT on 7 October 2010. The simulation results showed that the signals scattered by the AFAI in the F-layer of the ionosphere hit the receiving point through intermediate reflection from the Earth, and then from the ionosphere.

Experimental studies of the ionosphere modification induced by powerful HF radio waves with the X-mode of polarization of the SPEAR facility were carried out on 7 October 2010 in the daytime under favorable geomagnetic conditions ($K_p \approx 1$). Measurement data of the parameters of the background polar ionosphere on Spitsbergen (when SPEAR heating facility didn't work) showed a great variability of its regular characteristics and a high probability of diffuse formations at heights of the F2 layer with a partly inhomogeneous distribution of the ionospheric plasma density, which is typical for the polar ionosphere above SPEAR (Robinson et al., 2006) The influence of such large-scale features of the polar ionosphere as cleft/cusp, terminator, and auroral zone during heating experiments should also be noted.

The high variability of the polar ionosphere, along with the inevitable drift of the plasma even in weak natural electric fields or because of neutral winds, will mean that the plasma in the emission cycles of the heating facility will not be continuously heated, and, therefore, the conditions for the excitation of instability may not be met or violated due to rapid variability during a complete heater-on cycle. Plasma density changes can also lead to sharp local fluctuations in the electric field of the heating wave so that the threshold levels required to create instabilities could only be exceeded for short time intervals during the heater-on cycle.

Please, note that the maximum effective radiated power of the SPEAR facility is rather low ($P_{eff} = 15$ MW), while for EISCAT/Heating facility in Tromsø $P_{eff} = 190\text{--}250$ MW with the use of phased array No. 2, providing the antenna beam width of $12\text{--}14^\circ$. The above factors can explain the instability of the ionospheric response in experiments using the SPEAR heating facility.

During the experiment, small-scale artificial ionospheric irregularities during X-heating were created at heating frequencies both above and below the critical frequency of the F2 layer.

According to the measurements of the parameters of the polar ionosphere using the ESR in Longyearbyen, Spitsbergen, an increase in electron density N_e temperature T_e was observed at all cycles when AFAI were excited. An interesting and unexpected feature in the behavior of the altitude profiles of the electron density $N_e(h)$ was the formation of sporadic ionization at an altitude of 140–180 km under favorable geomagnetic conditions.

The analysis of the height $N_e(h)$ -profiles showed that there is a relationship between the time when additional ionization appears in the layer 140–180 km and the period of heater-on cycles of the SPEAR.

Numerical estimates of possible changes in electron density $\delta N_e/N_e$ due to the violation of the ionization-recombination balance during the heating of the ionospheric plasma in the field of a powerful wave using data from the works by Gurevich and Schwarzburg (1973), Shunk and Nagy (2000) and modeling data from the atmospheric model MSIS-E-90 (http://omniweb.gsfc.nasa.gov/vitmo/msis_vitmo.html) amounted to: $\delta N_e/N_e \approx 5\%$ at the height of 160 km and $\delta N_e/N_e \approx 2\%$ at a height of 225 km. According to the results of measurements by the ESR at the height of 161–163 km, the increase in $\delta N_e/N_e$ reached 50–200% in heater-on cycles in the time interval 13:00–13:35 UT.

We can assume that an increase in the electron density N_e at the height of 140–180 km on 7 October 2010 after 13:00 UT is caused by an increase in the intensity of natural precipitating particle fluxes with electron energies from hundreds of electron-volts to 1–2 keV, initiated by the effects of a powerful HF radio wave on the polar ionosphere. An increase in the flux intensity in heater-on cycles from 13:00 UT is confirmed by an increase in the integral Hall and Pedersen height-integrated conductivities in heater-on cycles.

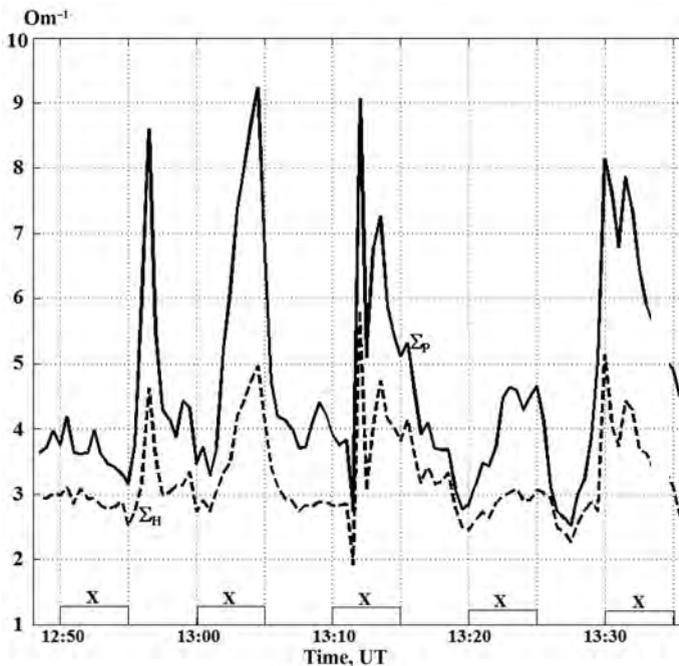


Fig. 4.1.7. Variations of the altitude-integrated Hall Σ_H and Pedersen Σ_P height-integrated conductivities of the ionosphere in the period from 12:48 to 13:32 UT on 7 October 2010, calculated from the data of the ESR in Longyearbyen for a height range of 80 to 350 km.

Fig. 4.1.7 shows the results of calculations of the height-integrated Hall Σ_h and Pedersen Σ_p conductivities (Lyatsky and Maltsev, 1983) based on the data of ionospheric measurements by the ESR in the layer from 80 to 350 km. The calculation results demonstrate an increase in the ionospheric conductivity Σ_p in four successive heater-on cycles from 13:00 UT. In the interval 12:55–13:00 UT (pause between heater-on cycles), the increase in Σ_h and Σ_p is due to the natural precipitation of electrons.

Botswana (South Africa)–SPEAR–St. Petersburg radio path

Measurements on the Botswana (South Africa)–SPEAR–St. Petersburg radio path, 13150 km long, were carried out on 29 January 2006, in the late evening hours under favorable magnetic conditions (Fig. 4.1.8). During the experiment, the HF SPEAR heating facility emitted at a frequency of 4450 kHz towards the magnetic zenith in cycles of 2 min on – 2 min off.

In contrast to the experiment on 7 October 2010, they used not the *X*-mode, but the *O*-mode polarization of a powerful HF radio wave to create artificial field-aligned irregularities (AFAI) on 29 January 2006. Fig. 4.1.8 shows the dynamic Doppler spectra (sonograms) of the heating signal at a frequency of 4,450 kHz, received in St. Petersburg, as well as diagnostic HF signals at Botswana (South Africa)–SPEAR–St. Petersburg radio path at frequency $f_{diag} = 17895$ kHz on 29 January 2006 from 18:50 to 19:50 UT.

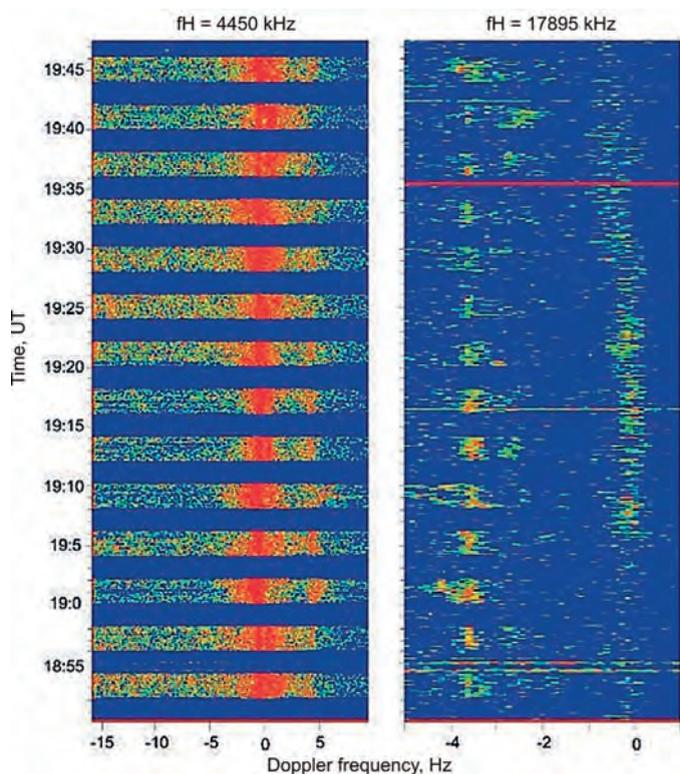


Fig. 4.1.8. Dynamic Doppler spectra (sonograms) of the heating signal at a frequency of 4,450 kHz, received in St. Petersburg, as well as diagnostic HF signals at Botswana (South Africa)–SPEAR–St. Petersburg radio path at frequency $f_{diag} = 17895$ kHz on 29 January 2006 from 18:50 to 19:50 UT.

The figure shows that while the SPEAR facility emitted signals, intense signals were recorded on this radio path; they were shifted in Doppler frequency by about 3.7 Hz relative to the zero frequency corresponding to the propagation of a radio wave at a frequency of 17895 kHz from Botswana to St. Petersburg along the great-circle. The spectra were rather narrow-band: their width did not exceed 1.5 Hz. The appearance of these additional signals in heater-on cycles is due to the bi-static scatter of the diagnostic signal at a frequency of 17895 kHz by artificial field-aligned irregularities (AFAI) in the F-layer of the polar ionosphere above the SPEAR facility. During the experiment, artificial field-aligned irregularities during *O*-heating were created at a heating frequency below or near the critical frequency of the F2 layer.

Zero Doppler frequency corresponds to the propagation of the diagnostic signal along the great-circle. A powerful HF radio wave of *O*-mode polarization was emitted towards the magnetic zenith by cycles of 2 min on, 2 min off.

To interpret the results of the experiment, we simulated the characteristics of the radio wave propagation trajectories using the model presented in Borisova et al. (2002) and Borisova (2014). The results of calculating the propagation trajectories of HF radio signals showed that HF radio signals from Botswana could fall on an artificially disturbed region of the ionosphere above the SPEAR facility and then, after bi-static scatter at the AFAI, reach a receiving point in St. Petersburg. Comparison of the characteristics of bi-static scattered signals on long-range radio paths during *O*- and *X*-heating showed that the intensity of the scattered signals is higher during *O*-heating, and the width of the Doppler spectra is smaller than during *X*-heating.

CONCLUSIONS

The experimental results related to the impact of artificial field-aligned irregularities (AFAI) in the polar ionosphere, excited by the HF heating facility SPEAR (Longyearbyen, Spitsbergen), on the propagation of decameter radio waves along long paths are presented. The measurements were carried out on two paths Okeechobee (USA)–SPEAR–St. Petersburg, 9210 km long, and Botswana (South Africa)–SPEAR–St. Petersburg, 13150 km long under favorable magnetic conditions.

It is shown that the bi-static scattered signals in heater-on cycles were recorded when the polar ionosphere was exposed to a powerful HF radio wave, with both ordinary (*O*-mode) and extraordinary (*X*-mode) polarization. During *O*-heating, the signals scattered from AFAI were recorded at frequencies below or near the critical frequency of the F2 layer. During *X*-heating, the AFAI were excited at heating frequencies both below and above foF2. Analysis of the characteristics of bi-static scattered signals from AFAI showed that the intensity of the scattered signals is higher during *O*-heating, and the width of the Doppler spectra is smaller than during *X*-heating.

Numerical modeling of the propagation parameters of diagnostic HF radio waves has been performed, which demonstrated the possibility of signal reception in St. Petersburg by the bi-static scatter method on long distance radio paths in the course of SPEAR heating experiments.

REFERENCES

Blagoveshchenskaya N.F., Baranets A.N., Borisova T.D., Bubnov V.A. The effects of the deviation of decameters of radio waves from the great-circle at high latitudes of the ionosphere. University News. Radiophysics. 1991, 34 (2): 119–122. [In Russian].

- Blagoveshchenskaya N.F., Borisova T.D., Kornienko V.A. et al.* Phenomena in the polar ionosphere initiated by the action of powerful HF radio waves of the SPEAR facility. University News. Radiophysics. 2008, 51 (11): 939–950. [In Russian].
- Blagoveshchensky D.V., Borisova T.D., Kalishin A.S.* Nonstandard (lateral) propagation modes on a high-latitude short-wave radio path. University News. Radiophysics. 2009, 52 (4): 1–12. [In Russian].
- Blagoveshchensky D.V., Zherebtsov G.A.* High-latitude geophysical phenomena and prediction of short-wave radio channels. Moscow: Nauka, 1987: 272 p. [In Russian].
- Blagoveshchensky D.V.* *Rasprostranenie dekametrovyykh radiovoln vo vremya geomagnitnykh vozmushchenij. Uchebnoe posobie.* Propagation of decameter radio waves during geomagnetic disturbances. Training book. St. Petersburg: GUAP, 2011: 393 p. [In Russian].
- Borisova T.D.* *Programmnoe obespechenie dlja modernizacii parametrov KV radiokanala, uchiyvajushchee jeffekty modifikacii vysokoshirotnoj ionosfery pri vozdeystvii moshhnykh KV radiovoln, predstavljajushchee model' KV radiokanala (CHATRASCA: TRASSA i CHANNEL).* Software for upgrading the parameters of the HF radio channel, taking into account the effects of the modification of the high-latitude ionosphere when exposed to powerful HF radio waves, representing the model of the HF radio channel (CHATRASCA: TRASSA и CHANNEL). Certificate of state registration of computer programs No. 2014618249, 2014. [In Russian].
- Borisova T.D., Blagoveshchenskaya N.F., Kalishin A.S. et al.* Modification effects of the polar ionosphere by powerful short-wave radiowave of extraordinary polarization of the SPEAR heating facility. *Izvestija vuzov. Radiofizika.* University News. Radiophysics. 2012, 55 (1–2): 140–157. [In Russian].
- Gurevich A.V., Schwarzburg A.B.* *Nelinejnaja teorija rasprostraneniya radiovoln v ionosfere.* Nonlinear theory of propagation of radio waves in the ionosphere. Moscow: Nauka, 1973: 272 p. [In Russian].
- Lyatsky V.B., Maltsev Yu.P.* *Magnitosferno-ionosfernoe vzaimodejstvie.* Magnetospheric-ionospheric interaction. Moscow: Nauka, 1983: 278 p. [In Russian].
- Blagoveshchenskaya N.F., Borisova T.D., Kornienko V.A. et al.* SPEAR-induced field-aligned irregularities observed from bi-static HF radio scattering in the polar ionosphere. *J. Atmos. Sol. Terr. Phys.* 2009, 71: 11–20.
- Blagoveshchensky D.V., Borisova T.D., MacDougall J.W.* Irregular HF radio propagation on a subauroral path during magnetospheric substorms. *Ann. Geophys.* 2006, 24 (7): 1839–1849.
- Borisova T.D., Blagoveshchenskaya N.F., Moskvina I.V. et al.* Doppler shift simulation of scattered HF signals during the Tromsø HF pumping experiment on 16 February 1996. *Ann. Geophys.* 1996, 20: 1479–1486.
- Dhillon R.S., Robinson T.R., Yeoman T.K.* EISCAT Svalbard radar observations of SPEAR-induced E- and F-layer spectral enhancements in the polar cap. *Ann. Geophys.* 2007, 25: 1801–1814.
- Hunsucker R.D., Hargreaves J.K.* *The high-latitude ionosphere and its effects on radio propagation.* Cambridge University Press, 2003: 477–482.
- Robinson T.R., Yeoman T.K., Dhillon R.S. et al.* First observations of SPEAR-induced artificial backscatter from CUTLASS and EISCAT Svalbard radars. *Ann. Geophys.* 2006, 24: 291–309.
- Schunk R.W., Nagy A.* *Ionospheres: physics, plasma physics, and chemistry.* Cambridge University Press, 2000: 554 p.
- Siddle D.R., Stocker A.J., Warrington E.M.* The time-of-flight and direction of arrival of HF radio signals received over a path along the mid-latitude trough: observations. *Radio Sci.* 2004, 39. RS4008; DOI:10.1029/2004RS003049.
- Stocker A.J., Warrington E.M., Jones T.B.* A comparison of observed and modeled deviations from the great circle direction for a 4490 km HF propagation path along the mid-latitude ionospheric trough. *Radio Sci.* 2003, 38: 1045; DOI: 10.1029/2002RS002RS002781.
- Yeoman T.K., Blagoveshchenskaya N.F., Kornienko V.A. et al.* SPEAR: Early results from a very high latitude ionospheric heating facility. *Adv. Space Res.* 2007, 40: 384–389.

4.2. POLAR IONOSPHERE MODIFICATION INDUCED BY POWERFUL HF RADIO WAVES: STUDY RESULTS ON SPITSBERGEN ARCHIPELAGO

N.F. Blagoveshchenskaya, T.D. Borisova, A.S. Kalishin

A theoretical basis for the ionosphere modification induced by powerful HF radio waves was formulated in the 60s–70s of the last century by V.L. Ginzburg and A.V. Gurevich (Ginzburg, 1967; Gurevich and Schwarzburg, 1973). Experiments on the effect of powerful HF radio waves on the ionosphere with the use of specially constructed ground-based HF radio transmitters with high effective radiated power became an important stimulus to develop this study direction P_{eff} ($P_{eff} = P \cdot G$, where P – power supplied to the antenna; G – antenna gain). The first such experiments were carried out in 1970 in the USA at heating facility in Boulder ($P_{eff} = 100$ MW) and Arecibo ($P_{eff} = 60$ MW), as well as in 1973 in the USSR at the heating facility in Zimenki, near Nizhny Novgorod ($P_{eff} = 20$ MW). The controlled injection of powerful HF radio waves into the ionosphere has opened up a fundamentally new possibility of conducting laboratory-type experiments for studying plasma physics, which can be performed regularly.

Since the 2000s, interest in studies of the effects of powerful HF radio waves on the high-latitude ionosphere has greatly increased. It is mostly due to the completion of construction and experimentation at the super-powerful HF heating facility at Gakona, Alaska, USA (HAARP project) (Sheerin and Cohen, 2015). Research at the EISCAT / Heating facility was also significantly intensified (Rietveld et al., 2016).

A powerful HF radio wave of ordinary polarization (*O*-mode) effectively interacts with the surrounding ionospheric plasma in the *F2* layer in the range between the reflection height of a powerful HF radio wave ($f_0^2 = f_H^2$) and the height of the upper hybrid resonance ($f_{UH}^2 = f_H^2 - f_{ce}^2$, where f_H and f_{ce} heating frequency and electron gyrofrequency, respectively), leading to the excitation of parametric decay (striction) and thermal parametric (resonance) instabilities, which cause the generation of various phenomena in the ionospheric plasma. These phenomena include intense excitation of plasma waves, an increase in the electron temperature, generation of artificial field-aligned irregularities and stimulated electromagnetic emission (SEE) from the ionosphere, electron acceleration of background plasma to superthermal velocities, which, in turn, leads to artificial optical emissions from the disturbed region of the ionosphere and artificial ionization of plasma (Robinson, 1989; Gurevich, 2007; Grach et al., 2016).

Generally, the ordinary polarization (*O*-mode) of a powerful HF radio wave is used to modify the *F*-layer of the ionosphere. It is explained by the fact that, per theoretical concepts, a powerful HF wave of extraordinary polarization (*X*-mode) cannot excite artificial ionospheric turbulence in the *F*-layer. A powerful HF radio wave of *X*-mode polarization reflected at height with local plasma frequency $f_X^2 = f_H(f_H - f_{ce})$, which is lower as the reflection heights of the HF radio wave of *O*-polarization ($f_0^2 = f_H^2$), as well as the height of the upper hybrid resonance ($f_{UH}^2 = f_H^2 - f_{ce}^2$). As a result, the excitation of artificial field-aligned irregularities (AFAI) due to thermal parametric (resonance) instability is also impossible. Nevertheless, the results of numerous experiments carried out by AARI specialists at the EISCAT / Heating HF heating facility in Tromsø, Northern Norway, have clearly demonstrated that a powerful HF radio wave of extraordinary polarization

(*X*-mode), injected into the high-latitude *F*-layer of the ionosphere in a parallel magnetic field (into the magnetic zenith), causes the generation of AFAI at heating frequencies both below and above the critical frequency of the ordinary component of the *F2* layer ($f_H/f_0F2 \leq 1$ and $f_H/f_0F2 > 1$) (Blagoveshchenskaya et al., 2011; 2013; 2015).

In 2004, a SPEAR (Space Plasma Exploration by Active Radar) heating facility was built near Longyearbyen on Spitsbergen (Robinson et al., 2006). SPEAR differs significantly from all previously built and operating HF heating facilities. First, SPEAR has no analogs in the world in terms of its geographical location and is the highest latitude HF heating facility (78.15 °N, 16.05 °E, a magnetic inclination $I = 82^\circ$). Second, the modification medium itself (the polar ionosphere) differs significantly not only from the mid-latitude zone but also from the auroral zone located south of the polar cap ionosphere. Note that the EISCAT / Heating facility at Tromsø is located in the auroral zone at night, while the HAARP facility in Alaska appears in the auroral ionosphere only at night under disturbed magnetic conditions. The polar ionosphere is characterized by strong variability of its parameters even under quiet magnetic conditions. Depending on the background geophysical conditions and local magnetic time, the SPEAR facility can be located either on the dayside auroral zone or in the polar cap. Therefore, it is of interest to study the phenomena initiated by the modification of the polar ionosphere under conditions when there are strong variations in the critical frequencies, even over relatively short time intervals.

In this research, we generalize the results of experimental studies of the AARI at Spitsbergen on the impact of powerful HF radio waves (SPEAR heating facility) on the polar ionosphere, partially published in the works of Blagoveshchenskaya et al. (2008); Blagoveshchenskaya et al. (2009); Yeoman et al. (2007); Borisova et al., (2009, 2012). In 2005–2007, the experiments were performed for several observation days, which were part of the heating campaigns carried out by the University of Leicester (UK) at Spitsbergen. In 2010–2013, the experiments were carried out within the framework of the Norwegian-Russian cooperation on the Polar Research Program (POLRES), project SPEAR–UNIS–AARI, number ES446799 (Study of Non-linear Phenomena in the Polar Ionosphere Induced by the SPEAR Heating Facility). Below, we consider the features of the behavior of artificial field-aligned irregularities and stimulated electromagnetic emission of the ionosphere based on the AARI experiments on modifying the polar ionosphere using the SPEAR facility. An analysis has been made of the characteristics of AFAI excited both in the *F*-layer of the polar ionosphere and in the “thick” sporadic E_s -layer upon pumping a powerful HF radio wave of ordinary polarization (*O*-mode) into the magnetic zenith. Attention is also paid to the study if it is possible to excite the AFAI by a powerful HF radio wave of extraordinary polarization (*X*-mode). Another aspect of this work concerns the study of stimulated electromagnetic emission of the ionosphere both in the *F*- and *E*-layers of the polar ionosphere under conditions of the wide variability of the critical frequencies of the *F2* and E_s layers.

DESCRIPTION OF EXPERIMENTS AND METHODS OF OBSERVATION

To modify the polar ionosphere, the SPEAR HF heating facility was used, the technical characteristics of which are given in Robinson et al. (2006). The effective radiated power of the heating facility is $P_{eff} = 15$ MW. The Antenna beam pattern was tilted 8° south of the vertical, providing a powerful HF radio wave towards the magnetic zenith. According to experimental and theoretical studies (Gurevich, 2007; Rietveld et al., 2003), the strongest disturbances of the ionospheric plasma arise precisely in the direction of

the magnetic flux tube, which based directly on the location of the heating facility. In experiments carried out in 2005–2007 (December 2005, July and December 2006, February and March 2007), a powerful HF radio wave of ordinary polarization (*O*-mode) was emitted at a frequency of 4450 kHz in heater-on cycles 2 – min on – 2 min off; 4 min on – 2 min off; 4 min on – 4 min off. In some observation sessions, continuous emission of a powerful radio wave was carried out for 48 minutes, starting from the 12th minute of every hour.

In the framework of the Norwegian-Russian cooperation on the Polar Research Program (POLRES), the SPEAR–UNIS–AARI project, experiments were carried out in October 2010, 2011, and 2012. Emission of a powerful HF radio wave of ordinary (*O*-mode) or extraordinary (*X*-mode) polarization was carried out at frequencies f_H equal to 4450, 4600, and 4900 kHz to the magnetic zenith (the antenna beam pattern was tilted to the south by 8°). The maximum effective radiated power was $P_{eff} = 15$ MW. Basically, the heater-on cycles were 5 min on – 5 min off. For experimental conditions when the *X*-wave was emitted, the “leakage” of the *O*-mode wave did not exceed 10–15 %.

The diagnostics of the phenomena initiated by the action of powerful HF radio waves of the SPEAR facility on the polar ionosphere was carried out by the following methods and means.

A multi-channel HF Doppler equipment (Blagoveshchenskaya et al., 2008), designed to register heating HF signals from the SPEAR facility and diagnostic HF radio signals by bi-static scatter (BS) on artificial field-aligned irregularities. The equipment was installed at the AARI Gorkovskaya observatory, located at a distance of 70 km from St. Petersburg and about 2000 km from the SPEAR facility. Signals scattered over the SPEAR facility were received by a double rhombic antenna oriented towards the SPEAR facility. The measurements were carried out on the radio paths London–SPEAR–St. Petersburg (at frequencies of 11820, 11955, 12095, 15485 and 17700 kHz), Pori–SPEAR–St. Petersburg (at frequencies 11755 and 15400 kHz) and Sitkunai (Lithuania)–SPEAR–St. Petersburg (at a frequency of 9710 kHz). During the experiments discussed below, spectral processing was carried out using the fast Fourier transform (FFT) method using the Hamming window. The sampling frequency was 102 Hz, providing a spectral analysis bandwidth of 51 Hz. 512 FFT coefficients were calculated, which provided a frequency resolution of 0.1 Hz. A 50 % overlap of the samples used to calculate the FFT coefficients was applied, which made it possible to obtain a Doppler spectrum every 5 seconds.

Equipment for registration of stimulated electromagnetic emission of the ionosphere (SEE) (Blagoveshchenskaya et al., 2008), installed in Barentsburg Spitsbergen, in close proximity of the SPEAR HF heating facility (about 40 km). The facility for registration of SEE provided one distribution (1000 amplitude values of the heating signal) in a 100 kHz band in less than 20 s. Scanning was performed in cycles within a given frequency range.

HF radar system CUTLASS (SUPERDARN) in Finland and Iceland (Lester et al., 2004); both CUTLASS radars emitted to a narrow beam antenna with a beam width of approximately 3.3°, oriented towards the artificially disturbed region of the ionosphere over Longyearbyen (“beam” 9 and 5 for radars in Finland and Iceland, respectively).

The analysis and interpretation of the results of experimental measurements were carried out, taking into account magnetic measurements (magnetometer in Longyearbyen) and ionospheric (ionosonde in Longyearbyen) data characterizing the background geophysical conditions. Ionograms of vertical ionosphere sounder were taken once every four minutes in pauses between heater-on cycles.

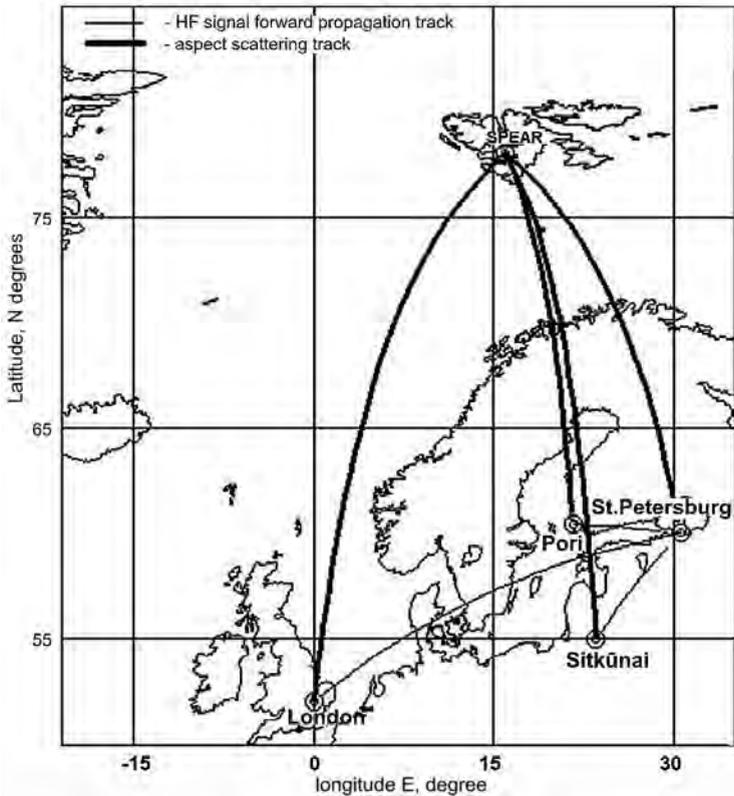


Fig. 4.2.1. Geometry of experiments on the SPEAR heating facility in Longyearbyen, Spitsbergen. Observations by the method of bi-static scatter of diagnostic HF signals at the AFAI were carried out on the radio paths London–SPEAR–St. Petersburg, Pori–SPEAR–St. Petersburg and Sitkūnai (Lithuania)–SPEAR–St. Petersburg.

ARTIFICIAL IONOSPHERIC IRREGULARITIES (AFAI) IN THE F -LAYER OF THE POLAR IONOSPHERE CAUSED BY THE INJECTION OF A POWERFUL HF RADIO WAVE WITH AN ORDINARY POLARIZATION (O -MODE)

This section discusses the results of experiments carried out at the SPEAR heating facility in winter (25 February 2007) and summer (21 July 2006), when a powerful HF radio wave of ordinary polarization (O -mode) reflected from the layer F_2 ($f_H/f_oF_2 \leq 1$). Both experiments were performed in quiet magnetic conditions. On 25 February 2007, according to the data of the ionosonde located in close proximity of the SPEAR facility, a sufficiently intense F_2 layer with critical frequencies f_o lying in the range from 4.5 to 5.0 MHz was observed, resulting in a powerful HF radio wave at a frequency $f_H = 4450$ kHz reflected from ionosphere: $f_H/f_oF_2 = 0.89–0.99$.

Fig. 4.2.2 shows the dynamic Doppler spectra (sonogram) of diagnostic HF signals on the London–SPEAR–St. Petersburg path at a frequency of $f = 12095$ kHz on 25 February 2007. Signals bi-static scattered from the AFAI were recorded during the periods of radiation of the SPEAR facility in the positive part of sonogram.

The figure shows that the bi-static scattered signals were characterized by strong spectral scattering ($\Delta f = 5\text{--}8\text{ Hz}$) and an increase in the median values of the Doppler frequency shift during the analyzed time interval. The Doppler frequency shift of scattered signals f_d during the experiment varied from +4 Hz at 10:51 UT (relative to the zero Doppler frequency corresponding to the propagation of a signal from London to St. Petersburg along the great-circle) to +10 Hz at 11:13 UT. It indicates a sharp increase in the background component of the plasma velocity southward in the polar ionosphere even under quiet magnetic conditions. Fig. 4.2.3 shows the dynamic Doppler spectra (sonogram) of diagnostic HF signals on the Pori–SPEAR–St. Petersburg path at a frequency of $f = 11755\text{ kHz}$ in the summer period on 21 July 2006 in the evening hours from 17:00 to 17:25 UT.

Signals scattered from the AFAI were recorded during the periods of radiation from the SPEAR facility in the negative part of the Doppler spectrum. Doppler width of the spectra of signals, Δf scattered from the AFAI did not exceed 2 Hz. Doppler shift of scattered signals f_d relative to the direct signal was approximately 7.5 Hz and did not change during the considered experiment. It is interesting to note that, according to the ionosonde data, a rather intense layer F2 with critical frequencies f was registered in the

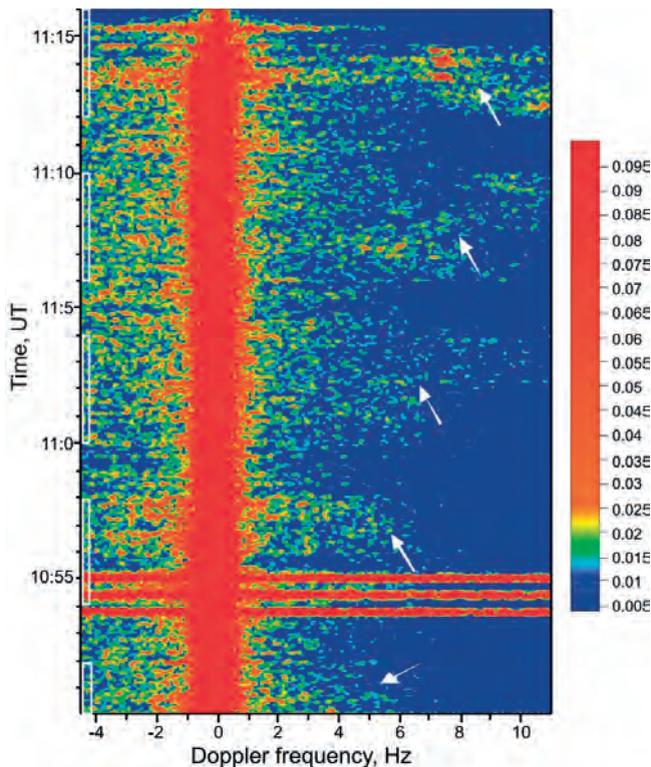


Fig. 4.2.2. Dynamic Doppler spectra (sonograms) of the diagnostic HF signals on the London–SPEAR–St.Petersburg path at a frequency $f = 12095\text{ kHz}$ on 25 February 2007 from 10:50 to 11:16 UT.

Signal propagation from London to St. Petersburg along the great-circle corresponds to zero Doppler frequency. A powerful HF radio wave of *O*-polarization was emitted into the magnetic zenith at a frequency of 4450 kHz in cycles of 4 min on – 2 min off. The emission time of the SPEAR facility is marked on the time axis with square brackets.

range from 4.2 to 4.5 MHz, $f_H/f_0F2 = 0.99-1.06$. Thus, the excitation of the AFAI in the F2-layer of the polar ionosphere was observed even when f_H exceeded f_0F2 by 0.2–0.3 MHz.

An important feature of artificial turbulence is the particular time for the growth and decay of the AFAI. During the period of experiments according to the modification of the polar F2 layer, the growth time of the AFAI (t_1) was about 10–30 s, and the time of their relaxation (t_2) about 15–40 s.

The results of the observations indicate that the generation of AFAI in the F2 layer of the polar ionosphere was observed both in winter and summer. However, the width of the Doppler spectra of the signals scattered from the AFAI in winter was significantly larger than in summer, even under quiet magnetic conditions. Artificial irregularities in the F-layer of the polar ionosphere were also recorded in experiments at the SPEAR facility based on observational data using the CUTLASS system of coherent HF Doppler radars at Hankasalmi (Finland) and Reykjavik (Robinson et al., 1989, 2006; Yeoman et al., 2007).

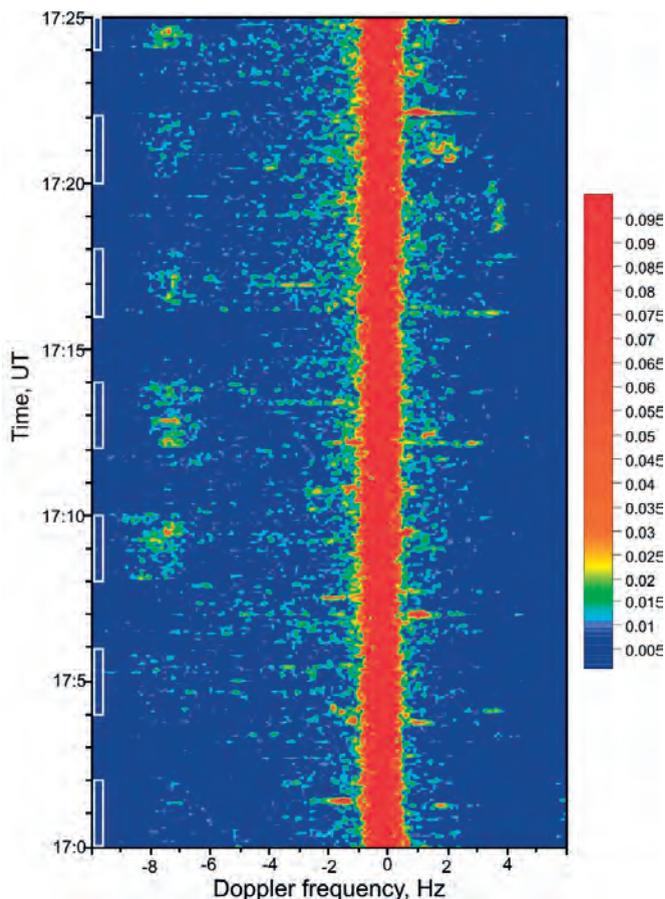


Fig. 4.2.3. Dynamic Doppler spectra (sonogram) of diagnostic HF signals along the Pori–SPEAR–St. Petersburg path at a frequency of $f = 11755$ kHz on Friday, 21 July 2006, from 17:00 to 17:25 UT. A powerful HF radio wave of *O*-polarization was emitted into the magnetic zenith at a frequency of 4450 kHz in cycles of 2 min on – 2 min off. The emission times of the SPEAR facility are marked on the time axis with square brackets.

To analyze and interpret the obtained experimental data, we simulated the dependences of the Doppler frequency shift f_d of the diagnostic HF signals bi-static scattered at the AFAI from the direction of motion of irregularities in the scattering volume. Fig. 4.2.4 shows the calculation results. The figure shows that there is a fairly wide range of azimuthal directions of motion of irregularities in an artificially disturbed region of the ionosphere, when there were either only positive or only negative f_d values on all paths. Positive values f_d correspond to the equatorial motion of the AFAI, and negative ones f_d correspond to the movement of the AFAI in the northern direction. Zero values of f_d scattered signals occur with the east and west directions of the velocity vector above the SPEAR facility. At the same time, there are relatively narrow azimuth sectors in which the signs f_d on the paths under consideration are different.

Further, according to the model developed at the AARI (Borisova et al., 2002; Borisova, 2014), we simulated the propagation trajectories of diagnostic HF signals during their scattering at AFAI over the SPEAR facility. The calculations were carried out for geophysical conditions corresponding to the conditions of the experiments at the SPEAR facility. The ionosphere model was corrected according to real data of vertical ionosphere sounder (VIS) in Longyearbyen and St. Petersburg. Fig. 4.2.5 shows the calculated propagation trajectories of diagnostic signals from London at frequencies of 12095 and 15485 kHz, received in St. Petersburg after bi-static scatter at the AFAI, created in the *F*-layer of the polar ionosphere above the SPEAR heating facility. The calculations were carried out for geophysical conditions at 11:00 UT on 25 February 2007.

The simulation results showed that different propagation modes are realized both on the path section of the *diagnostic transmitter – the scattering volume above the SPEAR*, and on the section of the *scattering volume – the receiver*, for which the condition of bi-static scattering from the AFAI located at the heights of the *F*-layer of the polar ionosphere

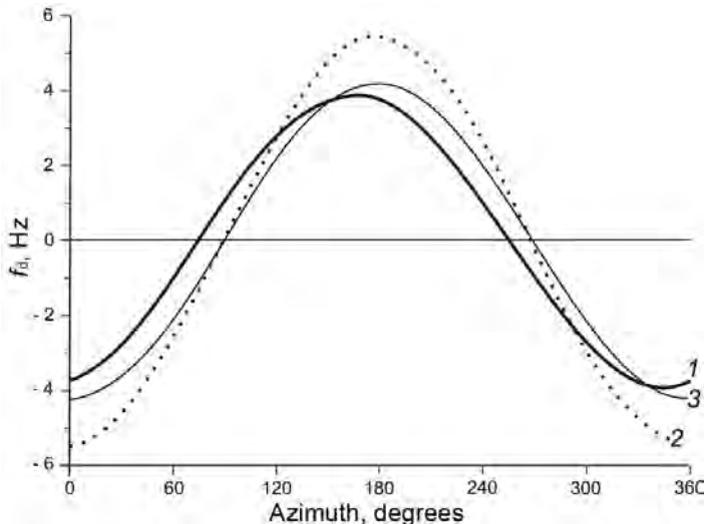


Fig. 4.2.4. Doppler frequency shift dependences f_d of HF diagnostic signals bi-static scattered from the AFAI from the direction of movement of irregularities in the scattering volume for the radio paths Pori–SPEAR–St. Petersburg at a frequency of $f = 11755$ kHz (1) and London–SPEAR–St. Petersburg at $f = 17770$ kHz (2) and 12095 kHz (3) for the movement speed of irregularities of 100 m/s.

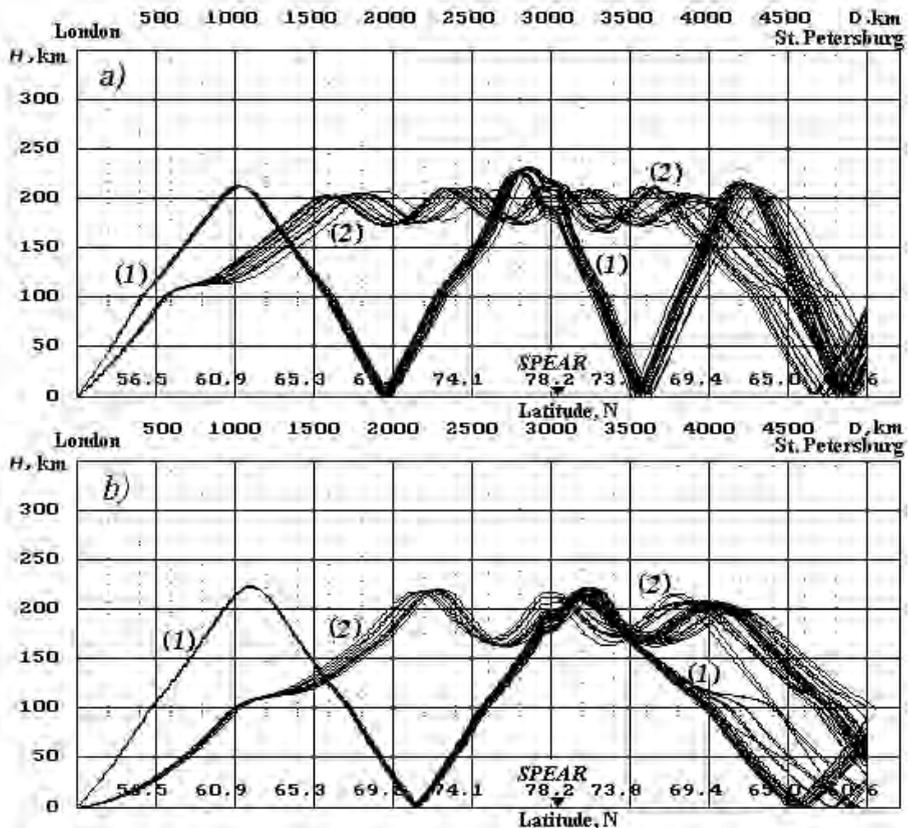


Fig. 4.2.5. The calculated propagation trajectories of diagnostic signals from London received in St. Petersburg after bi-static scatter at the AFAI, created in the F -layer of the polar ionosphere above the SPEAR heating facility for geophysical conditions at 11:00 UT on 25 February 2007.

a – frequency of the diagnostic signal 12095 kHz, b – 15485 kHz. 1 and 2 are propagation modes corresponding to the jump (1) and waveguide (2) mechanisms of radio wave propagation.

is satisfied. The signals scattered at the AFAI in the F -layer of the ionosphere hit the receiving point either through intermediate reflection from the Earth and then from the ionosphere (see Fig. 4.2.5 a), or, in the presence of gradients along the path; as a result, “direct” propagation of signals to the receiving point (Fig. 4.2.5 b).

EXCITATION OF AFAI IN A SPORADIC E -LAYER OF POLAR IONOSPHERE BY POWERFUL HF RADIO WAVE OF O -POLARIZATION

The results of experiments on the SPEAR heating facility have demonstrated that artificial field-aligned irregularities (AFAI) can be excited not only in the F - but also in the E -layer of the polar ionosphere. For studying the behavior and characteristics of AFAI in the sporadic layer E of polar ionosphere, let us consider the results of two experiments performed on 9 December 2005 and 2 December 2006. Both experiments were carried out under quiet magnetic conditions. It is interesting to note that, according to the ionosonde data, very weak reflections from the F -layer of the ionosphere (critical frequencies f_0F2 ranged from 3.0 to 4.0 MHz), as a result of which a powerful HF radio wave at a frequency of 4450 kHz could not be reflected from the F -layer. However, at the heights of the E -layer,

intense “thick” (with a group delay at high frequencies of ionogram) sporadic layers E_s with critical frequencies $f_0E_s = 4.2 \dots 6.5$ MHz ($f_H / f_0E_s = 0.68-1.06$) December 9, 2005 and $f_0E_s = 3.0 \dots 6.5$ MHz ($f_H / f_0E_s = 0.68-1.48$) on 2 December 2006. Considering the state of the polar ionosphere and the impossibility to excite AFAI in the F-layer, one can expect the excitation of AFAI in a thick sporadic E_s -layer in the considered experiments.

Fig. 4.2.6 shows the dynamic Doppler spectra of diagnostic HF signals on the Pori –SPEAR–St. Petersburg path on 9 December 2005. The measurements were carried out at a frequency of $f = 11755$ kHz. A powerful HF radio wave of ordinary polarization (O-mode) was emitted at a frequency of 4450 kHz in the direction of the magnetic zenith (antenna beam pattern was tilted 8° south of the vertical) in cycles of 2 min on – 2 min off. The figure shows that intense scattered signals were recorded in the emission cycles of the SPEAR facility.

There were two different components in the spectrum of the scattered signal: narrowband and wide-band. The narrowband component was recorded as an additional track in the positive part of the sonogram, shifted in frequency by +2.3 Hz relative to the zero Doppler frequency corresponding to the “direct” signal propagating from the

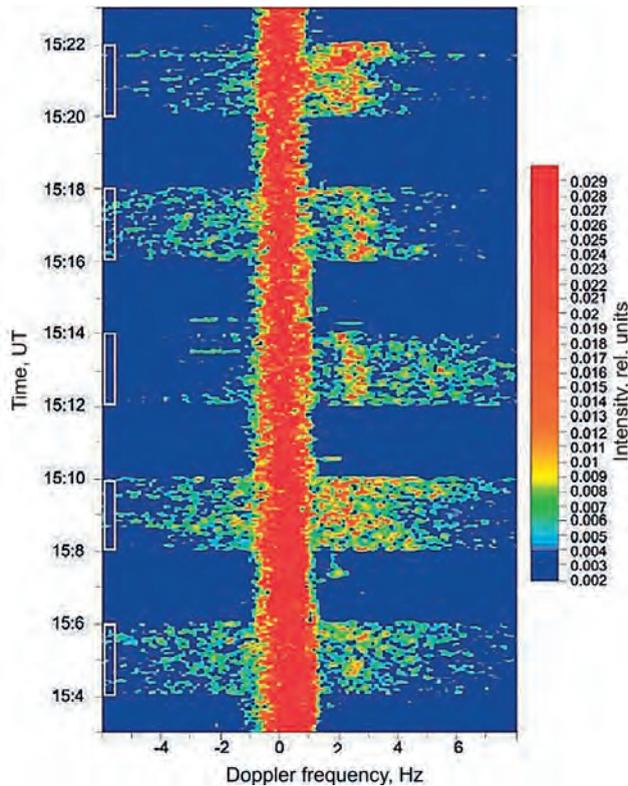


Fig. 4.2.6. Dynamic Doppler spectra (sonogram) of diagnostic HF signals along the Pori–SPEAR–St. Petersburg path 9 December 2005 at frequency = 11755 kHz from 14:56 to 15:29 UT.

A powerful HF radio wave of O-polarization was emitted into the magnetic zenith at a frequency of 4450 kHz in cycles of 2 min on- 2 min off. The emission time of the SPEAR facility is marked on the time axis with square brackets.

transmitter (Pori) to the receiver (St. Petersburg) along the great-circle. The broadband component is characterized by strong spectral scattering up to 20 Hz. These two spectral components were also clearly detected in the averaged signal spectra in heater-on cycles. Fig. 4.2.7 shows the averaged spectra of diagnostic signals for two heater-on cycles (15:16–15:18 and 15:08–15:10 UT) as well as for comparison in the pauses between heater-on cycles (15:18–15:20 and 15:10–15:12 UT).

The figure shows that the averaged spectra in heater-on cycles fundamentally differ from the spectra obtained in the pauses between heating intervals. Similar to the dynamic Doppler spectra (see Fig. 4.2.6), they demonstrate the presence of an additional narrowband maximum, most pronounced in the heater-on cycle 15:16–15:18 UT, and strong spectral scattering. It is interesting to note that the development and relaxation times of the AFAI, which are responsible for the appearance of the broadband and narrowband scattering components, differed significantly. Thus, for the broadband component of the scattering, the time of development and relaxation was no more than 1 s, and for the narrowband component, it was about 15–30 s.

Similar behavior of signals scattered at the AFAI in the *F*-layer of the mid-latitude ionosphere when heated at a frequency near the fourth electron gyroharmonic was observed in experiments on the mid-latitude HF heating facility SURA (Ponomarenko et al., 1999; Kagan et al., 2006). In our experiments at the SPEAR facility at the heights of the *E*-layer of the ionosphere, the heating frequency of 4450 kHz is close to the third gyroharmonic; therefore, essentially, this phenomenon is similar to the experiments on SURA. The theory developed by Gurevich and Zybin (2006) predicts the excitation of ultra-small-scale irregularities elongated along the magnetic field when the ionosphere is heated at frequencies near the gyroharmonics. In this case, the spectrum of bi-static scattered signals should contain two components. Stationary AFAI determines the narrowband spectral component, and the broadband one is determined by scattering at ultra-small-scale irregularities.

In the experiment carried out on 2 December 2006, as well as on 9 December 2005, a broadband spectral component was recorded in the Doppler spectrum of the signal scattered from AFAI. The narrowband spectral component was less expressed than on 9 December 2005.

Fig. 4.2.8 presents the calculated propagation trajectories of diagnostic signals from Pori at a frequency of 11755 kHz received in St. Petersburg after bi-static scatter from the AFAI, created in the *E*-layer of the polar ionosphere above the SPEAR heating facility. The calculations were performed according to the Borisova model (2014), Borisova et al. (2002), for the geophysical conditions observed on 9 December 2005 at 15:00 UT.

As the figure shows, the propagation of diagnostic signals from Pori, which reach the *E*-layer of the polar ionosphere above SPEAR, occurs in different modes. In this case, the signals scattered from the AFAI in the sporadic E_s -layer can reach the receiving point near St. Petersburg.

An analysis of the experimental data showed that in the polar *E*-layer of the ionosphere, the AFAI were excited only in “thick” sporadic *E*-layers, which are recorded as layers with a group delay in the ionograms of vertical ionospheric sounding. In thin semitransparent *E*-layers typical for the mid-latitude ionosphere, AFAI were not excited. In experiments carried out at the Tromsø heating facility, by using the methods of bi-static and back-scatter (Djuth et al., 1985; Blagoveshchenskaya et al., 1998; 2006), the generation of AFAI was also observed in the auroral *E*-layer at night at the reflection of a powerful HF radio wave of *O*-polarization from a thick sporadic *E*-layer.

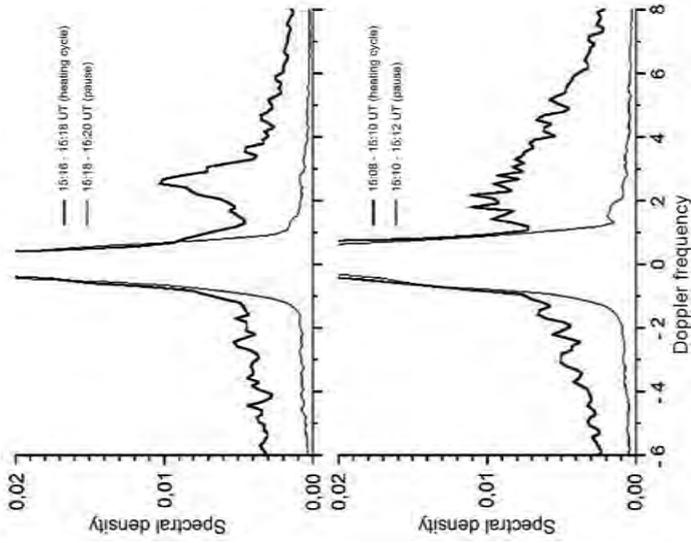


Fig. 4.2.7. Averaged spectra of diagnostic signals on the Port-SPEAR-St. Petersburg path on 9 December 2005 at a frequency of $f = 11755$ kHz for two heater-on cycles, as well as in the pauses between heater-on cycles.

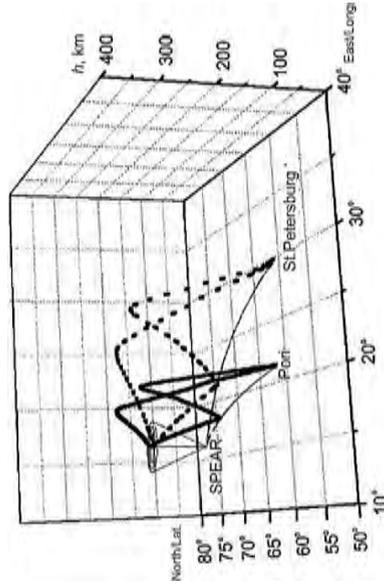


Fig. 4.2.8. The calculated propagation trajectories of diagnostic signals from Pori, received in St. Petersburg after bi-static scatter at the AFAI, created in the E -layer of the polar ionosphere above the SPEAR heating facility for the geophysical conditions observed on 9 December 2005 at 15:00 UT.

AFAI IN THE *F*-LAYER OF THE POLAR IONOSPHERE CAUSED BY THE INJECTION OF A POWERFUL HF RADIO WAVE WITH EXTRAORDINARY POLARIZATION (*X*-MODE)

During the ionosphere modification induced by powerful HF radio wave of extraordinary polarization (*X*-mode) in October 2010, diagnostic HF radio signals scattered in perspective at artificial field-aligned irregularities excited in the *F*-layer of the polar ionosphere above the SPEAR heating facility were recorded.

Fig. 4.2.9 shows the results of measurements by the method of bi-static scatter on 7 October 2010 from 12:19 to 12:26 UT as the example. Fig. 4.2.9 *a* shows a sonogram of a diagnostic radio signal at a frequency of $f_{diag} = 9610$ kHz on the Sitkunai–SPEAR–St. Petersburg path with a length of 4605 km, and Fig. 4.2.9 *b* – sonogram of the radio signal at $f_{diag} = 9710$ kHz on the London (Rampisham)–SPEAR–St. Petersburg path with

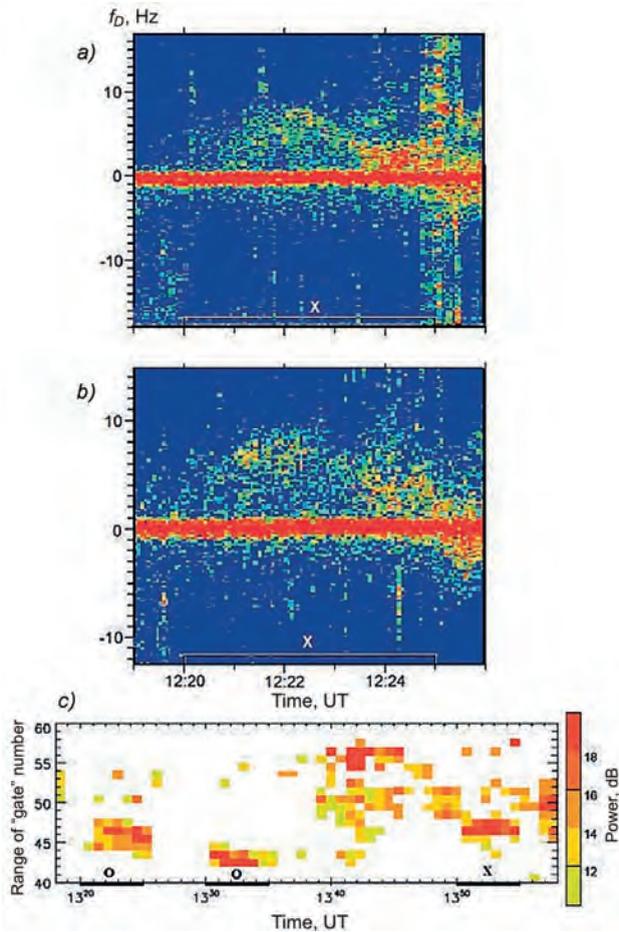


Fig. 4.2.9. Dynamic Doppler spectra of diagnostic HF signals during a heating experiment using the SPEAR facility on 7 October 2010 (*a* and *b*) and observation data using the coherent HF Doppler radar CUTLASS in Hankasalmi (beam 9, oriented towards the artificially disturbed region of the ionosphere above Longyearbyen) at a frequency of about 10 MHz on 8 October 2010 (*c*).

The heater-on cycles and the used polarization of the powerful HF radio wave are marked on the time axis.

a length of 5185 km. During the heater-on cycle from 12:20 to 12:25 UT, a powerful HF radio wave of extraordinary polarization (*X*-mode) was emitted towards the magnetic zenith at a frequency of 4450 kHz. For both diagnostic signals, there were intense signals in the emission cycle that were bi-static scattered at the ionospheric irregularities. Zero Doppler frequency shift values $f_D = 0$ on the sonograms in Fig. 4.2.9 correspond to the propagation of the signal from the transmitter to the receiver along the great-circle (“direct” signal). The figure shows that scattered diagnostic signals with frequency $f_{diag} = 9610$ kHz and $f_{diag} = 9710$ kHz formed diffuse tracks in the positive range f_D during the heater-on cycle 12:20–12:25 UT. The bi-static scattered signals on both diagnostic paths were characterized by diffuse spectral components in the range of positive f_D values. The frequency bands of the bi-static scattered signals ranged from 6–8 Hz for the HF radio signal from Sitkunai – up to 9 Hz for the radio signal from London (Rampisham).

During the heating experiments, observations were also carried out by using coherent HF radars CUTLASS in Finland and Iceland. Fig. 4.2.9 *c* shows the results of measurements on 8 October 2010 from 13:18 to 13:57 UT by the CUTLASS radar in Finland as an example at a frequency of about 10 MHz. The behavior of scattered signals (see Fig. 4.2.9 *c*) is presented in coordinates range (Range gate) – universal time UT. The scattered signals were recorded in the range from 1980 to 2880 km, corresponding to the “gate” from 40 to 60. The ionosphere was heated at frequency $f_H = 4450$ kHz in cycles 5 min on – 5 min off. In the first two heater-on cycles, in the interval 13:20–13:35 UT, a powerful HF radio wave of *O*-polarization was emitted into the magnetic zenith. In this time interval, for the heating frequency f_H and the critical frequency of the ionospheric layer F2 of ordinary polarization f_0F2 , the relation $f_H \leq f_0F2$ was met. As Fig. 4.2.9 *c* shows, in two heater-on cycles 13:20–13:25 and 13:30–13:35 UT, quite intense signals were recorded scattered at ionospheric irregularities. Then, from 13:35 to 13:50 UT, there was a pause in the operation of the heating facility. In the next heater-on cycle (13:50–13:55 UT), when the values of f_0F2 before the beginning of the heater-on cycle were already approximately 4.2–4.3 MHz, the polarization of the powerful HF radio wave was changed from *O*- to *X*- mode. Fig. 4.2.9 *c* shows, according to the CUTLASS radar data, the formation of intense signals scattered from ionospheric irregularities from 13:50 to 13:55 UT during *X*-heating of the polar ionosphere.

For the first time, the excitation of the AFAI during *X*-heating was detected at the EISCAT / Heating facility in Tromsø, Norway. The results of numerous experiments carried out by AARI specialists at the EISCAT / Heating facility (Blagoveshchenskaya et al., 2011, 2013, 2015) clearly demonstrated that the injection of powerful HF radio waves of *X*-polarization towards the Earth’s magnetic field (magnetic zenith) causes the generation of AFAI with scales transverse to the magnetic field approximately equal to 7.5–20 m. In this case, AFAI were excited by heating at frequencies both above and below the critical frequency of the layer F2 ($f_H / f_0F2 \leq 1$ and $f_H / f_0F2 > 1$). Please, note that the maximum effective radiated power of the EISCAT/Heating (P_{eff}) is high and is 190–250 MW with the use of phased array No. 2, while for the SPEAR facility in the polar ionosphere, the value of P_{eff} is only 15 MW.

The mechanism of the AFAI excitation upon reflection of a powerful HF radio wave of *O*-polarization from the F2 layer of the ionosphere is explained within the framework of the theory of thermal parametric (resonance) instability (Grach and Trakhtengerts, 1975; Vas’kov and Gurevich, 1976). An extraordinary wave (*X*-mode) is reflected at heights

below the upper hybrid resonance and below the reflection height of the O -wave; therefore, the excitation of the AFAI due to thermal (resonance) instability is impossible.

The mechanism of excitation of intense AFAI upon heating of F -layer in the high-latitude ionosphere by a powerful HF radio wave of X -polarization at frequencies both below and above the critical frequency of the F2 layer remains unclear. It requires further serious study, both experimental and theoretical. It seems possible to assume that the excitation of the AFAI upon X -heating is associated with the generation of large-scale inhomogeneities, which is possible upon heating at frequencies both below and above f_0F2 , due to the self-focusing instability of powerful HF beam (Gurevich, 1978). Under these conditions, a mechanism of small-scale stratification of large-scale plasma formations is possible. According to the theory proposed by Guzdar et al. (1998), first, kilometer-long structures develop along the magnetic field, which, after about 10 s, “break” into smaller-scale structures ranging in size from 10 to 100 m.

FEATURES OF THE BEHAVIOR OF THE STIMULATED ELECTROMAGNETIC EMISSION OF THE IONOSPHERE IN THE POLAR IONOSPHERE F -LAYER

Stimulated electromagnetic emission (SEE) was first detected at the EISCAT / Heating facility when the ionosphere was exposed to a powerful HF radio wave of ordinary polarization at a frequency below the critical frequency of the F2 layer (Thidé et al., 1982). Over the past three decades, intensive experimental studies of SEE in the F -layer of the ionosphere have been carried out (Gurevich, 2007; Grach et al., 2016; Leyser, 2001; Frolov et al., 1999) at various HF heating complexes of the world, such as the facility “Sura”, Arecibo, EISCAT / Heating, HAARP, located at middle and high latitudes.

Stimulated electromagnetic emission of the ionosphere arises as a result of various kinds of nonlinear interactions of electromagnetic waves and high-frequency plasma oscillations with low-frequency plasma turbulence, in the formation and development of which artificial field-aligned irregularities play a decisive role (Gurevich, 2007; Grach et al., 2016; Leyser, 2001; Frolov et al., 1999). The spectral and dynamic characteristics of the individual components of the SEE (about 15 names) were studied in detail in Leyser (2001) and the cited literature and are used to diagnose the properties of plasma processes both in artificially disturbed and in the natural ionospheric plasma. Among the main components of SEE, we note the following:

- the main spectral maximum of the emission also called the downshifted maximum (DM);
- broadband emission in the range of negative offsets (broad continuum, BC);
- maximum in the area of positive offsets (upshifted maximum, UM);
- broad-up-shifted maximum (BUM) emission, formed when the pump wave frequency is close to the gyroharmonic frequency, and BUM-like emission in the broad up-shifted structure (BUS) frequency range, etc.

The most intense and frequently observed thermal components of the stationary spectrum of SEE are the DM and BC components, where there is a certain clarity in the mechanisms of their generation. The BC emission is found in the range of negative offsets from the heating frequency up to a frequency of 60–120 kHz. The peak of DM emission appears at a frequency shifted downward by 8–15 kHz from the frequency of the disturbing wave. A study of the SEE characteristics shows that the generation of the DM component of the SEE is closely related to the processes in the range of the upper hybrid (UH) resonance and is determined by the development of thermal parametric (resonance)

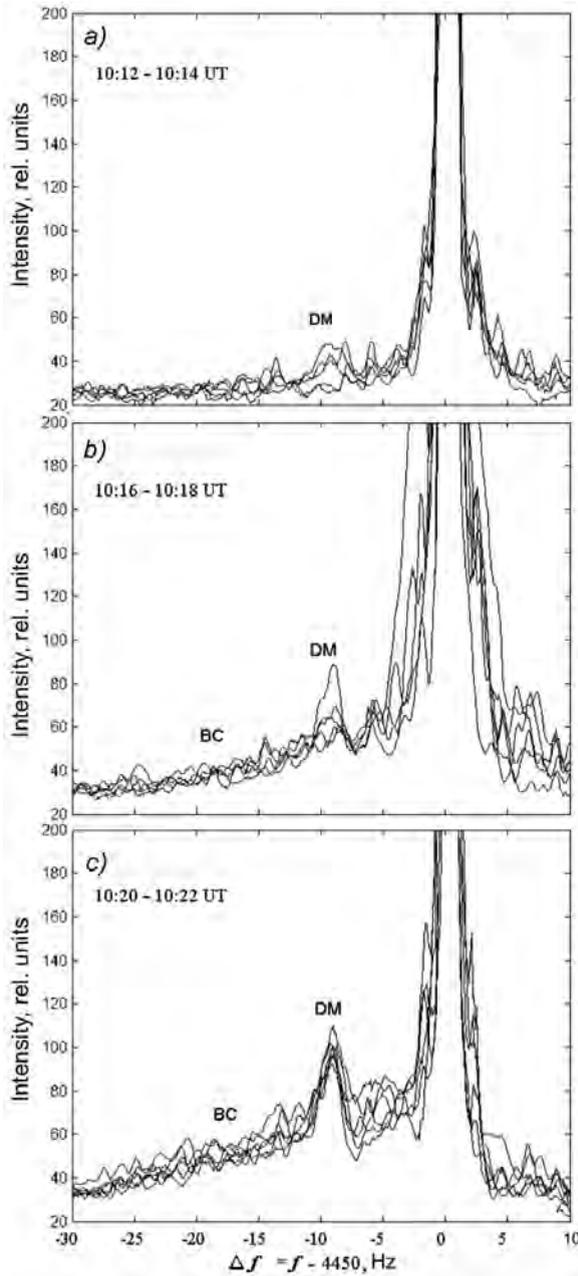


Fig. 4.2.10. Distribution of the intensity of the heating signal of the SPEAR facility, measured in Barentsburg, Spitsbergen, at positive (+10 kHz) and negative (-30 kHz) offsets from the heating frequency $f = 4450$ kHz, obtained on 10 March, 2007 in three consecutive heater-on cycles.

instability (Gurevich, 2007; Grach et al., 2016; Grach and Trakhtengerts, 1975; Vas'kov and Gurevich, 1976). The excitation of the DM component of the SEE was noted when F spread exists in the ionosphere (Leyser, 2001). Please, note that in all the publications cited above, studies of the features of the SEE behavior were carried out when the F -layer of the ionosphere was exposed to powerful HF radio waves.

Below are the results of experiments carried out in Barentsburg on Spitsbergen on March 9, 10, and 12, 2007, on the registration of stimulated electromagnetic emission of the ionosphere in the F -layer of the ionosphere of the polar cap. According to the ionosonde data, there was a rather intense layer of F2 with critical frequencies ranging from 3.6 to 4.6 MHz. Sporadic E_s layer was not detected. Magnetic conditions were favorable on March 9 and 10 2007 (three-hour planetary index $K_p = 1$, a sum of K_p indices per day $\sum K_p = 9^+$), and 12, 2007 the experiment was carried out with moderate magnetic activity ($K_p = 3^-$, $\sum K_p = 20^-$).

Fig. 4.2.10 shows the intensity distributions of the heating signal of the SPEAR facility at positive (+10 kHz) and negative (–30 kHz) offsets from the heating frequency $f_H = 4450$ kHz, registered on 10 March 2007 in three consecutive heater-on cycles: 10:12–10:14, 10:16–10:18 and 10:20–10:22 UT.

As Fig. 4.2.10 shows, in the first heater-on cycle, there was a weak maximum in the spectrum of the heating signal, shifted to the range of negative offsets from the heating frequency by about 9 kHz. The intensity of this maximum increased in the second and third heater-on cycles. Also, a broadband component appeared in the range of negative offsets from the heating frequency.

A powerful HF radio wave of O -mode polarization was emitted from 11:12 to 12:00 UT in cycles of 2 min on, 2 min off.

It is known that the most frequently observed component in the spectrum of stimulated electromagnetic emission of the ionosphere is the “downshifted maximum” (DM) relative to heating frequency f_H by $\Delta f_{DM} = \Delta f_{DM} \approx 2 \cdot 10^{-3} f_H$ (Leyser, 2001). Taking into account that during the experiment the heating was carried out at a frequency of $f_H = 4450$ kHz, the value of Δf_{DM} should be approximately 9 kHz, which we could see in the experiment. Therefore, there is no doubt that the observed maximum is the DM component in the SEE spectrum. The broadband component (see Fig. 4.2.10 *b* and *c*), apparently, is a broad continuum, (BC) observed in the range of negative offsets from the heating frequency Δf^- equal to about 30–40 kHz.

It is of interest to consider the dynamics of changes in time of the SEE spectra in the polar F -layer of the ionosphere. Fig. 4.2.11 and 4.2.12 show the distributions of the intensity of the heating signal of the SPEAR facility at positive (+50 kHz) and negative (–50 kHz) offsets from the heating frequency, obtained during the experiments on March 10 and 12, 2007. During the period of experiments, the ionosonde data showed significant variations in the critical F2 layer frequencies from 3.6 to 4.6 MHz. Fig. 4.2.11 and 4.2.12 also show significant variations in the intensity of the DM -component of the SEE. It is interesting to note that the DM -component was excited not only when a powerful HF radio wave was reflected from the F2 layer, but also under conditions when the heating frequency exceeded f_0F2 . So, on 10 March 2007 (see Fig. 4.2.11), a rather intense DM -component was registered in the first three heater-on cycles when the values f_0F2 were 4.5–4.6 MHz ($f_H/f_0F2 = 0.97 - 0.99$). In some heater-on cycles (11:24–11:26 and 11:28–11:30 and 11:32–11:34 UT), when the f_0F2 values decreased and were 4.0–4.2 MHz, the

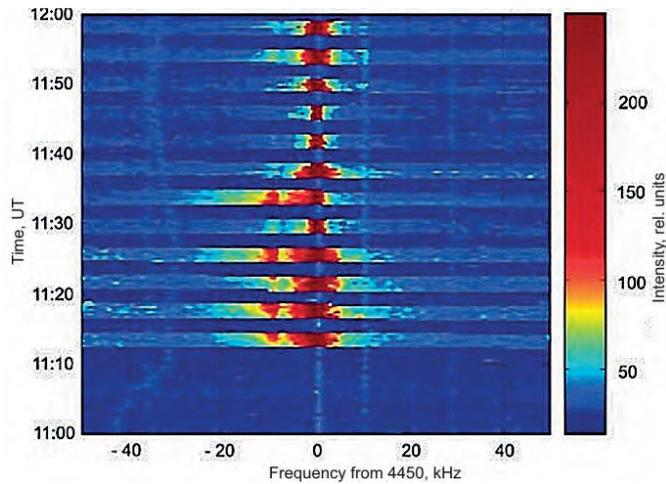


Fig. 4.2.11. Distribution of the intensity of the heating signal of the SPEAR facility, with positive (+50 kHz) and negative (−50 kHz) offsets from the heating frequency ($f_H = 4450$ kHz), obtained in the experiment on 10 March 2007 from 11:00 to 12:00 UT.

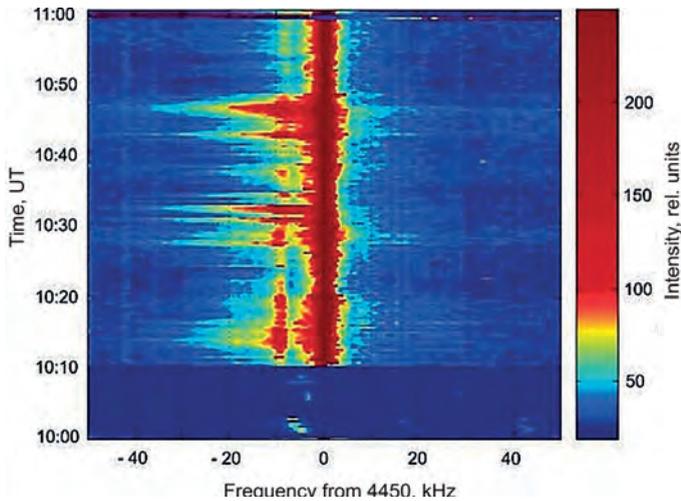


Fig. 4.2.12. Distribution of the intensity of the heating signal of the SPEAR facility, with positive (+50 kHz) and negative (−50 kHz) offsets from the heating frequency ($f_H = 4450$ kHz), obtained in the experiment on Monday, 12 March 2007 from 10:00 AM to 11:00 AM UT.

DM -component was also detected ($f_H/f_0F2 = 1.06\text{--}1.11$). Generally the relationship between the intensity of the DM -component and the ratio f_H/f_0F2 is uncertain. From 11:40 to 11:50 UT, the DM -component was not registered in the SEE spectrum, although the f_0F2 values were approximately the same as in the three previous heater-on cycles (4.0–4.2 MHz). On 12 March 2007, the polar ionosphere was heated in a continuous-wave mode from 10:12 to 11:00 UT (see Fig. 4.2.12). Here, the appearance of the DM -component was rather irregular, too.

A powerful HF radio wave of O -polarization was emitted in a continuous-wave mode from 10:12 to 11:00 UT.

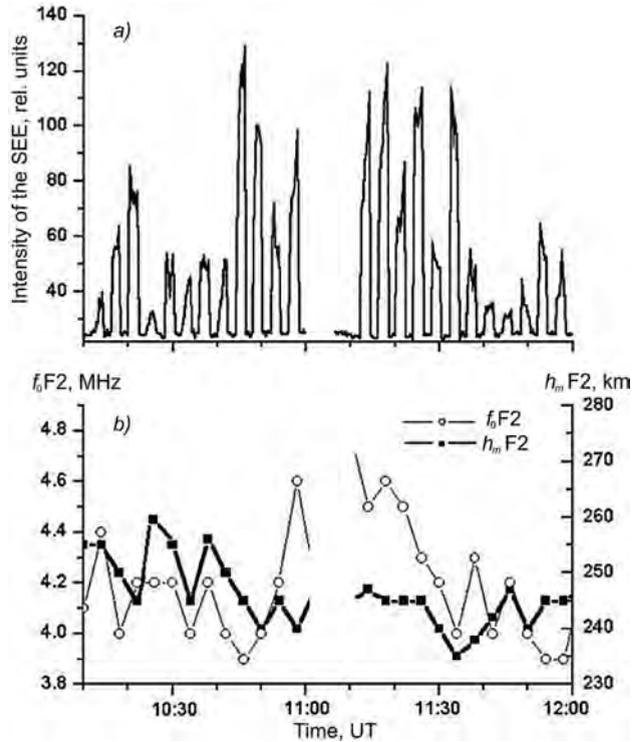


Fig. 4.2.13. Variations in the intensity of the *DM*-component of the SEE (a), as well as variations in the critical frequency f_0F2 and the height of the maxima h_mF2 (b) on March 10, 2007 from 10:00 to 12:00 UT on Saturday, March 10, 2007 from 10:00 to 12:00 PM UT.

Figure 4.2.13 shows variations in the intensity of the *DM*-component of the SEE (Fig. 4.2.13 a), as well as variations in critical frequencies f_0F2 and heights of h_mF2 maxima (Fig. 4.2.13 b) on March 10, 2007 from 10:00 to 12:00 UT. Generally, the relationship between the intensity of the *DM*-component and the ratio f_H/f_0F2 is uncertain. Noteworthy is the fact that the intense *DM*-component was recorded from 10:45 to 11:00 UT with a smooth increase in f_0F2 values from 3.9 to 4.6 MHz, as well as from 11:12 to 11:35 UT, when f_0F2 gradually decreased from 4.6 to 4.0 MHz. Thus, the analysis of experimental data obtained as a result of the registration of SEE in the polar ionosphere shows that the *DM*-component was excited not only upon heating at frequencies below f_0F2 , but also under conditions when the heating frequency exceeded f_0F2 by 0.5 MHz.

An analysis of the experimental data on bi-static scatter, obtained in 2005–2007, also indicates the excitation of AFAI in the polar ionosphere, when the frequency of a powerful HF radio wave exceeded the critical frequency f_0F2 (f_0E_s) by 0.3–0.3 MHz. It is known that nonlinear phenomena in the field of a powerful HF radio wave, such as artificial field-aligned irregularities and stimulated electromagnetic emission of the ionosphere, are excited in the upper hybrid resonance when $f_H^2 = f_{UH}^2 = f_0^2 + f_{ce}^2$, where f_0 upper hybrid frequency, f local frequency of ionospheric plasma, f_{ce} – electron gyrofrequency. This condition is met for the SPEAR facility during heated at a frequency $f_H = 4450$ kHz, the maximum plasma frequency (critical frequency) is approximately 4.25 MHz, which is 0.2 MHz less. Why the generation of the AFAI and the *DM*-component of the SEE occurs at lower than

4.25 MHz values of the critical frequency remains unclear. Please, note that the critical frequency, according to the ionosonde data, is measured in the vertical direction, while a powerful HF radio wave was emitted to the magnetic zenith. Under these conditions, when significant gradients of electron concentration are present, which is typical for the high-latitude ionosphere, a powerful HF radio wave could be reflected from the ionosphere.

In experiments on the heating facility in Tromsø, the generation of the AFAI was also observed at $f_H > f_0F2$ (f_0E_s), not only in the night auroral F -layer of the ionosphere (Blagoveshchenskaya et al., 2006), but also in sporadic E_s layer (Djuth et al., 1985; Blagoveshchenskaya et al., 2006). Observations of artificial luminescence in the red (630 nm) and green (557.7 nm) lines of atomic oxygen at the HAARP facility showed that the luminescence did not diminish when the critical frequency fell below the heating frequency. The artificial luminescence disappeared only when $f_0F2 < f_H - 0.5$ MHz (Mishin et al., 2005).

SOME FEATURES OF THE BEHAVIOR OF THE STIMULATED ELECTROMAGNETIC EMISSION OF THE IONOSPHERE IN THE SPORADIC E -LAYER OF THE POLAR IONOSPHERE

In the high-latitude ionosphere, the structure and parameters of the sporadic E -layer differ significantly from the mid-latitude E_s -layer. Both in the auroral zone and the polar cap, we can often observe a “thick” E_s -layer with a well-defined group delay in the altitude-frequency characteristics when approaching the limiting frequency f_0E_s . In such particular “thick” E_s the intense artificial field-aligned irregularities (AFAI) were excited with a spatial scale from several to tens of meters across the magnetic field in the nighttime auroral ionosphere (Djuth et al., 1985; Blagoveshchenskaya et al., 1998, 2006). In the experiment on 2 March 2007, performed by AARI specialists in Barentsburg, located 40 km from the SPEAR heating facility, stimulated electromagnetic emission of the ionosphere (SEE) was firstly detected in the sporadic E_s -layer of the polar ionosphere.

The experiment on 2 March 2007 was carried out in the late evening hours (from 19:00 to 20:00 UT) quiet magnetic conditions. Three-hour index K_p was 1^+ , the sum of indices K_p per day: $\sum K_p = 9^-$. According to the vertical sounding (VS) of the ionosphere, a sporadic E_s -layer, was recorded directly at the location of the SPEAR facility from 19:00 to 20:00 UT. Changes over time f_0E_s are shown in Fig. 4.2.14. The critical frequency f_0E_s during the experiment from 19:00 to 19:50 UT varied from 5.5 to 3.2 MHz. Taking into account that $f_H = 4450$ kHz, from the given VS data, it can be concluded that in three successive heater-on cycles (19:12–19:16, 19:20–19:24 and 19:28–19:32 UT) a powerful HF radio wave reflected from the ionospheric E_s layer. The values of the critical frequency of the f_0F2 layer of the ionosphere in the period under consideration did not exceed 3.0 MHz.

Let us consider the registration data on the distributions of the heating signal intensity of the SPEAR facility on 2 March 2007 in Barentsburg.

Fig. 4.2.15 shows the time-dynamic distributions of the intensity of the heating signal of the SPEAR facility (sonogram) at positive (+40 kHz) and negative (–40 kHz) offsets from the heating frequency $f_H = 4450$ kHz, for 19:10–19:42 UT. Please, note that the observations on 2 March 2007 were carried out under conditions of an increased level of radio interference in the frequency offset band. Fig. 4.2.15 shows that in the first three cycles of the SPEAR facility (19:12–19:16, 19:20–19:24, and 19:28–19:32 UT), spectral components intensified in a wide band of observations Δf from –40 to +40 kHz. Note

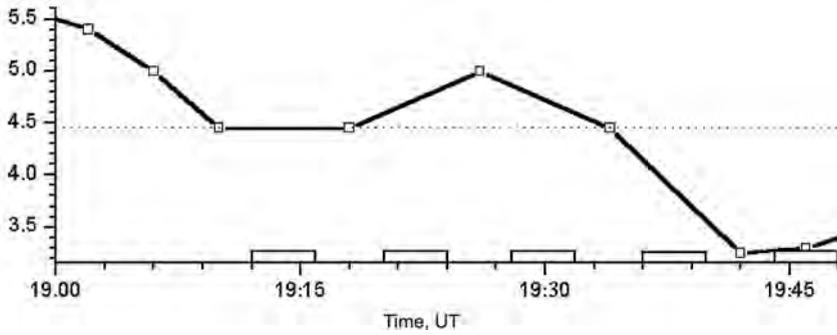


Fig. 4.2.14. Time variation of the critical frequency $f_0 E_s$ of the sporadic layer E_s on 2 March 2007 from 19:10 to 19:50 UT at the location of the SPEAR HF heating facility. The dashed line corresponds to the heating frequency $f_H = 4450$ kHz. SPEAR emission intervals are marked on the time axis with square brackets.

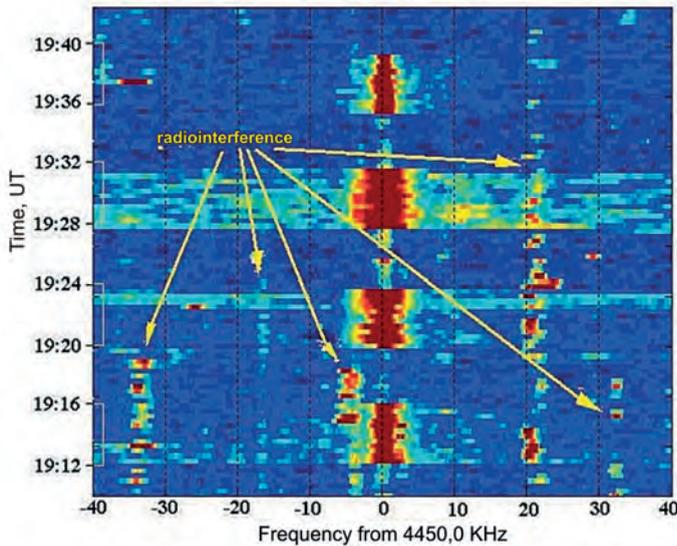


Fig. 4.2.15. Distribution of the intensity of the heating signal of the SPEAR facility, with positive (+40 kHz) and negative (-40 kHz) offsets from the heating frequency ($f_H = 4450$ kHz), obtained in the experiment on Friday, 2 March 2007, from 7:10 PM to 7:44 PM UT.

The SPEAR facility emitted from 19:12 UT in the cycles 4 min on – 4 min off. Arrows indicate radio interference.

that in the fourth heater-on cycle (19:36–19:40 UT), this intensity did not increase. When SPEAR was turned off, the spectral intensity was reduced to the noise level, excluding radio interference. The direct relationship between the increase in the intensity of the spectral components in the first three heater-on cycles with the periods of operation of the SPEAR facility suggests that the observed increase in the intensity in the spectrum of the heating signal is a stimulated electromagnetic emission of the ionosphere (SEE).

In the heater-on cycle 19:12–19:16 UT, the heating signal intensified in the form of a broadband increase in the intensity of spectral components by a factor of 1.5–2 both at

positive and negative frequency offsets relative to the heating frequency. The bandwidth Δf , in which the intensity increased, gradually narrowed during the heater-on cycle. In the next heater-on cycle (19:20–19:24 UT), emission was observed only at the last minute of the 4-minute cycle of the SPEAR facility (\approx 19:23–19:24 UT), but it occupied the entire range of Δf . The intensity of the broadband emission exceeded the noise level by 2–3 times. The most intense broadband emission was recorded during the entire third heater-on cycle (19: 28–19: 32 UT).

A specific feature of the third heater-on cycle is the formation of additional maxima in the spectrum of the radio emission intensity in the observation band Δf . Further, $f_H = 4450$ kHz, in the range of negative offsets at frequencies f^- approximately $-9 - 25$ kHz, additional maxima can be seen at different times. The width of the additional maxima occupied a frequency band of approximately 8–12 kHz. During the heater-on cycle, the frequencies of the additional maxima changed. The highest intensity of the additional maximum in the range of negative frequency offsets was observed during 19:29–19:31:30 UT.

Simultaneously with the maxima in the range of negative offsets in the heater-on cycle at 19:28–19:32 UT, additional maxima were observed in the radio emission spectra in the range of positive offsets from the heating frequency. The most intense in amplitude “positive” maximum was recorded at the offsets frequencies $f^+ \approx 8-12$ kHz and occupied the 8–10 kHz band. It should be noted that during the heater-on cycle, the spectral amplitude of the additional maximum of radio emission at positive offsets f^+ generally exceeded the amplitude of the additional maximum in the range of negative offsets in frequency f^- .

Summarizing the observational data on the intensity distributions of the heating signal in the 80 kHz frequency band, obtained under the action of a powerful HF radio wave from the SPEAR facility on the sporadic E_s -layer of the polar ionosphere, we can note the following features in the behavior of the radio emission spectra depending on the frequency of offsets relative to $f_H = 4450$ kHz:

- additional maxima in the range of negative offsets from the heating frequency $f^- \approx 9 \dots 25$ kHz with a width $\Delta f \approx 8-12$ kHz;
- additional maxima in the range of positive offsets from the heating frequency $f^+ \approx 8 \dots 30$ kHz with a width of $\Delta f \approx 8-20$ kHz;
- broadband increase in the intensity of spectral components in the range of negative offsets from the heating frequency $\Delta f^- \approx 10-40$ kHz;
- broadband increase in the intensity of spectral components in the range of positive offsets from the heating frequency $\Delta f^+ \approx 10-40$ kHz.

One of the characteristic features of the behavior of stimulated electromagnetic emission in the polar sporadic layer E_s is the temporal inconsistency of the frequency and width of additional maxima in the emission spectrum at both negative and positive offsets from f_H .

The Gorkovskaya observatory, located near St. Petersburg and at a distance of 2000 km from the SPEAR heating facility, received diagnostic signals bi-static scattered at the AFAI. The observation results indicate the excitation of AFAI in the sporadic E_s layer of the polar ionosphere.

As it is known, the effect of powerful HF radio waves on the F2 layer of the ionosphere leads to the generation of such thermal components of the SEE as DM and BC due to the re-emission of electrostatic plasma oscillations into secondary electromagnetic

waves during the development of resonance instability in the range of the upper hybrid (UH) resonance (Gurevich, 2007; Grach et al., 2016; Leyser, 2001; Frolov et al., 1999 and cited literature). The re-emission process is impeded by phase failure arising from collisions of electrons. Collision frequency ν_e in F -layer is low ($\nu_e < 10^2 \text{c}^{-1}$) and the phase failure is overcome when a sufficiently large amplitude of the main UH-wave (resonance) is reached. When SEE occurs in the F -layer of the ionosphere, the frequency shift of the maximum of the DM -component towards negative range from the frequency of the disturbing station is $f_{DM}^* \approx 8\text{--}15$ kHz and is determined by the frequency of the lower hybrid (LH) waves f_{LH} .

If we neglect the electron collision frequency ν_e , the value of f_{LH} in the F2 layer can be described by the expression (Ginzburg, 1967)

$$f_{LH} = \sqrt{\frac{f_0^2 f_{ge} f_{gi}}{f_0^2 + f_{ge}^2} \left(1 + \frac{\nu_i^2 + \nu_i \nu_e}{4\pi^2 f_{gi} f_{ge}} \right)}, \quad (4.2.1)$$

where f_0 – plasma frequency; f_{ge} and f_{gi} – gyrofrequency for electrons and ions, respectively.

In the F2 layer of the ionosphere, positive ions are mainly represented by atomic oxygen ions O^+ . The numerical value of the minimum frequency of LH waves (“cutoff” frequency) f_{LH} for the F2-layer, obtained using formula (4.2.1), is: $f_{LH} \approx 8$ kHz.

At the heights of the E -layer of the ionosphere, positive ions are predominantly represented by the ions of the O_2^+ and NO^+ molecules. The values obtained as a result of the calculation of f_{LH} for the E -layer by formula (4.2.1), taking into account the molecular mass of the ions, are approximately 5.5–6 kHz. Upon modification of the polar E_s -layer, the experimentally measured values of the shift of additional maxima of radio emission were $f^* \approx 9\text{--}25$ kHz, which is comparable to or exceeds the values of f_{DM}^- of component of SEE at the modification of the F2 layer of the ionosphere.

Please, note that at the heights of the E -layer of the ionosphere, the electron collision frequency $\nu_e < 10^4 \text{c}^{-1}$ therefore, the determination of f_{LH} should be carried out taking into account the influence of the collision frequency between electrons ν_e and ions ν_i . In this case, the expression for f_{LH} looks like

$$f_{LH} = \sqrt{\frac{f_0^2 f_{ge} f_{gi}}{f_0^2 + f_{ge}^2}} \approx \sqrt{f_{ge} f_{gi}}. \quad (4.2.2)$$

Estimates of f_{LH} made by formula (4.2.2) for the E_s -layer of the polar ionosphere with plasma frequencies $f_0 \approx 4.5$ MHz taking into account the positive ions of the O_2^+ molecules and NO^+ give values of $f_{LH} \approx 11\text{--}15$ kHz. When performing the calculations, we used model values of the collision frequency of electrons and ions: $\nu_e \approx 5\text{--}7 \cdot 10^5 \text{c}^{-1}$ (Nicolet, 1953), $\nu_i \approx 1\text{--}1.2 \cdot 10^4 \text{c}^{-1}$ (Shunk and Nagy, 2000). Under these conditions, the measured values of the frequency shift of the additional maximum of the observed radio emission are in acceptable agreement with the values of f_{LH} calculated by the formula (4.2.2), taking into account ν_e and ν_i for the E_s -layer of the polar ionosphere.

The estimates made allow us to assume that despite the high values of the electron collision frequency at the heights of the E -layer of the ionosphere ($\nu_e \approx 10^4\text{--}7 \cdot 10^5 \text{c}^{-1}$), the possibility of the development of resonance-type instability is realized, since the necessary condition of plasma “magnetization” is met: $2\pi f_{ge} > \nu_e$, $\nu_e / 2\pi f_{ge} \approx 10^{-1}\text{--}10^{-3}$ (Vas’kov and Gurevich, 1976). Thus, formally, in the ionospheric plasma of the polar E -layer, a situation is created for the generation of SEE and AFAI, similar to the conditions in

the F2 layer in the region of the UH resonance. The fundamental difference is the need to take into account the effect of the electron collision frequency ν_e . Higher (by two orders of magnitude) value of the ratio $\nu_e/2\pi f_{ge}$ in the polar E -layer in comparison with the conditions in the F2 layer does not allow stable additional maxima to form. Further study of the properties of stimulated electromagnetic emission in the polar E_s -layer will answer the question what is the reason for overcoming the phase failure during pumping of the resonance plasma UH wave in E_s -layer: lower values of ν_e or the formation of the large amplitude of the resonance plasma UH wave.

CONCLUSIONS

A summary of the results of experimental studies of the AARI on the effect of powerful HF radio waves emitted by the SPEAR heating facility (Longyearbyen, Spitsbergen) on the polar ionosphere is carried out. The results of the performed experiments indicate that SPEAR, which has no analogs in the world in terms of its geographic location, effectively modifies the polar ionosphere, causing the generation of artificial field-aligned irregularities (AFAI) and stimulated electromagnetic emission of the ionosphere (SEE). All considered experiments were carried out with the emission of a powerful HF radio wave towards the magnetic zenith (antenna beam pattern was tilted 8° south of the vertical). Observations were carried out simultaneously in two spatially separated points: in Barentsburg (Spitsbergen archipelago, at a distance of about 40 km from the SPEAR facility) and the Gorkovskaya observatory near St. Petersburg, located at a distance of about 2000 km from SPEAR.

Analysis of the experimental data showed that AFAI in the polar ionosphere are excited under different background geophysical conditions (season, time of day, the presence of sporadic layers in the E -layer). The emission frequency of diagnostic transmitters was in the range of 10–20 MHz, which corresponds to the minimum transverse scale of irregularities responsible for bi-static scatter, equal to about 7.5–15 m. The longitudinal scales of the AFAI, elongated along the direction of the magnetic field, are several tens of kilometers. It is shown that under the action of a powerful HF radio wave of ordinary polarization (O -mode) on the polar ionosphere, AFAI can be excited not only in the F -layer of the ionosphere but also in “thick” sporadic E_s -layers.

It should be noted that, in some heater-on cycles, the generation of the AFAI was observed when the heating frequency exceeded the critical frequency by 0.3–0.5 MHz. It is assumed that under these conditions, in the presence of electron density gradients typical for the polar ionosphere, the heating frequency, although exceeding the critical frequency, was comparable to the maximum upper hybrid frequency. The mechanism of the AFAI generation during O -heating is explained within the framework of the theory of thermal parametric (resonance) instability.

When AFAI is excited in the sporadic E_s -layer the presence of two different components in the spectrum of the scattered signal was found: a narrowband one, with a Doppler spectrum width of up to 2 Hz, and a broadband one, observed in a band up to 20 Hz. Note that the heating frequency of 4450 kHz is close to the third electron gyroharmonic at the SPEAR facility at the heights of the E -layer of the ionosphere. A possible mechanism for the generation of a broadband component can be scattering at ultra-small-scale elongated irregularities. In this case, the narrowband component is determined by scattering at stationary AFAI.

An analysis of the results of experimental measurements showed that the generation of the AFAI in the F -layer of the polar ionosphere is also possible during periods when powerful HF radio waves of extraordinary polarization (X -mode) are emitted. In this case, the AFAI excitation occurs at X -heating frequencies both above and below the critical frequency of the F_2 layer. It is assumed that the excitation of the AFAI upon X -heating is associated with the generation of large-scale irregularities due to the self-focusing instability of a powerful HF beam with the subsequent implementation of the mechanism of small-scale stratification of large-scale plasma formations.

For the geophysical conditions corresponding to the conditions of the experiments at the SPEAR facility, the trajectories of the propagation of diagnostic HF signals were simulated when they were scattered at the AFAI. The simulation results showed that the signals scattered at the AFAI in the F - or E -layer of the ionosphere in an artificially disturbed region of the ionosphere above SPEAR could get to a receiving point located near St. Petersburg.

The results of experiments on recording the spectra of the heating signal in Barentsburg, Spitsbergen, indicate the excitation of the DM -component in the spectrum of stimulated electromagnetic emission (SEE) in the F -layer of the polar ionosphere. The generation of the DM -component, which is the most typical structure of the SEE, was accompanied by the excitation of the AFAI. In general, the DM -component appeared rather irregularly, which is apparently due to significant variations in the critical frequencies of the F_2 layer (from 3.5 to 4.6 MHz). It is interesting to note that the generation of the DM -component was observed similarly to the excitation of the AFAI upon heating at frequencies above the critical frequency by up to 0.5 MHz.

For the first time, stimulated electromagnetic emission of the ionosphere in the E_s layer, accompanied by the generation of the AFAI, was discovered. Based on the analysis of the experimental data obtained in Barentsburg, the formation of a broadband “noise-like” component and the appearance of additional maxima in the spectrum of the heating signal was detected. Additional maxima were formed both at positive ($f^+ \approx 8\text{--}30$ kHz) and negative ($f^- \approx 9\text{--}25$ kHz) frequency offsets relative to the heating signal frequency f_H . One of the characteristic features of the behavior of the observed radio emission is the temporal variability of the frequency and width of additional maxima in the radiation spectrum.

REFERENCES

- Blagoveshchenskaya N.F., Borisova T.D., Kornienko V.A. et al. Izvestija vuzov. Radiofizika.* Phenomena in the polar ionosphere initiated by the action of powerful HF radio waves of the SPEAR facility. *Izvestija vuzov. Radiofizika.* University News. Radiophysics. 2008, 51 (11): 939–950. [In Russian].
- Borisova T.D., Blagoveshchenskaya N.F., Kornienko V.A. et al.* Features of artificial ionospheric radiosignal under the influence of powerful HF radio waves of the SPEAR stand on the sporadic E layer of the polar ionosphere. *Geomagnetizm i Aeronomija.* Geomagnetism and Aeronomy. 2009, 49 (5): 683–694. [In Russian].
- Borisova T.D., Blagoveshchenskaya N.F., Kalishin A.S. et al.* Modification effects of the polar ionosphere by powerful short-wave radiosignal of extraordinary polarization of the SPEAR heating facility. *Izvestija vuzov. Radiofizika.* University News. Radiophysics. 2012, 55 (1–2): 140–157.
- Borisova T.D.* *Programmnoe obespechenie dlja modernizacii parametrov KV radiokanala, uchiyvajushhee jeffekty modifikacii vysokoshirotnoj ionosfery pri vozdeystvii moshhnyh KV radiovoln, predstavljajushhee model' KV radiokanala (CHATRASCA: TRASSA i CHANNEL).* Software for upgrading the parameters of the HF radio channel, taking into account the effects of the modification

of the high-latitude ionosphere when exposed to powerful HF radio waves, representing the model of the HF radio channel (CHATRASCA: TRASSA и CHANNEL). Certificate of state registration of computer programs No. 20144618249. 13 August 2014. [In Russian].

Ginzburg V.L. Rasprostranenie jelectromagnitnyh voln v plazme. Propagation of electromagnetic waves in a plasma. Moscow: Nauka, 1967: 684 p. [In Russian].

Gurevich A.V., Schwarzburg A.B. Nelinejnaja teorija rasprostraneniya radiovoln v ionosfere. Nonlinear theory of propagation of radio waves in the ionosphere. Moscow: Nauka, 1973: 272 p. [In Russian].

Gurevich A.V. Nonlinear phenomena in the ionosphere. *Uspehi fizicheskikh nauk.* Advances in physical sciences. 2007, 177 (11): 1145–1177. [In Russian].

Grach S.M., Sergeev E.N., Mishin E.V., Shindin A.V. Dynamic characteristics of plasma turbulence of the ionosphere initiated by exposure to powerful short-wave radio signal. *Uspehi fizicheskikh nauk.* Advances in physical sciences. 2016, 186 (11): 1189–1228. [In Russian].

Frolov V.L., Kagan L.M., Sergeev E.N. Overview of RFS (Radio-frequency source) properties: New results obtained using the Sura facility. *Izvestija vuzov. Radiofizika.* University News. Radiophysics. 1999, 42 (7): 635–639. [In Russian].

Blagoveshchenskaya N.F., Borisova T.D., Kornienko V.A. et al. Probing of medium-scale traveling ionospheric disturbances using HF-induced scatter targets. *Ann. Geophys.* 2006a, 24: 2333–2345.

Blagoveshchenskaya N.F., Borisova T.D., Kornienko V.A. et al. Artificial field-aligned irregularities in the night-side auroral ionosphere, *Adv. Space Res.* 2006b, 38 (11): 2503–2510.

Blagoveshchenskaya N.F., Borisova T.D., Kornienko V.A. et al. SPEAR-induced field-aligned irregularities observed from bi-static HF radio scattering in the polar ionosphere. *J. Atmos. Sol.- Terr. Phys.* 2009, 71: 11–20.

Blagoveshchenskaya N.F., Borisova T.D., Yeoman T.K. et al. Artificial field-aligned irregularities in the high-latitude F region of the ionosphere induced by an X-mode HF heater wave. *Geophys. Res. Lett.* 2011, 38; DOI: 10.1029/2011GL046724.

Blagoveshchenskaya N.F., Borisova T.D., Yeoman T.K. et al. Plasma modifications induced by an X-mode HF heater wave in the high latitude F region of the ionosphere. *J. Atmos. Solar-Terr. Phys.* 2013, 105–106: 231–244.

Blagoveshchenskaya N.F., Borisova T.D., Yeoman T.K. et al. Modification of the high latitude ionosphere F region by X-mode powerful HF radio waves: Experimental results from multi-instrument diagnostics. *J. Atmos. Sol.-Terr. Phys.* 2015, 135: 50–63.

Blagoveshchenskaya N.F., Kornienko V.A., Petlenko A.V. et al. Geophysical phenomena during an ionospheric modification experiment at Tromsø. *Ann. Geophys.* 1998 (16): 1212–1225.

Borisova T.D., Blagoveshchenskaya N.F., Moskvina I.V. et al. Doppler shift simulation of scattered HF signals during the Tromsø HF pumping experiment on 16 February 1996. *Ann. Geophys.* 2002, 20: 1479–1486.

Djuth F.T., Jost R.J., Noble S.T. et al. Observations of E region irregularities generated at auroral latitudes by a high power radio wave. *J. Geophys. Res.* 1985, 90: 12293–12306.

Grach S.M., Trakhtengerts V.Y. Parametric excitation of ionospheric irregularities extended along the magnetic field. *Radiophys. Quant. Electron.* 1975, 18: 951–957.

Gurevich A.V. Nonlinear Phenomena in the Ionosphere. New York: Springer-Verlag, 1978: 380 p.

Gurevich A.V., Zybin K.P. Strong field-aligned scattering of UHF radio waves in ionospheric modification. *Phys. Lett. A.* 2006, 358: 159–165.

Guzdar P., Chaturvedi P., Papadopoulos K., Ossakow S. The thermal self-focusing instability near the critical surface in the high-latitude ionosphere. *J. Geophys. Res.* 1998, 103: 2231–2237.

Kagan L.M., Nicolls M.J., Kelley M.C. et al. Optical and radio frequency diagnostics of the ionosphere over the Sura facility: Review of results. *Radiophysics. & Radio Astronomy.* 2006, 11 (3): 221–241.

- Lester M. et al.* Stereo CUTLASS: A new capability for the SuperDARN radars. *Ann. Geophys.* 2004, 22: 459–473.
- Leysner T.B.* Stimulated electromagnetic emissions by high-frequency electromagnetic pumping of the ionospheric plasma. *Space Sci. Rev.* 2001, 98: 223–328.
- Mishin E.V., Burke W.J., Pedersen T.* HF-induced airglow at magnetic zenith: theoretical considerations. *Ann. Geophys.* 2005, 23: 47–53.
- Nicolet M.* The collision frequency of electrons in the ionosphere. *J. Terrest. Phys.* 1953, 3: 200–201.
- Ponomarevko P.V., Leysner T.B., Thidé B.* New electron gyroharmonic effects in HF scatter from pump-excited magnetic field-aligned ionospheric irregularities. *J. Geophys. Res.* 1999, 104: 10081–10087.
- Rietveld M.T., Kosch M.J., Blagoveshchenskaya N.F. et al.* Ionospheric electron heating, aurora, and striations induced by powerful HF radio waves at high latitudes: aspect angle dependence. *J. Geophys. Res.* 2003, 108 (A4): 1141; DOI: 10.1029/2002JA009543.
- Rietveld M.T., Senior A., Markkanen J., Westman A.* New capabilities of the upgraded EISCAT high-power HF facility. *Radio Sci.* 2016, 51 (9): 1533–1546.
- Robinson T.R.* The heating of the high latitude ionosphere by high power radio waves. *Physics Reports.* 1989, 179: 79–209.
- Robinson T.R., Yeoman T.K., Dhillon R.S. et al.* First observations of SPEAR-induced artificial back-scatter from CUTLASS and EISCAT Svalbard radars. *Ann. Geophys.* 2006, 24: 291–309.
- Schunk R.W., Nagy A.F.* *Ionospheres: Physics, Plasma Physics, and Chemistry.* Atmospheric and Space Science Series. Cambridge University Press., N.Y., 2000: 570 p.
- Sheerin J.P., Cohen M.B.* Nonlinear plasma experiments in geospace with gigawatts of RF power at HAARP. *AIP Conf. Proc.*, 2015; DOI: 10.1063/1.4936465.
- Thidé B., Kopka H., Stubbe P.* Observations of stimulated scattering of a strong high-frequency radio wave in the ionosphere. *Phys. Rev. Lett.* 1982, 49: 1561–1564.
- Vas'kov V.V., Gurevich A.V.* Nonlinear resonant instability of a plasma in the field of an ordinary electromagnetic wave. *Sov. Phys. JETP.* 1976, 42: 91–97.
- Yeoman T.K., Blagoveshchenskaya N.F., Kornienko V.A. et al.* SPEAR: Early results from a very high latitude ionospheric heating facility. *Adv. Space Res.* 2007, 40: 384–389.

4.3. STATE OF THE UPPER ATMOSPHERE ON SPITZBERGEN

R. Yu. Lukianova

The upper atmosphere is the outer part of the gaseous shell of Earth. It extends in height from about 50 km to several hundred kilometers, where it is gradually transformed into near-Earth space, filled by the Earth's magnetic field. Ionized particles formed under the influence of solar UV radiation play the central role in all processes developing in the upper atmosphere – the ionosphere. At high latitudes, there is an additional source of ionization in the form of sporadic fluxes of charged energetic particles of magnetospheric origin, precipitating into the ionosphere.

The properties of the neutral atmosphere determine the behavior of the ionized component at altitudes > 100 km. Above ~ 600 km, the motion of charged particles is controlled only by the Earth's magnetic field and the rapidly changing interplanetary magnetic field (IMF), which is associated with a supersonic flow of solar plasma, the solar wind (SW), constantly emanating from the solar corona. The ions at an altitude of ~ 120 km (E-layer of the ionosphere) are effectively carried away by neutrals, and move relative to the electrons. Here electric currents develop, which, even during moderate geomagnetic disturbances, reach several million amperes. The electron density maximum is, on average, at an altitude of ~ 250 km (the ionospheric F-layer).

When SW and IMF interact with the Earth's magnetosphere, about 10^{12} W of energy is supplied to the near-Earth space. The entry of this energy into the near-Earth space and its redistribution in the ionosphere occurs mostly in the high-latitude regions of the Earth. In the polar ionosphere, electrodynamic processes play the main role, and in the first turn it is the horizontal flow (convection) of the ionospheric plasma under the action of the SW electric field and the electric field generated due to the motion of the plasma in the magnetosphere. The high-latitude ionosphere is connected to the boundary layers of the magnetosphere through the electric currents flowing along the geomagnetic field lines.

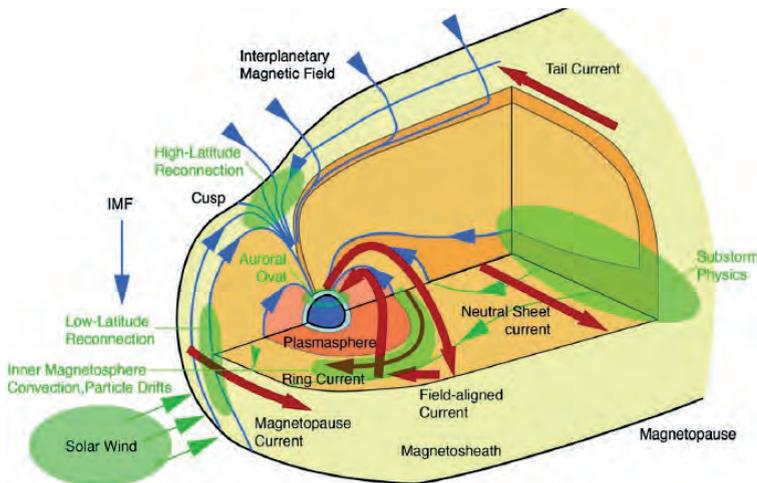


Fig. 4.3.1. Magnetosphere: main plasma domains (brown areas) and physical processes (green areas), systems of electric currents (brown arrows), geomagnetic field, and IMF lines (blue arrows) (after Hunsucker, 1991)..

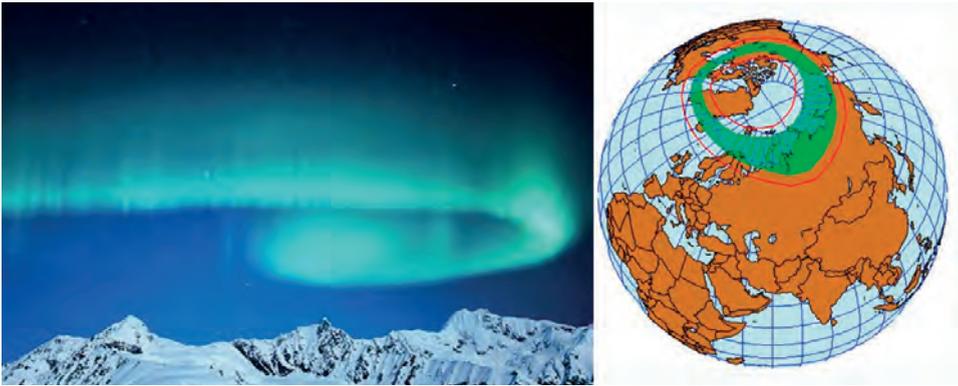


Fig. 4.3.2. Auroras and a geographic projection of the auroral zone in the Northern Hemisphere.

Right: green-shaded area shows the statistical auroral zone for favorable geomagnetic conditions, and green line show the equatorial boundary of the zone during a magnetic storm of moderate intensity.

Left: Photo: from open sources. Picture: <https://www.gi.alaska.edu/monitors/aurora-forecast>.

Fig. 4.3.1 shows the scheme of SW interaction with the Earth's magnetosphere and the structure of electric currents in the magnetosphere-ionosphere system. The IMF is "frozen in" the SW plasma and moves with its flow. The electrodynamic interaction between the SW energy and the Earth's magnetic field occurs mainly in the boundary layers and the magnetotail, which are conjugated along the magnetic field lines of the Earth's dipole with high-latitude ionospheric regions – the auroral zone and the polar cap. The geomagnetic field lines, conjugated with the polar cap, are extended far into the magnetotail and are directly open for the penetration of SW and IMF plasma. The lines, emerging from the auroral zone, are projected into the central plasma layer of the magnetosphere, occupied by plenty of charged energetic particles.

When the Sun is active, and the IMF and SW plasma velocity are large and highly variable, sporadic electrodynamic and plasma processes develop – these are magnetospheric storms and substorms. A sharp increase in plasma convection, intensification of electric fields and currents in the three-dimensional magnetosphere-ionosphere system, the formation of a substorm electrojet in the nighttime ionosphere, and fluxes of energetic particles from the magnetotail accompany these disturbances. The precipitation of energetic particles (mainly electrons), which ionize the air molecules and cause the glow of atmospheric gases – auroras (Fig. 4.3.2, left), are localized in the auroral zone. The right panel of Fig. 4.3.2 shows the geographic projection of the auroral zone in the Northern Hemisphere, and one can see that with increased magnetic activity the Spitsbergen archipelago turns out to locate within the auroral zone.

The level of solar activity, solar wind parameters, the state of the magnetosphere, ionosphere, and thermosphere – what is generally called space weather – have a significant impact on the conditions of operation and reliability of modern space and ground technological systems.

IONOSPHERIC OBSERVATIONS ON THE SPITZBERGEN

The Spitsbergen archipelago is located in the polar part of the auroral zone. The auroral zone shrinks towards the polar cap during the period of the minimum of the 11-year solar activity cycle, and one can observe manifestations of almost all electrodynamic processes

in the ionosphere over Spitsbergen that occur in the polar ionosphere during the interaction of the solar wind with the Earth's magnetosphere. Due to the mismatch between the two poles – geographic and geomagnetic – Spitsbergen is a unique place that can be located within the auroral zone, outside it, and directly in the auroral region during the day. Here, one can observe the processes occurring in the ionosphere due to disturbances of the underlying neutral atmosphere, in particular, high-altitude manifestations of atmospheric waves and sudden stratospheric warmings.

It is believed that Russian auroral research in the Arctic began with the Russian-Swedish expedition to Spitsbergen in 1899–1900, during which systematic visual observations of auroras were carried out. The concept of the auroral zone, first formulated by Russian scientists (Feldstein, Starkov, 1967), was mostly based on photometric observations at Spitsbergen.

Currently, several cooperative radar optical and magnetic observations are being carried out on the archipelago, which provides an integrated approach to the study of the ionosphere, ionosphere-magnetosphere interaction, and space weather. It should be noted that, despite the intense involvement of satellite measurements in solving space weather problems, the analysis of ground-based observations remains no less effective way to study the processes occurring in the upper atmosphere (especially from the point of view of the cost/productivity–balance).

The combination of the factors listed above determines the increased interest of the world geophysical community in research on Spitsbergen, which is currently being implemented in the creation of one of the best and most convenient international test sites in the Arctic with a developed infrastructure and stable international relations on the archipelago. On the Russian side, not only the Arctic and Antarctic Research Institute (AARI) carries out regular observations of space weather with the help of optical, radiophysical and magnetometric equipment but also the Polar Geophysical Institute (PGI) of the Russian Academy of Sciences. In particular, radio signals of the ultra-long-wave range are received, which is an important source of information about the structure of the lowest part of the ionosphere at an altitude of 50–90 km, where the electron density is very low. Within the framework of international cooperation, there are research opportunities to use the unique European radar facility EISCAT (European Incoherent Scatter Radar System) to study the characteristics of the polar ionosphere. An open competition of projects is held annually, based on new ideas for using radar observations, and radar operation time is free for the selected projects. Also, the radar data obtained in the course of the standard observation program are available for free and can be used for unique studies of the upper atmosphere and the ionosphere in the Arctic region. The following sections present the electrodynamic characteristics of the upper atmosphere obtained from the analysis of radar observations and regional modeling of ionospheric parameters.

EISCAT INCOHERENT SCATTER RADAR ON SPITZBERGEN ARCHIPELAGO

One of the most informative among the radiophysical methods for studying the ionosphere is the method of incoherent scattering (IS) of radio waves. Powerful radars are used in this method to obtain information about the vertical structure of the ionosphere and its dynamics. The IS allows one to obtain information on the distribution of such parameters of the ionospheric plasma as electron concentration, electron and ion temperature, plasma drift velocity along the sounding direction, and ionic composition. In contrast to ground-

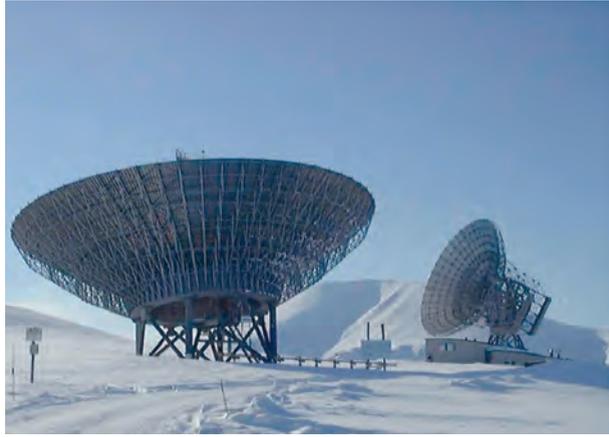


Fig. 4.3.3. Incoherent scatter radar ESR on Spitsbergen.

Photo: from open sources.

based high-frequency (HF) ionosondes, which can provide information only on the electron concentration below the main ionospheric maximum, the IS signals pass through the entire ionosphere. A relatively weak signal is returned, which can be registered and isolated using special processing and statistical averaging (Hunsucker, 1991). The large number of plasma parameters measured simultaneously over a considerable interval of altitude makes the data of the IS radars a very valuable tool to study the ionosphere, ionosphere-magnetospheric interaction, and the relationship between the ionosphere and the neutral atmosphere.

In 1996, one of the highest-latitude IS radar of the EISCAT system was put into operation – the ESR radar (European Svalbard Radar) located near Longyearbyen on Spitsbergen (geographic coordinates: 78.15° N, 16.03° E; geomagnetic latitude 75.3°). The radar consists of two paraboloid antennas operating at 500 MHz, with a maximum radiate power of 1 MW. One antenna, 42 m in diameter, is fixed towards the geomagnetic field lines (slightly tilted to the south from the vertical direction). The second antenna, 32 m in diameter, can change the direction of the beam over a wide range, which allows the radar to operate in different modes and sound the ionosphere not only directly above the facility location, but also in its vicinity (fig. 4.3.3).

The radar standard spatial resolution is units of kilometer, and the temporal resolution varies from fractions of a second to several minutes, depending on the operating mode. The characteristics of the ionospheric plasma in the direction of the beam are determined from the spectrum of the reflected signal using the standard GUISDAP software package (Lehtinen, Huuskonen, 1996).

CHARACTERISTICS OF IONOSPHERIC PLASMA CONVECTION ACCORDING TO THE EISCAT INCOHERENT SCATTER RADAR ON SPITZBERGEN AND THE RESULTS OF SIMULATION

The solar wind and the “frozen-in” IMF are the main factors controlling the polar ionosphere electrodynamics. The IMF intensity and direction determine the rate of plasma motion, the magnitude of the ionospheric electric field, the size of the polar cap and the latitudinal extension of the auroral oval. The vertical (B_z) component of the IMF is of primary importance. When the IMF is southward ($B_z < 0$), it is directed oppositely to

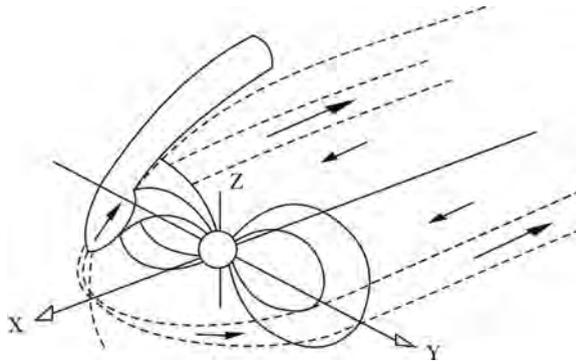


Fig. 4.3.4. Transfer of plasma tubes from the day side to the magnetotail due to the interaction of the solar wind with the magnetosphere.

In the solar-geomagnetic coordinate system, the X -axis is directed towards the Sun, the Y -axis – from dawn to dusk; black arrows show the direction of the convective drift of the plasma tubes.

the Earth's dipole magnetic field. This configuration results in a reconnection of the IMF the geomagnetic field lines at the dayside magnetopause and active transfer (convection) of magnetospheric plasma tubes from the daytime side to the magnetotail (Fig. 4.3.4).

Ionospheric plasma is also involved in the convective motion when it drifts along the lines of equal electric potential projected from the magnetosphere. If $B_z < 0$, at ionospheric altitudes, a two-vortex convection system, almost symmetric with respect to the noon-midnight meridian, is developed. Within the polar cap, the ionospheric plasma moves anti-sunward, and the return motion occurs at lower, auroral latitudes. When the IMF turns to the north ($B_z > 0$), the reconnection becomes weak and shifted to the night side, and plasma convection is also weakened. At the ionospheric altitudes, the convection pattern has the form of two relatively weak vortices located close to the pole, and the plasma moves sunward in the central part of the polar cap.

The azimuthal (B_y) IMF component distorts this symmetric picture. Asymmetry is determined by the sign of B_y , since the region of magnetic field lines is shifted either to the dawn or dusk flank of the magnetosphere depending on the B_y polarity. Thus, in the northern polar cap, at $B_y < 0$, the plasma moves more intensively counterclockwise, and at $B_y > 0$, clockwise.

Thus, depending on the orientation of the vector and the magnitude of the IMF modulus, as well as additional parameters such as the solar zenith angle, the level of solar and geomagnetic activity, specific structures of the convective drift of the ionospheric plasma are realized in the high-latitude ionosphere and large- and small-scale irregularities of electron density that directly influence the propagation conditions of radio waves.

CHARACTERISTICS OF A PLASMA FLOW NEAR THE POLAR CAP BOUNDARY OF ACCORDING TO RADAR OBSERVATIONS ON SPITZBERGEN

The polar cap boundary (PCB) separates the area of closed magnetic field lines of the Earth's dipole from the area, where the geomagnetic field lines are open to space and connecting with the IMF. Under the southward IMF conditions, the polar cap expands, and when the IMF turns to the north, the polar cap area decreases. Under the influence of the IMF B_y component, the PCB is shifted to the dawn or dusk side. The asymmetric part of the electric field controlled by B_y is manifested mainly at high geomagnetic latitudes. This is an area where the number and density of measurements are still relatively small,

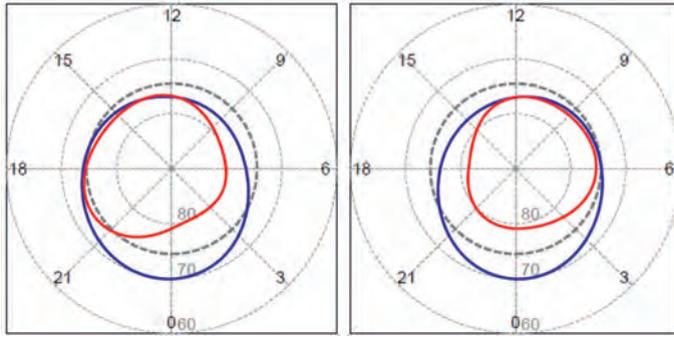


Fig. 4.3.5. Model position of the PCB at an altitude of 200–300 km if $B_y < 0$ (left) and $B_y > 0$ (right). The blue (red) line indicates the PCB at $B_z < 0$ ($B_z > 0$); the black dashed line shows the trajectory along which the radar moves during a day.

and the problem of obtaining accurate quantitative estimates remains very urgent. In this regard, the interpretation of the measurements the ESR radar located on Spitsbergen and constantly operating near PC, is of particular interest and makes it possible to collect large statistics of experimental data to study the trajectories and velocity of plasma flow, as well as to estimate the shift of the cap boundaries when the direction of the IMF vector changes.

The approximate position of the PCB at an altitude of 200–300 km can be determined from the topological model of the magnetosphere. Figure 4.3.5 shows the position of the PCB, calculated according to the model by Tsyganenko & Sitnov (2005) using the GEOPACK-2008 software package at average IMF values over the observation period,

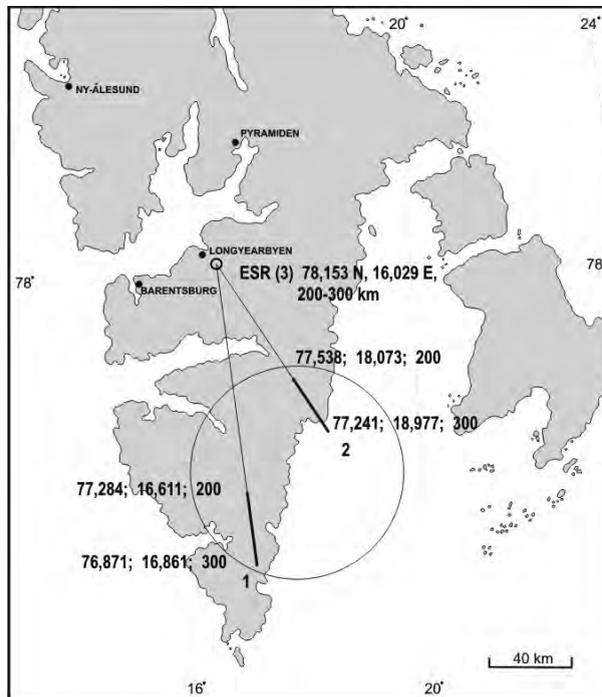


Fig. 4.3.6. The radar position and the direction of the beams in the CP2 experiment.

as well as the trajectory along which the observation point (i.e., the ESR) moves during a day. Based on the magnetospheric model, we can see that the radar can be located as in the region of open as closed field lines, depending on the time of day and IMF orientation.

Based on the analysis of ESR measurements, we obtained:

- statistical dependence of the meridional and zonal plasma drift velocity on the IMF parameters in the Spitsbergen region;
- the estimate of the PCB shift depending on the magnitude and sign of the IMF B_y and how this shift affects the zonal plasma drift.

Fig. 4.3.6 shows the radar position and the direction of the beams in the CP2 (Common Program 2) experiment, the data of which were used to determine the characteristics of the plasma flow near the PCB. The 32-meter antenna beam periodically scanned between three positions (one vertical and two oblique to the horizon at 63 or 66° with azimuth angles of 172 and 144°, respectively). The scanning cycle was about 6 minutes. Measurements were carried out with resolution in the horizontal plane about 100 km and referred to an altitude of 200–300 km (F -region of the ionosphere). The configuration made it possible to obtain data related to a geomagnetic latitude of $\sim 74.5^\circ$. The velocity vector of a large-scale plasma flow was calculated under the assumption that the flow is spatially uniform in the measurement region and its invariable during the scanning cycle. The electric field vector was determined under the assumption that the plasma moves with a drift velocity $E \times B$. In the period 2000–2007, the radar operated in CP2 mode for about 1700 hours. The entire dataset related to the CP2 experiment was selected from the MADRIGAL database (<http://madrigal.haystack.mit.edu/>).

ESTIMATION OF THE DEPENDENCE OF THE CONVECTION VELOCITY AND THE POLAR CAP BOUNDARY SHIFT ON THE IMF B_z AND B_y COMPONENTS

The subject of the analysis was the relationship between the ionospheric plasma convection velocity, measured by the radar, and the IMF. These dependencies are characterized primarily by the correlation coefficient C_{corr} and the linear regression coefficients for the parameters B_y and V_E . The linear regression coefficient K_R was calculated using the least-squares method:

$$V_E = V_{E0} + K_R B_y \quad (4.3.1)$$

where V_{E0} is flow caused by reconnection at the subsolar point and quasi viscous interaction and independent of sign of B_y . Confidential interval C_{corr} was calculated by the formula:

$$\partial C_{corr} = t_\gamma \frac{1 - C_{corr}^2}{\sqrt{n}}, \quad (4.3.2)$$

where n is the number of points, t_γ is a standard normal distribution (for 95 % confidence interval $t_\gamma = 1,96$).

During all MLT hours, there is a connection between V_E and B_y MMF, which can be approximated by a linear function with a regression coefficient K_R . Correlation coefficient C_{corr} between parameters V_E and B_y IMF reflects the current location of the radar relative to the PCB and the degree of influence B_y IMP on the structure of the trajectories of ionospheric plasma convection.

Fig. 4.3.7 shows how C_{corr} , K_R and PCB shift value change during the day (in degrees of magnetic latitude) when changing direction of B_y IMF. There are two curves for each parameter: at $B_z < 0$ and $B_z > 0$. Curves for C_{corr} and K_R have two well-defined minima – in the morning and evening hours MLT, and two maxima – at noon and night hours.

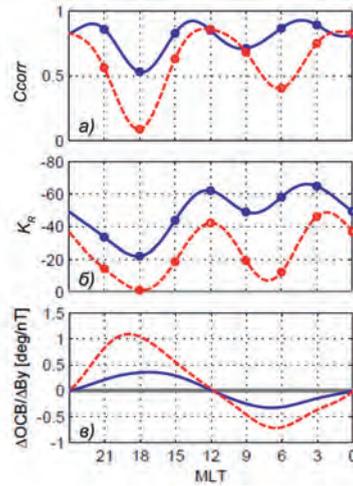


Fig. 4.3.7. Daily change (from top to bottom) in the correlation coefficient C_{corr} between B_y IMF and V_E ; coefficient of linear regression K_R between B_y and V_E ; and speed of PCB shift at the change of B_y . There are two curves for each parameter: at $B_z < 0$ (blue curve) and $B_z > 0$ (red curve).

The presence of minima confined to the 06–18 MLT meridian reflects the shift of PCB under B_y . Indeed, if we assume that the circular motion of plasma around the pole occurs on open lines of force, then when the observation point leaves this region, the zonal velocity component rapidly decays. This is reflected in a sharp decrease of C_{corr} . The figure shows that the evening minimum is much deeper than the morning one, which corresponds to a larger shift of the PCB at this time. In the change of K_R parameter, we can also see minima at 06–18 MLT and maxima at 00–12 MLT. The noon maximum is at precisely 12 MLT, and the night one is shifted to the early morning hours. The PCB shift along 06–18 MLT meridian at the change of B_y in the range under consideration is approximately 3° at $B_z > 0$ and 7° at $B_z < 0$. If we divide the full day along the midnight-noon MLT axis and compare the course of the curves for the ranges 0–12 and 12–24 MLT, then an asymmetry is found in the convection response, which consists in the fact that action B_y MLT is one and a half times more effective for the morning hours compared with the evening hours. For the coefficient K_R the difference is approximately 20 m/s per intensity unit, i.e. 1.5 times.

Thus, the observational data of the ESR CP2 experiment made it possible to obtain the statistical characteristics of the zonal and meridional plasma convection velocities driven by the IMF B_z and B_y components. The measurements showed that there is a well-defined asymmetry between the morning and evening local time sectors in the PCB position. The obtained relationships between the plasma drift velocity and IMF parameters are in agreement with the basic physical concept, which is that the complete picture of convection trajectories is given by a superposition of elements, which depend on the IMF B_z and B_y . The results also confirm the mechanism by which the vertical component of the solar wind electric field associated with the IMF B_y creates a radial electric field in the polar cap.

CONCLUDING REMARKS

The data of the European IS ESR radar obtained both during the standard observation program and during experiments with a particular orientation of the antenna are an important component of studies of the electrodynamics of the high-latitude ionosphere.

The physical interpretation of the results of experiments on measuring the electric field and the velocity of the ionospheric plasma convective drift made it possible to reveal the effects of asymmetry in the convection pattern and the position of the polar cap boundary, to obtain statistical characteristics of the ionospheric plasma drift velocity over the Spitsbergen region and to use them in a regional convection model. Based on the results of research carried out within the framework of international cooperation, several articles have been published in rating international journals (Lukianova, Christiansen, 2006; Lukianova, Christiansen, et al., 2011; Kozlovsky et al., 2014; Lukianova, Kozlovsky, 2011). In recent years, radar measurements on Spitsbergen have been actively developed, and a significant amount of new materials has been accumulated. In particular, it is of great interest to analyze the simultaneous measurements of the parameters of the high-latitude ionosphere using the ESR and the equipment installed on board the Swarm satellites (Friis-Christensen et al., 2008). All these data are free to access, available via the Internet on the corresponding portals, and the main task is their interpretation and use to create a new intellectual product.

The prospects for geophysical research on Spitsbergen are associated with both the development of the national base and the strengthening of international cooperation. Coordinated observations and an integrated approach, in which several instruments are involved at once, significantly increase the efficiency of the systems for diagnosing the state of the ionosphere in the Arctic zone. The radar system will continue to continuously monitor the areas of formation of large- and small-scale irregularities of the electron density and systems of ionospheric currents, since these characteristics, along with the areas of particle precipitation, mainly influence the formation of an interference environment and the quality of radio signal reception.

The upper atmosphere, which is located at altitudes of 80–1500 km and is one of the most important parts of the unified Sun-Earth system, plays a key role in the processes of interaction between the ionized and neutral gaseous shells of the Earth. At the same time, the influence of meteorological processes occurring in the high-latitude upper atmosphere on the state of the middle and lower atmosphere has been insufficiently studied. In this regard, it seems promising to supplement the existing radar system on Spitsbergen with a system of mesospheric-stratospheric-tropospheric radars, which are designed to determine the main thermodynamic parameters of the atmosphere up to an altitude of 100 km, such as air temperature, wind speed, and direction, as well as impurities: ozone, water vapor, aerosol.

Temperature and winds in the upper atmosphere are an important link in large-scale atmospheric circulation, including interhemispheric transport. They also affect the flight conditions of high-altitude aviation and the level of pollution during the combustion of space junk and other anthropogenic influences (Kozlovsky et al., 2014). Significant disturbances in the mesosphere and upper atmosphere can be observed during sudden stratospheric warmings (Lukianova et al., 2015). The speed and direction of high-altitude winds, air temperature, as well as the level of atmospheric turbulence at altitudes of 80–100 km can be determined by the transformation of meteor trails, the radio reflections from which are detected by meteor radars. The combination of data from ionospheric radar, ionosonde, and meteorological radar makes it possible to estimate variations in the amplitude of atmospheric gravitational waves, which are excited directly in the polar ionosphere, and also propagate upward from the lower layers of the atmosphere.

In 2013, a modern Australian-made SKiYMET interferometric meteor radar was put into operation on Spitsbergen at the Norwegian station Ny-Ålesund. This compact and easy-to-maintain serial unit comes complete with software and graphical interface. Already the first works published based on the radio sounding data obtained at latitudes above 75° N, i.e., in the inner region of the winter polar vortex, made it possible to estimate the energy fluxes carried by AGW (DeWit et al., 2014). However, access to Norwegian radar data is limited. If similar equipment is installed at the Russian station, it will be possible to conduct research on meteorological events and track long-term climatic changes in the upper atmosphere based on our own measurement data.

Relatively recently, Research and Production Association “Typhoon” (Rosgidromet) has developed a new meteor radar station (MRS). It allows registering the coordinates of the reflecting points of meteor trails, the speed of their drift under the influence of winds in the upper atmosphere, the duration of reflection, the speed, and radiants of meteors. On the territory of the Russian Federation, such stations have already been installed in Angarsk (52° N, 103° E), Petropavlovsk-Kamchatsky (53° N, 159° E), Obninsk (55° N, 37° E), Anadyr (65° N, 178° E), Kandalaksha (67° N, 33° E), Norilsk (69° N, 88° E), Tiksi (72° N, 129° E). A similar station can be installed on Spitsbergen in the area of Barentsburg – in the area of operation of the consortium “Russian Scientific Center on Spitsbergen”.

As for carrying out full-scale monitoring of the atmosphere at different altitude levels, the radiosonde system should be supplemented with an lidars, with which it is possible to monitor the state of the atmosphere up to an altitude of 80 km.

REFERENCES

- Lukianova R.Ju., Samokish B.A., Uvarov V.M. A numerical model of the global distribution of electric potential in the Earth's ionosphere. *Zhurnal vychislitel'noj matematiki i matematicheskoy fiziki*. J. Comput. Math. and Math. Physics. 1997. Vol. 37 (7). Pp. 862–868. [In Russian].
- Uvarov V.M., Lukianova R.Ju. Numerical modeling of the global distribution of electric potential excited by longitudinal current systems DPY and MTS for the equinox and solstice. *Geomagnetizm i ajeronomija*. Geomagnetism and aeronomy. 1999, 39 (3): 62–68. [In Russian].
- DeWit R.J., Hibbins R.E., Espy P.J., Orsolini Y.J., Limpasuvan V. and Kinnison D.E. Observations of gravity wave forcing of the mesopause region during the January 2013 major sudden stratospheric warming. *Geophys. Res. Lett.* 2014, 41: 4745–4752; DOI: 10.1002/2014GL060501.
- Feldstein Ya.I., Starkov G.V. Dynamics of Auroral Belt and Polar Geomagnetic Disturbances. *Planet. Space Sci.* 1967, 15 (2): 209–229.
- Frey H.U. Localized aurora beyond the auroral oval. *Rev. Geophys.* 2007, 45: RG1003; DOI: 10.1029/2005RG000174.
- Friis-Christensen E., Lühr H., Knudsen D. and Haagmans R. Swarm-An Earth Observation Mission investigating Geospace. *Adv. Space Res.* 2008, 41: 210–216.
- Hunsucker R.D. Methods of Measuring Ionospheric Absorption and Other D-Region Parameters. In: *Radio Techniques for Probing the Terrestrial Ionosphere. Physics and Chemistry in Space (Planetology)*. Springer, Berlin, Heidelberg. 1991, 22; DOI: https://doi.org/10.1007/978-3-642-76257-4_7.
- Kozlovsky A., Shalimov S., Koustov A.V., Lukianova R. and Turunen T. Dependence of the spectral width of ionospheric F region HF echoes on electric field. *J. Geophys. Res.* 2011, 116 (A07302); DOI: 10.1029/2011JA016804.

- Kozlovsky A., Shalimov S., Lukianova R., Lester M.* Ionospheric effects of the missile destruction on 9 December 2009. *J. Geophys. Res. Space Physics*. 2014, 119: 3873–3882; DOI: 10.1002/2013JA019531.
- Lehtinen M.S., Huuskonen A.* General incoherent scatter analysis and GUIDAP. *J. Atmos. Solar-Terr. Phys.* 1996, 58: 435–452.
- Lukianova R., Christiansen F.* Modeling of the global distribution of ionospheric electric fields based on realistic maps of field-aligned currents. *J. Geophys. Res.* 2006, 111 (A03213); DOI: 10.1029/2005JA011465.
- Lukianova R., Kozlovsky A.* IMF By effects in the plasma flow at the polar cap boundary. *Ann. Geophys.* 2011, 29: 1305–1315.
- Lukianova R., Kozlovsky A., Turunen T.* Comparison and validation studies related to the modeling ionospheric convection and the European incoherent scatter observations in the polar cap. *Int. J. Geomag. Aeron.* 2008, 7 (GI3005); DOI: 10.1029/2007GI000169.
- Lukianova R., Kozlovsky A., Shalimov S., Ulich T., Lester M.* Thermal and dynamical perturbations in the winter polar mesosphere-lower thermosphere region associated with sudden stratospheric warmings under conditions of low solar activity. *J. Geophys. Res. Space Physics*. 2015, 120; DOI: 10.1002/2015JA021269.
- Papitashvili V.O., Christiansen F., Neubert T.* A new model of field-aligned currents derived from high-precision satellite magnetic field data. *Geophys. Res. Lett.* 2002, 29 (14): 1683; DOI: 10.1029/2001GL014207.
- Papitashvili V.O., Rich F.J.* High-latitude ionospheric convection models derived from Defense Meteorological Satellite Program ion drift observations and parameterized by the interplanetary magnetic field strength and direction. *J. Geophys. Res.* 2002, 107 (A8): 1198; DOI: 10.1029/2001JA000264.
- Ruohoniemi J.M., Greenwald R.A.* Dependencies of high-latitude plasma convection: Consideration of IMF, seasonal, and UT factors in statistical patterns. *J. Geophys. Res.* 2005, 110 (A09204); DOI: 10.1029/2004JA010815.
- Tsyganenko N.A., Sitnov M.I.* Modeling the dynamics of the inner magnetosphere during strong geomagnetic storms. *J. Geophys. Res.* 2005, 110 (A03208); DOI: 10.1029/2004JA010798.
- Weimer D.R.* Models of high-latitude electric potentials derived with the least error fit of spherical harmonic functions. *J. Geophys. Res.* 1995, 100 (A10): 19595–19607.
- Zhang Y., Paxton L.J.* An empirical Kp-dependent global auroral model based on TIME/GUVI FUV data. *J. Atmos. Solar-Terr. Phys.* 2008, 79: 1231–1242.

Chapter 5.

The ecological state of the natural environment in the area of the Spitsbergen archipelago

5.1. ASSESSMENT OF ENVIRONMENTAL POLLUTION ON SPITZBERGEN IN THE AREA OF BARENTSBURG AND ADJACENT TERRITORIES

B.N. Demin, A.S. Demeshkin, S.V. Vlasov, K.A. Bazhukov

This chapter presents the results of a study of environmental pollution in the area of an operating Russian coal mining enterprise in Barentsburg on the Spitsbergen archipelago for the period 2002–2015. This research was carried out by the North-Western branch of the Research and Production Association “Typhoon”. The task was to obtain comprehensive information on the levels of pollution of the natural environment components to the extent necessary for the annual assessment of the existing ecological situation, as well as for the study of the interannual trend. The results of the first stage of work (2002–2010) were included in the monograph “State and trends in the environmental pollution in the places of economic activity of Russian enterprises on the Spitsbergen archipelago (Barentsburg and adjacent territories) for the period 2002–2010”, prepared by a group of authors from the North-West branch of the Research and Production Association “Typhoon”.

In the process of implementing the program in the period 2002–2015 in the Barentsburg region and adjacent reference areas, periodic sampling of atmospheric air, snow cover, sea, and fresh surface waters, sea and freshwater bottom sediments, soils, soil waters, and vegetation cover was carried out. The collected analytical material made it possible to obtain an objective assessment of the current pollution level of the environmental components of the studied territory, as well as to trace the interannual trend of their change.

ESTIMATION OF POLLUTION OF THE ATMOSPHERIC SURFACE LAYER

The main substances polluting the atmosphere in the area of mining, processing, or other use of coal are sulfur dioxide, carbon oxide and dioxide, nitrogen oxide and dioxide, hydrogen sulfide, polycyclic aromatic hydrocarbons (PAHs), volatile aromatic hydrocarbons (VAHs) and heavy metals (HMs). Six points of the reference background polygon and three points of the local polygon took part in atmospheric air research in 2002–2015. The concentration of dust, gas impurities, and volatile organic compounds (VOCs) was determined in the atmospheric surface layer. Samples of atmospheric aerosol were taken to determine the content of heavy metals (Fe, Mn, Ni, Co, Zn, Cd, Cu, Pb, Cr, Sn, Hg) and arsenic, organochlorine compounds (OCs), including polychlorinated biphenyls (PCBs), and polycyclic aromatic hydrocarbons (PAHs). Samples of atmospheric aerosol and air were analyzed for 79 indicators. In total, 205 samples of atmospheric air and 199 samples of aerosol were analyzed in 2002–2015.

Based on the materials of long-term observations carried out in the spring and summer-autumn of 2002–2015, materials were obtained that reflect the long-term and seasonal variability of the indicators of the state of the atmospheric surface layer. To assess this variability, we used the materials of observations carried out on the territory of Barentsburg – in the area of RHMO; on the opposite side of the Grønfjorden – in the area of Stemmevatnet; south of the settlement – at the mouth of the Grøndalselva; in the area of Kapp Dresselhuys – northeast of the settlement.

The quality of atmospheric air in Barentsburg was assessed under the Russian hygienic standards for settlements (GN 2.1.6.1338-03 ..., GN 2.1.6.2309-07 ...), as well as

the requirements of the “Council Directive 1999/30/EC of 22 April 1999 Relating to limit values for sulfur dioxide, nitrogen dioxide and oxides of nitrogen, particulate matter and lead in ambient air” (Council Directive 1999/30 / EC of 22.04.1999 ...).

According to the results of the observations carried out in 2002–2015, the concentration of all chemical compounds regulated in the atmospheric air in the area of Barentsburg did not exceed the MACs. The maximum values of the concentration of greenhouse gases in the atmospheric surface layer, recorded near the central power plant of the village (CPP), did not exceed:

- 0.11 of average daily MAC by the content of sulfur dioxide;
- 0.62 of average daily MAC by the content of nitrogen dioxide;
- for 0.21 of average daily MAC by the content of carbon monoxide;
- 0.28 of average daily MAC by the content of dust.

The levels of hydrogen sulfide, ammonia, phenol, formaldehyde, benzene, toluene, xylene, and ethylbenzene were below detection limits, which did not allow reliable detection.

At the same time, it should be noted that, according to the results of continuous automatic measurements of the content of gas impurities, carried out since September 2009 at Barentsburg RHMO, in the cold season, one-time concentrations of sulfur dioxide in the atmospheric air increased and exceeded the MAC by 2.6 times. The maximum one-time concentration of nitrogen dioxide, according to the observations of the RHMO in 2009–2010, reached 0.5 of MAC (Antsiferova et al., 2010). The measured values of the concentration of regulated organic compounds of the PAH group and the OC group, as well as heavy metals, were significantly lower than the current MACs and TSELs.

From 2006 to 2010 on the territory of Barentsburg, there were cases of long-term spontaneous combustion of waste rock, ignition of coal in a mine, burning of household waste. As a result, the content of combustion products increased significantly in the atmospheric air not only on the territory of the village itself but also at a considerable distance from it. It should be noted that the maximum values of all organochlorine compounds – Hexachlorocyclohexane (HCH), polyisobutylene, DDT, and PCBs – were recorded in the atmosphere of Barentsburg exactly in 2006–2015.

Assessing the overall nature of atmospheric pollution in Barentsburg from 2002 to 2015, it should be noted that the content of pollutants in the air complies with the current Russian and European hygienic standards and does not exceed the values of the standards (MACs and TSELs) approved by Directive No. 1999 / 30 / EC of 22.04.1999 (Council Directive 1999/30/EC of 22.04.1999 ...).

A comparative assessment of the obtained concentration values of the most toxic organic pollutants (pesticides of the HCH and DDT groups, hexachlorobenzene, PCBs, chlordane, PAHs and HMs) in the atmospheric surface layer with available data from Norwegian, North American and Canadian studies in the controlled area of the Arctic indicates that several groups of compounds, such as HCH, PAH compounds, zinc, lead, arsenic have reference values. At the same time, for some indicators (concentrations of polychlorobenzenes, DDT, PCBs, nickel, copper), there are cases when they exceed the reference levels established by international studies in the Arctic, it indicates that there are local sources of pollution in the area of Barentsburg.

ASSESSMENT OF SNOW COVER POLLUTION

The study of snow cover on the territory of Barentsburg and the surrounding area was produced in the winter-spring periods of 2003–2004 and 2007–2015. The components

of the mineral composition (chlorides, sulfates, alkaline and alkaline-earth metals (Na, K, Ca, Mg), nitrogen compounds (nitrites, nitrates, ammonium), petroleum hydrocarbons, phenols, PAHs, OCs, and HMs were detected in the snow cover samples.

Since the main supply source of water reserves in drinking water bodies is the melting of the snow cover, the accumulated pollutants (P) in it enter the drinking water supply systems. Therefore, the level of pollutants in the snow cover was assessed based on compliance with the established hygienic standards for the content of harmful substances in drinking water (SanPiN 2.1.3.559-96) and MAC of harmful substances in the water of water objects used for drinking and domestic recreation purposes (SanPiN 2.1.5.980-00) (GN 2.1.5.1315-03 ..., GN 2.1.5.2280-07 ...).

The concentration of pollutants exceeding the MAC for drinking water was noted in the snow cover of the studied areas for petroleum hydrocarbons (PH) (up to 2.9 MAC), for phenol (up to 1.3 MAC), for benzo(a)pyrene (up to 3.4 MAC in 3 % of samples), for lead (up to 1.29 MAC) and cadmium (up to 2.03 MAC) over the entire observation period. This exceedance was irregular and was most likely associated with the emergency ignition of waste rock and disposal sites.

Snow cover on the territory of Barentsburg and its adjacent areas have a relatively high concentration of pesticides of the HCH, DDT, and PCB groups.

The most significant pollution of snow with pesticides of the HCH group was observed in the spring periods of 2003 and 2004. During this period, the average levels of HCH in the snow of the village and its adjacent areas were 8.01 and 5.75 ng/l, respectively, and at the reference background polygon – 10.8 ng/l, which was 1–2 times higher than the HCH content in the snow cover of the Russian and Canadian Arctic (AMAP Assessment Report ... , 1998, Canadian Arctic Contaminants Assessment Report, 1997). In 2003, the HCH total reached the maximum values for the entire observation period – up to 23.9 ng/l near Stemmevatnet.

Assessment of the snow cover pollution with PCBs revealed a significant spatial heterogeneity of the PCB content in the study area. Significantly higher levels of pollution of the snow cover were noted in the village itself and its adjacent areas, and lower – at reference points. It indicates a significant impact of local pollution sources. Thus, the concentration of the total PCBs in the snow cover in the area of the helipad is 4–6 times as higher as the content of PCBs in the snow cover on the territory of the village and the locations of warehouses and disposal sites. The content of the total PCBs in the reference sampling points on average during the observation period varied from 0 to 19.8 ng/l (average – 2.9 ng/l), which is close to the values noted in the snow cover in the reference regions of the Arctic (Alert, Canada, 1992–1994 – from 1 to 8 ng/l) (AMAP Assessment ..., 2005).

Analysis of snow cover pollution with heavy metals (HM) revealed an excess of the maximum allowable concentration only for lead (up to 1.29 MAC) and cadmium (up to 2.03 MAC). The concentration of the rest of the regulated HM was below the MAC and was 0.9 for nickel, chromium, and iron; 0.66 and 0.32 MAC, respectively.

The concentration of manganese and zinc reached tenths of the MAC, copper, cobalt, mercury, and arsenic – thousandths of the MAC, according to SanPiN 2.15.980-00 in the water of water objects used for drinking and domestic recreation purposes.

The study of the long-term distribution of the heavy metals concentration in the snow cover in the area of Barentsburg has shown that the increased content of most metals

is confined to areas located near the place where they enter the atmosphere (thermal power station, helipad, waste rock, disposal sites). The further from the village, the more significantly concentration of most metals decreases. Thus, near the thermal power plant in the snow cover, there are the maximum concentrations of zinc, copper, lead, nickel, manganese, and cobalt. In the area of a warehouse for building materials and mining equipment, there are the maximum concentrations of cadmium and chromium in the snow.

ASSESSMENT OF SEAWATER QUALITY

Assessment of the seawater quality in the water area of the Grøn fjorden near Barentsburg was carried out based on the compliance of the values of the leading hydrochemical indicators and the concentration of the determined pollutants with the requirements of the current regulatory documents established by Roskomvod and Roskomekologiya (Water quality standards ..., 2010, RD 52.43.2–94).

In seawater samples, the main hydrochemical parameters were determined – hydrogen index (pH), electrical conductivity, oxidation-reduction potential (Eh), total alkalinity, dissolved oxygen, BOD₅, the content of biogenic elements in water (nitrites, nitrates, ammonium, total nitrogen, phosphates, total phosphorus, silicic acid) and the concentration of suspended solids, as well as pollutants – heavy metals and arsenic, OCs, including PCBs, PAHs, PH, saturated aliphatic hydrocarbons (NAHs), VAHs, individual phenols (alkylphenols, chlorophenols, and nitrophenols), synthetic surface-active substance (surfactants). In total, over the observation period from 2002 to 2015, more than five hundred samples of seawater were taken, each of them was analyzed for the content of about one hundred indicators.

The assessment of resistance and pollution level of sea waters in the controlled water area of the bay were carried out based on the frequency (%) and the multiplicity of exceeding the MAC of the regulated pollution indicators (Table 5.1.1).

Comparative analysis of the information received according to RD 52.23.643-2002/36/ showed that in the sea waters of the bay during the entire study period, there were mainly isolated cases of pollution of low (up to 2.0 MAC) and medium levels (from 2.0 to 10.0 MAC), and one case of high pollution with benzo/a/pyrene (over 10 MAC). The bottom horizons were the least polluted. Unstable pollution of the average level in terms of BOD₅, DDT and PCBs was typical for the spring period; it was noted at all horizons, as well as in the content of phenol in the surface water layer.

In general, from the entire list of regulated pollutants, the most significant number of indicators that exceeded the MAC was noted in the spring observation period.

Turning to the spatial-temporal analysis of the pollution distribution, it should be noted that over the entire period of research, the most polluted areas of the water were identified – these are the area of the confluence of the Gladdalen stream and the area of the port. The highest frequency of MAC excess was observed in the area of the confluence of the Gladdalen stream. It is also noteworthy that 2004 became the most unfavorable of the entire observation period in terms of seawater pollution (especially its spring period), when the maximum number of MACs exceeded at all horizons for the BOD₅ value, the total of DDT, PH, phenol, and a total of HCH, PCBs, as well as ions of heavy metals (iron, manganese, copper, and nickel). Most of the above cases of excess relate to the area of the confluence of the Gladdalen stream, which may indicate the influx of these pollutants with meltwater and municipal wastewaters from Barentsburg.

Table 5.1.1

Comparative characteristics of stability and pollution level of sea waters in the Grøn fjorden

Parameter	Surface horizon		Bottom horizon	
	Frequency (%) of cases Exceeding Maximum allowable concentrations (MACs)	Maximum multiplicity of exceeding MACs	Frequency (%) of cases Exceeding Maximum allowable concentrations (MACs)	Maximum multiplicity of exceeding MACs
<i>Spring period</i>				
BOD ₅ (5-day biological oxygen demand test)	9.5	4.2	8.0	3.9
Phosphate phosphorus	0.73	6.4	0.73	7.0
Total PH	3.6	1.4	–	–
Phenol	3.6	2.5	0.73	1.4
Total HCH	0.73	1.9	0.73	1.5
Total DDT	11.7	4.6	10.2	4.6
Iron	0.73	2.6	0.73	2.2
Manganese	0.73	2.0	0.73	1.7
Copper	0.73	1.3	0.73	1.1
Nickel	2.2	2.1	1.5	1.8
PCBs	3.6	8.3	3.6	8.2
Benzo/a/pyrene	–	–	0.73	1.0
<i>Summer-autumn period</i>				
BOD ₅	0.6	1.5	–	–
Nitrite nitrogen	1.8	1.7	–	–
Phosphate phosphorus	0.6	1.4	0.6	1.6
Total PH	6.4	7.6	3.5	1.5
Phenol	–	–	0.6	1.3
Total HCH	0.6	1.5	–	–
DDT	0.6	1.0	–	–
Nickel	–	–	1.8	1.6
Benzo/a/pyrene	1.8	13.8	–	–

To assess the pollution level and the dynamics of the qualitative state of waters in the water area, the water pollution index (WPI) was used (Methodological instructions ..., 1988). When calculating WPI for sea waters, the concentration values of dissolved oxygen, the values of BOD₅, as well as the two indicators with the highest values and exceeding the MAC from the general list of regulated hydrochemical indicators were used. So, for the spring period of research, such indicators were the concentration of the total DDT and PCBs; for the summer-autumn period – the total content of PCBs and petroleum hydrocarbons. Fig. 5.1.1 and 5.1.2 represent the long-term variability of WPI values in the form of histograms.

Comparative analysis of the results obtained for the average long-term WPI values allows us to make a conclusion about the state of pollution of sea waters near Barentsburg. The II water quality class, “clean”, prevailed in most of the surveyed water area, especially in the coastal area, in the spring period of observations. At the same time, water quality tended to improve with increasing depth and distance from the coast.

It should be noted that the water quality was at the level of I class, “very clean”, in 2007–2008 in the seaward part of Grøn fjorden. In 2003 and 2009, the quality of sea waters

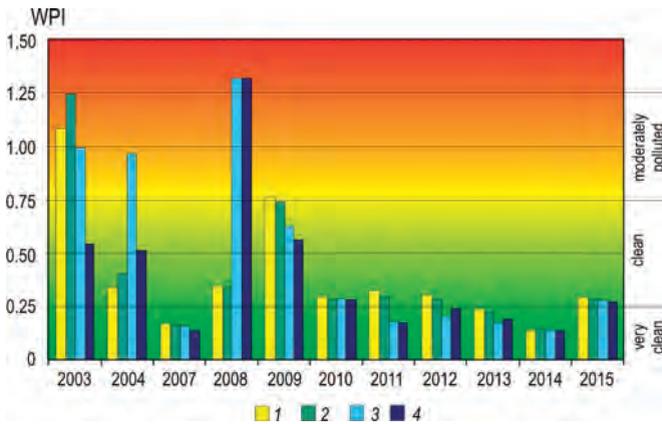


Fig. 5.1.1. Long-term variability of the water pollution index (WPI) in the areas of Grønxfjorden near Barentsburg during the spring observation period 2003–2015.
 1 - coastal, surface; 2 - coastal, bottom; 3 - seaward, surface; 4 - seaward, bottom.

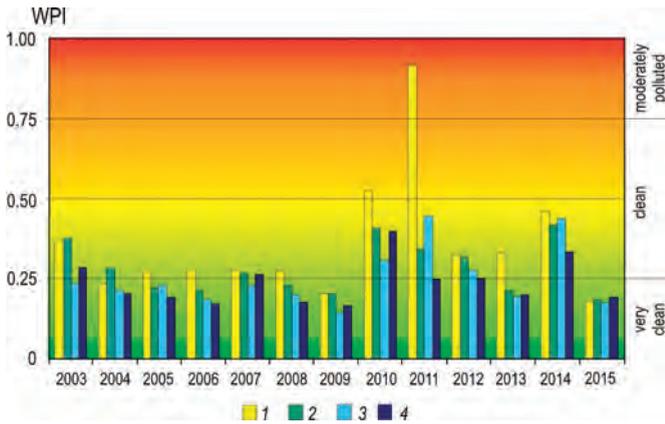


Fig. 5.2.1. Long-term variability of the water pollution index (WPI) in the areas of Grønxfjorden near Barentsburg in the summer-autumn period of observations in 2003–2015.
 See Fig. 5.1.1. for legend.

did not correspond to the average long-term dynamics, differing for the worse. Thus, in the spring of 2003, moderately polluted waters were observed practically throughout the entire water area, except for the bottom horizons of its seaward part. Here, the cases of MAC exceeding for BOD₅ noted everywhere influenced the WPI value the most. The content of pesticides of the DDT group influenced WPI values the most, resulting in moderate water pollution from the surface to bottom, recorded in the spring of 2009 in the coastal part of Grønxfjorden.

In the summer-autumn period of observations, the waters of the coastal part belonged to the II quality class (“clean”), and in 40 % of cases, the WPI value ranged from 0.25 to 0.75. An exception is the surface layer in the area of the stream’s confluence, where moderately polluted waters were observed in 2003, mostly due to the content of nitrite nitrogen with an excess of MAC up to 6.75. The WPI values of the surface horizons of the coastal areas of the water in 2004, 2006 and 2010 were also slightly increased against

the general reference (0.74, 0.74 and 0.69, respectively) due to the excess of MAC for nitrite nitrogen (2004, 2006) and the total content of petroleum products (2010). Waters of class I – “very clean” (31 % of cases) and class II – “clean” (22 % of cases) prevailed in the seaward part of the surveyed water area.

A comparison of the obtained data on the level of pollutants in the waters of the Grøn fjorden Bay with available international data (AMAP Assessment Report ..., 1998) confirms the above assessment of the quality of sea waters.

The concentrations of most groups of pollutants measured during the survey period 2002–2015 have values typical of the coastal regions of the Norwegian and North Seas with an average or insignificant level of impact of coastal pollution sources on the marine area (Arctic Pollution ..., 2009).

ASSESSMENT OF THE POLLUTION LEVEL OF BOTTOM SEDIMENTS

In the area of Barentsburg, there was an assessment of the pollution level of bottom sediments in the Grøn fjorden Bay, Stemmevatnet, and Grøn River. Russian regulatory documents do not regulate the content of pollutants in bottom sediments. Therefore, the assessment of the pollution level of bottom sediments was carried out under the recommendations of SP 11-102-97 (Engineering and environmental surveys ..., 1997), based on the compliance of the pollutants levels with the criteria for environmental assessment of soil pollution, according to the international standards “New Dutch List” (“Neue Niederlandische Liste). To assess the pollution level of bottom sediments with benzo(a)pyrene, recommendations R 52.24.581-97 “Organization and functioning of a special survey system of the natural environment status in the areas of developing coal mining industry and related industries” (R 52.23.581-97) were used.

ASSESSMENT OF THE POLLUTION LEVEL OF MARINE BOTTOM SEDIMENTS OF GRØNFJORDEN

From 2002 to 2015, 158 samples of bottom sediments were taken in the water area of Grøn fjorden to research the content of biogenic elements, heavy metals, and arsenic, OCs, including PCBs, PAHs, PH, NAHs, individual phenols, and surfactants. Samples were taken from the upper (0–5 cm) layer of bottom sediments; more than one hundred indicators were detected in the samples.

In the bottom sediments of Grøn fjorden, the maximum excess of allowable concentration (AC) for the total PH was regularly recorded in the central part of the fjord, the absolute maximum was observed in 2011 and amounted to 4.7 AC. In the coastal part of the bay, increased content of petroleum products was also regularly observed (up to 4.6 AC in 2009). 45 cases of AC exceeding for PH were recorded in total during the observation period in the coastal part of the water area and 71 cases in the seaward part (80 and 71 % of the total number of samples, respectively).

The highest values of the total PAH content were 4.9 AC in 2013. Since 2004, the content of the total PAH decreased and by 2011 amounted to tenths of the AC, and since 2012 the content of the total PAH began to increase, reaching 2–4 AC. During the observation period up to 2012, five cases of AC exceeding were recorded, and all of them were noted only in the coastal part. Since 2012, the PAH content has exceeded the MAC by 1.5–4 times in all areas of the bay. An increase in the share of PAHs with four or more aromatic rings indicates the local nature of the anthropogenic load on the coastal part of the bay associated with coal mining and processing. According to R 52.24.581–97, the bottom sediments of

Grønfjorden are characterized by a “moderate” degree of benzo(a)pyrene pollution over the observation period from 2003 to 2013 and “considerable” from 2013 to 2015.

Only for the DDT group (the organochlorine compounds) had the excess of AC in the bottom sediments of the Grønfjorden (up to 13 AC in 2012). Until 2011, there were only three cases of excess AC of the DDT group compounds, and since 2011, the content of DDT exceeds AC by two or more times.

The bottom sediments of the Grønfjorden, and primarily of the coastal water areas, are characterized by an increased content of PCBs compared to the regional reference (up to 9 AC). The maximum concentrations of PCBs were observed in 2011 when the content of PCBs increased several times (and even several tens of times) compared to previous years. Norwegian studies carried out in the villages of the archipelago also confirm the increased content of PCBs in the bottom sediments of the bay and associate it with the presence of local sources (Demeshkin, 2011; PCBs on Spitsbergen ..., 2008; Jartun et al., 2008). Such a source, in addition to transformer fluid and hydraulic mechanisms, can be, in particular, paints used in the 1970s–1980s both in Norwegian and in Russian settlements. A significant increase in the concentration of PCBs in bottom sediments in 2011 may be associated with construction work and the incineration of construction waste with paint and varnish coating.

The content of substances of the heavy metals did not exceed AC. An exception was a single case in 2004 when the nickel content in bottom sediments reached AC.

In general, a moderate level of pollution is typical for the marine bottom sediments of Grønfjorden during the period from 2002 to 2015. Petroleum products make the main contribution to the pollution of bottom sediments; the excess of AC by other pollutants is sporadic. Over the entire observation period, not a single case of exceeding the intervention limit for all determined pollutants was noted, which indicates an insignificant effect of the coal mining complex and the associated infrastructure on the ecosystem of the fjord.

ASSESSMENT OF THE POLLUTION LEVEL OF RIVER AND LAKE BOTTOM SEDIMENTS

In the period from 2002 to 2015, in the water area of Stemmevatnet, 40 samples from the upper (0–5 cm) layer of bottom sediments were taken for research and 24 samples of bottom sediments from the Grøndalselva. More than a hundred indicators were determined in all samples.

In the river bottom sediments during the observation period, 12 cases of exceeding the allowable concentration of petroleum products (50 % of the total number of samples) were recorded, the maximum value was detected in 2010 (2.7 AC). Three cases of the excess of the AC of the total content of petroleum products were recorded in lacustrine sediments, twice over the entire observation period: in 2004 (1.1 AC), in 2008 (1.5 AC) and 2011 (1.1 AC), and at the same station, located south of the source of the Blendadalen stream (Vasstakelva). The content of PAHs in the river sediments exceeded the AC by four times; the maximum value was noted in 2012 (2.5 AC). No excess of AC for the total PAH was recorded in lacustrine bottom sediments for the entire observation period. The source of PAH pollution of bottom sediments of the mouth of the Grøndalselva, apparently, is the wind transport of dust from the outcrops to the surface of the Barentsburg mine workings and waste rock heaps located on the terrace of the right slope of the Grøndalen.

The content of the DDT group compounds in the bottom sediments of Grøndalselva did not exceed AC during the entire observation period. The content of DDT in the bottom

sediments of Stemmevatnet until 2012, generally, did not exceed the values of the established AC, except for one case in 2002, when an excess (2.8 times) of the AC of the total content of pesticides of the DDT group was noted in lake bottom sediments. In 2012, the concentration increased dozens of times compared to previous years; the maximum value was 19 AC, then the DDT content dropped to 3–4 AC.

Bottom sediments of the Grøndalselva are characterized by an increased content of nickel (up to 1.4 AC, four cases during the observation period), and in 2006 the only case was recorded when the content of cobalt exceeded AC (by 1.1 times). In Stemmevatnet, over the entire observation period, there were 22 cases where the content of heavy metals exceeded the AC: five cases for zinc (all after 2013, the maximum in 2013 was 1.7 AC); seven cases for copper (five of them after 2012, maximum in 2012 – 4.7 AC); there are eight cases for nickel (five of them after 2012, the maximum in 2004 was 2.1 AC); one case for cobalt (1.6 AC in 2004) and chromium (1.1 AC in 2002). The content of other heavy metals in the bottom sediments did not exceed AC.

A “moderate” degree of pollution with benzo(a)pyrene is typical for both river and lake bottom sediments in 2002–2015 under the recommendations R 52.24.581–97.

In general, the technogenic component to the formation of levels of concentration of pollutants in the bottom sediments of the Grønfjorden and the surface waters of the land in the area of Barentsburg is insignificant. The concentration levels of pollutants are characterized by values close to the regional references. All the observed excess of AC in the bottom sediments of water bodies of land were significantly lower than the intervention limit for the entire observation period. Published data from international studies on the pollutants content in bottom sediments of freshwater bodies of the considered region and comparable regions of the Arctic as a whole confirm the above assessment.

QUALITY ASSESSMENT OF INLAND WATER

The main sources of pollution entering the surface waters of the land in the area of Barentsburg are the extraction, processing, and other use of hard coal, indirectly and/or directly affecting the quality of freshwater. The study of the composition of the surface waters of Stemmevatnet, used for drinking and domestic water supply to the village, has been carried out since 2002 in the winter-spring (in the presence of ice cover) and summer-autumn periods. The water of the Grøndalselva has been studied in the summer-autumn period since 2003.

For surface waters, the main hydrochemical characteristics were detected: oxidation-reduction potential (Eh); hydrogen index (pH); alkalinity; the content of biogenic elements (silicic acid, mineral forms of nitrogen and phosphorus and their total amount) and pollutants (heavy metals and arsenic; PAHs; PHs; NAHs; VAHs; individual phenols (alkylphenols, chlorophenols, and nitrophenols); synthetic surfactants; OCs, including organochlorine pesticides and PCBs).

The quality of surface water in various types of economic activity is regulated by hygienic requirements and standards contained in the Sanitary Rules and Norms (SanPiN) (GN 2.1.5.1315-03; GN 2.1.5.2280-07).

In addition to the above documents, the assessment was based on the water quality standards established by the “Council Directive 98/83/EC of 3 November 1998 on the quality of water intended for human consumption” (Council Directive 98/83/EC ..., 1998).

The current regulatory documents of Roskomvoda and Roskomekologii were used (Gokhman, 1988; Methodical instructions..., 1988; RD 52.23.643–2002) to assess the

level of anthropogenic load on aquatic biocenoses, the associated fisheries damage and the degree of degradation of water bodies as fishery water bodies.

ASSESSMENT OF WATER QUALITY ACCORDING TO HYGIENE STANDARDS AND STANDARDS FOR DRINKING AND DOMESTIC RECREATION PURPOSES

The quality of water used for drinking and domestic recreation purposes is regulated by regulatory documents that consider MACs for 54 compounds. Assessment of water quality according to hygienic standards and standards for water used for drinking and domestic recreation purposes was carried out for waters of Stemmevatnet, the primary source of central water supply in Barentsburg. The quality of the lake's surface waters for the spring and summer-autumn periods of 2002–2013 fully complied with the established Russian hygiene standards and MACs, as well as water quality standards established in the countries of the European Union. From 2014 to 2015, the MACs were exceeded for petroleum hydrocarbons, benzo(a)pyrene, and manganese (up to 1.6; 6.5 and 2.5 MAC, respectively).

Over the entire observation period (2002–2015), the maximum naphthalene content was hundredths of the established MAC (up to 0.064 MAC); the content of regulated OCs: the total HCH was 0.001 MAC, the total DDT – up to 0.061 MAC, the total PCBs – up to 0.0052 MAC. From the analyzed list of heavy metals, the values of the iron (0.2 MAC), nickel (0.6 MAC), lead (0.2 MAC), cadmium (0.5 MAC), cobalt (0.03 MAC), zinc (0.01 MAC) concentration were tenths and hundredths of MAC; copper – 0.003 MAC; mercury, arsenic – thousandths of the MAC.

Thus, the water of the Stemmevatnet can be used for drinking and household water use without additional water treatment.

“The list of fishery standards: maximum allowable concentrations (MAC) and tentatively safe exposure levels (TSELs) of harmful substances for the water of water bodies with fishery purposes” was used to assess the level of anthropogenic load on aquatic biocenoses and the associated fisheries damage and the degree of degradation of the reservoir as a fishery water body.

The assessment of the level of pollutants and the quality of surface waters in the studied areas was carried out based on the compliance of the values of hydrochemical indicators with the established MAC for waters of fishery reservoirs, taking into account the requirements of the current regulatory documents of Roskomvod and Rosgidromet. Water quality assessment according to fishery standards (Water quality standards ..., 2010) was carried out for the waters of Stemmevatnet in both seasons and Grøndalselva in the summer-autumn period.

During the observation period from 2002 to 2011 in the waters of the Stemmevatnet, the excess of MAC for waters of fishery reservoirs in spring was recorded in individual cases for the content of nitrite nitrogen (up to 1.5 MAC), ammonium nitrogen (up to 2.0 MAC), PH (up to 2.4 MAC), copper (up to 1, 3 MAC). In the summer-autumn period from 2002 to 2011, the excess of the MAC was noted for the content of nitrite nitrogen (up to 1.1 MAC), iron (up to 1.4 MAC), copper (up to 3.0 MAC), nickel (up to 1.2 MAC), the total HCH (up to 2.3 MAC). After 2012, both the number of cases of MAC exceeding and exceeding values increased. In the autumn of 2014 and the spring of 2015, the excess of the MAC for petroleum hydrocarbons is observed in 100 % of the samples and reaches 3.2 MAC. In 100 % of samples taken in the autumn observation period of 2014 and 2015, manganese exceeds MAC and reaches 25 MAC. The content of the total PCB congeners

exceeded the MAC in 71 % of the samples taken in the spring period from 2012 to 2015 and reached 10 MAC. Also, benzo(a)pyrene (up to 13 MAC) and the total DDT (up to 12 MAC) exceeded MAC in the period from 2013 to 2015.

In the water of the Grøndalselva, over the entire observation period, the following pollutants exceeded MAC: nitrite nitrogen up to 14 MAC, ammonium nitrogen up to 1.3 MAC, benzo(a)pyrene up to 5.4 MAC, manganese up to 410 MAC, zinc up to 40 MAC, copper up to 5.8 MAC, nickel up to 54 MAC, cobalt up to 21 MAC. Nitrite nitrogen, copper, and cobalt exceeded MAC only after 2013. Manganese, zinc, and nickel exceeded MAC in some years throughout the entire observation period from 2002 to 2015, but the values of the excess increased with time, reaching a maximum in 2014.

The assessment of the resistance and pollution level of surface waters was carried out based on calculating the frequency and multiplicity of exceeding the MAC for a water body as a whole or part of it. The characteristic of the stability of water pollution is the part of samples (in percent) in which MAC was reached or exceeded concerning the total number of samples (the frequency of exceeding the MAC). The stability assessment is determined using the following scale: no pollution (the concentration of pollutants does not reach the MAC), single pollution (pollution is observed in individual samples, the frequency of exceeding the MAC is less than 10 %), unstable pollution (the frequency of exceeding the MAC is from 10 to 30 %), stable pollution (recurrence of MAC exceeding from 30 to 50 %), typical pollution (frequency of exceeding MAC from 50 to 100 %).

The frequency of exceeding the MAC characterizes the level of water pollution for a specific ingredient. In contrast, the degree of pollution is determined according to the following scale: no pollution (the concentration of pollutants does not reach the MAC), low level pollution (the multiplicity of exceeding is less than two), moderate level pollution (the frequency of exceeding two up to ten), high level pollution (the frequency of exceeding from ten to 50), very high level pollution (the frequency of exceeding from 50 to 100).

Assessment of resistance and level of water pollution in Stemmevatnet was performed based on the frequency and the multiplicity of exceeding the MAC (Table 5.1.2).

Analysis of the information received in terms of resistance and pollution level showed that in the Stemmevatnet showed the unstable pollution of a high level in terms of PCB content

Table 5.1.2

Comparative characteristics of resistance and levels of water pollution in Stemmevatnet for the period 2002-2015 according to regulated hydrochemical indicators

Parameter	Frequency of exceeding the MAC,%		Multiplicity of exceeding the MAC,%	
	Winter – spring	Summer – autumn	Winter – spring	Summer – autumn
Nitrite nitrogen	2.8	3.4	1.5	1.7
Ammonia nitrogen	5.6	–	2.0	–
PH	8.3	6.8	2.4	3.2
Benzo(a)pyrene	8.3	4.6	1.7	13.1
Iron	–	1.1	–	1.4
Manganese	–	11.5	–	25.0
Copper	11.1	22.7	1.26	3.00
Nickel	–	1.1	–	1.2
Σ HCH	–	2.3	–	2.3
Σ DDT	13.9	2.3	4.4	12.1
Σ PCBs	27.8	1.1	10.4	1.6

Classification of surface waters according to the water pollution index (WPI)

Water quality class	Characteristic	WPI
I	Very clean	< 0.3
II	Clean	> [0.3–1]
III	Moderately polluted	> [1–2.5]
IV	Polluted	> [2.5–4]
V	Dirty	> [4–6]
VI	Very dirty	> [6–10]
VII	Extremely dirty	> 10

and unstable pollution of a moderate level in terms of DDT; isolated cases of moderate level pollution were noted for the content of ammonium nitrogen and PH, low levels – for nitrite nitrogen and benzo(a)pyrene. In the summer-autumn period, there was unstable high level pollution in terms of manganese content; isolated cases of high level pollution were detected for the content of benzo(a)pyrene and the total DDT, the average level – for the total PH and HCH, low level – for the total nitrite nitrogen, iron, nickel, and PCBs.

WPI calculations for surface waters of fresh land bodies in the Barentsburg area for the entire observation period were performed using the values of dissolved oxygen, BOD5, ammonium nitrogen, nitrite nitrogen, copper, and zinc.

WPI values obtained for Stemmevatnet in spring varied from 0.13 to 0.52, averaging 0.29 in a long-term perspective. In the summer-autumn period, the WPI value varied from 0.11 to 0.84, averaging 0.36 on a long-term perspective.

Thus, following the accepted classification of waters according to the WPI index (Table 5.1.3), the lake water for the entire observation period is classified as “clean” and “very clean”. The nature of the annual variability of WPI in waters of the lake is shown in Fig. 5.1.3. The figure shows that from 2005 to 2008, as well as in 2011 and 2013. The pollution of the lake water was the lowest (WPI less than 0.3), which, according to the classification of waters, makes it possible to refer it to the I quality class – “very clean”. In other years, the waters of the lake belong to the II quality class – “clean”.

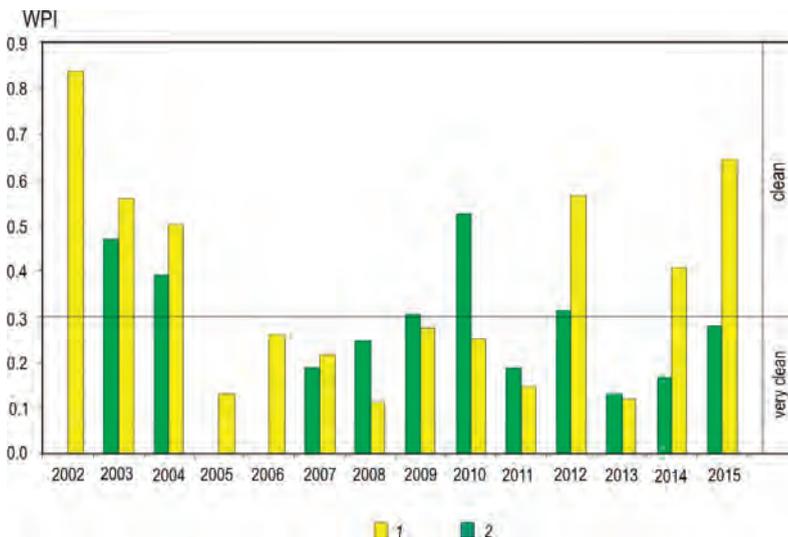


Fig. 5.1.3. Long-term variability of the water pollution index (WPI) of the Stemmevatnet in the spring and summer-autumn periods.

Assessment of resistance and level of pollution of the Grøndalselva, based on the frequency and the multiplicity of exceeding the MAC, is presented in Table 5.1.4.

Analysis of the received information showed that the river had a very high level of manganese pollution; unstable pollution was noted: very high level – nickel, high level – nitrite nitrogen, zinc and cobalt, medium level – copper; isolated medium-level pollution – ammonium nitrogen and benzo(a)pyrene. The calculated WPI values in the summer-autumn period had significant interannual variability and differed, depending on the location of the observation stations. For the gauging station located directly at the river mouth (station 6), the calculated WPI value for the observation period varied from 0.09 in 2005 to 17.8 in 2014, averaging 4.4.

The WPI index during the observation period varied from 0.23 in 2005 and 2012. to 75.2 in 2014, average 10.7 for the gauging station located upstream of the river at a distance of 3 km from the mouth.

Following the accepted classification of waters according to WPI (see Table 5.1.3), the water of Grøndalselva for the entire observation period in the estuary gauging station (station 6) can be ranged to the V quality class “Dirty”, the water in the station located above – to the VII quality class “Extremely dirty”.

Thus, summarizing the assessment of the quality of land surface waters in the area of Barentsburg, we can note the following:

- the water of Stemmevatnet for the entire observation period have insignificant pollution, meet the sanitary and hygienic standards for drinking and household water use, belong to the II quality class (“clean”) and do not have a well-defined trend towards the water quality deterioration;

- water quality of Grøndalselva has a well-defined trend of deterioration of the water body, observed from 2007 to the present. The overall assessment of the degree of water pollution of Grøndalselva is influenced by heavy metals, especially manganese, which is characterized by very high levels of pollution, as well as zinc, copper, nickel, and cobalt.

Studies of the soil water sampled in the valley of the Grøndalselva show a significant excess of AC and MAC for the content of iron (up to 35 MAC), manganese (up to 232 MAC), nickel (up to 23 MAC). Considering that, in addition to glaciers, groundwater and soil water are the sources of the river in the summer-autumn period, the significant deterioration in quality noted above is apparently explained by changes in hydrogeological conditions and the peculiarity of groundwater discharge in the region of the valley and the river bed of Grøndalselva.

Table 5.1.4

Comparative characteristics of resistance and levels of water pollution in Grøndalselva for the period 2002–2015 according to regulated hydrochemical indicators

Parameter	Frequency of exceeding the MAC, %	Multiplicity of exceeding the MAC
Nitrite nitrogen	16.7	13.75
Ammonia nitrogen	8.3	1.25
Benzo(a)pyrene	8.3	5.4
Manganese	66.7	410
Zinc	22.9	40
Copper	29.2	5.8
Nickel	20.8	54
Cobalt	16.7	42

Comparative characteristics of the HM content in the waters of Lapland lakes in 1993 and Stemmevatnet in 2002–2015

Metal	HM content, µg / l	
	Lapland lakes	Stemmevatnet
Cadmium	0.02	0.08
Chromium	0.24	0.45
Nickel	0.25	2.05
Lead	0.25	0.66
Copper	0.28	0.52
Zinc	1.84	2.20

The levels of heavy metals obtained in the course of research in Stemmevatnet are in good agreement with the materials of regular observations carried out by the Murmansk RHMO on Stemmevatnet and Kopan Lakes in similar periods (Antsiferova et al., 2010). The reference level of HM content in water bodies of West Spitsbergen significantly exceeds the reference metal levels typical for water bodies located in the north of Europe (Table 5.1.5) (Report on research ..., 2001, 2002; Mannion et al., 1995), which is associated with geological features, typical for the West Spitsbergen, where, in the course of geological exploration carried out in previous years, manifestations of iron, zinc, lead, copper and other metals were discovered (Russian geological research ..., 1998).

ASSESSMENT OF SOIL POLLUTION

The Barentsburg mine is the only Russian coal mining enterprise currently operating on Spitsbergen. As you know, the coal mining industry is one of those branches of economic activity, the development of which is accompanied by a significant negative impact on human health and disruption of the ecological state of the natural environment. The main sources of pollution from coal mining and processing are mine waters, waste rock, dust emissions, and emissions from coal-fired power plants.

The direct source of soil pollution in coal mining areas are gas and dust emissions into the atmosphere, containing suspended dust particles precipitating on the soil cover, on which most toxic compounds (heavy metals, petroleum products, OCs, PAHs, including benzo(a)pyrene, etc.), as well as wind-blown ash from dumps, settle. Also, soils are polluted by mine waters when they are discharged onto landscapes and during the infiltration of wastewater from ash dumps of power plants. In general, the level of soil pollution depends on many factors, and in particular on their type, migration abilities of toxic agents, terrain, dominant winds, power and nature of pollution sources, etc. Soil pollution can be local or regional in accordance with the nature of the distribution of atmospheric emissions. Most of the pollutants precipitate within a radius of 10–15 km from the emission site. The data on the concentration distribution of some heavy metals, as well as PAHs, in particular benzo(a)pyrene, are very informative, which serve as the most specific indicator in assessing the zones of the negative impact of the coal mining industry and coal-consuming industries.

In addition to local sources, soil cover pollution can be influenced by transboundary transport and remote sources. As you know, pollutants that enter the atmosphere in regions of industrial activity can be sorbed on the surface of atmospheric aerosols, form their solid micro-conglomerates, or be in the atmosphere in a gaseous state.

Depending on the distance from the settlement and the mine, on the altitude position of the test sites and the presence of local sources of pollution, eight regions were identified, within each of them, the data obtained as a result of studies of soil cover samples were generalized. Four sites are designated as local monitoring areas:

- Barentsburg (two test sites in the southern and northern areas of the settlement);
- outskirts of Barentsburg (three test sites in the area of a household disposal site, a mining equipment warehouse and a building materials warehouse);
- the area where the helipad is located;
- the area of the location of dumps of rocks and slag from the thermal power station.

One site is identified as an intermediate area, including two test sites located east of Barentsburg, the soils of which are not exposed to direct anthropogenic impact but are subject to pollution under appropriate meteorological conditions.

Three sites have been identified as reference monitoring areas:

- Grøndalselva (two test sites in the valley and the river delta);
- Stemmevatnet (two test sites in the lake valley);
- northeastern reference areas (two test sites in the Sahariassendalen and on the southern coast of Isfjorden).

191 samples of the upper (0–5 cm) soil cover layer and 191 samples of the underlying (5–20 cm) layer were taken on 16 test sites within the indicated areas during the summer-autumn period of expeditionary studies from 2002 to 2015. The concentration of petroleum hydrocarbons (PH), non-polar aliphatic hydrocarbons (NAHs), volatile aromatic hydrocarbons (VAHs), polycyclic aromatic hydrocarbons (PAHs), heavy metals and organochlorine compounds (OCs) was determined in soil samples. The levels of soil pollution were assessed under regulatory documents (GN 2.1.7.2041-06 ..., GN 2.1.7.2042-06 ..., GN 1.2.1323-03 ..., GOST 17.3.1.02-83 ..., MI 2.1.7.730-99 ..., RD 52.43.2-94 ..., SP 11-102-97 ..., Neue Niederlandische Liste).

Russian regulatory documents established MACs for 28 different pollutants (by individual value or by the total compounds of a particular group) from the entire list of quality indicators monitored in the soils of the study area. The Code of Rules (Engineering and environmental surveys ..., 1997) contains international standards for the content of pollutants in soil (Neue Niederlandische Liste), which establish allowable concentrations (AC) and intervention limit concentrations (ILC) for 62 substances and compounds.

Along with the established standards for allowable concentrations for assessing soil pollution, the reference values published in various literary sources, obtained as a result of international studies in other regions of the Arctic, were also used. The calculated averaged reference values of the concentration of the main pollutants are given in Table 5.1.6. The data sources were the reports of the international organization for monitoring and evaluation AMAP (Arctic Monitoring & Assessment Program) for 1998–2002. (AMAP Assessment ..., 1998; AMAP Assessment ..., 2004; AMAP Assessment ..., 2005).

The following number of cases of exceeding the MACs/ACs was noted in the soil cover of the study area for the entire research period 2002—2015: 371 for arsenic content, 230 for total petroleum hydrocarbons, 76 for total PAH content, 59 for total PCB content, 50 for benzo(a)pyrene, 8 for manganese, 19 for copper, 9 for nickel, 4 for lead, and 2 for ethylbenzene. There were also individual cases of exceeding the content of zinc, cobalt, chromium, the total DDT, and toluene.

Reference concentrations of pollutants in the soil

Pollutant	Concentration
Chlorobenzenes	0.64 ng/g
Total HCH	0.59 ng/g
Total DDT and its metabolites	0.90 ng/g
Total PCB	11.23 ng/g
Lead	3.33 µg /g
Cadmium	0.15 µg /g
Mercury	0.075 µg /g
Petroleum hydrocarbons	42.7 µg /g

A significant excess of the allowable content of petroleum products in the soil cover was noted both in the surface soil layer (up to 31.8 AC) and in the underlying layer (up to 24.7 AC). The highest concentrations of PH in the soil were typical for the territory of the village, its adjacent areas, and for the territory of the helipad. It suggests that the primary source of petroleum hydrocarbons entering the soil is the operation of road and air transport, especially the place of their maintenance.

The lowest PH concentrations were noted in the soils of the valley of the Stemmevatnet: 0.67–0.97 AC.

When comparing the levels of petroleum hydrocarbons in the studied soil samples with reference values, it should be noted that only the soils of the valley of Stemmevatnet and the transition area to the east of the village are on average correlated with the reference ones.

The content of regulated volatile aromatic hydrocarbons in samples of the surface soil layer ranged from 0.07 to 0.88 MAC / AC. However, in the underlying layer of the soil cover, the excess of MAC was recorded for toluene (up to 1.48 MAC) and ethylbenzene (up to 1.64 AC). Both these excesses were noted in the samples taken in the area of the dumps of rocks and slag from the TPP, which indicates a purely local nature of this pollution. The soils sampled at this test site also differed in an increased concentration of VAHs compared to other monitoring areas. For example, the content of VAHs in the soils of the village and its adjacent areas is 5–10 times less. Here, the maximum total content of VAHs in soils was noted for the entire observation period – 1.02 µg/g.

Only benzo(a)pyrene is regulated (priority PAHs) in the Russian Federation in terms of content in the soil; it is one of the most toxic substances entering the environment during the extraction and processing of coal. The maximum concentration of benzo(a)pyrene in the samples of the upper and lower soil layers exceeded the MAC by 49 and 46 times, respectively, for the entire observation period. Soils on the territory of the village and in its adjacent areas were the most contaminated with benzo(a)pyrene, as well as in the area of the helipad, which once again confirms the assumption that the main sources of this substance entering the environment in the study area are technogenic objects (mine “Barentsburg”, TPP, parking and service areas).

The total content of polycyclic aromatic hydrocarbons in soil samples reached values exceeding the AC by 18.3 (0–5 cm) and 12.5 times (5–20 cm). Four monitoring areas can be distinguished from all; their soils are most exposed to PAH pollution. It is the actual territory of the village, its surroundings, the area of the helipad, and the area located east

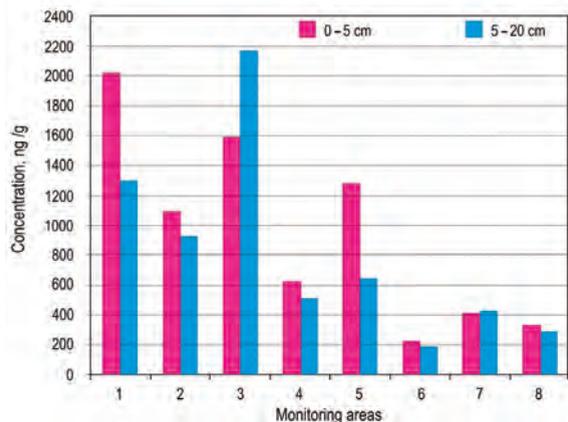


Fig. 5.1.4. Average long-term total values of PAH concentration in soil.

Monitoring areas: 1 – Barentsburg; 2 – outskirts of Barentsburg; 3 – Helipad; 4 – dumps of rocks and slag from the thermal power station; 5 – transition area; 6 – Stemmevatnet; 7 – Grøndalselva; 8 – northeastern reference territories.

of Barentsburg, designated above as transition area. The peculiarity of the latter region is that it is located at a small distance from the village, but at the same time, it is much higher (the height difference is about 100 m).

Fig. 5.1.4 shows the distribution of mean long-term total values of PAH concentration in the soils of the study area. As we can see from the presented histogram, PAHs in the soils of the adjacent areas of the village and the area of waste rock heaps are evenly distributed along the soil profile. At the same time, most of these pollutants are concentrated in the upper layer in the soils of the village and the transition area. On the contrary, the concentration of PAHs in the lower layers exceeds the concentration in the upper ones in the area of the helipad. In general, the concentration of Σ PAH was 0.18–0.43 MAC in the reference regions, both in the surface and in the underlying soil layer. The minimum values of the PAH concentration were typical for the soils of the valley of the Stemmevatnet.

The content of the main groups of organochlorine pesticides (OCs) in the soils of Barentsburg and its adjacent areas did not exceed the allowable values. It amounted to tenths of the MAC for the entire observation period:

- the total content of HCH isomers – up to 0.08 MAC;
- the total content of polychlorobenzenes – up to 0.45 MAC;
- the total content of DDT metabolites – up to 0.93 MAC.

When comparing the obtained data with reference values, it should be noted that the most polluted area is the area of the helipad: the concentration of polychlorobenzenes, Σ DDT and Σ HCH in the surface soil layer of the village exceeded the reference values typical for other regions of the Arctic, four, thirty and two times, respectively. The OCs content in the samples taken in the reference monitoring area is generally comparable to the reference values in the Arctic region.

The maximum total values of the concentration of polychlorinated biphenyls (PCBs) in the soils of the village exceeded the MAC by 21.6 times in the surface layer and 2.5 times in the underlying layer. The highest average long-term values of PCB concentration in soil were detected for the area of the helipad (up to 5.9 MAC), as well as for the territory of t Barentsburg (up to 3.5 MAC). Such pollution may be associated with the

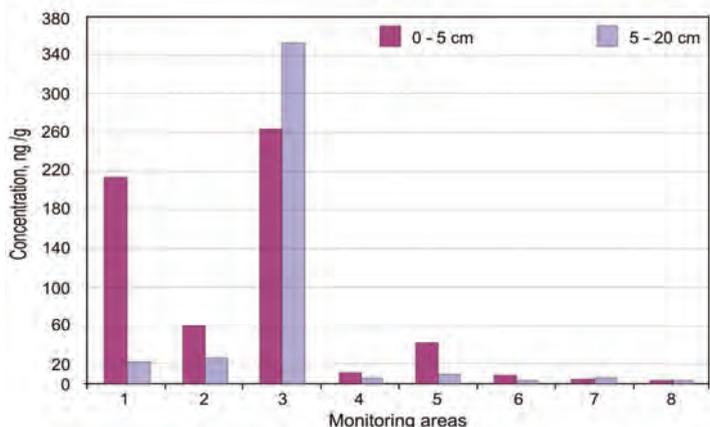


Fig. 5.1.5. Average long-term total concentrations of PCBs in soil.

Monitoring areas: 1 – Barentsburg ; 2 – outskirts of Barentsburg; 3 – Helipad; 4 – dumps of rocks and slag from the thermal power station; 5 – transition area; 6 – Stemmevatnet; 7 – Grøndalselva; 8 – northeastern reference territories.

active use of hydraulic fluids, transformer fluid, and other technical materials containing PCBs in these areas. According to Norwegian research data, confirmed by the results of the authors' research, in Spitsbergen, an active source of polychlorinated biphenyls entering the soil cover can be the paint crumbling from the walls of the settlement's buildings, which, being destroyed by atmospheric precipitation and wind, enters the soil surface in the form of fine particles and is carried by watercourses (Evenset, Ottesen, 2009; Evenset, 2010).

The low content of PCBs is typical for the soils in the reference monitoring areas: the concentration range is from 0.03 to 0.69 MAC. The total content of PCBs in soils in the outskirts of Barentsburg is at a level comparable to the MAC. Fig. 5.1.5 presents the average long-term total values of the PCB concentration in the soils of the study area. As can be seen from the above diagram, the highest amount of pollutants is accumulated in the upper soil layer everywhere, except for the area of the helipad. It indicates that PCBs enter the soil mainly as part of solid contaminated particles precipitating on the surface. Increased values of the PCB concentration in the underlying soil layer in the area of the helipad indicate that in this area pollutants enter the soil cover as part of materials that can penetrate the soil, or are transferred there along with petroleum products that dissolve them well (oils, fuel, etc. other technical fluids).

Heavy metals are more evenly distributed over the study area than organic pollutants. The highest average long-term values of the concentration of heavy metals exceeded the corresponding lowest values in various monitoring areas by 1.4–2.1 times, which once again indicates a very even distribution of heavy metals in the soil cover of Barentsburg and its surroundings.

The maximum values of the concentration of individual heavy metals were detected in the following areas: iron – on the northwestern slope of Grøn fjordfjellet mountain, east of Barentsburg; manganese – in the area of the building materials warehouse (2.4 MAC); zinc, chromium, and mercury – in Barentsburg (2.1 AC, 1.9 AC and 0.1 MAC, respectively); copper and nickel – in the area of the mining equipment warehouse (15.0 and 1.5 AC, respectively); cobalt and cadmium – in the valley of the Stemmevatnet (1.75 AC

and 0.6 AC, respectively); lead and arsenic – in the area of the helipad (2.0 MAC); arsenic – in the area of the Grøndalselva (16 MAC).

The concentration of many heavy metals in the underlying soil layer, in most cases, exceeded their concentration in the surface layer. That is because most of the compounds, which include HMs, are quite well soluble in water, in contrast to organic pollutants, and therefore can penetrate the soil with meltwater and surface runoff. The content of individual heavy metals in the upper and lower soil layers differed in different monitoring areas by only 0.70–1.29 times. Thus, it can be argued that heavy metals are contained in the same amount both in the surface and in the underlying soil layer.

Since the main economic activity in the study area is coal mining, most of the pollutants entering the soil are somehow related to coal mining. The main substances, the content of which is subject to control in the soils of such areas, under Appendix E of the Recommendations “Organization and functioning of a special survey system of the natural environment status in the areas of developing coal mining industry and related industries” P52.23.581–97 are PAHs, including benzo(a)pyrene, petroleum hydrocarbons, iron, manganese, cadmium, copper, arsenic, nickel, mercury, lead, zinc, etc.

A comprehensive assessment of the soil pollution level, according to (MI 2.1.7.730-99), was carried out according to the integrated indicator of chemical pollution (Z_c). The Z_c indicator is determined as the sum of the concentration factors of the individual components of pollution by the formula:

$$Z_c = K_{c_1} + \dots + K_{c_i} + \dots + K_{c_n} - (n - 1), \quad (5.1.1)$$

where n is the number of determined components; K_{c_i} is the concentration factor of the i -th component, which is equal to the multiplicity of the excess of this component over the reference content.

If the value of the Z_c indicator is less than 16, this indicates the allowable degree of soil pollution, when Z_c ranges from 16 to 32, the pollution level is considered moderately hazardous when Z_c is from 32 to 128 – dangerous, and if Z_c is more than 128 – extremely dangerous. For the selected soil samples, the total indicators of chemical pollution Z_c were calculated for those pollutants whose concentrations exceeded the established MAC / AC. In the surface soil layer, a dangerous degree of pollution ($Z_c > 32$) was recorded in four samples taken on the slope of a stream flowing through the territory of Barentsburg in the area where the consulate is located, in the area of the building materials warehouse and near the helipad. The maximum Z_c value was 93.7 (consulate area). In the rest of the processed samples, the value of the total indicator of soil pollution did not exceed 28.1, averaging 7.52.

In samples of the soil layer of 5–20 cm, a dangerous pollution level was observed in four samples taken in the area of the helipad and near the building materials warehouse. The maximum Z_c value was 79.5 (helipad).

In the rest of the processed samples, the value of the total indicator of soil pollution did not exceed 25.5, averaging 6.15. According to the results of calculations, a moderately dangerous pollution level was established: in 15 cases of the surface soil layer and nine cases of the underlying layer. The highest average long-term values of Z_c were detected for the soil cover of Barentsburg (14.0), its adjacent areas (9.6), and the helipad (19.9). The values of the total indicator of the chemical pollution of soils in the reference regions on average were: for the valley of the Stemmevatnet 2.47, for the Grøndalen 3.76, for northeastern reference areas 5.13.

Characterization of the soil pollution level with benzo(a)pyrene

Object	Units	MACs	Level of pollution		
			Moderate	Considerable	High
Soil	µg /g	20	20–30 and less	31–100	More than 100

The degree of soil pollution with benzo(a)pyrene is assessed using the scale given in Table 5.1.7, under the Recommendations (R 52.23.581–97).

According to the results of calculations, 13 cases of high soil pollution and 22 cases of considerable soil pollution with benzo(a)pyrene were identified. It should be noted that most of the recorded cases are confined to the soils of local monitoring areas (primarily the territory of Barentsburg and its adjacent areas).

Summing up, we can say that, in general, the soil pollution of the studied area is extremely heterogeneous, varies significantly from year to year, and it is not yet possible to distinguish stable changes in the levels of various groups of pollutants.

The characteristic that most revealingly reflects the heterogeneity of the interannual distribution of the content of pollutants in the soil cover of the study area is the integrated indicator of chemical pollution Z_c . Fig. 5.1.6 shows the Z_c values calculated for the period from 2002 to 2015 for the upper (0–5 cm) soil layer.

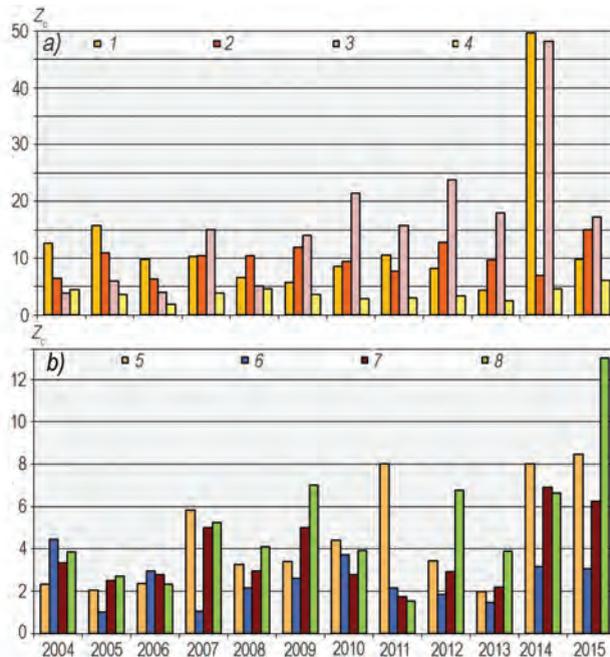


Fig. 5.1.6. The integrated indicator of chemical pollution Z_c , calculated for the period from 2004 to 2015 for samples of the upper (0–5 cm) layer of the soil cover.

Monitoring areas: a) 1 – Barentsburg; 2 – outskirts of Barentsburg; 3 – Helipad; 4 – dumps of rocks and slag from the thermal power station; b) 5 – transition area; 6 – Stemmevatnet; 7 – Grøndalselva; 8 – northeastern reference territories.

As we can see from the given histogram, the most polluted area is the area of local monitoring, and in different years there are different areas in terms of pollution. In general, the dynamics of the spatial distribution of pollutants in the soil cover can be characterized as follows:

- there is a decrease in anthropogenic load on the soils of the Barentsburg with a simultaneous increase in the load on the soils of the surrounding areas;
- there is an increase in soil pollution in the area of the helipad;
- there is an increase in soil pollution in the reference monitoring areas;
- there is an increase in the pollution of the northeastern reference areas in 2009–2015, after a relative decrease in the levels of pollutants in 2006–2008;
- the observed changes can be associated with a decrease in industrial load on the ecosystem of the area of Barentsburg, reclamation of old dumps and disposal sites, as well as an increase in the impact of booming tourism on it.

Comparing the data obtained during the 2002–2015 studies of soil pollution in the area of Barentsburg, with the materials of Russian studies (Dobrovolskiy, 1990; Kashulina, 2006; Kashulina, Kashulin, 2005), it should be noted that some of the results obtained are similar both from a qualitative and quantitative point of view. Certain difficulties in comparing the results are due to the difference in the methods of chemical and analytical studies of soil samples, as well as the discrepancy between the sampling points, which allows only conditionally correlate the literature data on different monitoring areas with the results we obtained.

From the mentioned works, it should be noted, first of all, the study of G.M. Kashulina (Kashulina, 2006). Not all data presented in work on the concentration of heavy metals in soil samples taken in 2004 agree with the results obtained during the expeditions of the Research and Production Association “Typhoon”. Fig. 5.1.7 presents a comparison of the results of the study of soil pollution by heavy metals, carried out based on the data of the N.A. Avrorin Polar-Alpine Botanical Garden and Institute (Kashulina, 2006) and the North-West Branch of Research and Production Association “Typhoon”.

Many international studies (primarily Norwegian) are devoted to the pollution of soils in the study area with polychlorinated biphenyls. Thus, Jartun et al. (2008) present the data of analytical studies of soils on the territory of Barentsburg for PCB content.

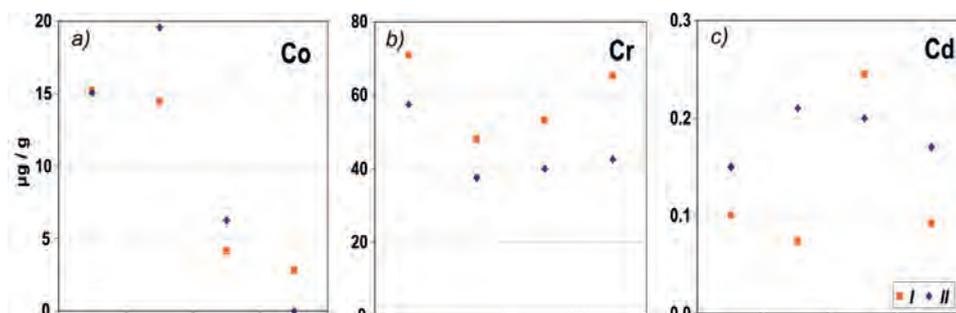


Fig. 5.1.7. Comparison of data on soil pollution of the study area with heavy metals: cobalt (Co), chromium (Cr), and cadmium (Cd) at the four most representative sampling points.

Monitoring areas: Grøndalen in the area of its mouth, the area of dumps of rocks and slag from the thermal power station, the coast of the Isfjorden in the area of Selisbukhta, a mountain range northeast of Barentsburg. I – data from the North-West Branch of Research and Production Association “Typhoon”, II – Kashulina, 2006.

Comparison of data on pollution of the surface soil layer with Σ PCB7

Source	Sampling area	Concentration, ng/g		
		Median value	Average	Maximum
Jartun et al., 2008	Barentsburg	268.0	2960	28700
	Piramiden	172.0	1140	13900
	Longyearbyen	< 3.0	10.0	131.0
	Research and Production Association "Typhoon", 2008	Barentsburg	40.6	52.0

Table 5.1.8 shows the data of Norwegian researchers (Jartun et al., 2008) in comparison with the data of monitoring carried out by the North-Western branch of the FSBI "NPO Typhoon". It is obvious that the values of Σ PCB7 concentration recorded in samples of the surface layer of soils taken during the expeditions of the Research and Production Association "Typhoon" are the closest to the values of Σ PCB7 concentration in the soils of Longyearbyen. It should be noted that there is a significant difference in the data on soil pollution in Barentsburg, which can be explained, first of all, by the differences in the methods of selecting the sites for soil sampling.

Norwegian researchers took samples in specially selected places (hotspot), where high PCB concentration values are most likely (places where old paint crumbling from the walls of buildings was concentrated, dismantled building structures were stored). At the same time, in some samples, quite expectedly, abnormally high concentration values were revealed. The significant discrepancy between the median and the averages in the Norwegian data indicates a significantly uneven distribution of PCB concentration in the samples.

Sampling sites during the research of the North-West Branch of Research and Production Association "Typhoon" were chosen to obtain an integral assessment of the soil pollution of In this case, as we can see, the median and average differ insignificantly, that means, the distribution of PCB concentration in the samples is more uniform.

ASSESSMENT OF SOIL WATER POLLUTION

At present, the maximum allowable concentrations of pollutants for soil waters have not been developed in Russian regulatory documents. According to the recommendations (SP 11-102-97), the assessment of the level of soil water pollution was carried out using the "Criteria for assessing the ecological situation in the territories for identifying zones of an environmental emergency and zones of ecological disaster", approved by the Ministry of Natural Resources of Russia on November 30, 1992, which establish assessment criteria for groundwater in the zones of influence of business objects. The MAC and TAC of chemical substances in the water of water objects used for drinking and domestic recreation purposes, established by the sanitary rules (GN 2.1.5.1315-03; GN 2.1.5.2280-07) were used as standard values. Additionally, under the recommendations (SP 11-102-97), the assessment of water pollution was carried out according to the criteria given in the work of Neue Niederlandische Liste.

Soil waters were studied according to 118 parameters; at the same time, 45 indicators are regulated by hygiene standards (by individual value or by the sum of the concentrations of a group of compounds), Neue Niederlandische Liste – 41.

For the soil waters of the area of In Barentsburg, an excess of AC established following international standards (Neue Niederländische Liste) was noted for compounds of the VAH group (benzene up to 14.9 AC, toluene 5.0 AC, ortho-xylene 2.5 AC); for the PAH group (naphthalene up to 9.2 AC, phenanthrene 4.9 AC, fluoranthene 10.9 AC, benzo(a)pyrene 25.0 AC, benzo(a)anthracene 6.5 AC, chrysene 13.0 AC, benzo(ghi)perylene 15.0 AC, benzo(j)fluoranthene 42.0 AC, indeno(1.2.3-cd)pyrene 135 AC and 2.7 HC); for heavy metals (zinc 5.5 AC, nickel 30.7 AC, and 6.1 HC, cobalt up to 16.5 AC or 3.3 HC, cadmium up to 2.8 AC, chromium up to 1.7 AC and the amount of PCBs up to 2.3 AC). For the rest of the regulated ones, there are no indicators of the excess of AC in the soil waters of the study area for the period 2002–2015.

In the soil waters of the study area, the maximum excess of MAC and TAC in terms of hygienic standards for the content of harmful substances (GN 2.1.5.1315-03; GN 2.1.5.2280-07) were recorded in the Grøndalselva valley in 2010 for heavy metals, including the content of iron (up to 35 MAC), manganese (up to 232 MAC), nickel (up to 31.4 MAC) and cadmium (up to 1.4 MAC). Such significant concentrations of metals in soil waters in this area are most likely due to the leaching of these elements from eroded rocks and, possibly, from dumps of abandoned mines located in the middle reaches of the Grøndalselva. No excess was found for other regulated indicators.

According to the criteria for the sanitary and hygienic assessment of the pollution danger of drinking water and water supply sources with chemical substances, the state of the soil waters of the study area corresponds to a “relatively satisfactory situation”.

When analyzing the spatiotemporal variability of the content of the main pollutants in soil waters, it should be borne in mind that the level of pollution depends mostly on the local physical and geographical conditions that form the characteristics of the penetration of surface and wastewaters into the soil. They are determined by the peculiar topography of the area, the arctic type of soil, the presence of pollution sources in the catchment basin, the migration characteristics of toxic agents, as well as the intensity of anthropogenic load associated with economic activities carried out at the Barentsburg mine. During the observation period, the economic activities carried out at the mine changed significantly due to economic conditions, the ignition of waste rock heaps, fires in the mine, and flooding of mine workings were repeatedly observed. All this affected the temporal variability of the priority pollutants content in the soil waters of particular regions of Barentsburg. The general trend over the observation period was a decrease in coal production and a decrease in the population of the village. Moreover, in 2008–2015, significant volumes of reclamation work were carried out, the TTP was re-equipped, and the main utility systems were updated.

The soil water samples show a decrease in PH content in the soil waters of the northern part of the village in the period from 2002 to 2007, a slight increase in PH concentration in 2005, and a significant increase in PH in 2011 and 2014.

The increase in the level of petroleum products in 2011 is clearly visible in the soil water sampled in the area of the household disposal site and the area of the mining equipment warehouse.

An increase in the level of petroleum products, recorded in 2010 and, especially, in 2011, was noted at almost all points of soil water extraction, including points of the reference background polygon. The highest increase in PH concentration in soil waters was noted in the northern part of the village and in the northeastern part of the reference

background polygon, where the content of petroleum products in soil waters was significantly higher than in 2008. PH concentration also increased in 2011 in the points of the reference background polygon located to the south and west of the village. All these features are associated with the nature of economic activity in the village and the degree of its intensity.

When considering the general state of soil water pollution in the area, the following characteristic features can be distinguished:

- the content of the main groups of pollutants (PH, PAH, OCs and some HMs, such as zinc, manganese, cadmium) in the soil waters of the village and its adjacent areas is much higher than the content of pollutants in the soil waters of the reference background polygon, which indicates the local nature of their pollution associated with production activities carried out in Barentsburg;

- interannual variability in the content of some determined pollutants, including PAHs, PCBs, zinc, copper, and cadmium, is characterized by a steady decrease in the level of their concentration in the soil waters of the local and reference background polygons to values close to the reference ones, starting from 2005 to the present;

- the content of some priority pollutants (PH, HCH, VAH, DDT, lead, nickel, and manganese) in the period from 2002 to 2015 does not show a well-defined tendency to decrease, and there is a multidirectional change in the level of their content in soil waters in the study period;

- the relocation of disposal sites within the framework of the reclamation program makes a significant contribution to soil water pollution, leading to an increase in the content of some pollutants and a decrease in the content of others, depending on the nature of the pollutants themselves, in particular, their ability to translocate. Still, this contribution is of a one-time nature, and subsequent reclamation will reduce the level of soil water pollution.

VEGETATION POLLUTION ASSESSMENT

Vegetation on the territory of the settlement and its adjacent areas is represented by mosses (*Aulacomnium turgidum*, *Racomitrium lanuginosum*, *Sphagnum lindbergii*, *Polytichum commune*, etc.), lichens (*Cetraria ericetorum*, *Cetraria islandica*, *Flavocetraria rotundis*, etc.) and vascular plants – sedges (*Carex*, *C. rariflora*, *C. aquatilis*), cotton grass (*Eriophorum russeolum*, *E. scheuchzeri*, *E. polystachion*), common bistort (*Polygonum bistorta*), Norwegian angelica (*Archangelica norvegica*), meadowsweet (*Filipendula ulmarlandia*), European goldenrod (*Solidago lapponica*), polar willow (*Salix polaris*, *Salix reticulata*), etc.

The concentration of PAHs, organochlorine compounds (including PCBs), and heavy metals (63 indicators in total) were determined in samples of vegetation taken in the territory of the village and its adjacent areas in 2002–2015. In total, from 2002 to 2015, 135 samples of vascular plants and 133 samples of mosses were taken at 16 sample sites of the study area. Taking into account the fact that mosses and vascular plants are the most representative species of vegetation found at all selected sites, the levels of pollutants in these groups of vegetation were studied.

The level of pollutant content in the vegetation cover of the studied region varies depending on the species of plants and is due to several factors. The content of pollutants in mosses, due to the lack of a developed root system, largely depends on the chemical composition of atmospheric precipitation. Also, mosses, due to their near-ground location, and also due to their larger surface compared to vascular plants, can accumulate a large

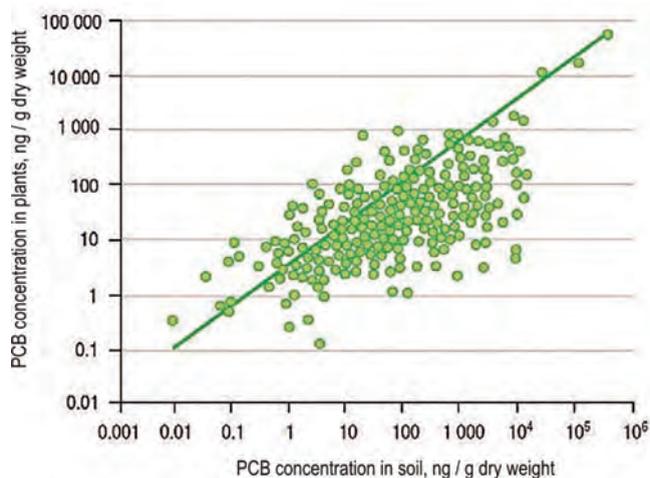


Fig. 5.1.8. Dependence of the PCBs content in vascular plants on the content in the soil (Gubala et al., 1995).

amount of dust and atmospheric aerosols, the composition of which also affects the level of their pollution. Besides, the concentration of some compounds may also depend on the morphological characteristics of individual species of mosses (on the surface area of the leaves and their roughness). Thus, moss pollution is largely dependent on air pollution.

The concentration of pollutants in vascular plants with a root system and a smoother leaf surface than mosses is less dependent on air pollution and precipitation. A more considerable influence on the pollution of vascular plants is exerted by the pollution of the soils on which they grow and the soil waters that feed them. Fig. 5.1.8 shows the correlation of the content of Σ PCB in samples of vascular plants with their concentration in the soil.

According to Russian studies (Kashulina et al., 2007), the chemical composition of both mosses and vascular plants is due to the strong influence of dust. The high dust content of the atmospheric air on Spitsbergen in summer is explained by the fact that soils with poor vegetation or its complete absence represent most of the archipelago's surface. Also, strong winds and steep mountainous terrain increases dustiness.

As in the case of zoning of territories for monitoring soil pollution, seven districts were chosen for sampling vegetation, depending on the distance from the village and the Barentsburg mine, on the altitude of the test sites and the presence of local sources of pollution, within each of them the data were generalized, obtained as a result of research samples. When studying the pollution of the vegetation cover, among other things, it is necessary to take into account that the test site is far from the coast since this microclimatic factor significantly affects the frequency and volume of precipitation, which is one of the determining factors in the formation of the level of pollution of the vegetation cover (primarily mosses) Thus, four local monitoring areas were identified:

- Barentsburg and its nearest eastern and northeastern outskirts (two test sites in the southern and northern areas of the village, as well as two test sites located to the east of the village, away from the coast of the Grønfjorden, where vegetation is not exposed to direct anthropogenic impact but is subject to pollution under appropriate meteorological conditions);
- outskirts of Barentsburg (three test sites in the area of a household disposal site, a mining equipment warehouse and a building materials warehouse);

- the area where the helipad is located;
 - the area of the location of dumps of rocks and slag from the thermal power station.
- Three reference monitoring areas were also identified:
- Grøndalselva valley (two test sites in the valley and the river delta);
 - the valley of Stemmevatnet (two test sites in the lake valley);
 - northeastern reference areas (two test sites in the Sahariassendalen Valley and on the southern coast of Isfjorden).

Unfortunately, the observation series for different sites differ markedly, as a result of which consideration of the pollution of the vegetation cover in individual sites is impossible from the temporal point of view. It is also problematic to thoroughly compare the data on vegetation and soil pollution in the areas of local monitoring, which, however, is compensated by a large amount of data on the pollution of reference areas.

From 2002 to 2015, 135 samples of vascular plants and 133 samples of mosses were studied, taken at 16 sample sites within the indicated monitoring areas in the summer-autumn period. The main objects of study were mosses (*Aulacomnium turgidum*, *Racomitrium lanuginosum*, *Sphagnum lindbergii*, *Polytrichum commune*) and vascular plants (sedges (*Carex rotundata*, *C. rariflora*, *C. aquatilis*), cotton grass (*Eriophorum russeolum*, *E. scheuchzeri*, *E. polystachion*), bistort (*Archangelica norvegica*, *Filipendula ulmaria*, *Solidago lapponica*). In vegetation samples, determination of the concentration of polycyclic aromatic hydrocarbons (PAHs), heavy metals and organochlorine compounds (OCs), including PCBs, was carried out. In total, during chemical-analytical studies, the concentration of 63 different compounds was determined, and six total values of the content of groups of pollutants were calculated.

In Russian environmental legislation, the concentration of pollutants in plants is not regulated. Therefore, we used the reference values calculated based on published data from Russian and international Arctic and subarctic studies to carry out a quantitative assessment of the level of the primary pollutants in the vegetation cover of the study area.

Table 5.1.9 shows the reference concentrations of pollutants typical for the vegetation cover of the Arctic calculated based on observational materials published in the collection of the international Arctic Monitoring & Assessment Program AMAP (AMAP Assessment ..., 1998). As we can see from the data presented, high concentrations of pollutants are typical for lower plants.

Table 5.1.9

Reference values of the concentration of the pollutant in the vegetation cover

Pollutant	Concentration	
	Mosses	Vascular plants
Total polychlorobenzenes, ng/g	0.75	0.30
Total HCH, ng/g	2.22	0.37
Total PCCD, ng/g*	0.35	0.25
Total DDT, ng/g	1.33	0.49
Total PCB, ng/g	7.13	3.64
Total PH, ng/g	180	88.0
Lead, µg /g	3.39	0.02
Cadmium, µg /g	0.17	0.01
Mercury, µg /g	0.085	0.060

* Sum of PCCD (polychlorocyclodienes) is given as the sum of cis- and trans-chlordane.

In addition to the reference values, the integrated indicators of the complex pollution were used for a comparative characteristic of the pollution of the vegetation cover of the study area.

Over the entire observation period (2002–2015) in vascular plants, there were 132 cases (98.0 % of samples) of exceeding reference concentrations in terms of the total PCB content; 124 cases (92 % of samples) by cadmium content; 119 cases by the content of lead (88.1 % of samples); 114 cases by the total content of polychlorobenzenes (84.4 % of samples); 113 cases by the total DDT and its metabolites (83.7 % of samples); 96 cases by the total HCH isomers (71.1 % of samples); 81 cases by the total PAHs (60 % of samples); 41 cases by the total PCCD (30.4 % of samples); 27 cases by mercury content (20 % of samples).

In mosses, the proportion of cases where reference concentrations were exceeded compared to vascular plants was lower and amounted to 118 cases of lead content (88.7 % of samples); 110 cases by the total PCBs (82.7 % of samples); 96 cases by the total polychlorobenzenes (72.2 % of samples); 90 cases by the total PAHs (68 % of samples); 74 cases by the total DDT and its metabolites (55.6 % of samples); 58 cases by cadmium content (43.6 % of samples); 57 cases by mercury content (42.8 % of samples); 50 cases by the total PCCD (37.6 % of samples); 17 cases by the total HCH isomers (12.7 % of samples).

For both studied groups of vegetation, similarly elevated levels of lead, polychlorobiphenyls, and polychlorobenzenes were observed, the concentration of which in the vegetation samples exceeded the reference level in 72–98 % of cases. In vascular plants, we note a high concentration of cadmium (92 %). No similar phenomenon was observed for other pollutants. Thus, it can be argued that lead, PCBs, and polychlorobenzenes are the priority pollutants of the vegetation cover of the study area.

The total values of the concentration of polycyclic aromatic hydrocarbons in vascular plants exceeded the calculated reference values by an average of 5.7 times, and the maximum recorded values – by 11.4 times. The multiplicity of the exceeding of the reference total values of PAH concentration in mosses averaged 11.6, reaching 10–30 in some cases. Despite the almost threefold difference in the quantitative content of pollutants in vascular plants and mosses, the spatial distribution of polycyclic aromatic hydrocarbons in both types of vegetation is almost identical.

The spatial distribution of pollutants in the vegetation cover and the frequency of the excess of the reference concentration in the vegetation samples are given in Table 5.1.10.

As we can see from the table below, the maximum frequency of the excess of the reference concentration is observed in the vegetation on the territory of Barentsburg. Somewhat less frequently, increased levels of pollutants were observed in the outskirts of the village, as well as in the area of the helipad. The areas of reference monitoring were distinguished by a low proportion of vegetation cover samples in which the concentration of pollutants exceeded the reference values. However, it should be noted that the values of the concentration of lead, cadmium, and polychlorinated biphenyls exceeded the reference in half or more cases, even in the areas considered to be the reference ones. At the same time, the frequency of excess of the reference level of pollutants in vascular plants is noticeably higher than in mosses, even though the absolute values of pollutant concentration in mosses are several times higher than in vascular plants.

Despite the significant difference in the levels of the main pollutants in mosses and vascular plants, the interannual variability of their content in the vegetation cover is largely

Frequency (%) of cases of the excess of the reference concentration of the main pollutants in the samples of the vegetation cover during the observation period 2002–2010

Vegetation type	Region	ΣΠΑΗ	Pb	Cd	Hg	ΣXB chloro-benzenes	ΣΗΧΗ	ΣΔΔΤ	ΣΠΧΧΔ	ΣΠΧΒ
Vascular plants	1	89.5	84.2	84.2	31.6	94.7	78.9	94.7	21 16.6	100
	2	100	66.7	33.3	33.3	100	83	100		100
	3	75	100	12.5	25	87.5	75	75	50	100
	4	75	91.6	91.6	8.3	91.6	50	83.3	33.3	100
	5	41	86.4	86.4	13.6	77.3	77.3	81.8	31.8	100
	6	50	80	100	10	85	55	80	25	95
	7	100	50	93.5	13	80.4	74	80.4	34.7	93.5
Mosses	1	94.1	64.1	70.6	76.4	82.3	64.7	29.4	76.5	100
	2	100	66.7	66.7	50	100	33.3	100	16.7	100
	3	87.5	100	75	62.5	87.5	25	50	87.5	100
	4	71.4	100	57.1	28.6	100	13.3	57.1	57.1	100
	5	71.4	100	42.9	28.6	78.6	0	13.3	42.9	71.4
	6	40	60	60	26.7	40	13.3	26.7	60	86.7
	7	66.7	100	22.2	22.2	66.7	0	33.3	55.6	55.6

similar for both types of vegetation. It is because the pollution of both mosses and vascular plants comes from the same sources, which means both types of plants accumulate the same pollutants, but in different proportions, depending on the accumulating capacity of each type of vegetation.

A comparative assessment of the degree of pollution of the vegetation cover was carried out based on calculating the integrated indicator of the complex pollution (K_k), taking into account the degree of accumulation of pollutants by various plant species and allowing to take into account the contribution of the pollutant groups controlled in this case. Larger K_k values correspond to higher pollution levels of the vegetation cover. The K_k coefficient was calculated by the formula:

$$K_k = \left(\sum \frac{|x_i - \bar{x}|}{s} \right) / n, \quad (5.1.2)$$

where x_i – natural logarithm of the parameter value, \bar{x} – mean of a logarithmic array, s – standard deviation of a logarithmic array, n – number of parameters.

The values of the concentration of the most significant toxic agents were used to calculate K_k , as well as the values of the total content of the main groups of pollutants (15 parameters in total): naphthalene, fluorene, anthracene, fluoranthene, benzo(b)luoranthene + perylene, benzo(k)fluoranthene, benzo(a)pyrene, ΣΠΑΗ, ΣΗΧΗ, ΣΔΔΤ, ΣPCB, zinc, cadmium, mercury, arsenic.

Fig. 5.1.9 shows the interannual variability of the K_k value for the vegetation cover samples taken on the territory of local and reference monitoring.

The figure shows that the interannual variability of the pollution level of the vegetation cover in the areas of reference and local monitoring is similar. The highest values of K_k in the territory of both local and reference monitoring were detected in 2006 and 2015; the

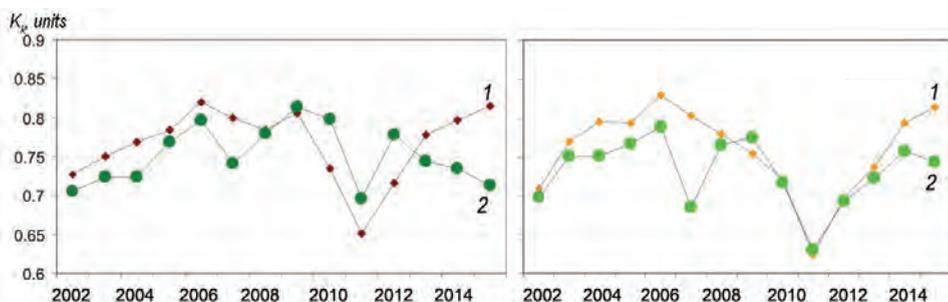


Fig. 5.1.9. Long-term variability of the integrated indicator of the complex pollution K_k for samples of vegetation cover according to the data of local (left) and reference (right) monitoring.

1 – mosses, 2 – vascular plants.

general minimum was in 2011. A similar pattern of long-term variability of the pollution of the vegetation cover is generally observed for each pollutant or group of pollutants.

Besides, the following features of changes in pollution should be noted. For the vegetation cover of both local and reference monitoring areas, there is a tendency towards a decrease in pollution levels up to 2011. It may be because, during the observation period (2002–2010), the sources of pollutants were localized, which narrowed the distribution area of pollutants entering the vegetation cover from local sources.

CONCLUSIONS

A comprehensive program of environmental monitoring in the area of the Barentsburg in 2002–2015 made it possible to obtain an objective assessment of the existing levels of pollution of natural environments in the study area and to trace the interannual trends of their changes. Based on the research results, the following conclusions can be drawn.

Air quality in the area of Barentsburg fully complies with the current Russian hygienic standards for air in populated areas and the directive of the Council Directive 1999/30/EC of 22 April 1999 relating to limit values for sulfur dioxide, nitrogen dioxide and oxides of nitrogen, particulate matter and lead in ambient air.

The seawaters of most of the Grøn fjorden in the winter-spring and summer-autumn periods are classified as “clean” for fishery standards. Local pollution of the coastal waters of the Grøn fjorden is associated with the flow of untreated domestic wastewater into the bay. It does not significantly affect the quality of the waters of the bay as a whole.

Waters of Stemmevatnet for the entire observation period are characterized by insignificant pollution, correspond to the sanitary and hygienic standards for drinking and domestic recreation purposes, belong to the II quality class (“clean”), and have no pronounced trend towards deterioration in quality.

Water quality in Grøndalselva from 2007 to the present is characterized by the presence of a well-defined tendency towards the deterioration of the state of the water body. If in 2007 the water quality in the river corresponded to the third class (“moderately polluted”), then in 2010 it was already the seventh class (“extremely dirty”). The heavy metals influence the overall assessment of the degree of water pollution of the Grøndalselva the most, especially manganese, which is characterized by very high levels of pollution, as well as zinc, copper, and nickel. Additional studies of the river catchment area are required to identify sources of pollution reliably.

The state of the soil waters of the study area, according to the criteria for the sanitary and hygienic assessment of the risk of pollution of drinking water and water supply sources with chemicals, corresponds to a “relatively satisfactory situation” and has the following features:

- the content of the main groups of pollutants (PHs, PAHs, OCs and some HMs, such as zinc, manganese, cadmium) in the soil waters of Barentsburg and its surroundings are significantly higher than the levels of pollutants in soil waters sampled at reference points, which indicates the local nature of their pollution associated with economic and industrial activities;
- the interannual variability of the content of PAHs, PCBs, zinc, copper, lead and cadmium in soil waters at all observation points since 2005 is characterized by a steady decrease in the level of their concentration down to values close to the values in the reference regions of the Arctic;
- the concentration of PHs, HCHs, VAHs, DDTs, nickel, and manganese in soil waters over the entire observation period (2002–2015) alternately rises and falls;
- the relocation and elimination of disposal sites within the framework of the reclamation program make an ambiguous contribution to soil water pollution, reducing the content of some pollutants and increasing the content of others.

Snow cover on the territory of Barentsburg and its surroundings are generally characterized by relatively high concentrations of organochlorine pesticides, PCBs, and some PAHs, HMs, compared with the reference regions of the Arctic. Pollution of the snow cover with OCs is mainly associated with global sources, PAHs, and PCBs – with regional and local sources.

The increased levels of HM concentration in the snow cover are associated with the influence of emissions from thermal power plants since it is the process of coal combustion that is the primary source of many metals entering the natural environment. Compounds of almost all metals are present in coal and petroleum; a significant amount of heavy metals is emitted into the atmosphere with exhaust gases, and, in addition, heavy metals contained in ash are a source of secondary pollution during swelling or erosion of ash dumps.

Contamination of the soil cover of the study area is subject to significant interannual variability and is extremely heterogeneous, especially in the territory of Barentsburg and its sanitary protection zone.

In terms of the total PH, VAH, OC, and HM soils in Barentsburg and its sanitary protection zone are characterized by an allowable degree of pollution. At the initial stages of observations, a reasonably significant content of PCBs and benzo(a)pyrene was noted in the soils. However, since 2005, the concentration of PCBs and benzo(a)pyrene in the soil cover has significantly decreased and is currently at a level below the MAC. These positive dynamics are directly related to a decrease in the volume of emissions from the TPP as a result of its modernization, with a reduction in coal production and transportation, and with a decrease in emissions from road and other transport.

Outside the territory of Barentsburg, soil pollution in it and its sanitary protection zone is at a level typical for the Arctic tundra region.

The nature of the pollution of the vegetation cover in the areas of reference and local monitoring differs markedly. The highest levels of vegetation pollution in the reference regions were recorded in 2003–2004. Subsequently, pollution tends to decrease steadily. The intensity of economic activity in the area of Barentsburg decreased, also existing

sources of pollution were localized, and there was reclamation work. All this created favorable conditions for weakening the anthropogenic load on the vegetation cover. There are no significant changes in the level of pollution of the vegetation cover on the territory of local monitoring.

The data obtained from the results of environmental monitoring and the performed assessments showed that the content of the main groups of pollutants in the area of Barentsburg and its surroundings are typical for the regions of the development of the coal mining industry in the Arctic. Moreover, in recent years (2008–2015), in several environmental objects (atmospheric air, snow cover, soils, soil waters) in the area of Barentsburg, the content of the main groups of pollutants decreased, due to environmental measures carried out by “Arktikugol” Trust, including the reconstruction of a thermal power plant and the elimination of some disposal sites.

It is necessary to continue work on reference and local environmental monitoring to obtain more complete and reliable information about the environmental situation in this area and other areas of Spitsbergen, where the economic activities of Russian enterprises were carried out. At the same time, a transition to a qualitatively new level of research should be carried out, which can be provided with the resources and infrastructure of the Russian Scientific Center created in Barentsburg.

Today Spitsbergen is actually an international testing ground for comprehensive research in various fields of geosciences. The creation of a modern Russian system for observing environmental pollution on the archipelago will ensure the integration of Russian researchers into the international scientific community and their participation in international scientific programs and projects. Such a system, in which a wide range of Russian scientific organizations will participate, will allow developing and testing the latest methods of environmental control and training highly qualified specialists capable of solving both scientific and practical problems. This system should include reference environmental monitoring and local monitoring in all areas where existing and mothballed Russian enterprises are located (the settlements of Barentsburg, Piramiden, Colesbay, and the waters of the Grønfjorden, Isfjorden and Billefjorden). This approach will provide systematic assessments of changes in the ecological situation in the controlled areas of the coast and sea area, taking into account the technogenic impact on the nature of industrial enterprises and the developing tourist infrastructure.

REFERENCES

GN 1.2.1323-03. *Gigienicheskie normativy sodержaniya pesticidov v ob#ektah okružhajushhej sredy (s izmenenijami ot 4 i 25 fevralja 2004 g., 6 marta 2006 g.)*. Hygienic norms of pesticide contents in environmental objects (as amended on February 4, 25, 2004, March 6, 2006). [In Russian].

GN 2.1.5.1315-03. *Predel'no dopustimye koncentracii (PDK) himicheskikh veshhestv v vode vodnyh ob#ektov hozjajstvenno-pit'evogo i kul'turno-bytovogo vodopol'zovanija*. Maximum allowable concentrations (MACs) of chemicals in the water of water objects used for drinking and domestic recreation purposes. [In Russian].

GN 2.1.5.2280-07. *Orientirovochnye dopustimye urovni (ODU) himicheskikh veshhestv v vode vodnyh ob#ektov hozjajstvenno-pit'evogo i kul'turno-bytovogo vodopol'zovanija i dopolnenijami k nim GN 2.1.5.2307-07 i GN 2.1.5.2312-08*. Estimated Safe Exposure Levels (ESDS) of chemicals in the water of water objects used for drinking and domestic recreation purposes and amendments to them GN 2.1.5.2307-07 and GN 2.1.5.2312-08. [In Russian].

GN 2.1.6.1338-03. *Predel'no dopustimye koncentracii (PDK) zagryznajushhih veshhestv v atmosfernom vozduhe naseleennyh mest.* Maximum allowable concentrations (MACs) of pollutants in the air of residential areas. [In Russian].

GN 2.1.6.2309-07. *Orientirovochnye bezopasnye urovni vozdeystvija (OBUV) zagryznajushhih veshhestv v atmosfernom vozduhe naseleennyh mest.* Tentative safe exposure levels (TSELs) of pollutants in the air of residential areas. [In Russian].

GN 2.1.7.2041-06. *Predel'no dopustimye koncentracii (PDK) himicheskikh veshhestv v pochve.* Maximum permissible concentration (MAC) of chemical substances in soil. [In Russian].

GN 2.1.7.2042-06. *Orientirovochno dopustimye koncentracii (ODK) himicheskikh veshhestv v pochve.* Tentative allowable concentrations (TAC) of chemical substances in soil. [In Russian].

GOST 17.3.1.02-83. *Ohrana prirody. Pochvy. Klassifikacija himicheskikh veshhestv dlja kontrolya zagryznenija.* Nature protection. Soils. Classification of chemicals for pollution control. [In Russian].

Gokhman V. V. The river runoff regime on West West Spitsbergen. *Materialy gljaciologicheskikh issledovanij.* Materials of glaciological studies. 1988, 62: 96–103. [In Russian].

Demeshkin A. S. The content of pollutants in the bottom sediments of Grønlfjorden in Spitsbergen. *Trudy Instituta prikladnoj geofiziki im. akademika E.K. Fjodorova.* Proc. of the Ye. K. Fedorov Institute of Applied Geophysics. 2011 (90): 260–265. [In Russian].

Direktiva Soveta Evropejskogo Sojuza 1999/30/ES ot 22.04.1999 po standartam zagryznenija atmosfernogo vozduha. Council Directive 1999/30/EC of 22 April 1999 Relating to limit values for sulfur dioxide, nitrogen dioxide and oxides of nitrogen, particulate matter and lead in ambient air. [In Russian].

Direktiva Soveta Evropejskogo Sojuza 98/83/ES ot 3.11.98 po kachestvu vody, prednaznachennoj dlja potreblenija chelovekom. Council Directive 98/83/EC of 3 November 1998 on the quality of water intended for human consumption. [In Russian].

Dobrovolsky V.V. Geochemistry of Spitsbergen soils. *Pochvovedenie.* Soil science. 1990, 2: 520 p.

Izuchenie meteorologicheskogo rezhima i klimaticeskikh izmenenij v rajone arhipelaga Shpicbergen: otchet o NIR. Study of the meteorological regime and climatic changes in the area of the Spitsbergen archipelago: R&D report. XXX (contract No. 1/23-01 of 26.05.2001) section “State of water resources on West Spitsbergen in current conditions”. Supervisor S. M. Pryamikov. St. Petersburg: AARI, 2001. [In Russian].

Izuchenie meteorologicheskogo rezhima i klimaticeskikh izmenenij v rajone arhipelaga Shpicbergen: otchet o NIR. Study of the meteorological regime and climatic changes in the area of the Spitsbergen archipelago: R&D report. XXX (contract No. 1/23-01 of 26.05.2001) section “Results of the expeditionary survey of the state of surface waters on West Spitsbergen based on hydrochemical indicators”. Supervisor S.M. Pryamikov. St. Petersburg: AARI, 2001. [In Russian].

Kashulina G. M. Geochemical features of soils nearby Barentsburg, Spitsbergen. *Kompleksnye issledovanija prirody Shpicbergena.* Comprehensive studies of the nature of Spitsbergen. Proc. of research to practice conference. Apatity: Publishing house of KSC RAS, 2006, 6: 321–330. [In Russian].

Kashulina G.M., Kashulin N.A. Chemical composition of surface waters nearby Barentsburg, Spitsbergen. *Kompleksnye issledovanija prirody Shpicbergena.* Comprehensive studies of the nature of Spitsbergen. Proceedings of research to practice conference. Apatity: Publishing house of KSC RAS, 2005, 5: 308–314. [In Russian].

Kashulina G.M., Baskova L.A., Likhachev A.Yu. The chemical composition of plants nearby Barentsburg. *Ezhegodnik Kol'skoj gorno-metallurgicheskoj kompaniji.* Yearbook of the Kola Mining and Metallurgical Company (MMC). 2007, 5 (2): 234 p. [In Russian].

Matishov G.G., Savinov V.M., Dale S., Savinova T.N., Killie B. The current level of pollution by chlorinated and petroleum hydrocarbons in bottom sediments of the Pechenga Bay, Barents Sea. *Doklady Rossijskoj akademii nauk.* Repost of RAS. 1998, 361 (3): 425–428. [In Russian].

Metodicheskie rekomendacii po formalizovannoj ocenke kachestva poverhnostnyh i morskij vod po gidrohimičeskim pokazateljam. Methodical instructions for the formalized assessment of the quality of surface and sea waters by hydrochemical indicators. Moscow: Goskomgidromet USSR, 1988. [In Russian].

MI 2.1.7.730-99. *Metodicheskie ukazanija. Gigieničeskaja ocenka kachestva pochvy naseleennyh mest.* Methodical instructions. Hygienic assessment of soil quality in populated areas. Water quality standards for fishery water bodies, including the maximum allowable concentration of pollutants in the water of fishery water bodies, enacted by order of the Federal Agency for Fishery No. 20 dated January 18, 2010. [In Russian].

Melnikov S.A., Graevsky A.P., Myakoshin O.I. *Obzor zagrjaznenija prirodnoj sredy v Rossijskoj Federacii za 2002 g. Arhipelag Shpicbergen.* Review of environmental pollution in the Russian Federation for 2002. Spitsbergen Archipelago. Moscow, 2003. [In Russian].

Melnikov S.A., Klopov V.P., Graevsky A.P., Darovskih A.N., Myakoshin O.I. *Obzor zagrjaznenija prirodnoj sredy v Rossijskoj Federacii za 2003 g. Arhipelag Shpicbergen.* Review of environmental pollution in the Russian Federation in 2003. Spitsbergen Archipelago. Moscow, 2004: 376–381. [In Russian].

Melnikov S.A., Kiyko O.A., Darovskikh A.N., Myakoshin O.I., Graevsky A.P. *Review of environmental pollution in the Russian Federation in 2004. Spitsbergen Archipelago.* Review of environmental pollution in the Russian Federation in 2004. Spitsbergen. Moscow, 2005: 160–163. [In Russian].

Melnikov S.A., Klopov V.P., Graevsky A.P., Myakoshin O.I., Krutelev S.P. *Obzor zagrjaznenija prirodnoj sredy v Rossijskoj Federacii za 2005 g. Arhipelag Shpicbergen.* Review of environmental pollution in the Russian Federation in 2005. Spitsbergen Archipelago. Moscow, 2006: 172–185. [In Russian].

Melnikov S.A., Klopov V.P., Graevsky A.P., Myakoshin O.I., Krutelev S.P. *Obzor zagrjaznenija prirodnoj sredy v Rossijskoj Federacii za 2006 g. Arhipelag Shpicbergen.* Review of environmental pollution in the Russian Federation in 2006. Spitsbergen Archipelago. Moscow, 2007: 150–156. [In Russian].

Demin B.N., Klopov V.P., Graevsky A.P., Myakoshin O.I., Demeshkin D.S. *Obzor zagrjaznenija prirodnoj sredy v Rossijskoj Federacii za 2007 g. Arhipelag Shpicbergen.* Review of environmental pollution in the Russian Federation in 2007. Spitsbergen Archipelago. Moscow, 2008: 152–159. [In Russian].

Demin B.N., Demeshkin A.S., Graevsky A.P. *Obzor sostojanija i zagrjaznenija okružhajushhej sredy v Rossijskoj Federacii za 2008 g. Kompleksnaja ocenka zagrjaznenija okružhajushhej sredy poberezhij arktičeskijh morej i arhipelaga Shpicbergen.* Review of environmental pollution in the Russian Federation in 2008. Comprehensive assessment of environmental pollution of the coasts of the Arctic seas and the Spitsbergen archipelago. Moscow, 2009: 161–170. [In Russian].

Demin B.N., Demeshkin A.S., Graevsky A.P. *Obzor sostojanija i zagrjaznenija okružhajushhej sredy v Rossijskoj Federacii za 2009 g. Kompleksnaja ocenka zagrjaznenija okružhajushhej sredy poberezhij arktičeskijh morej i arhipelaga Shpicbergen.* Review of environmental pollution in the Russian Federation in 2009. Comprehensive assessment of environmental pollution of the coasts of the Arctic seas and the Spitsbergen archipelago. Moscow, 2010: 156–164. [In Russian].

Demin B.N., Demeshkin A.S., Graevsky A.P. *Obzor sostojanija i zagrjaznenija okružhajushhej sredy v Rossijskoj Federacii za 2010 g. Kompleksnaja ocenka zagrjaznenija okružhajushhej sredy poberezhij arktičeskijh morej i arhipelaga Shpicbergen.* Review of environmental pollution in the Russian Federation in 2010. Comprehensive assessment of environmental pollution of the coasts of the Arctic seas and the Spitsbergen archipelago. Moscow, 2011: 163–174. [In Russian].

CBs on Svalbard. Governor of Svalbard, Nature Conservation Department. Report No. 1/2008: 45 p. Available at: www.sysselmannen.no (accessed 06.08.2018).

RD 52.23.581–97. *Rukovodjashhij dokument. Organizacija i funkcionirovanie sistemy special'nyh nabljudenij za sostojaniem prirodnoj sredy v rajonah razvitiya ugledobyvajushhej promyshlennosti i sopushtvujushhijh proizvodstv.* Organization and functioning of a particular survey system of the natural environment status in the areas of developing coal mining industry and related industries. [In Russian].

RD 52.23.643–2002. *Rukovodjashhij dokument. Metodicheskie ukazaniya. Metod kompleksnoj ocenki stepeni zagryaznennosti poverhnostnyh vod po gidrohimicheskim pokazateljam*. Methodical instructions. Method for a comprehensive assessment of the pollution degree of surface waters by hydrochemical indicators. [In Russian].

RD 52.43.2–94. *Rukovodjashhij dokument. Ohrana prirody. Kompleksnoe obsledovanie zagryaznenija prirodnyh sred promyshlennyh rajonov s intensivnoj antropogennoj nagruzkoj*. Nature protection. A comprehensive survey of environmental pollution in industrial areas with the intensive anthropogenic load. [In Russian].

Antsiferova A.R. Results of multiple hydrometeorological observations and monitoring of environmental pollution on the Spitsbergen archipelago. *Priroda shel'fa i arhipelagov Evropejskoj Arktiki. Kompleksnye issledovanija prirody Shpicbergena*. The nature of the shelf and archipelagos of the European Arctic. Comprehensive studies of the Nature of Spitsbergen. Research to practice conference. Moscow: Geos, 2010, 10: 338–345. [In Russian].

Krasilshikov A.A. (ed.). *Rossijskie geologicheskie issledovanija na Shpicbergene 1962–1996 gg.* Russian geological research on Spitsbergen 1962–1996. St. Petersburg, 1998: 228 p. [In Russian].

SP 11-102-97. Inzhenerno-jekologicheskie izyskanija dlja stroitel'stva. CR (construction regulations) 11-102-97. Engineering and environmental surveys for construction. Moscow: Gosstroj Russia, 1997. [In Russian].

AMAP Assessment 2002: Heavy Metals in the Arctic. Arctic Monitoring and Assessment Programme, 2005. Oslo, Norway: Published by Arctic Monitoring and Assessment Programme (AMAP), 2005.

AMAP Assessment 2002: Persistent Organic Pollutants in the Arctic. Oslo, Norway: Published by Arctic Monitoring and Assessment Programme (AMAP), 2004.

AMAP Assessment Report: Arctic Pollution Issues. Oslo, Norway: Published by Arctic Monitoring and Assessment Programme (AMAP), 1998.

Arctic Pollution, 2009. AMAP. Oslo, Norway: Published by Arctic Monitoring and Assessment Programme (AMAP), 2009.

Canadian Arctic Contaminants Assessment Report. Ottawa, 1997.

Evenset A. Forurensning ved bosetting på Svalbard. Behov for oppfølgende undersøkelser og tiltak APN-4900.01 (Akvaplan-niva AS Report: 4900-1, 2010). Available at: www.sysselmannen.no (accessed 06.08.2018).

Evenset A., Ottesen R.T. Norsk og russisk overvåking av PCB-forurensning ved bosettinger på Svalbard: Sammenligning av felt- og analysemetoder og resultater. Akvaplan-niva rapport 4330-1, 2009: 31 p.

Gubala C.P., Landers D.H., Monetti M., Heit M., Wade T., Lasorssa B., Allen-Gil S. The rates of accumulation and chronologies of atmospherically derived pollutants in Arctic Alaska, USA. *The Science of Total Environment*. 1995, 160/161: 373–380.

Jartun M., Ottesen R.T., Volden T. and Lundkvist Q. Local sources of polychlorinated biphenyls (PCBs) in Russian and Norwegian settlements on Spitsbergen Island, Norway. *J. Toxicology and Environmental Health*. May 4th, 2008.

Mannion J., Jarvinen O., Tuominen R. and Verta V. Survey of trace elements in lake waters of Finnish Lapland using ICP-MS technique. *The Science of the Total Environment*. 1995, 160/161: 433–439. *Neue Niederlandische Liste. Altlasten Spektrum* 3/95.

5.2. AEROSOL COMPONENT OF THE ATMOSPHERE IN BARENTSBURG

*V.F. Radionov, O.R. Sidorova, L.P. Golobokova, O.I. Khuriganova,
T.V. Khodzher, S.M. Sakerin, D.M. Kabanov, D.G. Chernov, V.S. Kozlov,
M.V. Panchenko*

There are three main aspects in the study of atmospheric aerosol (particles of a wide range of sizes 10–10,000 nm): the effect of aerosol on radiation processes and climate formation, its role in exchange processes (transfer of substance in the “continent–atmosphere–ocean” system) and anthropogenic impact on the environment. Obtaining initial information in these areas is based on measuring the concentration of aerosol particles and parameters of their microstructure, the content of absorbing matter (black carbon), determining the characteristics of aerosol extinction of solar radiation by the entire atmosphere and the chemical composition of particles.

The significant variability of aerosol properties is due to the variety of types of aerosol particles (shape, chemical composition, size) and processes of their transformation in the atmosphere under the influence of numerous factors: meteorological conditions, atmospheric circulation, solar insolation, as well as the type of the underlying surface as one of the important sources of aerosol. Spatial differences in geophysical conditions that form spatial irregularities in the aerosol distribution lead to the need for field studies in different regions of the planet. Observations of the aerosol component of the atmosphere in the polar regions are of particular interest. Since there are practically no sources of anthropogenic aerosol, one could hope to obtain the minimum values (which are reference values for the globe) characterizing this component of the atmosphere.

Aircraft measurements of aerosol characteristics carried out by American scientists in the second half of the 1970s showed that in the Arctic, the concentration of aerosol particles in winter is more than an order of magnitude higher than in summer. The concentration of particles increases with height, reaching its maximum at a level of 2–3 km, and sometimes higher (“arctic haze”). The particles contained increased concentrations of elements and compounds associated with industrial emissions. These facts indicate that the arctic haze is mainly a result of anthropogenic rather than natural influence.

Russian scientists carried out the first and most numerous expeditionary measurements of the optical and microphysical characteristics of the Arctic aerosol in the 1970s–1980s at high latitudes on the Arctic islands and at the “North Pole” drifting stations. As a result of the conducted studies, a relatively high aerosol content in the winter-spring period was identified, it is several times higher than the summer and autumn values. It seems unexpected, since the Arctic doesn’t have not only enough anthropogenic sources of aerosol, but also natural ones since it is mostly (in time and territory) covered with snow and ice. The reasons for the discovered feature are the drift of aerosol from the industrially developed and densely populated regions of Eurasia and America as well as seasonal changes in atmospheric circulation. The polluted air masses transfer from the middle to high latitudes occurs most intensively in winter. The inversion stratification of the atmosphere, typical for the cold period, facilitates the accumulation of aerosol. As a result, the main feature is a well-defined spring maximum of aerosol pollution of the atmosphere for all Arctic stations – the so-called Arctic haze (Kondratyev, Binenko,

1981; Marshunova, Mishin, 1988; Barteneva et al., 1991; Radionov et al., 1994; Rusina, Radionov, 2002).

**CHARACTERISTICS OF AEROSOL POLLUTION OF THE ATMOSPHERE
IN VARIOUS ARCTIC AREAS ACCORDING TO FIELD STUDIES
IN THE SECOND HALF OF THE XX CENTURY**

Analysis of the long-term observation of direct solar radiation at the actinometric network of the Arctic stations showed that since the end of the 1950s, the integral transparency tended to decrease, or the integral optical depth of the atmosphere (IOD) tended to increase (Fig.5.2.1). This effect, especially well-defined in spring, is associated primarily with an increase in the aerosol turbidity of the atmosphere by emissions from anthropogenic sources and sometimes with the consequences of powerful volcanic eruptions – El Chichón in 1982 and Pinatubo in 1991 (Radionov et al., 1994).

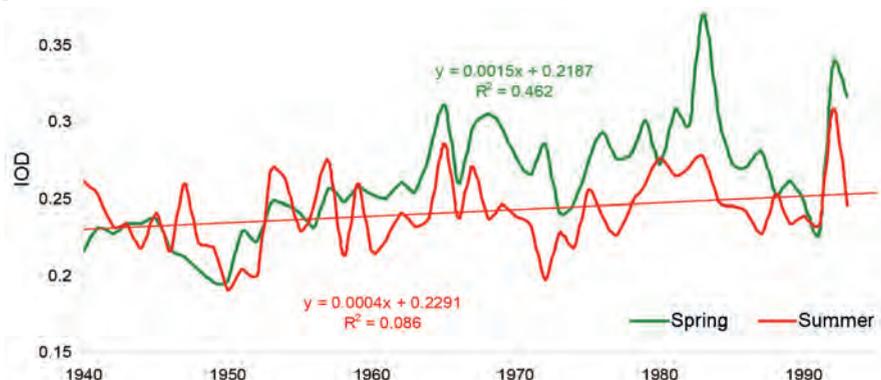


Fig. 5.2.1. Long-term variability of the average IOD values in the spring (March–May) and summer (July–August) on Dikson Island.

However, only direct observations could provide reliable quantitative estimates of the state and changes in the aerosol component of the atmosphere. Over the years, observations of the aerosol and optical characteristics of the atmosphere were organized in several areas in the Arctic (Table 5.2.1).

Table 5.2.1

Observations of the aerosol and optical characteristics of the atmosphere

Location	Coordinates	Period
Drifting station NP-22 (North Pole)	72–76° N, 135° W – 160° E	May–October 1979
Vavilov Ice Cap on October Revolution Island, Severnaya Zemlya archipelago	79° 29' N, 96° 50' E	1979, 1981–1986, 1988
Wrangel Island	71° 14' N., 179° 24' W	April–June 1984, April–May 1985 and 1986
Drifting station NP-28	82° N, 168° E	April–May 1987
Dikson Island	73° 31' N, 80° 20' E	1981, 1983–1990
Kotelny Island	75° 27' N, 140° 50' E	1985–1989
Expedition “Sever-44” (North-44)	69–82° N, 60–118° E and 68–76° N, 119–191° E	April–May 1992
Expedition “Sever-45” (North-45)	72–82° N, 60–120° E	March–April 1993
Ziegler Island, Franz Josef Land	80° 58' N, 57° 25' E	March–April 1994

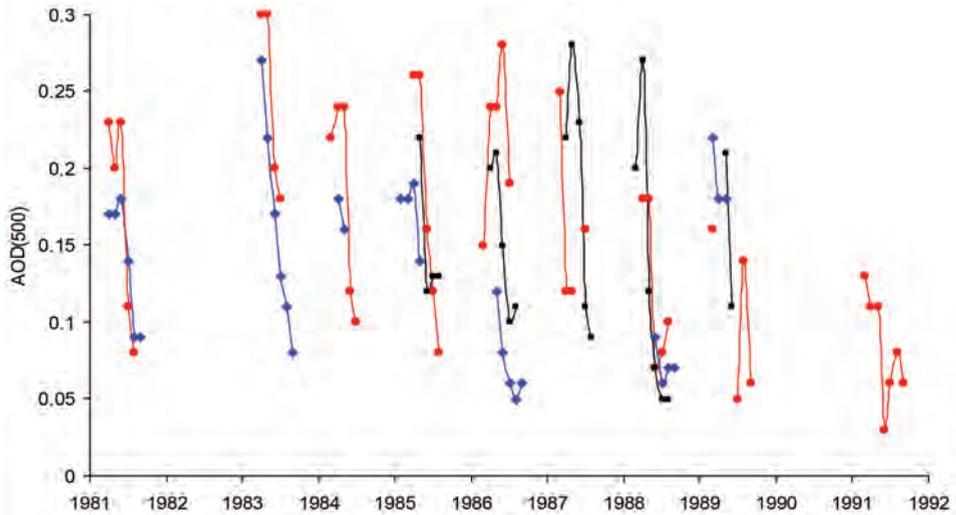


Fig. 5.2.2. Intra-annual and long-term variability of aerosol extinction of solar radiation at the stations in the Russian Arctic in 1981–1991.

1 – Severnaya Zemlya arch., 2 – Dikson Island, 3 – Kotelny Island.

The spectral aerosol optical depth of the atmosphere makes it possible to obtain detailed information about the features of extinction of solar radiation by aerosol in different parts of the spectrum. Fig. 5.2.2 shows the average monthly values of the spectral aerosol optical depth of the atmosphere at the wavelength 500 nm – AOD (500). They were measured at three points in the Russian Arctic: Vavilov Ice Cap on October Revolution Island (79° 29' N, 96° 50' E) on the Severnaya Zemlya archipelago; Dikson Island (73° 31' N, 80° 20' E); Kotelny Island (75° 27' N, 140° 50' E).

Fig. 5.2.2 shows that the aerosol component of the atmosphere, with its maximum at the end of winter – the beginning of spring of each year, sharply decreases by several times by summer at the Arctic stations.

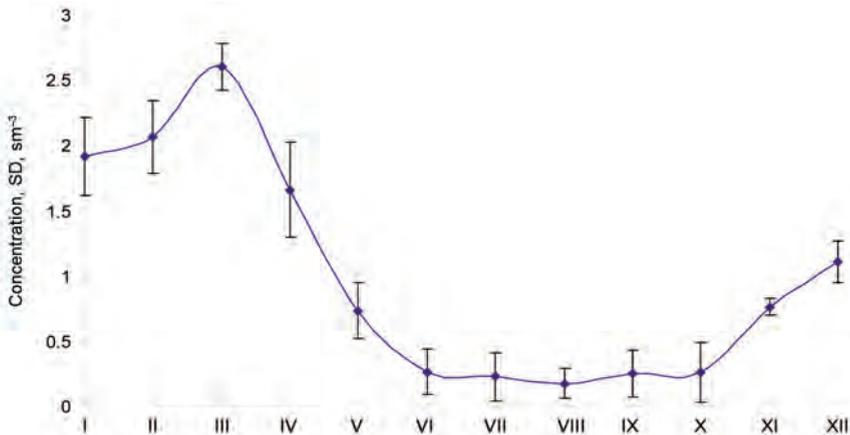


Fig. 5.2.3. Average monthly values of total particulate count larger than 0.4 μm and their standard deviation (SD) on Severnaya Zemlya archipelago according to observations for 1979, 1981, 1983, 1984–1986.

The results of measurements of the spectral transparency of the atmosphere carried out in 1978 and 1979. at the NP-22 drifting station, confirmed a very small aerosol extinction of solar radiation in the Central Arctic Basin in summer (Sakunov et al., 1981).

Regular studies of aerosol in the surface layer of the atmosphere in the Russian Arctic began in May–June 1979 on the Severnaya Zemlya archipelago and continued in subsequent years (Sakunov et al., 1981; Barteneva et al., 1991).

Total particulate count. There is a seasonal variation in the total particulate count with its maximum in the winter-spring period and its minimum in the summer months (Fig. 5.2.3).

The figure shows that the average monthly values of the total particulate count in summer (June–October) is less than in winter (January–March), more than an order of magnitude. All areas of the Arctic, where observations were carried out in different years, have the same regularity in the annual variation of the aerosol concentration in the surface air layer. It is the main feature of the aerosol component of the Arctic atmosphere.

An analysis of aerosol observation data showed that the annual and interannual variability of the total particulate count depends on synoptic processes, the characteristics of the transported air masses, and meteorological characteristics during the observation period (Barteneva et al., 1991). The aerosol drift from the industrially developed regions of Eurasia and North America influence the composition of the Arctic air a lot. Consequently, the aerosol content in the Arctic substantially depends on the intensity of anthropogenic emissions in middle latitudes and the long-range transport of polluted air masses to high latitudes.

Aerosol size distribution function. Photoelectric counters made most of the measurements of the disperse composition of aerosol in the Arctic; they make it possible to reconstruct the particle size distribution function only for relatively large particles, the effective diameter of which exceeds 0.4 μm . Aerosol measurements covered the size range from 0.005 to 10 μm only twice, in May 1985 on Wrangel Island and in April 1994 on Ziegler Island, Franz Josef Land.

In general, the nature of particle size distribution remained the same throughout the year and from year to year, despite the wide ranges of variability in particle concentration according to the data of all measurements at various points in the Arctic. The size spectrum of the Arctic aerosol of submicron ($0.1 \mu\text{m} < R < 1 \mu\text{m}$) and coarse ($R \geq 1 \mu\text{m}$) fractions in the first approximation is described by Young's law $dN/d(\lg R) \sim R^{-n}$ (R is the particle radius).

The exponent n at various points in the Arctic varied from 3 to 3.5. Only in May 1985, its average value was $n = 4$ on Wrangel Island.

Fig. 5.2.4 shows an example, the particle size distribution function based on measurements on Ziegler Island (Smirnov et al., 1998). Young's law well describes it with exponent $n = 3$.

The seasonal difference in aerosol size spectra is that the range of recorded particle sizes is wider in the cold season than in the warm one. In summer, as a rule, there were no particles larger than 4 μm , and in some cases – 1.5 and 2 μm . From February to May, particles larger than 1 μm were the main ones in the mass concentration of aerosol, from 60 to 80 %.

Surface aerosol chemical composition. The first ideas about the chemical composition of atmospheric aerosol on the Spitsbergen archipelago, obtained at the Norwegian research

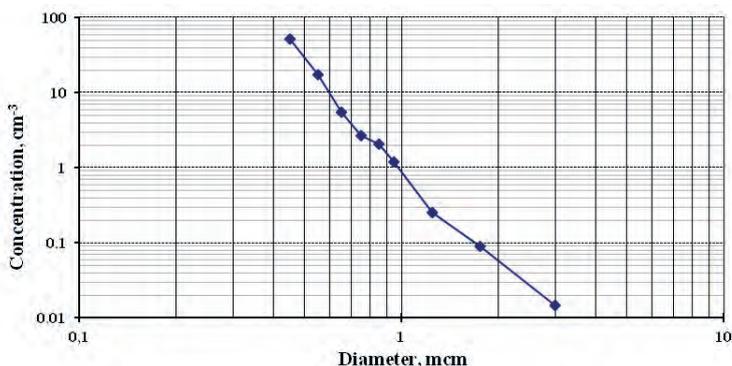


Fig. 5.2.4. The aerosol particle size distribution function in April 1994 on Ziegler Island, Franz Josef Land Archipelago.

center in Ny-Ålesund, date back to the late 1970s (Larsson et al., 1979). The concentration of the main ions (SO_4^{2-} , Cl^- , NO_3^- , Na^+ , Ca^{2+} , K^+ , Mg^{2+} , NH_4^+) and some elements (Ti, Cr, Mn, Ca, Fe, Cu, Zn, Pb, Ni) was determined in the aerosol. A comparison of the chemical composition and size distribution of particles with the results obtained in other Arctic regions confirmed the hypothesis of that time. It said that in winter, the Arctic aerosol is strongly influenced by anthropogenic sources located in middle latitudes. Later, the scientists revealed that air currents carry a wide range of pollutants into the Arctic, including sulfur and nitrogen compounds (Fenger et al., 2013). Cruise ships also pollute the archipelago's atmosphere a lot. Per Zhan et al. (2014), The concentration of Ca^{2+} ions increased in the aerosol by an average of ten times, K^+ ions by five times, and SO_4^{2-} ions by three times when the ships came to Ny-Ålesund.

The above mentioned (mainly episodic) observations in the Arctic latitudes made it possible to obtain estimates of the main characteristics of the atmosphere aerosol component and their annual variability: spectral aerosol optical depth of the atmosphere, total particulate count, and parameters of particle size distribution. It was found that they are formed under the influence of long-distance transport of polluted air masses from the middle to high latitudes.

In subsequent years, the list of measured parameters expanded, and their monitoring began – regular long-term observations at stationary stations (AMAP, 2011). In 2011, such observations started at the Russian Scientific Center on Spitsbergen (RSCS) in Barentsburg.

CHARACTERISTICS OF THE ATMOSPHERIC AEROSOL IN THE BARENTSBURG REGION (2011–2019)

Features of the study area and measured aerosol characteristics. Measurements of atmospheric aerosol characteristics at Barentsburg station, where the Russian Scientific Center on Spitsbergen (RSCS) is located (Savatyugin, Solovyanova, 2011), are organized and carried out in cooperation of three organizations – AARI (St. Petersburg), V.E. Zuev Institute of Atmospheric Optics (Tomsk) and Limnological Institute, Siberian Branch of the Russian Academy of Sciences (Irkutsk). The research is aimed to identify the features of the variability of optical, microphysical characteristics and chemical composition of aerosols in the western sector of the Russian Arctic. The accumulation of a sufficient amount of data will make it possible to develop empirical aerosol models, which are necessary for radiation-climatic calculations and assessment of the ecological state of the Arctic region in the current period.

The laboratory, which houses the equipment, is located in a building on the southwestern outskirts of Barentsburg. On the east side, there is a height of about 250 m, in the west – the Grøn fjorden. Industrial activities influence the state of the environment in the study area. Sludge dumps of the coal mining industry lead to the degradation of vegetation cover and geological formations, which subsequently create conditions for surface erosion (Tomczyk, Ewertowski, 2010). Air emissions from a thermal power plant located about 0.5 km south-south-west of the measurement point affect air pollution levels in the surface air. The underlying surface not covered with snow is also the source of dust and black carbon particles with the appropriate direction and wind speed. Recently, the tourism industry and the construction of new infrastructure increased the load on the ecosystem as well.

Regular measurements of the physicochemical characteristics of atmospheric aerosol on the territory of the RSCS (78° 06' N, 14° 22' E) began in the spring of 2011. The list of optical and microphysical characteristics includes total particulate count (N_A), the mass concentration of the absorbing substance in the aerosol (black carbon – M_{BC}), an aerosol optical depth of the atmosphere (AOD) in the spectral range of 0.34–2.14 μm .

AOD measurements were carried out during the periods of the polar day (April–September) using sun photometers SPM and SP-9 (Sakerin et al., 2013). Based on the data obtained, the spectral AOD τ_λ^a and parameters α and β of the Angstrom formula were calculated, which describes well the spectral dependence of the AOD in the spectrum range up to 1 μm :

$$\tau^a(\lambda) = \beta \cdot \lambda^{-\alpha}. \quad (5.2.1)$$

Also, according to the measurements in the IR spectral range ($\lambda > 1 \mu\text{m}$), two AOD components were determined, due to the extinction of radiation by coarse and fine aerosol:

$$\tau^a(\lambda) = \tau^c + \tau^f(\lambda) = \tau^c + m \cdot \lambda^{-n}, \quad (5.2.2)$$

where τ^c – coarse component of AOD, practically independent of wavelength; $\tau^f(\lambda)$ – selective fine component; m and n – parameters are similar to those of Angstrom formula.

The minimal AOD values, measured in the range 1.24–2.14 μm , were taken as the coarse component τ^c ; and the fine component was estimated for a wavelength of 0.5 μm as a residual depth (Sakerin et al., 2014): $\tau_{0.5}^f = \tau_{0.5}^a - \tau^c$.

Note that the parameter α characterizes the slope of the spectral path of AOD in logarithmic scale. It mainly depends on the ratio of fine and coarse components of AOD ($\tau_{0.5}^f / \tau^c$) (e.g., Sakerin et al., 2014).

Measurements of aerosol and black carbon concentrations in the near-ground layer of the atmosphere are carried out in a 24-hour hourly monitoring mode: in 2011–15 during the polar day (April–September), and since 2016 throughout the year.

When measuring the concentrations, a two-channel aethalometer MDA-02 (Kozlov et al., 2008) and optical particle counters were used: AZ-10 in radius range $R = 0.15 \dots 2.5 \mu\text{m}$ or Grimm 1.108 ($R = 0.15 \dots 5 \mu\text{m}$). The MDA-02 aethalometer provides registration of the mass concentration of black carbon in aerosol with a sensitivity of about 10 ng/m³ when 30 liters of air is pumped through the device.

Analysis of the seasonal and interannual variability of the total particulate count was carried out separately for fine N_f ($R = 0.15 \dots 0.5 \mu\text{m}$) and coarse N_c ($R = 0.5 \dots 5 \mu\text{m}$) particles, which have different nature of origin, transformation processes in the atmosphere and lifetime. Moreover, variability was additionally considered:

Table 5.2.2

The number of days (hours) of aerosol characteristics measurements and the number of aerosol samples taken for filters

Year, a period of measurements	AOD	Microphysical characteristics		The number of aerosol samples
		N_A, M_A	M_{BC}	
2011: April 19 – August 31	31 (194)	74 (1469)	58 (1093)	37
2012: April 21 – August 28	25 (73)	58 (1079)	92 (1904)	37
2013: April 15 – September 8	13 (64)	35 (655)	35 (725)	35
2014: April 22 – August 30	37 (135)	75 (1402)	69 (1448)	76
2015: April 30 – September 28	68(393)	95 (2124)	150 (3289)	54
2016: April 14 – December 31	61 (298)	245 (4908)	261 (4755)	55
2017: whole year	76 (402)	312 (4077)	336 (6513)	56
2018: whole year	51 (173)	352 (5550)	350 (6271)	52
2019: January 1 – September 30	75 (420)	271 (5841)	271 (5049)	12
Total	437 (2152)	1517 (27105)	1622 (31047)	414

- 1) volumetric particle size distribution $(dV/dR_i) = 4/3 \cdot \pi \cdot R_i^3 \cdot dN_i$ ($\mu\text{m}^2/\text{cm}^3$), where dN_i and R_i – number concentrations and average radii for the i -th particle size interval;
 2) aerosol mass concentration $M_A = \rho \cdot \sum 4/3 \cdot \pi \cdot R_i^3 \cdot \Delta N_i$ for the aerosol substance density $\rho = 1.5 \text{ g/cm}^3$.

It was very important to reject the realizations influenced by local sources of aerosol (first of all, smoke emissions from the thermal power stations chimney), as well as unfavorable meteorological conditions (low clouds, fog, precipitation) to process the measurement data correctly.

After excluding such data, for each year, the daily, monthly, and annual values of aerosol characteristics were sequentially calculated. Table 5.2.2 shows the amount of analyzed data – total and for each year of measurements.

Samples were taken for filters by pumping at least 10–12 m³ of air to determine the chemical composition of the aerosol and the content of gaseous impurities in the air. Sampling and analysis of samples were carried out following the Guidelines used for observations in international monitoring networks EANET (Acid Deposition Monitoring Network in East Asia) and EMEP (European Monitoring and Evaluation Programme) (EMEP, 1996). The ionic composition analysis of aerosols (Na⁺, K⁺, Mg²⁺, Ca²⁺, NH⁴⁺, Cl⁻, NO₃⁻, Br⁻, SO₄²⁻) was performed with the help of the ion chromatography method in the certified laboratory of hydrochemistry and atmospheric chemistry of the Limnological Institute, Siberian Branch of the RAS (Irkutsk). The introduction of a standardized method of quantitative chemical analysis for the identification of ions made it possible to obtain measurement results at a confidence level of P = 0.95 with 4 %. Detection of trace elements Li, Al, Ti, V, Cr, Mn, Fe, Co, Ni, Cu, Zn, As, Se, Sr, Mo, Cd, Sn, Sb, Ba, W, Pb, Th, Ag, Tl in soluble and solid aerosol fractions on an “Agilent 7500 ce” mass spectrometer (USA) was carried out by inductively coupled plasma mass spectrometry. Aerosol samples for the detection of polycyclic aromatic hydrocarbons (PAHs) were collected on fibrous glass filters by “Sartorius”. The amount of PAHs in the aerosol was measured using the internal standards method. Solutions of fenatrene-d10, chrysene-d12, and perylene-d12 were used as standards; they were added to the sample before extraction. The prepared samples were

analyzed on a gas chromatography-mass spectrometer “Agilent, GC System 7890B, 7000 CGC/MS Triple Quad” (Gorshkov et al., 2014 (A)). The quality of the analyzes performed has been repeatedly confirmed by comparing the results in inter-laboratory comparison tests under international programs under the authority of EMEP, WMO, and EANET network (Khodzher et al., 2004).

Aerosol optical depth (AOD) of the atmosphere. Forty years of research in various regions of the Arctic (Barteneva et al., 1991; Radionov et al., 1994; Herber et al., 2002; Tomasi et al., 2015; 2012) showed that monthly AOD values (0.5 microns) range from 0.03 to 0.15. In the same range of values, AOD also varied at three observation points on Spitsbergen (Ny-Ålesund, Hornsund, and Barentsburg) in 2002–2013 (e.g., Tomasi et al., 2015); average AOD (0.5 μm) decreased from 0.08–0.11 in spring to 0.03–0.07 in autumn.

In spring, high turbidity of the atmosphere, known as Arctic haze (e.g., Shaw, 1995; Quinn et al., 2007; Tomasi et al., 2015), are associated with long-range transport of anthropogenic aerosol from continents and accumulation of aerosol in the sub-inversion layers of the troposphere. One could observe significant short-term (several days) anomalies of atmospheric transparency during long-distance transport of smoke from forest and agricultural fires in summer. (e.g., Stohl et al., 2007; Stone et al., 2008; Tomasi et al., 2015). The influence of the drift of various pollution from middle latitudes is confirmed by the statistics of the trajectories of the movement of air masses (e.g., Vinogradova and Ponomareva, 2012; Vinogradova, 2014).

The total range of changes in spectral AOD in Barentsburg was about 1.5 orders of magnitude in 2011–2019. Daily AOD (0.5 μm) changes by almost 8 times due to variations in the aerosol content in the atmospheric column, and about the same AOD changes due to spectral differences in radiation extinction at different wavelengths. Fig. 5.2.5 shows average spectral dependences of AOD for various data samples (in smoke situations, annual and seasonal averages). In the spectral range up to 1 μm , power-law decrease AOD with increasing wavelength is observed, which is well described by the Angstrom formula. While the average AOD values decrease, the magnitude of variations also decreases. In the IR-range, spectral differences become insignificant, and the AOD value approaches the value of τ^c .

Table 5.2.3 shows the statistical characteristics of daily and annual variations in AOD at a wavelength of 0.5 μm , as well as parameters α , β . The statistical data show that fine aerosol makes the main contribution to the AOD and its variations: the relative fraction ($\tau_{0.5}^f / \tau_{0.5}^a$) is 77 %, and the coefficients of variation $V(\tau_{0.5}^f) = 95$ %. The most stable

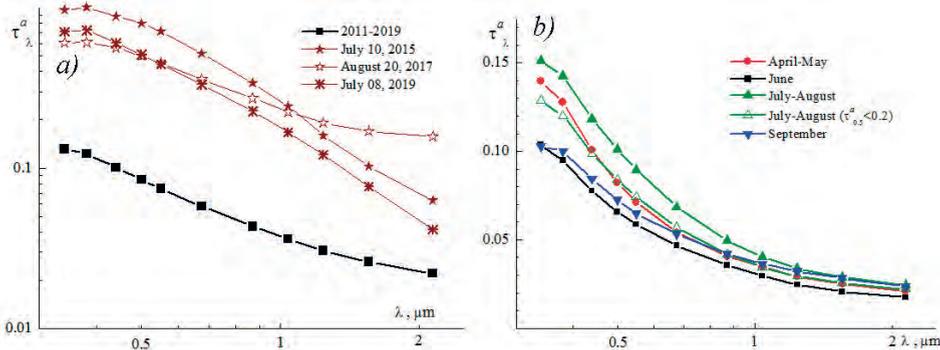


Fig. 5.2.5. Spectral dependences of AOD: *a*) – long-term averages and in a smoke-drift situation; *b*) – during periods of extreme seasonal variation.

Statistical characteristics of the daily (1st row) and annual (2nd row) AOD values in Barentsburg (2011–2019): mean, minimum (Min), maximum (Max) values, standard deviations (SD) and coefficients of variation (V)

Parameter	Mean	SD	Min	Max	V, %
$\tau_{0.5}^a$	0.091	0.074	0.011	0.799	82
	0.085	0.014	0.069	0.116	16
$\tau_{0.5}^f$	0.070	0.066	0.008	0.736	95
	0.063	0.015	0.044	0.096	23
τ^c	0.021	0.015	0.002	0.158	71
	0.022	0.005	0.015	0.030	23
α	1.28	0.34	0.37	2.30	26
	1.25	0.18	1.01	1.60	14
β	0.038	0.030	0.004	0.296	81
	0.036	0.006	0.025	0.047	18

characteristic is the Angstrom selectivity index α . Its relative variability is 23 %, and the average ($\alpha = 1.28$) is in the range of values typical for continental middle latitude regions ($\alpha = 1.2\text{--}1.4$) (Holben et al., 2001; Chubarova et al., 2014; Kabanov et al., 2019). This fact shows only to the same ratio of fine and coarse components of AOD ($\tau_{0.5}^f / \tau^c$) in different regions. For example, in the reference region of Siberia (Kabanov et al., 2019) the ration ($\tau_{0.5}^f / \tau^c$) = 3.2, and in Barentsburg ($\tau_{0.5}^f / \tau^c$) = 3.3.

Fig. 5.2.6a shows a daily AOD frequency (in logarithmic scale) for the entire measurement period in Barentsburg. The figure shows that the AOD histogram is close to the lognormal distribution with a modal (most probable) value of 0.07. Most (95 %) of AOD values are in the range $\tau_{0.5}^a < 0.2$.

Comparison with observational data at neighboring Arctic stations (Ny-Ålesund, Hornsund) in different seasons, 2011–2017 showed that AOD in Barentsburg is slightly higher (Kabanov et al., 2018); on average by 0.01–0.02.

Seasonal variability. Fig. 5.2.6 b shows the variability of AOD depending on the day according to the Julian calendar. For individual years (2011, 2013), we previously noted a decline in AOD from spring to autumn (Sakerin et al., 2014; 2018a). However,

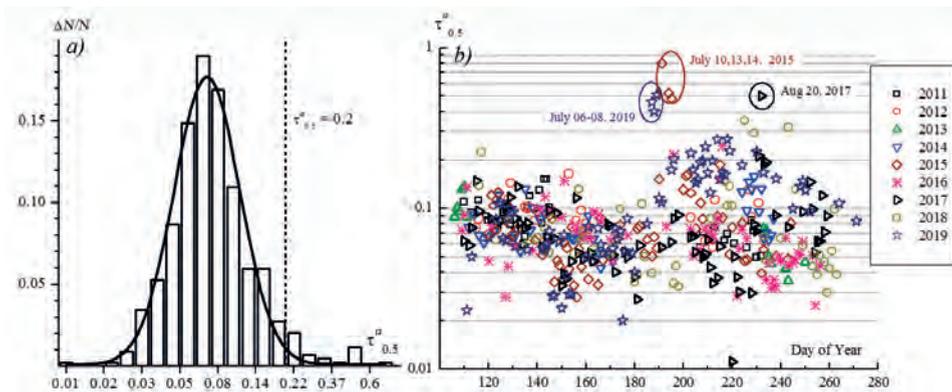


Fig. 5.2.6. Histogram of distributions $\tau_{0.5}^a$ (a) and variations $\tau_{0.5}^a$ (b) in Barentsburg in 2011–2019 (at the x-axis – Julian days).

in the general dataset (2011–2019), the seasonal variation of AOD is not so well-defined, it is associated with synoptic processes – the change in air masses. One can see seasonal dynamics only in the behavior of the maximum and minimum AOD values: a spring decline to about 170 days according to the Julian calendar, a summer increase to 220 days, and a subsequent decline until the end of the measuring season.

Occasionally observed high AOD values were caused by invasions of smoke aerosol into the Arctic atmosphere (see Fig. 5.2.6 *b* and 5.2.5 *a*). The most significant AOD fluctuations were observed on July 10–14, 2015, August 20, 2017, and July 6–8, 2019. A specific feature of 2019 was more prolonged turbidity of the atmosphere from mid-July to the end of the measurement period (~ 190 –260 Julian days). Despite the short duration of smoke inflow situations (1–4 days, except for 2019), they have influenced the character of seasonal AOD variability significantly.

Let us consider the case of maximum smoke turbidity separately. On July 10–14, 2015, the highest turbidity of the atmosphere was observed in Barentsburg for the entire time of measurements (Sakerin et al., 2018a). Daily AOD ($0.5 \mu\text{m}$) during this period reached 0.8, which is about an order of magnitude higher than the average long-term values (see Table 5.2.3). The following facts show that the measurement data, in this case, were not false (cloudiness or local plume of smoke). The increase in AOD was not short-time: it began on the evening of July 9 and lasted more than three days. In the same period, the aerosol content in the surface layer of the atmosphere increased, especially the total particulate count of small particles. A similar increase in AOD was recorded at the neighboring stations Ny-Ålesund and Hornsund (Pakszys and Zielinski, 2017; Markowicz et al., 2016), located at a distance of about 120 km from Barentsburg.

All listed facts show that the extreme turbidity of the atmosphere was caused not by local sources of aerosol, but by the long-distance transport of polluted air. The trajectory analysis data indicate that the source of atmospheric pollution was the drift of smoke from forest fires in Alaska. The following information confirms it (Sakerin et al., 2018a): satellite fire maps (<http://lance-modis.eosdis.nasa.gov/cgi-bin/imagery/firemaps.cgi>); AOD measurements at the AERONET station in Barrow/Alaska (<http://aeronet.gsfc.nasa.gov>); as well as the dynamics of AOD fields from satellite observations (<http://giovanni.sci.gsfc.nasa.gov>), which reflected the movement of a smoke cloud from Alaska to Spitsbergen in the period from 7 to July 9, 2015.

Thus, the turbidity of the atmosphere on Spitsbergen is influenced by the inflow of forest fire smoke not only from the middle latitudes of Eurasia but also from the north of the American continent. Given the enormous impact of such events, the analysis of seasonal and interannual variability of AOD was carried out in two versions: for the general dataset (“All data”) and except for situations of smoke turbidity (“No smoke”), when $\tau_{0.5}^a > 0.2$ (see Fig. 5.2.6 *a*). They were only 5 % of the total number of observations.

The seasonal variability of AOD is clearly seen when considering its monthly average values. (Fig. 5.2.7 *a*). The seasonal variation of AOD has two maximums (April–May and July–August), separated by a June minimum, comparable with the AOD minimum in September. Table 5.2.4 shows the statistical characteristics of AOD for different periods of the year.

The spring AOD maximum is typical for most areas, including the Arctic (e.g., Tomasi et al., 2015). The primary reason for the increased AOD values in spring is the annual cycle of solar radiation entering the surface. The spring rise in insolation and

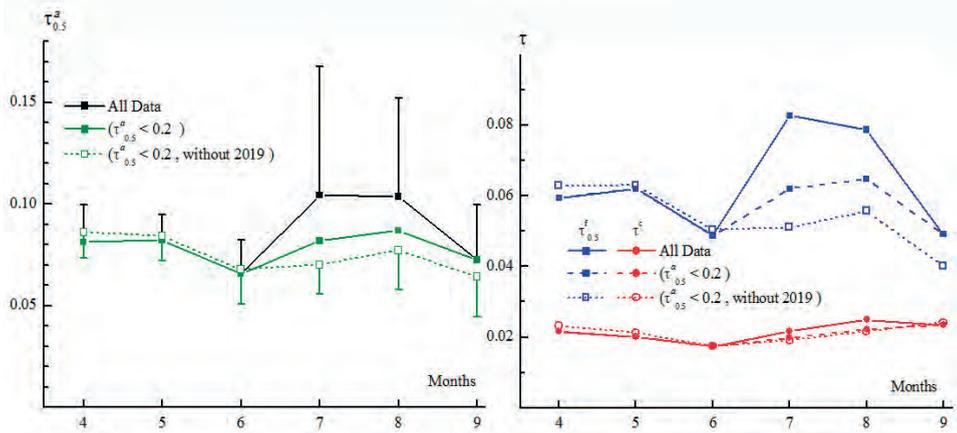


Fig. 5.2.7. Average seasonal $\tau_{0.5}^a$, $\tau_{0.5}^f$ and τ^c (All data and “No smoke” – $\tau_{0.5}^a < 0.2$).

temperature triggers several processes: a) the snow cover evaporates and melts; b) the atmosphere is enriched with various substances that have deposited and accumulated in the snow cover over the winter; c) soil aerosol begins to flow from the underlying surface (d) photochemical processes of aerosol formation in the atmosphere and organic aerosol emissions are activated (e.g., Kondratyev et al., 2006).

The presence of the summer maximum AOD is more typical for middle latitudes (e.g., Kabanov et al., 2019; Chubarova et al., 2014; Holben et al., 2001). Let us compare the results of AOD observations with and without smoke situations to find out the reasons for its appearance in the Arctic region. Fig. 5.2.7 a and Table 5.2.4 shows that the summer maximum AOD decreases to 0.085 (becoming less than the spring maximum) when we exclude smokes ($\tau_{0.5}^a > 0.2$). When the “smoke” 2019 is excluded from the analysis, the summer maximum becomes even smaller: $\tau_{0.5}^a \approx 0.075$. Consequently, the main reason for the high AOD values in Barentsburg in July–August was the inflow of forest fire smoke from the boreal zone, which has become more frequent in the last 5 years.

We should note that the spring and summer maxima of AOD are determined by the behavior of fine component – $\tau_{0.5}^f$ (Fig. 5.2.7 b) and we can better see them in the shortwave part of the spectrum (Fig.5.2.5 b). Seasonal changes in the AOD coarse component during the measurement period are insignificant. As a consequence, the seasonal variation of the selectivity index α , depending on the ratio ($\tau_{0.5}^f / \tau^c$), repeats the change from a qualitative point of view $\tau_{0.5}^a$: maximum values are observed in spring ($\alpha = 1.38$), minimum – in September ($\alpha = 1.05$).

Table 5.2.4.

Average AOD (\pm SD) characteristics in Barentsburg in selected periods

Parameter	April–May	June	July–August		September
			All data	“No smoke”	
$\tau_{0.5}^a$	0.088 ± 0.028	0.066 ± 0.016	0.104 ± 0.053	0.085 ± 0.033	0.073 ± 0.027
$\tau_{0.5}^f$	0.066 ± 0.027	0.049 ± 0.016	0.080 ± 0.049	0.064 ± 0.031	0.049 ± 0.027
τ^c	0.021 ± 0.009	0.017 ± 0.003	0.024 ± 0.007	0.021 ± 0.007	0.023 ± 0.014
α	1.38 ± 0.27	1.15 ± 0.20	1.30 ± 0.22	1.30 ± 0.23	1.05 ± 0.47
β	0.035 ± 0.012	0.030 ± 0.005	0.042 ± 0.023	0.035 ± 0.015	0.036 ± 0.014

The nature of the seasonal variation in AOD in Barentsburg in the last 9 years differs from other Arctic regions in the previous decades (Barteneva et al., 1991; Radionov et al.; Herber et al., 2002; Tomasi et al., 2015). The difference is: a summer maximum appears, and the value of the decline in AOD decreases from spring to autumn. Observation results at the nearby Hornsund station in 2008–2013 (Chen et al., 2016) show that after 2010 the magnitude of the seasonal decline in AOD (spring-autumn) decreased. It decreased because of the fine component of AOD and mainly in the spring period: from $\tau_{0.5}^f \sim 0.1$ in 2008–2010 to $\tau_{0.5}^f = 0.04 \dots 0.08$ in 2011–2013. Spring values $\tau_{0.5}^f$ at Hornsund station in 2011–2013 are consistent with measurements in Barentsburg: $\tau_{0.5}^f = 0.066$ (See Table 5.2.4). Besides, good agreement is observed between the long-term average AOD values: in Barentsburg $\tau_{0.5}^a = 0,091$ (see Table 5.2.3), in Hornsund $\tau_{0.5}^a = 0.09$ (Chen et al., 2016).

Thus, the seasonal variability of AOD in Barentsburg in the last decade has two distinctive features: a) more frequent smoke aerosol drifts led to the formation of the summer maximum AOD; b) due to as yet unknown reasons (possibly due to a decrease in inversions and Arctic haze situations), there was a decrease in AOD in the spring.

Interannual variability. The fluctuations of annual AOD reflected above episodes of high turbidity of the atmosphere (Fig. 5.2.8 a). The maximum AOD in 2015 was due to the short-term (July 10–14) drift of the smoke plume from Alaska (Sakerin et al., 2018a). If this situation was excluded (see the dashed line), the maximum AOD leveled out. Two other AOD peaks (in 2012 and 2019) were the result of the impact of large forest fires in Siberia in July 2012 (Zhuravleva et al., 2017) and July–August 2019. The exception of increased turbidity ($\tau_{0.5}^a > 0.2$) reduced the annual AOD values in 2012 and 2019 only partially, as, in those years, there was general and more prolonged pollution of the Arctic atmosphere.

The second rows of Table 5.2.3 provide quantitative data on the magnitude of interannual fluctuations in various AOD characteristics. The fine component influences the variations of annual AOD the most: SD and the range (Max-Min) of $\tau_{0.5}^f$ is 3 times as much as τ^c . Feature of long-term variability τ^c is the presence of a statistically significant trend (for a dataset without smoke): decline τ^c by 0,012 during nine observation years. Other AOD characteristics have no trend component.

The lowest rates of variation (14–16 %) are observed for the α and $\tau_{0.5}^a$. Relative variability of $\tau_{0.5}^f$, τ^c component slightly higher. Average value and range of variability

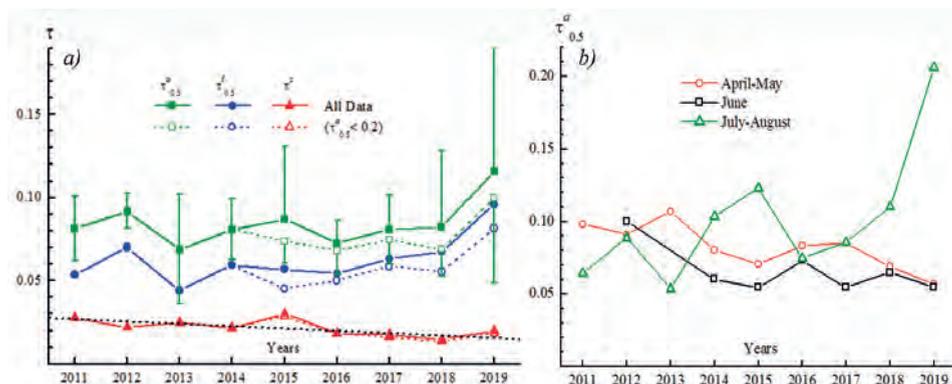


Fig. 5.2.8. Interannual variability: a) – annual values $\tau_{0.5}^a$, $\tau_{0.5}^f$ and τ^c (dash line – data without smoke); b) – average values $\tau_{0.5}^a$ in selected seasons.

of α (from 1 to 1.6) in Barentsburg, as already noted, correspond to those observed in the continental atmosphere of middle latitudes. But it significantly exceeds the values over the seas and oceans, varying from 0.25 to 1 (Smirnov et al., 2002; Sakerin et al., 2008; 2017).

Long-term variability of averages of AOD in April–May, June, and July–August is shown in Fig. 5.2.8 *b*. Due to the smaller scale of averaging (1–2 months), the amplitude of interannual fluctuations of seasonal AOD values as 2–4 times as much as the annual AOD. The biggest fluctuation in $\tau_{0.5}^a$ and $\tau_{0.5}^f$ we can observe in 2019. In the long-term perspective, the AOD values for different seasons are not correlated with each other: in the same year, the maximum in one of the seasons is combined with the minima in the others. Estimates of the trend components of seasonal AOD showed the presence of: a) statistically significant increase (0.011 a year) $\tau_{0.5}^a$ and $\tau_{0.5}^f$ in July–August; b) decrease $\tau_{0.5}^a$ (0.0045 a year) and τ^c (0.002 a year) in April–May.

These tendencies reflected in the change in the nature of the seasonal variation of AOD in the last period (2011–2019), which was noted above: a summer maximum formed and a spring maximum slightly decreased.

Table 5.2.3 follows that all characteristics of AOD variability (SD, V , and the total range of Max–Min) of annual values are 2–6 times as less as daily values. Consequently, the day-to-day variations associated with circulation processes (change in air masses) influence the AOD variations the most. Moreover, in some cases, these processes determine the features of the seasonal and interannual variability of AOD. In particular, the more frequent drift of forest fire smoke from the boreal zone led to the appearance of the summer maximum AOD exceeding the spring one.

Aerosol and black carbon concentrations. The aerosol and black carbon concentrations in the surface layer of the atmosphere are more variable than AOD. A large range of concentration variability of NA and MBC caused not only by changes in meteorological

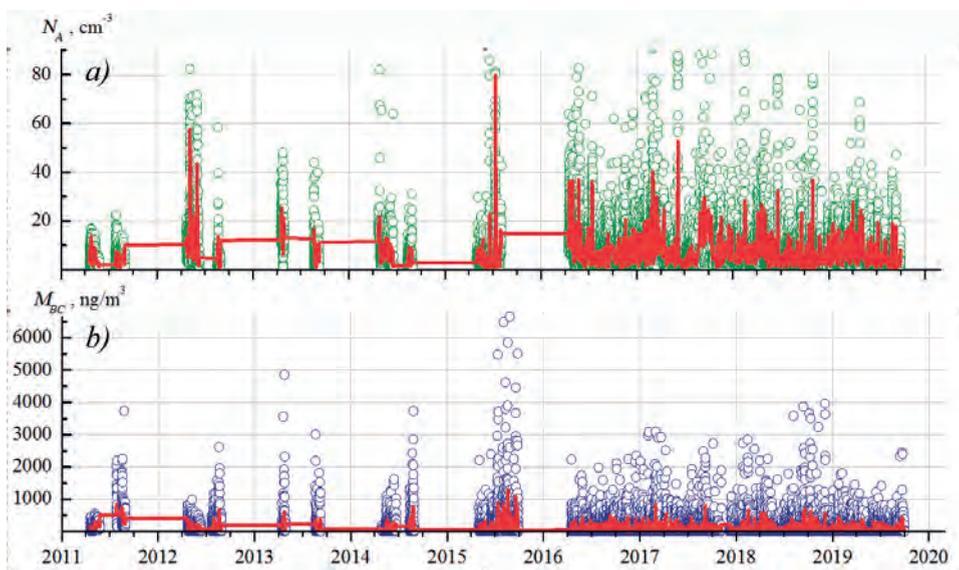


Fig. 5.2.9. Long-term variability of hourly values of aerosol (*a*) and black carbon (*b*) concentrations in Barentsburg (solid red lines – daily smoothing).

and synoptic conditions (change of air masses) but also by the episodic impact of local sources of aerosol in Barentsburg (coal dust, smoke from a thermal power plant, etc.). Fig 5.2.9 illustrates the time course of aerosol and black carbon concentrations over the entire measurement period in Barentsburg. The total range of hourly variation of the concentration values exceeds three orders of magnitude. With daily averaging, the range of relative variability NA and MBC decreases to 220–230 times (see Max/Min in the first rows of Table 5.2.5). The range of variations in annual concentration values decreases by another two orders of magnitude (see the second rows of Table 5.2.5). Consequently, short-period fluctuations in the daily and synoptic ranges influence the variability of NA and MBC the most. Among the given characteristics, the black carbon concentration ($V = 109\%$) has the maximum day-to-day variations.

We should also note that the average values of aerosol characteristics given in the 1st and 2nd rows of Table 5.2.5 are slightly different (see also Table 5.2.3). The methodological peculiarities of statistical calculations of daily and annual values can explain the difference of about 10 %. But in the case of N_c and M_{BC} concentrations in Barentsburg, the difference was much higher. Apparently, this is because they are very sensitive to local impacts.

Table 5.2.5

Statistical characteristics of the variability of daily (1st row) and annual (2nd row) values of aerosol and black carbon concentration in Barentsburg in 2011–2019

Parameter	Mean	SD	Min	Max	V, %
N_A , cm^{-3}	7.10	6.65	0.36	80	94
	7.75	1.75	4.62	10.6	23
N_p , cm^{-3}	7.04	6.63	0.35	79.7	94
	7.65	1.72	4.5	10.3	23
N_c , cm^{-3}	0.07	0.07	0.002	0.80	100
	0.10	0.06	0.05	0.24	60
M_A , $\mu\text{g}\cdot\text{m}^{-3}$	1.58	1.34	0.064	12.8	85
	1.91	0.77	1.07	3.47	40
M_{BC} , ng/m^3	120	131	5	1163	109
	148	69	93	311	47

Seasonal variability. Fig. 5.2.10 shows the average annual variation of the calculated aerosol concentrations and the mass concentration of black carbon in Barentsburg. Fig. 5.2.10 *a* shows that the main maximum in August was well manifested ($M_{BC} = 168 \text{ ng}/\text{m}^3$) and secondary in April in the annual course of black carbon concentrations. The lowest concentrations of black carbon are observed in December ($M_{BC} = 68 \text{ ng}/\text{m}^3$), and also in early summer.

Annual variation of fine aerosol concentrations (Fig. 5.2.10 *b*) characterized by a well-defined maximum in spring (in March $N_f = 12.3 \text{ cm}^{-3}$), decline until June, and a subsequent low level of values ($4\text{--}6 \text{ cm}^{-3}$) until November. Seasonal decline amplitude N_f (from maximum to minimum) is about 60 %. In December, the winter increase of fine aerosol concentrations begins and continues until March. This behavior of N_f occurs because the meridional drift of pollutants from mid-latitudes increases during the cold period in combination with temperature inversions that lead to the accumulation of aerosol in the Arctic atmosphere (e.g., Quinn et al., 2007; Tomasi et al., 2015).

The variability of the large particle content during the year (Fig. 5.2.10 *c*) has large inter-monthly fluctuations – $\pm 20\%$. But from April to September, when there were much more observations than in other months of the year, it is necessary to pay attention to the N_c maximums in April and July.

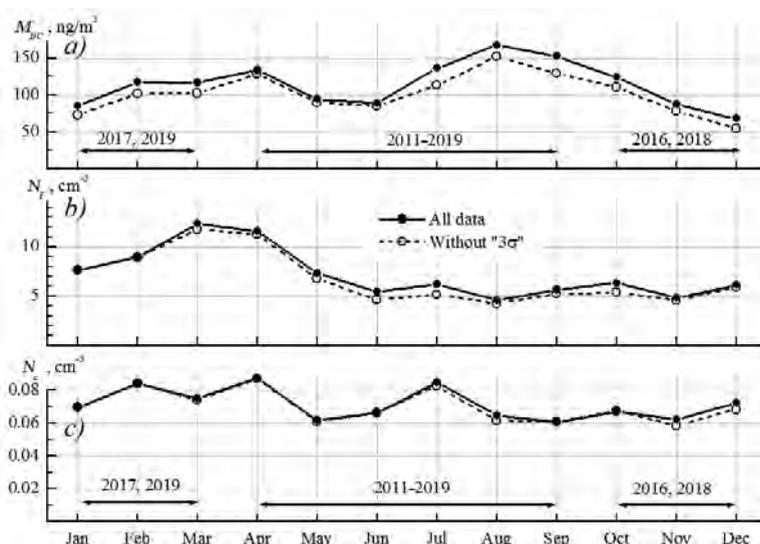


Fig. 5.2.10. Annual course of monthly concentration values MBC (a), N_f (b) и N_c (c) in Barentsburg. The horizontal arrows indicate the years and the period of averaging monthly values, the dashed line - the data after filtering by the “3 sigma” criterion.

The particle volume distribution functions give a more detailed understanding of the seasonal transformation of the aerosol disperse composition during the polar day (dV/dR) (Fig. 5.2.11). The maximum values (dV/dR) in the fine fraction range are observed in April and the minimum – in June and at the end of the polar day. That is, the volumetric distribution of the fine fraction changes similarly to the concentrations N_f (see Fig. 5.2.10 b). In the range of the largest particles ($R > 1 \mu\text{m}$), we can observe a different nature of seasonal variability: high values (dV/dR) in the middle of the warm period (June–July) and low values at the beginning (April) and end (August–September) of the polar day. The underlying surface gets free from the snow cover and ice cover, which prevents the generation of soil and sea aerosol. It explains the increased volume content of large particles in the middle of the warm period.

It is necessary to explain why the highest N_c concentrations in April (Fig. 5.2.10 c) are combined with low values (dV/dR) in most of the broad particle range (Fig. 5.2.11). The apparent contradiction is due to the fact that, in comparison with other months, April has the highest content of particles with an average radius $R = 0.75 \mu\text{m}$, which makes a decisive contribution to the N_c concentration.

Estimates of seasonal variability were carried out not only for the general dataset but also with a rejection of short-term sharp increase in concentration (splash) according to the “3 sigma” criterion (see the dashed line in Fig. 5.2.10) to at least partially exclude the effect of local anthropogenic sources of aerosol on the values of the measured parameters. When excluding the splashes, the monthly concentration values are partially reduced (for M_{BC} , to 20 %), but the nature of the annual variation does not change. Therefore, we can draw two conclusions. First, the increased concentrations are formed not only by short-term splashes but also by the general (higher) average level of atmospheric pollution in Barentsburg. Second, splashes in aerosol and black carbon concentrations are relatively evenly distributed throughout the year and do not affect the nature of seasonal variability.

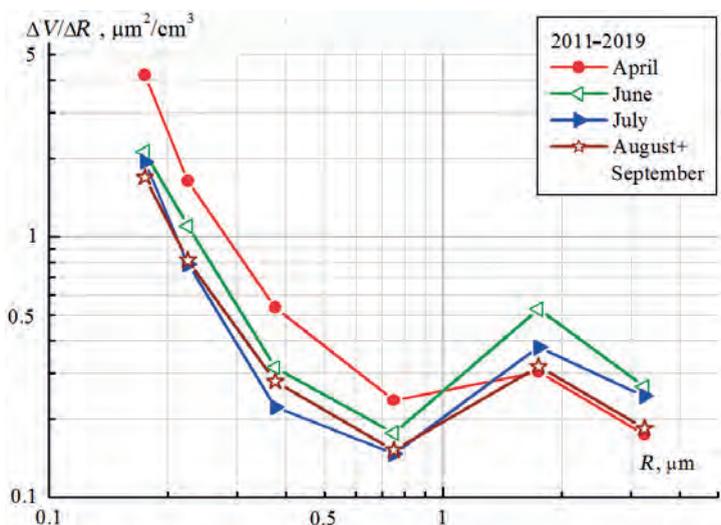


Fig. 5.2.11. Average volumetric distributions of particles (dV/dR) in Barentsburg at different times of the year.

Let's pay attention to the different statistical availability of estimates of the annual variation of N_A and M_{BC} at different times of the year. For the polar day, the calculations were carried out for nine years of measurements (2011–2019) and for the polar night – only for two years: at the beginning of 2017, 2019, and at the end of 2016, 2018. For this reason, quantitative information on the seasonal variability of aerosol and black carbon concentrations in Barentsburg is presented only for the polar day (Table 5.2.6.).

We can see from the statistical data that the total particulate count N_A decreases from 11.7 cm^{-3} in April to $4.6\text{--}5.7 \text{ cm}^{-3}$ at the end of the polar day. The fine fraction particles influence the aerosol concentration the most (about 99 %). However, the coarse aerosol is the main contributor to the aerosol mass concentration (M_A), which is proportional to the particle volume. Therefore, the M_A seasonal variation qualitatively repeats the N_c variation.

Table 5.2.6.

Statistical characteristics of monthly values of aerosol and black carbon concentrations in Barentsburg in the period April – September (2011–2019): first row – average \pm SD, second row – minimum and maximum values

Month	N_A, cm^{-3}	N_p, cm^{-3}	N_c, cm^{-3}	$M_A, \mu\text{g}/\text{m}^3$	$M_{BC}, \text{ng}/\text{m}^3$
April	11.7 ± 7.23	11.6 ± 7.19	0.087 ± 0.104	1.81 ± 1.32	134 ± 114
	2.05 – 36.0	2.05 – 36.0	0.003 – 0.80	0.24 – 8.73	14 – 550
May	7.39 ± 6.32	7.32 ± 6.30	0.061 ± 0.060	1.17 ± 0.95	94.7 ± 77.6
	0.65 – 58.1	0.64 – 58.1	0.002 – 0.41	0.09 – 6.82	5 – 446
June	5.48 ± 6.48	5.41 ± 6.47	0.066 ± 0.057	1.60 ± 1.32	89.2 ± 67.4
	0.44 – 57.7	0.42 – 57.6	0.003 – 0.29	0.13 – 7.67	6 – 338
July	6.31 ± 8.67	6.22 ± 8.63	0.085 ± 0.102	2.06 ± 2.16	137 ± 152
	0.67 – 79.9	0.67 – 79.7	0.002 – 0.61	0.11 – 12.8	10 – 1004
August	4.64 ± 3.64	4.58 ± 3.60	0.065 ± 0.068	1.34 ± 1.13	168 ± 176
	0.78 – 27.8	0.77 – 27.7	0.006 – 0.34	0.06 – 5.09	6 – 1163
September	5.70 ± 5.75	5.64 ± 5.74	0.061 ± 0.083	1.42 ± 1.28	152 ± 169
	0.55 – 43.5	0.52 – 43.5	0.001 – 0.54	0.09 – 7.24	5.5 – 1052

As noted above, the second half of the polar day – from July to September shows the highest content of black carbon (137–168 ng/m³). The high concentrations of black carbon during this period, along with the local anthropogenic impact, were influenced by the drift of forest fire smoke, which has become more frequent in recent years.

Comparison with measurement data in 1989–2011 at Arctic stations Zeppelin (Svalbard), Alert (Canada) and Barrow (Alaska) (Eleftheriadis et al., 2009; Stone et al., 2014) showed that average concentrations M_{BC} in Barentsburg are much higher: 1.7 times as much as in April and almost 5 times as much as in summer. Also, at international stations, there is no maximum concentration of black carbon in the warm period, and the monthly M_{BC} values continuously decrease from April to September. The increased contribution of anthropogenic sources and dust (including coal) coming from the underlying surface can explain such a difference in the nature of seasonal variability and the average content of black carbon in the surface atmosphere of Barentsburg with the above mentioned Arctic stations.

Interannual variability. Interannual changes in aerosol concentrations and mass concentration of black carbon were estimated only for the periods of the polar day, according to the average values of concentrations measured from April to September of each year. Analysis of long-term variability of surface aerosol and black carbon concentrations showed (Fig. 5.2.12) that the most stable characteristic is the fine aerosol concentration. According to the data in Table 5.2.5 (see second rows), the ratio (Max/Min) of the N_f values is 2.3 times, and the coefficient of variation is 23 %. The N_c and M_{BC} concentrations have significantly large interannual fluctuations. Their coefficients of variation are 60 % and 47 %, respectively.

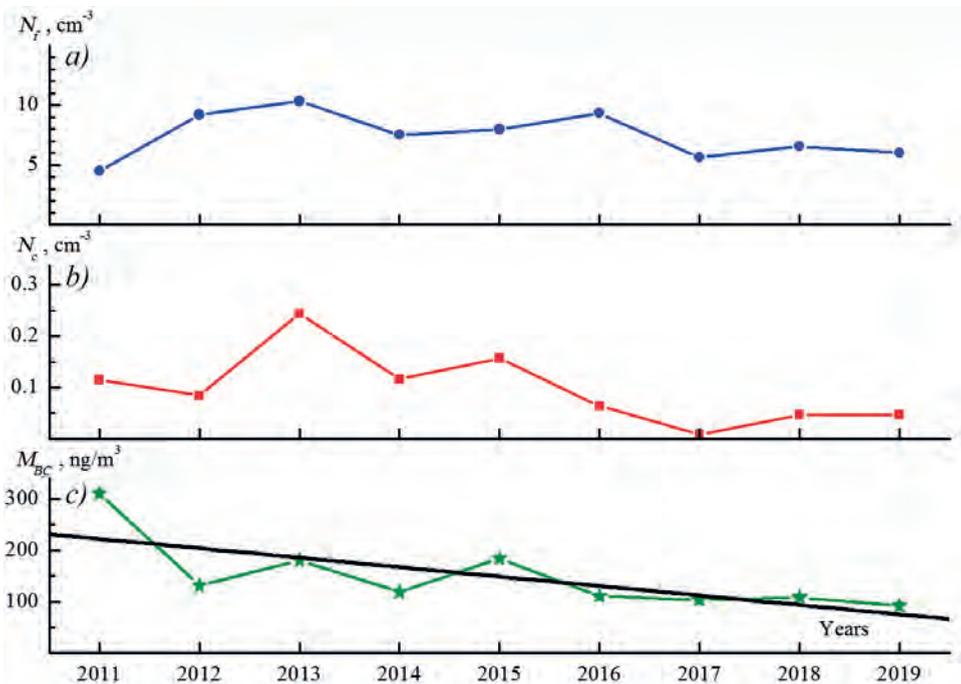


Fig. 5.2.12. Interannual variability of N_f (a), N_c (b), and M_{BC} (c) concentrations measured during the polar day in Barentsburg (the straight line indicates the long-term M_{BC} trend).

In the long-term variability of all characteristics, there is a tendency for a slight decline. Still, a statistically significant (at the 0.05 level) trend manifested itself only in the black carbon concentrations: a decrease in M_{BC} by 18.4 ng/m³ per year. The very high content of black carbon in 2011 is noteworthy. The summer period of this year was characterized by increased exposure to soil aerosol and coal dust from local sources (Chernov et al., 2014; Sakerin et al., 2018b). The maximum concentration of M_{BC} in 2015 was formed due to the short-term (July 10–14), but the powerful drift of forest fire smoke from North America (Sakerin et al., 2018a; Markowicz et al., 2016).

The tendency for a decrease in aerosol concentrations (N_p , N_c), a negative trend in MBC, as well as a decrease in interannual fluctuations in N_c and MBC indicate that the impact of anthropogenic factors (coal dust and emissions from the power stations) on the atmosphere of Barentsburg gradually decreases.

There are distinctive features in the regularities of the seasonal and interannual variability of the surface aerosol and AOD characteristics of the atmosphere, along with the general properties (spring maximum and decay trends in N_p , N_c , τ^c). The main reasons for the differences in the behavior of the surface and integral aerosol characteristics are as follows.

The transport of smoke aerosol from the boreal zone significantly influences the atmospheric AOD, as noted above. Regardless of the height of the long-range transport of smoke, we can well detect them in the change in AOD if observations were made at that time. Local sources of aerosol in the near-ground layer, due to their local nature, affect the integral characteristic very little.

There is the opposite situation with local measurements of surface concentrations of aerosol and black carbon, which are very sensitive to the influence of local sources. If long-distance transport of smoke or other pollutants from middle latitudes is accompanied by a plume settling into the surface layer in the measurement area, they can also affect surface concentrations. If it does not happen, then the continental impact manifests itself indirectly. In the process of long-distance transport of pollutants, they are scattered (advection, diffusion), then set into the near-ground layer of the atmosphere. That means each transport of continental aerosol and their total contribution increase the average level of aerosol content in the Arctic atmosphere.

CHEMICAL COMPOSITION OF AEROSOL PARTICLES IN THE NEAR-GROUND AIR LAYER AT BARENTSBURG STATION

According to the results of chemical analysis of 284 aerosol samples collected during the daytime (2011–2016, see Table 5.2.2), the average values of the concentrations of the measured ions were calculated for each calendar month and the seasons – “spring: April–May”, “summer: June–July”, “autumn: August–October”. Statistical characteristics: mean, minimum, maximum values and standard deviations (SD) were determined from the average results calculated for each year. The total content of ions in the aerosol composition varied in a wide range from 0.24 to 6.41 µg/m³. Fig. 5.2.13 illustrates that the highest total ion concentrations were observed in 2011–2012.

So, for example, the content of SO_4^{2-} , one of the main ions in the aerosol composition, reached 5.6 µg/m³ in June 2012. High sulfate concentrations in Barentsburg are inconsistent with data in other regions of the Arctic. At Nord station (northeastern Greenland), the SO_4^{2-} content in late winter and early spring, when the Arctic atmosphere is most affected by anthropogenic sources, ranged from 0.54 to 1.09 µg/m³ (Fenger et al., 2013). At Kevo

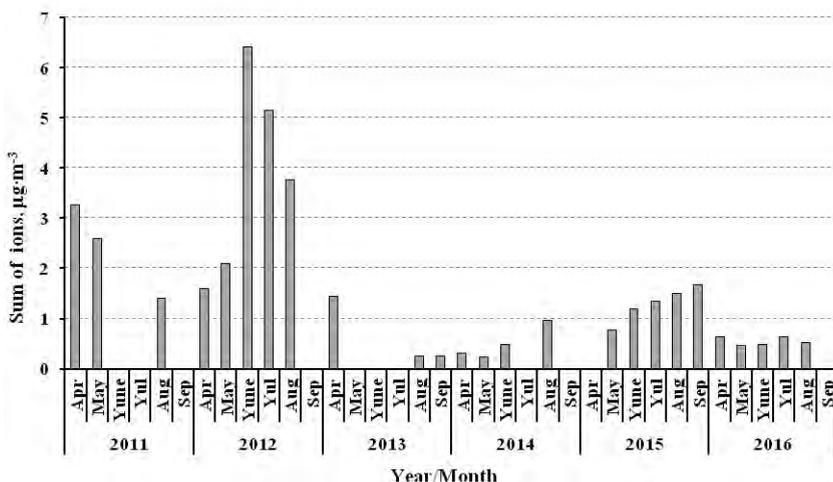


Fig. 5.2.13. Changes in the total ions content in the aerosol composition, 2011–2016 (April–September).

station (Finland), located 350 km north of the Arctic Circle and affected by the industrial zone of the Kola Peninsula, the sulfate content varied from 0.004 to 0.10 $\mu\text{g}/\text{m}^3$ (Yli-Tuomi et al., 2003). The high content of sulfates in the territory of Barentsburg in 2011–2012 could be due to intensive construction and capital repairs of housing and infrastructure. The atmosphere got significant pollution from the thermal power plant, which annually consumes about 30 thousand tons of coal. In 2012, the thermal power plant upgraded the pollution abatement system and replaced the ash and dust removal system. As a result, in 2013–2016, the total content of ions in the aerosol composition on average decreased by more than four times (see Fig. 5.2.13). In this regard, the data of 2011–2012 were excluded from the statistical calculations. They reflect the state of the atmosphere during the period of intense anthropogenic impact and are not typical for the study region. Further calculations and analysis of statistical characteristics were carried out for 210 samples taken in 2013–2016, of which 76 samples were taken at the beginning of the light period, 61 samples – in the middle, 73 – at the end. Table 5.2.8 presents the results of calculations of ion concentrations in individual seasons of 2013–2016.

The data in Table 5.2.8 demonstrate that the total ions content decreased from the initial (spring) sampling period to summer months and again increased in the colder (autumn) final period. The number of ions in the aerosol of the summer period was 1.5 times as less as in the spring and 1.6 times as less as in the autumn. The summer minimum was noted both in total concentrations and for individual ions. The average values of ions total in Barentsburg in autumn are higher than in spring. The difference between spring and autumn data was observed for higher concentrations of predominant ions (Na^+ , Ca^{2+} , Cl^- , SO_4^{2-}). Sulfates of marine (ss-SO_4^{2-}) and non-marine (nss-SO_4^{2-}) origin were calculated. In this case, the well-known formulas were used:

$$\begin{aligned}
 (\text{nss-SO}_4^{2-}) &= (\text{SO}_4^{2-}) - 0.06028 (\text{Na}^+), \\
 (\text{ss-SO}_4^{2-}) &= (\text{SO}_4^{2-}) - (\text{nss-SO}_4^{2-}), \\
 (\text{nss-Ca}^{2+}) &= (\text{Ca}^{2+}) - 0.02161 (\text{Na}^+), \\
 (\text{ss-Ca}^{2+}) &= (\text{Ca}^{2+}) - (\text{nss-SO}_4^{2-}).
 \end{aligned}$$

where (SO_4^{2-}) is the sulfate concentration, (Ca^{2+}) is the calcium concentration, (Na^+) is the sodium concentration in the ionic composition of the aerosol, the initial content of the sought components is presented in molar concentration (EANET, 2010). The long-term average value of (ss-SO_4^{2-}) was 10 %, the highest (August 2012) – 21 %, (ss-Ca^{2+}) – the average 9.6 %, the highest (June 2015) – 20 %. Thus, these ions drifted into the atmosphere predominantly (on average more than 90 %) from the continents during daylight hours.

Table 5.2.8.

Statistical characteristics of the ionic composition of aerosol in Barentsburg
(upper row – average \pm SD, lower – minimum and maximum ion concentrations, $\mu\text{g}/\text{m}^3$),
2013–2016

Ions	April – May	June – July	August – October
Na^+	0.104 \pm 0.096 0.038–0.245	0.100 \pm 0.093 0.026–0.204	0.166 \pm 0.087 0.082–0.274
NH_4^+	0.088 \pm 0.120 0.010–0.266	0.037 \pm 0.002 0.036–0.040	0.055 \pm 0.056 0.001–0.131
K^+	0.037 \pm 0.024 0.008–0.064	0.016 \pm 0.016 0.005–0.034	0.037 \pm 0.028 0.007–0.067
Mg^{2+}	0.028 \pm 0.038 0.001–0.084	0.014 \pm 0.010 0.003–0.021	0.017 \pm 0.009 0.005–0.027
Ca^{2+}	0.050 \pm 0.061 0.016–0.141	0.046 \pm 0.009 0.035–0.052	0.081 \pm 0.041 0.050–0.137
Cl^-	0.349 \pm 0.405 0.092–0.948	0.259 \pm 0.210 0.099–0.497	0.364 \pm 0.084 0.330–0.486
NO_2^-	0.006 \pm 0.011 0.000–0.022	0.002 \pm 0.002 0.000–0.004	0.003 \pm 0.005 0.000–0.002
Br^-	0.000 \pm 0.001 0.000–0.001	0.000 \pm 0.000 0.000–0.000	0.002 \pm 0.002 0.000–0.003
NO_3^-	0.067 \pm 0.087 0.015–0.197	0.053 \pm 0.044 0.015–0.102	0.039 \pm 0.023 0.013–0.067
SO_4^{2-}	0.385 \pm 0.365 0.080–0.914	0.230 \pm 0.103 0.149–0.346	0.415 \pm 0.199 0.157–0.578
PO_4^{3-}	0.011 \pm 0.016 0.000–0.035	0.009 \pm 0.014 0.000–0.025	0.014 \pm 0.010 0.004–0.024
Total ions	1.125 \pm 1.211 0.270–2.916	0.769 \pm 0.433 0.481–1.267	1.198 \pm 0.358 0.649–1.796

From April 2016 to March 2019, measurements of the chemical composition of the aerosol were carried out throughout the year: both during the light period of the year and during the polar night (Table 5.2.9). Estimates of the variability of the aerosol chemical composition for this period (April 2016–March 2019) were carried out depending on the light period and stable negative and positive air temperatures. The polar night in Barentsburg lasts from October 26 to February 15, the polar day from April 20 to August 23. The following periods were identified: winter from December to March (polar night), when there was a negative average monthly air temperature, spring from April to May – the period of intense snow melting (the beginning of the polar day), summer from June to August (polar day) – the period of the highest air temperatures, autumn from September to November (the end of the polar day and the beginning of the polar night) – a decrease in air temperature and an ice cover in Grøn fjorden. During the period of entire year observations

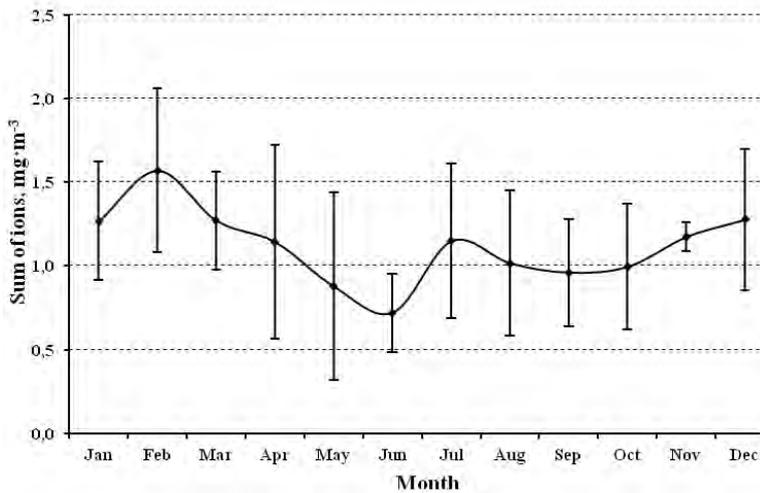


Fig. 5.2.14. Intraannual variability of average values of ions concentration and their standard deviation (SD) in the near-ground aerosol in Barentsburg, April 2016 – March 2019, $\mu\text{g}/\text{m}^3$.

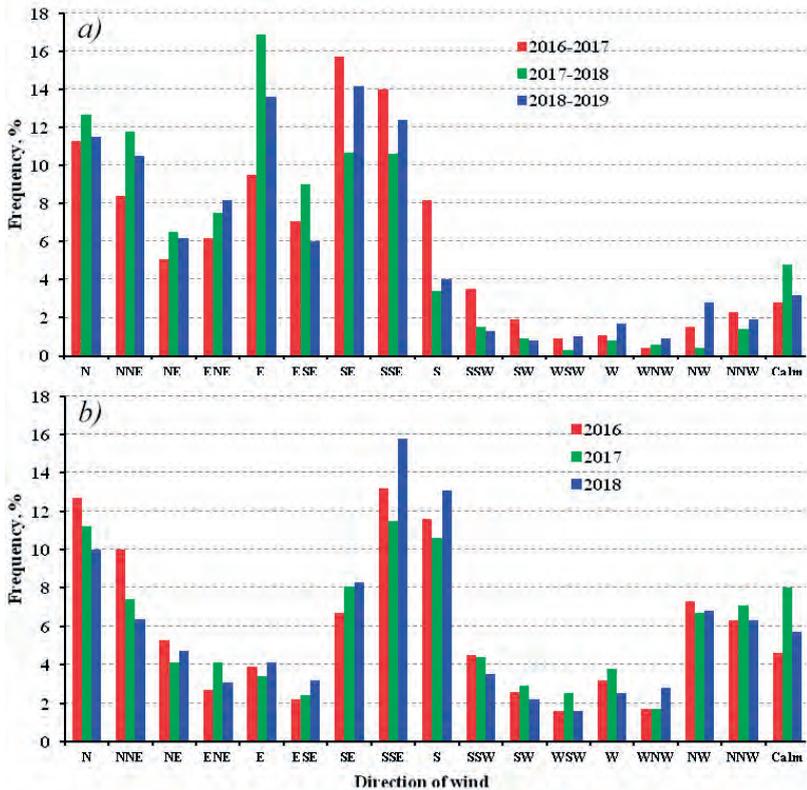


Fig. 5.2.15. The frequency of wind directions in the area of Barentsburg on average for the periods of the polar night (a) on 26.10.2016–02.15.2017, 26.10.2017–02.15.2018, 26.10.2018–02.15.2019, and the polar day (b) 20.03–23.08.2016, 20.03–23.08.2017, 20.03–23.08.2018 (Weather archive, 2013–2019).

Table 5.2.9.

Mean monthly values of ion concentrations and their standard deviations in aerosol composition in Barentsburg (April 2016 – March 2019), g/m³

Month	Na ⁺	NH ₄ ⁺	K ⁺	Mg ²⁺	Ca ²⁺	Cl ⁻	NO ₃ ⁻	SO ₄ ²⁻
January	0.174 ± 0.040	0.155 ± 0.144	0.020 ± 0.017	0.020 ± 0.010	0.048 ± 0.035	0.344 ± 0.037	0.032 ± 0.016	0.474 ± 0.224
February	0.332 ± 0.117	0.080 ± 0.025	0.033 ± 0.018	0.044 ± 0.027	0.058 ± 0.043	0.520 ± 0.196	0.045 ± 0.025	0.460 ± 0.076
March	0.179 ± 0.063	0.159 ± 0.094	0.025 ± 0.022	0.024 ± 0.005	0.066 ± 0.038	0.255 ± 0.113	0.036 ± 0.006	0.528 ± 0.121
April	0.144 ± 0.064	0.139 ± 0.138	0.024 ± 0.020	0.017 ± 0.009	0.054 ± 0.026	0.240 ± 0.122	0.024 ± 0.012	0.502 ± 0.292
May	0.144 ± 0.142	0.079 ± 0.036	0.019 ± 0.019	0.014 ± 0.008	0.030 ± 0.007	0.236 ± 0.197	0.023 ± 0.006	0.332 ± 0.168
June	0.131 ± 0.091	0.037 ± 0.007	0.020 ± 0.009	0.014 ± 0.002	0.034 ± 0.015	0.249 ± 0.110	0.019 ± 0.007	0.217 ± 0.031
July	0.195 ± 0.118	0.068 ± 0.031	0.040 ± 0.038	0.022 ± 0.004	0.053 ± 0.022	0.379 ± 0.161	0.028 ± 0.007	0.365 ± 0.137
August	0.171 ± 0.096	0.058 ± 0.034	0.039 ± 0.038	0.017 ± 0.002	0.050 ± 0.024	0.298 ± 0.131	0.022 ± 0.011	0.362 ± 0.152
September	0.177 ± 0.041	0.071 ± 0.047	0.030 ± 0.029	0.017 ± 0.004	0.044 ± 0.023	0.324 ± 0.081	0.022 ± 0.014	0.276 ± 0.148
October	0.173 ± 0.053	0.071 ± 0.061	0.033 ± 0.021	0.023 ± 0.017	0.051 ± 0.036	0.331 ± 0.102	0.023 ± 0.018	0.291 ± 0.285
November	0.234 ± 0.067	0.071 ± 0.053	0.028 ± 0.015	0.025 ± 0.007	0.064 ± 0.042	0.379 ± 0.105	0.028 ± 0.016	0.346 ± 0.114
December	0.249 ± 0.146	0.089 ± 0.053	0.028 ± 0.021	0.021 ± 0.009	0.051 ± 0.022	0.437 ± 0.221	0.028 ± 0.012	0.375 ± 0.031

(April 2016–March 2019), the average monthly total ion content in the composition of the soluble fraction of the aerosol varied from 0.45 to 2.05 $\mu\text{g}/\text{m}^3$. In the interannual dynamics of the total ion content, there are three periods of decrease and increase in their concentrations. February and December showed the greatest accumulation of impurities in the atmosphere during the polar night, and July – during the polar day. The lowest ion concentrations were determined in June. There was a slight decrease in the number of ions in September (Fig. 5.2.14). The variability of ion concentrations as a result of entire year measurements coincided with the results of measurements in the light season when the highest values of the ions total were determined in April–May and August–October.

The study of the frequency of surface wind directions at the height of 10–12 m during the polar night revealed the highest frequency of winds blowing from the northern, eastern, and southeastern directions. On a polar day, one could observe the highest frequency of wind from the northern, southern, and northwestern directions (Fig. 5.2.15). Coal warehouses became the primary source of aerosol particles for the north and north-east direction of the wind, and sludge dumps and emissions from the power plants for the south, southeast, and south-west directions.

The seasonal dynamics of the concentrations of ions prevailing in the aerosol is considered. The predominant ions in the composition of the soluble aerosol fraction, as in 2011–2016, in all periods were Na^+ , NH_4^+ , SO_4^{2-} , Cl^- . The highest concentrations of these ions are determined mainly in cold winter and autumn periods corresponding to the polar night (Fig. 5.2.16). It is noted that the concentrations of K^+ , Ca^{2+} , and SO_4^{2-} ions of predominantly continental origin, increase in July–August. The concentrations of Na^+ , Mg^{2+} , and Cl^- ions of marine origin increased in July.

The observed decrease in the concentration of ions in the aerosol from spring to summer is consistent not only with long-term studies in Spitsbergen (Ny-Ålesund, Zeppelin) (Yamagata et al., 2009; Udisti et al., 2016) but also at other stations of the Arctic region – Barrow (Alaska) (Quinn et al., 2009), Nord (Greenland) (Fenger et al., 2013), Alert (Canada) (Sirois, Barrie, 1999). The same ions are dominant in the aerosol composition in Barentsburg as at other Arctic stations with long-term observation series.

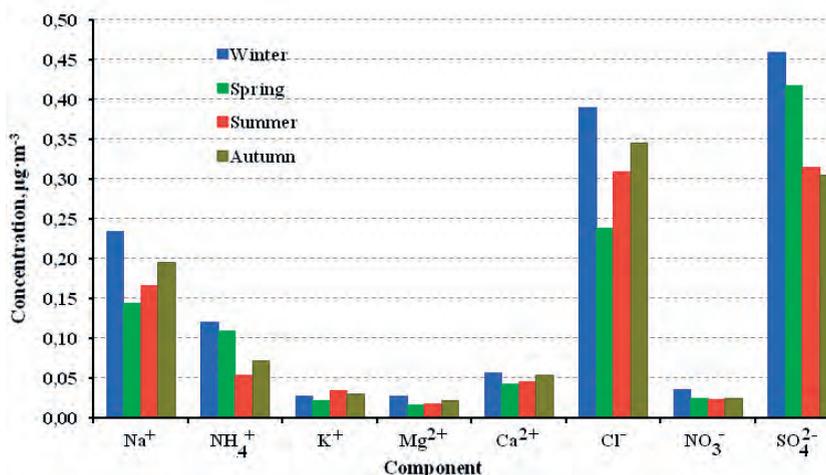


Fig. 5.2.16. Seasonal variability of ion concentrations in the surface aerosol composition in the area of Barentsburg, April 2016 – March 2019, $\mu\text{g}/\text{m}^3$.

The similarity of the aerosol ionic composition is observed at different measurement periods. On the polar night, there is a high correlation in the concentrations of pairs of ions Na^+ , Cl^- ($r = 0.94$), Mg^{2+} , Cl^- ($r = 0.77$), which confirms the marine source to be the main sources of aerosol formation during this period. It may be due to an increased inflow of warmer and saltier waters of Atlantic origin into the inner regions of the fjords of West Spitsbergen, which does not contribute to the stable ice cover (Nilsen et al., 2008; Tislenko et al., 2015). The correlation between NH_4^+ , SO_4^{2-} ($r = 0.66$), K^+ , SO_4^{2-} ($r = 0.38$), Ca^{2+} , NO_3^- ($r = 0.52$) ions is less significant. If there is snow cover on the surface this most likely indicates their anthropogenic origin associated with the combustion of coal at power plant. In the summer period, the correlation coefficients of the concentrations of the pairs of ions K^+ , NO_3^- ($r = 0.40$) and K^+ , SO_4^{2-} ($r = 0.41$), Ca^{2+} , SO_4^{2-} ($r = 0.68$) indicate an additional source of impurities entering from the surface.

The influence of various factors on the change in the aerosol composition is confirmed by the analysis of the enrichment factors K of aerosol particles with various substances in comparison with their content in seawater (see Fig. 5.2.17). The K value was calculated using the formula from (Yli-Tuomi et al., 2003).

$$K_i = \left[\left(\frac{C_i}{\text{Na}^+} \right)_{aer} \right] / \left[\left(\frac{C_i}{\text{Na}^+} \right)_{sw} \right], \tag{5.2.3}$$

where K is the enrichment factor, (C_i/Na^+) is the concentration of the i -th element relative to Na^+ in aerosol (*aer*) and seawater (*sw*).

Figure 5.2.17 shows that the enrichment of aerosol particles in magnesium (Mg^{2+}) and chlorides (Cl^-) in all seasons is close to one, which indicates their predominantly marine origin. Unlike Mg^{2+} and Cl^- , aerosol particles are enriched with calcium (Ca^{2+}), potassium (K^+), and sulfate ions (SO_4^{2-}). The most significant enrichment with Ca^{2+} , K^+ was noted in the spring-summer and autumn periods, in SO_4^{2-} – throughout the year. If at the beginning of April in Barentsburg the snow is mostly loose or packed and covers the soil completely, then by the end of the month, there are thaw holes. The intense

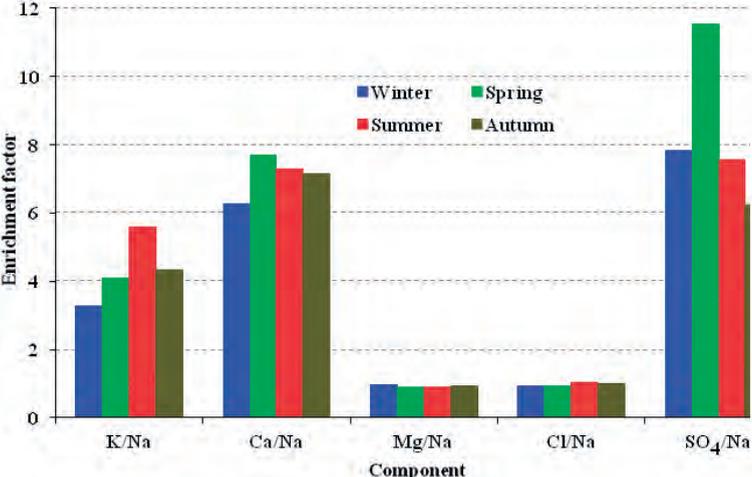


Fig. 5.2.17. Enrichment factors of aerosol particles in the atmosphere of Barentsburg (Spitsbergen) in different seasons of the year.

melting of the snow cover occurs in May (Weather archive, 2013–2019). The emission of soil aerosol and chemical compounds accumulated in the snow increases, turbulent heat exchange over bare soil intensifies, contributing to the accumulation of impurities in the atmosphere at low relative humidity. Air dustiness increases in the spring, it was also noted at the continental sampling stations. For example, in Eastern Siberia, at the reference station Mondy (51° 41' N, 100° 59' E), located at an altitude of 2000 m and far from large industrial centers, one of the peaks of the increase in the total ion concentration in the aerosol is observed in April. A similar increase in the concentration of ions in aerosol in the spring period was also detected in a large industrial center – the city of Irkutsk (Golobokova et al., 2005). An increase in atmosphere turbidity associated with the transfer of impurities released during snowmelt in the western regions of Siberia. (Panchenko et al., 1994). The natural influx of Ca²⁺ and K⁺ into the atmosphere in Barentsburg may come from degraded surfaces not covered with snow and ice located near the sampling station (Tomczyk et al., 2010). In an industrial center, sulfur oxides in the air in the presence of strong oxidants and high humidity become the main producers of sulfates (Isidorov, 2001). In summer, the tourism industry and the operation of the marine port increase the load on the island's ecosystem (Zhan et al., 2014). The relief features influence the accumulation of pollutants in the atmosphere. With the northwestern winds, dust is supplied to the atmosphere from the side of the coal warehouse. South-south-west winds bring smoke emissions from the thermal power plant, while with the south-west winds, the sea component prevails. Frequent calm weather conditions, especially in spring (up to 13.5 %) and autumn (up to 18 %), do not contribute to the dispersion of substances entering the atmosphere (Weather archive, 2013–2019).

A comparison of the average concentration of the ion totals in the aerosol of Barentsburg for the period 2016–2018 with our data in other Arctic regions showed the following. The average total content of ions in Barentsburg (average over the year – $1.14 \pm 0.23 \mu\text{g}/\text{m}^3$) is consistent with the data obtained in August-September 2013 in the atmosphere of the Asian sector of the Arctic Ocean ($1.38 \mu\text{g}/\text{m}^3$) (Sakerin et al., 2015). The concentration of ions in aerosol over the Barents Sea is almost 3.0 times higher ($3.42 \mu\text{g}/\text{m}^3$) (Sakerin et al., 2018c). The content of ions is even higher over other seas of this region: over the subarctic White Sea – 15 times ($17.1 \mu\text{g}/\text{m}^3$), over the Kara Sea – almost 8 times higher ($8.9 \mu\text{g}/\text{m}^3$) (Polkin et al., 2007). Continental aerosol sources influence the atmosphere of these seas. Their contribution to the White Sea is about 38 %, in the central regions of the Kara Sea – 30 % and in its coastal waters – 60–80 % (Polkin et al., 2007). Comparison of the total ion concentration in the aerosol of Barentsburg with the data obtained during the 58th Russian Antarctic Expedition (2012) in the area of the Antarctic stations Molodezhnaya ($0.29 \mu\text{g}/\text{m}^3$) and Mirny ($0.50 \mu\text{g}/\text{m}^3$) indicates higher atmosphere pollution of the Arctic station (Golobokova et al., 2016).

Microelement composition of ground-level aerosol. In aerosol samples collected in 2012–2018, one studied the trace element composition in the water-soluble fraction of the aerosol. From 2014 to 2018, the total (solid) fraction was additionally researched, including the fraction soluble and insoluble in deionized water (Golobokova et al., 2020). The results of the analysis showed a variety and a broad range of variations in the absolute concentrations of elements, reaching four orders of magnitude. In the soluble fraction, Sr, Al, Fe, Zn were predominant in the composition of the aerosol with an average concentration of $> 1.0 \text{ ng}/\text{m}^3$, in the composition of the solid fraction – Ba, Mn, Sr, Zn,

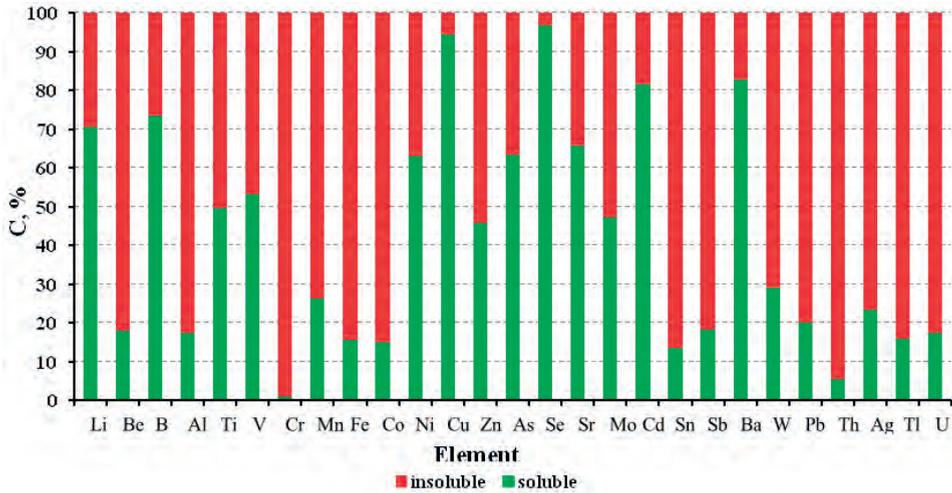


Fig. 5.2.18. The ratio of the average long-term concentrations of trace elements in the water-soluble and water-insoluble fractions in the aerosol.

Cr, Al, Fe. The lowest concentrations ($< 0.010 \text{ ng/m}^3$) in both fractions were determined for Th, Tl, Ag, Be, U. Comparison of the average long-term concentrations of trace elements in the aerosol showed that such elements as Al, Cr, Mn, Fe, Co, Zn, Mo, W, Pb, Th, Ag, Tl are mainly contained in the water-insoluble aerosol fraction (Fig. 5.2.18). Most of the elements that are tracers of anthropogenic pollution (Ni, V, As, Se, Cd) are in the soluble, more mobile fraction.

To identify the influence of local sources on the composition of aerosol particles, samples of coal, waste from the coal mining industry, the underlying surface and the road surface were analyzed. The calculation of the elements content in the composition of the samples taken, in contrast to the content in the aerosol substance (ng/m^3), was carried out per kilogram of their mass (mg/kg). There is an identity of variations in the ranges of element concentrations and sample composition. Ca, Ti, Na, Mg, K, Fe, Al dominated in the samples with a concentration range of $1500\text{--}75000 \text{ mg/kg}$, including the maximum content determined for K, Fe, Al. Content of Mn, Li, V, Sr, B, Ba ranged $100\text{--}900 \text{ mg/kg}$; Th, Co, As, Cu, Ni, Cr, Zn – ranged $6\text{--}90 \text{ mg/kg}$. The concentrations of the latter group of elements were lower in samples of waste from the coal mining industry. The next group of elements was W, Be, Se, Sn, Mo, U with concentrations of $0.85\text{--}5.40 \text{ mg/kg}$. The lowest concentrations are determined for Ag, Cd, Sb with concentration limits of $0.19\text{--}0.64 \text{ mg/kg}$.

Typically, the concentrations of elements dominating in the aerosol composition ($> 1.0 \text{ ng/m}^3$) prevail in the composition of coal, sludge, and soil. Ag, Cd, Sb, which make up the group with minimum concentrations in samples of coal, sludge, and soil, are contained in the aerosol in the range of average concentrations in the soluble fraction from 0.001 to 0.1 ng/m^3 , in the solid fraction – up to 1.0 ng/m^3 .

Quantitative estimates of the difference in the ratios of the concentrations of elements relative to the sodium ion in aerosol (aer) and seawater (sw) for the soluble fraction are used to determine the degree of influence of various sources on the formation of the aerosol chemical composition according to the formula (Xu, Gao, 2014):

$$K_i = ((C_i/\text{Na}^+)_{\text{aer}})/((C_i/\text{Na}^+)_{\text{sw}}), \quad (5.2.4)$$

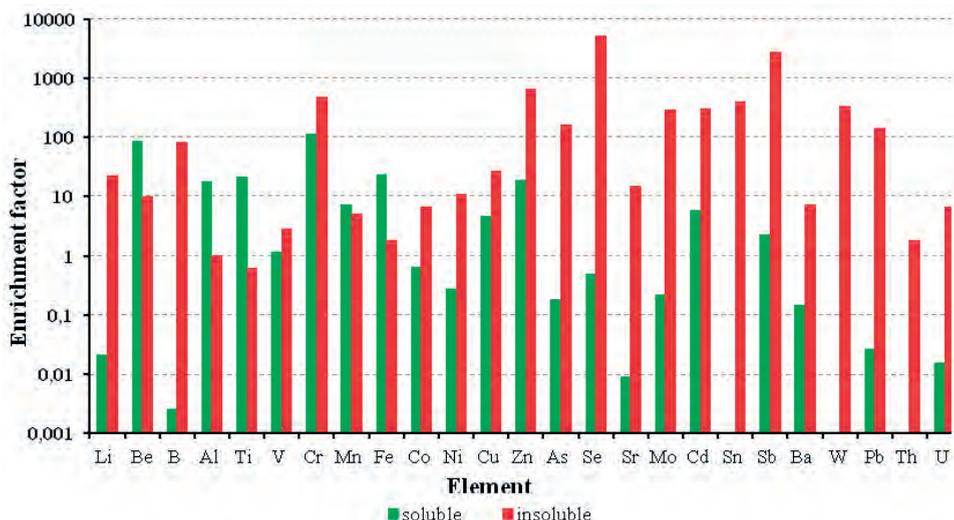


Fig. 5.2.19. Element enrichment factors for soluble (2012–2018) and solid (2014–2018) aerosol fractions.

and average concentrations (clarks) of elements in the earth’s crust (Earth) relative to Al for the solid fraction by the formula:

$$K_i = ((C_i/Al)_{aer}) / ((C_i/Al)_{Earth}), \quad (5.2.5.)$$

where (C_i/Na^+) and (C_i/Al) is the concentration of the i -th element relative to Na^+ or Al, K is the enrichment factor (Xu, Gao, 2014).

It is generally accepted that the enrichment factor from 1 to 10 indicates the marine or lithophilic origin of the element, more than 10 indicates the presence of an additional source of inflow of the element into the air. Calculations showed that the soluble aerosol fraction is less enriched with B, Li, Ni, As, Se, Sr, Ba, Pb, U, Mo, Co. Average values of the coefficients from 1 to 10 were found for V, Mn, Sb, Cu, Cd. Increased enrichment is determined for such elements as Al, Zn, Ti, Be, Fe ($K = 17 - 85$), the highest is for Cr ($K = 111$). In the solid fraction, the smallest enrichment was found for Ti; V, Fe, Co, Mn, Ba, Th, U ($K < 10$) are of lithophilic origin. Increased enrichment was found for Li, B, Cu, Sr ($K = 15 - 82$), high – for As, Cr, Zn, Mo, Cd, Sn, Sb, W, Pb ($K = 140 - 2800$), (Fig. 5.2.19). The enrichment factors for elements in the composition of coal, sludge, and soil, calculated relative to the content in the earth’s crust and normalized to Al, indicate their predominantly lithophilic origin.

It should be noted that emissions into the atmosphere from local sources are not always critical for the aerosol composition in the Arctic atmosphere. The maximum enrichment coefficients of elements in aerosol (> 100) indicate their origin in other regions. For example, As, Cd, Cr, Pb, Mn, Hg, Ni, V are emitted into the atmosphere of Western Europe; in European Russia, their spectrum is somewhat different – Pb, Cd, As, Zn, Ni, Cr, Cu (Vinogradova et al., 2018). Elements such as Cd, Ni, Cu, V, Pb, As, Fe, Co prevail in the pollution plumes of the Kola Peninsula (Virkkula et al., 1997). About 8 % of the world’s production of metal Cd is provided by Canada, in Europe – Belgium, in Russia – Chelyabinsk, and Vladikavkaz. Trajectory analysis data are likely to indicate the transfer of air masses from these territories (ARL NOAA).

Polycyclic aromatic hydrocarbons in the surface aerosol. Polycyclic aromatic hydrocarbons (PAHs), a persistent organic pollutant with mutagenic and carcinogenic properties, represent a class of important indicators of air pollution. Aerosol samples for PAH detection were taken from September 28 to October 8, 2017. 16 PAHs were identified (naphthalene, acenaphthylene, acenaphthene, fluorene, phenanthrene, anthracene, fluoranthene, pyrene, chrysene, benzo(a)anthracene, chrysene, benzo(b)fluoranthene, benzo(k)fluoranthene, benzo(e)pyrene, benzo(a)pyrene, indeno(1,2,3-c,d)pyrene, benzo(g,h,i)perylene), their total concentrations were determined on level from 0.36 to 1.7 ng/m³ (Table 2, (Golobokova et al., 2020)). Increased content of the total PAHs was recorded in an air sample on October 7–8, 2017, with a southeast wind from the thermal power plant (1.7 ng/m³). Low values of the PAH sum were determined on October 5–6, 2017, with an east wind (0.37 ng/m³) and September 28–30, 2017, during the rainy season, when the atmosphere was cleared (0.36 ng/m³). The obtained content of the total PAHs in the air of the study area is comparable with the data of the Research and Production Association “Typhoon” (0–4.4 ng/m³) and Norwegian researchers (Demin et al., 2011).

A slight increase in benzo(a)pyrene concentration was recorded on October 7–8, 2017 with a southeasterly wind from the TPP and is consistent with the data of the Research and Production Association “Typhoon” for the summer-autumn period of 2008, when the maximum PAH concentrations varied from 0.1 to 2.4 ng/m³ (Demin et al., 2011).

Using the diagnostic ratios of individual PAHs and percentage profiles, an attempt was made to identify sources of pollution in the study area. It is known that the fluoranthene/fluoranthene + pyrene ratio for petrogenic sources is below 0.4; if it is above 0.4, the sources are pyrogenic (Tobiszewski et al., 2012). On the territory of Barentsburg, this ratio indicated pyrogenic sources (0.59–0.63). The ratio indeno(1,2,3-c,d)pyrene / indeno(1,2,3-c,d)pyrene + benzo(g,h,i)perylene below 0.5 indicates the combustion of liquid fuel, and above 0.5 – the combustion of coal and wood (Tobiszewski et al., 2012). Considering that in Barentsburg, this ratio varies from 0.52 to 0.57, local pollution is caused by the burning of coal and wood. It is believed that the ratio benzo(a)pyrene / benzo(g,h,i)perylene below 0.6 indicates vehicle emissions, above 0.6 – stationary sources (Tobiszewski et al., 2012). The content of PAHs in the aerosol of Barentsburg was correlated with emissions from stationary sources (0.76–1.75). According to (Omar et al., 2002), for aerosol samples collected near pollution sources, the ratio benzo (e) pyrene/benzo (e) pyrene + benzo (a) pyrene is 0.50–0.57, at a considerable distance from of PAH sources, the ratio varies from 0.70 to 0.83. The calculated ratios of benzopyrenes, presented in the air over Barentsburg, are determined at the level from 0.42 to 0.59.

According to (Ravindra et al., 2008), naphthalene and phenanthrene are present in emissions from fossil fuel power plants. 26–33 % of these compounds were found in aerosols from Barentsburg. Calculation of the individual PAHs percentage from their total amount showed that the amount of fluoranthene and pyrene associated with coal combustion in aerosol in winter reached 22–30 % (see Table 2, (Masclat et al., 2000)). The content of chrysene, the dominant substance in the atmosphere of the village during the combustion of biomass (Masclat et al., 2000), varied within 2–3 % of the total of detected PAHs. The total number of benzo (g, h, i) perylene, indeno (1,2,3-s, d) pyrene and dibenzo (a, h) anthracene, indicators of urban air pollution by road transport reached 5–13 % (see Table 2, (Masclat et al., 2000)).

CONCLUSION

Since 2011, Barentsburg has been conducting annual observations of the spectral aerosol extinction of solar radiation throughout the entire atmosphere, the microphysical characteristics of aerosol particles and their chemical composition in the surface air layer. Most of the measurements were taken during the daytime from April to October. Based on the data obtained, the physicochemical composition of the aerosol and its variability in the atmosphere of Barentsburg were determined over nine years.

Due to the orographic features in the area of Barentsburg, calm weather conditions and northern and southern winds are frequent, which contribute to the accumulation of various impurities of both natural and anthropogenic origin from local sources in the lower atmosphere. These specifics of the region have almost no effect on the integral characteristics of the levels of atmospheric pollution, but significantly affect the local characteristics in the surface air layer – the total particulate count, the content of black carbon, as well as the ionic and elemental composition of the aerosol.

The highest average black carbon concentrations recorded in 2011 were mainly due to local sources. The multiple (1.7–5 times) excess of the average concentration of black carbon in Barentsburg in comparison with other polar stations is also explained by the increased contribution of local anthropogenic sources.

Statistical analysis of the physicochemical characteristics of atmospheric aerosol obtained based on observations in 2011–2019 in Barentsburg, allows us to draw the following conclusions.

AOD of the atmosphere. The average AOD characteristics in the period under study were: $\tau^a(0.5 \mu\text{m}) = 0.091$; $\tau^f(0.5) = 0.07$; $\tau^c = 0.021$; $\alpha = 1.28$; $\beta = 0.038$. AOD is highly influenced by occasional inflows of forest fire smoke from Eurasia and North America into the Arctic. The maximum impact of inflow of forest fire smoke was recorded on July 10–14, 2015. AOD at a wavelength of $0.5 \mu\text{m}$ in this situation reached 0.8.

The frequency plot of AOD repeatability is close to the lognormal distribution, with the most probable value of 0.07. The fine component influences AOD and its short-period variations the most: the relative fraction of $\tau^f(0.5)$ is 77 %, and the coefficients of variation of $\tau^f(0.5)$ are 95 %. The average value and range of variability of the Angstrom exponent in Barentsburg ($\alpha = 1 \dots 1.6$) are the same as in the continental atmosphere of middle latitudes and greater than in the marine atmosphere ($\alpha = 0.25 \dots 1$).

In general, after 2013, two distinctive features appeared in the pattern of inter-monthly AOD variability, which influenced the decrease in the magnitude of the seasonal decline from spring to autumn: (a) due to the more frequent drifts of smoke aerosol, the summer maximum AOD was formed; (b) there was a decrease in AOD in the spring, the reasons for which are still unclear.

Interannual fluctuations in the annual AOD were mainly determined by the frequency and power of inflow of forest fire smoke from the boreal zone. Average annual AOD values ($0.5 \mu\text{m}$) varied from 0.069 in 2013 to 0.116 in 2019. The fine component influences the interannual fluctuations of AOD the most: the range of variability of $\tau^f(0.5)$ is three times as much as that of τ^c . The long-term variability of τ^c showed a statistically significant trend (a decline of 0.012 over 9 years). Other AOD characteristics have no trend component.

Aerosol and black carbon concentrations. The average values of aerosol characteristics in the surface layer of the Barentsburg atmosphere for the entire measurement period were: $N_A = 7,1 \text{ cm}^{-3}$ (including, $N_f = 7,04 \text{ cm}^{-3}$, $N_c = 0,07 \text{ cm}^{-3}$); $M_A = 1,58 \mu\text{g}/\text{m}^3$; $M_{BC} = 120 \text{ ng}/\text{m}^3$.

Surface aerosol and black carbon concentrations differ in a wide range of variability (N_A from 0.36 to 80 cm⁻³, M_{BC} from 5 to 1163 µg/m³), short-period fluctuations in the diurnal and synoptic ranges influence them the most.

The average annual course of black carbon concentrations showed the main maximum in August ($M_{BC} = 168$ ng/m³) and secondary in April. The lowest concentrations of black carbon are observed in December (68 ng/m³), and also in early summer. The more frequent emissions of forest fire smoke into the Arctic atmosphere increased M_{BC} values in the second half of the polar day, along with the anthropogenic impact.

Seasonal dynamics of the fine aerosol is characterized by a well-defined decrease in concentrations from March ($N_f = 12.3$ cm⁻³) to June – by 60 %. From June to November, N_f concentrations remain at a low level (4–6 cm⁻³), and in December, winter increase begins and continues until March. Large inter-monthly fluctuations veil the regular component of the seasonal variability of aerosol coarse concentrations. However, an analysis of the volumetric distribution functions (dV/dR) in the range of the largest particles ($R > 1$ µm) showed higher values (dV/dR) in the middle of the warm period as compared to the beginning and end of the polar day. The increased volumetric content of large particles in June–July is explained by an increase in the generation of soil and sea aerosol during the melting of the snow cover.

In the long-term variability of all characteristics, there is a tendency for a slight decline. Still, a statistically significant (at the 0.05 level) trend manifested itself only in the black carbon concentrations: a decrease in M_{BC} by 18.4 ng / m³ per year. According to the relative value of interannual fluctuations, the fine aerosol concentration is more stable, followed by N_c and M_{BC} . The coefficients of variation for the annual values of N_p , N_c , and M_{BC} are 23 %, 47 %, and 60 %, respectively. The tendency for a decrease in aerosol concentrations, negative M_{BC} trend, as well as a decrease in interannual fluctuations in N_c and M_{BC} in recent years, indicate a gradual decrease in the impact of anthropogenic factors (coal dust and emissions from the thermal power stations) on the atmosphere of Barentsburg.

Aerosol chemical composition. The chemical composition of atmospheric aerosol (ions, elements, polycyclic aromatic hydrocarbons) in the surface layer of the atmosphere at the Barentsburg station was studied. From 2011 to 2016, observations of the chemical composition of the surface atmosphere were carried out during the daylight period, from April 2016 to March 2019 all year round. The highest total ion concentrations were observed in 2011–2012. After the installation of new pollution abatement systems and repair work at the coal-fired thermal power plant in Barentsburg, the content of ions in the aerosol in 2013–2016 decreased almost four times. High values characterized seasonal variability of ion concentrations in aerosol during the cold period (October–February), and low values during the warm period (May–June). High values of the correlation coefficients of pairs of ions Na⁺, Cl⁻ ($r > 0.90$), and Mg²⁺, Cl⁻ ($r > 0.70$) throughout the year indicate that the main source of the aerosol is the sea surface. A significant correlation between ions K⁺, NO₃⁻, NH₄⁺, SO₄²⁻, K⁺, SO₄²⁻ and increased concentrations of polycyclic aromatic hydrocarbons on a polar night indicates the influence of local sources: coal mining at the mine and its combustion at thermal power plants. Among the elements, the maximum enrichment in aerosol was found for As, Cr, Zn, Mo, Cd, Sn, Sb, W, Pb, with a low content of Cd, Sn, Sb, W, Pb in coal, sludge, and soil. In the annual course, the purification of the atmosphere is detected during the summer months (June–July), which is consistent with measurements of the ionic composition of aerosol at other Arctic stations with long-term observation series – Nord, Alert, Barrow, Zeppelin, Ny-Ålesund.

REFERENCES

- ARL NOAA. Atmospheric Resource Laboratory NOAA. <http://www.arl.noaa.gov>.
- Barteneva O.D., Nikitinskaya N.I., Sakunov G.G., Veselova L.K. Atmospheric transmittance in the visible and near IR spectral range. Leningrad: Gidrometeoizdat, 1991: 224 p. [In Russian].
- Chen Y.-C., Hamre B., Frette Q., Muyimbwa D., Blindheim S., Stebel K., Sobolewski P., Toledano C., Stamnes J. Aerosol optical properties in Northern Norway and Svalbard. *Applied Optics*. 2016, 55 (4); DOI: 10.1364/AO.55.000660.
- Chernov D.G., Kozlov V.S., Panchenko M.V., Turchinovich Yu.S., Radionov V.F., Gubin A.V., Prakhov A.N. Features of the variability of aerosol and black carbon concentrations in the surface air layer in Barentsburg (Spitsbergen) in 2011–2013. *Problems of Arctic and Antarctic*, 2014, 102 (12): 34–44 [In Russian].
- Chubarova N.E., Nezval' E.I., Belikov I.B., Gorbarenko E.V., Eremina I.D., Zhdanova E.Yu., Korneva I.A., Konstantinov P.I., Lokoshchenko M.A., Skorokhod A.I., Shilovtseva O.A. Climatic and environmental characteristics of Moscow megalopolis according to the data of the Moscow State University Meteorological Observatory over 60 years. *Russian Meteorology and Hydrology*. 2014, 39 (9): 602–613. DOI: 10.3103/S1068373914090052.
- Demin B.N., Graevsky A.P., Demeshkin A.S., Vlasov S.V., Krylov S.S., Laletin N.A. The state and trends in the environmental pollution in the places of economic activity of Russian enterprises on the Svalbard archipelago (Barentsburg and adjacent territories) for the period of 2002–2010. St. Petersburg: Arctic and Antarctic Research Institute, 2011: 316 p. [In Russian].
- EANET: Technical manual for wet deposition monitoring in East Asia. Available at: <http://www.eanet.asia/product/manual/techwet.pdf>, 2010 (accessed March 20, 2019).
- EMEP: Manual for sampling and chemical analysis, Norwegian Institute for Air Research. EMEP/CCC-Report 1/95. 1996, O-7726: 176 p.
- Eleftheriadis K., Vratolis S. and Nyeki S. Aerosol black carbon in the European Arctic: measurements at Zeppelin station, Ny-Ålesund, Svalbard from 1998–2007. *Geophys. Res. Lett.* 2009, 36, L02809; DOI: 10.1029/2008GL035741.
- Fenger M., Sørensen L. L., Kristensen K., Jensen B., Nguyen Q. T., Nøjgaard J. K., Massling A., Skov H., Becker T., Glasius M. Sources of anions in aerosols in northeast Greenland during late winter. *Atmospheric Chemistry and Physics*. 2013, 13: 1569–1578.
- Golobokova L.P., Latysheva I.V., Mordvinov V.I., Khodzher T.V., Obolkin V.A., Potemkin V.L. Peculiarities in the chemical composition of atmospheric aerosol against the background of extreme weather conditions in Southern Siberia. *Atmospheric and Oceanic Optics*. 2005, 18 (08): 616–620.
- Golobokova L.P., Polkin V.V., Onischuk N.A., Khuriganova O.I., Tikhomirov A.B., Terpugova S.A., Polkin Vas.V., Turchinovich U.S., Radionov V.F. Chemical composition of aerosol in the atmospheric surface layer of the East Antarctica coastal zone. *Ice and Snow*, 2016, 2 (56): 177–188 [In Russian].
- Golobokova L.P., Khodzher T.V., Chernov D.G., Sidorova O.R., Khuriganova O.I., Onishchuk N.A., Zhuchenko N.A., Marinaite I.I. The chemical composition of surface atmospheric aerosol in Barentsburg (Svalbard archipelago) according to the results of many years of research. *Ice and Snow*. 2020, 1 (60): 85–97; DOI: 10.31857/S2076673420010025 [In Russian].
- Gorshkov A.G., Marinaite I.I., Zhamsueva G.S., Zayakhanov A.S. Benzopyrene Isomer Ratio in Organic Fraction of Aerosols over Water Surface of lake Baikal. *J. Aerosol Sci.* 2004, 35 (2): 1059–1060.
- Herber A., Thomason L.W., Gernandt H., Leiterer U., Nagel D., Schulz K., Kaptur J., Albrecht T., and Notholt J. Continuous day and night aerosol optical depth observations in the Arctic between 1991 and 1999. *J. Geophys. Res.* 2002, 107 (D10); DOI: 10.1029/2001JD000536.
- Holben B.N., Tanre D., Smirnov A., Eck T.F., Slutsker I., Abuhassan N., Newcomb W.W., Schafer J.S., Chatenet B., Lavenu F., Kaufman Y.J., J. Vande Castle, Setzer A., Markham B., Clark D., Frouin R., Halthore R., Karneli A., O'Neill N.T., Pietras C., Pinker R.T., Voss K., and Zibordi G. An emerging

ground-based aerosol climatology: Aerosol optical depth from AERONET. *J. Geophys. Res.* 2001, 106 (D1): 12 067–12 097.

Isidorov V.A. Ecological chemistry. St. Petersburg: Khimizdat, 2001: 304 p. [In Russian].

Kabanov D.M., Sakerin S.M., Kruglinsky I.A., Ritter C., Sobolewski P.S., Zielinski T. Comparison of atmospheric aerosol optical depths measured with different sun photometers in three regions of Spitsbergen Archipelago. *Proc. SPIE 10833, 24th International Symposium on Atmospheric and Ocean Optics: Atmospheric Physics*, 2018, 1083342; DOI: 10.1117/12.2503949.

Kabanov D.M., Sakerin S.M., Turchinovich Yu.S. Interannual and seasonal variations in the atmospheric aerosol optical depth in the region of Tomsk (1995–2018). *Atmospheric and Oceanic Optics*. 2019, 32 (6): 663–670; DOI: 10.1134/S1024856019060071.

Khodzher T.V., Golobokova L.P., Netsvetaeva O.G., Domyshcheva V.M., Pogodaeva T.V., Korovyakova-Tomberg I.V. Results of testing the chemical parameters of artificial standard samples of rains and surface freshwaters. *Atmospheric and Oceanic Optics*. 2004, 17 (05–06): 425–429 [In Russian].

Kondratyev K.Ya., Binenko V.I. Extended cloud cover and radiation. In: *Polar aerosol, cloudiness and radiation*. Leningrad: Gidrometeoizdat, 1981: 73–89. [In Russian].

Kondratyev K.Ya., Ivlev L.S., Krapivin V.F., Varotsos C.A. Atmospheric aerosol properties, formation processes, and impacts: from nano- to global scales. Springer/PRAXIS, Chichester, UK, 2006: 572 p.

Kozlov V.S., Shmargunov V.P., and Polkin V.V. Spectrometers to study the properties of light absorption by aerosol particles. *Instrum. Exp. Tech.* 2008, 5: 155–157 [In Russian].

Larsson S., Hanssen J.E. Annual variation and origin of aerosol components in the Norwegian Arctic-subarctic region. *WMO Technical Conference on Regional and Global Observation of Atmospheric Pollution Relative to Climate*, Boulder. WMO. 1979, 549: 251–258.

Masclat P., Hoyau V., Jaffrezo J.L., Cachier H. Polycyclic aromatic hydrocarbon deposition on the ice sheet of Greenland. Part I: superficial snow. *Atmospheric Environment*. 2000, 34: 3195–3207; DOI: 10.1016/S1352-2310(99)00196-X.

Markowicz K.M., Pakszys P., Ritter Ch., Zielinski T., Udusti R., Cappelletti D., Mazzola M., Shiobara M., Zawadzka O., Lisok J., Petelski T., Makuch P., Karasiński G. Impact of North American intense fires on aerosol optical properties measured over the European Arctic in July 2015 *J. Geophys. Res.* 2016, 121: 14487–14512.

Marshunova M.S., Mishin A.A. Monitoring of the polar atmospheric turbidity. In: *Arctic Climate Monitoring*. Leningrad: Gidrometeoizdat, 1988: 132–140 [In Russian].

Nilsen F., Cottier F., Skogseth R., Mattsson S. Fjord-shelf exchanges controlled by ice and brine production: the interannual variation of Atlantic Water in Isfjorden, Svalbard. *Continental Shelf Research*. 2008, 28(14): 1838–1853; DOI: 10.1016/j.csr.2008.04.015.

Omar N.Y.V.J., Abas M.R.B., Ketuly K.A., Tahir N.M. Concentrations of PAHs in atmospheric particles (PM-10) and roadside soil particles collected in Kuala Lumpur, Malaysia. *Atmospheric Environment*. 2002, 36 (2): 247–254.

Pakszys P., Zielinski T. Aerosol optical properties over Svalbard: a comparison between Ny-Ålesund and Hornsund. *Oceanologia*. 2017, 59: 431–444. Available at: <http://dx.doi.org/10.1016/j.oceano.2017.05.002>.

Panchenko M.V., Terpigova S.A., Tumakov A.G., Belan B.D., Rasskazchikova T.M. Some aspects of a technique for airborne nephelometric studies of the tropospheric aerosol on a regional scale. *Atmospheric and Oceanic Optics*. 1994, 7 (08): 546–551. [In Russian].

Polkin V.V., Panchenko M.V., Golobokova L.P., Filippova U.G., Khodzher T.V., Lisitsyn A.P., Shevchenko V.P. Surface aerosol of the White and Kara Seas in August – September 2007. *Meteorological and Geophysical Studies*. Moscow: Paulsen, 2011: 199–214. [In Russian].

Quinn P., Shaw G., Andrews E., Dutton E.G., Ruoho-Airola T., Gong S.L. Arctic haze: current trends and knowledge gaps. *Tellus*, 2007, 59B (1): 99–114. Available at: <http://dx.doi.org/10.1111/j.1600-0889.2006.00238.x>.

- Radionov V.F., Marshunova M.S., Rusina E.N., Lubo-Lesnichenko K.E., Pimanova Yu.E.* Atmospheric aerosol turbidity in Polar Regions. *Izvestiya RAS, Atmospheric and Oceanic Physics*. 1994, 30 (6): 797–801. [In Russian].
- Ravindra K., Sothi R., Grieken R.* Atmospheric polycyclic aromatic hydrocarbons: Source attribution, emission factors and regulation. *Atmospheric Environment*. 2008, 42(13): 2895–2921. DOI: 10.1016/j.atmosenv.2007.12.010.
- Rusina E.N., Radionov V.F.* Estimation of “preindustrial” optical depth of the atmosphere in a polar haze in the arctic and recent contribution of anthropogenic emissions. *Meteorology and Hydrology*. 2002, 5: 35–39. [In Russian].
- Sakerin S.M., Kabanov D.M., Smirnov A.V., Holben B.N.* Aerosol optical depth of the atmosphere over the ocean in the wavelength range 0.37–4 μm . *Int. J. Remote Sensing*, 2008, 29 (9): 2519–2547; DOI: 10.1080/01431160701767492.
- Sakerin S.M., Kabanov D.M., Rostov A.P., Turchinovich S.A., and Knyazev V.V.* Sun photometers for measuring spectral air transparency in stationary and mobile conditions. *Atmospheric and Oceanic Optics*. 2013, 26 (4): 352–356. DOI: 10.1134/S102485601304012X.
- Sakerin S.M., Andreev S.Yu., Kabanov D.M., Nikolashkin S.V., Prakhov A.N., Radionov V.F., Turchinovich Yu.S., Chernov D.G., Holben B.N., Smirnov A.* On results of studies of atmospheric aerosol optical depth in arctic regions. *Atmospheric and Oceanic Optics*. 2014, 27 (6): 517–528; DOI: 10.1134/S1024856014060165.
- Sakerin S.M., Kabanov D.M., Polkin V.V., Radionov V.F., Holben B.N., and Smirnov A.* Variations in aerosol optical and microphysical characteristics along the route of Russian Antarctic Expeditions in the East Atlantic. *Atmospheric and Oceanic Optics*. 2017, 30 (1): 89–102; DOI: 10.1134/S1024856017010122.
- Sakerin S.M., Kabanov D.M., Radionov V.F., Chernov D.G., Turchinovich Yu.S., Lubo-Lesnichenko K.E., and Prakhov A.N.* Generalization of results of atmospheric aerosol optical depth measurements on Spitsbergen Archipelago in 2011–2016. *Atmospheric and Oceanic Optics*. 2018a, 31 (2): 163–170; DOI: 10.1134/S1024856018020112.
- Sakerin S.M., Chernov D.G., Golobokova L.P., Kabanov D.M., Khodzher T.V., Khuriganova O.I., Kozlov V.S., Radionov V.F., Sidorova O.R., Turchinovich Yu.S.* Seasonal and interannual variations of aerosol characteristics in the Arctic settlement Barentsburg (Spitsbergen archipelago, 2011–2017). *Proc. SPIE 10833, 24th International Symposium on Atmospheric and Oceanic Optics: Atmospheric Physics*. 2018b. 1083338; DOI: 10.1117/12.2502011.
- Sakerin S.M., Golobokova L.P., Kabanov D.M., Kozlov V.S., Pol'kin V.V., Radionov V.F., Chernov D.G.* Comparison of average aerosol characteristics in the neighboring Arctic regions. *Atmospheric and Oceanic Optics*. 2018c, 31 (08): 640–646. [In Russian].
- Sakunov G.G., Barteneva O.D., Radionov V.F., Timerev A.A., Voskresenskiy A.I., Adnashkin V.N.* Optical properties of the Arctic atmosphere. In: *Polar aerosol, cloudiness and radiation*. Leningrad: Gidrometeoizdat, 1981: 73–89. [In Russian].
- Savatyugin L.M., Solovyanova I.Yu.* The Russian Scientific Center on Spitsbergen archipelago. *Russian Polar Research*. 2011, 1 (3): 13–15. [In Russian]. <http://www.aari.ru/main.php?lg=0&id=318>.
- Shaw G.E.* The Arctic haze phenomenon. *Bull. Amer. Meteor. Soc.* 1995, 76 (12) 2403–2414.
- Sirois A., Barrie L.A.* Arctic lower tropospheric aerosol trends and composition at Alert, Canada: 1980–1995. *J. Geophys. Res.* 1999, 104 (D9): 11599–11618.
- Smirnov A., Holben B.N., Kaufman Y.J., Dubovik O., Eck T.F., Slutsker I., Pietras C., Halthore, R.N.* Optical Properties of Atmospheric Aerosol in Maritime Environments. *J. Atmos. Sciences*. 2002, 59 (3-1): 501–523.
- Stohl A., Berg T., Burkhardt J.F., Fjérraa A.M., Forster C., Herber A., Hov Ø., Lunder C., McMillan W.W., Oltmans S., Shiobara M., Simpson D., Solberg S., Stebel K., Ström J., Tørseth K., Trefeisen R., Virkkunen K., Yttri K.E.* Arctic smoke – record high air pollution levels in the European

- Arctic due to agricultural fires in Eastern Europe in spring 2006. *Atmos. Chem. Phys.* 2007, 7 (2): 511–534. <http://dx.doi.org/10.5194/acp-7-511-2007>.
- Stone R.S., Anderson G.P., Shettle E.P., Andrews E., Loukachine K., Dutton E.G., Schaaf C., Roman III M.O. Radiative impact of boreal smoke in the Arctic: Observed and modeled. *J. Geophys. Res.* 2008, 113, D14S16. Available at: <http://dx.doi.org/10.1029/2007JD009657>.
- Stone R.S., Sharma S., Herber A., Eleftheriadis K., and Nelson D.W. A characterization of Arctic aerosols on the basis of aerosol optical depth and black carbon measurements. *ELEMENTA, Science of the Anthropocene*. 2014; DOI: 10.12952/journal.elementa.000027.
- Tislenko D.I., Ivanov B.V. Long-term variability of Atlantic water temperature in the Svalbard fjordsin conditions of past and recent global warming. *Czech Polar Reports*. 2015. 5(2): 134–142.
- Tobiszewski M., Namiesnik J. PAH diagnostic ratios for the identification of pollution emission sources. *Environmental Pollution*. 2012, 162: 110–119; DOI: 10.1016/j.envpol.2011.10.025.
- Tomasi C., Lupi A., Mazzola M., Stone R.S., Dutton E.G., Herber A., Radionov V.F., Holben B., Sorokin M., Sakerin S.M., Terpigova S.A., Lanconelli C., Petkov B., and Vitale V. An update of the long-term trend of aerosol optical depth in the polar regions using POLAR-AOD measurements performed during in International Polar Year. *Atmos. Environ.* 2012. Vol. 52. Pp. 29–47.
- Tomasi C., Kokhanovsky A.A., Lupi A., Ritter C., Smirnov A., Mazzola M., Stone R.S., Lanconelli C., Vitale V., Holben B.N., Nyeki S., Wehrli C., Altonen V., de Leeuw G., Rodriguez E., Herber A.B., Stebel K., Stohl A., O'Neill N.T., Radionov V.F., Zielinski T., Petelski T., Sakerin S.M., Kabanov D.M., Xue Y., Mei L., Istomina L., Wagener R., McArthur B., Sobolewski P.S., Butler J., Kivi R., Courcoux Y., Larouche P., Broccardo S., and Piketh S.J. Aerosol remote sensing in polar regions. *Earth-Science Reviews*. 2015, 140: 108–157.
- Tomczyk A.M., Ewertowski M. Changes of arctic landscape due to human impact, north part of Billefjorden area. Svalbard, *Quaestiones Geographicae*. 2010, 29 (1): 75–83.
- Udisti R., Bazzano A., Becagli S., Bolzacchini E., Caiazzo L., Cappelletti D., Ferrero L., Frosini D., Giardi F., Grotti M., Lupi A., Malandrino M., Mazzola M., Moroni B., Severi M., Traversi R., Viola A., Vitale V. Sulfate source apportionment in the Ny-Ålesund (Svalbard Islands) Arctic aerosol. *Environmental Changes in Arctic*, 2016; DOI: 10.1007/s12210-016-0517-7.
- Vinogradova A.A., Ponomareva T.Ya. Atmospheric transport of anthropogenic impurities to the Russian Arctic (1986–2010). *Atmospheric and Oceanic Optics*. 2012, 25 (6): 414–422.
- Vinogradova A.A. Seasonal and long-term variations in atmospheric circulation indices and air mass transport to the Russian Arctic. *Opt. Atmos. Okeana*. 2014, 27 (6): 463–472. [In Russian].
- Vinogradova A.A., Kotova E.I. Contributions of European sources to lead and cadmium pollution in northern regions of European Russia. Live and bio-kos systems. 2018, 23. Available at: <http://www.jbks.ru/archive/issue-23/article-2> [In Russian].
- Weather archive in Barentsburg. <http://www.rp5.ru>.
- Virkkula A., Hillamo R.E., Kerminen V.-M., Stohl A. The influence of Kola Peninsula, continental European and marine sources on the number concentrations and scattering coefficients of the atmospheric aerosol in Finnish Lapland. *Boreal Environment Research*. 1997, 2: 317–336.
- Zhuravleva T., Kabanov D., Nasrtdinov I., Russkova T., Sakerin S., Smirnov A., and Holben B. Radiative characteristics of aerosol under smoke mist conditions in Siberia during summer 2012. *Atmos. Meas. Tech.* 2017, 10: 179–198. Available at: <http://www.atmos-meas-tech.net/10/179/2017>. DOI: 10.5194/amt-10-179-2017.
- Zhan J., Gao Y., Li W., Chen L., Lin H., Lin Q. Effects of ship emissions on summertime aerosols at Ny-Ålesund in the Arctic. *Atmospheric Pollution Research*. 2014, 5: 500–510.
- Xu G., Gao Y. Atmospheric trace elements in aerosols observed over the Southern Ocean and coastal East Antarctica. *Polar Research*. 2014, 33: 23973. doi.org/10.3402/polarv.33.23973.

Yamagata S., Kobayashi D., Ohta S., Murao N., Shiobara M., Wada M., Yabuki M., Konishi H., Yamanouchi T. Properties of aerosols and their wet deposition in the arctic spring during ASTAR2004 at Ny-Ålesund, Svalbard. *Atmospheric Chemistry and Physics*. 2009, 9: 261–270.

Yli-Tuomi T., Venditte L., Hopke P.K., Basunia M. S., Landsberger S., Viisanen Y., Paatero J. Composition of the Finnish Arctic aerosol: collection and analysis of historic filter samples. *Atmospheric Environment*. 2003, 37 (17): 2355–2364.

Электронный ресурс: 1 CD

Формат PDF. Размер файла 72 Мб [12, 75 п.л.].

Системные требования: процессор с частотой 1,3 ГГц (Intel,AMD);
оперативная память от 1 Гб, Windows (XP; Vista; 7; 10); Acrobat Reader, либо его аналог.

Издание подготовлено в ГНЦ РФ ААНИИ. 199397, Санкт-Петербург, ул. Беринга, 38